SANDIA REPORT

SAND97-3109
Unlimited Release
Printed August 2000

Interpretations of Tracer Tests Performed in the Culebra Dolomite at the Waste Isolation Pilot Plant Site

Lucy C. Meigs, Richard L. Beauheim, and Toya L. Jones, Editors

Prepared by
Sandia National Laboratories
Albuquerque, New Mexico 87185 and Livermore, California 94550

Sandia is a multiprogram laboratory operated by Sandia Corporation, a Lockheed Martin Company, for the United States Department of Energy under Contract DE-AC04-94AL85000.

Approved for public release; further dissemination unlimited.

Sandia National Laboratories

Issued by Sandia National Laboratories, operated for the United States Department of Energy by Sandia Corporation.

NOTICE: This report was prepared as an account of work sponsored by an agency of the United States Government. Neither the United States Government, nor any agency thereof, nor any of their employees, nor any of their contractors, subcontractors, or their employees, make any warranty, express or implied, or assume any legal liability or responsibility for the accuracy, completeness, or usefulness of any information, apparatus, product, or process disclosed, or represent that its use would not infringe privately owned rights. Reference herein to any specific commercial product, process, or service by trade name, trademark, manufacturer, or otherwise, does not necessarily constitute or imply its endorsement, recommendation, or favoring by the United States Government, any agency thereof, or any of their contractors or subcontractors. The views and opinions expressed herein do not necessarily state or reflect those of the United States Government, any agency thereof, or any of their contractors.

Printed in the United States of America. This report has been reproduced directly from the best available copy.

Available to DOE and DOE contractors from
U.S. Department of Energy
Office of Scientific and Technical Information
P.O. Box 62
Oak Ridge, TN 37831

Telephone: (865)576-8401
Facsimile: (865)576-5728
E-Mail: reports@adonis.osti.gov
Online ordering: http://www.doe.gov/bridge

Available to the public from
U.S. Department of Commerce
National Technical Information Service
5285 Port Royal Rd
Springfield, VA 22161

Telephone: (800)553-6847
Facsimile: (703)605-6900
E-Mail: orders@ntis.fedworld.gov
Online order: http://www.ntis.gov/ordering.htm

SAND97-3109
Unlimited Release
Printed August 2000

Interpretations of Tracer Tests Performed in the Culebra Dolomite at the Waste Isolation Pilot Plant Site

Lucy C. Meigs, Editor
Geohydrology Department

Richard L. Beauheim, Editor
Repository Performance and Certification Department

Sandia National Laboratories
P.O. Box 5800
Albuquerque, NM 87185-0735

Toya L. Jones, Editor
Duke Engineering and Services, Inc.
9111 Research Boulevard
Austin, TX 78758

ABSTRACT

This report provides (1) an overview of all tracer testing conducted in the Culebra Dolomite Member of the Rustler Formation at the Waste Isolation Pilot Plant (WIPP) site, (2) a detailed description of the important information about the 1995-96 tracer tests and the current interpretations of the data, and (3) a summary of the knowledge gained to date through tracer testing in the Culebra. Tracer tests have been used to identify transport processes occurring within the Culebra and quantify relevant parameters for use in performance assessment of the WIPP. The data, especially those from the tests performed in 1995-96, provide valuable insight into transport processes within the Culebra. Interpretations of the tracer tests in combination with geologic information, hydraulic-test information, and laboratory studies have resulted in a greatly improved conceptual model of transport processes within the Culebra. At locations where the transmissivity of the Culebra is low ($<4 \times 10^{-6}$ m^2/s), we conceptualize the Culebra as a single-porosity medium in which advection occurs largely through the primary porosity of the dolomite matrix. At locations where the transmissivity of the Culebra is high ($>4 \times 10^{-6}$ m^2/s), we conceptualize the Culebra as a heterogeneous, layered, fractured medium in which advection occurs largely through fractures and solutes diffuse between fractures and matrix at multiple rates. The variations in diffusion rate can be attributed to both variations in fracture spacing (or the spacing of advective pathways) and matrix heterogeneity. Flow and transport appear to be concentrated in the lower Culebra. At all locations, diffusion is the dominant transport process in the portions of the matrix that tracer does not access by flow.

Acknowledgements

We greatly appreciate the assistance of numerous individuals without whose help the 1995-96 tracer tests and this report would not have been possible. Numerous people from Duke Engineering and Services (formerly INTERA, Inc.) assisted with test design, implementation, and data reduction. Joanna Ogintz reduced and organized most of the tracer-test data and assisted with compilation of tracer-test information. Wayne Stensrud, George Saulnier, John Pickens, Don Fulton, Dave Chace, Curtis Chester, Ronnie Lewis, Kermit Riley, Carl Young, Patricia Johnson, Bryan Bullard, and Bob Coupland assisted with the implementation of the experiment from equipment design and installation to tracer injection and sample collection. Charles Tilburg assisted with some pretest design calculations. Irene Farnham and Klaus Stetzenbach of the University of Nevada-Las Vegas (UNLV) and Robert Bowman of the New Mexico Institute of Mining and Technology provided assistance with selection of tracers. Irene Farnham carefully coordinated the analysis of approximately one thousand samples, assisted by Kaz Lindley, Martha Dominguez, Amy Smiecinski, and Jeanette Daniels of UNLV and Connie Chocas of Sandia National Laboratories (SNL). Yvonne Tsang of Lawrence Berkeley National Laboratory and Ray Ostensen of SNL provided valuable insights for the design of the SWIW tests. Richard Lark of DOE provided strong programmatic support and constructive technical criticism throughout the design and performance of the tests. Peter Davies of SNL assisted with test design and logistical support. Allan Sattler and Al Lappin of SNL also provided valuable logistical support. Thomas Doe and Bill Thompson of Golder Associates provided technical review of the well locations, test design, and preliminary analyses. Susan Altman, Robert Holt, Mike Kelley, James McCord, and Sean McKenna of SNL, Roy Haggerty of Oregon State University, Yvonne Tsang and numerous others listed above provided insights into the details of the test data and interpretations. Tom Corbet, Peter Davies, Al Lappin, Randy Roberts, Vince Tidwell, and provided valuable reviews of drafts of portions of this report.

Contents

Chapter 1 Introduction 1
By Lucy C. Meigs, Toya L. Jones, and Richard L. Beauheim
1.1 Background and Purpose of Recent Tests 2
1.2 Previous Studies 3
1.3 Description of Contents 4
1.4 References 5

Chapter 2 Characteristics of the Culebra 9
By Lucy C. Meigs and Richard L. Beauheim
2.1 Culebra Geology and Sedimentology 9
2.2 Core Studies 11
2.3 Culebra Hydraulic Testing 12
2.4 Culebra Water Chemistry 13
2.5 References 13

Chapter 3 Experimental Design and Observed Tracer Recoveries for the 1995-96 Tracer Tests 17
By Lucy C. Meigs, Richard L. Beauheim, and Toya L. Jones
3.1 Tracer Tests Performed in the Culebra 17
3.2 Conceptual Transport Model for the Culebra to be Tested 19
3.3 1995-96 Tracer Tests 20
    3.3.1 Experimental Description and Methodologies 20
    3.3.2 Tracer Data Observations and Discussion 25
3.4 Summary and Preliminary Evaluation of Conceptual Model 32
3.5 References 34

Chapter 4 Controls on Mass Recovery for Single-Well Injection-Withdrawal Tracer Tests 37
By Susan J. Altman, Toya L. Jones, and Lucy C. Meigs
Abstract 37
4.1 Introduction 37
4.2 Motivation and Objectives for Study 38
4.3 Test Design 40
4.4 Numerical Simulations 41
    4.4.1 Approach to Representing Heterogeneity 41
    4.4.2 Approach to Representing Flow and Transport 41
    4.4.3 Model Domain and Boundary Conditions 43
    4.4.4 Input Parameters 44
4.5 Results and Discussion 47
    4.5.1 Single-Porosity Sensitivity Studies 47
    4.5.2 Comparison of Single- and Double-Porosity Responses 53
    4.5.3 WIPP-Specific Study 61
4.6 Summary and Conclusions 64
4.7 References 65

Chapter 5 Controls on Multiwell Convergent-Flow Tracer-Breakthrough-Curve Tailing for a Single-Porosity, Heterogeneous Conceptualization 69
By Sean A. McKenna
Abstract 69
5.1 Introduction 69
5.2 Approach 71
  5.2.1 Conceptual Model of Heterogeneity 71
  5.2.2 Variations in Correlation Length 73
  5.2.3 Advective Porosity 73
5.3 Flow and Transport Model 74
5.4 Results 74
  5.4.1 Model of Spatial Correlation 74
  5.4.2 Correlation Length and Porosity 75
  5.4.3 Comparison to Field Data 78
5.5 Conclusions 81
5.6 References 82

Chapter 6 Evaluation of Single-Well Injection-Withdrawal Tracer-Test Data with a Multirate-Diffusion Model 85
By Roy Haggerty, Sean W. Fleming, Lucy C. Meigs, and Sean A. McKenna
Abstract 85
6.1 Introduction 85
6.2 Multirate Diffusion: Mathematical Model 86
  6.2.1 Radially Divergent Flow (Injection Period) 89
  6.2.2 No Flow (Resting Period) 89
  6.2.3 Radially Convergent Flow (Pumping Period) 89
6.3 Modeling of SWIW Tests 90
  6.3.1 Conventional Double-Porosity and Radial Transport 91
  6.3.2 Multirate Diffusion and Radial Transport 91
6.4 Discussion 95
  6.4.1 Sensitivity Analysis 95
  6.4.2 Discussion of Estimated Parameters and Comparison with Other Data 96
  6.4.3 The Late-Time Slope of the Data 97
  6.4.4 Conventional Double-Porosity vs. Multirate Diffusion 98
6.5 Conclusions 99
6.6 References 99

Chapter 7 Evaluation of Multiwell Convergent-Flow Test Data with a Multirate Model 103
By Sean A. McKenna, Lucy C. Meigs, and Roy Haggerty
Abstract 103
7.1 Introduction 103
7.2 Multirate Transport Modeling in Multiwell Systems 104
7.3 Results of MWCF Tracer Test Simulations 108
  7.3.1 Experimental Data 108
  7.3.2 Parameter Estimation 108
  7.3.3 Discussion of Results 111
7.4 Alternative Conceptual Models 113
7.5 Uniqueness and Testing of the Estimated Models 114
7.6 Comparison of SWIW and MWCF Test Results 115
7.7 Mass-Transfer Processes at Larger Scales 116

7.8 Conclusions 117
7.9 References 118

Chapter 8 Discussion and Conclusions 119
By Lucy C. Meigs, Richard L. Beauheim, and Toya L. Jones
8.1 Introduction 119
8.2 Summary of Geologic, Hydrologic, and Chemistry Information 119
8.3 Summary of Observations from Examination of Tracer-Test Data 120
8.4 Summary of Numerical Simulations 122
8.5 Evaluation and Revision of Conceptual Transport Model for the Fractured Culebra 124
8.6 Remaining Issues and Future Research Directions 126
8.7 Conclusions 127
8.8 References 127

Appendix A Sources of Information 129
By Lucy C. Meigs and Toya L. Jones

Appendix B Transport Input Parameter Spreadsheets (TIPS) 131
By Toya L. Jones

Appendix C WIPP Tracer-Test Data 169
By Toya L. Jones, Irene M. Farnham, Lucy C. Meigs, and Joanna B. Ogintz

Appendix D Well Configurations, Test Equipment, and Hydraulic Data 217
By Richard L. Beauheim

Appendix E Summary of Hydraulic Tests Performed at Tracer-Test Sites 253
By Richard L. Beauheim

Appendix F Summary of Tracer Testing in the Culebra During the 1980s 259
By Toya L. Jones and Timothy F. Dale

Appendix G Design of H-19 Well Layout 267
By Richard L. Beauheim

Appendix H Evaluation of Tracers Used for the WIPP Tracer Tests 273
By Irene M. Farnham, Lucy C. Meigs, Martha E. Dominguez, Kazumasa Lindley, Jeanette M. Daniels, and Klaus J. Stetzenbach

Appendix I Liquid Chromatographic Separations of Fluoro- and Chlorobenzoates Used as Groundwater Tracers 291
By Irene M. Farnham, Jeanette M. Daniels, Martha E. Dominguez, Kazumasa Lindley, Klaus J. Stetzenbach, and Lucy C. Meigs

Appendix J Tracer-Mixing Methodology 301
By Irene Farnham and Kazumasa Lindley

Appendix K Development of Late-Time Slopes on Log-Log Breakthrough Curves After a Pulse-Type Injection for the Case of Infinite Matrix Blocks 305
By Roy Haggerty

Appendix L Calculation of the Standard Deviation of the Natural Log of Transmissivity ($\sigma \ln T$) for WIPP-Specific Data 309
By Toya L. Jones and Susan J. Altman

Appendix M Comparison of Results for an SWIW Tracer Test Using the Numerical Codes SWIFT II and THEMM 313
By Toya L. Jones and Susan J. Altman

Appendix N Calculation of Diffusion of Tracer Trapped in the Borehole During Injection 317
By Toya L. Jones and Lucy C. Meigs

Appendix O Effects of Sorption on Tracer Breakthrough for an SWIW Test 321
By Toya L. Jones and Susan J. Altman

Appendix P Double-Porosity Single-Rate Interpretations of Multiwell Convergent-Flow Tracer-Test Data 327
By Toya L. Jones, Joanna Ogintz, Susan J. Altman, Sean A. McKenna, and Lucy C. Meigs

Appendix Q Laplace-Domain Solution for Multirate Model 351
By Roy Haggerty

Appendix R Estimation of Diffusive Mass-Transfer for Continuous Rate Distributions from a Single-Well Injection-Withdrawal Tracer Test 355
By Winston Yu and Charles Harvey

Appendix S Double-Porosity Single-Rate and Multirate Interpretations of Multiwell Convergent-Flow Tracer-Test Data 363
By Michael J. Kelley, Lucy C. Meigs, Richard L. Beauheim, Sean A. McKenna, and Roy Haggerty

Figures

1-1 Location of the WIPP site. 1
1-2 WIPP area stratigraphic column. 2
1-3 Well locations in the vicinity of the WIPP site. 2

2-1 Schematic of vertical variations in Culebra lithologies and porosity types (from Holt, 1997). 10
2-2 Variations in transmissivity values measured in Culebra wells near the WIPP site. 12

3-1 Well locations at the H-11 hydropad. 20
3-2 Well locations at the H-19 hydropad. 21
3-3 SWIW tracer-recovery curves from (a) one test at the H-11 hydropad and (b) two tests at the H-19 hydropad. 26
3-4 Normalized cumulative mass recovered for the first tracer from the SWIW tests at the H-11 and H-19 hydropads. 27
3-5 MWCF tracer-breakthrough curves from the H-11 hydropad. 27
3-6 MWCF tracer-breakthrough curves for the 4-well test at the H-19 hydropad. 28
3-7 Cumulative mass recovered versus volume pumped per radius squared for the H-19 4-well test and the early tests conducted at H-3, H-6, and H-11 28
3-8 MWCF tracer-breakthrough curves from full-thickness injections for the high-pumping-rate H-19 hydropad data. 29
3-9 Comparison of MWCF breakthrough curves for tracer injections repeated for two different pumping rates. 29
3-10 Comparison of benzoic-acid and iodide data for (a) one pathway at H-11 and (b) two pathways at H-19. 29
3-11 Comparison of injections into the upper and lower Culebra at the H-19 hydropad. 30
3-12 Comparison of MWCF data from all pathways. 31
3-13 Cumulative mass recovered at time of breakthrough-curve peak and calculated advective porosity. 32

4-1 Simulated (a) tracer-recovery curve and (b) mass-recovery curve for a homogeneous single-porosity medium without drift. 39
4-2 Comparison of Gaussian and bimodal distributions for transmissivity used in the sensitivity studies. 41
4-3 Simulated (a and c) tracer-recovery curves and (b and d) mass-recovery curves showing decrease in mass recovery with increase in plume drift in a heterogeneous system 49
4-4 Demonstration of the cause of reduced mass recovery in a single-porosity system due to the movement of the plume during the resting phase (irreversibility of transport paths) 50
4-5 Effect of the structure of heterogeneity on mass recovery: (a) standard deviation of ln *T*, (b) range, and (c) ln *T* frequency distribution for a metric of time to 90% mass recovery, and (d) ln *T* frequency distribution for a metric of time to 99% mass recovery 51
4-6 Comparison of drift distance for the four sets of simulations used to investigate the controls on plume drift 53
4-7 Ranges in time to 90% mass recovery for simulations examining the relative effects of porosity, resting-phase duration, and regional gradient on mass recovery 53

4-8 Comparison of (a) tracer-recovery curves, (b) mass-recovery curves, (c) tracer distribution between the advective porosity (ϕ_a) and the diffusive porosity (ϕ_d), and (d) derivative plots for single- and double-porosity conceptualizations assuming a homogeneous transmissivity field and no plume drift. 54
4-9 Comparison of (a) tracer-recovery curves and (b) mass-recovery curves for single- and double-porosity conceptualizations assuming a heterogeneous transmissivity field and no plume drift........ 56
4-10 Comparison of (a) tracer-recovery curves and (b) mass-recovery curves for single- and double-porosity conceptualizations assuming a homogeneous transmissivity field and plume drift during the resting phase. 56
4-11 Comparison of (a) tracer-recovery curves and (b) mass-recovery curves for single- and double-porosity conceptualizations assuming a heterogeneous transmissivity field and plume drift during the resting phase. 57
4-12 Comparison of (a) tracer-recovery curves and (b) mass-recovery curves for a single-porosity simulation in the heterogeneous transmissivity field that gave the slowest mass recovery in the sensitivity studies to double-porosity simulations in the heterogeneous transmissivity field that gave the fastest mass recovery in the sensitivity studies........ 58
4-13 Comparison of (a) tracer-recovery curves, (b) mass-recovery curves, and (c) derivative plots for single-porosity simulations in the heterogeneous transmissivity field that gave the slowest mass recovery in the sensitivity studies to double-porosity simulations in the heterogeneous transmissivity field that gave the fastest mass recovery in the sensitivity studies........ 60
4-14 Comparison of simulated and observed results for (a and b) tracer 1 from the H-19 SWIW test 1, (c and d) tracer 2 from the H-19 SWIW test 1, and (e and f) the H-19 SWIW test 2........ 62
4-15 Comparison of simulated and observed results for (a and b) tracer 1 from the H-11 SWIW test using a $\sigma \ln T$ of 2.64, (c and d) tracer 2 from the H-11 SWIW test using a $\sigma \ln T$ of 2.64, and (e and f) tracer 1 from the H-11 SWIW test using a $\sigma \ln T$ of 2.1 63

5-1 Two spatially heterogeneous transmissivity fields created with (a) maximum entropy and (b) indicator geostatistical algorithms........ 75
5-2 Magnified views of the two spatially heterogeneous fields shown in Figure 5-1........ 76
5-3 Volumetric flux ($\log_{10}$ m^3/s) through the two heterogeneous fields shown in Figure 5-2 for a simulation with an advective porosity of 0.005........ 76
5-4 Tracer concentrations twelve hours after injection for a simulation with an advective porosity of 0.005. 77
5-5 Amount of tailing, defined as time to 90% mass recovery, as a function of relative correlation length and advective porosity for (a) maximum entropy realizations and (b) indicator realizations. 77
5-6 Comparison of the H-19b7 tracer test results to the numerical results in two-dimensional space........ 79
5-7 Cumulative particle breakthrough distributions for the H-19b7 data and the 25 realizations with a relative correlation length of 0.19 and an advective porosity of 0.005........ 80
5-8 Particle breakthrough curves in double-log space for the H-19b7 data and the 25 realizations with a relative correlation length of 0.19 and an advective porosity of 0.005........ 80
5-9 Cumulative particle breakthrough distributions for the H-19b7 data and the 25 realizations with a relative correlation length of 0.19 and an advective porosity of 0.05........ 81
5-10 Particle breakthrough curves in double-log space for the H-19b7 data and the 25 realizations with a relative correlation length of 0.19 and an advective porosity of 0.05........ 81

6-1 Conceptual model for multirate diffusion 86
6-2 Best fits of conventional double-porosity models to the H11-1 and H19S2 data 91
6-3 Best fits of multirate diffusion model to all SWIW data 93
6-4 Cumulative distribution functions (CDFs) estimated from each of the SWIW data 94
6-5 Normalized sensitivity for estimated parameters of multirate diffusion model at H11-1 and at H19S2 96
6-6 Sensitivity analysis for σ_d (standard deviation of $\ln(\alpha_d)$) in multirate diffusion model 98

7-1 Schematic diagram of polar coordinate transformation from coordinates with respect to the injection well to coordinates with respect to the pumping well. 106
7-2 Observed breakthrough curve data and the limits of the 95% confidence intervals for the two H-11b3 to b1 tracer tests. 109
7-3 Observed breakthrough curve data and the limits of the 95% confidence intervals for the two H-19b7 to b0 tracer tests. 109
7-4 Normalized sensitivities of the BTC model to each of the four estimated parameters 110
7-5 Multirate diffusion transport model fits to the H-11 data for both pumping rates 111
7-6 Multirate diffusion transport model fits to the H-19 data for both pumping rates 111
7-7 Cumulative distributions of diffusion rate coefficients as estimated from the four two-well tests 112
7-8 Single-rate model fit to the H-11 low data 114
7-9 Single-rate model fit to the H-19 low data 114
7-10 Model fits to the H-11 high tracer test data using both multirate and single-rate models estimated on the H-11 low tracer test data. 115
7-11 Model fits to the H-19 high tracer test data using both multirate and single-rate models estimated on the H-19 low tracer test data. 115

Tables

2-1 Physical Properties of the Culebra at the Tracer-Test Hydropads 11
2-2 Chemical Properties of Culebra Brines at the Tracer-Test Hydropads 13

3-1 Summary of Tracer Tests Performed in the Culebra 18
3-2 Tabulated Information on the SWIW Tracer Tests at the H-11 and H-19 Hydropads 22
3-3 Tabulated Information on the MWCF Tracer Tests at the WIPP Site 23

4-1 Input Parameters for the Sensitivity Studies. 44
4-2 Input Parameters for the Comparison of Single- and Double-Porosity Responses. 45
4-3 Input Parameters for the WIPP-Specific Study 46
4-4 Calculated Gradients Across the H-11 and H-19 Hydropads. 47

5-1 Numerical Simulation Parameters 72
5-2 Relative Correlation Lengths Used in Creating the Geostatistical Realizations of Hydraulic Conductivity 73

6-1 Fixed Parameters Used in Simulations 90
6-2 Single-Rate Double-Porosity Estimation Results 92
6-3 Multirate Estimation Results 92

7-1 Fixed Parameters for MWCF Tracer Tests 109
7-2 Multirate Parameter Estimation Results for MWCF Tracer Tests 111
7-3 Values of Parameters Estimated Using a Single-Rate MWCF Model 112

8-1 Summary of Inferred Multirate Diffusion Coefficients 125

Chapter 1
Introduction

By Lucy C. Meigs[1], Toya L. Jones[2], and Richard L. Beauheim[3]

Tracer testing of the Culebra Dolomite Member of the Rustler Formation has been conducted as part of the overall evaluation of the Waste Isolation Pilot Plant (WIPP) site located near Carlsbad, New Mexico (Figure 1-1). The WIPP is a U.S. Department of Energy (DOE) research and development facility designed to demonstrate the safe disposal of transuranic wastes resulting from the United States' defense programs. The WIPP repository is excavated in bedded halite of the Salado Formation at a depth of about 655 m below ground surface. At the WIPP, the Salado Formation is approximately 600 m thick and is overlain by the approximately 95-m-thick Rustler Formation, the 150-m-thick Dewey Lake Redbeds, and approximately 16 m of surficial deposits (Figure 1-2). Site-characterization studies at the WIPP site have shown that, if radionuclides were to be released from the repository through inadvertent human intrusion and introduced into other geologic formations, groundwater transport through the Culebra would be the most significant pathway to the accessible environment (US DOE, 1996).

The Culebra is a 7-m-thick, variably fractured dolomite with massive and vuggy layers lying approximately 440 m above the WIPP repository. Tracer tests have been used to identify transport processes occurring within the Culebra and quantify relevant parameters for use in performance assessment of the WIPP. The purposes of this report are to: (1) provide a single document describing all of the important information about the Culebra tracer tests conducted in 1995 and 1996, (2) provide a single document discussing all tracer

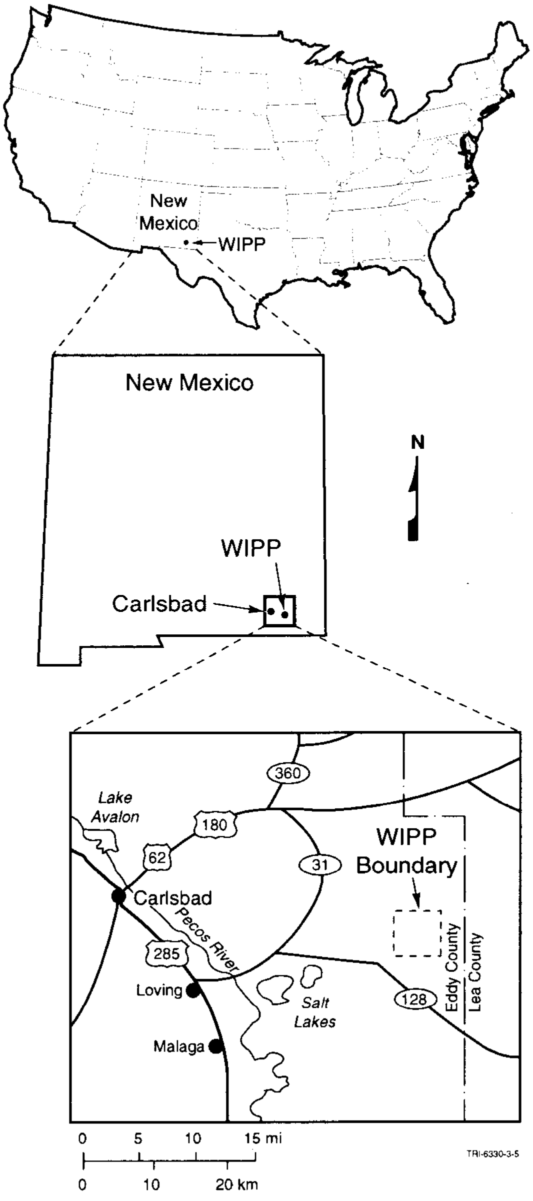

Figure 1-1. Location of the WIPP site.

---

[1] Sandia National Laboratories, Geohydrology Department, P.O. Box 5800, MS-0735, Albuquerque, NM 87185-0735. Email: lcmeigs@sandia.gov.

[2] Duke Engineering & Services, Inc., 9111 Research Boulevard, Austin, TX 78758.

[3] Sandia National Laboratories, Repository Performance and Certification Department, P.O. Box 5800, MS-1395, Albuquerque, NM 87185-1395.

System	Series	Group	Formation	Member	Approximate Thickness* (m)	Approximate Thickness* (ft)
Quaternary	Recent		Surficial Deposits		3	10
	Pleistocene		Mescalero Caliche		10	30
			Gatuña			
Triassic		Dockum	Undivided		3	10
Permian	Ochoan		Dewey Lake Redbeds		150	500
			Rustler	Forty-niner	18	60
				Magenta	7	24
				Tamarisk	26	85
				Culebra Dolomite	7	24
				Los Medaños	37	120
			Salado		600	2000
			Castile		400	1300
	Guadalupian	Delaware Mountain	Bell Canyon		310	1000
			Cherry Canyon		335	1100
			Brushy Canyon		550	1800

* At center of WIPP site.

TRI-6115-38-4

Figure 1-2. WIPP area stratigraphic column.

testing at the WIPP, (3) provide a summary of the interpretations of the 1995-96 tracer tests conducted to date and review reinterpretations of several of the earlier tests conducted in the 1980's, and (4) summarize the knowledge gained to date through tracer testing in the Culebra.

1.1 Background and Purpose of Recent Tests

Tracer tests were performed in the Culebra at five multiple-well sites, designated the H-2, H-3, H-4, H-6, and H-11 hydropads (Figure 1-3), between February 1980 and July 1988. The tracer tests at the H-2 and H-4 hydropads showed slow tracer transport, consistent with a porous-medium conceptualization of the Culebra at those locations. Tracer transport at the H-3, H-6, and H-11 hydropads was much more rapid, particularly along certain flow paths, suggesting transport through fractures. Hydraulic testing performed at the five tracer-test hydropads showed that transmissivities are nearly two orders of magnitude higher at H-3, H-6, and H-11 than at H-2 and H-4. The hydraulic-test data from H-2 and H-4 can be simulated using single-porosity (porous-medium) models, whereas simulation of the hydraulic tests at H-3, H-6, and H-11 requires the use of double-porosity models (Beauheim, 1987; Beauheim and Ruskauff, 1998).

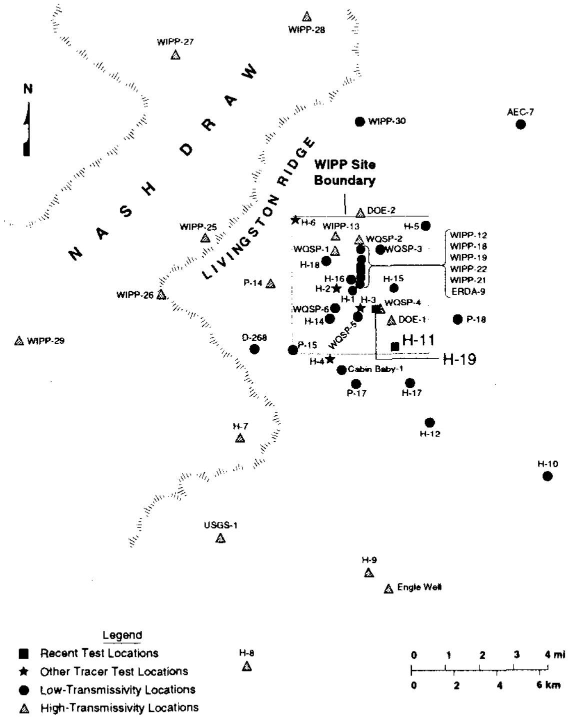
N
NASH DRAW
LIVINGSTON RIDGE
WIPP Site Boundary
WIPP-27
WIPP-28
WIPP-30
AEC-7
DOE-2
H-6
WIPP-13
H-5
WIPP-25
WQSP-2
WQSP-1
WQSP-3
H-18
WIPP-12
WIPP-18
WIPP-19
WIPP-22
WIPP-21
ERDA-9
H-16
H-15
P-14
H-2
WIPP-26
H-1
H-3
WQSP-4
WQSP-6
H-14
DOE-1
P-18
WQSP-5
WIPP-29
D-268
P-15
H-11
H-19
H-4
Cabin Baby-1
P-17
H-17
H-12
H-7
H-10
USGS-1
H-9
Engle Well
H-8
Legend
■ Recent Test Locations
★ Other Tracer Test Locations
● Low-Transmissivity Locations
▲ High-Transmissivity Locations
0 1 2 3 4 mi
0 2 4 6 km
TRI-6115-488-0

Figure 1-3. Well locations in the vicinity of the WIPP site.

Jones et al. (1992) interpreted the early tests at the H-3, H-6, and H-11 hydropads using a homogeneous, one-dimensional (radial), double-porosity continuum model with three orthogonal, equally spaced fracture sets and a single rate of diffusion between fractures and matrix. Their simulations suggest that the observed transport behavior can be explained by a combination of anisotropy in horizontal hydraulic conductivity and matrix diffusion, and demonstrated that the tailing observed in the breakthrough-curve data could not be adequately represented with a homogeneous single-porosity model.

To evaluate the performance of the WIPP repository under various human-intrusion scenarios, a model of solute transport through the Culebra is necessary. Transport through the matrix porosity of the Culebra is sufficiently slow to not be of concern over the regulatory timeframe of 10,000 years, but transport through fractures could be much faster. Therefore, to be conservative, performance-assessment modeling of the Culebra (WIPP PA Department, 1993) treated the entire unit as a double-porosity medium with transport parameters derived from the interpretations of Jones et al. (1992).

However, independent reviewers of the Jones et al. (1992) interpretations questioned the assumption that matrix diffusion was the primary or sole mechanism causing physical retardation during these tests. Hautojärvi and Vuori (1992) suggest that other processes in addition to matrix diffusion, such as channeling caused by variations in fracture apertures or delayed release of tracer from the injection well to the formation, may have contributed to the long tails observed in the tracer-breakthrough curves. As a result of these and other criticisms of the test interpretations from a variety of regulatory and review groups, a series of additional hydraulic and tracer tests was designed and implemented to address specific issues. The tests were conducted in 1995 and 1996 at both the existing H-11 hydropad and at a new seven-well site designated the H-19 hydropad (Figure 1-3). The additional tracer tests consisted of both single-well injection-withdrawal (SWIW) tests and multiwell convergent-flow (MWCF) tests. The objectives of the tests were to collect detailed and accurate data sets under carefully controlled conditions to test the validity of the double-porosity conceptual model for the fractured portion of the Culebra and to define appropriate transport parameters for the fractured Culebra. In addition, the tests were designed to evaluate the extent to which heterogeneity, anisotropy, layering, and the scale of testing affect flow and transport.

1.2 Previous Studies

Understanding and predicting the movement of solutes in groundwater is critical not only for evaluating the WIPP but also for many other environmental-protection problems. Accurate models are needed to predict the movement of contaminant plumes, evaluate the potential success of contaminant-remediation technologies, assess the risks associated with various remediation or containment schemes, and evaluate sites for potential waste disposal. Many countries in addition to the United States are designing geologic repositories for the storage of radioactive waste. Understanding the details of transport processes is of critical importance in assessing those repositories as well as the repository at the WIPP site.

Over the last fifteen years, several detailed field tracer tests have been conducted that have provided valuable insight into the complexities of contaminant-transport processes (e.g., Mackay et al., 1986; Killey and Moltyaner, 1988; LeBlanc et al., 1991; Abelin et al., 1991; Boggs et al., 1992; Novakowski and Lapcevic, 1994; Volckaert and Gautschi, 1997). Some of these experiments, like those at the Borden and Cape Cod sites (e.g., Mackay et al., 1986; LeBlanc et al., 1991), have provided detailed and accurate data bases that have been analyzed by numerous scientists and have spawned many fruitful follow-on studies. Several large-scale tracer tests and numerous simpler and smaller scale tests have provided invaluable data for testing and improving the overall knowledge of the processes that control the transport of solutes in groundwater.

Most of the tracer tests to date that have produced a large data base have focused on advection, dispersion, and chemical reactions (e.g., sorption). Few field studies have focused on the diffusion of solutes from the high-permeability (advection-dominated) domains of a porous medium into low-permeability (diffusion-dominated) domains. Diffusion has been recognized, however, as potentially having an important role in transport processes (e.g., Neretnieks, 1980; Wood, 1996). Most of the quantitative studies of diffusion processes have been laboratory studies (e.g., Grisak et al., 1980; Moreno and Neretnieks, 1985; Skagius and Neretnieks, 1986, 1988; Wood et al., 1990; Ball and Roberts, 1991; Shackelford, 1991; Byegård et al., 1998; Tidwell et al., 2000). The relatively slow rates of diffusion, especially for hard rocks such as granite, make quantifying the effects of matrix diffusion difficult in the field. However, several field studies have provided valuable insights into matrix-diffusion processes (e.g., Abelin et al., 1991; Jones et al., 1992; Novakowski and Lapcevic, 1994; Moench, 1995; Haderman and Herr, 1996; Volckaert and Gautschi, 1997).

One goal of the 1995-96 Culebra tracer tests was to conduct well-controlled tests to produce a detailed and accurate data base for evaluation of advective and diffusive transport processes in fractured, saturated, permeable media. Although past studies at the WIPP and elsewhere have provided valuable insights into diffusion processes, this is the first extensive field tracer-test study primarily focused on providing a data set to evaluate matrix-diffusion processes.

1.3 Description of Contents

Chapter 2 of this report provides a general description of the geology and hydrology of the Culebra at the WIPP site. Chapter 3 describes the field setting, goals, design, implementation, and data obtained for the tracer tests conducted in the Culebra in 1995 and 1996 at the H-11 and H-19 hydropads. Chapter 4 discusses the effect of heterogeneity in the hydraulic-conductivity field and plume drift due to a regional gradient on SWIW test results for a single-porosity system. Conditions under which single- and double-porosity responses can be confused are also investigated. Numerical simulations are then presented that demonstrate that the recovery curves from the WIPP SWIW tests cannot be explained with a single-porosity model employing heterogeneity and plume drift, suggesting that the observed data cannot be explained without incorporating matrix diffusion. Chapter 5 discusses single-porosity simulations of an observed breakthrough curve from the 1995-96 MWCF tracer tests at the H-19 hydropad. The purpose of the simulations was to evaluate the role of heterogeneity in breakthrough-curve tailing. The tailing observed in the MWCF breakthrough-curve data could not be reproduced with single-porosity numerical simulations, suggesting that matrix diffusion may be required. In addition, the conceptual model used to create the heterogeneous hydraulic-conductivity fields, the changes in advective porosity, and the variability in the relative correlation length were examined with respect to their effects on breakthrough-curve tailing. Chapter 6 discusses interpretations of the SWIW tracer tests used to determine the effectiveness of multiple rates of mass transfer (diffusion) in a double-porosity model at matching field data. Simulations show that the observed recovery behavior for the Culebra SWIW tests can be matched assuming a double-porosity conceptualization with multirate diffusion. Chapter 7 presents interpretations using a double-porosity model with multirate diffusion of selected MWCF tracer-test data from sites at which SWIW tracer tests were also performed. Also included is a comparison of the results obtained for the MWCF and SWIW tracer tests and a discussion of the implications of the multirate-diffusion model on solute transport at time and length scales greater than those for the tracer tests. Chapter 8 provides a summary and further integration of the information presented in both the Chapters and Appendices of this report. Chapter 8 also includes a discussion of our revisions to the conceptual model of transport for the Culebra, remaining issues and possible future research, and conclusions. Portions of Chapters 2, 3, 4, 6, and 7 were originally prepared as articles for publication in Water Resources Research.

This report contains a large quantity of supporting information in the form of appendices. Appendix A summarizes the sources of information used in this report and provides assistance for finding that information in the Sandia WIPP Central Files. Appendix B contains tracer input parameter sheets (TIPS) for all interpreted data sets. These sheets contain the detailed information needed for interpretations of the tracer-test data. Appendix C contains plots of the tracer-breakthrough and -recovery data for the interpreted tracer tests, a discussion of the method used to calculate the 95% confidence intervals for the data collected during the 1995-96 tracer tests, and tables that summarize information regarding the tracer-breakthrough curves. Appendix D contains hydraulic and injection information for the recent tracer tests at the H-11 and H-19 hydropads. This includes plots of pressures and pumping rates versus time and diagrams of well and tool configurations. Appendix E summarizes hydraulic testing that has been conducted at tracer test sites at the WIPP. Appendix F provides a brief summary of the tracer tests that were performed at the H-2, H-3, H-4, H-6, and H-11 hydropads during the 1980's. Appendix G discusses the rationale for the final well layout at the H-19 hydropad. Appendix H discusses the tracers used during the 1995-96 tracer tests and the batch tests conducted to demonstrate the conservative nature of those tracers in the Culebra. Appendix I discusses the reversed-phase high-performance liquid chromatographic (RP-HPLC) conditions developed to separate the tracers used for the 1995-96 tracer tests during sample analysis. Appendix J briefly presents the methodology used to dissolve the tracers used in the 1995-96 tests in Culebra brine. Appendix K contains a derivation of the -3/2 (log-log) late-time slope observed in the tracer-breakthrough curve after a pulse-type injection for a double-porosity medium with infinite matrix blocks and a single diffusion rate (see Chapter 4 for the significance of this slope). Appendix L contains the calculation of the standard deviation of the natural logarithm of transmissivity for the Culebra at the WIPP site. Appendix M contains a comparison of single-porosity results for the two finite-difference codes used for the interpretations presented in Chapter 4. Appendix N presents calculations that show that mass recovery during a tracer test due to the diffusion of tracer trapped in the bottom of the injection well is insignificant. Appendix O discusses the effects of tracer sorption to the aquifer on tracer breakthrough for a SWIW tracer test. Appendix P presents conventional double-porosity (i.e., single diffusion rate) interpretations of some of the data from the MWCF tracer tests that have been performed at the WIPP. Appendix Q presents the derivation of the Laplace-domain solution for the advective-dispersive equation in radial coordinates with multirate diffusion for the injection, resting, and pumping periods of a SWIW tracer test. Appendix R contains additional multirate interpretations of the SWIW tracer tests using a piecewise-linear distribution of diffusion-rate coefficients. Appendix S contains preliminary interpretations of the 1995-96 MWCF data from H-11 and H-19 using both multirate and single-rate diffusion models. Selected MWCF data from the tests at the H-3 and H-6 hydropads and the 1988 tests at the H-11 hydropad are also interpreted.

1.4 References

Abelin, H., L. Birgersson, L. Moreno, H. Widén, T. Ågren, and I. Neretnieks. 1991. "A Large-Scale Flow and Tracer Experiment in Granite. 2. Results and Interpretation," *Water Resources Research.* Vol. 27, no. 12, 3119-3135.

Ball, W.P., and P.V. Roberts. 1991. "Long-Term Sorption of Halogenated Organic Chemicals by Aquifer Material. 1. Equilibrium," *Environmental Science and Technology.* Vol. 25, no. 7, 1223-1237.

Beauheim, R.L. 1987. *Interpretations of Single-Well Hydraulic Tests Conducted At and Near the Waste Isolation Pilot Plant (WIPP) Site, 1983-1987.* SAND87-0039. Albuquerque, NM: Sandia National Laboratories.

Beauheim, R.L., and G.J. Ruskauff. 1998. *Analysis of Hydraulic Tests of the Culebra and Magenta Dolomites and Dewey Lake Redbeds Conducted at the Waste Isolation Pilot Plant Site.* SAND98-0049. Albuquerque, NM: Sandia National Laboratories.

Boggs, J.M., S.C. Young, L.M. Beard, L.W. Gelhar, K.R. Rehfeldt, and E.E. Adams. 1992. "Field Study of Dispersion in a Heterogeneous Aquifer. 1. Overview and Site Description," *Water Resources Research.* Vol. 28, no. 12, 3281-3291.

Byegård, J., H. Johansson, M. Skålberg, and E.-L. Tullborg. 1998. *The Interaction of Sorbing and Non-Sorbing Tracers with Different Äspö Rock Types: Sorption and Diffusion Experiments in the Laboratory Scale.* Technical Report TR-98-18. Stockholm, Sweden: Swedish Nuclear Fuel and Waste Management Company.

Grisak, G.E., J.F. Pickens, and J.A. Cherry. 1980. "Solute Transport Through Fractured Media, 2. Column Study of Fractured Till," *Water*

Resources Research. Vol. 16, no. 4, 731-739.

Hadermann, J., and W. Heer. 1996. "The Grimsel (Switzerland) Migration Experiment: Integrating Field Experiments, Laboratory Investigations and Modelling," *Journal of Contaminant Hydrology.* Vol. 21, no. 1-4, 87-100.

Hautojärvi, A., and S. Vuori. 1992. *Comments on Tracer Tests and Data Interpretation.* TVO/KPA Turvallisuus Ja Tekniikka Työraportti 92-01. Helsinki, Finland: Technical Research Centre of Finland, Nuclear Engineering Laboratory.

Jones, T.L., V.A. Kelley, J.F. Pickens, D.T. Upton, R.L. Beauheim, and P.B. Davies. 1992. *Integration of Interpretation Results of Tracer Tests Performed in the Culebra Dolomite at the Waste Isolation Pilot Plant Site.* SAND92-1579. Albuquerque, NM: Sandia National Laboratories.

Killey, R.W.D., and G.L. Moltyaner. 1988. "Twin Lake Tracer Tests: Setting, Methodology, and Hydraulic Conductivity Distribution," *Water Resources Research.* Vol. 24, no. 10, 1585-1612.

LeBlanc, D.R., S.P. Garabedian, K.M. Hess, L.W. Gelhar, R.D. Quadri, K.G. Stollenwerk, and W.W. Wood. 1991. "Large-Scale Natural Gradient Tracer Test in Sand and Gravel, Cape Cod, Massachusetts. 1. Experimental Design and Observed Tracer Movement," *Water Resources Research.* Vol. 27, no. 5, 895-910.

Mackay, D.M., D.L. Freyberg, P.V. Roberts, and J.A. Cherry. 1986. "A Natural Gradient Experiment on Solute Transport in a Sand Aquifer. 1. Approach and Overview of Plume Movement," *Water Resources Research.* Vol. 22, no. 13, 2017-2029.

Moench, A.F. 1995. "Convergent Radial Dispersion in a Double-Porosity Aquifer with Fracture Skin: Analytical Solution and Application to a Field Experiment in Fractured Chalk," *Water Resources Research.* Vol. 31, no. 8, 1823-1835.

Moreno, L., and I. Neretnieks. 1985. "Analysis of Some Laboratory Runs in Natural Fissures," *Water Resources Research.* Vol. 21, no. 7, 951-958.

Neretnieks, I. 1980. "Diffusion in the Rock Matrix: An Important Factor in Radionuclide Retardation?," *Journal of Geophysical Research.* Vol. 85, no. B8, 4379-4397.

Novakowski, K.S., and P.A. Lapcevic. 1994. "Field Measurement of Radial Solute Transport in Fractured Rock," *Water Resources Research.* Vol. 30, no. 1, 37-44.

Shackelford, C.D. 1991. "Laboratory Diffusion Testing for Waste Disposal – A Review," *Journal of Contaminant Hydrology.* Vol. 7, no. 3, 177-217.

Skagius, K., and I. Neretnieks. 1986. "Porosities and Diffusivities of Some Nonsorbing Species in Crystalline Rocks," *Water Resources Research.* Vol. 22, no. 3, 389-398.

Skagius, K., and I. Neretnieks. 1988. "Measurements of Cesium and Strontium Diffusion in Biotite Gneiss," *Water Resources Research.* Vol. 24, no. 1, 75-84.

Tidwell, V.C., L.C. Meigs, T. Christian-Frear, and C.M. Boney. 2000. "Effects of Spatially Heterogeneous Porosity on Matrix Diffusion as Investigated by X-ray Absorption Imaging," *Journal of Contaminant Hydrology.* Vol. 42, no. 2-4, 285-302.

US DOE (U.S. Department of Energy). 1996. *Title 40 CFR Part 191 Compliance Certification Application for the Waste Isolation Pilot Plant.* DOE/CAO-1996-2184. Carlsbad, NM: United States Department of Energy, Waste Isolation Pilot Plant, Carlsbad Area Office. Vol. I- XXI.

Volckaert, G., and A. Gautschi. 1997. "Field Tracer Experiments in Clay," *Field Tracer Experiments: Role in the Prediction of Radionuclide Migration, Synthesis and Proceeding of an NEA/EC GEOTRAP Workshop, Cologne, Germany, 28-30 August 1996*. Paris: Nuclear Energy Agency, Organisation for Economic Co-Operation and Development. 95-101.

WIPP Performance Assessment Department. 1993. *Preliminary Performance Assessment for the Waste Isolation Pilot Plant, December 1992, Volume 2: Technical Basis.* SAND92-0700/2. Albuquerque, NM: Sandia National Laboratories.

Wood, W.W. 1996. "Editorial. Diffusion: The Source of Confusion?," *Ground Water*. Vol. 34, no. 2, 193.

Wood, W.W., T.F. Kraemer, and P.P. Hearn, Jr. 1990. "Intragranular Diffusion: An Important Mechanism Influencing Solute Transport in Clastic Aquifers?," *Science*. Vol. 247, no. 4950, 1569-1572.

This page intentionally left blank.

Chapter 2
Characteristics of the Culebra

By Lucy C. Meigs[1] and Richard L. Beauheim[2]

The Culebra Dolomite Member of the Rustler Formation is the most transmissive saturated unit overlying the WIPP repository horizon. As such, it is the most likely geologic pathway to the accessible environment in the event of a breach of the repository by human intrusion. Because of its potential importance as an off-site pathway, a variety of studies have been performed of the Culebra to characterize its hydraulic and solute-transport processes and properties. The characteristics of the Culebra, as determined from shaft and core descriptions, borehole video logs, core studies, hydraulic testing, and water analyses, are described in this chapter.

2.1 Culebra Geology and Sedimentology

At the WIPP site, the Culebra is located approximately 230 m below land surface. It is underlain by a mudstone unit and overlain by an anhydrite unit (Holt and Powers, 1988). The Culebra varies in thickness between approximately 6 and 9 m in the vicinity of the WIPP. The thickness of the Culebra is approximately 7.4 m at both the H-11 and H-19 hydropads (Holt, 1997), 6.1 m at the H-2 hydropad, 7.2 m at the H-3 hydropad, 7.7 m at the H-4 hydropad, and 7.0 m at the H-6 hydropad (Cauffman et al., 1990). The Culebra is a regionally persistent bed within the Rustler Formation and currently occupies an area of greater than 25,000 km^2 (Holt, 1997). Stratigraphic layering within the Culebra changes little across the WIPP area, apparently as a result of the large size of facies tracts within the Culebra depositional system (Holt and Powers, 1988; Holt, 1997). Lateral variations in the Culebra across the WIPP site appear to be confined to post-depositional features including fractures and distribution of gypsum cements. Holt and Powers (1988) suggest that fracture intensity in the Culebra increases from east to west across the WIPP site.

On the basis of shaft descriptions (Holt and Powers, 1984; 1986; 1990), core descriptions (Holt and Powers, 1988; Holt, 1997), and borehole video logs, four distinct Culebra units (CU) can be identified (Figure 2-1) in the subsurface across the entire WIPP area (Holt, 1997). The upper Culebra comprises CU-1 and the lower Culebra comprises CU-2, 3, and 4. CU-1 consists primarily of well-indurated intercrystalline dolomite and is more massively bedded than the underlying units. Porosity in the well-indurated dolomite is primarily intercrystalline in nature. Fractures are less common in CU-1 than in lower units and usually appear to be bedding-plane separations. Small vugs are common in the upper Culebra and frequently occur in zones parallel to stratification. A portion of the vugs and fractures are typically filled with gypsum. CU-1 has an average thickness across the site area of approximately 3.0 m.

The Culebra units below CU-1, especially CU-2 and 3, are typically more intensely fractured, have more vugs, and contain interbeds of poorly indurated dolomite. The intensely fractured nature of CU-2 and 3 results in very poor core recovery of these two units at many locations. Where core has been recovered (e.g., H-19), portions of it often have a jigsaw-puzzle-like appearance with fractures spaced less than a centimeter to several centimeters apart. Many of the fracture surfaces display dark brown or orange staining suggestive of current or past fluid flow. Vugs in the lower

---

[1] Sandia National Laboratories, Geohydrology Department, P.O. Box 5800, MS-0735, Albuquerque, NM 87185-0735. Email: lcmeigs@sandia.gov.

[2] Sandia National Laboratories, Repository Performance and Certification Department, P.O. Box 5800, MS-1395, Albuquerque, NM 87185-1395.

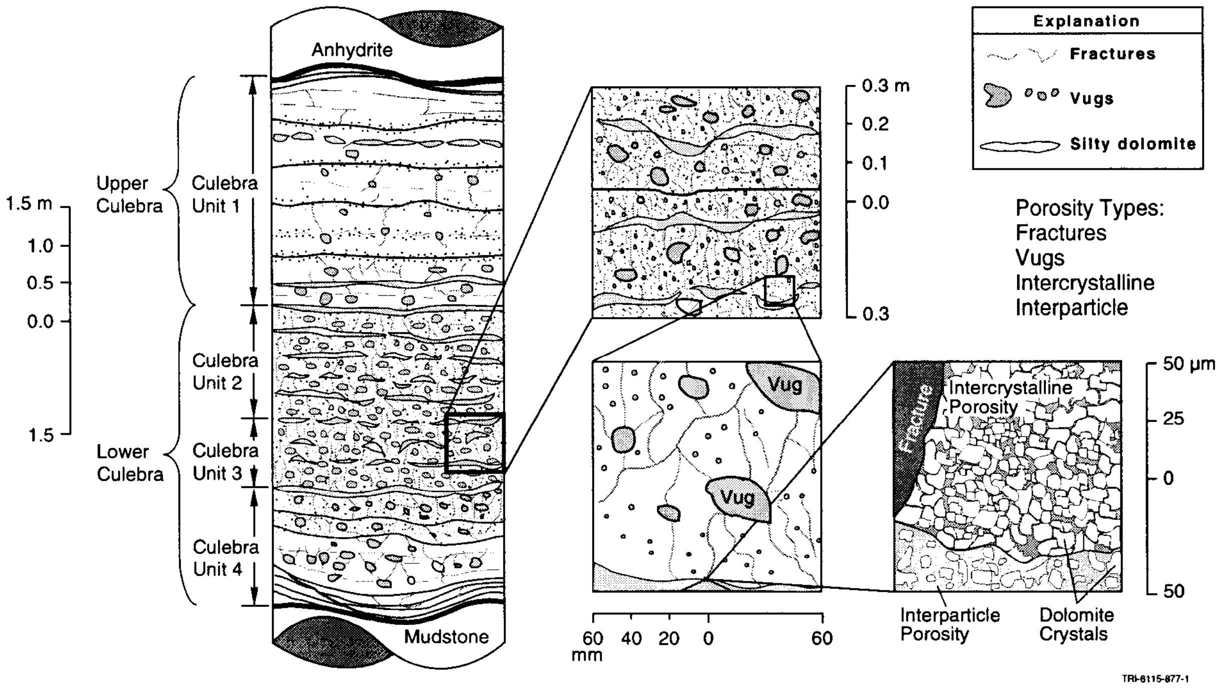
Explanation
Fractures
Vugs
Silty dolomite
Porosity Types:
Fractures
Vugs
Intercrystalline
Interparticle
Anhydrite
1.5 m
1.0
0.5
0.0
1.5
Upper Culebra
Lower Culebra
Culebra Unit 1
Culebra Unit 2
Culebra Unit 3
Culebra Unit 4
Mudstone
0.3 m
0.2
0.1
0.0
0.3
Vug
Vug
60 40 20 0 60
mm
Fracture
Intercrystalline Porosity
Interparticle Porosity
Dolomite Crystals
50 µm
25
0
50
TRI-6115-877-1

Figure 2-1. Schematic of vertical variations in Culebra lithologies and porosity types (from Holt, 1997).

Culebra (CU-2, 3, and 4) range in size from a millimeter to a few centimeters and are often connected by microfractures. The vugs are often partially filled with poorly indurated dolomite or gypsum. The poorly indurated dolomite is also referred to as silty dolomite because it is composed of poorly cemented clay- to silt-sized dolomite. The poorly indurated dolomite has a higher interparticle porosity and permeability than the well-indurated dolomite that makes up most of the Culebra. CU-4 is less intensely fractured than CU-2 and 3 and has more clearly defined bedding planes that are undulatory in nature. CU-2 and 3 combined have an average thickness of 2.8 m across the WIPP area and CU-4 has an average thickness of 1.6 m. The combined thicknesses of the lower three units at hydropads where tracer tests have been conducted are given in Table 2-1. For a more complete description of Culebra lithologies and porosity variations, see Holt (1997).

The different porosity types described above and shown graphically in Figure 2-1 each have a range of permeabilities associated with them. On the time and length scales of our tracer tests, tracer(s) accesses some of this porosity primarily by advection and other portions of the porosity primarily by diffusion. Hence, we use the expressions "advective porosity" and "diffusive porosity" to denote the portions of the porosity in which the different processes are dominant. Note that this distinction relies to some degree on the contrast in permeability between different porosity types. Where fracture permeabilities are low, the permeability of the interparticle porosity in the poorly indurated dolomite may be of similar magnitude, so that advection occurs in both porosity types. Where fracture permeabilities are high, the interparticle porosity may play only a diffusive role. Thus, whether a particular porosity type is considered advective or diffusive depends on the properties of the other porosity types at any given location. The advective and diffusive porosities together make up the "effective" (i.e., interconnected) porosity commonly measured in core tests.

The fractures observed in the Culebra differ from the common conceptualization of fractures based largely on fracturing in crystalline rocks. Fractures in crystalline rock are often related to regional tectonic forces and tend to be relatively planar, persist over distances of meters to tens of meters, occur in parallel sets with regular

Table 2-1. Physical Properties of the Culebra at the Tracer-Test Hydropads

	H-11 Hydropad	H-19 Hydropad	H-2 Hydropad	H-3 Hydropad	H-4 Hydropad	H-6 Hydropad
Field Transmissivity	4.7×10^{-5} m^2/s	6.8×10^{-6} m^2/s	5.9×10^{-7} m^2/s	2.1×10^{-5} m^2/s	8.3×10^{-7} m^2/s	4.0×10^{-5} m^2/s
Thickness of Full Culebra	7.4 m	7.4 m	6.1 m	7.2 m	7.7 m	7.0 m
Thickness of Lower Culebra	4.4 m	4.4 m	3.1 m	4.2 m	4.7 m	4.0 m
Average Core Hydraulic Conductivity	2.2×10^{-8} m/s (10)[1]	1.5×10^{-8} m/s (20)	1.9×10^{-9} m/s (9)	6.1×10^{-8} m/s (2)	-[2]	5.7×10^{-10} m/s (3)
Average Core Porosity	0.16 (10)	0.15 (21)	0.13 (10)	0.20 (6)	0.25 (2)	0.15 (4)
Average Core Formation Factor	66 (4)	110 (21)	327 (1)	-	-	-
Average Calculated Tortuosity	0.11 (4)	0.09 (21)	0.03 (1)	-	-	-

[1] Numbers in parentheses denote number of samples.
[2] Denotes no value available.

spacings, and have definable orientations (strike and dip). In contrast, regional or local tectonic activity has not caused significant fracturing within the Culebra. The Culebra has primarily fractured in response to differential unloading, dissolution of evaporites from above or below the Culebra, and dissolution of fillings within large vugs and/or zones of vugs in the Culebra (Beauheim and Holt, 1990). The majority of the fractures in the Culebra are subvertical and occur within vuggy zones in CU-2 and 3. These fractures usually extend from vug to vug (Holt and Powers, 1990), over distances of mm to cm, with no preferred orientation. Horizontal fractures, parallel to bedding planes, occur throughout the Culebra. These bedding-plane separations were probably caused by stress relief accompanying the erosion of overburden or dissolution of overlying evaporites. Bedding-plane separations have greater lateral extent within the upper Culebra (CU-1) than in the lower Culebra units where more soft-sediment deformation has occurred, disrupting bedding planes. Similarly, high-angle subvertical fractures locally persist vertically for nearly one meter within the more massive CU-1, but terminate at bedding-plane separations in the lower Culebra. However, the high-angle fractures in CU-1 are typically filled with gypsum in most locations and have little hydraulic significance. Fracture apertures measured in thin sections are highly variable, even in individual fractures, and range from <10 to 500 μm (Holt, 1997). West and south of the WIPP site, the dominant cause of fracturing in the Culebra is collapse following dissolution of the underlying Salado Formation, which caused more extensive fracturing than is observed at the WIPP site.

2.2 Core Studies

Over 100 Culebra core samples have been tested for permeability, porosity, and/or electrical-resistivity formation factor (Kelley and Saulnier, 1990; Holt, 1997). Horizontal permeabilities (parallel to bedding) have been found to range from 2×10^{-18} to 4×10^{-13} m^2, corresponding to hydraulic conductivities between approximately 10^{-11} and 10^{-6} m/s. The higher values are believed to reflect fractures in the core. The measured Culebra porosities range from 3 to 30%, with an average of 15%. Formation factors have been found to range from 12 to 407, with an average value of 108.

An approximation of the tortuous nature of the Culebra pore structure can be calculated from the measured formation factors. Tortuosity, τ, is expressed as:

$$\tau = \frac{1}{F\phi} \tag{2-1}$$

where F and ϕ are the measured formation factor and effective porosity for a given sample, respectively (Kelley and Saulnier, 1990). Tortuosities so calculated range from 0.02 to 0.33. Table 2-1 lists the average property values for core from the hydropads at which tracer tests have been performed. The average core hydraulic conductivities are approximately two orders of magnitude lower than the hydraulic conductivities calculated by dividing the field transmissivities by the Culebra thickness, showing the importance of fractures at the field scale that are not captured in core tests.

2.3 Culebra Hydraulic Testing

Within the 41.4 km^2 area of the WIPP site, 44 wells at 26 locations (hydropads) and four shafts penetrate the Culebra dolomite (Figure 2-2). An additional 27 wells have been completed to the Culebra at 21 locations within 15 km of the WIPP site. Hydraulic testing completed in these wells has shown that the transmissivity of the Culebra varies by six orders of magnitude in the vicinity of the WIPP site. Beauheim and Holt (1990) suggest that much of the variation in transmissivity is due to variations in the relative percentages of open and filled fractures. Where transmissivity values are less than ~4 x 10^{-6} m^2/s, hydraulic tests can be best interpreted with a single-porosity conceptualization (Appendix E). Where transmissivities are greater than ~4 x 10^{-6} m^2/s, a double-porosity conceptualization best explains the data. Double-porosity hydraulic behavior reflects the dominance of open fractures in determining transmissivity and the dominance of the matrix in determining the storage capacity of the medium (Gringarten, 1984).

The hydraulic testing performed at the tracer-test hydropads is summarized in Appendix E. Values of transmissivity inferred from the tests are discussed in Appendix E, and representative values for each hydropad are given in Table 2-1. Variations in transmissivity (heterogeneity) are almost certainly present on the hydropad (tens of meters) scale, but are difficult to quantify because the pressure transient created by any type of hydraulic test quickly propagates beyond that scale. As a result, transmissivity values interpreted from hydraulic tests of the Culebra represent average properties over distances of hundreds of meters. No evidence of leakage from overlying anhydrite or underlying mudstone confining beds is seen in Culebra hydraulic tests.

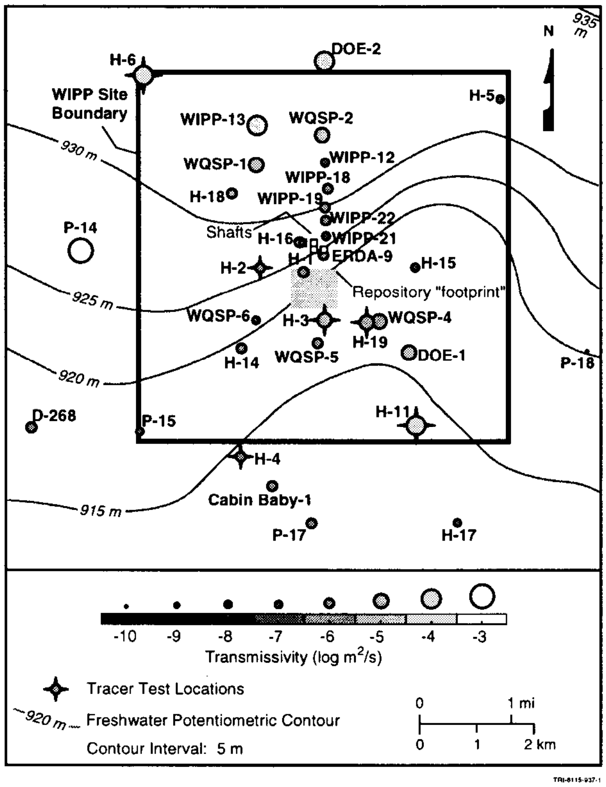
N
935 m
H-6
DOE-2
WIPP Site Boundary
H-5
WIPP-13
WQSP-2
930 m
WQSP-1
WIPP-12
WIPP-18
H-18
WIPP-19
WIPP-22
Shafts
H-16
WIPP-21
P-14
H-2
H-1
ERDA-9
H-15
Repository "footprint"
925 m
WQSP-6
H-3
WQSP-4
H-19
H-14
WQSP-5
DOE-1
P-18
920 m
D-268
P-15
H-11
H-4
Cabin Baby-1
915 m
P-17
H-17
-10
-9
-8
-7
-6
-5
-4
-3
Transmissivity (log m²/s)
Tracer Test Locations
920 m Freshwater Potentiometric Contour
Contour Interval: 5 m
0
1 mi
0
1
2 km
TRI-6115-937-1

Figure 2-2. Variations in transmissivity values measured in Culebra wells near the WIPP site.

Flow in the Culebra is generally to the south across the WIPP site (Crawley, 1988; Corbet and Knupp, 1996), with hydraulic gradients ranging from approximately 0.001 to 0.01 meters of fresh water per meter distance (Figure 2-2). Calculated Darcy velocities on the WIPP site range from approximately 1 x 10^{-11} to 2 x 10^{-9} m/s (LaVenue et al., 1990). Transmissivities are higher in a zone near the H-3, H-11, and H-19 hydropads than elsewhere in the southern portion of the WIPP site (Figure 2-2). This high-transmissivity zone is potentially important because it could represent a fast transport path to the site boundary for WIPP contaminants released to the Culebra through inadvertent human intrusion of the repository.

Hydraulic tests and logging at several locations suggest that the hydraulic properties of the Culebra vary vertically, in some places significantly. Cross-hole sinusoidal pumping tests of the upper and lower Culebra indicate that the permeability of the upper portion of the Culebra (CU-1) is significantly lower than the permeability of the lower Culebra (CU-2, 3, and 4) at the H-19 hydropad (Beauheim et al., 1997). Hydrophysical (fluid) logging and pressure responses during drilling also suggest that most flow occurs in the lower portion of the Culebra at H-19 (Beauheim et al., 1997). The results of a tracer (^{131}I) and temperature survey conducted at the H-3 hydropad indicated that, within the resolution of the test, all flow was in the lower 3 m of the Culebra (See Appendix E and Mercer and Orr, 1979). In addition, most of the fluid flow observed in the Air-Intake Shaft came from the lower portion of the Culebra (Holt and Powers, 1990). Transmissivity values reported for the Culebra (e.g., Beauheim and Ruskauff, 1998, and Table 2-1) represent integrated values over the entire thickness of Culebra.

2.4 Culebra Water Chemistry

In the vicinity of the WIPP site, Culebra water is a moderate- to high-ionic-strength brine of predominantly sodium-chloride type composition. The properties of brines sampled from wells at each of the tracer-test hydropads are presented in Table 2-2. On the basis of major and minor solute concentrations, a few different hydrochemical facies have been defined (Siegel and Anderholm, 1994). Brines in hydrochemical facies A are characterized by ionic strengths of 1.5 to 3 molal and Mg/Ca molar ratios between approximately 1.3 and 2.0. Brines from the H-11 and H-19 hydropads belong to this facies. Brines in hydrochemical facies C have lower ionic strengths (0.3 to 1.6 molal) and lower Mg/Ca molar ratios (0.5 to 1.2). Brines from the H-2, H-3, H-4, and H-6 hydropads belong to this facies. The density of the Culebra brine ranges between 1.01 and 1.09 g/cm^3 at the six tracer-test hydropads (Table 2-2). Culebra water temperatures typically range from 23 to 27°C (e.g., INTERA Technologies, Inc., 1986; Stensrud et al., 1990).

2.5 References

Beauheim, R.L., and R.M. Holt. 1990. "Hydrogeology of the WIPP Site," *Geological and Hydrological Studies of Evaporites in the Northern Delaware Basin for the Waste Isolation Pilot Plant (WIPP), New Mexico, Field Trip #14 Guidebook, November 1-4, 1990,* Geological Society of America 1990 Annual Meeting. Dallas, TX: Dallas Geological Society. 131-179.

Beauheim, R.L., and G.J. Ruskauff. 1998. *Analysis of Hydraulic Tests of the Culebra and Magenta Dolomites and Dewey Lake Redbeds Conducted at the Waste Isolation Pilot Plant Site.* SAND98-0049. Albuquerque, NM: Sandia National Laboratories.

Table 2-2. Chemical Properties of Culebra Brines at the Tracer-Test Hydropads

Well	Facies	Ionic strength (molal)[1]	Mg/Ca (mole/mole)[1]	pH (field)[1]	Density (g/cm^3)[2]
H-11b3	A	2.23	1.29	7.25	1.09
H-19b5	A	1.79	1.41	7.4	1.07
H-2a	C	0.27	0.38	8.0	1.01
H-3b3	C	1.08	0.89	7.4	1.04
H-4c	C	0.45	1.21	7.8	1.01
H-6b	C	1.13	0.85	6.9	1.04

[1] Chemical data for H-19b5 are from Siegel (1997). Chemical data for other wells are from Siegel and Anderholm (1994).

[2] Density for H-11b3 is from Randall et al. (1988). All other densities, except for H-19b5, are from Bodine et al. (1991). H-19b5 data in ERMS #251278.

Beauheim, R.L., L.C. Meigs and P.B. Davies. 1997. "Rationale for the H-19 and H-11 Tracer Tests at the WIPP Site," *Field Tracer Experiments: Role in the Prediction of Radionuclide Migration, Synthesis and Proceeding of an NEA/EC GEOTRAP Workshop, Cologne, Germany, August 28-30, 1996.* Paris, France: Nuclear Energy Agency, Organisation for Economic Co-Operation and Development. 107-118.

Bodine, M.W., Jr., B.F. Jones, and S.J. Lambert. 1991. "Chapter 4. Normative Analysis of Groundwaters from the Rustler Formation Associated with the Waste Isolation Pilot Plant, Southeastern New Mexico," *Hydrogeochemical Studies of the Rustler Formation and Related Rocks in the Waste Isolation Pilot Plant Area, Southeastern New Mexico.* Eds. M.D. Siegel, S.J. Lambert, and K.L. Robinson. SAND88-0196. Albuquerque, NM: Sandia National Laboratories. 4-1 through 4-140.

Cauffman, T.L., A.M. LaVenue, and J.P. McCord. 1990. *Ground-Water Flow Modeling of the Culebra Dolomite Volume II: Data Base.* SAND89-7068/2. Albuquerque, NM: Sandia National Laboratories.

Corbet, T.F., and P.M. Knupp. 1996. *The Role of Regional Goundwater Flow in the Hydrogeology of the Culebra Member of the Rustler Formation at the Waste Isolation Pilot Plant (WIPP), Southeastern New Mexico.* SAND96-2133. Albuquerque, NM: Sandia National Laboratories.

Crawley, M.E. 1988. *Hydrostatic Pressure and Fluid Density Distribution of the Culebra Dolomite Member of the Rustler Formation Near the Waste Isolation Pilot Plant, Southeastern New Mexico.* DOE/WIPP 88-030. Carlsbad, NM: Westinghouse Electric Corporation.

Gringarten, A.C. 1984. "Interpretation of Tests in Fissured and Multilayered Reservoirs With Double-Porosity Behavior: Theory and Practice," *JPT, Journal of Petroleum Technology.* Vol. 36, no. 4, 549-564.

Holt, R.M. 1997. *Conceptual Model for Transport Processes in the Culebra Dolomite Member, Rustler Formation.* SAND97-0194. Albuquerque, NM: Sandia National Laboratories.

Holt, R.M., and D.W. Powers. 1984. *Geotechnical Activities in the Waste Handling Shaft, Waste Isolation Pilot Plant (WIPP) Project, Southeastern New Mexico.* WTSD-TME 038. Carlsbad, NM: U.S. Department of Energy, Waste Isolation Pilot Plant.

Holt, R.M., and D.W. Powers. 1986. *Geotechnical Activities in the Exhaust Shaft.* DOE-WIPP 86-008. Carlsbad, NM: U.S. Department of Energy.

Holt, R.M., and D.W. Powers. 1988. *Facies Variability and Post-Depositional Alteration Within the Rustler Formation in the Vicinity of the Waste Isolation Pilot Plant, Southeastern New Mexico.* DOE-WIPP 88-004. Carlsbad, NM: Westinghouse Electric Corporation.

Holt, R.M., and D.W. Powers. 1990. *Geologic Mapping of the Air Intake Shaft at the Waste Isolation Pilot Plant.* DOE-WIPP 90-051. Carlsbad, NM: Westinghouse Electric Corporation.

INTERA Technologies, Inc. 1986. *WIPP Hydrology Program, Waste Isolation Pilot Plant, Southeastern New Mexico, Hydrologic Data Report #3.* SAND86-7109. Albuquerque, NM: Sandia National Laboratories.

Kelley, V.A., and G.J. Saulnier, Jr. 1990. *Core Analyses for Selected Samples from the Culebra Dolomite at the Waste Isolation Pilot Plant Site.* SAND90-7011. Albuquerque, NM: Sandia National Laboratories.

LaVenue, A.M., T.L. Cauffman, and J.F. Pickens. 1990. *Ground-Water Flow Modeling of the Culebra Dolomite, Volume I: Model Calibration.* SAND89-7068/1. Albuquerque, NM: Sandia National Laboratories.

Mercer, J.W., and B.R. Orr. 1979. *Interim Data Report on the Geohydrology of the Proposed Waste Isolation Pilot Plant Site Southeast*

New Mexico. U.S. Geological Survey Water-Resources Investigations 79-98. Albuquerque, NM: U.S. Geological Survey.

Randall, W.S., M.E. Crawley, and M.L. Lyon. 1988. *1988 Annual Water Quality Data Report for the Waste Isolation Pilot Plant.* DOE-WIPP 88-006. Carlsbad, NM: Westinghouse Electric Corporation.

Siegel, M.D. 1997. "Recipe for H19 Brine." Memo to C. Boney, September 26, 1997. Albuquerque, NM: Sandia National Laboratories. (Copy on file in the Sandia WIPP Central Files (SWCF)as ERMS #248941.)

Siegel, M.D., and S.A. Anderholm. 1994. "Geochemical Evolution of Groundwater in the Culebra Dolomite Near the Waste Isolation Pilot Plant, Southeastern New Mexico, USA," *Geochimica et Cosmochimica Acta.* Vol. 58, no. 10, 2299-2323.

Siegel, M.D., K.L. Robinson, and J. Myers. 1991. "Chapter 2. Solute Relationships in Groundwaters from the Culebra Dolomite and Related Rocks in the Waste Isolation Pilot Plant Area, Southeastern New Mexico," *Hydrogeochemical Studies of the Rustler Formation and Related Rocks in the Waste Isolation Pilot Plant Area, Southeastern New Mexico.* Eds. M.D. Siegel, S.J. Lambert, and K.L. Robinson. SAND88-0196. Albuquerque, NM: Sandia National Laboratories. 2-1 through 2-164.

Stensrud, W.A., M.A. Bame, K.D. Lantz, J.B. Palmer, and G.J. Saulnier, Jr. 1990. *WIPP Hydrology Program, Waste Isolation Pilot Plant, Southeastern New Mexico, Hydrologic Data Report #8.* SAND89-7056. Albuquerque, NM: Sandia National Laboratories.

This page intentionally left blank.

Chapter 3
Experimental Design and Observed Tracer Recoveries for the 1995-96 Tracer Tests

By Lucy C. Meigs[1], Richard L. Beauheim[2], and Toya L. Jones[3]

Hydropad-scale tracer tests have been performed in the Culebra at the WIPP site to characterize its solute-transport processes and properties because of the potential importance of this unit as an off-site pathway. Between 1980 and 1988, tracer testing was performed at the H-2, H-3, H-4, H-6, and H-11 hydropads (Figure 2-2). The tests at H-2 and H-4 showed slow transport, reflecting flow through a porous (rather than fractured) medium. The tests at H-3, H-6, and H-11, however, showed rapid initial tracer breakthrough along some flow paths followed by long "tails" of declining tracer concentrations. These tests were thought to reflect transport through fractures, with the tails caused by diffusion of tracer between the fractures and the adjacent rock matrix, a form of physical retardation. Due to criticism of interpretations of these tests that assumed matrix diffusion was the sole mechanism causing the observed physical retardation, additional tests were planned and conducted in 1995 and 1996 to obtain detailed and accurate data under carefully controlled conditions in order to test the validity of the double-porosity conceptual model for the Culebra. This chapter summarizes all of the tracer tests that have been performed in the Culebra and provides a detailed description of the tracer tests conducted in 1995 and 1996.

3.1 Tracer Tests Performed in the Culebra

Three types of tracer tests have been performed in the Culebra dolomite at the WIPP: two-well recirculating (TWR) tests at the H-2 and H-6 hydropads, multiwell convergent-flow (MWCF) tests at the H-3, H-4, H-6, H-11, and H-19 hydropads, and single-well injection-withdrawal (SWIW) tests at the H-11 and H-19 hydropads. Table 3-1 summarizes the hydropads at which tracer tests have been performed, the type(s) of test(s) conducted, and the time period(s) of the test(s). The TWR tracer tests entailed withdrawing fluid from one well, adding a tracer to the fluid, and injecting the now-traced fluid into a second well in a continuous recirculation loop. Because the tracer was recirculated between two wells, the formation was tested along the flow paths developed between those two wells. MWCF tracer tests were conducted at hydropads containing three or more wells. The tests involved pumping one well until an effectively steady-state flow field was established and then injecting traced fluid followed by untraced fluid (chaser) into the other wells at the hydropad. Because the tracers were injected into several wells and recovered from a different well, the formation was tested along individual well-to-well flow paths at the hydropad. For the SWIW tests, one or more tracers were injected sequentially into a well followed by the injection of chaser designed to displace the traced fluid from the borehole. After a pause period of about 18 hr, the well was pumped to recover the tracer(s). Because the tracer was injected and recovered from the same well, the formation was tested only in the immediate vicinity of a single well.

The early tests conducted in the 1980's have been previously described and discussed in numerous publications as indicated in Table 3-1. This

---

[1] Sandia National Laboratories, Geohydrology Department, P.O. Box 5800, MS-0735, Albuquerque, NM 87185-0735. Email: lcmeigs@sandia.gov.

[2] Sandia National Laboratories, Repository Performance and Certification Department, P.O. Box 5800, MS-1395, Albuquerque, NM 87185-1395.

[3] Duke Engineering & Services, Inc., 9111 Research Boulevard, Austin, TX 78758.

Table 3-1. Summary of Tracer Tests Performed in the Culebra

Hydro-pad	Test	SWIW	MWCF	TWR	Previous Publications
H-2	#1			02/80 to 06/80[b] (126 d)[c]	Hydro Geo Chem (1985; 1986); Jones et al. (1992)
	#2			07/80 to 04/81 (274 d)	Hydro Geo Chem (1985; 1986); Jones et al. (1992)
H-3			04/84 to 06/84 (50 d)		Hydro Geo Chem (1985); INTERA (1986); Kelley and Pickens (1986); Jones et al. (1992)
H-4			10/82 to 10/84 (722 d)		Hydro Geo Chem (1985); Kelley and Pickens (1986); Jones et al. (1992)
H-6	#1 & #2		08/81 to 09/81 (23 d)		Hydro Geo Chem (1985); Jones et al. (1992)
	#3 & #4		09/82 to 10/82 (15 d)		Hydro Geo Chem (1985); Jones et al. (1992)
	#5		10/82 to 11/82 (36 d)		Hydro Geo Chem (1985); Jones et al. (1992)
	#6			04/83 to 05/83 (29 d)	Hydro Geo Chem (1985); Jones et al. (1992)
	#7			06/83 to 07/83 (39 d)	Hydro Geo Chem (1985); Jones et al. (1992)
H-11	1988		05/88 to 07/88 (63 d)		Stensrud et al. (1990) Jones et al. (1992)
	1996	02/96 to 04/96 (50 d)			
	1996		02/96 to 04/96 (41 d)		
H-19	4-well	06/95 to 07/95 (32 d)			
	4-well		06/95 to 07/95 (37 d)		
	7-well	12/95 to 01/96 (26 d)			
	7-well		12/95 to 04/96 (106 d)		

(a) TWR: Two-Well Recirculating; MWCF: Multiwell Convergent-Flow; SWIW: Single-Well Injection-Withdrawal

(b) Intermittent pumping between 04/80 and 06/80

(c) Test duration, in days, is included in parentheses

chapter does not include any discussion of those tests. However, a brief overview of each early test can be found in Appendix F. The following sections deal with the tests conducted in 1995 and 1996 at the existing and previously tested H-11 hydropad and at the H-19 hydropad that was constructed specifically for the tests. The objectives of the sections below are to describe the conceptual model that the 1995-96 tracer tests were designed to evaluate; describe the experimental design and methodologies of those tests; discuss tracer selection, mixing, and injection; discuss sample collection and analysis; present and discuss the observed data; and provide a preliminary evaluation of the consistency of the data with our initial conceptual model.

3.2 Conceptual Transport Model for the Culebra to be Tested

Based on the results of both hydraulic and tracer tests, we believe that the Culebra is best conceptualized as a single-porosity medium at some locations and as a double-porosity medium at other locations. Where the Culebra transmissivity is found to be less than approximately 4 x 10^{-6} m^2/s, hydraulic-test data are best simulated using a single-porosity (porous-medium) model (Beauheim, 1987; Beauheim and Ruskauff, 1998). Where the Culebra transmissivity is greater than 4 x 10^{-6} m^2/s, hydraulic-test data are best simulated using a double-porosity model. Double-porosity hydraulic models assume the presence of fractures and matrix with contrasting hydraulic properties (Gringarten, 1984, 1987). The fractures have high permeability and low storage capacity, while the matrix has low permeability and high storage capacity. Double-porosity hydraulic conditions are observed in the northwestern and southeastern portions of the WIPP site, whereas single-porosity conditions are observed in the northeastern, southwestern, and central portions of the site (see Figure 2-2).

Of the tracer-test locations, the H-2 and H-4 hydropads fall in the region where single-porosity hydraulic responses are observed. The H-3, H-6, H-11, and H-19 hydropads lie in regions where double-porosity hydraulic responses are observed. As described in Hydro Geo Chem (1986) and Kelley and Pickens (1986), the tracer tests at the H-2 and H-4 hydropads showed slow tracer transport, reflecting flow through a porous (rather than fractured) medium. The tests at H-3, H-6, and H-11, however, showed rapid initial tracer breakthrough along some flow paths followed by long "tails" of declining tracer concentrations. These tests were thought to reflect transport through fractures, with the tails caused by diffusion of tracer between the fractures and the adjacent rock matrix, a form of physical retardation (Jones et al., 1992). Thus, the tracer-test interpretations are consistent with the hydraulic-test interpretations in differentiating single-porosity regions of the Culebra from double-porosity regions.

To evaluate the performance of the WIPP repository under various human-intrusion scenarios, a model of solute transport through the Culebra is necessary. Transport through the matrix porosity of the Culebra is sufficiently slow to not be of concern over the regulatory timeframe of 10,000 years, but transport through fractures could be much faster. Therefore, to be conservative, performance-assessment modeling of the Culebra (WIPP PA Department, 1993) treated the entire unit as a double-porosity medium with transport parameters derived from the interpretations of Jones et al. (1992). However, some reviewers criticized these interpretations of the tracer tests, which assumed that matrix diffusion was the sole mechanism causing the observed physical retardation in the double-porosity regions of the Culebra. They suggested that other mechanisms, such as channeling within the most permeable portions of fractures and delayed tracer release from injection wells, might have contributed to the observed physical retardation, and that these other processes might be less effective at retarding transport on the regional scale than matrix diffusion.

To resolve the criticisms, additional tests were planned and conducted in 1995 and 1996 to test the validity of the double-porosity conceptual model for the Culebra. The model used for the interpretations of Jones et al. (1992) can be stated as follows:

- Advective flow and transport occur only through fractures;
- Diffusion is the only mechanism transferring tracers between the fractures and matrix, and is the only active physical retardation mechanism;
- Transport along all flow paths at an individual hydropad can be modeled using a single matrix-block size; and
- Differences in transport along different flow paths at an individual hydropad are caused by hydraulic anisotropy.

Thus, the new tests were designed to provide data that could be used to evaluate the assumptions listed above, as well as provide information on: 1) the importance of vertical heterogeneity in the Culebra, and 2) the effects of transport scale on inferred transport mechanisms and parameters.

3.3 1995-96 Tracer Tests

The tracer testing performed at the H-11 and H-19 hydropads in 1995 and 1996 consisted of SWIW tests followed by MWCF tests. For the SWIW tests, one or two tracers were injected. The MWCF tests were initiated after pumping for the SWIW tests had created effectively steady-state hydraulic gradients at the hydropad. Numerous benzoic acids were used as conservative tracers to allow the collection of tracer-recovery and breakthrough data from multiple pathways simultaneously.

Numerical simulations by Tsang (1995) suggest that an SWIW test is an excellent way of evaluating the importance of matrix diffusion, even in a highly heterogeneous aquifer. Her results show that the rate of mass recovery is always much slower when matrix diffusion is occurring than when it is not. Because slow mass recovery can also be caused by tracer plume drift under ambient flow conditions, as discussed in Chapter 4 and Lessoff and Konikow (1997), the pause period between injection and pumping was kept relatively short (18 hr) for the SWIW tests to minimize drift.

Two features of the MWCF tests were designed to evaluate matrix diffusion. First, after tracers had been injected and recovered while the central well was pumped at one rate, the pumping rate was changed and new tracers were injected to show the effects of advective residence time on diffusion. Second, two conservative tracers having different aqueous diffusion coefficients were injected simultaneously to investigate the effects of different amounts of diffusion. Another feature of the MWCF tests was the injection of tracers into isolated upper and lower subsections of the Culebra at H-19 to evaluate the importance of vertical variations in Culebra properties at this site. The testing at H-19 involved more flow paths (six) and a greater variety of path lengths than at any other MWCF test location at the WIPP.

3.3.1 Experimental Description and Methodologies

The H-11 hydropad comprises four wells (Figure 3-1) which were used for a tracer test conducted in 1988 (see Appendix F and Jones et al., 1992). Details regarding drilling and completion of the wells at the H-11 hydropad can be found in Beauheim and Ruskauff (1998). Prior to the 1996 tracer tests at H-11, a workover rig was used to remove materials that had sloughed into the wells. Twenty-foot (6.1-m) lengths of 4.5-inch (11.4-cm) outside diameter (O.D.) PVC pipe were then set at the bottom of each well below the Culebra to prevent further sloughing.

Seven wells were drilled at the H-19 hydropad (Figure 3-2) in the spring and summer of 1995 using brine- and air-rotary methods (Mercer et al., 1998). The wells were located to allow examination of flow paths in multiple directions and maximize the volume of Culebra that could be tested. Fiberglass casing was cemented in the wells from ground surface to within 3 m of the Culebra, and the Culebra intervals were completed as open holes. The Culebra interval of the central well, H-19b0, was drilled to a diameter of approximately 20 cm and the Culebra intervals of the surrounding wells were drilled to diameters of approximately 15 cm. After all drilling was completed (which was after the preliminary test discussed below), 20-ft (6.1-m) lengths of 5.5-inch (14.0-cm) O.D. PVC pipe were set below the Culebra in all of the wells, except H-19b0, to stop sloughing of clay from the Los Medaños Member of the Rustler into the holes.

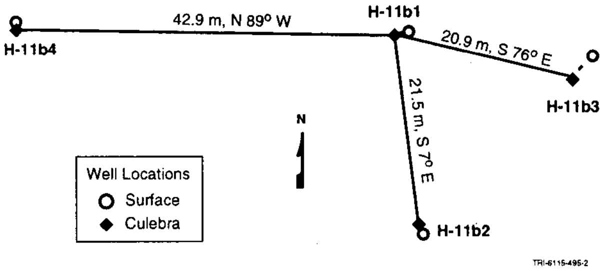

Figure 3-1. Well locations at the H-11 hydropad.

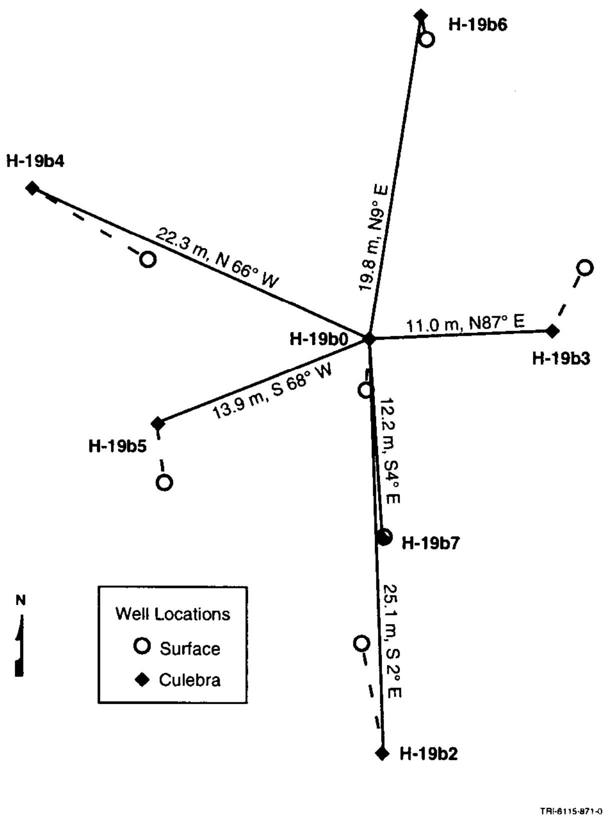

Figure 3-2. Well locations at the H-19 hydropad.

After the first four wells were drilled at the H-19 hydropad (H-19b0, H-19b2, H-19b3, and H-19b4), preliminary SWIW and MWCF tracer tests were conducted (referred to as the H-19 4-well test). The preliminary MWCF test was designed to evaluate transport rates to aid in both siting the locations for the final two wells at the hydropad (H-19b6 and H-19b7) and determining final test design. (The location for H-19b5 was determined independently of the preliminary test results as discussed in Appendix G). The preliminary test also served as a test of equipment. The preliminary tracer test revealed two differences between tracer transport at H-19 and at previous MWCF test sites (i.e., H-3, H-6, and H-11). First, none of the H-19 flow paths showed tracer breakthrough as rapid as that observed along some of the paths at the other hydropads, even though the H-19 well separations are, for the most part, shorter. Second, the rates of mass recovery for two pathways (H-19b2 to H-19b0 and H-19b4 to H-19b0) were much higher than those from the slower pathways in earlier tests at the other hydropads although the peak arrival times were similar. As a result of observing no fast arrivals and slow arrival times with high mass recoveries, the decision was made to drill H-19b6 and H-19b7 much closer to H-19b0 than had been originally planned. See Appendix G for details regarding the original design for the well layout at the H-19 hydropad and a discussion of how the final well locations were selected.

The preliminary test at the H-19 hydropad began on 15 June 1995 and lasted 43 days. This test had two phases, beginning with an SWIW test and ending with an MWCF test. The details of the tests are tabulated in Tables 3-2 and 3-3. The tracer test began with the sequential injection of two tracers followed by a chaser across the full Culebra thickness in H-19b0 for the SWIW test. Following an 18-hr pause, pumping of H-19b0 began. After pumping for approximately three days, the MWCF test was initiated by injecting different distinct tracers across the full Culebra thickness in the three other wells on the hydropad at that time (H-19b2, H-19b3, and H-19b4). The test was conducted at a pumping rate of approximately 0.24 L/s, which created hydraulic gradients ranging from 1.4 to 3.0 meters of fresh water per meter distance along the three pathways tested (Table 3-2).

The final tracer tests at the H-19 hydropad (referred to as the H-19 7-well test) began on 14 December 1995, lasted 121 days, and had four tracer-injection phases: injection for the SWIW test; round 1 of MWCF injections at a high pumping rate; round 2 of MWCF injections at a high pumping rate; and round 3 of MWCF injections at a low pumping rate. The details of each test phase are tabulated in Tables 3-2 and 3-3. The high pumping rate was selected to be slightly below the estimated maximum sustainable rate (about 0.3 L/s). The low pumping rate was selected to be slightly more than half the high pumping rate. The lower rate was selected as a compromise between the desire to maximize the difference in pumping rates and the need to minimize the time to complete the tests. The tracer test began with tracer and chaser (Culebra brine) injection into the lower portion of H-19b0 for the SWIW test, followed by an 18-hr pause before pumping began in H-19b0. After pumping for five days, round 1 of tracer injection was initiated with the injection of

Table 3-2. Tabulated Information on the SWIW Tracer Tests at the H-11 and H-19 Hydropads[1]

Test	Pumping Rate (L/s)	Injection Date	Culebra Interval	Tracer[2]	Tracer Concentration (g/L)	Calculated Aqueous Diffusion Coefficient[3] (m^2/s)	Tracer Injection Rate (L/s)	Injected Tracer Volume (L)	Chaser Injection Rate[4] (L/s)	Injected Chaser Volume[4] (L)	Time to Final Sample (days)	Calculated Mass Recovered (fraction)
H-11 SWIW (H-11b1)	0.22	02/06/96	full	2,4-DCBA	8.07 ± 0.40	7.3×10^{-10}	0.12	996	0.13	1920	50	0.98
				3,4-DFBA	5.02 ± 0.32	8.2×10^{-10}	0.13	1010	0.12	910	50	0.97
H-19 4-well SWIW (H-19b0)	0.24	06/15/95	full	2,4-DCBA	4.94 ± 0.21	7.3×10^{-10}	0.13	997	0.13	2020	32	0.95
				o-TFMBA	1.91 ± 0.04	7.4×10^{-10}	0.13	1005	0.13	1015	32	0.98
H-19 7-well SWIW (H-19b0)	0.27	12/14/95	lower	2,4-DCBA	5.97 ± 0.17	7.3×10^{-10}	0.12	849	0.12	1697	26	0.94

[1] see Appendix B which contains the tracer input parameter spreadsheets (TIPS) for more complete details of each test

[2] 2,4-DCBA = 2,4-dichlorobenzoic acid
3,4-DFBA = 3,4-difluorobenzoic acid
o-TFMBA = ortho-trifluoromethylbenzoic acid

[3] Aqueous diffusion coefficient calculated using Hyduk and Laudie method as described by Tucker and Nelken (1982).

[4] For 6/15/95 and 2/6/96 tests, injection sequence consisted of injection of tracer 1 (2,4-DCBA), followed by tracer 2 (o-TFMBA or 3,4-DFBA), followed by chaser (Culebra brine). For tracer 1 listed above, chaser injection rate and volume are calculated as the rate or volume for injection of both tracer 2 and the chaser fluid.

different distinct tracers into each of the six surrounding wells, with injections over the full Culebra thickness in all wells except H-19b5, into which separate tracers were injected into the upper and lower Culebra. Estimated hydraulic gradients on the H-19 hydropad during this phase of testing ranged from 1.7 to 3.7 meters of fresh water per meter distance (Table 3-2). Approximately 26 days later, round 2 began with the injection of different tracers into the upper and lower Culebra in H-19b3 and H-19b7 and over the full Culebra interval in H-19b5. Hydraulic gradients along these pathways during this phase of testing ranged from 2.8 to 3.5 m/m. After another approximately 32 days, the pumping rate was decreased from 0.25 L/s to 0.16 L/s and tracer injections were repeated (round 3) over the full Culebra thickness in H-19b3, H-19b6, and H-19b7. Hydraulic gradients along these pathways ranged from 1.3 to 2.0 m/m.

The tracer test at the H-11 hydropad began on 6 February 1996, lasted 50 days, and had three injection phases: injection for the SWIW test; round 1 of MWCF injections at a low pumping rate (0.22 L/s); and round 2 of MWCF injections at a high pumping rate (0.38 L/s). Tables 3-2 and 3-3 present details about the injections. H-11b1 served as the pumping well and H-11b2 and H-11b3 were used as injection wells. H-11b4 was not used due to poor tracer resolution (low concentrations near the analytical detection limit) and late peak arrival during the 1988 test (see Jones et al., 1992). Hydraulic gradients from H-11b2 and H-11b3 to H-11b1 were approximately 0.31 and 0.30 meters of fresh water per meter distance, respectively, during round 1, and 0.70 and 0.72 m/m during round 2 (Table 3-2). The H-11 tracer tests were terminated earlier than planned due to equipment problems, and tracers were only injected over the full Culebra interval.

3.3.1.1 Tracer Selection

Five different tracers were used at H-19 during the 4-well test, 16 different tracers were used at H-19 during the 7-well test, and seven different tracers were used at H-11. Fluoro and chlorobenzoic acids were selected as the primary tracers because they behave conservatively and could be chromatographically separated (see Appendices H and I). Batch and field tests conducted using several benzoic acids (Benson and Bowman, 1994; Bowman and Gibbens, 1992; Jones et al., 1992) suggest that many of the fluorobenzoic acids used for the tests at WIPP should behave conservatively in waters, such as those of the Culebra, with low potential for biotransformation and near neutral pH. In

Table 3-3. Tabulated Information on the MWCF Tracer Tests at the WIPP Site[1]

Test	Pumping Rate (L/s)	Path	Average Hydraulic Gradient (m/m)[2]	Injection Date	Tracer[3]	Tracer Concentration (g/L)	Calculated Aqueous Diffusion Coefficient[4] (m^2/s)	Tracer Injection Rate (L/s)	Injected Tracer Volume (L)	Chaser Injection Rate (L/s)	Injected Chaser Volume (L)	Time to Final Sample (days)	Calculated Mass Recovered (fraction)
H-3	0.19	b1-b3		05/09/84	m-TFMBA	13.21	7.4×10^{-10}	0.063	76	0.067	303	33	0.55
		b2-b3		05/09/84	DFBA	26.42	7.7×10^{-10}	0.063	38	0.063	189	33	0.15
H-6	1.04	a-c		08/23/81	m-TFMBA	9.53	7.4×10^{-10}	0.167	100	0.088	100	19	0.20
		b-c		08/23/81	PFBA	8.94	7.7×10^{-10}	0.167	100	0.088	100	19	0.79
				09/02/81	p-FBA	5.69	9.3×10^{-10}	0.128	100	0.128	100	9	0.63
H-11 1998 Test	0.38	b2-b1		05/14/88	PFBA	12.5	7.7×10^{-10}	0.073	189	0.061	188	54	0.53
		b3-b1		05/14/88	m-TFMBA	10.0	7.4×10^{-10}	0.099	189	0.100	373	54	0.77
		b4-b1		05/14/88	o-TFMBA	15.8	7.4×10^{-10}	0.131	189	0.080	187	54	0.29
H-11 1996 Round 1	0.22	b2-b1	0.31	02/15/96	2,6-DFBA	10.38 ± 0.05	8.2×10^{-10}	0.068	189	0.060	213	41	0.40
		b3-b1	0.30	02/15/96	2,3,4,5-TFBA	10.85 ± 0.24	7.9×10^{-10}	0.096	189	0.098	372	41	0.74
H-11 1996 Round 2	0.38	b2-b1	0.70	03/14/96	p-TFMBA	10.78 ± 0.11	7.4×10^{-10}	0.072	189	0.062	213	13	0.21
		b3-b1	0.72	03/13/96	2,5-DFBA	10.30 ± 0.15	8.2×10^{-10}	0.095	190	0.097	373	14	0.56
					NaI	10.87 ± 0.03	18.0×10^{-10}					14	0.53
H-19 1995 (Preliminary 4-Well Test)	0.24	b2-b0	1.4	06/19/95	2,3-DFBA	7.30 ± 0.34	8.2×10^{-10}	0.11	246	0.11	246	37	0.54
		b3-b0	3.0	06/20/95	2,3,4,5-TFBA	7.77 ± 0.27	7.9×10^{-10}	0.15	259	0.14	206	37	0.69
		b4-b0	1.6	06/19/95	2,6-DFBA	7.06 ± 0.58	8.2×10^{-10}	0.13	265	0.11	255	37	0.41
H-19 1995-96 (7-Well Test) Round 1	0.27	b2-b0	1.7	12/22/95	2,3,4-TFBA	8.18 ± 0.25	8.0×10^{-10}	0.13	202	0.15	154	104	0.88
		b3-b0	3.7	12/22/95	m-TFMBA	9.52 ± 0.51	7.4×10^{-10}	0.18	198	0.23	173	104	0.88
					NaI	12.71	18.0×10^{-10}					63	0.80
		b4-b0	2.1	12/22/95	3,5-DFBA	8.46 ± 1.95	8.2×10^{-10}	0.12	198	0.12	143	104	0.84
		b5(u)-b0	3.0	12/20/95	2,3-DCBA	11.45 ± 0.31	7.3×10^{-10}	0.015	147	0.010	105	106	0.18
		b5(l)-b0	3.0	12/20/95	2,5-DCBA	13.49 ± 1.26	7.3×10^{-10}	0.011	149	0.009	65	106	0.84
		b6-b0	2.3	12/21/95	2,5-DFBA	9.49 ± 0.13	8.2×10^{-10}	0.12	199	0.12	154	106	0.88
		b7-b0	3.3	12/21/95	2,4-DFBA	7.58 ± 0.53	8.2×10^{-10}	0.21	198	0.22	168	105	1.03
H-19 1995-96 (7-well Test) Round 2	0.25	b3(u)-b0	3.5	01/19/96	p-TFMBA	14.13 ± 0.32	7.4×10^{-10}	0.016	132	0.015	69	82	0.13
		b3(l)-b0	3.4	01/19/96	o-TFMBA	9.69 ± 0.25	7.4×10^{-10}	0.028	198	0.033	143	82	0.89
		b5-b0	2.8	01/19/96	2,4-DCBA	9.85 ± 0.66	7.3×10^{-10}	0.19	199	0.17	169	82	0.83
		b7(u)-b0	3.0	01/20/96	PFBA	14.51 ± 0.10	7.7×10^{-10}	0.008	131	0.010	64	81	0.05
		b7(l)-b0	3.1	01/20/96	3,5-DCBA	7.67 ± 0.41	7.3×10^{-10}	0.016	197	0.015	139	81	0.90
H-19 1995-96 (7-well Test) Round 3	0.16	b3-b0	2.0	02/22/96	2,34,5-TFBA	9.95 ± 0.34	7.9×10^{-10}	0.100	198	0.12	173	48	0.80
		b6-b0	1.3	02/22/96	2,4,6-TCBA	9.87 ± 0.35	6.8×10^{-10}	0.070	197	0.068	168	48	0.74
		b7-b0	1.8	02/22/96	2,3,6-TFBA	9.54 ± 0.27	8.0×10^{-10}	0.12	199	0.12	168	48	0.91
					NaI	HPLC 10.54 ± 0.11	18.0×10^{-10}					47	0.86
						IC 10.68 ± 1.50						48	0.88

[1] see Appendix B which contains the tracer input parameter spreadsheets (TIPS) for more complete details of each test

[2] meters of fresh water per meter distance

[3] x,y-DFBA = x,y-difluorobenzoic acid (e.g., 2,6-DFBA = 2,6-difluorobenzoic acid)
2,3,4,5-TFBA = 2,3,4,5-tetrafluorobenzoic acid
m-, o-, or p-TFMBA = meta-, ortho-, or para-trifluoromethylbenzoic acid
NaI = sodium iodide
x,y,z-TFBA = x,y,z-trifluorobenzoic acid
x,y-DCBA = x,y-dichlorobenzoic acid
PFBA = pentafluorobenzoic acid
2,4,6-TCBA = 2,4,6-trichlorobenzoic acid
HPLC = high-performance liquid chromatography
IC = ion chromatography

[4] aqueous diffusion coefficients calculated using Hyduk and Laudie method as described by Tucker and Nelken (1982)

conjunction with the 1995-96 field tracer tests, a series of batch tests was conducted for all of the chloro and fluorobenzoic acids used in the H-11 and H-19 tests with crushed Culebra sediment. These tests showed no apparent sorption of the benzoic acids to Culebra sediments over a 90-day period (Appendix H). Natural background concentrations of the benzoic acids in Culebra brines were below detection limits (0.01 to 0.05 mg/L).

For two of the injections during the H-19 7-well test and one injection during the H-11 test, iodide, in the form of sodium iodide, was injected in addition to the benzoic-acid tracer. Iodide was selected because it has a higher aqueous diffusion coefficient than the benzoic acids and has been shown to behave conservatively in many environments (Davis et al., 1980; Meigs and Bahr, 1995). Iodide also was selected because it has a relatively low background concentration in the Culebra (less than 0.1 mg/L). Bromide or chloride could not be used as tracers because their background concentrations in Culebra brine are too high.

3.3.1.2 Tracer Mixing and Injection

Culebra brine pumped from the hydropad or a nearby well prior to the tracer test was used to mix the tracer solution and as the chaser fluid. Tracer solutions were mixed in 300-gallon (1,135-L) polyethylene containers equipped with circulation systems used to ensure uniform tracer concentration during injection. For most of the MWCF test injections, approximately 200 L of a nominally 10-g/L solution were used (see Table 3-3 for exact volumes and concentrations). Based on past tests, we estimated that a 2-kg mass of tracer was needed for adequate breakthrough-curve definition (i.e., peak concentrations between 2 and 10 mg/L and significant breakthrough-curve tails before concentrations dropped below detection). Chaser-solution volumes for the MWCF tests were selected to be approximately two to three times the borehole volume to flush tracer from the borehole. For the SWIW tests, larger masses of tracer were used (at lower concentrations) to provide recovery concentrations ranging over several orders of magnitude (see Table 3-2). For two of the SWIW tests, approximately 1,000-L volumes of each of the two tracers and chaser were used so as to be similar to SWIW design calculations by Tsang (1995). For the second SWIW test at H-19, only 850 L of tracer solution followed by 1,700 L of chaser solution were injected into the lower portion of the Culebra.

For all tests, tracer solutions were injected using a centrifugal magnetic-drive pump to deliver the tracer and chaser solutions from mixing and holding tanks to the wells. Injection rates were constant within ±5% in most cases. The tracer-distribution and pumping assemblies used in H-19b0 and H-11b1 for the SWIW and MWCF tests are shown in Figures D-1, D-2, and D-4. Tracer injection for the SWIW tests was performed by pumping tracer and chaser downhole through 1.27-cm polyethylene tubing at rates of 0.12 to 0.13 L/s (Table 3-2). An injection manifold at the top of each injection assembly split the tracer solution into four smaller tubes, through which the tracer was injected at different depths and different radial positions within the Culebra. For the H-11 and preliminary H-19 SWIW tests, tracers were injected over the full thickness of the Culebra. For the final H-19 SWIW test, tracers were injected only into the lower Culebra. Packers were positioned above the top of the Culebra to provide isolation during tracer injection and pumping. During the final H-19 SWIW test, additional packers were set at the base of CU-1 and below the Culebra in H-19b0. The packer at the base of CU-1 was deflated after tracer injection was completed and pumping for tracer recovery had begun.

The tracer-injection tools used in H-19b2, H-19b3, and H-19b4 for the H-19 4-well test were the tools previously used during the 1988 tracer test at H-11. Those tools consisted of 10.2-cm tubing with four 1.9-cm perforations every 61 cm (Figure D-1). The tracer-injection tools for the H-19 7-well test injections into H-19b2, H-19b4, and H-19b6 (full Culebra injections) and the H-11 injections were constructed to a different design (Figures D-3 and D-4). For these tools, tracer (and chaser) were delivered to the injection manifold through a single tube and then split into four sets of injection ports. Injection-port sizes were carefully graded (larger at the bottom than at the top) to provide relatively uniform delivery of tracer to the formation. At each of the three wells closest to H-19b0 (H-19b3, H-19b5, and H-19b7), tools with two injection assemblies were used during the H-19 7-well test (Figure D-2). Those tools included a middle packer that could be inflated to allow distinct tracer injection into the upper and lower portions of the Culebra. With the packer deflated, a single tracer could be injected through both injection assemblies simultaneously.

For all tests, packers were positioned above the top of the Culebra to provide isolation during tracer injection and pumping. During the 7-well test, all H-19 boreholes were equipped with another packer at or near the base of the Culebra (Figures D-2 and D-3). At H-11, packers could not be placed at the base of the Culebra due to sloughing of the boreholes. Pressures were monitored in all wells during both H-19 tests and the H-11 test. Each borehole was equipped with at least one test-zone pressure transmitter and one annulus transmitter. Plots of measured pressures during the tests can be found in Appendix D.

3.3.1.3 Sample Collection and Analysis

At each hydropad, tracer testing began with injection into the pumping well for the SWIW test, followed by an 18-hr pause after which pumping was initiated. Pumping-rate fluctuations were minor and did not significantly affect the tracer data. Appendix D contains plots of the pumping-rate data collected by the data-acquisition system (DAS) and calculated from totalizer and standpipe measurements. Also shown on the plots are the average pumping rates calculated for each test segment (e.g., SWIW, MWCF round 1, MWCF round 2, etc.). After pumping began, 60-mL samples were collected in duplicate from a port on the discharge line at the surface. Sampling frequency varied from minutes to once a day over the duration of the tests. Many more samples were collected than were analyzed to ensure that adequate samples were available as needed to define the tracer-recovery and -breakthrough curves. Samples also were collected from the tracer-mixing tanks during injection.

Samples were analyzed for benzoic acids by reverse-phase high-performance liquid chromatography (HPLC) with ultraviolet adsorption detection, and for iodide using an ion chromatograph (IC) with an ampterometric detector or by HPLC. To measure low concentrations of the benzoic acids and iodide in the Culebra brine, new analysis methodologies were developed (see Appendix I). To evaluate analytical precision, numerous duplicate samples, including blind duplicates, were analyzed. Data from duplicate sample analyses were used to calculate 95% confidence intervals for each data set (see Appendix C). A time correction was made for all the tracer data to reflect relative time in the Culebra since the start of injection. This correction included subtracting the time for the tracer solution to flow down the tubing in the injection borehole (the approximately 230 m to the Culebra) and back up the tubing in the pumping well to the sampling port (most times were corrected by between 30 and 90 minutes).

3.3.2 Tracer Data Observations and Discussion

The tracer-concentration data derived from analysis of the samples collected are presented in graphical format (recovery and breakthrough curves) and discussed in the following sections.

3.3.2.1 SWIW Test Results

Figure 3-3 shows the tracer-recovery curves and the 95% confidence intervals (lines bounding the data) for the three SWIW tests. The concentration data have been normalized by the concentrations of the injectate solutions as listed in Table 3-2. The times are relative to the time since the start of injection of the first tracer. In Figure 3-3a, the data for both the first and second tracers injected into H-11b1 are shown. Figure 3-3b shows the data from both the H-19 4-well SWIW test (SWIW1), which was nearly identical to the H-11 SWIW test in design, and the H-19 7-well SWIW test (SWIW2) for which tracer was only injected into the lower portion of the Culebra. The periods of time for which data are presented are, in part, functions of the injectate concentrations (Table 3-2). For example, the data set for tracer 2 terminates sooner than that for tracer 1 at H-19 in part because the concentration falls below the minimum detection limit earlier. For all data sets, if multiple samples were analyzed for a given sampling time, the average value is plotted. The lack of significant data scatter and the tightness of the confidence intervals demonstrate the high precision of these analyses.

The late-time (≥100 hr) log-log slopes of the data plotted in Figure 3-3 vary between approximately -2 and -2.8. These are much lower slopes than those predicted by Tsang (1995) for single-porosity (fractured), heterogeneous media with no diffusion. However, the slopes of all five data sets are steeper than the -1.5 late-time log-log slope predicted by conventional double-porosity models (Tsang, 1995; Hadermann and Heer, 1996; Appendix K). The similarity in the late-time slopes of all five data sets suggests that a similar process is controlling the gradual mass recovery at both hydropads. Additional discussion of this point is presented in Chapter 6.

Figure 3-4 shows the normalized cumulative mass recoveries for the first tracers at the H-11 and H-19 hydropads. The mass recoveries are gradual, as would be expected in simulations of an SWIW test in a double-porosity medium (Tsang, 1995; Chapter 6). For each tracer used in the SWIW tests, Appendix C contains a series of six diagrams showing the tracer data plotted in various ways.

3.3.2.2 MWCF Test Results

The following paragraphs address the MWCF tracer-test results for the testing at the H-11 and H-19 hydropads in 1995 and 1996. Results for the earlier testing at H-3, H-6, and H-11 can be found in Appendix F. Appendix C contains a series of six diagrams showing observed tracer data plotted in various ways for all of the MWCF tests, and a table showing several calculations made on the observed data (e.g., time to 50% mass recovery, volume pumped at the time of the peak concentration, etc.).

Figure 3-5 shows the results of the MWCF test at the H-11 hydropad. As was seen in the test conducted in 1988 (Jones et al., 1992; Appendix F), the breakthrough curves for the H-11b2 to H-11b1 and H-11b3 to H-11b1 pathways differ

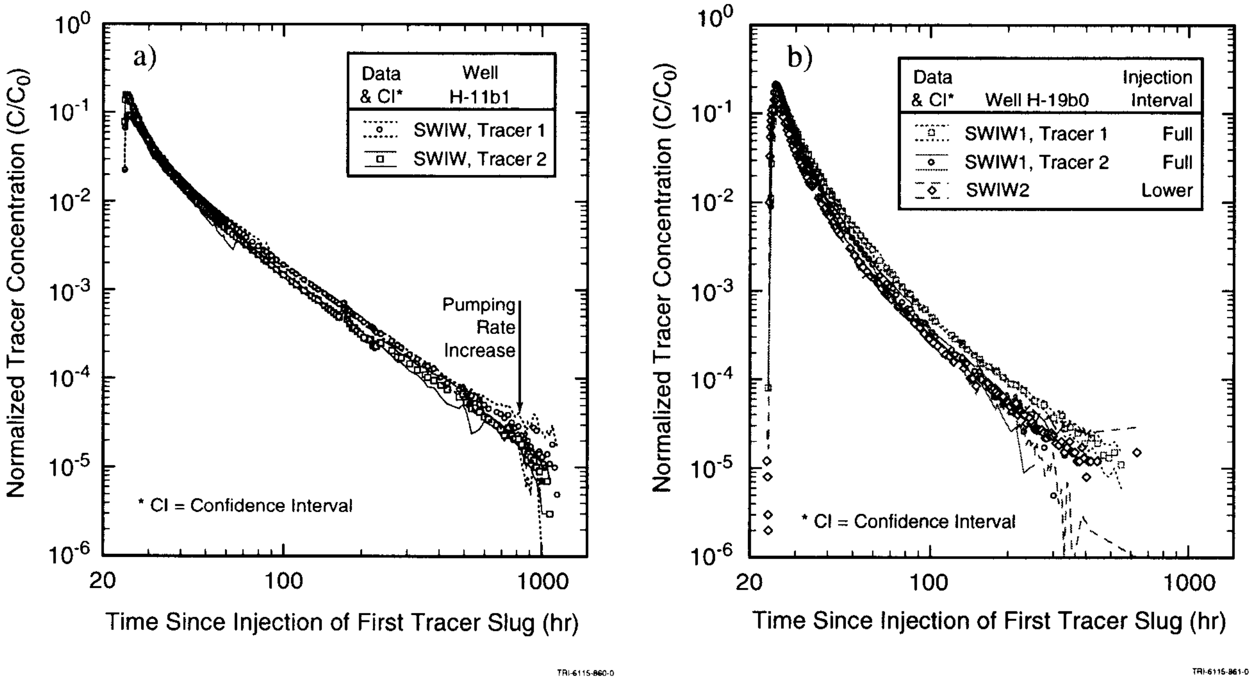

Figure 3-3. SWIW tracer-recovery curves from (a) one test at the H-11 hydropad and (b) two tests at the H-19 hydropad.

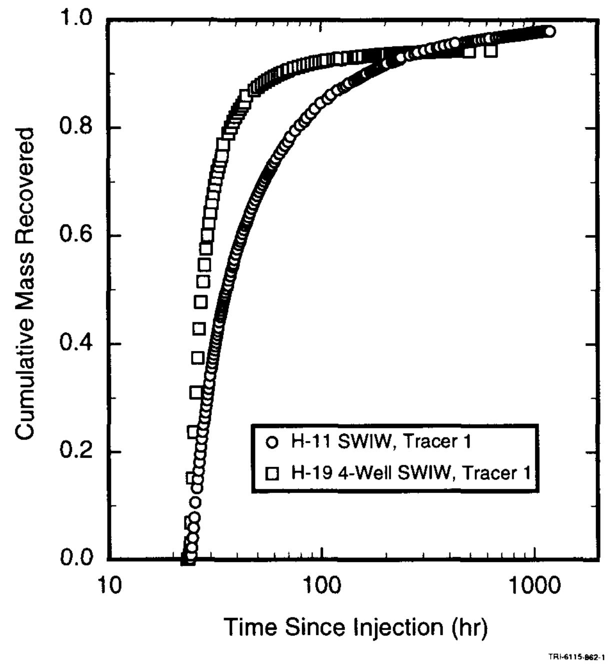

Figure 3-4. **Normalized cumulative mass recovered for the first tracer from the SWIW tests at the H-11 and H-19 hydropads.**

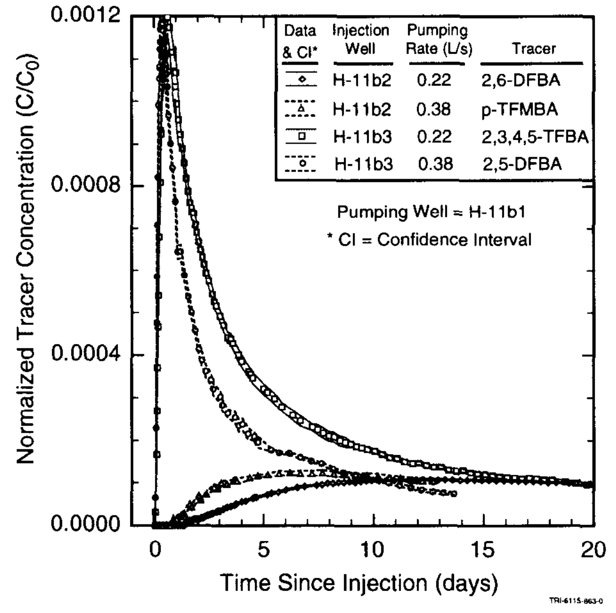

Figure 3-5. **MWCF tracer-breakthrough curves from the H-11 hydropad.**

dramatically, even though the well separations are approximately the same length. For the lower pumping rate (0.22 L/s), the peak concentration arrives about 20 times faster (0.65 days compared to 12.2 days) and is about 10 times higher for the H-11b3 to H-11b1 path compared to the H-11b2 to H-11b1 path. Similar dramatic differences in breakthrough curves for different pathways of similar lengths were seen for previous MWCF tracer tests conducted at the H-3 and H-6 hydropads (Jones et al., 1992, Appendix F). For both pathways at the H-11 hydropad, the peak concentrations are approximately the same for both pumping rates. Based on pretest simulations, we expected that the data for the lower pumping rate would have a lower peak height resulting from more time for matrix diffusion (See Section P.5).

Figure 3-6 shows the results of the H-19 4-well MWCF test. These results differ from the results obtained from tests conducted at the H-3, H-6, and H-11 hydropads in that the H-19 breakthrough curves showed no rapid transport path similar to those observed at the other three hydropads. Figure 3-7 shows a plot of the cumulative mass recovered versus the volume pumped divided by the radius (well separation) squared for the three H-19 flow paths and the flow paths from the earlier tests at H-3, H-6, and H-11. Dividing the volume pumped by the radius squared provides a measure similar to pore volumes pumped, assuming that the porosity is the same at all four hydropads, which allows easier comparison of tracer recoveries from flow paths of different lengths. Plotted in this way, we see that larger proportionate volumes had to be pumped to get initial tracer recovery for all three H-19 flow paths than for all of the flow paths at the other hydropads except for the slow H-6a to H-6c flow path. This could indicate higher porosity at H-19 than at the other hydropads. Once tracer recovery began at H-19, mass was recovered faster than along many of the flow paths at the other hydropads. This might reflect less matrix diffusion along the H-19 flow paths than along those other flow paths.

Figure 3-8 shows the results of the tracer injections over the full thickness of Culebra for the 7-well MWCF test at the H-19 hydropad for the high pumping rate, revealing significant differences in

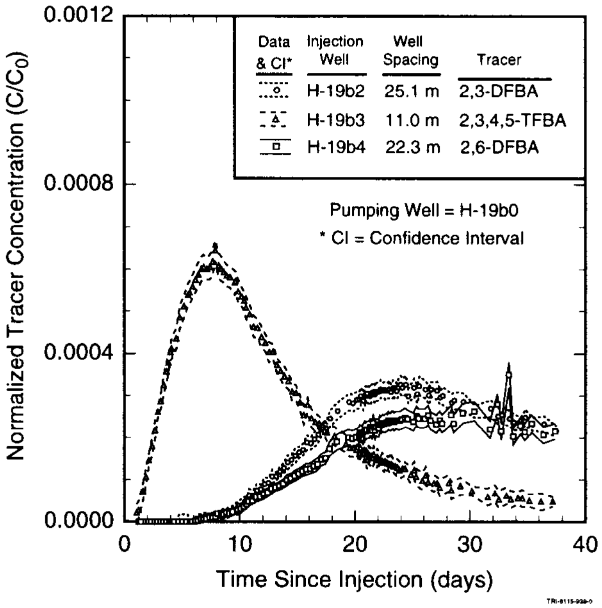

Figure 3-6. **MWCF tracer-breakthrough curves for the 4-well test at the H-19 hydropad.**

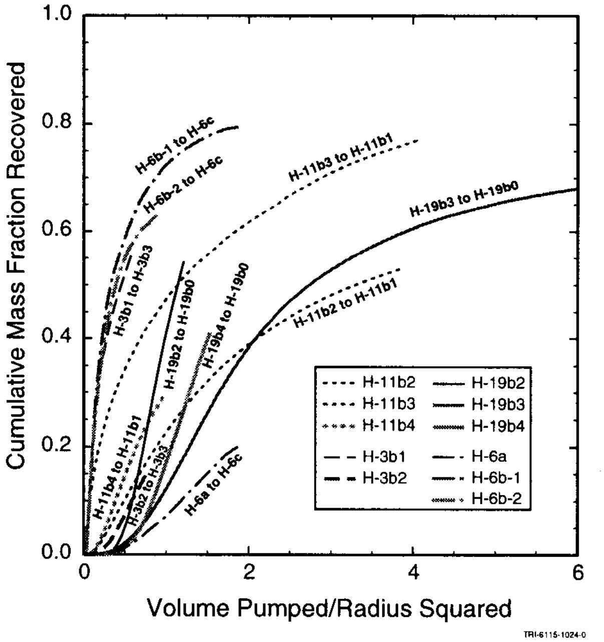

Figure 3-7. **Cumulative mass recovered versus volume pumped per radius squared for the H-19 4-well test and the early tests conducted at H-3, H-6, and H-11.**

the breakthrough curves that cannot be accounted for by the differences in path lengths alone. For example, the fastest peak-arrival time is not from the shortest travel distance and the slowest time for peak arrival is not from the longest travel distance. At H-19, the differences between peak arrival times for different pathways of similar lengths are much less dramatic than those found at the H-3, H-6, and H-11 hydropads (compare Figure 3-8 to Figure 3-5 and Figures C-32 to C-39 in Appendix C), suggesting that the Culebra is less heterogeneous (and/or less anisotropic) at the H-19 hydropad. No pathways were found at the H-19 hydropad with tracer breakthroughs as rapid as those observed at the H-3, H-6, and H-11 hydropads. Given that only two to three pathways were tested at the H-3, H-6, and H-11 hydropads and that six pathways were tested at the H-19 hydropad, the H-19 hydropad apparently lacks the rapid transport pathways found at the other three hydropads.

Figure 3-9 compares the breakthrough curves for the three H-19 pathways where tracer injections were repeated while pumping at two different rates. For each pathway, the differences in peak height are not significant when comparing the 95% confidence intervals for the analyses. As with the H-11 peak heights, this behavior is not what we had expected based on simulations with a conventional double-porosity medium with a single diffusion rate.

Figure 3-10 shows a comparison of the benzoic-acid data and the iodide data for the three pathways for which the pairs of tracers were injected during the H-11 and H-19 tests. A lower peak height for the iodide data would be expected if diffusion is an important process because the estimated aqueous diffusion coefficient for iodide is about two to three times that of the benzoic acids (Table 3-3). For both the H-19b3 to H-19b0 and H-19b7 to H-19b0 pathways, the iodide data show significant scatter due to difficulties analyzing iodide in brine (Figure 3-10b). Comparisons of the 95% confidence intervals for the H-19 data leave us uncertain whether the iodide and benzoic-acid breakthrough curves are essentially the same or whether the iodide data have a slightly lower peak height. The quality of the iodide data from the

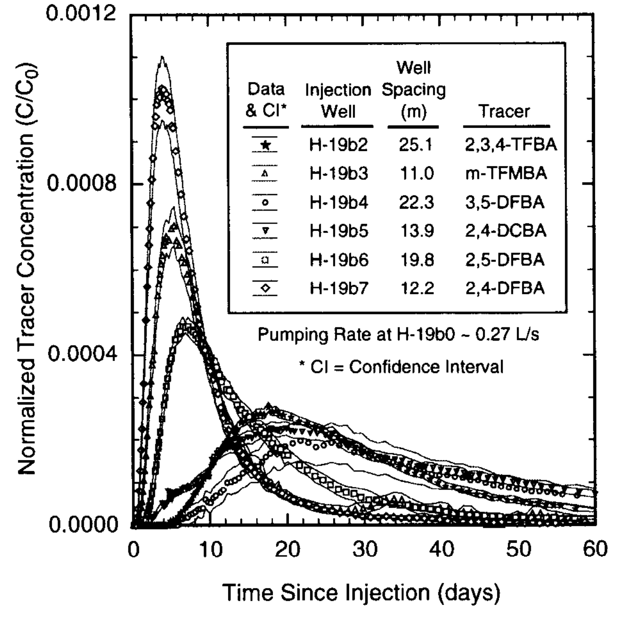

Figure 3-8. **MWCF tracer-breakthrough curves from full-thickness injections for the high-pumping-rate H-19 hydropad data.**

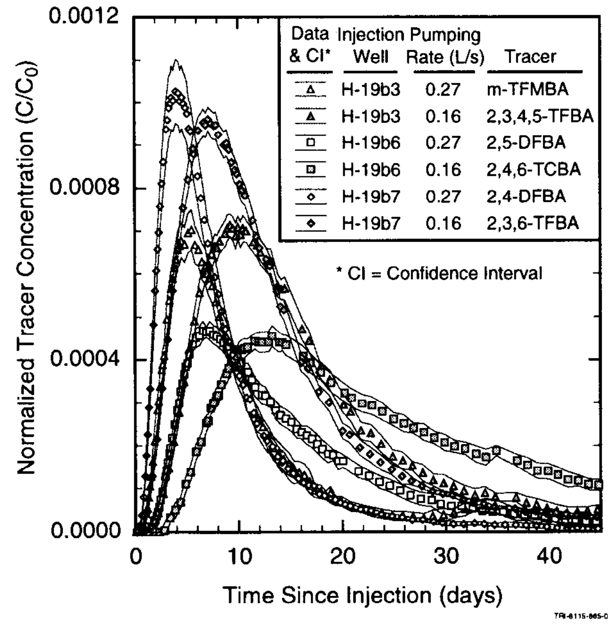

Figure 3-9. **Comparison of MWCF breakthrough curves for tracer injections repeated for two different pumping rates.**

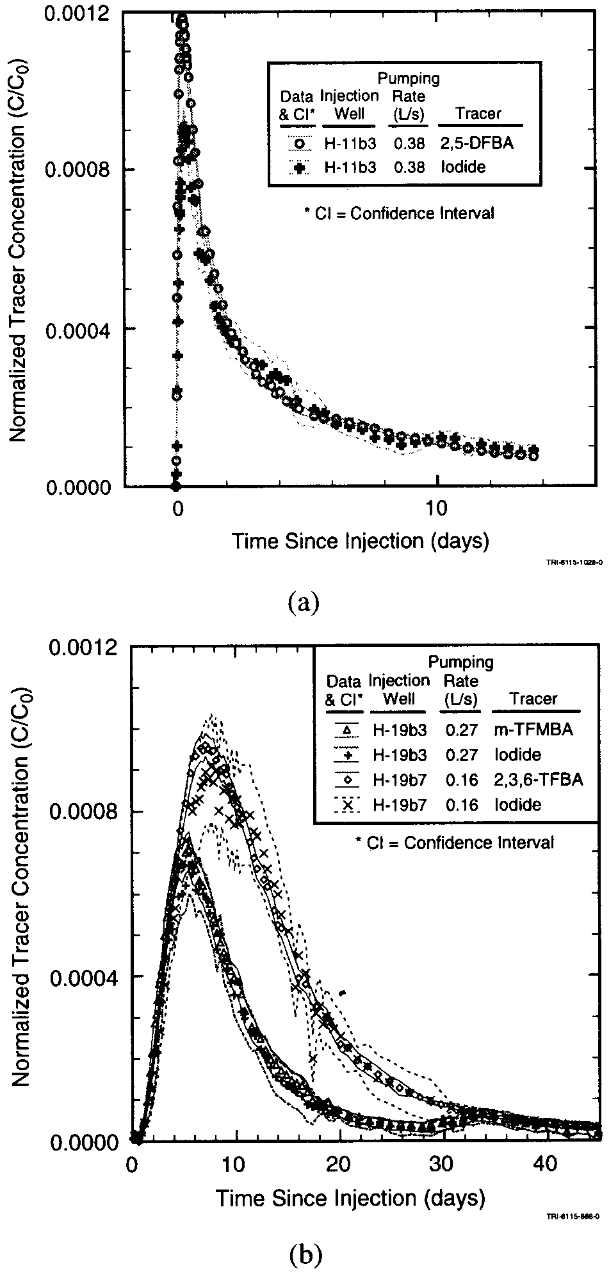

Figure 3-10. **Comparison of benzoic-acid and iodide data for (a) one pathway at H-11 and (b) two pathways at H-19.**

H-11 hydropad is better due to analysis-method refinements, and the peak height of the iodide data is clearly lower than the peak height of the benzoic-acid data (Figure 3-10a).

For three pathways at the H-19 hydropad, tracers were injected into packed-off intervals of both the upper and lower Culebra during the 7-well test.

The injections into the upper Culebra (CU-1) resulted in very little mass produced at the pumping well (Figure 3-11, Table 3-3). This suggests that the low permeability of the upper Culebra results in extremely slow transport. The injections into the lower Culebra (CU-2 to 4) produced breakthrough curves quite similar to those from the full-thickness injections (Figure 3-8). These results suggest that most of the transport of injected tracers is occurring in the lower portion of the Culebra at H-19.

Figure 3-12 shows almost all of the MWCF benzoic-acid tracer data for both the H-11 and H-19 tests. Figure 3-12a contains data from both the 1988 and 1996 tests at the H-11 hydropad (see Appendix F for details on the 1988 test). Data from tracers injected into the upper Culebra are not included in Figure 3-12b for clarity. The normalized-concentration data are plotted versus matrix pore volumes pumped rather than time to facilitate comparison of tracer recoveries from flowpaths of different lengths. The matrix pore volumes pumped at any time is defined as the cumulative volume pumped since start of injection divided by the pore volume of a cylinder with a radius equal to the separation between the tracer-injection well and the pumping well, a thickness of7.4 m, and a porosity of 0.15. Given that tracer is initially distributed in a cylindrical shell around each injection well rather than as a line source, this definition of matrix pore volumes pumped is not rigorously correct. However, it provides a useful metric for comparison of different breakthrough curves.

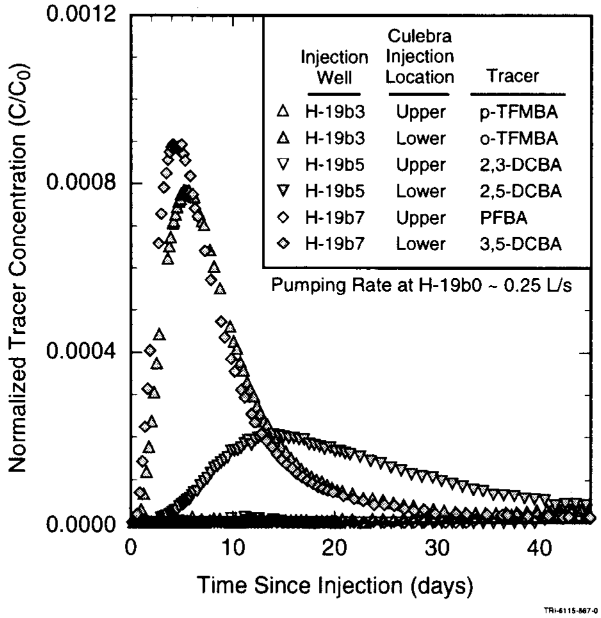

Figure 3-11. Comparison of injections into the upper and lower Culebra at the H-19 hydropad.

From Figure 3-12, we see strong similarities among repeated injections along the same pathways, even when the pumping rates differ. This repeatability of experimental results provides confidence in the measurements, but also indicates that less-than-twofold differences in pumping rates have little effect on the observed tracer behavior.

All of the tracer-breakthrough curves presented in Figure 3-12 show tracers arriving at the pumping well and reaching their peak concentrations long before even a single matrix pore volume has been pumped. These fast arrivals demonstrate that advection cannot be occurring through the entire matrix pore volume, as defined. Advection must be concentrated in a lower percentage of the porosity and/or a lower percentage of the total Culebra thickness.

At each hydropad, the fastest pathways are those for which the fewest matrix pore volumes are pumped before peak concentration is reached. From Figure 3-12a, we see that the H-11b3 to H-11b1 pathway is much faster than the H-11b4 to H-11b1 pathway, even though their azimuths differ by only 13°, and that the H-11b2 to H-11b1 pathway is the slowest. At the H-19 hydropad, the H-19b6 to H-19b0 pathway appears to be the fastest, followed by the H-19b7 and H-19b2 to H-19b0 pathways. These pathways have nearly north-south orientations, with azimuths differing by 2° to 13°. The H-19b3 and H-19b4 to H-19b0 pathways are slower and appear to be nearly equivalent. The H-19b5 to H-19b0 is the slowest pathway on the hydropad. At H-19, faster pathways do not always have higher peaks than slower pathways because the well separations and time to peak are sometimes longer, allowing more dilution and diffusion than occurs along some of the slower pathways (compare H-19b6 data to H-19b7 data in Figure 3-12b). For those pathways that require approximately the same number of matrix

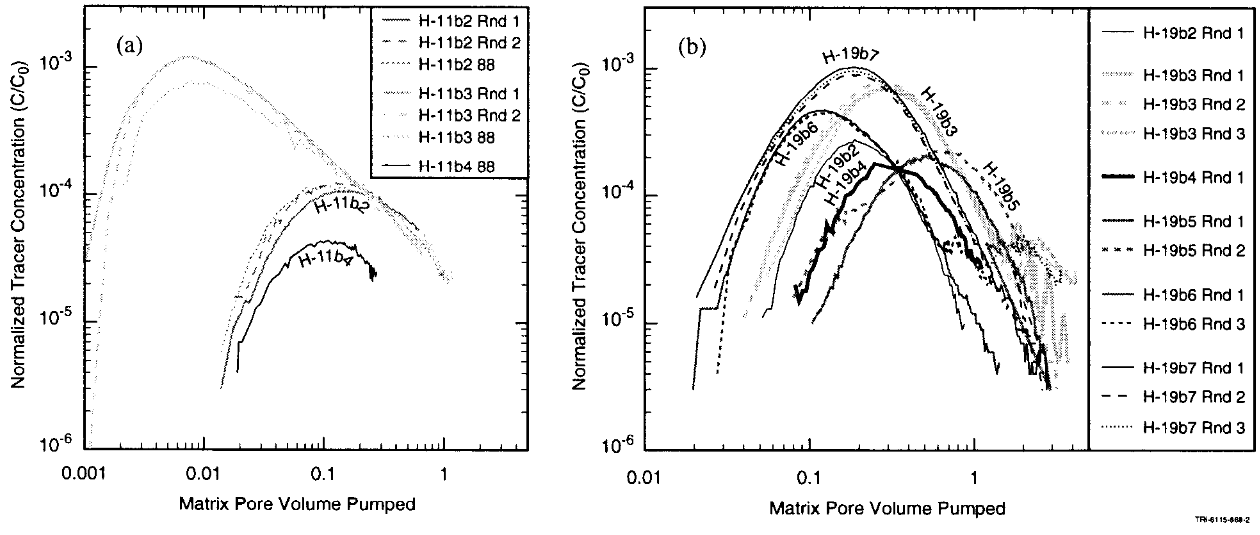

Figure 3-12. Comparison of MWCF data from all pathways.

pore volumes pumped to reach peak concentrations, the longer pathways always have lower peaks, consistent with increased dilution and diffusion (compare H-19b7 data to H-19b2 data and H-19b3 data to H-19b4 data in Figure 3-12b.)

Only the fastest pathway on the H-19 hydropad (H-19b6 to H-19b0) was nearly equivalent to the slowest pathway on the H-11 hydropad (H-11b2 to H-11b1) in terms of matrix pore volumes pumped to reach peak concentration. All other H-19 pathways were slower than the slowest H-11 pathway. This observation could be explained by lower advective porosity at H-11 than at H-19. The shapes and late-time slopes of the breakthrough curves at the two hydropads are also quite different. The H-11 breakthrough curves tend to be more asymmetric than the H-19 curves, reflecting greater tailing. The late-time slopes of the H-19 breakthrough curves are much steeper than the late-time slopes of the H-11 curves. These observations are consistent with tracers being released more slowly from the matrix through diffusion at H-11 than at H-19, perhaps reflecting larger matrix blocks at H-11.

3.3.2.3 Calculation of Advective Porosity

In order to compare tracer-test data from different pathways and different hydropads, a simple analytic expression was used to provide an initial rough estimate of the advective porosity. Based on the theoretical direct plug-flow travel time between the injection well and the pumping well in an MWCF tracer test, and assuming no diffusive interaction between the advective and diffusive porosities present, the advective porosity, ϕ_A, for a given MWCF pathway was calculated using the relationship:

$$\phi_A = \frac{Qt_p}{\pi r^2 b} \qquad (3\text{-}1)$$

where Q is the pumping rate, t_p is the peak arrival time, r is the distance between the injection and pumping wells, and b is the thickness of the permeable medium. This relationship was used to calculate an advective-porosity value for each breakthrough curve from the recent tests (see Tables C-1 and C-2 in Appendix C). The results are plotted in Figure 3-13 as advective porosity versus cumulative normalized mass recovered at the time of peak concentration. For comparison purposes, advective porosities calculated from the results of the early tracer tests at the H-3, H-6, and H-11 hydropads (see Appendix F) are also included on the figure.

Figure 3-13 reveals that the H-19 data plot as a group distinct from the data from the other hydropads. All of the H-19 data sets (injections into the upper Culebra are not included) have greater than 15% mass recovered at the time of peak concentration. All of the calculated advective porosities

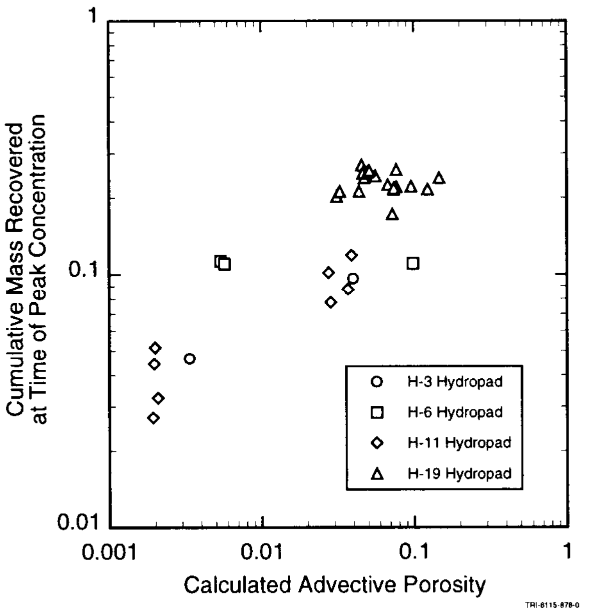

Figure 3-13. Cumulative mass recovered at time of breakthrough-curve peak and calculated advective porosity.

are relatively high, between 0.03 and 0.16. The data from the three other hydropads fall into two distinct groups. One group has low advective porosity, between 0.002 and 0.005, and very low mass recovery (less than 12%) at the time of peak concentration. This group represents the pathways at these hydropads that had the most rapid tracer breakthrough (e.g., the H-11b3 to H-11b1 pathway). The second group has a calculated porosity range between 0.03 and 0.10, which is similar to a portion of the H-19 data, but the mass recovery is always less than 13% at the time of peak concentration. The lower mass recovery at the H-3, H-6, and H-11 hydropads suggests that some process, possibly matrix diffusion, is causing more mass to be lost from the advective pathways.

The advective porosity estimated with Equation 3-1 provides a very rough estimate of the porosity needed to fit the peak arrival time of the data with an isotropic, homogeneous or heterogeneous single-porosity model. Such an estimate can be in error for a variety of reasons. Anisotropy in horizontal hydraulic conductivity could, depending on the orientation of the flow path, cause the estimate to be either too high or too low. Flow channeling in a heterogeneous hydraulic-conductivity field can effectively increase the porosity required to match the peak arrival time (e.g., Moreno and Tsang, 1994). Heterogeneity can also decrease the required porosity by creating a more tortuous flow pathway (i.e., increasing the value of r in Equation 3-1).

The calculated porosity also provides an upper bound on the value that could be used to fit the data with an isotropic, homogeneous, double-porosity model. In a double-porosity model, diffusion into the matrix (non-advective porosity) retards transport, which results in the need to decrease the advective porosity from the value calculated for a single-porosity model in order to match the peak-arrival time of the data.

Based on these plug-flow calculations and numerical simulations of the data (see Chapters 5 and 7), significant variations may exist in the proportions of advective transport occurring in the different types of Culebra porosity. The contrast in transmissivity between H-11 and H-19 may provide some insight into these differences. For rapid-transport pathways, such as from H-11b3 to H-11b1, advection may be concentrated in fractures with a permeability significantly higher than that of the rock matrix. At lower transmissivity locations where peak-arrival times are longer (e.g., H-19), less of a permeability contrast may exist between the fractures and a portion of the matrix. As a result, significant advection may be occurring not just in fractures, but also in relatively high-permeability portions of the matrix such as vugs connected by microfractures or poorly cemented zones with high interparticle porosity (see Figure 2-2).

3.4 Summary and Preliminary Evaluation of Conceptual Model

The series of tracer tests performed at the H-11 and H-19 hydropads in 1995 and 1996 met the goal of producing a detailed and accurate data base to evaluate advective and diffusive transport processes in the fractured portions of the Culebra. The lack of significant data scatter and the tight 95% confidence intervals on most data sets demonstrate the high quality of the tracer analyses.

The data from the three SWIW tests show gradual mass recovery as would be anticipated if matrix diffusion is the dominant process. The late-time slope of the data on a log-log plot is lower than was predicted by Tsang (1995) for a highly heterogeneous single-porosity (fractures only) system but is higher than the -1.5 log-log slope predicted by conventional double-porosity models with a single rate of diffusion.

The breakthrough curves from the MWCF tests at the H-11 and H-19 hydropads are quite different, but curves from both sites show gradual mass recovery as would be expected with matrix diffusion. However, the similar peak heights for the breakthrough curves for two different pumping rates cannot be explained with a conventional double-porosity conceptualization. The results of the injection of tracers at H-19 with two different aqueous diffusion coefficients are somewhat ambiguous, in part due to the poor quality of the iodide data. The H-11 iodide data have a lower peak height than the benzoic-acid data, which is consistent with a double-porosity conceptualization. The extremely low mass recoveries for all tracers injected into the upper portion of the Culebra at H-19 indicate that most tracer transport takes place in the lower Culebra. This is consistent with available hydraulic data.

Tracer-transport behavior at the H-19 hydropad differs from that at the H-3, H-6, and H-11 hydropads. The tracer-test results for the latter three hydropads can be characterized by one rapid transport path with a rapid rate of mass recovery and one or more slow transport path(s) with a very slow rate of mass recovery. At the H-19 hydropad, however, differences in the mass-recovery rates for the different flow paths exist but are small. In general, the rate of mass recovery, once tracer breaks through, for all paths at the H-19 hydropad is faster, or just as fast, as the fastest rate at the other three hydropads. This indicates a difference in the transport mechanisms at the H-19 hydropad compared to those at H-3, H-6, and H-11. This difference may be due to significant advection occurring in relatively high-permeability portions of the matrix at the H-19 hydropad, such as vugs connected by microfractures or poorly cemented zones with high interparticle porosity, while advection is concentrated in fractures at the other three hydropads. Given that some samples of Culebra matrix materials from H-19 were found to have relatively high permeabilities, the permeability contrast between the fractures and the matrix is likely small enough at some locations to result in advection in more than just connected fractures. This hypothesis is consistent with the advective porosities calculated for the H-19 flow paths which, ranging from 3 to 16%, are too high to be representative of fractures alone.

The complexity of the tracer-test results suggests that the conventional double-porosity conceptual model for transport in the Culebra used to explain past tests (Jones et al., 1992) is overly simplistic. The fact that the data do not appear consistent with a single-porosity conceptualization but also do not exhibit the slopes and/or different peak heights that would be predicted for a conventional double-porosity medium led to a detailed reexamination of the Culebra geology (e.g., Holt, 1997). A double-porosity model with a single rate of diffusion is often used to represent a medium in which advection occurs in numerous discrete fractures, based on an assumption that the numerous fractures provide fairly uniform access to all parts of a uniform matrix. Examination of Culebra core does not support assumptions that the matrix is uniform or that all parts of the matrix are uniformly accessed by fractures and other advective pathways. The descriptions of Holt (1997) of the variations in the porosity structures of the Culebra and recent laboratory diffusion measurements (Tidwell et al., 2000) also suggest that diffusion within the matrix probably could not be accurately modeled using a single rate. In addition, geologic and hydrologic observations, as well as the tracer-test results, indicate that flow and transport are not uniform over the entire thickness of Culebra, but are concentrated in the more fractured lower Culebra. Thus, a more complex conceptual model is needed.

Other chapters and appendices in this report provide interpretations of a portion of the large data set presented in this chapter, contributing to the development of a revised conceptual model. Additional efforts to provide a more complete explanation of the data set are warranted. Other researchers are invited to study this data set to improve the understanding of transport processes in fractured, permeable media and test-interpretation methodologies. Electronic versions of the data sets presented here and in Appendix C are available to those interested in analyzing the tests in the Sandia WIPP Central Files ERMS #251278 or by contacting Lucy Meigs.

3.5 References

Beauheim, R.L. 1987. *Interpretations of Single-Well Hydraulic Tests Conducted At and Near the Waste Isolation Pilot Plant (WIPP) Site, 1983-1987.* SAND87-0039. Albuquerque, NM: Sandia National Laboratories.

Beauheim, R.L., and G.J. Ruskauff. 1998. *Analysis of Hydraulic Tests of the Culebra and Magenta Dolomites and Dewey Lake Redbeds Conducted at the Waste Isolation Pilot Plant Site.* SAND98-0049. Albuquerque, NM: Sandia National Laboratories.

Benson, C.F., and R.S. Bowman. 1994. "Tri- and Tetrafluorobenzoates as Nonreactive Tracers in Soil and Groundwater," *Soil Science Society of America Journal.* Vol. 58, no. 4, 1123-1129.

Bowman, R.S., and J.F. Gibbens. 1992. "Difluorobenzoates as Nonreactive Tracers in Soil and Ground Water," *Ground Water.* Vol. 30, no. 1, 8-14.

Davis, S.N., G.M. Thompson, H.W. Bentley, and G. Stiles. 1980. "Ground-Water Tracers - A Short Review," *Ground Water.* Vol. 18, no. 1, 14-23.

Gringarten, A.C. 1984. "Interpretation of Tests in Fissured and Multilayered Reservoirs With Double-Porosity Behavior: Theory and Practice," *JPT, Journal of Petroleum Technology.* Vol. 36, no. 4, 549-564.

Gringarten, A.C. 1987. "How To Recognize 'Double-Porosity' Systems From Well Tests," *JPT, Journal of Petroleum Technology.* Vol. 39, no. 6, 631-633.

Hadermann, J., and W. Heer. 1996. "The Grimsel (Switzerland) Migration Experiment: Integrating Field Experiments, Laboratory Investigations and Modelling," *Journal of Contaminant Hydrology.* Vol. 21, no. 1-4, 87-100.

Holt, R.M. 1997. *Conceptual Model for Transport Processes in the Culebra Dolomite Member, Rustler Formation.* SAND97-0194. Albuquerque, NM: Sandia National Laboratories.

Hydro Geo Chem, Inc. 1985. *WIPP Hydrology Program, Waste Isolation Pilot Plant, SENM Hydrologic Data Report #1.* SAND85-7206. Albuquerque, NM: Sandia National Laboratories.

Hydro Geo Chem, Inc. 1986. *Two-Well Recirculation Tracer Tests at the H-2 Hydropad, Waste Isolation Pilot Plant (WIPP), Southeastern New Mexico.* SAND86-7092. Albuquerque, NM: Sandia National Laboratories.

INTERA Technologies, Inc. 1986. *WIPP Hydrology Program, Waste Isolation Pilot Plant, Southeastern New Mexico, Hydrologic Data Report #3.* SAND86-7109. Albuquerque, NM: Sandia National Laboratories.

Jones, T.L., V.A. Kelley, J.F. Pickens, D.T. Upton, R.L. Beauheim, and P.B. Davies. 1992. *Integration of Interpretation Results of Tracer Tests Performed in the Culebra Dolomite at the Waste Isolation Pilot Plant Site.* SAND92-1579. Albuquerque, NM: Sandia National Laboratories.

Kelley, V.A., and J.F. Pickens. 1986. *Interpretation of the Convergent-Flow Tracer Tests Conducted in the Culebra Dolomite at the H-3 and H-4 Hydropads at the Waste Isolation Pilot Plant (WIPP) Site.* SAND86-7161. Albuquerque, NM: Sandia National Laboratories.

Lessoff, S.C., and L.F. Konikow. 1997. "Ambiguity in Measuring Matrix Diffusion with Single-Well Injection/Recovery Tracer Tests," *Ground Water.* Vol. 35, no. 1, 166-176.

Meigs, L.C., and J.M. Bahr. 1995. "Three-Dimensional Groundwater Flow Near Narrow Surface Water Bodies," *Water Resources Research.* Vol. 31, no. 12, 3299-3307.

Mercer, J.W., D.L. Cole, and R.M. Holt. 1998. *Basic Data Report for Drill Holes on the H-19 Hydropad (Waste Isolation Pilot Plant—WIPP).* SAND98-0071. Albuquerque, NM: Sandia National Laboratories.

Moreno, L., and C-F. Tsang. 1994. "Flow Channeling in Strongly Heterogeneous Porous Media: A Numerical Study," *Water Resources Research.* Vol. 30, no. 5, 1421-1430.

Stensrud, W.A., M.A. Bame, K.D. Lantz, J.B. Palmer, and G.J. Saulnier, Jr. 1990. *WIPP Hydrology Program Waste Isolation Pilot Plant Southeastern New Mexico Hydrologic Data Report #8.* SAND89-7056. Albuquerque, NM: Sandia National Laboratories.

Tidwell, V.C., L.C. Meigs, T. Christian-Frear, and C.M. Boney. 2000. "Effects of Spatially Heterogeneous Porosity on Matrix Diffusion as Investigated by X-ray Absorption Imaging," *Journal of Contaminant Hydrology.* Vol. 42, no. 2-4, 285-302.

Tsang, Y.W. 1995. "Study of Alternative Tracer Tests in Characterizing Transport in Fractured Rocks," *Geophysical Research Letters.* Vol. 22, no. 11, 1421-1424.

Tucker, W.A., and L.H. Nelken. 1982. "Diffusion Coefficients in Air and Water," *Handbook of Chemical Property Estimation Methods: Environmentall Behavior of Organic Compounds.* Eds. W.J. Lyman, W.R. Reehl, and D.H. Rosenblatt. New York, NY: McGraw-Hill Book Co. 17-1 through 17-25.

WIPP Performance Assessment Department. 1993. *Preliminary Performance Assessment for the Waste Isolation Pilot Plant, December 1992, Volume 2: Technical Basis.* SAND92-0700/2. Albuquerque, NM: Sandia National Laboratories.

This page intentionally left blank.

Chapter 4
Controls on Mass Recovery for Single-Well Injection-Withdrawal Tracer Tests

By Susan J. Altman[1], Toya L. Jones[2], and Lucy C. Meigs[1]

Abstract

Numerical-modeling studies by Tsang (1995) suggest that single-well injection-withdrawal (SWIW) tracer tests may be an excellent method for distinguishing between double- and single-porosity media. However, Lessoff and Konikow (1997) suggest that differentiating the response for a double-porosity conceptualization from the response for a heterogeneous, single-porosity conceptualization that incorporates plume drift due to the presence of a regional gradient may be difficult. An investigation was conducted to determine whether SWIW tracer tests are an effective tool for evaluating the presence or absence of matrix diffusion in a geologic medium. This chapter presents results for numerical modeling performed in conjunction with the Culebra SWIW tracer tests which were designed, in part, to determine whether matrix diffusion is an important transport process in the Culebra dolomite. The goals of the investigation were to evaluate the effects of heterogeneity and plume drift on simulated tracer-recovery curves for a single-porosity conceptualization, evaluate the conditions under which single- and double-porosity responses can be confused, and evaluate the ability of a single-porosity conceptualization to reproduce the tracer recovery observed for the Culebra SWIW tests.

4.1 Introduction

One of the primary objectives for performing the single-well injection-withdrawal (SWIW) tracer tests at the WIPP site was to determine whether matrix diffusion within the formation dominated the behavior of the observed data. Matrix diffusion is defined as the transfer of mass via diffusion from high-permeability, advection-dominated domains into and out of low-permeability, diffusion-dominated domains. Two types of simulations (single-porosity and double-porosity) were performed in an effort to evaluate the role of matrix diffusion in the Culebra based on the results of the SWIW tracer tests. The single-porosity simulations assumed that the Culebra is a heterogeneous formation with a small porosity and, therefore, they considered advective flow and transport through a heterogeneous fracture-type advective porosity and did not include any interaction with a diffusive porosity. In addition, mixing within the advective porosity was controlled by the heterogeneity and not by dispersion or diffusion. The double-porosity simulations assumed advective flow and transport through a heterogeneous fracture-type advective porosity but also included diffusion of tracer mass between the advective and diffusive porosities. Advective transport did not occur in the diffusive porosity for the double-porosity simulations.

Matrix diffusion is recognized as a potentially important process in the transport of solutes in the subsurface. For example, the National Research Council (1994, p. 2-3) identified diffusion of solutes into "immobile" regions of the subsurface as one of the key technical reasons leading to difficulty in predicting and accomplishing aquifer restoration. Matrix diffusion can significantly affect contaminant migration at any scale and, in addition, can be an important process in providing access to sorption sites within the matrix (Ball and

---

[1] Sandia National Laboratories, Geohydrology Department, P.O. Box 5800, MS-0735, Albuquerque, NM 87185. Email: sjaltma@sandia.gov.

[2] Duke Engineering & Services, Inc., 9111 Research Boulevard, Austin, TX 78758.

Roberts, 1991; Wood et al., 1990). Thus, in modeling transport of solutes in the subsurface, recognition of the role of diffusion is important.

Field tracer tests can be used to provide valuable insight on transport processes such as matrix diffusion (e.g., Volckaert and Gautschi, 1997; Moench, 1995; Jones et al., 1992; Abelin et al., 1991). Although the SWIW tracer tests at the WIPP site are, to our knowledge, the first designed to investigate the role of matrix diffusion in an aquifer, the use of SWIW tests in the field is not uncommon. Historically, they have been conducted to measure residual oil saturation (Seetharam and Deans, 1989; Majoros and Deans, 1980; Tomich et al., 1973), investigate microbial metabolic activities (Istok et al., 1997), and measure advective groundwater velocity (Leap and Kaplan, 1988).

As described in Section 3.1, a SWIW tracer test consists of injecting and recovering tracer from a single well with a pause time between the end of injection and the start of withdrawal. For a system in which the tracer pathway into the formation during injection is identical to the tracer pathway out of the formation during withdrawal (i.e., a perfectly reversible flow system), all tracer injected during a SWIW test would be recovered when the volume pumped equaled the injected volume assuming no non-reversible sorption. Natural systems, however, are not completely reversible. Dispersion and mixing always cause additional spreading of a tracer plume so that the volume withdrawn must always be greater than the volume injected before all mass can be recovered. In addition, chemical processes within the formation will affect the transport behavior and can lead to non-reversible transport.

A homogeneous, single-porosity medium with no ambient hydraulic gradient provides the simplest "real" system in which a SWIW test might be conducted. Figure 4-1 shows model-predicted results for such a system. The normalized concentration versus time results (Figure 4-1a) form a single, slightly asymmetrical hump with the increasing-concentration (rising) limb steeper than the decreasing-concentration (falling) limb. The plot of normalized cumulative mass recovered versus log time (Figure 4-1b) shows that the majority of the mass is recovered very rapidly and the final few percent of mass is recovered more slowly.

The results in Figure 4-1 are presented as both normalized concentration versus time since injection in log-log space (referred to as the tracer-recovery curve) and normalized cumulative mass recovered versus log time (referred to as the mass-recovery curve). Both types of plots are presented because each one is useful for determining how different characteristics of the medium affect the simulated results. If the pumping rate remains constant for the duration of the test, the tracer-recovery curve has the same shape as a plot of tracer-recovery rate versus time. This relationship allows one to draw direct inferences about rates from the tracer-recovery curve.

Most natural systems are more complex than the simple example shown in Figure 4-1. A variety of factors can cause the falling limb of the tracer-recovery curve to be less steep than the rising limb and the associated mass-recovery curve to have a shallower initial slope. These factors include: (1) an ambient hydraulic gradient that causes the plume to drift during the resting phase of the SWIW test; (2) aquifer heterogeneity if accompanied by plume drift; (3) diffusion into porosity that does not participate in advective transport; and (4) chemical sorption.

4.2 Motivation and Objectives for Study

Tsang (1995) conducted several numerical simulations for multiwell and SWIW tracer tests in heterogeneous media to determine which test(s) could be used to evaluate the occurrence of matrix diffusion in the transport process. She assumed no significant regional gradient and used a conventional model (i.e., one with a single rate of diffusion) for her double-porosity simulations. Tsang (1995) found that, for multiwell tests in which tracer is injected into one well and recovered from a second, heterogeneity within the advective porosity may cause gradual mass recovery similar to that caused by matrix diffusion, making differentiation between single and double-porosity

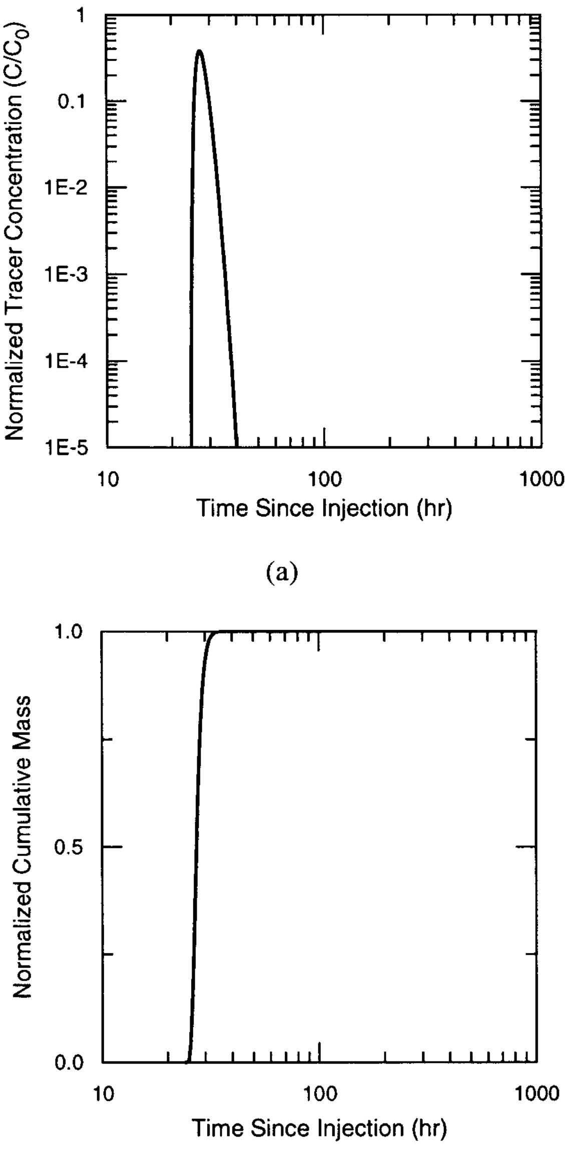

(a)

(b)

Figure 4-1. Simulated (a) tracer-recovery curve and (b) mass-recovery curve for a homogeneous single-porosity medium without drift. This SWIW simulation assumed a 23,580-s injection period (tracer injection for 8,160 s and chaser injection for 15,420 s) and a 63,583-s resting period. Most of the mass was recovered within 63,230 s after the start of pumping, which corresponded to a withdrawal volume approximately five times the injected volume.

media difficult. Her simulations of SWIW tracer tests, in contrast, showed significantly faster mass recovery for a single-porosity conceptualization as compared to a double-porosity conceptualization. The dramatically different mass-recovery curves for the two different conceptualizations suggest that SWIW tests can be used to detect the presence of matrix diffusion. Tsang (1995) also noted that the late-time slope of the tracer-recovery curve on a log-log plot is always -1.5 for the conventional double-porosity simulations, regardless of the degree of heterogeneity in the advective porosity. Thus, heterogeneity does not change the asymptotic $t^{-1.5}$ dependence for double-porosity transport (Heer and Hadermann, 1994; Appendix K). Tsang's work suggests that a -1.5 slope in recovery curves for a SWIW test may be a diagnostic indication of matrix diffusion.

Recent numerical modeling of SWIW tracer tests by Lessoff and Konikow (1997) incorporated heterogeneity, as did Tsang's work, but also included a significant regional gradient. Plume drift caused by a regional gradient during the resting phase can cause the injection and withdrawal transport pathways to be different, unlike simulations that ignore or have a negligible drift and have reversible pathways. Lessoff and Konikow (1997) created 90 highly heterogeneous transmissivity fields and simulated transport for a SWIW test with a single-porosity conceptualization incorporating drift. The injection and extraction rates and times and the resting-phase length used by Lessoff and Konikow (1997) were similar to those initially considered for the WIPP SWIW tracer tests. Lessoff and Konikow (1997) found that under some conditions involving regional drift, determining whether a single-porosity or a double-porosity conceptualization of the system is appropriate may be difficult. They describe a single-porosity simulation in which, during the resting phase, the plume is pushed into or across a low-transmissivity area located downgradient of the well. Once withdrawal pumping begins, the tracer is slowly drawn across this lower transmissivity area and the recovered tracer is diluted by fresh water from areas of higher transmissivity. The simulations by Lessoff and Konikow (1997) show that the effect of a regional gradient and the resultant plume drift during the resting phase is to reduce the rate of mass recovery in a heterogeneous, single-porosity system. In some cases, that reduction in recovery rate is large enough to yield results similar to those obtained for a double-porosity system. Based on the Lessoff and Konikow (1997) work, the design of the WIPP SWIW tracer tests was revised to shorten the length of the resting phase and increase the length of the withdrawal phase.

As stated earlier, the simulations by Tsang (1995) incorporated a negligible gradient and, as a result, the effects of plume drift during the resting phase were not investigated. Although the study by Lessoff and Konikow (1997) did include a significant regional gradient, the volume of fluid pumped during the withdrawal phase of the test was only three times the injected volume. As we will discuss below, we now consider this ratio of withdrawal volume to injected volume to be too small for a clear evaluation of the ability to distinguish between single- and double-porosity media.

Like the Lessoff and Konikow (1997) work, we conducted numerical modeling of SWIW tracer tests incorporating both a regional gradient and heterogeneity in the transmissivity field. For our simulations, the ratio of the volume of withdrawn fluid to the volume of injected fluid was over 250. This increase in the ratio between the withdrawn and injected volumes over that used by Lessoff and Konikow (1997) was designed to eliminate ambiguity in the results by increasing the amount of tracer recovered during the simulations, thus allowing for a greater range in the normalized concentrations for the simulated tracer-recovery curves. Lessoff and Konikow (1997) show that plume drift during the resting phase affects a SWIW test by decreasing the mass-recovery rate. Expanding on this, we wanted to determine the factors that control plume drift. Additional objectives of our study were to determine which controls on heterogeneity have the greatest impact on tracer recovery and under what conditions can single- and double-porosity responses be confused.

The study by Tsang (1995) suggests that a −1.5 log-log slope in the recovery curve for a SWIW test may be an indication that matrix diffusion has played a role in transport of the tracer in the formation. The observed data for the SWIW tests performed in the Culebra, for which a double-porosity conceptualization has been proposed, have a slope that is steeper than −1.5. Because the observed data do not have the characteristic −1.5 slope proposed by Tsang (1995), numerical simulations were also performed as part of this study to assess the possibility of matching the observed data with a single-porosity conceptualization that incorporates formation heterogeneity and a regional gradient.

In summary, this study consisted of three sets of simulations. The objective of the first set, referred to as the sensitivity studies, was to evaluate the conditions that can lead to gradual mass recovery with a single-porosity conceptualization. The relative importance of factors influencing mass recovery (degree of heterogeneity and the amount of drift) and the physical controls on drift (regional gradient, resting-phase duration, and porosity) were explored. The objective of the second set was to determine under what conditions single- and double-porosity responses can be confused. The objective of the third set, the WIPP-specific study, was to evaluate data from the SWIW tracer tests conducted at the WIPP and assess the possibility of ruling out a single-porosity conceptualization for the Culebra.

4.3 Test Design

SWIW tracer tests were conducted at the H-11 and H-19 hydropads (Figure 2-2). The tests consisted of: (1) tracer-solution injection; (2) chaser injection; (3) a resting phase of approximately 18 hr; and (4) pumping and collection of samples. Fluoro- and chlorobenzoic acids were used as non-sorbing tracers (Appendix H). The chaser was composed of either Culebra brine or a second slug of a different tracer followed by Culebra brine. The wells were pumped for 26 to 50 days, until the tracer concentrations were close to or below detection levels. Pumping and tracer-injection information for the SWIW tests can be found in Table 3-2, and the observed tracer-recovery curves are shown in Figures 3-3 and 3-4 as well as Figures C-1, C-20, and C-21 in Appendix C.

4.4 Numerical Simulations

For the purposes of the simulations presented here, the transmissive portion of the Culebra was assumed to be homogeneous in the vertical direction (two-dimensional approximation) and to be a confined layer because it is underlain by mudstone with an expected permeability orders of magnitude lower than that of the Culebra (Beauheim, 1987) and overlain by a significantly less permeable portion of the Culebra. No anisotropy was included in the simulations, an assumption consistent with the analysis of hydraulic tests at H-19 that showed little to no hydraulic anisotropy in the horizontal plane in the Culebra (Beauheim and Ruskauff, 1998). Based on extensive hydraulic testing conducted at five hydropads at the WIPP site, including H-11 and H-19 (Beauheim and Ruskauff, 1998), the Culebra fractures appear to have a high enough density and be well enough connected to be reasonably approximated by a heterogeneous stochastic continuum for advective transport.

4.4.1 Approach to Representing Heterogeneity

The heterogeneous transmissivity fields were created using sequential simulation algorithms as described in Deutsch and Journel (1998). Generation of the transmissivity fields utilized a spherical model of spatial correlation with isotropic ranges and no nugget effect. A grid-block size was chosen so that each range comprised at least ten blocks. Two distributions of ln T were used to create two different conceptual models of the transmissivity distribution. The first conceptualization assumed a Gaussian distribution and used the sequential Gaussian simulation algorithm (*sgsim*) to generate the fields. The second conceptualization assumed a bimodal distribution of ln T and used the sequential indicator simulation algorithm (*sisim*). The means and univariate ranges of the Gaussian and bimodal distributions were kept approximately the same (Figure 4-2). The two peaks of the bimodal distribution differ by approximately two orders of magnitude. These two peaks can be conceptualized as: (1) highly transmissive fractures; and (2) permeable zones in the rock matrix where advection takes place.

In addition to the distribution of ln T (Figure 4-2), the two algorithms differ in their reproduction of the model of spatial correlation. By design, for the *sgsim* algorithm, the variogram model is reproduced at the median of the Gaussian distribution, and extreme high and low values tend to be poorly correlated. With the *sisim* algorithm, the model is reproduced for each specified centile in the generated random-transmissivity fields, thus generating well-correlated structures for transmissivity values throughout the distribution. Gaussian distributions created with both *sgsim* and *sisim* have been compared for simulations of MWCF tracer tests (see Chapter 5). In a few simulations, the transmissivity fields created with *sgsim* result in slower mass-recovery rates. The differences in the recovery curves are not significant, however, for most realizations.

4.4.2 Approach to Representing Flow and Transport

The single-porosity simulations for the sensitivity studies and the WIPP-specific study used the numerical code THEMM (transport in heterogeneous

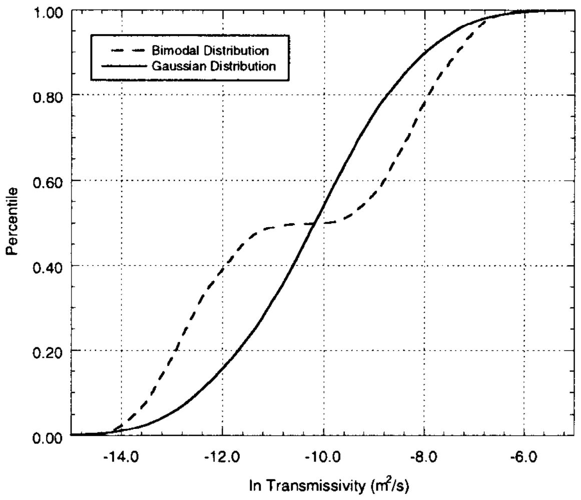

Figure 4-2. **Comparison of Gaussian and bimodal distributions for transmissivity used in the sensitivity studies.**

media with matrix diffusion) (Tsang and Tsang, 1999). The single-porosity and conventional double-porosity simulations for the comparison of single- and double-porosity systems used SWIFT II (the Sandia Waste-Isolation Flow and Transport Model for Fractured Media) (Reeves et al., 1986a).

The approach to representing transport in THEMM is very efficient and results in quick runtimes, making numerous simulations possible in a short time period. Calculating transport with SWIFT II is computationally more intensive, resulting in longer run times. Therefore, the large number of single-porosity simulations required for the sensitivity studies and the WIPP-specific study were conducted using THEMM. Although THEMM has the capability of simulating conventional double-porosity transport, that capability does not extend to the condition of plume drift due to an ambient gradient. SWIFT II, on the other hand, has no limitations with respect to conventional double-porosity transport of a drifting plume. Therefore, all double-porosity simulations were conducted with SWIFT II. The method of simulating transport with SWIFT II results in some numerical spreading that does not occur with THEMM. Consequently, a comparison of single-porosity simulations using THEMM and SWIFT II shows some differences (see Appendix M). As a result, the SWIFT II double-porosity simulations could not be directly compared to the THEMM single-porosity simulations. To enable direct comparison between single- and conventional double-porosity results, all single-porosity simulations for the comparison of single- and double-porosity responses were conducted using SWIFT II.

4.4.2.1 General Approach

Flow and transport in the heterogeneous system were simulated in three steps. First, the heterogeneous transmissivity field was imbedded within a coarser mesh to provide adequate distance between the transport region and the model boundaries. Second, a steady-state flow field was calculated using a finite-difference approach for each flow regime (i.e., injection, resting phase, and withdrawal). Third, transient transport in the heterogeneous continuum was simulated.

4.4.2.2 Single-Porosity THEMM Simulations

The THEMM computer code models flow through a heterogeneous continuum using a finite-difference solution to the steady-state groundwater-flow equation, which is based on mass-balance principles and Darcy's law (Hale and Tsang, 1996). Solution of the flow equation yields a steady-state head field, and a discretized nonuniform velocity field is subsequently computed by multiplying gradients in the head field by the heterogeneous hydraulic-conductivity field. Transient advective transport is simulated by a particle-tracking method. For a detailed description of the THEMM code, see Hale and Tsang (1996).

With the particle-tracking method for simulating advective transport, a large number of particles is introduced at the injection well. The residence time (t_w) for a particle within each discretized element is determined based on the element porosity divided by the flux through the element (Moreno et al., 1990):

$$t_w = \frac{b\phi\Delta x\Delta y}{\frac{1}{2}\sum_j |Q_{ij}|} \tag{4-1}$$

where b is the thickness [L] of the model layer, ϕ is the porosity, Δx and Δy are the grid dimensions [L], and Q_{ij} is the flow rate [L^3/T] through element (i) and the connecting elements (j). Each particle moves through the calculated flow field, and the residence times within each element along the particle paths are summed. Particles are distributed to the neighboring grid cells according to steady-state stream tubes. To minimize numerical dispersion, particles do not diffuse across stream tubes (Moreno et al., 1988). Arrival times of the particles at the element containing the withdrawal well are calculated to generate tracer-recovery and mass-recovery curves. The number of particles in each element at specified times is also calculated in order to determine the spatial distribution of the tracer.

4.4.2.3 Single- and Conventional Double-Porosity SWIFT II Simulations

For this application, SWIFT II was used to solve the steady-state fluid-flow and transient radionuclide-transport equations in heterogeneous single- and double-porosity media using a Cartesian coordinate system. The equations used to describe transient radionuclide transport in a single-porosity system and in the advective porosity of a double-porosity system are identical with the exception of the source/sink term representing exchange processes between the advective and diffusive porosities in the double-porosity system. SWIFT II assumes that the interaction between the advective porosity and diffusive porosity in a double-porosity system is via diffusion only. The only means for large-scale movement provided by SWIFT II in a double-porosity system is within the advective porosity. The bulk of the storage for the double-porosity system is provided by the diffusive porosity. The advective porosity can be one-, two-, or three-dimensional. The diffusive porosity is assumed to be one-dimensional in a direction orthogonal to the movement in the advective porosity. The geometry of the diffusive porosity within SWIFT II can be either parallel slabs or cubes. Parallel-slab geometry was used for this application. A reflective no-flow boundary is assumed for the interior boundary of the diffusive porosity. The advective porosity/diffusive porosity interface provides a source to the diffusive porosity that is identical to the loss from the advective porosity to within a geometrical scaling factor.

For double-porosity applications, SWIFT II solves two sets of equations, one for the processes in the advective porosity and another for the processes in the diffusive porosity. The approach used by SWIFT II to treat an advective porosity-diffusive porosity system is similar to that used by Bear and Braester (1972), Huyakorn et al. (1983), Pruess and Narasimhan (1982), Tang et al. (1981), Grisak and Pickens (1980), Streltsova-Adams (1978), and Rasmuson et al. (1982).

A complete discussion of the theory and implementation of SWIFT II and the basic limitations of the methodology can be found in Reeves et al. (1986a). A guide to the SWIFT II input data is provided by Reeves et al. (1986b). Comparisons of the results from SWIFT II to analytical solutions appear in Finley and Reeves (1981), Reeves et al. (1986c), and Ward et al. (1984).

4.4.3 Model Domain and Boundary Conditions

The model domain and boundary conditions for the THEMM and SWIFT II simulations were identical with the exception of how the injection/withdrawal well was represented (see below). The models consisted of a 4.4-m-thick layer extending 634 m in both the x- and y-directions. The central 120 m x 120 m area was heterogeneous with each grid block assigned a different transmissivity value. The remaining portion of the model was homogeneous and assigned a transmissivity equal to the geometric mean value for the heterogeneous region. The model grid blocks were 0.5 m x 0.5 m in the heterogeneous region and increased from 0.5 m to 128 m in the homogeneous region with the largest grid blocks located at the model's outer edge. Solute transport occurred only within the heterogeneous region.

Constant-head boundary conditions were set on the four sides of the model domain such that a gradient was induced from the top to the bottom (north to south). The average of the head values assigned at the top and bottom was assigned to the lateral boundaries. Simulations confirmed that these lateral boundaries were far enough from the inner region to not affect plume movement. For the THEMM simulations, an internal, constant-rate, source/sink term was specified to represent the injection/withdrawal well (located at 60 m, 80 m within the heterogeneous region). For the SWIFT II simulations, the injection/withdrawal well was explicitly incorporated into the simulations using a model well located at 60 m, 80 m within the heterogeneous region. A constant injection rate was assigned during injection, a zero rate during the resting phase, and a constant extraction rate during the withdrawal phase. A transmissivity value ten times greater than the maximum transmissivity of the entire field was assigned to the grid block containing the well to represent the increased conductivity of the well. Because the grid block containing the well was sufficiently small compared to the size and movement of the plume, the increased transmissivity did not significantly affect plume movement.

4.4.4 Input Parameters

The parameter values for the sensitivity studies (Table 4-1) were based on the first tracer injected during the Culebra SWIW test performed at the H-11 hydropad. Parameters for which values were varied for the sensitivity studies fall into one of two groups: (1) parameters that affect the heterogeneity of the system (standard deviation of the natural logarithm of transmissivity ($\sigma \ln T$), range, and transmissivity distribution); and (2) parameters that affect drift (porosity, regional gradient, and resting-phase duration). Thirty equally plausible, heterogeneous, random transmissivity-field realizations were used for these sensitivity studies.

Parameter values for the comparison of single- and double-porosity responses (Table 4-2) were, like those for the sensitivity studies, consistent with conditions for the first tracer injected during the H-11 SWIW test. The comparison was conducted for several situations designed to address the roles of heterogeneity and plume drift in creating confusion between single- and double-porosity results. The effects of heterogeneity were investigated by considering a homogeneous and two heterogeneous transmissivity fields. The two heterogeneous fields selected for use in the comparison were those found by the sensitivity studies to have produced close to the most gradual and most rapid mass recovery. The effects of plume drift were investigated by considering no regional gradient, the same regional gradient as used for the sensitivity studies (0.011 m/m), and some intermediate gradients (0.001 and 0.006 m/m) to look at the sensitivity to the gradient in additional detail.

In order to investigate how the amount of matrix diffusion might contribute to ambiguity between single- and double-porosity results, the double-porosity simulations considered four matrix-block lengths ranging from 0.01 to 2.0 m (see Table 4-2). The diffusive porosity used for the double-porosity simulations was assigned a value equal to the smallest hydropad-average porosity determined from core measurements (see records

Table 4-1. Input Parameters for the Sensitivity Studies

Parameter	Base-Case Value	Comparison Sensitivity Value(s) (--- indicates no change from base case)
Mean transmissivity (T) (m^2/s)	5.10×10^{-5}	---
Standard deviation of ln T ($\sigma \ln T$)	1.76	0.88, 2.64, 3.52
Range (λ) (m)	15	5, 25, 40
Transmissivity distribution	Gaussian	Bimodal
Culebra thickness (b) (m)	4.4	---
Porosity (ϕ)	1×10^{-3}	5×10^{-4}, 5×10^{-3}
Injection rate (m^3/s)	1.24×10^{-4}	---
Pumping rate (m^3/s)	2.23×10^{-4}	---
Regional gradient (dh/dl)	0.011	0.0011, 0.0054, 0.014
Mass of tracer injected (kg)	8.035	---
Tracer-injection duration (s)	8160	---
Chaser-injection duration (s)	15420	---
Resting-phase duration (s)	63583	0, , 64800, 129600

Note: 30 realizations of transmissivity fields were generated and used in the single-porosity simulations.

Table 4-2. Input Parameters for the Comparison of Single- and Double-Porosity Responses

Parameter	Single-Porosity Simulations	Double-Porosity Simulations
Mean transmissivity (T) (m^2/s)	5.1 x 10^{-5}	5.1 x 10^{-5}
Standard deviation of ln T (σln T)	1.76	1.76
Range (λ) (m)	15	15
Transmissivity distribution	Gaussian	Gaussian
Culebra thickness (b) (m)	4.4	4.4
Advective porosity (ϕ)	1 x 10^{-3}	1 x 10^{-3}
Diffusive porosity (ϕ)	na	0.10
Diffusive tortuosity (τ)	na	0.11
Matrix-block length (m)	na	2.0, 1.0, 0.1, and 0.01
Free-water diffusion coefficient (m^2/s)	na	7.3 x 10^{-10}
Injection rate (m^3/s)	1.24 x 10^{-4}	1.24 x 10^{-4}
Pumping rate (m^3/s)	2.23 x 10^{-4}	2.23 x 10^{-4}
Mass of tracer injected (kg)	8.035	8.035
Tracer-injection duration (s)	8160	8160
Chaser-injection duration (s)	15420	15420
Resting-phase duration (s)	63583	63583
Regional gradient (dh/dl) (m/m)	0.0, 0.001, 0.006, and 0.011	0.0, 0.001, 0.006, and 0.011

package ERMS #237228). The smallest value was selected in an effort to minimize diffusion and thus maximize the possibility of getting double-porosity responses similar to single-porosity responses. The diffusive tortuosity for the double-porosity simulations was assigned a value equal to the average tortuosity determined for the H-11 hydropad from core measurements (see records package ERMS #237226).

Parameter values for the WIPP-specific simulations (Table 4-3) were chosen based on the test design or, when uncertain, considered to be within realistic bounds for the H-11 and H-19 hydropads. When the tracer- and chaser-injection rates differed, a time-weighted average was used in the simulations. A comparison of this simplified method to the use of two different injection rates showed insignificant differences in simulated mass recovery. For parameters that were uncertain (e.g., porosity and hydraulic gradient), a reasonable value leading to the most drift and, as a result, the slowest rate of mass recovery, was selected.

An estimate of advective porosity was calculated from the MWCF tracer-test results at each hydropad assuming direct plug flow between the injection well and the pumping well (see Section 3.3.2.3 and Appendix C). The porosity used for the WIPP-specific simulations described here was the minimum calculated porosity for each hydropad reduced by a factor of five (Table 4-3). This reduction was made in an effort to minimize simulated mass-recovery rates while maintaining parameter values that appear to be reasonable because, as discussed below, the smaller the porosity, the greater the drift and the slower the mass-recovery rates.

Periodic water-level measurements are taken in Culebra wells on and near the WIPP site. The measurements for September and December 1996 and March, June, and July 1997 were used to estimate the hydraulic gradient across the H-11 and H-19 hydropads. The gradient across the H-11 hydropad was estimated using water-level measurements at DOE-1 and H-17 (see Figure 2-2). The gradient across the H-19 hydropad was

Table 4-3. Input Parameters for the WIPP-Specific Study

Parameter	H-11			H-19		
				4-Well Test		7-Well Test
Tracer	2,4-DCBA		3,4-DFBA	2,4-DCBA	o-TFMBA	2,4-DCBA
Mean transmissivity (*T*) (m^2/s)	5.10×10^{-5}	5.10×10^{-5}	5.10×10^{-5}	6.8×10^{-6}	6.8×10^{-6}	6.8×10^{-6}
Standard deviation of ln *T* ($\sigma \ln T$)	2.64	2.1	2.64	2.64	2.64	2.64
Range (λ) (m)	15	15	15	15	15	15
Culebra thickness (*b*) (m)	4.4	4.4	4.4	4.4	4.4	4.4
Porosity (ϕ)	4×10^{-4}	4×10^{-4}	4×10^{-4}	6×10^{-3}	6×10^{-3}	6×10^{-3}
Injection rate (m^3/s)	1.24×10^{-4}	1.24×10^{-4}	1.25×10^{-4}	1.29×10^{-4}	1.28×10^{-4}	1.16×10^{-4}
Pumping rate (m^3/s)	2.23×10^{-4}	2.23×10^{-4}	2.23×10^{-4}	2.37×10^{-4}	2.37×10^{-4}	2.74×10^{-4}
Regional gradient (dh/dl) (m/m)	5.7×10^{-3}	5.7×10^{-3}	5.7×10^{-3}	1.30×10^{-2}	1.30×10^{-2}	1.30×10^{-2}
Mass of tracer injected (kg)	8.035	8.035	5.050	4.9	1.9	4.995
Tracer-injection duration (s)	8160	8160	7980	7620	7950	7320
Chaser-injection duration (s)	15420	15420	7440	15780	7830	14580
Resting-phase duration (s)	63583	63583	63583	63362	63362	63800

Note: 100 realizations of transmissivity fields were generated and used in these simulations. Contents of table taken from the TIPS found in Appendix B.

estimated using water-level measurements at four well-pair combinations: H-1 and WQSP-5, H-15 and DOE-1, H-2b2 and DOE-1, and H-1 and DOE-1. To calculate the gradients, the water level at each well was converted to a freshwater-head. This conversion was done using a specific gravity of 1.1 at the upgradient well and a specific gravity of 1.0 at the downgradient well. These two specific gravities represent the near maximum and minimum specific gravities measured for Culebra fluid. The use of maximum and minimum values of specific gravity to convert water levels to freshwater heads ensures conservative (i.e., maximum) calculations of the gradients. Table 4-4 summarizes the calculated gradients along with their means and standard deviations. The gradients used for the simulations were taken as slightly higher than and exactly equal to the mean gradients plus three times the standard deviations for the H-11 and H-19 hydropads, respectively. The gradient used in the simulations for H-19 was calculated using the well-pair combination that gave the highest gradients (i.e., H-1 and WQSP-5).

In estimating bounding values of porosity and gradient for the WIPP-specific simulations, the porosity was most likely underestimated and the gradient overestimated. This may have resulted in simulations that have more gradual mass recovery than is realistic. However, use of these values provided a good test of whether or not the field data can be matched with a single-porosity model.

Although numerous hydraulic tests have been conducted in the vicinity of the WIPP site, relatively little information on the spatial structure of transmissivity at the hydropad scale (tens of meters) is available. Evaluating the transmissivity distribution for a given location is difficult because of the dependence of transmissivity on scale (Clauser, 1992; Gelhar et al., 1992). An estimate of the $\sigma \ln T$ for the Culebra was calculated based on results of hydraulic tests performed in the

Table 4-4. Calculated Gradients Across the H-11 and H-19 Hydropads

Date	Calculated Gradient				
	H-11 Hydropad	H-19 Hydropad			
	DOE-1 to H-17	H-1 to WQSP-5	H-15 to DOE-1	H-2b2 to DOE-1	H-1 to DOE-1
September 1996	0.00486	0.01200	0.00645	0.00890	0.00932
December 1996	0.00503	0.01206	0.00705	0.00905	0.00994
March 1997	0.00515	0.01181	0.00742	0.00920	0.01032
June 1997	0.00522	0.01202	0.00765	0.00941	0.01068
July 1997	0.00523	0.01261	0.00768	0.00944	0.01072
Mean	0.005098	0.01210	0.00725	0.00920	0.010196
Standard Deviation	0.000155	0.000301	0.000513	0.000231	0.000582
Mean + 3*Std. Dev.	0.0056	0.013	0.00879	0.00989	0.01194
Simulation Value	0.0057(1)	0.013	na	na	na

(1) The simulation value is slightly different from the calculated mean plus three standard deviations because the simulation value was developed using an early version of the calculated gradients that differs slightly from the final version presented here.

41.4-km^2 region located within the WIPP-site boundaries. That calculation yielded a $\sigma \ln T$ value of 2.1 (see Appendix L).

Because mass recovery is expected to be slower with an increase in $\sigma \ln T$, a higher value of 2.64 for $\sigma \ln T$ was used for the WIPP-specific simulations. For the first tracer injected during the SWIW test at H-11, simulations were also conducted using the $\sigma \ln T$ value of 2.1 calculated for the entire WIPP-site area. All transmissivity fields for the WIPP-specific simulations were generated with a Gaussian distribution of ln T. The mean transmissivity values used in the simulations were from Beauheim and Ruskauff (1998)[3] (Table 4-3). One hundred transmissivity-field realizations were considered for the SWIW tests at both the H-11 and H-19 hydropads.

4.5 Results and Discussion

The single-porosity sensitivity studies, comparison of single- and double-porosity responses, and the WIPP-specific study are described below.

4.5.1 Single-Porosity Sensitivity Studies

The single-porosity sensitivity studies can be divided into two types: (1) simulations where values of parameters affecting the structure of the heterogeneous transmissivity fields were varied; and (2) simulations for which values of parameters affecting drift were varied. Prior to providing detailed results of the sensitivity studies, a comparison of a set of simulations is discussed to elucidate the factors affecting mass-recovery rates for a single-porosity conceptualization of an SWIW test with plume drift. Given the large number of simulations, a simple metric was needed to compare results. Because our primary interest is the rate at which mass is recovered, the time to 90% mass recovery was selected as the metric.

---

[3] The transmissivity value we used for H-11 was actually an early estimation of the transmissivity as part of Beauheim and Ruskauff's (1998) work. The final value published in Beauheim and Ruskauff (1998) is 4.7 x 10^{-5} m^2/s. The value used in this work (Table 4-3) is higher, leading to slightly slower mass recovery.

4.5.1.1 Factors Affecting Mass-Recovery Rates

Two factors affect the time to 90% mass recovery in a single-porosity system: (1) the amount of plume drift during the resting phase; and (2) the structure of the heterogeneity relative to the location of the well.

Figure 4-3 illustrates how increasing plume drift (by increasing the resting-phase duration at a constant gradient of 0.011 m/m) in two different heterogeneous systems increases the time to 90% mass recovery. In order to compare the results easily, the times since injection for the simulations having resting-phase durations of 0 or 36 hr were shifted to be consistent with the times since injection for the simulations with an 18-hr resting phase. The heterogeneous fields used for the simulations presented in Figure 4-3 correspond to the fields that resulted in close to the fastest mass-recovery rate (Figures 4-3a and b) and close to the slowest mass-recovery rate (Figures 4-3c and d) for all of the sensitivity simulations. The use of these two fields for this demonstration indicates that the trend that increasing plume drift increases time to 90% mass recovery appears to be true regardless of the structure of the heterogeneous transmissivity field. In some circumstances, plume drift can lead to a loss of mass. For the simulation with a 36-hr resting-phase duration shown in Figures 4-3c and d, approximately 1.5% of the mass is carried beyond the well's capture zone during the resting phase and is permanently lost. In another case (not shown), a gradient of 0.014 in a system with an advective porosity of 1 x 10^{-3} leads to mass loss as great as 18%. Clearly, steep gradients combined with low advective porosities can lead to significant mass loss beyond the capture zone of the withdrawal well.

Although the heterogeneous transmissivity fields used in generating the results shown in Figure 4-3 were defined by the same variogram using the base-case parameter values given in Table 4-2, they produced greatly varying times to 90% mass recovery. In Figures 4-3a and b, the time to 90% mass recovery for the heterogeneous case with an 18-hr resting phase is quite similar to that for the homogeneous case because the transmissivity field is relatively homogeneous in the region of the plume. In Figures 4-3c and d, the time to 90% mass recovery is significantly longer in the heterogeneous transmissivity field with an 18-hr resting phase than in a homogeneous transmissivity field.

The results of one flow and transport simulation (Figure 4-4) illustrate the process by which plume drift in a heterogeneous medium can result in slower mass recovery. The origin in this figure is the lower left-hand corner of the heterogeneous region in the model. The base-case transmissivity-field realization (Figure 4-4a) producing the slowest mass recovery is chosen for this demonstration (the same simulation presented as the bold line in Figures 4-3c and d). The flow paths that dominate plume movement during the resting phase are those that carry the plume in a southeastern direction through high-transmissivity areas located both southeast and southwest of the well (Figure 4-4b). The shape of the plume after the resting phase illustrates the influence of these high-transmissivity regions (Figure 4-4c). During the withdrawal phase, the high-flux (primary) flow paths to the well are from the southwest and southeast (Figure 4-4d). Tracer that is transported during the resting phase along the high-transmissivity feature located southwest of the well must return to the well along lower flux (secondary) flow paths (Figure 4-4d). Transport along these secondary flow paths is through a lower transmissivity region. These new transport paths cause mass recovery to be slower than if the transport paths had been reversible.

In summary, results of the simulation presented in Figure 4-4 suggest that, if high-transmissivity areas are equally connected to the well by primary flow paths during the injection, resting, and withdrawal phases, then drift will have only a small effect on recovery; the transport pathways are essentially reversible. In contrast, if tracer is carried during the resting phase to regions where the most direct path during withdrawal is through a low-transmissivity area, mass recovery will slow significantly.

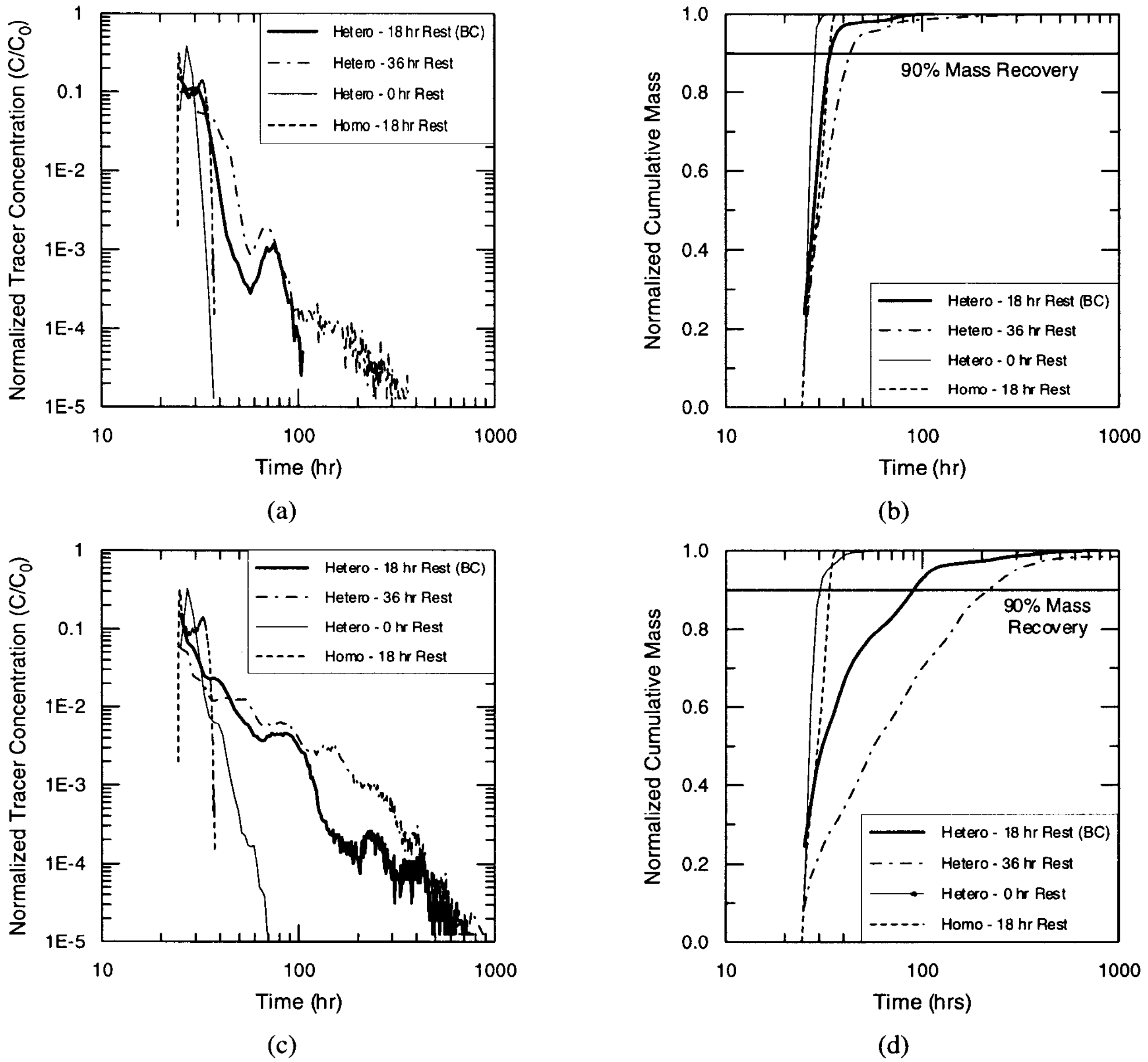

(a) (b)

(c) (d)

Figure 4-3. Simulated (a and c) tracer-recovery curves and (b and d) mass-recovery curves showing decrease in mass recovery with increase in plume drift in a heterogeneous system. The difference between the curves shown in (a and b) and (c and d) is the random number seed used to generate the heterogeneous transmissivity fields (i.e., the realization number). All parameters are the same as the base case (Table 4-1). Base case (BC) shown in (c,d), bold line, is the same realization as shown in Figure 4-4.

4.5.1.2 Heterogeneity

To understand the effects of heterogeneity on mass recovery, several suites of simulations were conducted varying values of parameters that define the variograms and transmissivity frequency distributions. Parameter values for these sensitivity studies are summarized in Table 4-1.

The parameter with the greatest effect on the time to 90% mass recovery is $\sigma \ln T$ (Figure 4-5a). As $\sigma \ln T$ increases, the time to 90% recovery increases. This result is similar to that reported in Tsang (1995). The larger the $\sigma \ln T$, the greater the degree of flow channeling. This channeling increases the likelihood that, during the resting-phase, tracer will travel into or further within

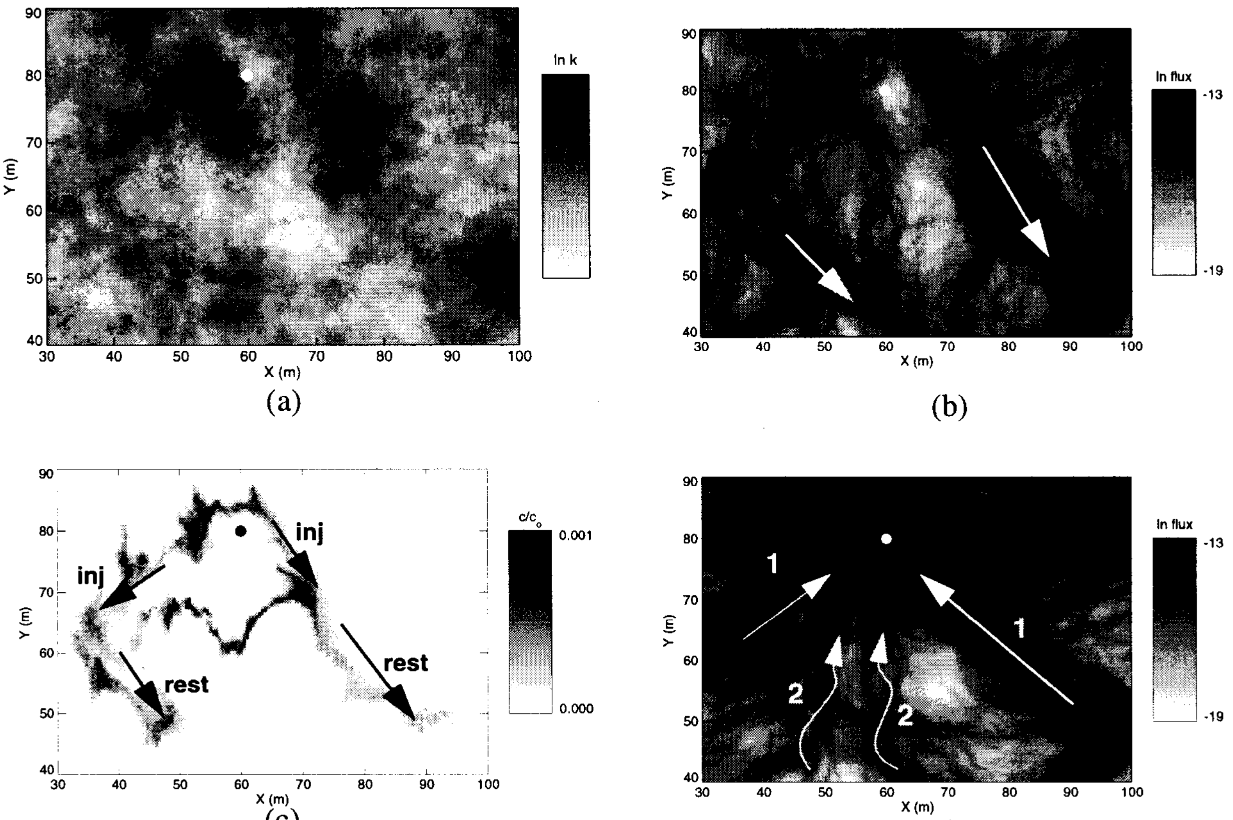

(a) (b) (c) (d)

Figure 4-4. **Demonstration of the cause of reduced mass recovery in a single-porosity system due to the movement of the plume during the resting phase (irreversibility of transport paths). (a) Transmissivity distribution of area; (b) flux distribution during the resting phase with arrows showing primary flow and transport paths; (c) tracer distribution after resting phase annotated with flow paths at different SWIW stages (inj = injection, rest = resting phase); and (d) flux distribution during the withdrawal phase. Ones and twos indicate primary and secondary flow paths, respectively.**

areas where the flux to the well is low during the withdrawal phase. As σ ln T increases, the contrast in the magnitude of the transmissivity between the primary and secondary flow paths also increases. Larger contrasts in transmissivities (and fluxes) between primary and secondary flow paths result in the tracer being more easily diluted or trapped in lower transmissivity areas. All of these factors lead to slower mass recovery.

The spread of time to 90% mass recovery also increases as σ ln T increases. For simulations that are highly heterogeneous in the vicinity of the solute plume (e.g., Figures 4-3c and d and Figure 4-4), an increase in σ ln T leads to greater contrasts between high- and low-transmissivity areas leading to longer mass-recovery times. However, for simulations that have relatively homogeneous transmissivities in the region of the plume (e.g., Figures 4-3a and b), 90%-mass-recovery times do not change significantly with changing σ ln T.

The results of simulations presented in Figure 4-5b suggest that the range (λ) does not have a strong effect on mass recovery. If the range is extremely large or small relative to the area occupied by the plume, mass recovery is anticipated to be fast because the system will appear homogeneous in the area of interest. These sensitivity simulations investigated intermediate values of λ that produced hetergeneous conditions in the vicinity of the plume. The results of the simulations indicate that no critical range exists that minimizes or maximizes 90%-mass-recovery times. The range in mass-recovery times is largest for a range of 15 m, suggesting the possibility of a

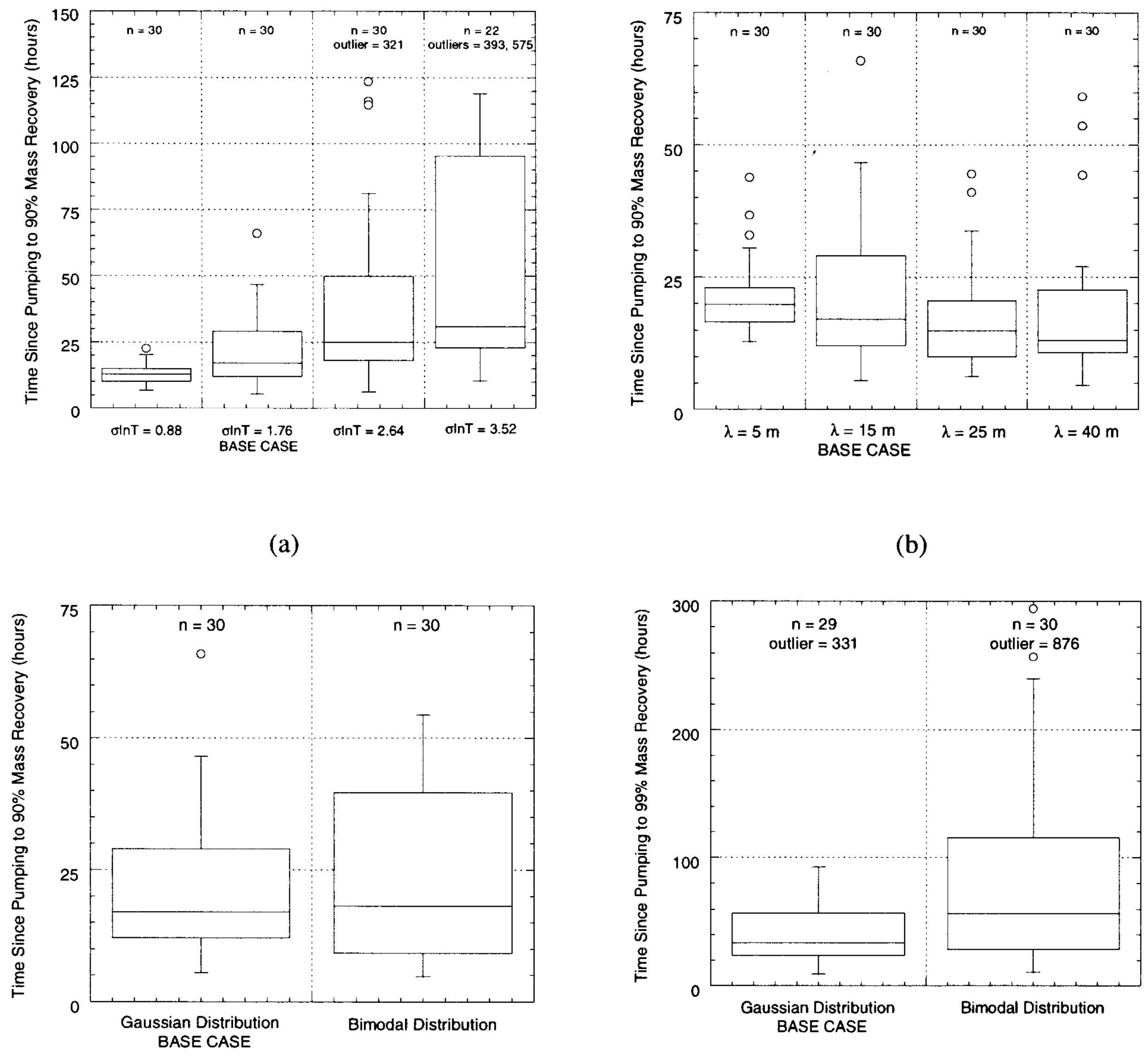

(a)

(b)

(c)

(d)

Figure 4-5. Effect of the structure of heterogeneity on mass recovery: (a) standard deviation of ln *T*, (b) range, and (c) ln *T* frequency distribution for a metric of time to 90% mass recovery, and (d) ln *T* frequency distribution for a metric of time to 99% mass recovery. The number of simulations was less than 30 when a ln *T* of 3.52 was used because several simulations did not converge. Each box encloses 50% of the values with the central line representing the median value. Outliers, circles, are defined as [upper 25% + ((1.5)*(upper 25% - lower 25%))]. The bars show the minimum and maximum values that are not outliers.

greater likelihood of slow mass recovery for that range. However, as long as the system is heterogeneous, the range of the system appears to play a secondary role in controlling 90%-mass-recovery times.

Simulations with bimodal and Gaussian distributions were compared to examine the effects of the shape of the transmissivity frequency distribution on mass-recovery times (Figures 4-5c and d). Figure 4-5c shows that no significant difference in mass-recovery times is observed when using bimodal or Gaussian distributions based on the time to 90% mass recovery. If, however, the metric for comparison is 99%-mass-recovery times, a difference in the two sets of results is apparent. Figure 4-5d shows that, in most cases, times to 99% mass recovery are longer for simulations using the bimodal distribution as compared to simulations using the Gaussian distribution. The slower mass recoveries for simulations using a bimodal distribution are explained by the higher probability that a low-transmissivity area is located between the tracer location at the end of the resting phase and the pumping well. This increased likelihood is due to regions of low transmissivity being present in the bimodal distribution and these regions tending to be well connected. In summary, the mass-recovery rates are not significantly different for the two distribution types until over 90% of the mass is recovered, and recovery of the final 10% of the mass is slower for the simulations using the bimodal distribution.

4.5.1.3 Controls on Plume Drift

In addition to heterogeneity, the amount of plume drift strongly controls mass recovery. Plume drift within a given transmissivity field is primarily controlled by three factors: (1) porosity; (2) hydraulic gradient, and (3) resting-phase duration. From Darcy's law, the magnitude of plume drift is defined as:

$$Drift = \frac{T}{b\phi}\frac{dh}{dl}(t_r) \qquad (4\text{-}2)$$

where T is the mean transmissivity [L^2/T], b is the thickness of the transmissive layer [L], ϕ is the advective porosity, dh/dl is the regional gradient [L/L], and t_r is the resting-phase duration [T]. This definition is correct only for a homogeneous system, but can provide a good approximation of the relative magnitude of drift when heterogeneous systems are compared.

Porosity controls the volume of rock occupied by a fixed tracer volume. As porosity decreases, the tracer plume covers a larger area and moves farther per unit time, both of which increase its potential to be influenced by heterogeneity. The hydraulic gradient controls the rate at which the tracer plume drifts during the resting phase, and also affects the capture zone of the well during pumping. As the gradient increases, a greater portion of the capture zone lies upgradient of the well. Thus, tracer lying downgradient of the well is recovered more slowly as the gradient increases. If the gradient is large enough, some tracer may never be recovered. The resting-phase duration determines how far a plume will drift for a given gradient and porosity. As the duration increases, plume drift also increases, which increases the likelihood of encountering heterogeneity and escaping the capture zone of the well.

To examine the relative importance of the three variables controlling plume drift (porosity, gradient, and resting-phase duration) in a heterogeneous system, four sets of simulations were conducted in each of the 30 transmissivity fields. For each set, the values of two of the three variables were varied in a coordinated fashion such that the expected plume drift, as calculated by Equation 4-2, remained constant. A comparison of the range in actual plume drifts for the four sets of simulations shows that the amount of drift was approximately the same for all simulation sets (Figure 4-6). The drift distances shown in Figure 4-6 were calculated as the distance in the direction of flow (north-south) between the center of the plume after the injection period and the center of the plume after the pause period. The center of the plume was defined as the mid-point (along the north-south line) between the extreme extent of the plume in the north and south directions.

The results in Figure 4-7 show the relative effects of porosity, resting-phase duration, and gradient on times to 90% mass recovery for an expected constant drift distance. Changing the regional gradient while also changing either porosity (compare sets A and B) or resting-phase duration (compare sets B, C, and D) has a clear effect on the times to 90% mass recovery. As the magnitude of the regional gradient increases, the rate of mass recovery decreases and the range in 90%-mass-recovery times increases. Variations in porosity and resting-phase duration while holding regional gradient constant, in contrast, do not appear to affect 90%-mass-recovery times significantly (compare sets A and C). Thus, for a given drift distance, the hydraulic gradient appears to

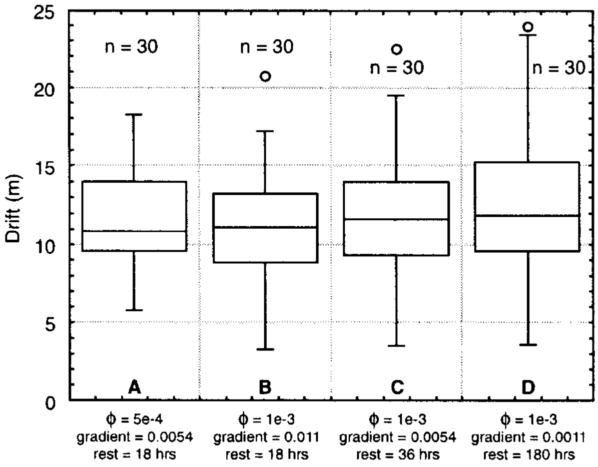

Figure 4-6. Comparison of drift distance for the four sets of simulations used to investigate the controls on plume drift. See Figure 4-5 caption for an explanation of the box plots.

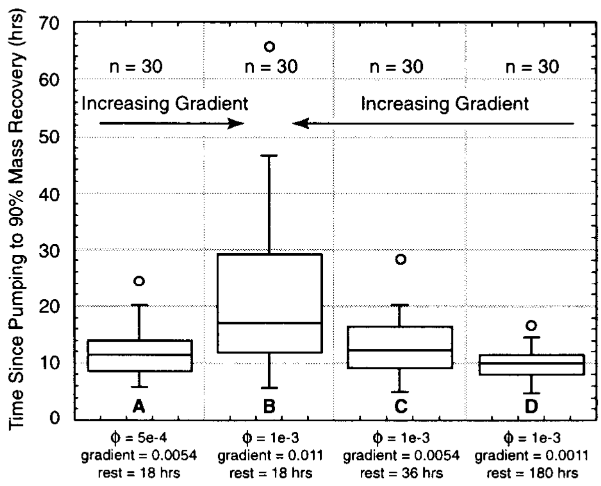

Figure 4-7. Ranges in time to 90% mass recovery for simulations examining the relative effects of porosity, resting-phase duration, and regional gradient on mass recovery. Drift is approximately the same for all sets of simulations as shown in Figure 4-6. See Figure 4-5 caption for an explanation of the box plots.

affect times to 90% mass recovery more than porosity or the resting-phase duration for the parameter values considered in this study. This probably occurs because the gradient not only affects the position of the plume, but also the capture zone of the well, as discussed above.

4.5.2 Comparison of Single- and Double-Porosity Responses

The objective of this section is to provide insight into conditions for which single- and double-porosity responses for an SWIW tracer test can be easily distinguished and difficult to distinguish. Simulations of SWIW tests were performed using the parameters listed in Table 4-2 to compare and contrast the responses that would be expected from single- and double-porosity systems. The factors controlling the tracer response considered in this analysis are plume drift during the resting phase due to a regional gradient, heterogeneity in the formation transmissivity, and the degree of matrix diffusion for the double-porosity simulations. A low porosity value of 10^{-3}, representative of fractures, was used for the single-porosity simulations rather than a higher value typical of a matrix porosity because plume drift increases as porosity decreases and, as will be shown below, confusion between single- and double-porosity systems is unlikely without plume drift. For all figures discussed in this section, the first data point represents the start of the withdrawal phase, which also coincides with the end of the resting phase.

The effects of plume drift and heterogeneity on single- and double-porosity responses were investigated by first looking at the simple case of a homogeneous system with no plume drift (Figure 4-8). For this system, the responses for the single- and double-porosity simulations are easily distinguished looking at both the tracer-recovery (Figure 4-8a) and mass–recovery (Figure 4-8b) curves. The mass-recovery curves show that 100% recovery is achieved very shortly after withdrawal begins for the single-porosity simulation, full mass recovery is not reached by 1000 hr for the double-porosity simulations with the three largest matrix-block lengths, and 100% recovery occurs at about 400 hr for the double-porosity simulation with the smallest matrix-block length.

For the two double-porosity simulations with the largest matrix-block lengths, the rate of mass recovery is initially very rapid but then slows substantially at about 40 day. The change in recovery

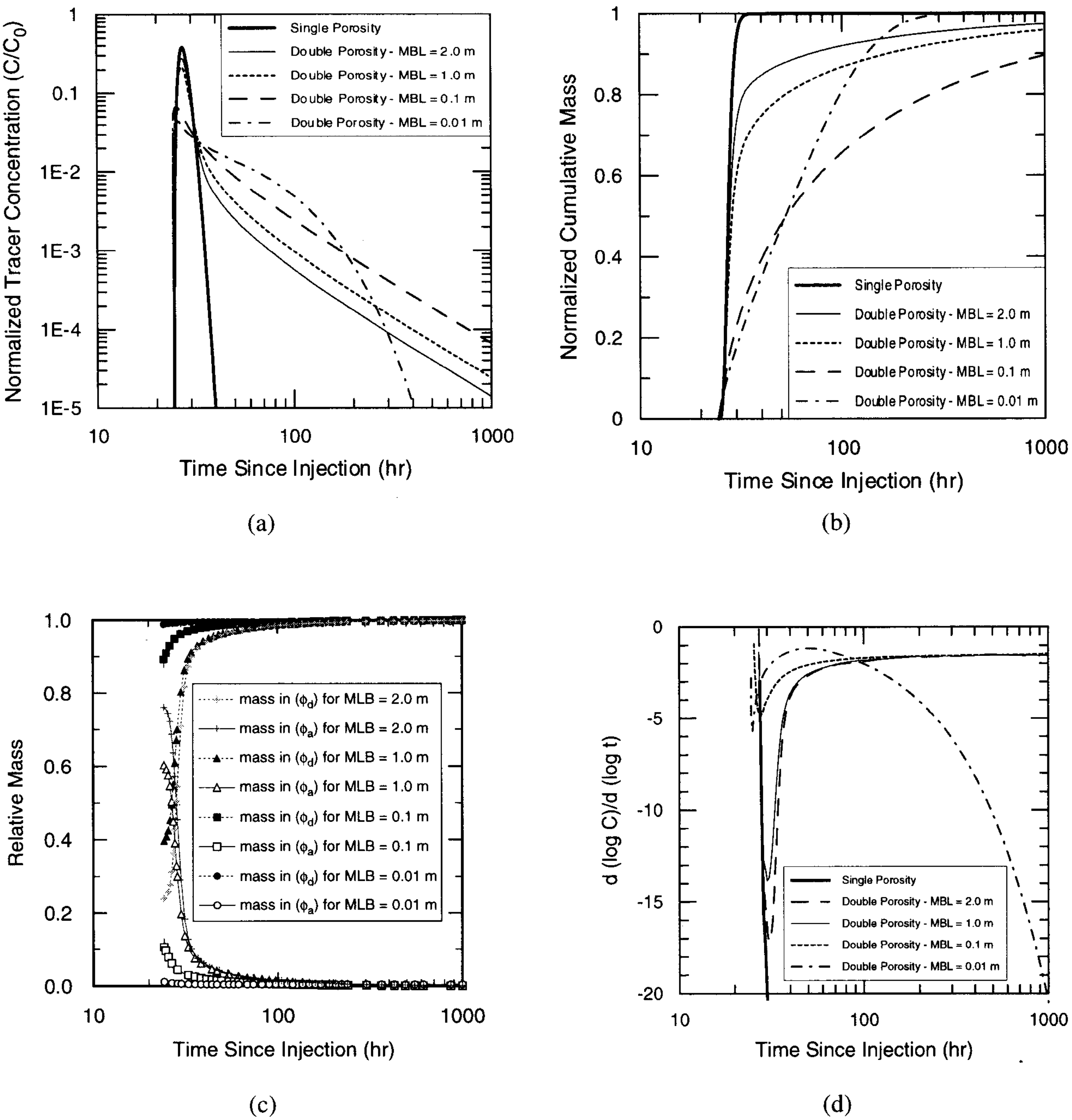

(a)

(b)

(c)

(d)

Figure 4-8. Comparison of (a) tracer-recovery curves, (b) mass-recovery curves, (c) tracer distribution between the advective porosity (ϕ_a) and the diffusive porosity (ϕ_d), and (d) derivative plots for single- and double-porosity conceptualizations assuming a homogeneous transmissivity field and no plume drift.

rate reflects the change from advection-dominated transport to diffusion-dominated transport. Figure 4-8c shows the relative mass of tracer in the advective porosity and the diffusive porosity during the withdrawal period for the SWIW test. The relative mass is defined as the mass of tracer in the advective porosity or diffusive porosity relative to the total mass of tracer in the system at a given time. The transition from rapid to slow mass recovery begins when the relative tracer mass in the advective porosity drops below about 0.1. Once the mass of tracer residing in the advective porosity at the end of the pause period is nearly depleted, tracer enters the advective porosity predominantly by diffusion from the diffusive porosity, and the rate of tracer recovery is then controlled by the rate of diffusion.

For the double-porosity simulation with a matrix-block length of 0.1 m, the relative mass of tracer in the advective porosity at the end of the pause period is very small (~10%). This mass is quickly recovered during a very short period of advection-dominated transport. The rate of mass recovery is then controlled by diffusion-dominated transport during the remainder of the withdrawal period. For the double-porosity simulation with a matrix-block length of 0.01 m, essentially all tracer is located in the diffusive porosity at the end of the pause period, which results in diffusion-dominated transport controlling the rate of mass recovery for the entire withdrawal period. The large surface area available for diffusion and short diffusion distance associated with this smallest matrix-block length allows for complete diffusion of tracer from the diffusive porosity into the advective porosity over the time period of the withdrawal portion of the test, resulting in full mass recovery.

Derivative plots show that the slopes of the falling limbs of the tracer-recovery curves for the double-porosity simulations with the three largest matrix-block lengths are approximately -1.5 for the final approximately 800 hr of the simulation (Figure 4-8d). As the derivation in Appendix K shows, diffusion from infinite matrix blocks produces tracer-recovery curves in log-log space with late-time slopes of -1.5. The agreement between the -1.5 slope obtained with the derivation and observed in the simulated results suggests that, over the time period of the simulations, the matrix blocks appear to be infinite. The tracer-recovery curve for the double-porosity simulation with the smallest matrix-block length does not have a late-time slope of -1.5, suggesting that, over the time period of the test, the diffusive porosity was finite and tracer reached the inner boundaries of the matrix blocks. The slope of the falling limb of the tracer-recovery curve for the single-porosity simulation rapidly becomes very steep, as reflected in Figure 4-8d. The derivative plot shows striking differences in tracer-recovery behavior from a single-porosity system, a double-porosity system with an infinite-acting diffusive porosity, and a double-porosity system with a finite diffusive porosity.

Figure 4-9 shows that single- and double-porosity responses are also easily distinguished for a heterogeneous system with no regional gradient (i.e., plume drift is absent). The transmissivity field for the simulations shown in Figure 4-9 is the same as that used for the simulations shown in Figures 4-3c and d and 4-4; that is, the field in the sensitivity studies that gave close to the slowest mass-recovery rates (i.e., has close to the largest effect of heterogeneity on mass recovery). If drift is included but the aquifer is assumed to be homogeneous, the single- and double-porosity responses are also easily distinguished (Figure 4-10). The regional gradient used for these simulations is the same as that used for the sensitivity studies (0.011 m/m). These results indicate that heterogeneity alone or drift alone is not sufficient to cause confusion between single- and double-porosity media. Lessoff and Konikow (1997) also concluded that the effect of drift in a homogeneous system would not "have a significant effect on the expected tracer-recovery curves". The double-porosity results for a matrix-block length of 0.01 m are not included in Figures 4-9 through 4-10, for reasons discussed below.

Most natural systems will have some degree of heterogeneity and some regional gradient. Therefore, single- and double-porosity simulations were conducted assuming both a heterogeneous transmissivity field and a regional gradient in order to represent natural systems more closely. The heterogeneous transmissivity field used for the simulations was the same as that used for the simulations shown in Figure 4-9 (i.e., the one that gave close to the slowest mass recovery for the sensitivity studies). The regional gradient used for the simulations was the same as that used for the sensitivity studies (0.011 m/m). The results show that the tracer-recovery curve for the single-porosity simulation is very similar to those for the double-porosity simulations until about 100 hr after injection or until the normalized tracer concentration is over two orders of magnitude less than the peak concentration (Figure 4-11a). From that time until about 400 hr after injection, or over

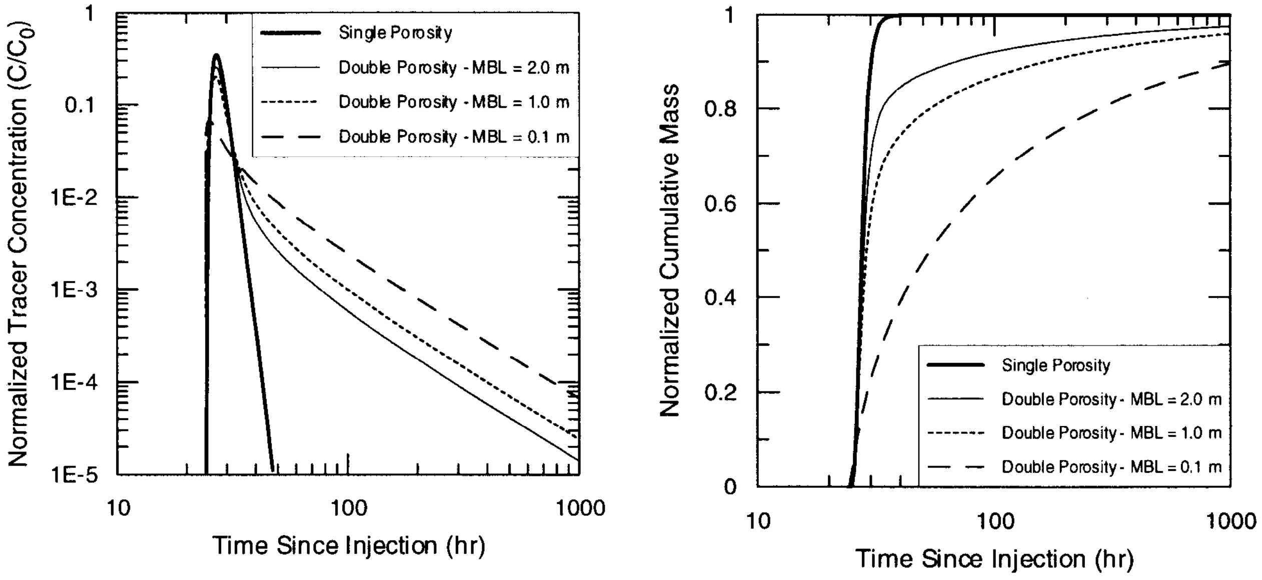

(a) (b)

Figure 4-9. Comparison of (a) tracer-recovery curves and (b) mass-recovery curves for single- and double-porosity conceptualizations assuming a heterogeneous transmissivity field and no plume drift.

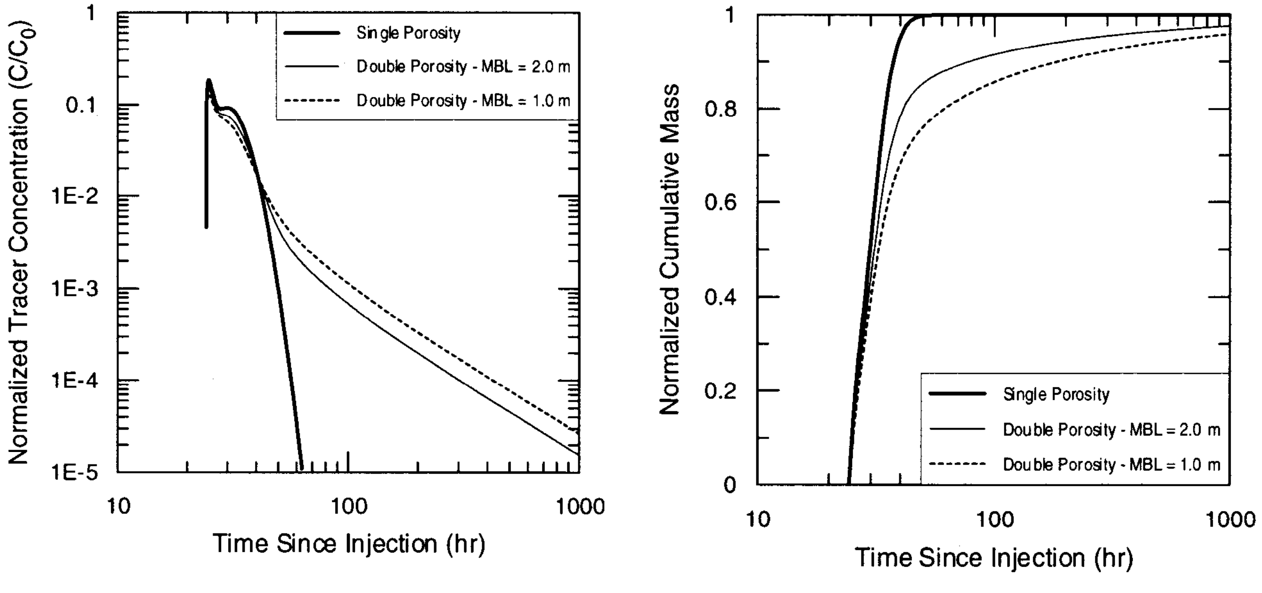

(a) (b)

Figure 4-10. Comparison of (a) tracer-recovery curves and (b) mass-recovery curves for single- and double-porosity conceptualizations assuming a homogeneous transmissivity field and plume drift during the resting phase.

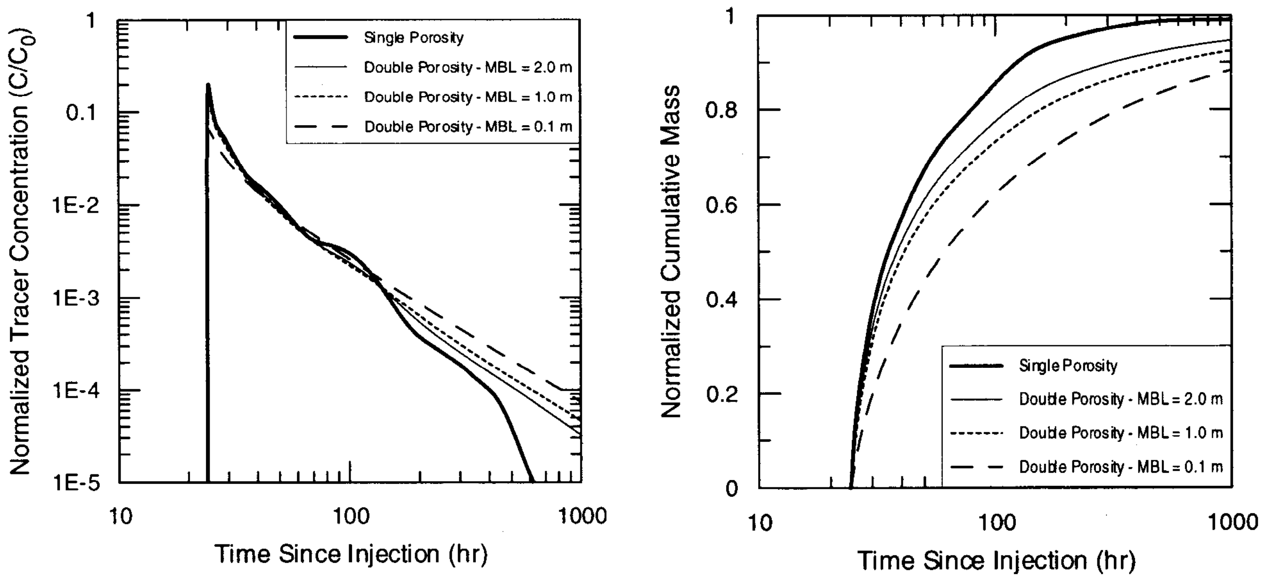

(a) (b)

Figure 4-11. **Comparison of (a) tracer-recovery curves and (b) mass-recovery curves for single- and double-porosity conceptualizations assuming a heterogeneous transmissivity field and plume drift during the resting phase.**

another one order of magnitude decrease in the normalized concentration, the slope of the single-porosity curve is essentially identical to the slope of the double-porosity curves. However, beyond that time and over another order of magnitude reduction in concentration, the slope of the double-porosity curves remains constant at approximately -1.5 while the slope of the single-porosity curve increases substantially. The mass-recovery curves show that a higher mass fraction is recovered for the single-porosity simulation than for the double-porosity simulations at all times (Figure 4-11b).

The simulations presented to this point indicate that the double-porosity results show no sensitivity to the nature of the transmissivity field unless a regional gradient is also present. That is, for systems with no gradient, the simulations assuming a homogeneous and a heterogeneous transmissivity field yield identical results. As the matrix-block length increases, the sensitivity of the simulated results to the regional gradient also increases due to a larger areal extent of the plume in the advective porosity resulting from less physical retardation by matrix diffusion. Double-porosity results for simulations using a matrix-block length of 0.01 m are not shown in Figures 4-9, 4-10, and 4-11 because they are identical to the results shown in Figure 4-8. This indicates that, for simulations with this matrix-block length, the effect of matrix diffusion on transport dominates because matrix diffusion significantly restricts the areal extent of the plume in the advective porosity, which is where the effects of heterogeneity and gradient are manifested.

Double-porosity simulations were also conducted using the heterogeneous transmissivity field from the sensitivity studies that gave close to the fastest mass recovery. This field is the one used for the simulations depicted in Figures 4-3a and b. In Figure 4-12, these double-porosity simulations are compared to the results of the single-porosity simulation shown in Figure 4-11 that was conducted with the heterogeneous transmissivity field that resulted in close to the slowest mass recovery in the sensitivity study. The purpose of this comparison was to look at the single-porosity simulation in this study having the slowest recovery versus the double-porosity simulations in this study having the fastest recovery based on heterogeneous effects. This comparison shows that the overall trend of the tracer-recovery curve for a single-porosity simulation is quite similar to that for the double-porosity simulations until the normalized tracer concentration drops below about 10^{-4} (i.e., is over three orders of magnitude less than the peak concentration). The mass-recovery curves (Figure 4-12b) show that the double-porosity simulations with matrix-block lengths of 2.0 and 1.0 m reached approximately 93% and 84% mass recovery, respectively, faster than the single-porosity simulation. This implies that using the time to some percentage mass recovery does not provide a basis for differentiating between single- and double-porosity media.

Figures 4-11a and 4-12a show that the most distinctive difference between the single- and double-porosity responses is observed late in the simulation where the slope of the tracer-recovery curves remains constant at a value of -1.5 for the double-porosity simulations but decreases significantly to a value of ≤ -6 for the single-porosity simulation. However, until the normalized concentration fell below 10^{-4}, or was over three orders of magnitude less than the peak concentration, the responses of the two types of systems could not be definitively distinguished based on slope. Therefore, key factors for differentiating between single- and double-porosity media are the use of tracers with low detection thresholds and the collection of data for as long as possible.

Heterogeneity and plume drift work together to generate plumes that have no consistent structure and, as a result, the rate of tracer flux to the well can be extremely variable from plume to plume. For the single-porosity simulation shown in Figures 4-11a and 4-12a, the increases and reductions in tracer influx to the well during withdrawal are reflected by "humps" in the tracer-recovery curve. In the double-porosity simulations, this effect is significantly dampened by the presence of diffusion processes. Once transport in the double-porosity simulations switches from advection-dominated to diffusion-dominated, the effect of the diffusion processes on tracer transport dominates over the effects of heterogeneity. Therefore, the tracer-recovery curves for the double-porosity simulations do not exhibit pronounced humps.

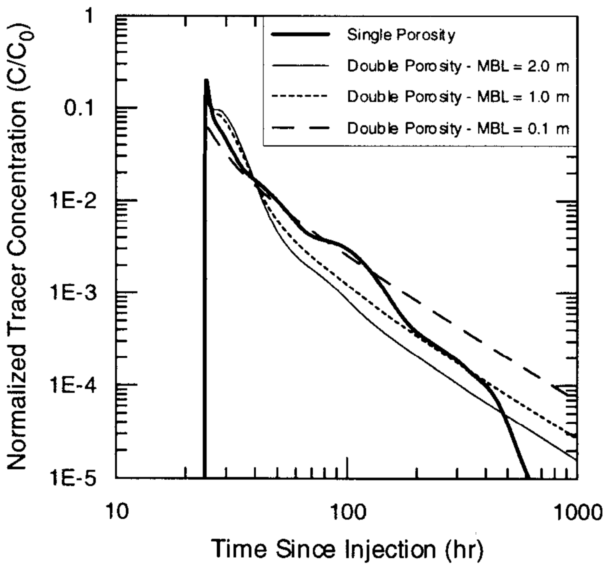

(a)

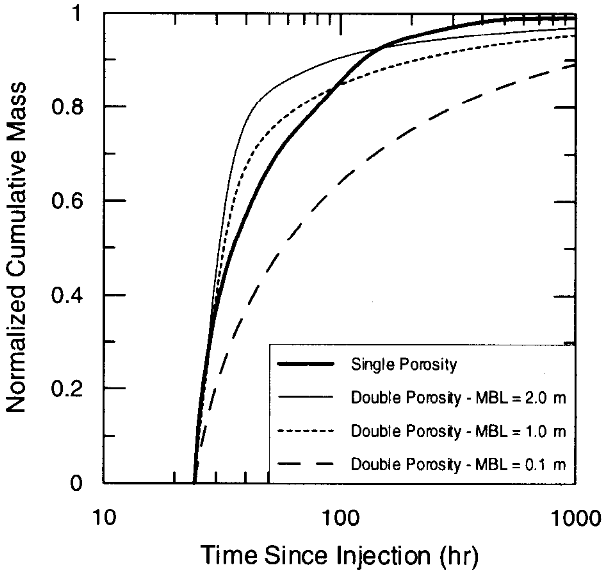

(b)

Figure 4-12. Comparison of (a) tracer-recovery curves and (b) mass-recovery curves for a single-porosity simulation in the heterogeneous transmissivity field that gave the slowest mass recovery in the sensitivity studies to double-porosity simulations in the heterogeneous transmissivity field that gave the fastest mass recovery in the sensitivity studies. All simulations included a regional gradient of 0.011 m/m.

Very subtle humps are present in the tracer-recovery curves for the double-porosity simulations with a matrix-block length of 2.0 m because matrix diffusion was significantly minimized by using a very large matrix-block size (i.e., equal to one-half the model-layer thickness). When the block length is reduced to 1.0 m, the humps completely disappear from the double-porosity simulations. If data from a given test are not collected long enough to differentiate between single- and double-porosity conditions on the basis of the slope of the data collected at the end of the test, differentiation may be feasible by evaluating the frequency and magnitude of slope changes in the tracer-recovery curve, provided the data are of high precision and accuracy.

In order to gain greater insight regarding the role plume drift plays in causing confusion between responses from single- and double-porosity systems, single- and double-porosity simulations were conducted using regional gradients of 0.0, 0.001, 0.006, and 0.011 m/m. The greatest possibility for confusion occurs when parameter values are selected so that the mass-recovery rate for the single-porosity simulations is minimized and the mass-recovery rate for the double-porosity simulations is maximized. Therefore, the single-porosity simulations were conducted using the heterogeneous transmissivity field that gave the slowest mass recovery in the sensitivity studies and the double-porosity simulations were conducted using the heterogeneous transmissivity field that gave the fastest mass recovery in the sensitivity studies. In addition, the double-porosity simulations assumed a matrix-block length of 2.0 m in order to minimize diffusion and increase the rate of mass recovery. The simulation results show that the single- and double-porosity results are easily distinguishable for regional gradients less than or equal to 0.006 m/m (Figure 4-13a). Notice, however, that the normalized tracer concentration must be at least two orders of magnitude lower than the peak concentration before the single-porosity simulation with a gradient of 0.006 m/m can be distinguished from the double-porosity simulations. The time to 90% mass recovery is longer for the single-porosity simulation than for the double-porosity simulation when a regional gradient of 0.011 m/m is used. The distinction between the single- and double-porosity responses is easily seen in the derivative plots shown in Figure 4-13c. The late-time slope is near -1.5 for all of the double-porosity simulations. For the single-porosity simulations, the slope is either very steep or has several peaks and valleys in the late-time data before steepening significantly.

Prior to conducting a SWIW tracer test, the likelihood of collecting data that may be difficult to interpret should be estimated. The performance of pre-test simulations using a single-porosity model and worst-case values for the regional gradient and the parameters describing the heterogeneous nature of the system is recommended. If those simulations produce tracer-recovery curves having steep slopes, the SWIW test will probably provide a definitive means of determining the proper conceptualization for the system. Simulated tracer-recovery curves having shallow slopes, however, will be an indication that the test may not be definitive or that, at a minimum, high-precision data spanning at least three to four orders of magnitude in concentration will be needed to evaluate the system's conceptualization definitively. As seen from the simulated results, a large span in the observed data is required in order to determine whether the tracer-recovery curve will maintain a constant slope, indicating a double-porosity system with an infinite-acting matrix over the time period of the test, or will increase in slope, indicating a single-porosity system.

In summary, the results presented here illustrate that, for some situations, responses from single- and double-porosity systems can be confused. The likelihood for confusion increases as both the regional gradient and the degree of heterogeneity increase. If one or the other of these factors is absent from the system or is small, misinterpreting the response is unlikely. For cases where confusion is likely, the collection of high-resolution late-time data is critical in order to eliminate ambiguity between single- and double-porosity conditions. Pre-test simulations can provide a means for evaluating the potential for confusion in the observed data and, if a potential exists, will provide guidance for determining the concentration

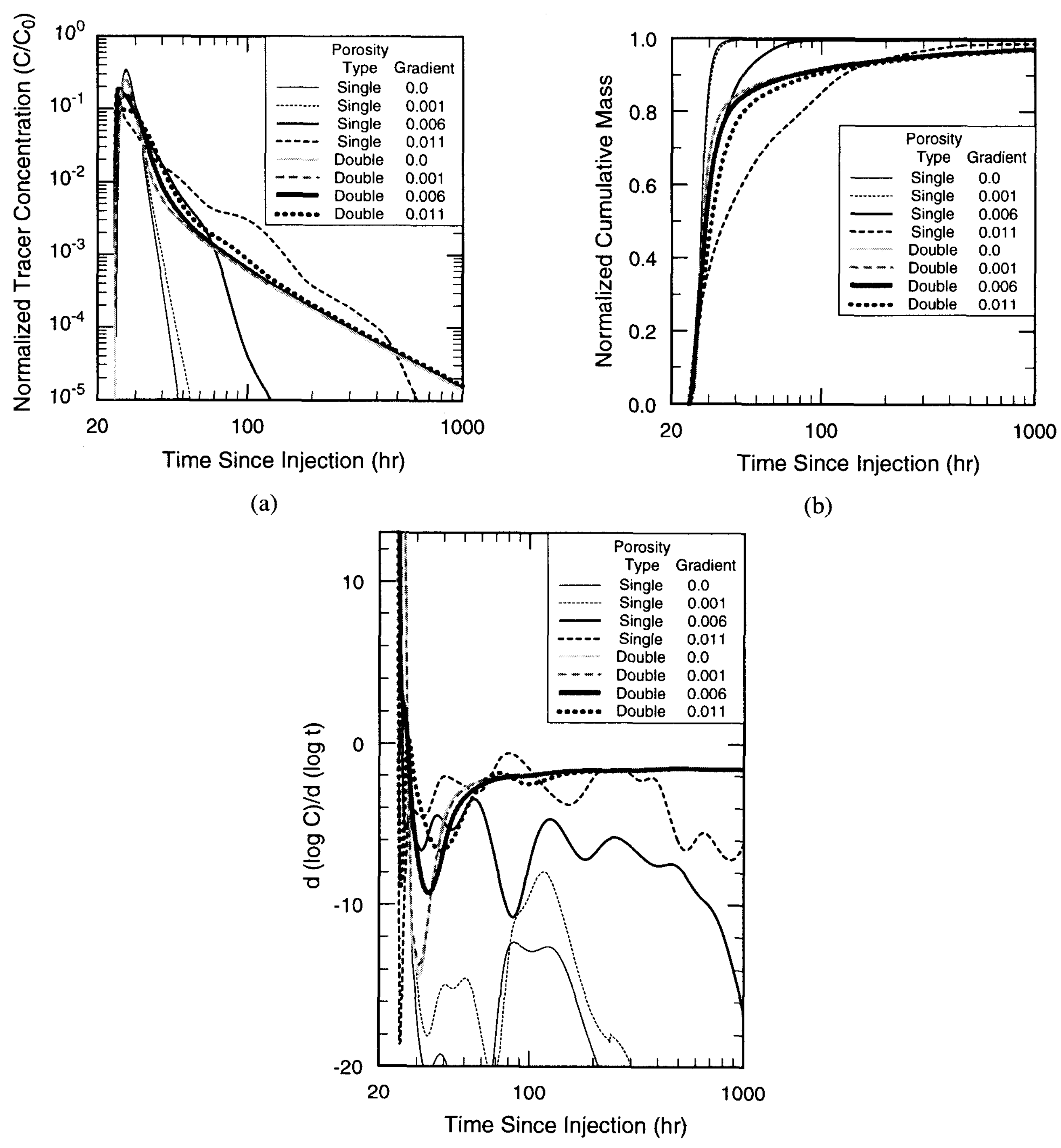

(a)

(b)

(c)

Figure 4-13. Comparison of (a) tracer-recovery curves, (b) mass-recovery curves, and (c) derivative plots for single-porosity simulations in the heterogeneous transmissivity field that gave the slowest mass recovery in the sensitivity studies to double-porosity simulations in the heterogeneous transmissivity field that gave the fastest mass recovery in the sensitivity studies. The single- and double-porosity simulations assumed regional gradients of 0.0, 0.001, 0.006, and 0.011 m/m. The matrix-block length for the double-porosity simulations was 2.0 m.

reduction needed in the tracer-recovery curve to minimize the ambiguity.

The simulations presented in this section also show that the effects of heterogeneity and plume drift on simulated results are qualitatively the same for both single- and double-porosity simulations. A comparison of the double-porosity results shown in Figures 4-10 through 4-12 indicates that mass recovery slows as the degree of heterogeneity increases, a result identical to that observed for the single-porosity simulations in the sensitivity studies. In addition, the trend of slower mass recovery with increasing plume drift observed for the single-porosity simulations is also observed for the double-porosity simulations, as seen in Figure 4-13. However, these effects decrease in importance in double-porosity simulations as the matrix-block length decreases (i.e., as diffusion increases).

4.5.3 WIPP-Specific Study

The sensitivity studies described in Section 4.5.1 provide insight into the roles model parameters representing characteristics of an aquifer play in affecting mass recovery in a single-porosity system. These insights are used in this section to determine whether observed mass recovery from the SWIW tracer tests conducted at the WIPP site could be explained with a single-porosity conceptualization. WIPP-specific simulations were conducted for all SWIW tracer tests at the H-19 and H-11 hydropads (Table 4-3). As stated in Section 4.4.4, all tests were simulated using a heterogeneous transmissivity field generated with a $\sigma \ln T$ of 2.64, and the first tracer injected at H-11 was also simulated using a heterogeneous transmissivity field generated with a $\sigma \ln T$ of 2.1.

When the simulations for the H-19 tests (Figure 4-14) and H-11 tests (Figure 4-15) are compared, a much wider variation in simulated mass recovery is observed for H-11 conditions. If the values for mean transmissivity, thickness, porosity, gradient, and resting-phase duration given in Table 4-3 for the H-11 and H-19 hydropads are substituted into Equation 4-2, the calculated drift magnitude for the H-11 hydropad is a factor of about 50 greater than for the H-19 hydropad. Because the amount of simulated drift is much less at H-19, the H-19 simulations have less spread and faster mass recovery.

For the SWIW test conditions at the H-19 hydropad, single-porosity simulations produce recovery curves with longer times to peak concentration and higher peak concentrations than the observed test data and simulated mass recovery is much faster than observed mass recovery (Figure 4-14). These results indicate that single-porosity simulations using realistic end-member parameter values cannot reproduce the observed data.

The results for the H-11 simulations also show that the observed SWIW test data cannot be matched with a single-porosity conceptualization (Figure 4-15). For one transmissivity-field realization using a $\sigma \ln T$ value of 2.64, the simulated tracer-recovery and mass-recovery curves are similar to the observed data for both tracers up to approximately 100 hr into the test (Figures 4-15a, b, c, and d). However, two important differences between the simulated results and the observed data at later times are noted. First, the slopes of the simulated mass-recovery curves approach zero between 400 and 500 hr into the test (Figures 4-15b and d). In contrast, the slope of the observed data remains positive, indicating continued mass recovery at these later times. In addition, the slope of the simulated tracer-recovery curve increases relative to the data.

For the first tracer injected during the SWIW test at H-11, simulations were also conducted using a heterogeneous transmissivity field generated with a $\sigma \ln T$ value of 2.1. This value is calculated for the entire WIPP-site area (see Appendix L). The simulation results (Figures 4-15e and f) show that the spread in the tracer-recovery and mass-recovery curves is smaller than when the larger $\sigma \ln T$ value is used. This result is consistent with that found by the sensitivity study (see Figure 4-5a). In addition, the length of time over which the results for any transmissivity field match the observed data decreases from about 100 hr with the higher $\sigma \ln T$ value to about 35 hr with the lower value. Beyond that time, the simulated results deviate significantly from the observed data,

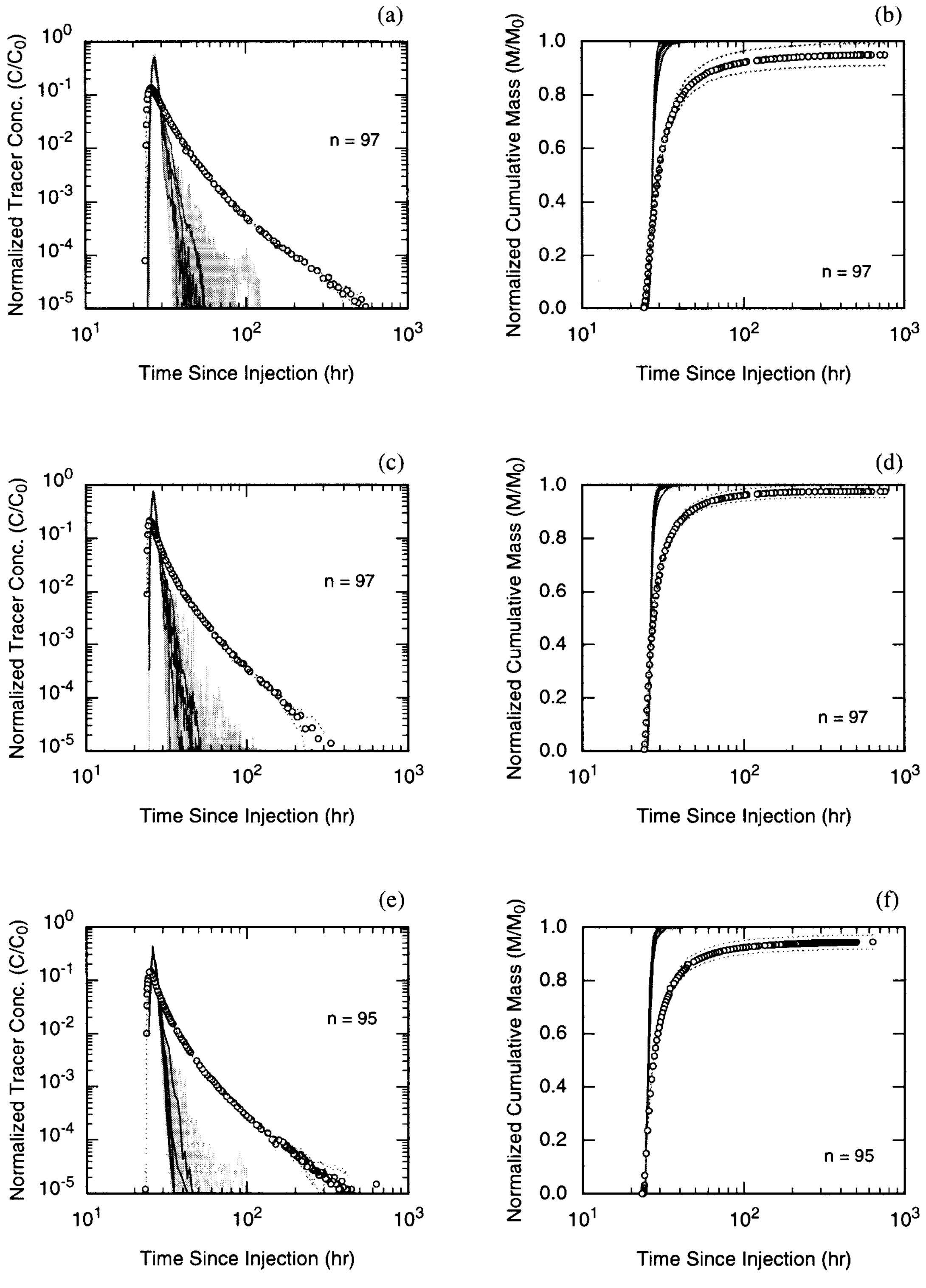

Figure 4-14. Comparison of simulated and observed results for (a and b) tracer 1 from the H-19 SWIW test 1, (c and d) tracer 2 from the H-19 SWIW test 1, and (e and f) the H-19 SWIW test 2. Solid gray lines are simulation results. Solid black lines are 1, 25, 50, 75, and 100 percentile results of time to 90% mass recovery. Circles represent observed data with 95% analytical confidence intervals (dashed black lines). Only 97 out of 100 simulations converged for the H-19 SWIW test 1realizations, and 95 out of 100 for the H-19 SWIW test 2 realizations.

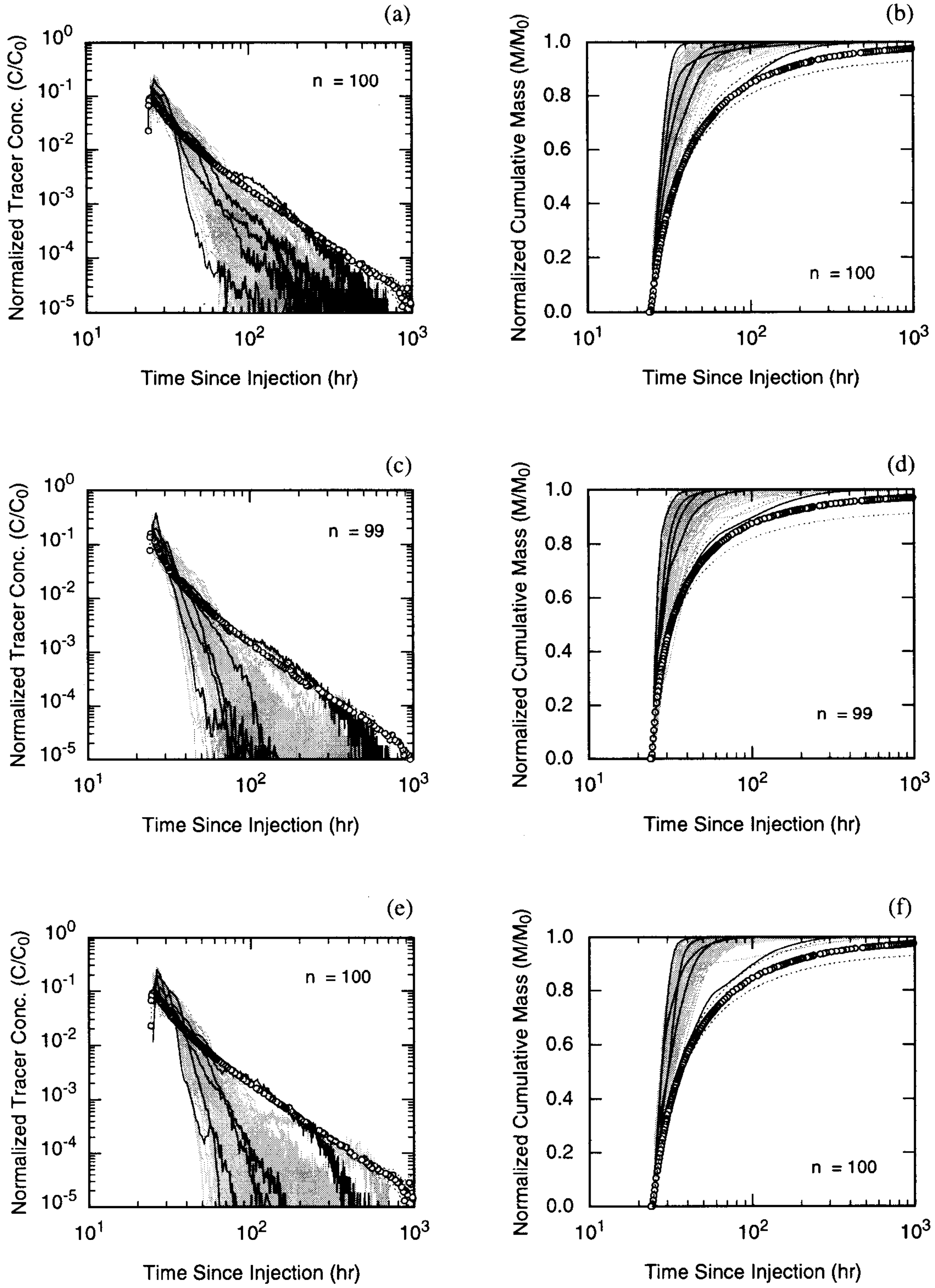

Figure 4-15. **Comparison of simulated and observed results for (a and b) tracer 1 from the H-11 SWIW test using a $\sigma \ln T$ of 2.64, (c and d) tracer 2 from the H-11 SWIW test using a $\sigma \ln T$ of 2.64, and (e and f) tracer 1 from the H-11 SWIW test using a $\sigma \ln T$ of 2.1. Solid gray lines are simulation results. Solid black lines are 1, 25, 50, 75, and 100 percentile results of time to 90% mass recovery. Circles represent observed data with 95% analytical confidence intervals (dashed black lines).**

indicating that a single-porosity conceptualization is not appropriate.

Additional data suggest that a single-porosity conceptualization is not an appropriate model for the Culebra at both the H-11 and H-19 hydropads. Laboratory diffusion studies suggest that solutes diffuse significantly into the Culebra matrix (Dykhuizen and Casey, 1989; Tidwell et al., 2000). Hydraulic-test data from both hydropads also cannot be matched using single-porosity models (Beauheim, 1989; Beauheim and Ruskauff, 1998).

In addition to regional flow combined with aquifer heterogeneity, two other scenarios have been proposed that could cause gradual mass recovery without matrix diffusion. These two scenarios were investigated prior to conducting the WIPP-specific simulations and eliminated as explanations for gradual mass-recovery rates. The first scenario involves the loss of mass from the injection system to the bottom of the borehole during the tracer-injection phase of the test. During the withdrawal phase, this mass could diffuse back into the test interval, resulting in gradual mass recovery at late time. Even with conservative assumptions for diffusion rates and surface areas for diffusion, the amount of mass that could diffuse from the bottom of the borehole is very small and has an insignificant effect on the observed mass-recovery curves. A complete discussion of the investigation of diffusion from the bottom of the borehole can be found in Appendix N. The second scenario for gradual mass-recovery rates is tracer sorption to the aquifer materials. Simulations that included linear sorption show that the peak concentration, the length of the rising limb of the tracer-recovery curve, and the rate of mass recovery immediately after the peak decrease as the amount of sorption increases. Although sorption does decrease the rate of mass recovery, the characteristics of the tracer-recovery curve for simulations with linear sorption are not consistent with the characteristics of the observed tracer-recovery curve. For simulations that include sorption and have a well-defined peak, the slope of the falling limb is much steeper than the slope of the observed data. However, simulations that include sorption and have a shallow falling-limb slope do not have a rising limb on the tracer-recovery curve (i.e., do not have a peak), unlike the observed data. A complete discussion of the effects of sorption on simulated results is provided in Appendix O.

In summary, the late-time data from the H-19 and H-11 SWIW tracer tests cannot be matched if a single-porosity conceptualization is assumed. These results suggest that diffusion is occurring in the aquifer and reinforces the value of collecting late-time data. However, the late-time slope of the observed tracer-recovery data does not match the characteristic -1.5 log-log slope predicted by conventional double-porosity models. The late-time slopes for the observed SWIW test data vary between -2.05 and -2.75. Chapter 6 shows that a double-porosity model with multiple rates of diffusion provides an excellent explanation for the observed data, including the late-time slopes.

4.6 Summary and Conclusions

Through numerical simulations, the effect of plume drift in a heterogeneous, single-porosity system on simulated results for SWIW tracer tests has been demonstrated. In addition, the conditions under which single- and double-porosity responses can be confused have been evaluated. The insights gained from these simulations were then used to assess whether a single-porosity conceptual model in a heterogeneous system with plume drift can explain the data from the SWIW tracer tests performed at the WIPP site.

Site-specific factors that affect mass recovery in SWIW tracer tests include the structure of the heterogeneity, the porosity, the regional gradient, and matrix diffusion. Of the factors affecting the heterogeneity structure, the magnitude of the heterogeneity in the transmissivity field (as defined by $\sigma \ln T$) has the strongest influence on the occurrence of channeling and, therefore, also has the strongest influence on whether plume drift will result in reduced mass recovery. The porosity, regional gradient, and resting-phase duration affect mass recovery because of their direct control on plume drift during the resting phase. Of these factors, the regional gradient has the largest impact on mass recovery because it also affects the capture zone of the well during pumping.

The evaluation of conditions for which single- and double-porosity responses can be confused indicated that both formation heterogeneity and a regional gradient, which causes plume drift during the resting phase, must be present in order to encounter difficulty in distinguishing between the two types of responses. Both the degree of heterogeneity and the magnitude of the gradient must be fairly large before differentiating between responses for the two systems becomes difficult. For systems with very high background gradients and significant heterogeneity, the SWIW test results may not provide definitive evidence for matrix diffusion due to possible loss of mass outside the capture zone of the pumping well and tailing due to drift.

If background gradients are low and a relatively short resting period is used (i.e., very little plume drift occurs during the resting phase), a SWIW test is likely to be a definitive test for demonstrating the presence of significant matrix diffusion. For moderate background gradients, results from single-porosity numerical simulations using worst-case parameters (lowest porosity, highest background gradient, and most heterogeneity) should provide insight into the likelihood that the test results will provide a definitive means of differentiating between a single- or double-porosity response. For example, if the pre-test calculations with worst-case parameters yield rapid mass recovery and a steep falling-limb slope in log concentration versus log time, then the SWIW test should provide a definitive means of determining the presence or absence of matrix diffusion in the tested medium. If the calculations show the potential for confusion between single- and double-porosity conditions for some period of time, the test may not be definitive unless it can be continued until the time or concentration at which confusion no longer exists. For any test to be definitive, a tracer with the potential for several orders of magnitude of resolution in concentration should be selected, data should be collected over a long enough time period to get several orders of magnitude in concentration in the tracer-recovery curve, and the data should be of high precision and accuracy. In systems with high background gradients in which tracer may drift outside of the capture zone of the well, a SWIW test may not be useful in differentiating between a single- and double-porosity system.

The observed data from the SWIW tracer tests performed at the WIPP H-11 and H-19 hydropads cannot be matched assuming a single-porosity conceptualization even when a small porosity is used and heterogeneity and plume drift are incorporated into the analysis. The effects of heterogeneity and plume drift decrease as the porosity increases due to the decreased area of the plume. Therefore, use of a small porosity in the WIPP-specific simulations resulted in worst-case (i.e., reduced mass-recovery rate) results. These results indicate that matrix diffusion is likely an important process in controlling the slow mass recovery observed in the WIPP test data. The late-time slopes of the observed tracer-recovery data are steeper than the -1.5 log-log slope predicted by conventional double-porosity models. Chapter 6 demonstrates that a double-porosity model with multiple rates of diffusion can provide an excellent explanation for the observed data, including the late-time slopes.

4.7 References

Abelin, H., L. Birgersson, L. Moreno, H. Widén, T. Ågren, and I. Neretnieks. 1991. "A Large-Scale Flow and Tracer Experiment in Granite. 2. Results and Interpretation," *Water Resources Research*. Vol. 27, no. 12, 3119-3135.

Ball, W.P., and P.V. Roberts. 1991. "Long-Term Sorption of Halogenated Organic Chemicals by Aquifer Material. 1. Equilibrium," *Environmental Science and Technology*. Vol. 25, no. 7, 1223-1237.

Bear, J., and C. Braester. 1972. "On the Flow of Two Immiscible Fluids in Fractured Media," *Fundamentals of Transport Phenomena in Porous Media*. Developments in Soil Science 2. New York, NY: Elsevier Publishing Company. 177-202.

Beauheim, R.L. 1987. *Interpretations of Single-Well Hydraulic Tests Conducted At and Near the Waste Isolation Pilot Plant (WIPP) Site, 1983-1987.* SAND87-0039. Albuquerque, NM: Sandia National Laboratories.

Beauheim, R.L. 1989. *Interpretation of H-11b4 Hydraulic Tests and the H-11 Multipad Pumping Test of the Culebra Dolomite at the Waste Isolation Pilot Plant (WIPP) Site.* SAND89-0536. Albuquerque, NM: Sandia National Laboratories.

Beauheim, R.L., and G.J. Ruskauff. 1998. *Analysis of Hydraulic Tests of the Culebra and Magenta Dolomites and Dewey Lake Redbeds Conducted at the Waste Isolation Pilot Plant Site.* SAND98-0049. Albuquerque, NM: Sandia National Laboratories.

Clauser, C. 1992. "Permeability of Crystalline Rocks," *Eos Transactions, American Geophysical Union.* Vol. 73, no. 21, 233 and 237-238.

Deutsch, C.V., and A.G. Journel. 1998. *GSLIB: Geostatistical Software Library and User's Guide.* 2nd ed. New York, NY: Oxford University Press.

Dykhuizen, R.C., and W.H. Casey. 1989. *An Analysis of Solute Diffusion in the Culebra Dolomite.* SAND89-0750. Albuquerque, NM: Sandia National Laboratories.

Finley, N.C., and M. Reeves. 1981. *SWIFT Self-Teaching Curriculum: Illustrative Problems to Supplement the User's Manual for the Sandia Waste-Isolation Flow and Transport Model (SWIFT).* SAND81-0410, NUREG/CR-1968. Albuquerque, NM: Sandia National Laboratories.

Gelhar, L.W., C. Welty, and K.R. Rehfeldt. 1992. "A Critical Review of Data on Field-Scale Dispersion in Aquifers," *Water Resources Research.* Vol. 28, no. 7, 1955-1974.

Grisak, G.E., and J.F. Pickens. 1980. "Solute Transport Through Fractured Media 1. The Effect of Matrix Diffusion," *Water Resources Research.* Vol. 16, no. 4, 719-730.

Hale, F.V., and Y.W. Tsang. 1996. *THEMM User Guide Version 1.0 (7-16-96).* Berkeley, CA: Lawrence Berkeley National Laboratory. (Copy on file in the Sandia WIPP Central Files (SWCF) as ERMS #235261.)

Heer, W., and J. Hadermann. 1994. *Grimsel Test Site, Modelling Radionuclide Migration Field Experiments.* PSI-Bericht Nr. 94-13. Würenlingen, Switzerland: Paul Scherrer Institut.

Huyakorn, P.S., B.H. Lester, and J.W. Mercer. 1983. "An Efficient Finite Element Technique for Modeling Transport in Fractured Porous Media 1: Single Species Transport," *Water Resources Research.* Vol. 19, no. 3, 841-854.

Istok, J.D., M.D. Humphrey, M.H. Schroth, M.R. Hyman, and K.T. O'Reilly. 1997. "Single-Well, 'Push-Pull' Test for In Situ Determination of Microbial Activities," *Ground Water.* Vol. 35, no. 4, 619-631.

Jones, T.L., V.A. Kelley, J.F. Pickens, D.T. Upton, R.L. Beauheim, and P.B. Davies. 1992. *Integration of Interpretation Results of Tracer Tests Performed in the Culebra Dolomite at the Waste Isolation Pilot Plant Site.* SAND92-1579. Albuquerque, NM: Sandia National Laboratories.

Leap, D.I., and P.G. Kaplan. 1988. "A Single-Well Tracing Method for Estimating Regional Advective Velocity in a Confined Aquifer: Theory and Preliminary Laboratory Verification," *Water Resources Research.* Vol. 24, no. 7, 993-998.

Lessoff, S.C., and L.F. Konikow. 1997. "Ambiguity in Measuring Matrix Diffusion with Single-Well Injection/Recovery Tracer Tests," *Ground Water.* Vol. 35, no. 1, 166-176.

Majoros, S., and H.A. Deans. 1980. *Single-Well Chemical Tracer Tests Since 1968.* DOE/BC/20006-17. Houston, TX: Rice University for U.S. Department of Energy, Washington, DC.

Moench, A.F. 1995. "Convergent Radial Dispersion in a Double-Porosity Aquifer with Fracture Skin: Analytical Solution and Application to a Field Experiment in Fractured Chalk," *Water Resources Research.* Vol. 31, no. 8, 1823-1835.

Moreno L., Y.W. Tsang, C.F. Tsang, F.V. Hale, and I. Neretnieks. 1988. "Flow and Tracer Transport in a Single Fracture: A Stochastic Model and Its Relation to Some Field Observations," *Water Resources Research.* Vol. 24, no. 12, 2033-2048.

Moreno, L., C.F. Tsang, Y. Tsang, and I. Neretnieks. 1990. "Some Anomalous Features of Flow and Solute Transport Arising from Fracture Aperture Variability," *Water Resources Research.* Vol. 26, no. 10, 2377-2391.

National Research Council. 1994. *Alternatives for Ground Water Cleanup.* Washington, DC: National Academy Press.

Pruess, K., and T.N. Narasimhan. 1982. "A Practical Method for Modeling Fluid and Heat Flow in Fractured Porous Media," *Proceedings, Sixth SPE Symposium on Reservoir Simulation, New Orleans, LA, January 31-February 3, 1982.* SPE 10509. Dallas, TX: Society of Petroleum Engineers. 269-284.

Rasmuson, A., T.N. Narasimhan, and I. Neretnieks. 1982. "Chemical Transport in a Fissured Rock: Verification of a Numerical Model," *Water Resources Research.* Vol. 18, no. 5, 1479-1492.

Reeves, M., D.S. Ward, N.D. Johns, and R.M. Cranwell. 1986a. *Theory and Implementation for SWIFT II, the Sandia Waste-Isolation Flow and Transport Model for Fractured Media Release 4.84.* SAND83-1159, NUREG/CR-3328. Albuquerque, NM: Sandia National Laboratories.

Reeves, M., D.S. Ward, N.D. Johns, and R.M. Cranwell. 1986b. *Data Input Guide for SWIFT II, the Sandia Waste-Isolation Flow and Transport Model for Fractured Media, Release 4.84.* SAND83-0242, NUREG/CR-3162. Albuquerque, NM: Sandia National Laboratories.

Reeves, M., D.S. Ward, P.A. Davis, and E.J. Bonano. 1987. *SWIFT II Self-Teaching Curriculum: Illustrative Problems for the Sandia Waste-Isolation Flow and Transport Model for Fractured Media.* SAND84-1586 Revision, NUGER/CR-3925. Albuquerque, NM: Sandia National Laboratories.

Seetharam, R.V., and H.A. Deans. 1989. "CASTEM – A New Automated Parameter-Estimation Algorithm for Single-Well Tracer Tests," *Society of Petroleum Engineers Reservoir Engineering.* Vol. 4, no. 1, 35-44.

Streltsova-Adams, T.D. 1978. "Well Hydraulics in Heterogeneous Aquifer Formations," *Advances in Hydroscience.* Ed. V.T. Chow. New York, NY: Academic Press. Vol. 11, 357-423.

Tang, D.H., E.O. Frind, and E.A. Sudicky. 1981. "Contaminant Transport in Fractured Porous Media: Analytical Solution for a Single Fracture," *Water Resources Research.* Vol. 17, no. 3, 555-564.

Tidwell, V.C., L.C. Meigs, T. Christian-Frear, and C.M. Boney. 2000. "Effects of Spatially Heterogeneous Porosity on Matrix Diffusion as Investigated by X-ray Absorption Imaging," *Journal of Contaminant Hydrology.* Vol. 42, no. 2-4, 285-302.

Tomich, J.F., R.L. Dalton, Jr., H.A. Deans, and L.K. Shallenberger. 1973. "Single-Well Tracer Method to Measure Residual Oil Saturation," *JPT, Journal of Petroleum Technology.* Vol. 25, no. 2, 211-218.

Tsang, Y.W. 1995. "Study of Alternative Tracer Tests in Characterizing Transport in Fractured Rocks," *Geophysical Research Letters*. Vol. 22, no. 11, 1421-1424.

Tsang, Y.W., and C.F. Tsang. 1999. *A Particle Tracking Method for Advective Transport with Diffusion into Finite Matrix Blocks*. LBNL-42634. Submitted to Water Resources Research. Berkeley, CA: Ernest Orlando Lawrence Berkeley National Laboratory. (Draft copy on file in the SWCF as ERMS #508903).

Volckaert, G., and A. Gautschi. 1997. "Field Tracer Experiments in Clay," *Field Tracer Experiments: Role in the Prediction of Radionuclide Migration, Synthesis and Proceeding of an NEA/EC GEOTRAP Workshop, Cologne, Germany, August 28-30 1996*. Paris, France: Nuclear Energy Agency, Organisation for Economic Co-Operation and Development. 95-101.

Ward, D.S., M. Reeves, and L.E. Duda. 1984. *Verification and Field Comparison of the Sandia Waste-Isolation Flow and Transport Model (SWIFT)*. SAND83-1154, NUREG/CR-3316. Albuquerque, NM: Sandia National Laboratories.

Wood, W.W., T.F. Kraemer, and P.P. Hearn, Jr. 1990. "Intragranular Diffusion: An Important Mechanism Influencing Solute Transport in Clastic Aquifers?," *Science*. Vol. 247, no. 4950, 1569-1572.

Chapter 5

Controls on Multiwell Convergent-Flow Tracer-Breakthrough-Curve Tailing for a Single-Porosity, Heterogeneous Conceptualization

By Sean A. McKenna[1]

Abstract

A series of convergent-flow tracer tests has been conducted in the fractured Culebra dolomite at the Waste Isolation Pilot Plant site. Recovery/breakthrough curves from both single-well injection-withdrawal and multiwell convergent-flow tracer tests have tails that are believed to be the result of matrix diffusion. Numerical-modeling studies have been conducted to evaluate diffusion parameters and whether the effects of heterogeneity on tailing can be separated from the effects due to matrix diffusion. Numerical simulations of the multiwell convergent-flow tracer-test data indicate that the early arrival portion of a tracer-breakthrough curve is mainly controlled by the fracture porosity, and is independent of whether a single- or double porosity conceptualization of the system is used. Single-porosity simulations with several conceptual models of heterogeneous transmissivity fields were conducted to evaluate the role of heterogeneity in breakthrough-curve tailing. The different types of transmissivity fields were created using geostatistical simulation. Transport modeling results on the heterogeneous fields indicate that the amount of tailing in a single-porosity medium is influenced by the style of heterogeneity, the correlation length of transmissivity, and the porosity.

5.1 Introduction

As described in Chapter 3, multiwell convergent-flow (MWCF) tracer tests involve pumping one well to create a converging flow field with effectively steady-state gradients, and then injecting tracer(s) (followed by a chaser solution) into one or more nearby wells to be drawn to the pumping well. The concentration of the tracer in the pumped water is then monitored through time to define a tracer-breakthrough curve. Tracer-breakthrough curves are typically plotted in terms of concentration (often normalized with respect to the injectate concentration) versus pumping time since injection on a log-log graph. The data may also be plotted as cumulative mass recovered (normalized if desired) versus pumping time since injection. In general, single-porosity breakthrough curves have a relatively steep decline in concentration for times beyond that of the peak concentration. Increased tailing (a less steep decline in concentration) in the falling limb of a breakthrough curve can be caused by a variety of factors, including plume drift, heterogeneity, and matrix diffusion.

MWCF tracer tests were conducted in the Culebra at the H-3, H-4, H-6, and H-11 hydropads in the 1980's. Interpretations of the tests at H-3, H-6, and H-11 relied on matrix diffusion in a double-porosity system to explain the long tails observed in the tracer-breakthrough curves (Jones et al., 1992). Independent reviewers suggested that some or all of the tailing might be explainable as the result of heterogeneity in a single-porosity system leading to multiple channels or tortuous flow paths with different effective lengths and fluxes. The purpose of this chapter is to use simulations to examine the effects that heterogeneity can have on breakthrough-curve tailing in a single-porosity medium. The simulations are compared to data collected from the H-19b7 to H-19b0 flow path during the 1995-96 H-19 7-well tracer test. This particular data set was selected for the comparison because it exhibits one of the fastest mass recoveries of all the H-19 data sets and should, therefore, be easist to simulate using a single-porosity model.

---

[1] Sandia National Laboratories, Geohydrology Department, P.O. Box 5800, MS-0735, Albuquerque, NM 87185. Email: samcken@sandia.gov.

Tracer tests are often employed to characterize flow and solute-transport properties of an aquifer. Important information regarding solute-transport properties can be determined from examining the tails of breakthrough curves. For both single-well injection-withdrawal tests (SWIW) and MWCF tests, the rate of decrease in tracer concentration as a function of time is indicative of the hydraulic and/or mass-transfer processes acting within the aquifer. As discussed by Tsang (1995), the signature of diffusion processes in a MWCF test is more difficult to discern than in a SWIW test because of the added complexity in the physics governing the flow system. Specifically, this added complexity is due to: (1) tailing caused by flow-field heterogeneity, a process the SWIW test is designed to mitigate by reversing the injection flow paths during withdrawal; and (2) the sensitivity of the MWCF tracer-transport results to advective porosity. Results of SWIW tests are insensitive to the advective porosity, while the time to peak concentration and the slope of the rising limb of the breakthrough curve in a MWCF test are controlled by the value of advective porosity.

MWCF tracer tests have been used by a number of researchers to estimate groundwater flow and transport parameters over a volume of aquifer between the injection and recovery wells. As pointed out by Moench (1989), a strength of MWCF tests is that 100% recovery of the injected tracer is theoretically possible, thus providing confidence in the conceptual model used to interpret the tracer recovery. Numerous tracer tests have been conducted with the goal of determining dispersivity (e.g., Novakowski et al., 1985; Moench, 1989; Welty and Gelhar, 1994). Other researchers have used MWCF tracer tests to determine the effective porosity and anisotropy of the flow system (e.g., Sánchez-Vila and Carrera, 1997). MWCF tracer tests can also provide information on sorption and diffusion processes in fractured rock (Moench, 1995; Haderman and Heer, 1996; D'Alessandro et al., 1997; Garcià Gutiérrez et al., 1997).

Tracer-breakthrough curves from MWCF tests can generally be described as exhibiting a relatively rapid rise to a peak concentration and then a decline in concentration after the peak. The latter portion, or tail, of the breakthrough curve may be of the same time scale as the rise in concentration or considerably longer. Tortuous flow paths between the injection well and the pumping well caused by spatial heterogeneity in the transmissivity field can be a source of tailing in the breakthrough curve, as can diffusion of tracer between fractures and matrix. Due to the number of processes that can cause tracer-breakthrough-curve tailing, differentiating the effects of heterogeneity from mass-transfer processes such as diffusion can be difficult.

Numerical simulations of the MWCF tracer tests conducted in the 1980's in the Culebra by Jones et al. (1992) attributed all breakthrough-curve tailing to matrix diffusion. Independent reviewers, such as Hautojärvi and Vuori (1992), questioned whether most if not all of the observed tailing could be due to other processes such as flow-field heterogeneity or delayed release of tracer. Numerical simulations of the SWIW tests clearly indicate that neither flow-field heterogeneity (Chapter 4), nor delayed release of tracer from the borehole (Appendix N), nor linear sorption (Appendix O) can cause the extensive tailing observed in the SWIW tests.

The general objective of this chapter is to show the amount of tailing that would be possible for a breakthrough curve from a MWCF test if the Culebra is conceptualized as a heterogeneous single-porosity medium. Specifically, results of heterogeneous single-porosity simulations are compared to the observed tailing for a selected breakthrough curve from the H-19 7-well test. The effect of the conceptual model used to create the heterogeneous transmissivity fields, the effect of changes in advective porosity, and variability in the relative correlation length are examined with respect to the observed breakthrough-curve tailing.

5.2 Approach

In a manner similar to numerical simulations in Chapter 4, the effect of heterogeneity on breakthrough-curve tailing was examined by creating a large number of heterogeneous transmissivity fields and modeling tracer transport through those fields. Two different conceptual models of transmissivity spatial correlation were examined: *maximum entropy*, created with a gaussian simulation algorithm, and *indicator*. For each conceptual model, an ensemble (set) of 25 realizations was created at each of 12 relative correlation lengths for a total of 300 realizations for each conceptual model (600 realizations in total). For either conceptual model at a given relative correlation length, all 25 realizations are equally probable representations of the transmissivity field. For this study, the spatially heterogeneous transmissivity fields were created on a grid with 0.333- x 0.333-meter grid blocks. The domain for each heterogeneous field is 250 x 250 grid blocks for a size of 83.333 x 83.333 meters.

The multiple, spatially heterogeneous realizations of transmissivity were used as input to a series of single-porosity tracer-transport studies. Tracer transport was introduced to the system through injection at a point source and the breakthrough curve was computed at a pumping well located a specified distance away. For this study, the tracer transport was simulated using the well spacing, pumping rates, and injection rates and times for the Round 1 injection into H-19b7 during the H-19 7-well test (Table 5-1). A single injection regime was used with the injection rate of the tracer for the combined time of the tracer and chaser injections as measured for the H-19b7 Round 1 injection. The H-19b7 data were chosen because they provide one of the longest data sets collected in the tracer tests and also show the fastest time to full mass recovery. This model setup allows the results of the numerical simulations to be compared directly to the results of the H-19b7 data.

5.2.1 Conceptual Model of Heterogeneity

Under the dual constraints of a known mean and a known variance, the distribution that provides for the maximum amount of entropy, or the acceptance of the largest amount of uncertainty in other information about the system, is the gaussian (normal) distribution (Harr, 1987). Within the realm of spatial statistics, gaussian distributions can be constructed in two ways: the maximum-entropy approach (only constrained to a mean and variance) and a more highly constrained approach that requires construction of the cumulative distribution function at a finite number of predetermined thresholds. This second approach is known as the indicator approach. For this study, both maximum-entropy and indicator approaches were employed to create heterogeneous transmissivity fields.

Most published studies examining groundwater flow and mass transport in heterogeneous media have used fields created with maximum-entropy geostatistical simulation algorithms (e.g., the turning-bands algorithm; see Journel and Huijbregts, 1978; Mantoglou and Wilson, 1982). Recent work (e.g., Gómez-Hernández, 1997) has pointed out the inherent bias of advective travel-time results when using maximum-entropy fields in modeling radionuclide transport. Because the maximum-entropy fields do not reproduce the model of spatial correlation (i.e., variogram) at the extremes of the distribution, well-connected high-transmissivity channels cannot exist and the modeled transport times will not include the possibility of transport through such channels. Gómez-Hernández (1997) has pointed out the potential nonconservative bias of maximum-entropy fields in modeling radionuclide transport due to the spatial disorder at the extreme values inherent within these models. The effects of maximum-entropy models on MWCF tracer-breakthrough-curve tailing have not previously been addressed.

Table 5-1. Numerical Simulation Parameters

Parameter	Value(s) Used in Simulations
Distance Between Wells (m)	12.2
Pumping Rate (m^3/s)	2.72×10^{-4}
Tracer Injection Time (s)	1740
Tracer Injection Rate (m^3/s)	2.06×10^{-4}
Tortuosity	0.09
Aquifer Thickness (m)	4.4
Aqueous Diffusion Coefficient (m^2/s) (2,4-DFBA)	8.2×10^{-10}
Advective Porosity	0.05, 0.01, 0.005, 0.001, and 0.0005

In this chapter, results of tracer transport in heterogeneous maximum-entropy fields are compared to results from indicator-based heterogeneous fields. In contrast to maximum-entropy spatial fields, spatial fields created with an indicator geostatistical algorithm reproduce the model of spatial correlation at all specified thresholds of the transmissivity distribution. In other words, the maximum-entropy models only reproduce the model variogram at the mean of the transmissivity distribution, while the indicator fields reproduce the variogram model across the full range of transmissivity.

Two ensembles of unconditional geostatistical realizations of transmissivity consistent with the information available at the H-19 hydropad were generated. Each ensemble, or set, was created using a different conceptual model (maximum entropy and indicator) for the type of spatial correlation that may exist in a heterogeneous aquifer such as the Culebra. These conceptual models of heterogeneity are possible representations of the transmissivity of the Culebra; however, the modeling discussed in this chapter is of a general nature with the results being applicable to other heterogeneous aquifers. Hydraulic tests at the H-19 hydropad showed insignificant anisotropy in the Culebra (Beauheim and Ruskauff, 1998). Therefore, isotropic correlation lengths were used for all geostatistical realizations.

The ensembles of statistically isotropic heterogeneous fields were created using the sequential gaussian simulation algorithm, *sgsim*, and the sequential indicator simulation algorithm, *sisim*, as described in Deutsch and Journel (1998). In all cases, the variable $Y=ln(K)$, where K is the hydraulic conductivity, was simulated using a spherical variogram model, and a gaussian distribution of Y with a mean of -11.9 and a standard deviation of 1.76. This corresponds to a mean transmissivity of 6.6×10^{-6} m^2/s and is representative of a fairly significant degree of heterogeneity as would be expected at the H-19 hydropad[2]. For the flow and transport, the K values were multiplied by the modeled aquifer thickness (4.4 meters; see Table 5-1) to produce the transmissivity values used in the model.

The sequential gaussian simulation algorithm, *sgsim*, is a maximum-entropy simulation technique (Journel and Deutsch, 1993). In a maximum-entropy spatial simulation, the specified variogram model is reproduced (honored) at the mean of the gaussian distribution, but the spatial correlation of the values in the tails of the distribution is minimized (see Journel, 1989). The sequential indicator simulation algorithm, *sisim*, was also used to create log-gaussian fields of hydraulic conductivities by discretizing the Gaussian distribution of Y into 16 classes at 15 selected centiles. Values were simulated between the thresholds by drawing from a log-gaussian distribution. The major difference between the realizations created with the *sgsim* and *sisim* algorithms is that the model of spatial correlation is reproduced at all 15 centiles of the *Y* distribution in the random fields created with the *sisim* algorithm but only reproduced at the median of the *Y* distribution of the fields created using *sgsim*. No previous study has been performed comparing the effects of maximum-entropy and indicator-based models on breakthrough-curve tailing.

---

[2] This mean transmissivity value is close to the transmissivity value reported in Chapter 2 and was the best estimate of transmissivity at the time these simulations were done.

5.2.2 Variations in Correlation Length

Tsang (1995) hypothesized that the largest amount of tailing would occur during a MWCF tracer test at a relative correlation length (correlation length/distance between injection and pumping wells) of 0.2 to 0.5. Relative correlation lengths less than this would allow the tracer transport to integrate all of the aquifer variability over the transport distance and the resulting breakthrough curves would suggest transport through a homogeneous medium. Relative correlation lengths approaching 1.0 would create fields with little conductivity variation between the two wells. In the range of relative correlation lengths between 0.2 and 0.5, the injected tracer could experience several discrete transmissivity values and be diverted around or through these discrete pockets, thus creating a variety of flow path lengths and breakthrough-curve tailing.

In order to test this hypothesis, realizations were created for 12 different relative correlation lengths. The distance between the injection and pumping wells was set to12.2 m. The relative correlation lengths were systematically varied from 0.08 to 1.0 as shown in Table 5-2 and the effect on breakthrough-curve tailing for both heterogeneity models was examined. Twenty-five T-field realizations were created using both *sgsim* and *sisim* for each of the 12 relative correlation lengths for a total of 600 realizations.

5.2.3 Advective Porosity

To evaluate the effect of advective porosity on breakthrough-curve tailing, five values from 0.0005 to 0.05 were used for the numerical simulations (see Table 5-1). These values were selected to encompass the range of possible advective porosities at the H-19 hydropad (see Section 3.3) as well as lower advective porosities generally observed in fractured rock. The high value of 0.05 is based on the advective porosity calculated

Table 5-2. Relative Correlation Lengths Used in Creating the Geostatistical Realizations of Hydraulic Conductivity

Relative Correlation Length	Actual Correlation Length (m)	Gridblocks per Correlation Length
0.03	0.3	1
0.08	1.0	3
0.14	1.7	5
0.19	2.3	7
0.25	3.0	9
0.30	3.7	11
0.36	4.3	13
0.41	5.0	15
0.49	6.0	18
0.63	7.7	23
0.82	10.0	30
1.01	12.2	37

from theoretical direct plug-flow travel time between the injection well (H-19b7) and the pumping well (H-19b0) (see Section 3.3.2.3). The lower advective-porosity estimate is based on interpretations of the tracer tests using a multirate double-porosity model (see Chapter 8).

5.3 Flow and Transport Model

The particle-tracking-based solute-transport code THEMM ver. 1.01 (Hale and Tsang, 1996) was used to model the movement of the tracer through the aquifer. (See Section 4.4.2 for an additional description of THEMM.) For each different flow regime, injection and pumping or pumping only, a steady-state flow field was solved using a finite-difference approach. Heterogeneity was incorporated into the flow solution on a grid block by grid block basis. A small regional gradient, based on estimates for the Culebra in the vicinity of the H-19 hydropad, was prescribed from north to south by using fixed heads on the north and south boundaries and no-flow boundaries to the east and west. The central heterogeneous portion of the model extends 83.333 m in the x and y directions. A telescoping mesh was used to place the fixed-head boundaries 85 m from the outer boundary of the central heterogeneous transmissivity field. The geometric mean of the heterogeneous transmissivity fields was assigned to these additional grid blocks. Tracer transport was modeled by simulating the movement of 100,000 particles through the system.

5.4 Results

Numerical simulations were conducted to determine if spatial heterogeneity in the distribution of transmissivity (specifically *ln(T)*) can account for the tailing observed in the MWCF breakthrough curve for the case of a single tracer test at the H-19 hydropad. To compare the numerical simulations to one another and to the breakthrough-curve data, a small number of readily calculable parameters that describe the general shape and tailing of the breakthrough curve have been selected. These metrics were chosen to provide information not only on the length of the post-peak breakthrough curve, but also on the overall shape of the breakthrough curve. The transport results were examined with respect to: 1) the model of spatial correlation; 2) the relative correlation length and porosity; and 3) the field data.

5.4.1 Model of Spatial Correlation

Six hundred heterogeneous transmissivity fields were created using geostatistical simulation. The two ensembles of spatially correlated random fields were created using the same vector of seeds for the random-number generator and thus allow for direct comparison of transport results between each realization created with the indicator model *sisim* and the corresponding realization created with the maximum-entropy (gaussian) model *sgsim* (Table 5-2).

In general, this comparison shows no systematic bias toward more or less tailing for one conceptual model over the other; however, all of the individual cases of extreme tailing occur for the fields created with the maximum-entropy model of spatial correlation. Examination of these extreme cases relative to the corresponding indicator transport results suggests that the discontinuous nature of the high-transmissivity values in the maximum-entropy fields causes streamlines to sample a large range of the full transmissivity distribution. The fields created with the indicator model, with the more continuous high-transmissivity channels, allow for faster flushing of the tracer from the system and consequently less tailing in the breakthrough curve.

Flow and transport results were compared for one realization (number 2) of the heterogeneous fields as shown in Figure 5-1. These fields were created with *sgsim* and *sisim* using the same relative correlation length (0.19) and the same seed for the random-number generator. This particular pair of realizations was chosen for detailed examination because of the extreme amount of breakthrough-curve tailing, relative to other realizations, produced by the *sgsim* realization. Note the similarity in the spatial distribution of high- and low-transmissivity values between the two images in Figure 5-1. The mean and variance of the Y values is identical for the two fields. Close examination of the images in Figure 5-1 shows the differences between the maximum-entropy and indicator simulations. The maximum-entropy constraint of the gaussian simulation results in limited connectivity of the high- and low-transmissivity values. The transmissivity field created with the indicator simulation algorithm shows a markedly mosaic arrangement of the transmissivities. Within the indicator simulation, the distribution of individual transmissivity values is more uniform within the regions of high and low transmissivity, providing more continuity in these values relative to the maximum-entropy simulation.

Figure 5-2 shows the area near the injection and withdrawal wells from the same fields as shown in Figure 5-1. The subtle differences in the spatial arrangement of the transmissivity values between the two fields produce differences in the spatial distribution of the volumetric flux between the injection and withdrawal wells. A map of $\log_{10}$ flux for the simulation with an advective porosity of 0.005 is shown for each heterogeneous transmissivity field in Figure 5-3. Tracer transport through the two heterogeneous fields, represented by concentrations at 12 hr after injection, is shown in Figure 5-4.

5.4.2 Correlation Length and Porosity

For all 600 transmissivity fields, transport was simulated for five different advective porosities. To evaluate the amount of tailing, a tailing metric is defined as the time to 90% mass recovery normalized by the time to pump a single pore volume. The pore volume is defined as the porosity times the volume of a cylinder with a radius equal to the distance between the injection and pumping wells and a height equal to the modeled aquifer thickness. This normalization allows tailing results to be compared across the different porosities. The normalized times to 90% mass recovery are shown in Figure 5-5. Each line in Figure 5-5 connects the median of the results for the 25 transmissivity fields across each relative correlation length.

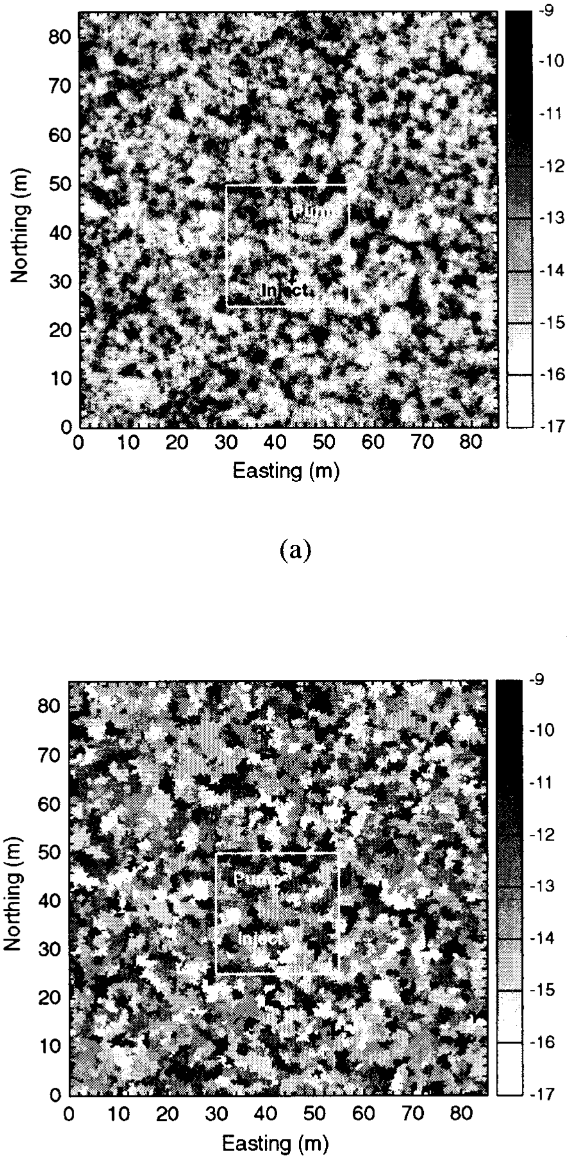

(a)

(b)

Figure 5-1. Two spatially heterogeneous transmissivity fields created with (a) maximum entropy and (b) indicator geostatistical algorithms. Both fields were created with the same random seed and have a relative correlation length of 0.19.

For the maximum-entropy simulations (Figure 5-5a), the amount of tailing is only slightly influenced by the relative correlation length. For each advective porosity, the maximum amount of tailing occurs at either a relative correlation length less than 0.4 or at a relative correlation length of 1.0. Similar results were obtained for the indicator simulations (Figure 5-5b); however, the indicator results do not show the same monotonic

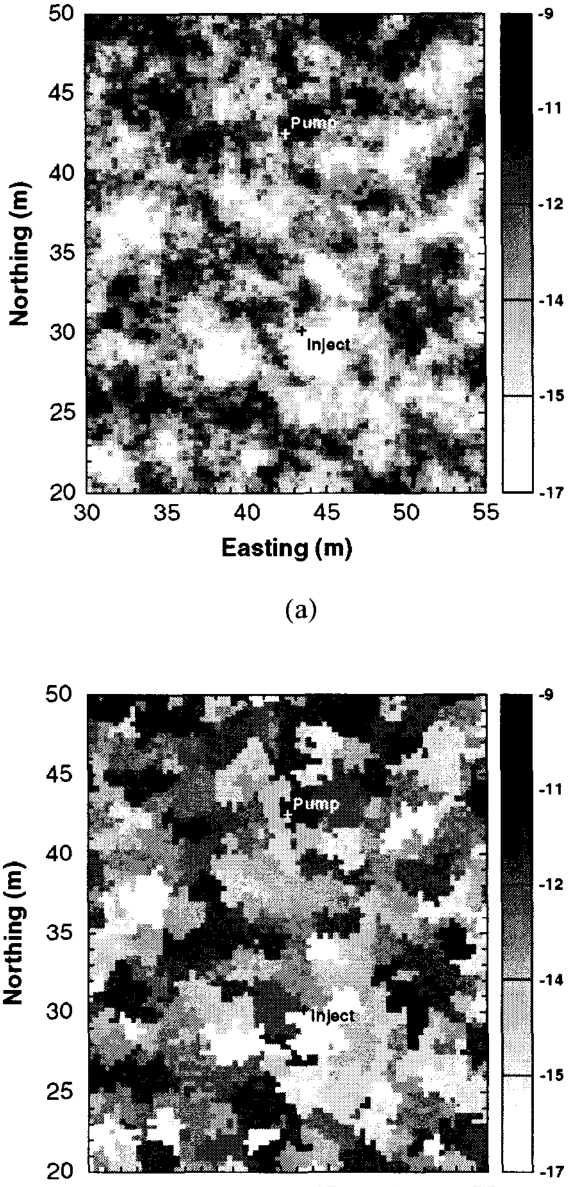

(a)

(b)

Figure 5-2. Magnified views of the two spatially heterogeneous fields shown in Figure 5-1. The heterogeneous transmissivity fields created with (a) maximum entropy and (b) indicator geostatistical algorithms. Both fields were created with the same random seed and have a relative correlation length of 0.19.

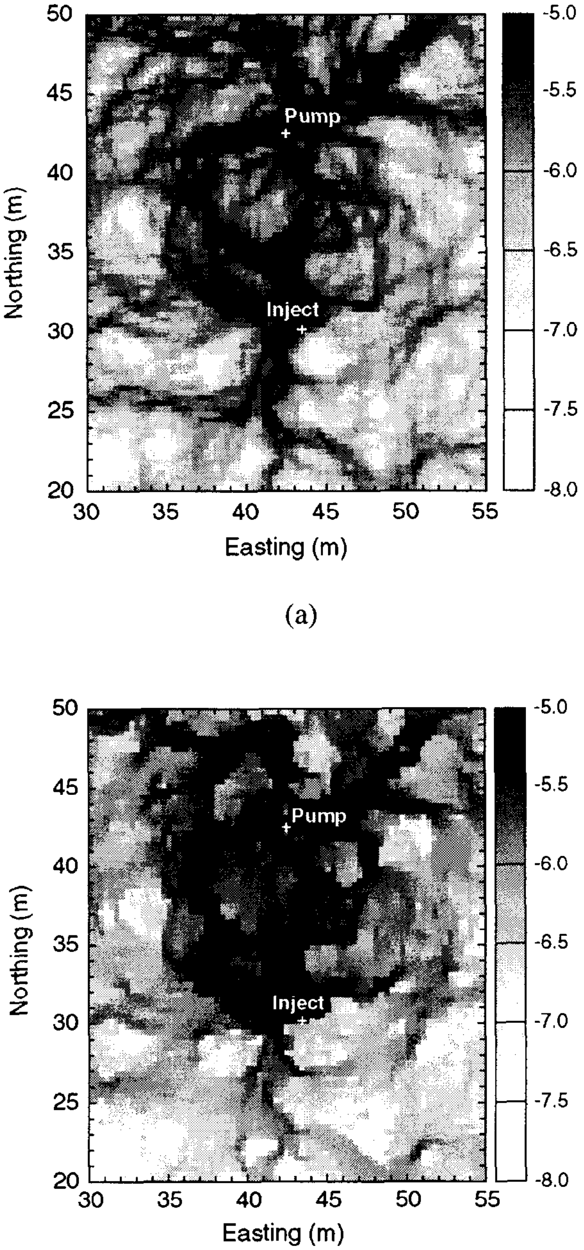

(a)

(b)

Figure 5-3. Volumetric flux ($\log_{10}$ m^3/s) through the two heterogeneous fields shown in Figure 5-2 for a simulation with an advective porosity of 0.005. The fields are created with (a) maximum entropy and (b) indicator geostatistical algorithms.

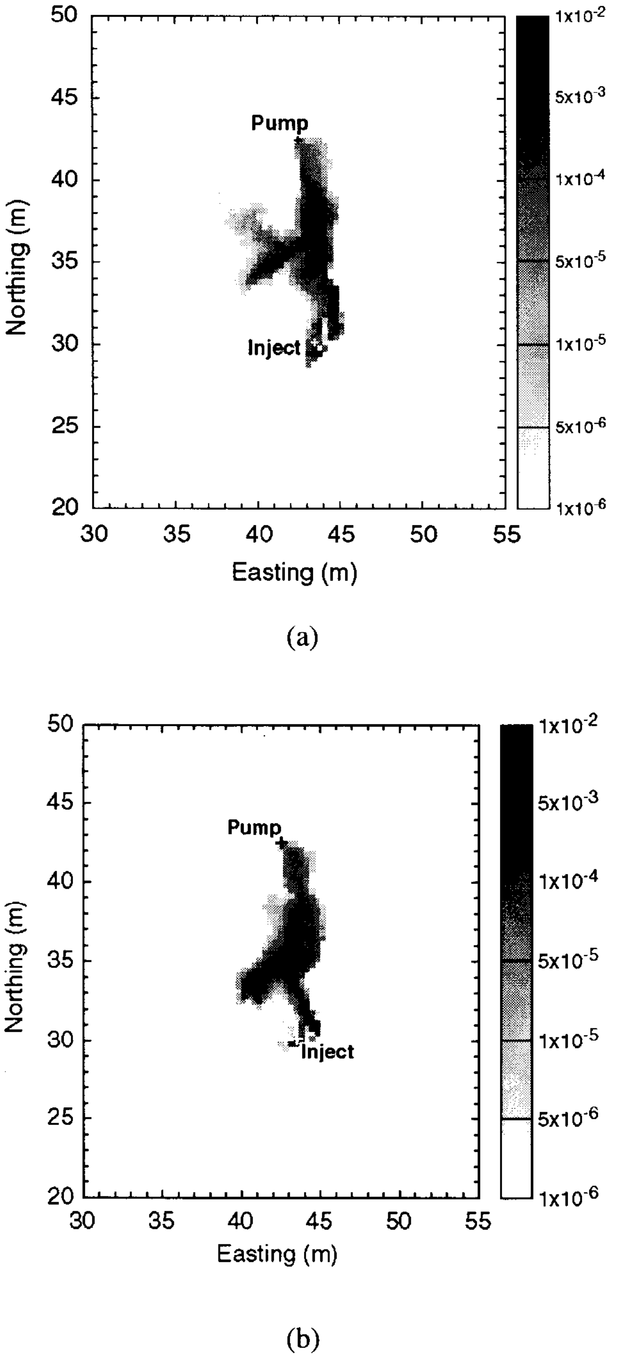
Pump
Inject
Northing (m)
Easting (m)
1x10-2
5x10-3
1x10-4
5x10-5
1x10-5
5x10-6
1x10-6
(a)
(b)

Figure 5-4. **Tracer concentrations twelve hours after injection for a simulation with an advective porosity of 0.005. The concentrations are shown in the (a) maximum entropy and (b) indicator fields shown in Figure 5-2.**

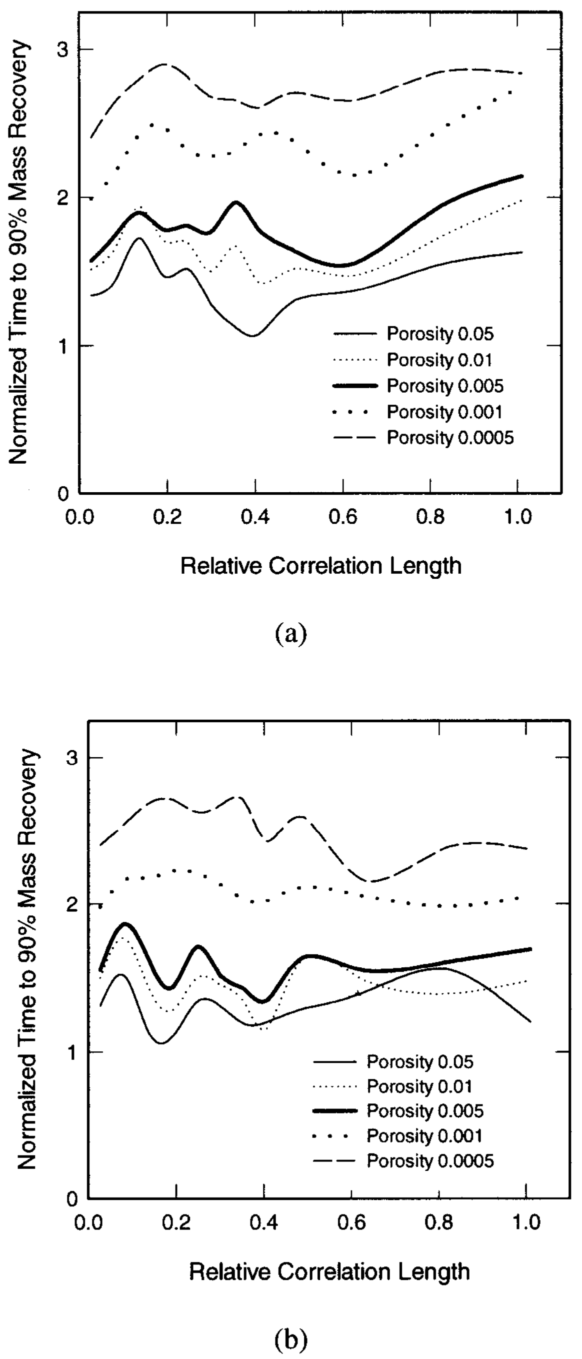

Figure 5-5. **Amount of tailing, defined as time to 90% mass recovery, as a function of relative correlation length and advective porosity for (a) maximum entropy realizations and (b) indicator realizations.**

increase in tailing as the relative correlation length approaches 1.0. The maximum amount of breakthrough-curve tailing for the indicator simulations occurs between relative correlation lengths of 0.1 and 0.4 for all five porosity values. However, the difference between the maximum and minimum amount of tailing is less than 50% across all porosity values.

An intuitive hypothesis regarding the relationship between tailing and relative correlation length was put forth by Tsang (1995). This hypothesis predicted maximum tailing occurring at correlation-lengths between 0.15 and 0.4. At relative correlation lengths less than 0.15, the tracer would sample all of the relevant heterogeneity and the small-scale effects would be averaged out by the time the tracer reached the pumping well. At large relative correlation lengths, the tracer would only sample a small number of discrete features and the transport would be controlled by the transmissivity value of these features. In the range of maximum tailing, relative correlation lengths from 0.15 to 0.40, the tracer must pass through or around three to six discrete zones of transmissivity and the dispersive effects of this variability would create greater tailing in the breakthrough curve.

The results shown in Figure 5-5 indicate that, at least for the cases modeled here, the intuitive hypothesis presented by Tsang (1995) does not hold. Elucidation of the specific reasons why this intuitive hypothesis does not hold is beyond the scope of this paper. One condition that may explain the similarity of the tailing results across relative correlation lengths in Figure 5-5 is that for the case modeled here, the flow regime is not dispersive, but advective. A dispersive flow regime, characterized by relatively low hydraulic gradients, would allow for the tracer to move around the areas of relatively low transmissivity and be transported through the relatively higher transmissivity regions. Under an advective flow regime, such as immediately adjacent to a pumping well, the transport pathways are dominated by the hydraulic gradient and the effect of the spatial heterogeneity is minimized. Transport through a dominantly advective flow regime may explain the similarity of the results in Figure 5-5, but more work would be necessary to confirm this conjecture. The flux maps in Figure 5-3 (the realization that produced the maximum tailing at an advective porosity of 0.005) show that flux is dominated by the hydraulic gradient created by the pumping well, but that the heterogeneity also has some influence on the flux map.

The results of Figure 5-5 demonstrate a correlation between the normalized time to 90% mass recovery and the advective porosity: the lower the porosity, the longer the time to 90% mass recovery. This result is explained by the injection of the tracer into a heterogeneous aquifer. The injected tracer will move out from the injection well in a series of "fingers" that follow the high-transmissivity pathways away from the well. Transport away from the injection well will be less advective and more dispersive than transport to the pumping well. This transport along high-transmissivity pathways is accentuated for lower advective porosities relative to higher porosities due to the reduced volume for advection (see Chapter 3). In the case of the MWCF tracer tests, lower porosity results in increased migration of the tracer out from the injection well along high-transmissivity pathways. The pumping well pulls the tracer through the heterogeneous medium along different pathways that create the tailing in the breakthrough curve.

5.4.3 Comparison to Field Data

Results of the single-porosity simulations are compared to the observed data by locating all results in a two-dimensional space defined by two tailing metrics (Figure 5-6). The x-axis of Figure 5-6 represents the value of dispersion, *D*, defined as:

$$D = \frac{\left(t_{90} - t_{10}\right)}{t_{50}} \qquad (5\text{-}1)$$

where t_n is the elapsed time since injection to the *nth* percentile of cumulative mass recovery. This representation of dispersion has been used in previous studies of transport in fractured rock (e.g., Neretnieks et al., 1982). The y-axis is the raw (unnormalized) time to 90% cumulative mass recovery. Results for all 12 relative correlation lengths created with both conceptual models at all five porosities are shown. Rather than plotting the results of each individual realization, the median value of the tailing metric from all 25 realizations is shown.

Examination of Figure 5-6 shows that the observed data do not fall into the same space as the simulation results. That is, the time to 90% mass recovery is more than twice as long for the observed data, ~14 days, as it is for the median of any simulations. The simulations with low porosities (0.001 and 0.0005) produce values of dispersion that include the value calculated for the observed data. However, the longest times to 90% mass recovery for simulations at these porosities are over an order of magnitude shorter than for the observed data. Even for the simulations with a porosity of 0.05, the time to 90% mass recovery is significantly shorter than for the H-19b7 data. The observed data also show a large amount of dispersion relative to the simulation results with the most similar times to 90% mass recovery. Figure 5-6 demonstrates that simulated transport through a single-porosity, heterogeneous transmissivity field cannot reproduce the observed breakthrough-curve data, as represented by this metric.

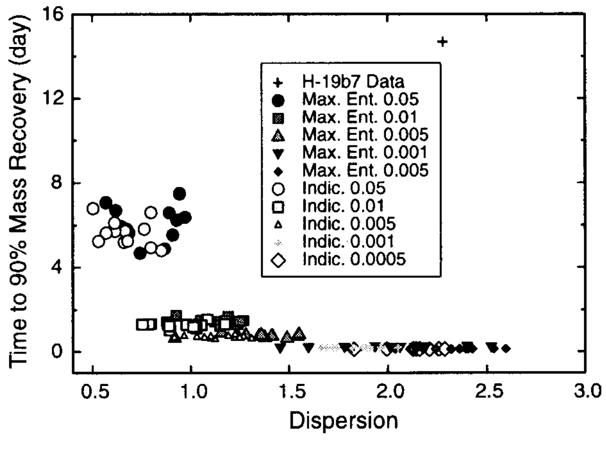

Figure 5-6. Comparison of the H-19b7 tracer test results to the numerical results in two-dimensional space. Each circle represents the median value of 25 realizations. The open symbols are results from the maximum entropy realizations and the solid symbols are results from the indicator simulations.

In order to get a better understanding of how tracer transport in individual realizations compares to the H-19b7 data, a series of individual breakthrough curves are compared to the data in Figures 5-7 through 5-10. Figures 5-7 and 5-8 show the simulated breakthrough curves as cumulative mass recovered versus time and relative concentration versus time in log-log space, respectively, for all 25 realizations of the transmissivity fields created with a relative correlation length of 0.19 and a porosity of 0.005. Realization 2 is presented in Figures 5-1 to 5-4 and highlighted in Figures 5-7 and 5-8. Relative to the simulations, the H-19b7 data show a much more gradual rise to the peak concentration and a significantly longer tail after the peak concentration. The sharp rise and consequent steep decline in concentration that is characteristic of the simulated breakthrough curves leads to the smaller amount of dispersion for the simulations relative to the H-19b7 data as seen in Figure 5-6. The different conceptual models of heterogeneity produce similar amounts of tailing, and both conceptual models of heterogeneity produce tailing that is significantly less than is seen in the observed data.

Figure 5-8 shows that the simulated breakthrough curves all have times to peak concentration that are significantly less than the time to peak concentration for the observed data. This observation suggests that a porosity of 0.005 is not the correct porosity to use when simulating the H-19b7 data. Better matches to the H-19b7 data with respect to time to peak concentration can be achieved by comparing the simulations done with a porosity of 0.05. The simulated breakthrough curves and the observed data are compared as both cumulative mass recovered and relative concentration versus time in log-log space in Figures 5-9 and 5-10 respectively. These two figures, similar to Figures 5-7 and 5-8, show 25 breakthrough curves created with a relative correlation length of 0.19.

The relative-concentration curves (Figure 5-10) demonstrate that, on average, single-porosity simulations with a porosity of 0.05 can match the time to peak concentration. Although difficult to discern in Figure 5-10, a steep rise and decline in concentration relative to the H-19b7 data generally characterize the simulated breakthrough

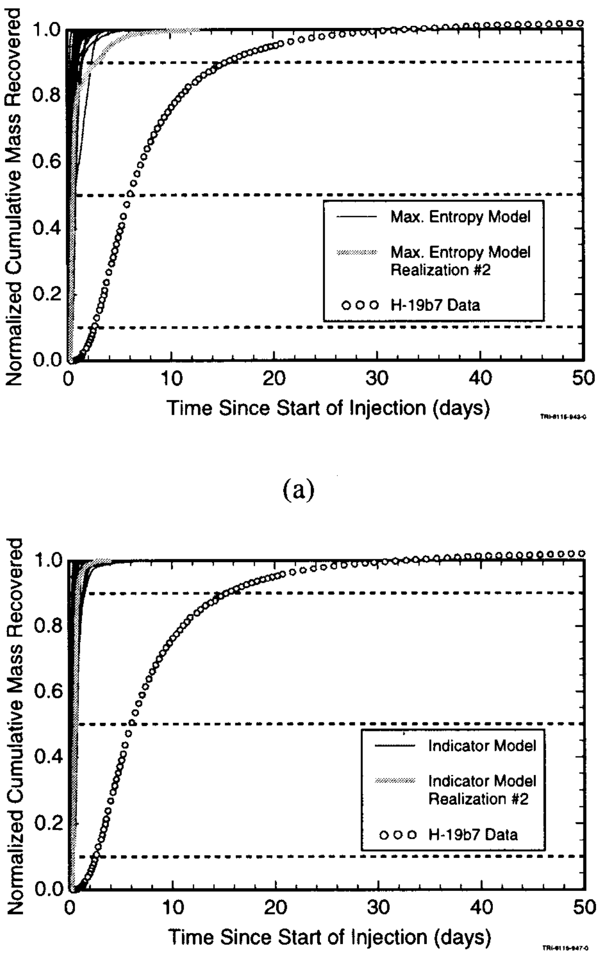

(a)

(b)

Figure 5-7. Cumulative particle breakthrough distributions for the H-19b7 data and the 25 realizations with a relative correlation length of 0.19 and an advective porosity of 0.005. Results for the (a) maximum entropy realizations and (b) indicator realizations are shown.

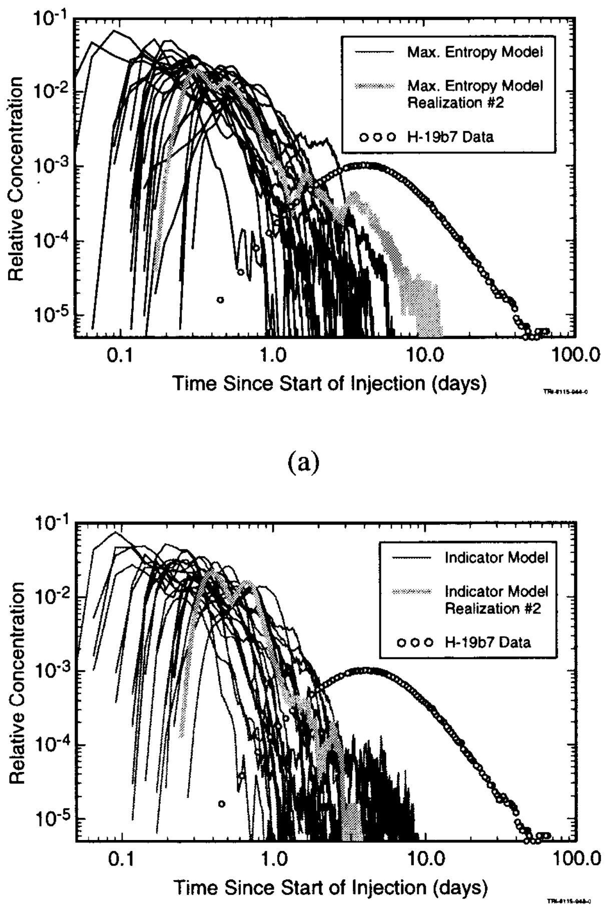

(a)

(b)

Figure 5-8. Particle breakthrough curves in double-log space for the H-19b7 data and the 25 realizations with a relative correlation length of 0.19 and an advective porosity of 0.005. Results for the (a) maximum entropy realizations and (b) indicator realizations are shown.

curves. This result is expected from the relatively small amount of dispersion seen in Figure 5-6 for simulations done with a porosity of 0.05. However, several simulations come close to matching the tailing of the observed data. These simulations are more readily seen in Figure 5–9. Simulated breakthrough curves with long tails, in several cases longer than the observed data, demonstrate a breakthrough curve with a different shape than the observed data. The simulated curves with long tails are defined by a discontinuous change in slope. These changes are attributed to tracer being transported along several discrete pathways. Transport along different pathways gives rise to the multimodal-tailing behavior seen in the breakthrough curves (e.g., realization number 2 in the upper image of Figure 5-10). Also note that the several simulated breakthrough curves with long tails have first arrivals that are much later (approximately four days beyond the start of injection) than the observed data (Figure 5-9).

Numerical simulations of transport for a MWCF tracer test were performed with two different

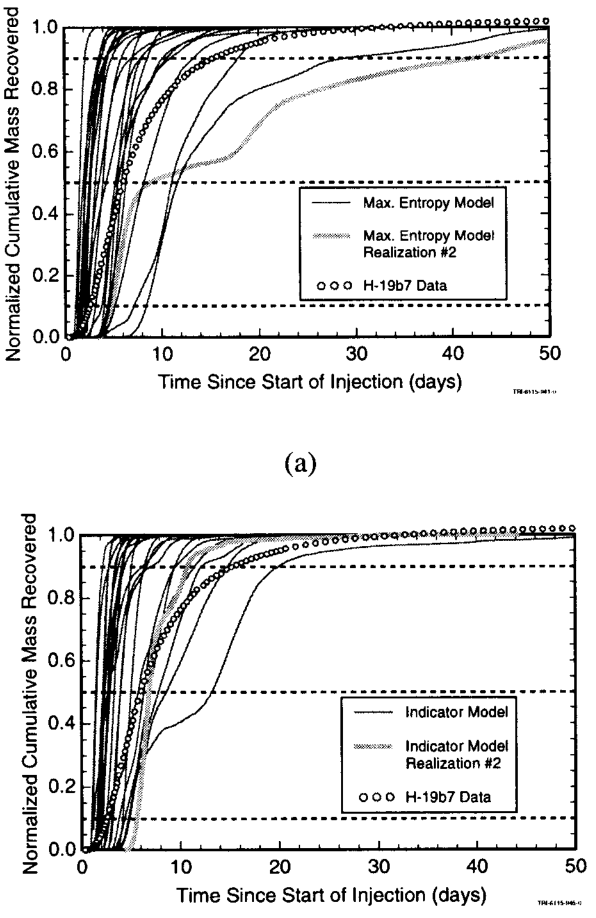

(a)

(b)

Figure 5-9. Cumulative particle breakthrough distributions for the H-19b7 data and the 25 realizations with a relative correlation length of 0.19 and an advective porosity of 0.05. Results for the (a) maximum entropy realizations and (b) indicator realizations are shown.

conceptualizations of heterogeneity: maximum entropy and indicator. Comparison of the two conceptual models of heterogeneity shows that breakthrough-curve tailing is not a strong function of the conceptual model of heterogeneity. However, for any combination of relative correlation length and porosity, the largest amount of tailing occurs when using the maximum-entropy conceptual model of heterogeneity (Figure 5-7).

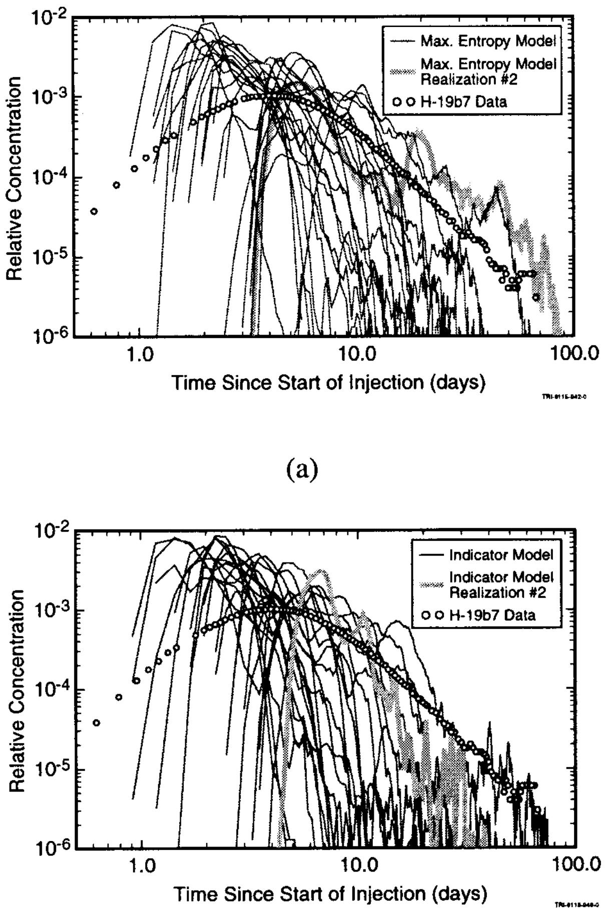

(a)

(b)

Figure 5-10 Particle breakthrough curves in double-log space for the H-19b7 data and the 25 realizations with a relative correlation length of 0.19 and an advective porosity of 0.05. Results for the (a) maximum entropy realizations and (b) indicator realizations are shown.

5.5 Conclusions

The fraction of the total porosity that is associated with advection is often difficult to determine. However, results of this study suggest that, across a range of porosity from 0.0005 to 0.05, breakthrough-curve tailing is not a function of the relative correlation length. These results indicate that the intuitive hypothesis stated by Tsang (1995), that maximum tailing should occur at normalized correlation lengths of 0.15 to 0.4, is not necessarily applicable. One reason for this hypothesis not holding may be that the transport system is overly influenced by the local hydraulic gradient and the effects of heterogeneity on the breakthrough curves are only minimal.

Comparisons of the numerical results presented here to the observed H-19b7 tracer data suggest that single-porosity simulations will not result in the long tails observed in the data. Because this H-19b7 data set has one of the fastest mass recoveries of all the H-19 data sets, we doubt that many, if any, of the other H-19 MWCF tracer test data sets could be adequately simulated with this heterogeneous single-porosity conceptualization. The gradual mass recovery observed in the data is likely a result of diffusion into the rock matrix (see Chapter 7 and Appendices P and S).

5.6 References

Beauheim, R.L., and G.J. Ruskauff. 1998. *Analysis of Hydraulic Tests of the Culebra and Magenta Dolomites and Dewey Lake Redbeds Conducted at the Waste Isolation Pilot Plant Site.* SAND98-0049. Albuquerque, NM: Sandia National Laboratories.

D'Alessandro, M., F. Mousty, G. Bidoglio, J. Guimerà, I. Benet, X. Sánchez-Vila, M. García Gutiérrez, and A. Yllera De Llano. 1997. "Field Tracer Experiment in a Low Permeability Fractured Medium: Results from El Berrocal Site," *Journal of Contaminant Hydrology.* Vol. 26, no. 1-4, 189-201.

Deutsch, C.V., and A.G. Journel. 1998. *GSLIB: Geostatistical Software Library and User's Guide.* 2nd ed. New York, NY: Oxford University Press.

García Gutiérrez, M.G., J. Guimerà, A. Yllera De Llano, A. Hernández Benitez, J. Humm, and M. Saltink. 1997. "Tracer Test at El Berrocal Site Site," *Journal of Contaminant Hydrology.* Vol. 26, no. 1-4, 179-188.

Gómez-Hernández, J.J. 1997. "Issues on Environmental Risk Assessment," *Geostatistics Wollongong '96, International Geostatistics Congress, Wollongong, Australia, September 1996.* Quantitative Geology and Geostatistics Vol. 8. Eds. E.Y. Baafi and N.A. Schofield. Boston, MA: Kluwer Academic Publishers. 15-26.

Hadermann, J., and W. Heer. 1996. "The Grimsel (Switzerland) Migration Experiment: Integrating Field Experiments, Laboratory Investigations and Modelling," *Journal of Contaminant Hydrology.* Vol. 21, no. 1-4, 87-100.

Hale, F.V., and Y.W. Tsang. 1996. *THEMM User Guide Version 1.0 (7-16-96).* Berkeley, CA: Lawrence Berkeley National Laboratory. (Copy on file in the Sandia WIPP Central Files (SWCF) as ERMS #235261.)

Harr, M.E. 1987. *Reliability-Based Design in Civil Engineering.* New York, NY: McGraw-Hill.

Hautojärvi, A., and S. Vuori. 1992. *Comments on Tracer Tests and Data Interpretation.* TVO/KPA Turvallisuus Ja Tekniikka Työraportti 92-01. Helsinki, Finland: Technical Research Centre of Finland, Nuclear Engineering Laboratory.

Jones, T.L., V.A. Kelley, J.F. Pickens, D.T. Upton, R.L. Beauheim, and P.B. Davies. 1992. *Integration of Interpretation Results of Tracer Tests Performed in the Culebra Dolomite at the Waste Isolation Pilot Plant Site.* SAND92-1579. Albuquerque, NM: Sandia National Laboratories.

Journel, A.G. 1989. *Fundamentals of Geostatistics in Five Lessons.* Short Course in Geology Vol. 8. Washington, DC: American Geophysical Union.

Journel, A.G., and C.V. Deutsch. 1993. "Entropy and Spatial Disorder," *Mathematical Geology.* Vol. 25, no. 33, 329-355.

Journel, A.G., and Ch. J. Huijbregts. 1978. *Mining Geostatistics*. New York, NY: Academic Press. Mantoglou, A., and J.L. Wilson. 1982. "The Turning Bands Method for Simulation of Random Fields Using Line Generation by a Spectral Method," *Water Resources Research*. Vol. 18, no. 5, 1379-1394.

Moench, A.F. 1989. "Convergent Radial Dispersion: A Laplace Transform Solution for Aquifer Tracer Testing," *Water Resources Research*. Vol. 25, no. 3, 439-447.

Moench, A.F. 1995. "Convergent Radial Dispersion in a Double-Porosity Aquifer with Fracture Skin: Analytical Solution and Application to a Field Experiment in Fractured Chalk," *Water Resources Research*. Vol. 31, no. 8, 1823-1835.

Neretnieks, I., T. Eriksen, and P. Tahtinen. 1982. "Tracer Movement in a Single Fissure in Granitic Rock: Some Experimental Results and Their Interpretation," *Water Resources Research*. Vol. 18, no. 4, 849-858.

Novakowski, K.S., G.V. Evans, D.A. Lever, and K.G. Raven. 1985. "A Field Example of Measuring Hydrodynamic Dispersion in a Single Fracture," *Water Resources Research*. Vol. 21, no. 8, 1165-1174.

Sánchez-Vila, X., and J. Carrera. 1997. "Directional Effects on Convergent Flow Tracer Tests," *Mathematical Geology*. Vol. 29, no. 4, 551-569.

Tsang, Y.W. 1995. "Study of Alternative Tracer Tests in Characterizing Transport in Fractured Rocks," *Geophysical Research Letters*. Vol. 22, no. 11, 1421-1424.

Welty, C., and L.W. Gelhar. 1994. "Evaluation of Longitudinal Dispersivity from Nonuniform Flow Tracer Tests," *Journal of Hydrology*. Vol. 153, no. 1-4, 71-102.

This page intentionally left blank.

Chapter 6
Evaluation of Single-Well Injection-Withdrawal Tracer-Test Data with a Multirate-Diffusion Model

By Roy Haggerty[1], Sean W. Fleming[1,2], Lucy C. Meigs[3], and Sean A. McKenna[3]

Abstract

We investigated multiple-rate diffusion as a possible explanation for observed behavior in a suite of single-well injection-withdrawal (SWIW) tracer tests conducted in the fractured Culebra dolomite. We first investigated the ability of a conventional double-porosity model and a multirate-diffusion model to explain the data. This revealed that the multirate-diffusion hypothesis/model is most consistent with all available data, and is the only model to date that is capable of matching each of the recovery curves entirely. Second, we studied the sensitivity of the SWIW recovery curves to the distribution of diffusion-rate coefficients and other parameters. We concluded that the SWIW test is very sensitive to the distribution of rate coefficients, but is relatively insensitive to other flow and transport parameters such as advective porosity and dispersivity. Third, we examined the significance of the constant double-log late-time slopes (-2.1 to -2.8) that are present in several data sets. The observed late-time slopes are significantly different than would be predicted for either conventional double-porosity or single-porosity media, and are found to be a distinctive feature of multirate diffusion. Fourth, we found that the estimated distributions of diffusion-rate coefficients are very broad, with the distributions spanning a range of at least 3.6 to 5.7 orders of magnitude.

6.1 Introduction

The effects of multiple rates of mass transfer (or "multirate" mass transfer) have been theoretically predicted in the past, and are now being observed in an increasing number of laboratory experiments; these effects have not, until now, been documented at the field scale. In this chapter, we investigate the multirate-diffusion hypothesis as it relates to the single-well injection-withdrawal (SWIW) tracer tests performed at the H-19 and H-11 hydropads at the WIPP site. The hypothesis postulates that a distribution of apparent diffusion coefficients and diffusion-length scales is responsible for anomalously long tails and scale-dependent rate coefficients in many laboratory and field tracer experiments. As such, the goals of this chapter are to: (1) investigate the hypothesis that multirate diffusion could be responsible for the observed recovery behavior in the Culebra SWIW tests; (2) develop a methodology for estimating the distribution of rate coefficients responsible for the observed behavior; (3) examine whether the hypothesis and resulting model are consistent with other data; and (4) examine the significance of the late-time slope of the observed SWIW recovery curves, a slope that is common to data collected from several single-well and multiwell tests.

As a model of mass transfer, multirate diffusion invokes diffusion between an advection-dominated ("mobile") zone and a diffusion-dominated rock matrix ("immobile zone") that is heterogeneous at the pore scale. The multirate-diffusion model (Haggerty and Gorelick, 1995, 1998) is essentially a modified double-porosity model consisting of advective porosity and diffusive porosity, with diffusion of mass from one to the other described by a range of rate coefficients.

---

[1] Oregon State University, Department of Geosciences, 104 Wilkinson Hall, Corvallis, OR 97331-5506. Email: haggertr@geo.orst.edu.

[2] Now at Waterstone Environmental Hydrology and Engineering, 1650 38th St., Suite 201E, Boulder, CO 80301.

[3] Sandia National Laboratories, Geohydrology Department, P.O. Box 5800, MS-0735, Albuquerque, NM 87185-0735.

A growing body of literature now documents the existence, observability, and effects of multiple rates of mass transfer on solute transport in the subsurface. Multiple rates of diffusive or sorptive mass transfer are theoretically and intuitively reasonable (e.g., Ruthven and Loughlin, 1971; Villermaux, 1981; Rao et al., 1982; Cooney et al., 1983; Rasmuson, 1985; Wu and Gschwend, 1988; Brusseau et al., 1989; Fong and Mulkey, 1990; Valocchi, 1990; Lafolie and Hayot, 1993; Haggerty and Gorelick, 1995; Cunningham et al., 1997), and have now been observed and modeled in a number of laboratory experiments (e.g., Ball and Roberts, 1991; Connaughton et al., 1993; Pedit and Miller, 1994, 1995; Chen and Wagenet, 1995, 1997; Culver et al., 1997; Werth et al., 1997; Haggerty and Gorelick, 1998; Lorden et al., 1998; and others). However, to date, no field study that documents the effects of multirate diffusion has been reported.

6.2 Multirate Diffusion: Mathematical Model

In this section, we present and discuss the mathematical model used to describe advective-dispersive solute transport with multirate diffusion. The solutions to these equations are obtained in the Laplace domain and then numerically inverted using the de Hoog algorithm (de Hoog et al., 1982). The solutions are performed sequentially for each of the injection, resting, and pumping periods of the SWIW test. More details of the solution method are presented in Haggerty et al. (2000) and Appendix Q. The multirate-diffusion model is a distributed model of diffusion representing a medium with pore-scale heterogeneity in diffusive-mass transfer. As conceptualized in this paper, the multirate-diffusion model is similar to that described by Cunningham et al. (1997) and by Haggerty and Gorelick (1998). Figure 6-1 illustrates fractures and matrix (i.e., advective and diffusive porosity) in a small volume of rock, where the matrix is heterogeneous with respect to diffusion at spatial scales much smaller than a representative elementary volume (REV). We assume that this sub-REV-scale heterogeneity is replicated in approximately the same fashion everywhere in the formation. This is necessary because the same variability in diffusion properties is assumed to exist everywhere in the formation.

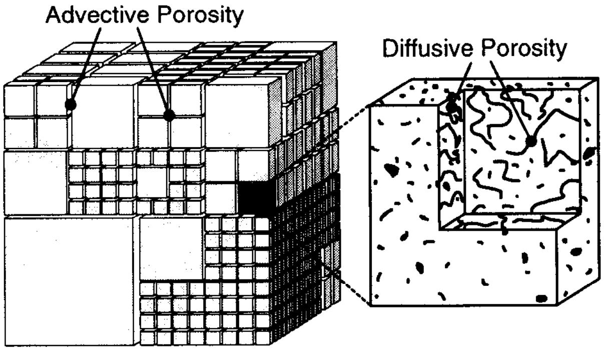

Figure 6-1. Conceptual model for multirate diffusion. Although the illustrated blocks are cubes, the blocks may be of any shape. The volume of rock shown in the diagram is less than the REV.

The multirate-diffusion model is a generalization of the conventional double-porosity model (e.g., Neretnieks, 1980, 1993) in that porosity is divided into two broad categories: advective porosity (where transport is by advection and dispersion) and diffusive porosity (where transport is by diffusion). However, in the multirate model, the diffusion-rate coefficient ($\alpha_d = D_a/l^2$, see below) is described by a distribution rather than a single value. The model assumes one-dimensional diffusion along a distribution of individual pathways within matrix blocks. The distribution describes the fraction of rock characterized by a given diffusion-rate coefficient. Although Figure 6-1 shows cubic matrix blocks in the model, the pathways and the blocks can be any shape, provided that each pathway is one-dimensional, homogeneous, and independent of other pathways. With these criteria, each diffusive pathway in the distribution can be modeled with a one-dimensional diffusion equation. In the likely case that the pathways are not one-dimensional and independent, the distribution of rate coefficients becomes an effective distribution representing the range of rates of mass transfer.

Variability in the diffusion-rate coefficient is due to a combination of factors, including variability in at least the following: (1) matrix-block size; (2) tortuosity; (3) pore geometry; (4) restricted diffusion within pores (i.e., diffusion is slowed by small cross-sectional area of the pore); and (5) interaction with pore walls, including sorption (though the tracers employed in our experiments are believed to be non-sorbing). In addition to diffusion into the rock matrix, diffusion probably occurs in the fractures into dead-ends and immobile zones, and into clay and other material within the fractures. All of these sources of variability are implicit to the distribution of D_a/l^2. For further discussion on these sources of variability, see Pedit and Miller (1994), Haggerty and Gorelick (1995, 1998), and Pignatello and Xing (1996).

The distribution of diffusion-rate coefficients may be defined in any appropriate manner, but most commonly is defined as a statistical distribution. Culver et al. (1997), Cunningham et al. (1997), and others have used a gamma distribution, while Pedit and Miller (1994, 1995), Haggerty and Gorelick (1998), and others have employed a lognormal distribution. Although we employ a lognormal distribution primarily due to ease of use, independent evidence suggests a lognormal distribution is an appropriate choice. Several geologic properties frequently appear to be lognormally or near lognormally distributed, including hydraulic conductivity (Neuman, 1982; Hoeksema and Kitanidis, 1985; Gelhar, 1993, p. 19, p. 99) and grain size (Buchan, 1989; Buchan et al., 1993). The distribution coefficient and the sizes of the micropores may also be approximately lognormally distributed. The product of lognormal distributions is a lognormal distribution (Aitchison and Brown, 1957, p. 11). Additionally, the product of many independent, positive variates is also lognormally distributed (Aitchison and Brown, 1957, p. 14). Therefore, because properties of a medium such as grain size and the distribution coefficient contribute multiplicatively to the diffusion-rate coefficient, we hypothesize that the rate coefficient may be characterized by a lognormal distribution.

The mathematical models presented here make the following important simplifications: (1) the regional hydraulic gradient is negligible; and (2) the formation is isotropic, confined, horizontal, homogeneous with respect to groundwater flow, and of constant thickness. The second set of assumptions simply guarantees that flow is radially symmetric. This is much less significant for an SWIW test than for other types of tests, particularly if the first assumption is approximately valid, because the tracer leaves the well and comes back to the well along close to the same paths. Numerical simulations presented in Chapter 4 demonstrate that the SWIW data from the tests at H-11 and H-19 cannot be explained by a single-porosity or conventional double-porosity model that incorporates aquifer heterogeneity and drift due to a regional gradient. In this chapter, we evaluate whether a double-porosity model with a distribution of diffusion coefficients can explain the data. We leave the evaluation of combined effects of heterogeneity, drift, and multiple rates of diffusion for future research.

The equations for solute transport into or out of a well, in the presence of a lognormal distribution of matrix-diffusion rates, are given by:

$$\frac{\partial c_a}{\partial t} + \int_0^\infty b(\alpha_d) \frac{\partial \hat{c}_d(\alpha_d)}{\partial t} \, d\alpha_d = \frac{1}{r}\frac{\partial}{\partial r}\left(\frac{r\alpha_L |v|}{R_a}\frac{\partial c_a}{\partial r}\right) - \frac{v}{R_a}\frac{\partial c_a}{\partial r} \tag{6-1}$$

$$b(\alpha_d) = \frac{\beta_{tot}}{\sqrt{2\pi}\sigma_d \alpha_d} \exp\left\{ - \frac{\left[\ln(\alpha_d) - \mu_d\right]^2}{2\sigma_d^2} \right\} \tag{6-2a}$$

where

$$\alpha_d \equiv \frac{D_a}{l^2} \tag{6-2b}$$

and

$$\beta_{tot} = \frac{\phi_d R_d}{\phi_a R_a} \tag{6-2c}$$

and where c_a [M/L^3] is the solute concentration in the advective porosity (e.g., fractures); $\hat{c}_d(\alpha_d)$ [M/L^3] is the average solute concentration in the portion of the matrix associated with a particular diffusion-rate coefficient; α_d [1/T] is the diffusion-rate coefficient described in Equation 6-2b, which is continuously distributed; $b(\alpha_d)$ [-] is the PDF of diffusion-rate coefficients, which we assume to be lognormal in Equation 6-2a; β_{tot} [-] is the total capacity coefficient of the formation, which is the ratio of mass in the matrix to mass in the fractures at equilibrium; α_L [L] is the longitudinal dispersivity; v [L/T] is the pore-water velocity; R_a [-] is the retardation factor in the advective porosity; r [L] is the radial coordinate (positive away from well); t [T] is time elapsed since the beginning of injection of the first tracer; σ_d is the standard deviation of the log-transformed diffusion-rate coefficients; μ_d is the natural log of the geometric mean of the diffusion-rate coefficients; D_a [L^2/T] is the apparent diffusion coefficient in the matrix, which may be defined most simply as the product of the aqueous diffusion coefficient of the tracer and diffusive tortuosity, although this expression may be modified to incorporate processes such as immobile-zone sorption; l [L] is the length of the diffusion pathway within the matrix; ϕ_d [-] is the diffusive porosity of the formation; R_d [-] is the retardation factor due to sorption within the diffusive porosity; and ϕ_a [-] is the advective porosity. In Equation 6-1, we do not consider transverse dispersion because the flow is radially symmetric and transverse dispersion plays no role.

The time-derivative of the spatially averaged solute concentration in the matrix is given by:

$$\frac{\partial \hat{c}_d(\alpha_d)}{\partial t} = \frac{1}{l}\int_0^l \frac{\partial c_d(\alpha_d)}{\partial t}\,dz\ , \qquad 0 < \alpha_d < \infty \tag{6-3a}$$

where c_d [M/L^3] is the concentration at a point within the portion of the matrix associated with a particular diffusion-rate coefficient; and z [L] is the coordinate along the pathway. Note that l is a variable part of α_d and, therefore, is implicitly dependent upon α_d. The concentration at a point within the portion of the matrix associated with a particular diffusion-rate coefficient is given by the solution to the diffusion equation:

$$\frac{\partial c_d(\alpha_d)}{\partial t} = D_a \frac{\partial^2 c_d(\alpha_d)}{\partial z^2}, \qquad 0 < \alpha_d < \infty \tag{6-3b}$$

This equation represents diffusion in a distribution of one-dimensional paths. The boundary condition for diffusive mass transfer is that the concentration at the edge of the matrix is equal to the concentration in the mobile zone:

$$c_d(\alpha_d) = c_a, \qquad z = l, 0 < \alpha_d < \infty \tag{6-3c}$$

The boundary condition at the internal end of each path is:

$$\frac{\partial c_d(\alpha_d)}{\partial z} = 0 \qquad z = 0, 0 < \alpha_d < \infty \tag{6-3d}$$

To solve these equations, we use the approach outlined by Haggerty and Gorelick (1995, 1998), where we substitute a series of first-order equations for Equations 6-3a and 6-3b (Appendix Q). The substitution is done in such a way that the resulting solution for c_a is mathematically identical to that which would be obtained by solving the above equations directly. The solutions are obtained in the Laplace domain and then numerically inverted to the time domain (Appendix Q). The code STAMMT-R (Solute Transport and Multirate Mass Transfer in Radial Coordinates (Haggerty et al., 2000) was used to solve these equations.

To model the experiments for diffusion into a sphere (e.g., Rao et al., 1980; Ball and Roberts, 1991), we also employ Equation 6-1. However, Equations 6-2a and 6-3a-c are replaced by the following five equations:

$$b(\alpha_d) = \beta_{tot}\delta(\alpha_d - \alpha_d^*) \tag{6-4}$$

$$\frac{\partial \hat{c}_d(\alpha_d)}{\partial t} = \frac{3}{l^3}\int_0^l z^2 \frac{\partial c_d}{\partial t}\,dz\ , \quad \alpha_d = \alpha_d^* \tag{6-5}$$

$$\frac{\partial c_d}{\partial t} = \frac{D_a \partial}{z^2 \partial z}\left(z^2 \frac{\partial c_d}{\partial z}\right) \tag{6-6a}$$

$$c_d = c_a, \quad at\ z = l \tag{6-6b}$$

$$\frac{\partial c_d}{\partial z} = 0, \qquad at\ z = 0 \tag{6-6c}$$

where $\delta(\alpha_d - \alpha_d^*)$ is the Dirac delta (α_d^* represents a single value of α_d instead of a distribution); and l is now defined as the radius of the spherical matrix block, which is constant.

The choice of spherical geometry for the single-rate model is not important. Several authors have shown that diffusion into spheres and cylinders, layers, or cubes does not differ significantly, other than that the mean residence time differs for a fixed value of l (e.g., Villermaux, 1981; Rao et al., 1982; Goltz and Roberts, 1987). The mean residence time in a slab is five times the mean residence time in a sphere of the same half-thickness. Therefore, the multirate model for 1-D pathways with $\sigma_d = 0$ is approximately the same as the single-rate model provided that μ_d [multirate] = $\exp(D_a/5l^2)$ [sphere].

6.2.1 Radially Divergent Flow (Injection Period)

For each of the three parts of an SWIW test (the injection, resting, and pumping periods), the pore-water velocities, initial conditions, and boundary conditions differ. Let us first consider the injection period.

The pore-water velocity in Equation 6-1 during the injection period is given by:

$$v = \frac{Q_{inj}}{2\pi r \phi_a b} \qquad (6\text{-}7)$$

where Q_{inj} [L^3/T] is the injection rate and b [L] is the formation thickness. The boundary conditions for use with Equation 6-1 for conditions of radially divergent flow (injection) are:

$$c_a - \alpha_L \frac{\partial c_a}{\partial r} = c_{inj} \qquad at\, r = r_w \qquad (6\text{-}8a)$$

$$\frac{\partial c_a}{\partial r} = 0 \qquad r \to \infty \qquad (6\text{-}8b)$$

where r_w [L] is the well radius and c_{inj} is the injected concentration (which may be a function of time). Equation 6-8a is the flux boundary at the well accounting for dispersion and Equation 6-8b is the boundary condition at infinity during injection. Initial conditions for radially divergent flow are that concentrations in both the advective and diffusive porosities (i.e., matrix and fracture porosities) are initially zero.

The equations described in this section must be solved over all space at the end of the injection period. We solved these equations on a one-dimensional grid (because we assumed that concentrations change only radially away from the well). The grid used 25 equally spaced nodes and was terminated at a distance where mobile concentrations fell below 10^{-4} of the injected concentration. With this number of nodes placed to the edge of the concentration field, results were insensitive to grid spacing. An independent mass-balance calculation ensured all injected mass was accounted for.

6.2.2 No Flow (Resting Period)

After the injection period, the well is turned off. During the resting period, the pore-water velocity in the formation is assumed to be zero. This is justified because velocities near a well very rapidly come to steady state after a change in pumping rate, even though heads may continue to change for some time. This assumption is supported and discussed by Harvey et al. (1994). Therefore, Equation 6-1 may be simplified to:

$$\frac{\partial c_a}{\partial t} + \int_0^\infty b(\alpha_d) \frac{\partial \hat{c}_d(\alpha_d)}{\partial t}\, d\alpha_d = 0 \qquad (6\text{-}9)$$

and all other equations remain the same. In the absence of a velocity field, no boundary conditions are required. Initial conditions for the resting period are taken as the concentrations in both the advective and the diffusive domains at the end of the injection period. Concentrations are solved at the end of the resting period, spatially along the grid discussed above.

6.2.3 Radially Convergent Flow (Pumping Period)

The pore-water velocity in Equation 6-1 during the pumping period is given by:

$$v = \frac{Q_{out}}{2\pi r \phi_a b} \qquad (6\text{-}10)$$

where Q_{out} [L^3/T] is the pumping rate. We also assume that the velocity in Equation 6-10 is constant because velocities quickly come to steady state in a radial system (see reasoning in Section 6.2.2). The boundary conditions for use with Equation 6-1 for conditions of radially convergent flow (pumping) are:

$$\frac{\partial c_a}{\partial r} = 0 \qquad r = r_w \qquad \text{(6-11a)}$$

$$c_a = 0 \qquad r \to \infty \qquad \text{(6-11b)}$$

Initial conditions for radially convergent flow are that concentrations (both advective and diffusive) at every point on the grid (see the end of Section 6.2.1) are initially identical to those at the end of the resting period.

6.3 Modeling of SWIW TESTS

In this section, we present two models of the SWIW tests. First, we present results from our effort to model the five SWIW tests using conventional (single-rate) diffusion into a spherical matrix block and transport assuming radial flow. Second, we show the multirate-diffusion model of the SWIW test data. We also present results from a sensitivity analysis with the multirate-diffusion model, including confidence bounds on the parameter estimates.

We refer to the five SWIW data sets as follows: (1) the first H-19 test (SWIW1), tracer 1 as H19S1-1; (2) the first H-19 test (SWIW1), tracer 2 as H19S1-2; (3) the second H-19 test (SWIW2), only one tracer added, as H19S2; (4) the H-11 test (SWIW), tracer 1 as H11-1; and (5) the H-11 test (SWIW), tracer 2 as H11-2. Details of the injected volumes, injection rates, pumping rates, etc., are given in Table 3-2. Parameters used by the models were defined in one of two ways: (1) values were fixed based on knowledge of the tracer tests and the Culebra geology; and (2) values were estimated by fitting the models to the data. All parameters that could be fixed are shown in Table 6-1.

Estimation of parameters was done using a nonlinear least-squares algorithm (e.g., Marquardt, 1963). For each data set and model of that data, we found the set of parameters that minimized the sum of squared errors on the logarithm of concentrations. We estimated the natural logs of those parameters that are strictly positive-valued. For purposes of comparison, we used the root-mean square error (RMSE), defined for natural logs of concentration and corrected for the number of parameters estimated (e.g., Bard, 1974, p. 178). The logs of concentration were fit because of our interest in mass transfer and the fact that the low-concentration tails are very sensitive to mass transfer (see Section 6.4.1.). Estimation from log concentrations allows us to take advantage of the information contained in the tails without losing the information contained in the peak of the breakthrough. A first-order approximation to the estimated parameter covariance matrix (V_p) is given by (e.g., Bard, 1974; Draper and Smith, 1981):

Table 6-1. Fixed Parameters Used in Simulations

Parameter	Test				
	H11-1	H11-2	H19S2	H19S1-1	H19S1-2
solute injection time [s]	8.16×10^3	7.98×10^3	7.32×10^3	7.62×10^3	7.95×10^3
chaser injection time [s]	1.54×10^4	7.44×10^3	1.46×10^4	1.58×10^4	7.83×10^3
pause length, t_{rest} [s]	6.36×10^4	6.36×10^4	6.38×10^4	6.22×10^4	6.22×10^4
injection rate, Q_{inj} [m^3/s]	1.22×10^{-4}	1.27×10^{-4}	1.16×10^{-4}	1.31×10^{-4}	1.26×10^{-4}
pumping rate, Q_{out} [m^3/s]	2.24×10^{-4}	2.24×10^{-4}	2.74×10^{-4}	2.37×10^{-4}	2.37×10^{-4}
well radius, r_w [m]	0.065	0.065	0.113	0.113	0.113
thickness, b [m]	4.4	4.4	4.4	4.4	4.4
matrix porosity, ϕ_d [-]	0.160	0.160	0.147	0.147	0.147
grid radius [m]	8.00	8.00	3.75	3.75	3.75

$$V_p = \sigma^2 \left(J^T J\right)^{-1} \qquad (6\text{-}12)$$

where σ is the replicate variance defining the uncertainty in concentration (assumed to be uniform and equal to the RMSE), J is the Jacobian, which is the matrix of sensitivities of the model output to the parameter estimates, and the superscript T indicates the transpose of the matrix. In the analyses that follow, σ_p is the standard deviation of the estimated parameter, which is the square root of the respective diagonal from V_p.

6.3.1 Conventional Double-Porosity and Radial Transport

Figure 6-2 shows the best obtainable fit of the conventional double-porosity model (assuming spherical diffusion) to the H19S2 and H11-1 recovery curves. Modeling of the other recovery curves is not shown for conventional double-porosity because the two attempts with H19S2 and H11-1 clearly demonstrate that a conventional double-porosity model is inadequate. Numerical simulations incorporating the effects of heterogeneity and plume drift presented in Chapter 4 also suggest that the late-time slope of the data cannot be explained with a conventional double-porosity model. The parameters estimated from these fits and the RMSEs are given in Table 6-2.

We used only early-time data (first 50 hr) in the inversion procedure, roughly corresponding to the advection/dispersion-dominated portion of the recovery curve. This was necessary because we found that the conventional double-porosity model could not possibly match the late-time data (see Figure 6-2). When matching the late-time data was attempted, other estimated parameters in the model were made physically unreasonable (e.g., advective porosity close to 100%, or dispersivity larger than several meters, close to the spatial scale of the experiment) and the estimation algorithm would fail. In dozens of scoping runs with a conventional double-porosity model, no set of parameters was able to reproduce the late-time slope of the data. For conventional double-porosity, the log-log slope is -1.5 for times after the advection-dominated early part of the test, and before the diffusion time scale of approximately l^2/D_a, (see Appendix K; Hadermann and Heer, 1996 and Tsang, 1995). At times greater than the diffusion time scale, the double-log slope predicted for a conventional double-porosity model quickly goes to infinity (in other words, the matrix is quickly emptied of solute once the time scale of diffusion is reached). For these reasons, we also decided not to produce confidence bounds on the parameter estimates shown in Table 6-2.

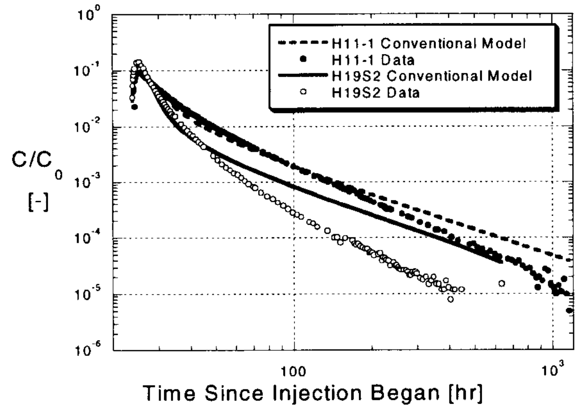

Figure 6-2. Best fits of conventional double-porosity models to the H11-1 and H19S2 data. Parameters are given in Table 6-2.

6.3.2 Multirate Diffusion and Radial Transport

Figures 6-3a-e show the multirate-diffusion model results (assuming a lognormal distribution of rate coefficients) for the five SWIW recovery curves. From these figures, we note two points. First, the data for all five SWIW tracers sets are fit very well by the multirate-diffusion model. The RMSE values (Table 6-3) range from 0.150 to 0.424, which are four to eight times smaller than the values from the conventional double-porosity model for the same respective SWIW data sets. This improvement over the conventional double-porosity model is achieved with one additional estimated parameter, σ_d. Second, the models fit the observed recovery curves over the entire range of data, including both early and late concentrations.

Table 6-2. Single-Rate Double-Porosity Estimation Results

Test	Log[mean (D_d/a^2)] μ_d	Advective Porosity ϕ_a [-]	Dispersivity α_L [m]	RMSE
H19S2	-16.2	0.0540	0.159	1.27
H11-1	-18.8	0.00714	0.458	0.527

Table 6-3. Multirate Estimation Results

Test	Log[mean (D_d/a^2)] $\mu_d \pm 2\sigma$ range	Std. Dev. Log(D_d/a^2) σ_d $ln(\sigma_d) \pm 2\sigma$ range	Advective Porosity ϕ_a [-] $ln(\phi_a) \pm 2\sigma$ range	Dispersivity α_L [m] $ln(\alpha_L) \pm 2\sigma$ range	RMSE
H11-1	-15.8 ± 1.09 -14.7, -16.9	3.55 *1.27 ± 0.245* 2.79, 4.54	0.00175 *-6.35 ± 4.59* 1.77×10^{-5}, 0.174	0.0566 *-2.87 ± 4.35* 7.33×10^{-4}, 4.37	0.151
H11-2	-15.7 ± 0.942 -14.7, -16.6	3.83 *1.34 ± 0.238* 3.02, 4.858	0.00430 *-5.45 ± 2.53* 3.43×10^{-4}, 0.0538	0.0365 *-3.31 ± 5.08* 2.28×10^{-4}, 5.84	0.152
H19S2	-10.9 ± 1.67 -9.23, -12.5	5.83 *1.76 ± 0.237* 4.60, 7.38	0.0151 *-4.19 ± 2.74* 9.78×10^{-4}, 0.233	0.173 *-1.76 ± 0.237* 0.136, 0.219	0.161
H19S1-1	-11.9 ± 3.96 -7.94, -15.9	6.87 *1.93 ± 0.297* 5.12, 9.272	0.00485 *-5.33 ± 12.8* 1.34×10^{-8}, >1	0.213 *-1.55 ± 0.356* 0.149, 0.303	0.276
H19S1-2	-10.1 ± 3.98 -6.12, -14.1	2.56 *0.940 ± 0.822* 1.13, 5.83	0.0202 *-3.90 ± 12.7* 6.18×10^{-8}, >1	0.117 *-2.15 ± 1.80* 0.019, 0.705	0.424

For a given test, 1st row in each column (except that for μ_d) gives the best-fit parameter value; 2nd row gives the natural logarithm of the best-fit parameter value and 95% confidence limits; and 3rd row gives the range of possible parameter values to within 95% confidence. μ_d was directly estimated (as opposed to its logarithm), so confidence limits are given in arithmetic space. See text for details.

The parameters estimated from these fits, their 95% confidence intervals (i.e., $2\sigma_p$), and the associated RMSEs are given in Table 6-3. Because the natural logarithms of positive-valued parameters were estimated, the confidence intervals are on the logs of the estimates for all parameters except μ_d. From Table 6-3, we note four points. First, the parameters indicate that the estimated distribution of α_d is very broad, spanning several orders of magnitude. Second, the distribution of α_d appears to be different at H-11 than at H-19. This is discussed below in more detail. Third, μ_d and σ_d have relatively small confidence intervals, while ϕ_a and α_L generally have very large confidence intervals. In particular, we note that the confidence interval on the estimate of advective porosity suggests that this parameter is essentially unestimable in an SWIW test. Conversely, σ_d appears to be particularly well-measured by this type of test. However, the terms "large" and "small" are somewhat subjective and a more detailed analysis is given in the following sections. Fourth, parameters estimated from tests at the same well (with the exception of σ_d for the H19S1-2 recovery curve) have values that are statistically the same (i.e., their confidence intervals greatly overlap).

Figure 6-4 shows the estimated cumulative distribution functions (CDFs) of the diffusion-rate

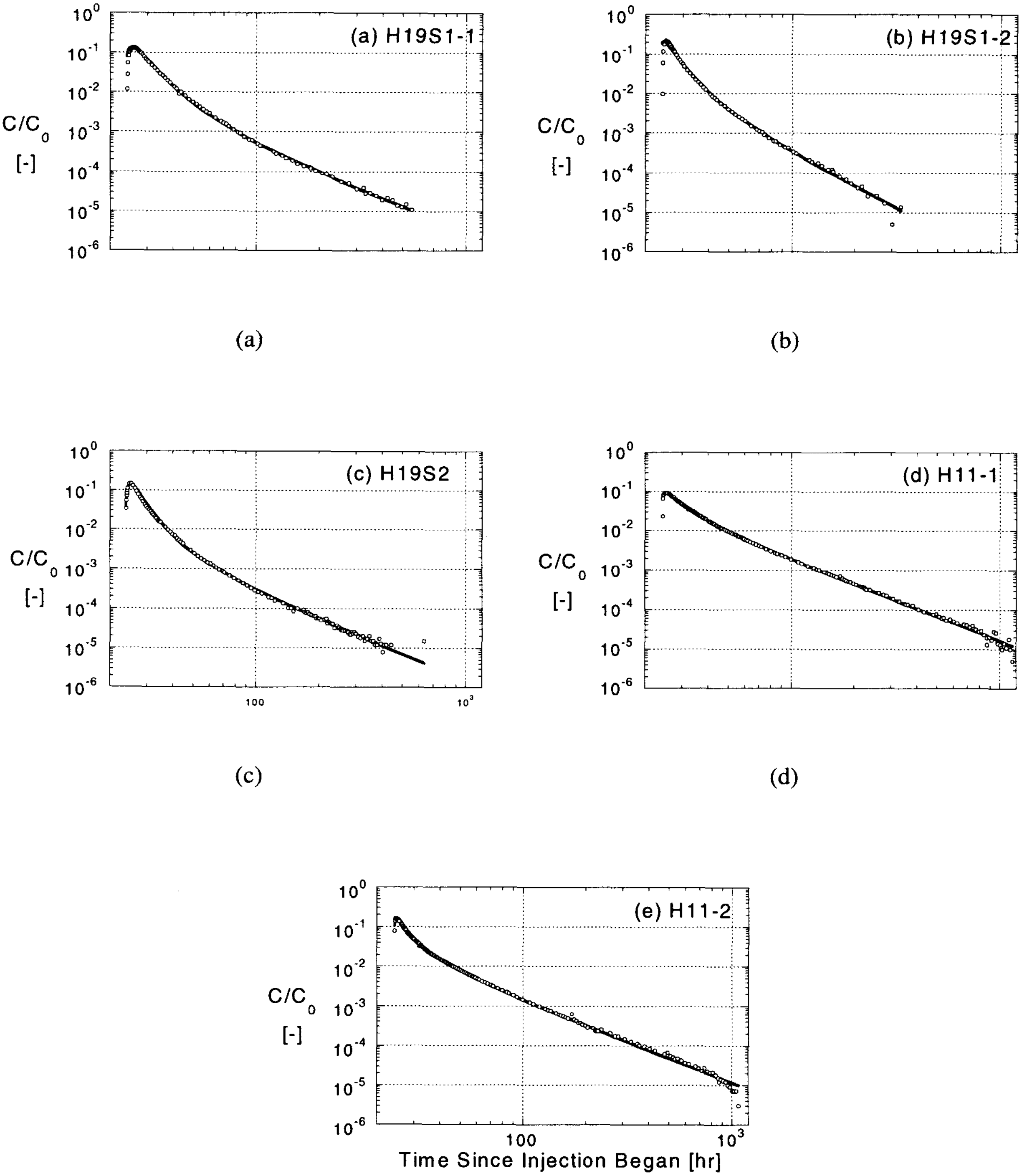

(a)

(b)

(c)

(d)

(e)

Figure 6-3. Best fits of multirate diffusion model to all SWIW data. Parameters are given in Table 6-3.

coefficient for the five models. The graph shows the cumulative matrix volume associated with a diffusion-rate coefficient smaller than a given value. The variance of the estimated distribution is large for all tests, but is somewhat larger, in general, for the H-19 tests than for the H-11 tests. The estimated CDFs display 95% of the distribution spanning a range of 4.4 to 11.7 orders of magnitude. We also note that the CDFs from the H-11 and H-19 tests appear to be self-consistent, with the exception of the CDF for H19S1-2, which has a different estimated σ_d than the other two at H-19 (discussed in Section 6.4.2).

Figure 6-4 contains a shaded region, indicating the portion of the CDF of diffusion-rate coefficients that could be assayed (i.e., "observed") by the tracer tests. Upper and lower limits were calculated by considering the diffusive time scale for different parts of the CDF. The diffusive time scale is the amount of time it takes for a solute to diffuse into a particular region, and is roughly the inverse of the diffusion coefficient for a one-dimensional micropore (e.g., Crank, 1975). For example, a one-dimensional micropore that is characterized by a α_d of 2.3×10^{-9} s^{-1} would require approximately 4.3×10^8 s (1.2×10^5 hr) for solute to diffuse into it. Therefore, we would not expect that such a micropore would affect a tracer test at time scales 100 times smaller (on the order of 1200 hr, the time of the last data point in H11-1). This reasoning is consistent with arguments based on Damkohler numbers (e.g., Bahr and Rubin, 1987). Therefore, we draw an approximate lower limit of the shaded zone at 2.3×10^{-9} s^{-1}. Thus, the portion of the CDF with values of α_d smaller than the shaded region corresponds to that part of the diffusive porosity that could not be assayed by the SWIW tests. A longer duration test would be needed to "observe" that portion of the matrix.

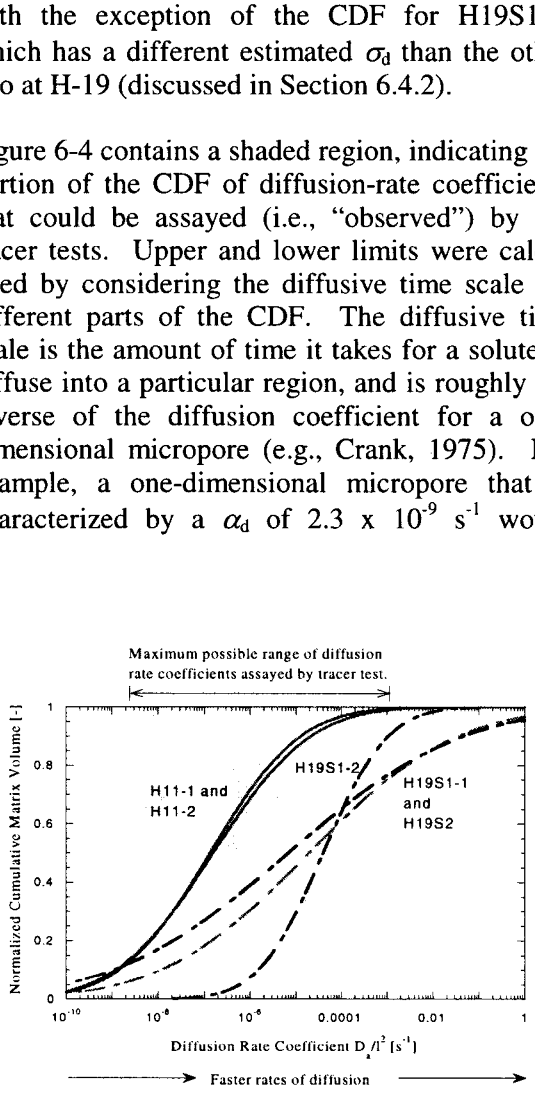

Figure 6-4. Cumulative distribution functions (CDFs) estimated from each of the SWIW data. CDFs shown here correspond to the models shown in Figure 6-3 and the parameters given in Table 6-3.

On the other end of the time-scale spectrum, diffusive mass transfer that is very fast will be obscured by advective processes. Because we do not know the ratio of advective to diffusive porosity, we cannot distinguish between pores dominated by advection and small micropores into which diffusion occurs quickly. In other words, diffusive porosity that interacts very rapidly with advective porosity is indistinguishable from the advective porosity itself, even in an SWIW test. Therefore, the fastest observable diffusion processes will occur at a minimum of approximately one percent of transport time through the system. For our system, this initial recovery time also includes the injection and resting time (a total of about 24 hr), which corresponds to a α_d of 1.2×10^{-3} s^{-1}. In reality, the fastest observable diffusion process is probably slower than this, but this provides an approximate upper bound. Again, this reasoning is consistent with an argument based on the Damkohler number.

The fringes of the estimated CDFs, lying outside the bounds in Figure 6-4, are highly nonunique and are not supported by data. They appear on the CDF only because we have chosen, *a priori*, a lognormal distribution. We have the largest degree of confidence about the part of the CDF near the center of the shaded region, with decreasing confidence toward the edges.

As discussed above, the estimated CDFs suggest that 95% of the distribution is spread over 4.4 to 11.7 orders of magnitude. However, not all of this distribution is supported by data. If the unsupported portions of the CDFs are ignored, the distributions are spread over 3.6 to 5.7 orders of magnitude. This spread should be considered a minimum, as a longer duration experiment would likely support a wider spread.

6.4 Discussion

6.4.1 Sensitivity Analysis

In this subsection, we discuss the sensitivity of the multirate-diffusion model to the estimated parameters.

The Jacobian (sensitivity matrix of dependent variable to model parameter) can be normalized to allow comparison of parameter sensitivities through time and from one parameter to another (Harvey et al., 1996):

$$\mathbf{J}_{ij} = \frac{p_j \partial C_i}{\sigma \partial p_j} \qquad (6\text{-}13)$$

where J_{ij} is the sensitivity of the modeled concentration at the ith time to the jth parameter; C_i is the ith component of the vector of normalized concentrations through time; and p_j is the jth component of the vector of estimated parameters. The Jacobian is a useful instrument for investigating the sensitivity of the model to the estimated parameters as a function of time (e.g., Wagner and Harvey, 1997), and gives insight into the correlation between estimated parameters. A large value (either positive or negative) in the Jacobian indicates that the model, at a particular time, is sensitive to a given parameter; a small value would indicate that the model is insensitive to the parameter. The parameter covariance matrix from Equation 6-12 was also used to examine cross-correlation.

Plots of the columns of the Jacobians for H11-1 and H19S2 are given in Figures 6-5a and 6-5b, respectively; each is representative of the sensitivity matrices computed for other SWIW tests at their respective locations. In both plots, the nature of all sensitivities changes significantly between the advection/dispersion- and mass-transfer-dominated parts of the simulations, a transition that occurs at roughly 40 hr (1.44 x 10^5 s) at the H-11 well and roughly 30 hr (1.08 x 10^5 s) at H-19.

For H11-1, the sensitivity of the model to the mass-transfer parameters is much larger than to the flow parameters, and increases over time. The sensitivities to dispersivity and advective porosity are small and essentially constant for times greater than 40 hr (1.44 x 10^5 s), suggesting strong correlation. Consequently, neither parameter can be estimated with any confidence. In contrast, the sensitivities of the mean and standard deviation of the distribution of log-diffusion-rate coefficients are larger and increase through time. Thus, the mass-transfer parameters can be estimated with a reasonable degree of confidence, provided that good data are available at late time. These conclusions are supported both by the covariances and by the confidence intervals of the estimated parameters (see Table 6-3).

The sensitivity matrix for H19S2 exhibits greater complexity than that for H11-1. First, μ_d shows a fairly high degree of correlation with ϕ_a, but the sensitivities are somewhat larger for ϕ_a than in H11-1. This is explained as follows. The largest coefficients in the distribution of diffusion-rate coefficients represent near-instantaneous mass transfer. Hence, the corresponding diffusive porosity effectively acts as part of the advective porosity (i.e., they are indistinguishable). The fraction of the distribution of diffusion-rate coefficients that are large is determined in part by μ_d (larger μ_d means that the geometric mean of α_d is larger and diffusive mass transfer is faster). Therefore, μ_d determines the fraction of the diffusive porosity that is indistinguishable from advective porosity. Consequently, μ_d and ϕ_a can be strongly correlated if μ_d is relatively large (as is the case in H19S2). Nonetheless, calculated confidence limits indicate that μ_d can still be estimated for H19S2 with reasonable confidence, though with somewhat less confidence than for H11-1.

Second, in H19S2, the sensitivities exhibit a higher degree of scatter and numerical error. The scatter and oscillations in the sensitivity plot are due to numerical error at very low concentrations and do not have physical significance. Sensitivities are calculated numerically as derivatives, which are very sensitive to small numerical errors.

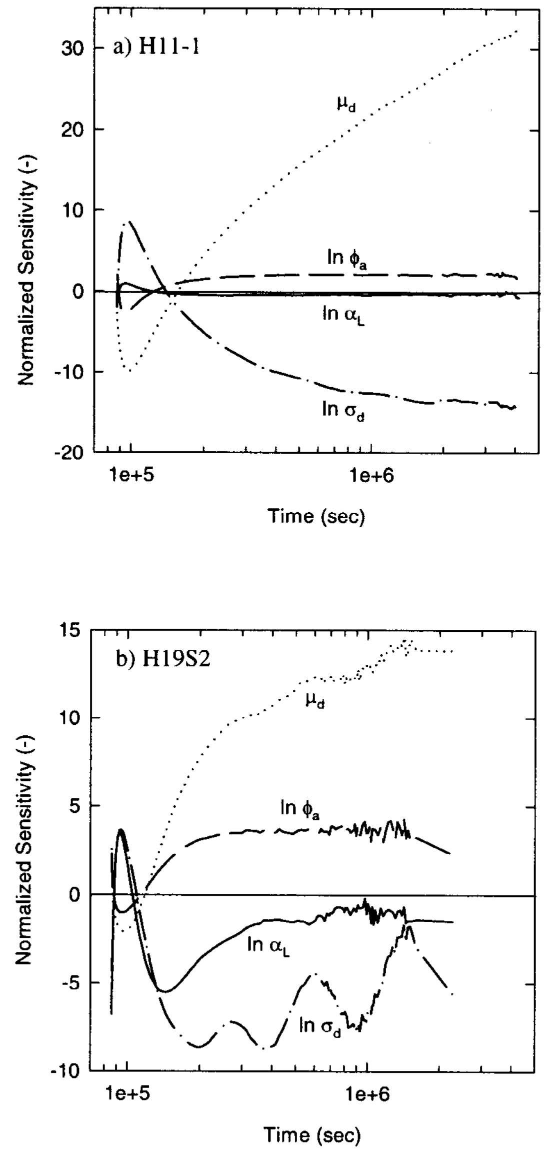

Figure 6-5. Normalized sensitivity for estimated parameters of multirate diffusion model at H11-1 and at H19S2.

6.4.2 Discussion of Estimated Parameters and Comparison with Other Data

In this subsection, we discuss the estimated parameters, their confidence intervals, and compare these values to data external to the SWIW tests.

The values of ϕ_a and α_L (see Table 6-3) cannot confidently be estimated by the SWIW test: both parameters have extremely large confidence intervals. In the case of ϕ_a, the confidence intervals span all possible values of advective porosity. Dispersivity has slightly smaller confidence intervals, but the confidence intervals still span all possible values. Surprisingly, however, all estimated values of both ϕ_a and α_L are in reasonable agreement with independent information. The estimated values of α_L, for example, lie within the bounds of field-scale dispersivities observed in other types of tests at similar scales (Gelhar et al., 1992). The advective porosities we estimate are within the range expected for fractured rock, and lie between the high advective porosities calculated for the multiwell test data assuming plug flow (see Chapter 3 and Appendix C) and the lower advective porosities predicted based on multirate interpretations of the multiwell test data (see Chapter 7 and Appendix S).

Advective porosity and dispersivity are not estimable by an SWIW test because the flow field is approximately reversed in the middle of the experiment. Large and small values of these two parameters result in very similar early-time recoveries, and the late-time recovery is almost completely insensitive to the parameters. In contrast, diffusion should not be significantly affected by the flow-direction changes. Additionally, the late-time recovery is very sensitive to diffusive mass transfer. Consequently, the parameters describing the distribution of diffusion-rate coefficients, μ_d and σ_d (discussed below), are quite estimable in an SWIW test.

The parameters μ_d and σ_d are estimated with small confidence intervals relative to their range of reasonable values. Because diffusion-rate coefficients can vary over an extremely wide range, 95% confidence intervals on μ_d of about ± 1 to 2 indicate a reasonable degree of confidence for this parameter. The value of ln (σ_d) appears to be well-estimated by the SWIW test also (with the exception of H19S1-2, which is a much shorter data set). Other than H19S1-2, the confidence intervals on ln (σ_d) range from ± 0.24 to ± 0.30.

The mean and standard deviation of diffusion-rate coefficients are both generally larger for the H-19 recovery curves than for the H-11 recovery curves. This corresponds well to our current understanding of the hydrogeology at the two hydropads. On the basis of advective porosities inferred from interpretations of MWCF tracer tests (see Chapter 7), transmissivities determined for many wells at the WIPP site (Beauheim and Ruskauff, 1998), and examination of drill core (Holt, 1997), we believe that advective transport in the Culebra dolomite at the H-11 hydropad tends to be channeled along well-connected fractures that form comparatively direct flow paths. At the H-19 hydropad, advective porosity appears to consist not only of fracture porosity but also interparticle porosity and vugs connected by microfractures, and flow thus follows a more circuitous route (see Chapters 2, 3, and 8). Mass that is advectively transported near the H-11 hydropad experiences: (1) exposure to a smaller surface area of matrix, resulting in less matrix diffusion during a given time or space scale of experiment and thus lower effective matrix-diffusion rates; and (2) incomplete exposure to the range of porosity types, resulting in a narrower spread to the distribution of diffusion-rate coefficients.

The distributions of α_d estimated from the SWIW tests appear consistent from test to test and data set to data set, with the exception of H19S1-2. The H-11 data set and the other two H-19 data sets yielded very similar values of μ_d and σ_d for tests conducted at the same well. The estimated values of μ_d and σ_d for H19S1-2 are larger and smaller, respectively, than for H19S2 and H19S1-1. The confidence interval on σ_d for H19S1-2 is large enough, however, that the value of σ_d is very uncertain. The larger uncertainty and different estimates of μ_d and σ_d at H19S1-2 may be due to two factors. First, the lower detection limit was reached in H19S1-2 several hundred hours before it was reached in the other H-19 data sets. The data in H19S1-2 sample a smaller range of mass-transfer time scales and the test is, therefore, insensitive to the slowest rates of mass transfer. This resulted in a larger estimated mean diffusion-rate coefficient and a lower estimated standard deviation. The influence of the time scale of the experiment on the estimated parameters was confirmed by performing a parameter estimation on a H19S1-1 data set truncated to the length of the H19S1-2 data. The resulting estimates for μ_d and σ_d from this scoping run were intermediate between those from the H19S1-1 and H19S1-2 runs.

Second, the Culebra is heterogeneous. Of the three SWIW tests at H-19, the H19S1-2 injection appears to have been conducted over the smallest volume of the Culebra (see Table 6-2). As a result, the H19S1-2 tracer may have encountered the smallest amount of heterogeneity and, therefore, may be expected to have a smaller estimated σ_d.

The CDFs of diffusion-rate coefficients estimated from all recovery curves are very broad. The portions of the CDFs that are supported by data span at least 3.6 to 5.7 orders of magnitude (see Section 6.3.2). The significance of this for long-term solute transport in the Culebra is as follows. Diffusive mass transfer results in the average solute-transport velocity decreasing as a function of time. A distribution of diffusion-rate coefficients means that the decrease in average velocity occurs over a longer period of time than if there were a single diffusion-rate coefficient. A spread in the diffusion-rate coefficients of 3.6 to 5.7 orders of magnitude means that the average tracer velocity will decrease over time scales ranging from at least minutes to tens of years. Because this is a minimum, the average tracer velocity could decrease over an even greater range in time.

6.4.3 The Late-Time Slope of the Data

The SWIW data shown in Figure 6-3 have late-time slopes that are very nearly constant after 200 hr (7.2×10^5 s). Plots of the derivatives of these log-transformed data reveal that both H-11 data sets have a constant late-time slope of -2.1. The late-time slopes for H19S1-1 and H19S2 are both approximately -2.2, while the late-time slope for H19S1-2 is approximately -2.8. For all five SWIW data sets, these slopes are remarkably different from those predicted for a conventional double-porosity medium. For conventional double-porosity, the slope is -1.5 for times after the advection-dominated early part of the test, and before the diffusion time scale of approximately l^2/D_a, (Appendix K, Hadermann and Heer, 1996). At times greater than the diffusion time scale, the slope predicted for a conventional double-porosity medium quickly goes to infinity.

Figure 6-6 shows the effect of varying σ_d from 0 (conventional double-porosity) to the estimated value of 3.55 for H11-1. For the conventional double-porosity model, we see that the slope of the graph is -1.5 from approximately 100 hr (3.6 x 10^5 s) to 500 hr (1.8 x 10^6 s). However, after 500 hr, the slope steepens considerably, and would ultimately go to $-\infty$ as all mass is removed from the single-rate immobile zone. For the multirate-diffusion models, the late-time slopes are constant, with values of -1.9 for σ_d = 2.00, and -2.1 for σ_d = 3.55.

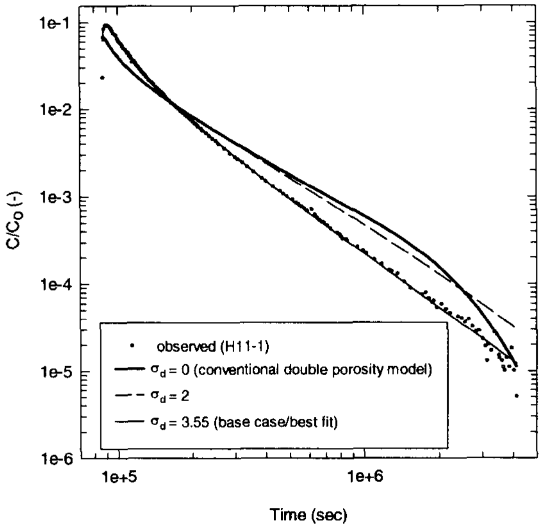

Figure 6-6. Sensitivity analysis for σ_d (standard deviation of ln(α_d)) in multirate diffusion model. The curve for σ_d = 0 is equivalent to the conventional double-porosity model.

In all of the SWIW data sets, the late-time slope is both constant and steeper than -1.5. We ran the multirate model for a range of parameters (many are not shown), and found that the late-time slopes are always approximately constant and steeper than -1.5 for σ_d greater than 0. In addition, data from other types of tests (e.g., one-dimensional column experiments with a pulse or square-wave injection) also show straight-line recovery curves at late times with slopes greater than -1.5, and scoping runs performed on these data have required non-zero values for σ_d in order to match the entire length of the recovery curve adequately. Therefore, we suggest that a constant late-time slope steeper than -1.5 for a pulse-injection tracer test is diagnostic of multirate mass transfer. Further investigation of this conclusion is warranted, however. Other effects may produce slopes similar to multirate diffusion, including significant tracer drift, the injection well not being cleared of solute, or nonlinear sorption. This is not believed to be the case for the WIPP data. Both single-porosity and conventional double-porosity simulations presented in Chapter 4 suggest that the combination of aquifer heterogeneity and drift may cause some bumps in the late-time portion of the curve, but will not result in a constant late-time slope slightly steeper than -1.5, similar to the WIPP data (see also Haggerty et al., in review and Haggerty et al., in press). In addition, diffusion of mass from the bottom of the borehole could not cause the late-time tailing observed in the WIPP data (see Appendix N).

6.4.4 Conventional Double-Porosity vs. Multirate Diffusion

A growing body of literature has concluded that multirate diffusion is a significant phenomenon. The majority of this literature has shown that the estimated distributions of rate coefficients have surprisingly large variances, even in relatively homogeneous media. Direct comparison of the various models is not straightforward because of different mathematical formulations, but Pedit and Miller (1995), Culver et al. (1997), Werth et al. (1997), Haggerty and Gorelick (1998), and Lorden et al. (1998) all found variability in mass-transfer-rate coefficients that span many orders of magnitude. Our study, based on field experiments, adds to this list: estimated variability in the diffusion-rate coefficient spans at least five orders of magnitude (see Figure 6-4). In our study, we find that we cannot fit all parts of the field data using a conventional, single-rate double-porosity model (assuming diffusion into spherical blocks). We can fit the earliest data, but these data are dominated by advection rather than mass transfer.

6.5 Conclusions

1. A double-porosity model incorporating distributed diffusion, such as the multirate-diffusion model presented here, appears necessary to represent the recovery curves for the SWIW tests in the Culebra dolomite. A conventional, single-rate double-porosity model, assuming spherical diffusion, is not able to reproduce the observed late-time slope of the data. This is a serious short-falling of the conventional double-porosity model, because the late-time data are dominated by diffusive mass transfer. The portion of the recovery curve matched well by the conventional double-porosity model is dominated by advection and dispersion.

2. Parameter estimation and sensitivity analyses indicate that the SWIW tests in the Culebra dolomite are generally insensitive to advective porosity and dispersivity. This is due to the design of this test in which the tracer goes out from the well and returns to the same well along approximately the same flow paths. However, the SWIW tests appear to be particularly sensitive to matrix diffusion, and from these tests we can estimate a distribution of diffusion-rate coefficients with a reasonable degree of reliability, although care must be taken to address the effects of data length and quality and the nonuniqueness of the estimated lognormal distribution of diffusion rates outside the assay range of a given tracer test.

3. The distribution of diffusion-rate coefficients is particularly sensitive to late-time data. In fact, the sensitivity to these parameters generally grows through time. Therefore, accurate estimation of the distribution relies on accurate concentration data in the tail of the test, where the effects of matrix diffusion dominate the effects of advection and dispersion. We doubt that distributions of rate coefficients can be estimated from SWIW recovery curves that either do not contain the tail concentrations or have very low-accuracy tails.

4. The late-time slope of the recovery curves obtained from SWIW tests in the Culebra dolomite have constant double-log slopes between -2.1 and -2.8. Late-time slopes obtained from conventional double-porosity models, however, are -1.5 before the diffusion time scale l^2/D_a (Appendix K; Hadermann and Heer, 1996), and quickly go from -1.5 to a slope much steeper than -2.5 after the diffusion time scale. Therefore, a constant late-time slope steeper than -2 is tentatively suggested as diagnostic of a distribution of diffusion-rate coefficients. However, more research must be done on this topic to confirm this finding and to examine its consequences.

5. The estimated distribution of diffusion-rate coefficients is very broad for the Culebra dolomite. The estimated CDFs, which assume a lognormal distribution of rate coefficients, have a standard deviation in ln (α_d) from 2.56 to 6.87. The portions of these CDFs that are supported by data are spread over at least 3.6 to 5.7 orders of magnitude. Consequently, if these distributions are accurate for the entire formation, approximately this many orders of magnitude in time would be needed to experience all of the mass-transfer variability in the formation. Given the range of the particular distributions, the advective velocity of a solute in the Culebra would continue to slow over time scales from minutes to decades and possibly much longer. Any experiments or modeling conducted within these time frames would need to account for a distribution of mass-transfer-rate coefficients in order to predict advective velocities accurately on another time scale.

6.6 References

Aitchison, J., and J.A.C. Brown. 1957. *The Lognormal Distribution with Special Reference to Its Uses in Economics.* New York, NY: University Press. 11.

Bahr, J.M., and J. Rubin. 1987. "Direct Comparison of Kinetic and Local Equilibrium Formulations for Solute Transport Affected by Surface Reactions," *Water Resources Research.* Vol. 23, no. 3, 438-452.

Ball, W.P., and P.V. Roberts. 1991. "Long-Term Sorption of Halogenated Organic Chemicals by Aquifer Material. 2. Intraparticle Diffusion," *Environmental Science & Technology*. Vol. 25, no. 7, 1237-1249.

Bard, Y. 1974. *Nonlinear Parameter Estimation*. New York, NY: Academic Press.

Beauheim, R.L., and G.J. Ruskauff. 1998. *Analysis of Hydraulic Tests of the Culebra and Magenta Dolomites and Dewey Lake Redbeds Conducted at the Waste Isolation Pilot Plant Site*. SAND98-0049. Albuquerque, NM: Sandia National Laboratories.

Brusseau, M.L., R.E. Jessup, and P.S.C. Rao. 1989. "Modeling the Transport of Solutes Influenced by Multiprocess Nonequilibrium," *Water Resources Research*. Vol. 25, no. 9, 1971-1988.

Buchan, G.D. 1989. "Applicability of the Simple Lognormal Model to Particle-Size Distribution in Soils," *Soil Science*. Vol. 147, no. 3, 155-161.

Buchan, G.D., K.S. Grewal, and A.B. Robson. 1993. "Improved Models of Particle-Size Distribution: An Illustration of Model Comparison Techniques," *Soil Science Society of America Journal*. Vol. 57, no. 4, 901-908.

Chen, W., and R.J. Wagenet. 1995. "Solute Transport in Porous Media with Sorption-Site Heterogeneity," *Environmental Science & Technology*. Vol. 29, no. 11, 2725-2734.

Chen, W., and R.J. Wagenet. 1997. "Description of Atrazine Transport in Soil with Heterogeneous Nonequilibrium Sorption," *Soil Science Society of America Journal*. Vol. 61, no. 2, 360-371.

Connaughton, D.F., J.R. Stedinger, L.W. Lion, and M.L. Shuler. 1993. "Description of Time-Varying Desorption Kinetics: Release of Naphthalene from Contaminated Soils," *Environmental Science & Technology*. Vol. 27, no. 12, 2397-2403.

Cooney, D.O., B.A. Adesanya, and A.L. Hines. 1983. "Effect of Particle Size Distribution on Adsorption Kinetics in Stirred Batch Systems," *Chemical Engineering Science*. Vol. 38, no. 9, 1535-1541.

Crank, J. 1975. *The Mathematics of Diffusion*. 2nd ed. New York, NY: Oxford University Press.

Culver, T.B., S.P. Hallisey, D. Sahoo, J.J. Deitsch, and J.A. Smith. 1997. "Modeling the Desorption of Organic Contaminants from Long-Term Contaminated Soil Using Distributed Mass Transfer Rates," *Environmental Science & Technology*. Vol. 31, no. 6, 1581-1588.

Cunningham, J.A., C.J. Werth, M. Reinhard, and P.V. Roberts. 1997. "Effects of Grain-Scale Mass Transfer on the Transport of Volatile Organics Through Sediments 1. Model Development," *Water Resources Research*. Vol. 33, no. 12, 2713-2726.

de Hoog, F.R., J.H. Knight, and A.N. Stokes. 1982. "An Improved Method for Numerical Inversion of Laplace Transforms," *SIAM Journal on Scientific and Statistical Computing*. Vol. 3, no. 3, 357-366.

Draper, N.R., and H. Smith. 1981. *Applied Regression Analysis*. 2nd ed. New York, NY: John Wiley & Sons.

Fong, F.K., and L.A. Mulkey. 1990. "Solute Transport in Aggregated Media: Aggregate Size Distribution and Mean Radii," *Water Resources Research*. Vol. 26, no. 6, 1291-1303.

Gelhar, L.W. 1993. *Stochastic Subsurface Hydrology*. Englewood Cliffs, NJ: Prentice-Hall. pp. 19, 99.

Gelhar, L.W., C. Welty, and K.R. Rehfeldt. 1992. "A Critical Review of Data on Field-Scale Dispersion in Aquifers," *Water Resources Research*. Vol. 28, no. 7, 1955-1974.

Goltz, M.N., and P.V. Roberts. 1987. "Using the Method of Moments to Analyze Three-

Dimensional Diffusion-Limited Solute Transport from Temporal and Spatial Perspectives," *Water Resources Research.* Vol. 23, no. 8, 1575-1585.

Hadermann, J., and W. Heer. 1996. "The Grimsel (Switzerland) Migration Experiment: Integrating Field Experiments, Laboratory Investigations and Modelling," *Journal of Contaminant Hydrology.* Vol. 21, no. 1-4, 87-100.

Haggerty, R., and S.M. Gorelick. 1995. "Multiple-Rate Mass Transfer for Modeling Diffusion and Surface Reactions in Media with Pore-Scale Heterogeneity," *Water Resources Research.* Vol. 31, no. 10, 2383-2400.

Haggerty, R., and S.M. Gorelick. 1998. "Modeling Mass Transfer Processes in Soil Columns with Pore-Scale Heterogeneity," *Soil Science Society of America Journal.* Vol. 62, no. 1, 62-74.

Haggerty, R., S.W. Fleming, and S.A. McKenna. 2000. *STAMMT-R: Solute Transport and Multirate Mass Transfer in Radial Coordinates, Version 1.01.* SAND99-0164. Albuquerque, NM: Sandia National Laboratories.

Haggerty, R., S.W. Fleming, L.C. Meigs, and S.A. McKenna. In review. "Tracer Tests in a Fractured Dolomite. 3. Analysis of Mass Transfer in Single-Well Injection-Withdrawal Tests," resubmitted to *Water Resources Research, 3/00.* SAND98-2573J. (Copy on File in the Sandia WIPP Central Files (SWCF) as ERMS #502440).

Haggerty, R, S.A. McKenna, and L.C. Meigs. In press. "On the Late-Time Behavior of Tracer Test Breakthrough Curves," Accepted by *Water Resources Research*, 7/00. SAND99-3120J. (Copy on file in the SWCF as ERMS #508873)

Harvey, C.F., R. Haggerty, and S.M. Gorelick. 1994. "Aquifer Remediation: A Method for Estimating Mass Transfer Rate Coefficients and an Evaluation of Pulsed Pumping," *Water Resources Research.* Vol. 30, no. 7, 1979-1991.

Harvey, J.W., B.J. Wagner, and K.E. Bencala. 1996. "Evaluating the Reliability of the Stream Tracer Approach to Characterize Stream-Subsurface Water Exchange," *Water Resources Research.* Vol. 32, no. 8, 2441-2451.

Hoeksema, R.J., and P.K. Kitanidis. 1985. "Analysis of the Spatial Structure of Properties of Selected Aquifers," *Water Resources Research.* Vol. 21, no. 4, 563-572.

Holt, R.M. 1997. *Conceptual Model for Transport Processes in the Culebra Dolomite Member, Rustler Formation.* SAND97-0194. Albuquerque, NM: Sandia National Laboratories.

Lafolie, F., and Ch. Hayot. 1993. "One-Dimensional Solute Transport Modelling in Aggregated Porous Media Part 1. Model Description and Numerical Solution," *Journal of Hydrology.* Vol. 143, no. 1-2, 63-83.

Lorden, S.W., W. Chen, and L.W. Lion. 1998. "Experiments and Modeling of the Transport of Trichloroethene Vapor in Unsaturated Aquifer Material," *Environmental Science & Technology.* Vol. 32, no. 13, 2009-2017.

Marquardt, D.W. 1963. "An Algorithm for Least-Squares Estimation of Nonlinear Parameters," *Journal of the Society for Industrial and Applied Mathematics.* Vol. 11, no. 2, 431-441.

Neretnieks, I. 1980. "Diffusion in the Rock Matrix: An Important Factor in Radionuclide Retardation?," *Journal of Geophysical Research.* Vol. 85, no. B8, 4379-4397.

Neretnieks, I. 1993. "Solute Transport in Fractured Rock -- Applications to Radionuclide Waste Repositories," *Flow and Contaminant Transport in Fractured Rock.* Ed. J. Bear, C-F. Tsang, and G. de Marsily. San Diego, CA: Academic Press. 39-127.

Neuman, S.P. 1982. "Statistical Characterization of Aquifer Heterogeneities: An Overview," *Recent Trends in Hydrogeology.* Ed. T.N. Narasimhan. Special Paper 189. Boulder, CO: Geological Society of America. 81-102.

Pedit, J.A., and C.T. Miller. 1994. "Heterogeneous Sorption Processes in Subsurface Systems. 1. Model Formulations and Applications," *Environmental Science & Technology*. Vol. 28, no. 12, 2094-2104.

Pedit, J.A., and C.T. Miller. 1995. "Heterogeneous Sorption Processes in Subsurface Systems. 2. Diffusion Modeling Approaches," *Environmental Science & Technology*. Vol. 29, no. 7, 1766-1772.

Pignatello, J.J., and B. Xing. 1996. "Mechanisms of Slow Sorption of Organic Chemicals to Natural Particles," *Environmental Science & Technology*. Vol. 30, no. 1, 1-11.

Rao, P.S.C., D.E. Rolston, R.E. Jessup, and J.M. Davidson. 1980. "Solute Transport in Aggregated Porous Media: Theoretical and Experimental Evaluation," *Soil Science Society of America Journal*. Vol. 44, no. 6, 1139-1146.

Rao, P.S.C., R.E. Jessup, and T.M. Addiscott. 1982. "Experimental and Theoretical Aspects of Solute Diffusion in Spherical and Nonspherical Aggregates," *Soil Science*. Vol. 133, no. 6, 342-349.

Rasmuson, A. 1985. "The Effect of Particles of Variable Size, Shape and Properties on the Dynamics of Fixed Beds," *Chemical Engineering Science*. Vol. 40, no. 4, 621-629.

Ruthven, D.M., and K.F. Loughlin. 1971. "The Effect of Crystalline Shape and Size Distribution on Diffusion Measurements in Molecular Sieves," *Chemical Engineering Science*. Vol. 26, no. 5, 577-584.

Tsang, Y.W. 1995. "Study of Alternative Tracer Tests in Characterizing Transport in Fractured Rocks," *Geophysical Research Letters*. Vol. 22, no. 11, 1421-1424.

Valocchi, A.J. 1990. "Use of Temporal Moment Analysis to Study Reactive Solute Transport in Aggregated Porous Media," *Geoderma*. Vol. 46, no. 1/3, 233-247.

Villermaux, J. 1981. "Theory of Linear Chromatography," *Percolation Processes: Theory and Applications*. Eds. A.E. Rodrigues and D. Tondeur. NATO Advanced Study Institutes Series. Series E: Applied Sciences No. 33. Rockville, MD: Sijthoff & Noordhoff. 83-140.

Wagner, B.J., and J.W. Harvey. 1997. "Experimental Design for Estimating Parameters of Rate-Limited Mass Transfer: Analysis of Stream Tracer Studies," *Water Resources Research*. Vol. 33, no. 7, 1731-1741.

Werth, C.J., J.A. Cunningham, P.V. Roberts, and M. Reinhard. 1997. "Effects of Grain-Scale Mass Transfer on the Transport of Volatile Organics Through Sediments. 2. Column Results," *Water Resources Research*. Vol. 33, no. 12, 2727-2740.

Wu, S-C., and P.M. Gschwend. 1988. "Numerical Modeling of Sorption Kinetics of Organic Compounds to Soil and Sediment Particles," *Water Resources Research*. Vol. 24, no. 8, 1373-1383.

Chapter 7
Evaluation of Multiwell Convergent-Flow Test Data with a Multirate Model

By Sean A. McKenna[1], Lucy C. Meigs[1], and Roy Haggerty[2]

Abstract

Multiwell convergent-flow (MWCF) tracer tests conducted in the Culebra dolomite are analyzed with both single-and multiple-rate, double-porosity models. Parameter estimation is used to determine the mean and standard deviation of a lognormal distribution of diffusion-rate coefficients as well as the advective porosity and longitudinal dispersivity. At two different test sites, both multirate and single-rate models are capable of accurately modeling the observed data. Estimated model parameters are tested against breakthrough curves obtained along the same transport pathway at a different pumping rate. Implications of the multirate mass-transfer model at time and length scales greater than those of the tracer tests include effectively instantaneous equilibrium between solute concentration in the advective porosity and in a fraction of the diffusive porosity, with the concentration in the remainder of the diffusive porosity remaining in disequilibrium with the advective porosity solute concentration at long times.

7.1 Introduction

In Chapter 4, numerical simulations of the single-well injection-withdrawal (SWIW) tracer tests are presented that suggest that matrix diffusion is an important transport process within the Culebra. In Chapter 5, numerical simulations of one of the multiwell convergent-flow (MWCF) data sets suggest that a mass-transfer process is necessary to create the breakthrough-curve (BTC) tailing observed in the data. In Chapter 6, the conceptual model of matrix diffusion within the Culebra was extended from a conventional double-porosity model (i.e., one with a single rate of diffusion) to a double-porosity model with a continuous log-normal distribution of mass-transfer rates. The multirate diffusion model is shown to provide superior model fits to the observed SWIW test data relative to the conventional double-porosity model.

The signature of multirate-diffusion processes in an MWCF test is more difficult to discern than in an SWIW test because of added complexity in the physics governing the flow system. Specifically, this added complexity is due to: (1) tailing caused by flow-field heterogeneity, a process the SWIW test is designed to mitigate by reversing the flow paths; and (2) the sensitivity of the tracer-transport results to advective porosity. In this chapter, we examine the applicability of the multi-rate-diffusion model to a subset of the data from the MWCF tracer tests performed at the H-11 and H-19 hydropads.

The simulations presented here examine a single pathway (i.e., one injection well to the pumping well) at each hydropad. As used in this chapter, an MWCF tracer test is defined as a test with a single injection well and a single withdrawal well having a constant pumping rate. Prior to tracer injection, the pumping rate has been maintained for sufficient time to allow velocities to be considered at steady state within the domain of the tracer test. A slug of tracer is injected into this steady-state convergent-flow system from a second well located a distance, r_o, away from the pumping well. Immediately following the injection of the tracer, a chaser of Culebra brine (con-

---

[1] Sandia National Laboratories, Geohydrology Department, P.O. Box 5800, MS-0735, Albuquerque, NM 87185-0735. Email: samcken@sandia.gov.

[2] Oregon State University, Department of Geosciences, 104 Wilkinson Hall, Corvallis, OR 97331-5506. Email: haggertr@geo.orst.edu.

taining no tracer) is injected to flush the injection well of any remaining tracer. At the end of the chaser injection, the injection rate is reduced to zero for the remainder of the tracer test. The discharge at the pumping well remains constant throughout the tracer and chaser injections and throughout the collection of tracer data (up to 50 days). Other researchers have employed MWCF tracer tests to estimate flow and transport parameters in fractured and porous aquifers. A number of these works are cited in the Introduction to Chapter 5.

The goal of this chapter is to elucidate the processes responsible for mass transfer in the Culebra dolomite. Toward this goal, we are interested in developing a model of mass transfer between fracture and matrix porosity, or more generally between advective porosity and diffusive porosity, and testing that model on data for one flow path from the MWCF tracer tests conducted at the H-11 and H-19 hydropads. In this chapter, we will: (1) extend the methodology of estimating distributions of multirate mass-transfer rates from the SWIW to the MWCF tests; (2) model the observed MWCF breakthrough curves with a multirate-diffusion model; (3) examine the uniqueness of the estimated model and compare the results to those obtained with conventional single-rate models; and (4) discuss the extension, or scale-up, of the multirate model to scales larger than that of the multiwell tracer test (i.e., the scale of repository performance assessment).

7.2 Multirate Transport Modeling in Multiwell Systems

The multirate-diffusion transport model described in Chapter 6 is extended here to work with MWCF tests. The multirate model (Haggerty and Gorelick, 1995) enables mass transfer to be modeled with a continuous distribution of diffusion-rate coefficients. A distribution of diffusion rate coefficients may arise from variability in the following: matrix-block sizes, cross-sectional area of the pore space normal to the direction of diffusion, and tortuosity. The multirate mass-transfer model presented here is similar to that described by Cunningham et al. (1997) and Haggerty and Gorelick (1998). Diffusion is assumed to occur along one-dimensional pathways within the matrix blocks and we assumed that mass-transfer properties are homogeneous along each pathway and that each pathway is independent of all other pathways. The pathways and matrix blocks can be any shape as long as the diffusion-rate coefficients form a continuous distribution. In this work, we employ a lognormal distribution of diffusion-rate coefficients for reasons discussed in Haggerty and Gorelick (1998) and for direct comparison to SWIW tracer-test results (Chapter 6).

For the analysis, the aquifer is assumed to be fully confined with a constant thickness in all directions and to have spatially isotropic and homogeneous flow and transport properties. Mechanical mixing due to small-scale variations in the flow field is approximated with a longitudinal dispersivity term. The regional gradient is considered to be negligible. Given these conditions, the process of solute transport in a convergent, or divergent, flow field is described by:

$$\frac{\partial c_a}{\partial t} + \int_0^\infty b(\alpha_d)\frac{\partial \hat{c}_d(\alpha_d)}{\partial t}d\alpha_d = \frac{1}{r}\frac{\partial}{\partial r}\left(\frac{r\alpha_L|v|}{R_a}\frac{\partial c_a}{\partial r}\right) - \frac{v}{R_a}\frac{\partial c_a}{\partial r} \quad (7\text{-}1)$$

where the distribution of diffusion rates is represented as a probability density function of diffusion-rate coefficients, $b(\alpha_d)$, defined by a lognormal distribution:

$$b(\alpha_d) = \frac{\beta_{tot}}{\sqrt{2\pi}\sigma_d\alpha_d}\exp\left\{-\frac{[\ln(\alpha_d) - \mu_d]^2}{2\sigma_d^2}\right\} \quad (7\text{-}2a)$$

where

$$\alpha_d = \frac{D_a}{l^2} \quad (7\text{-}2b)$$

and

$$\beta_{tot} = \frac{\phi_d R_d}{\phi_a R_a} \quad (7\text{-}2c)$$

where c_a [M/L^3] is the solute concentration in the advective porosity (e.g., fractures); $\hat{c}_d(\alpha_d)$ [M/L^3] is the average solute concentration in the portion of the matrix associated with a particular diffusion-rate coefficient; α_d [1/T] is the diffusion-rate coefficient defined by Eq. 7-2b, which is continuously distributed; β_{tot} [-] is the total capacity coefficient of the formation, which is the ratio of the solute mass in the diffusive porosity to solute mass in the advective porosity at equilibrium; α_L [L] is the longitudinal dispersivity along the flow path; v [L/T] is the pore-water velocity; R_a [-] is the retardation factor in the advective porosity; r [L] is the radial coordinate (positive away from the well); t [T] is the time elapsed since the beginning of injection of the first tracer; σ_d [1/T] is the standard deviation of the log-transformed diffusion-rate coefficients; μ_d [1/T] is the natural log of the geometric mean of the diffusion-rate coefficients; D_a [L^2/T] is the apparent matrix-diffusion coefficient, defined for this work as the product of the aqueous diffusion coefficient and the diffusive tortuosity (τ); l [L] is the length of the diffusion pathway within the matrix; ϕ_d [-] is the diffusive porosity of the formation; R_d [-] is the retardation factor due to sorption within the diffusive porosity; and ϕ_a [-] is the advective porosity.

A distribution of mass-transfer rates arising from variation in block sizes is geologically more plausible than the single matrix-block size ("sugar cube") conceptualization employed in conventional double-porosity models. Equation 7-2 not only defines this distribution of diffusion-rate coefficients, lognormal in this work, but provides a critical link between the diffusion-rate coefficients and the solute-storage capacity of the diffusive porosity associated with each rate coefficient. Equation 7-2 ties each diffusion-rate coefficient, α_d, to a specific volume of storage. This volume is specified as a fraction of the total storage capacity of the medium, β_{tot}, and is expressed as a function of the diffusion-rate coefficient $b(\alpha_d)$. For non-sorbing tracers, $\beta_{tot} \equiv \phi_d/\phi_a$. Also, variability in α_d is due to variability in both l and τ (Eq. 7-2b) and the joint variability cannot be further refined.

The time derivative of the spatially averaged solute concentration in the matrix is given by:

$$\frac{\partial \hat{c}_d(\alpha_d)}{\partial t} = \frac{1}{l}\int_0^l \frac{\partial c_d(\alpha_d)}{\partial t}\partial z, \quad 0 < \alpha_d < \infty \tag{7-3a}$$

where c_d [M/L^3] is the concentration at a point within a portion of the diffusive porosity (matrix) associated with a certain diffusion-rate coefficient; and z [L] is the coordinate along the one-dimensional diffusion pathway. This concentration at a point within the diffusive porosity is given by a solution to the diffusion equation:

$$\frac{\partial c_d(\alpha_d)}{\partial t} = D_a \frac{\partial^2 c_d(\alpha_d)}{\partial z^2}, \quad 0 < \alpha_d < \infty \tag{7-3b}$$

The boundary condition for diffusive mass transfer is that the concentration at the edge of the diffusive porosity (matrix) is equal to the concentration in the advective porosity (fracture) and that the concentration gradient in the center of the matrix, or the internal end of the pore is zero:

$$c_d(\alpha_d) = c_a, \quad 0 < \alpha_d < \infty \tag{7-3c}$$

$$c_d \frac{\partial c_d}{\partial z}(\alpha_d, z = 0) = 0, \quad 0 < \alpha_d < \infty \tag{7-3d}$$

To solve these equations, we use the approach developed by Haggerty and Gorelick (1995, 1998) where a series of first-order equations is used in place of Eqs. 7-3a and 7-3b (see Appendix Q). The code STAMMT-R (Haggerty et al., 2000) was used to solve these equations. These equations are solved in the Laplace domain and then numerically inverted back to the time domain. The resulting solution for c_d from the first-order equations is mathematically identical to that which would be obtained if solving the above equations directly.

Boundary conditions and fluid velocities must also be specified at the injection well. Pore-water velocity during the injection of the tracer and chaser fluid at a radius, r, away from the injection well is given by:

$$v = \frac{Q_{inj}}{2\pi r \phi_a b} \tag{7-4}$$

where Q_{inj} [L^3/T] is the rate of injection for the tracer or chaser and b [L] is the aquifer thickness. The boundary conditions for use with Eq. 7-1 under radially divergent flow are:

$$c_a - \alpha_L \frac{\partial c_a}{\partial r} = c_{inj} \quad \text{at } r = r_{iw} \tag{7-5a}$$

$$\frac{\partial c_a}{\partial r} = 0 \quad r \to \infty \tag{7-5b}$$

where c_{inj} [M/L^3] is the injectate concentration and r_{iw} [L] is the radius of the injection well.

The combined shape of the injected tracer and chaser within the aquifer is assumed to be unaffected by the convergent-flow field during the time of injection. In general, this assumption remains valid if (1) the ratio of the volume of fluid injected to the volume of fluid contained within a single pore volume within the area defined by the two wells is small and (2) the ratio of fluid velocity caused by injection to fluid velocity due to pumping is large at the location of the injection well. These two constraints can be expressed, respectively, as (after Guvanasen and Guvanasen, 1987):

$$\frac{Q_{inj1}T_{inj1} + Q_{inj2}T_{inj2}}{b\phi_a \pi r_o^2} << 1 \tag{7-6a}$$

$$\frac{Q_{inj} r_o}{Q_{out} r_{iw}} >> 1 \tag{7-6b}$$

where Q_{inj1} and Q_{inj2} refer to the injection rates of the tracer and chaser respectively, T_{inj1} and T_{inj2} refer to the elapsed time of injection for the tracer and chaser respectively, and r_{iw} is the radius of the injection well. The injection rate denoted as Q_{inj} in Eq. 7-6b is taken as the larger of the two injection rates (tracer or chaser) and Q_{out} refers to the discharge rate of the pumping well. We will use the equations described above to test the conceptual model of multirate diffusion against observed tracer-test data, but first we need to devise a means of modeling the movement of tracer along the transport pathway from the injection well to the pumping well.

A three-step process is used to determine the breakthrough curve at the pumping well after the initial injection of tracer and chaser. The first step is to transform the post-injection concentration distribution from polar coordinates centered on the injection well (r_{in}, θ_{in}) to polar coordinates centered on the pumping well (r_{out}, θ_{out}). The second step is to reduce the dimensionality of the problem through azimuthal averaging. The final step in simulating the breakthrough curve is to model the transport through the aquifer to the pumping well under a radially convergent flow field with the multirate-diffusion model described in Eqs. 7-1 through 7-5. Completion of these three steps provides a semi-analytical solution for the BTC at the pumping well.

Step one involves transformation of the polar coordinates from the injection well to the pumping well. Figure 7-1 shows the relationship between the polar-coordinate system with respect to the two wells along with an intermediate cartesian-coordinate system. The transformations from the injection-well coordinate system to the pumping-well coordinate system are:

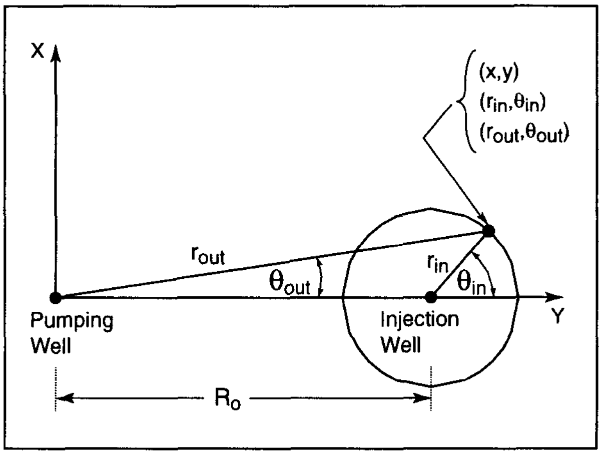

Figure 7-1. Schematic diagram of polar coordinate transformation from coordinates with respect to the injection well to coordinates with respect to the pumping well.

$$r_{out} = \sqrt{r_o^2 + 2r_o r_{in}\cos\theta_{in} + r_{in}^2} \qquad \text{(7-7a)}$$

$$\theta_{out} = \tan^{-1}\left(\frac{r_{in}\sin\theta_{in}}{r_o + r_{in}\cos\theta_{in}}\right) \qquad \text{(7-7b)}$$

where r_{out} [L] is the distance from the pumping well, r_{in} [L] is the distance from the injection well, θ_{out} [°] is the angle from the pumping well between the mass at r_{out} and the axis intersecting the pumping and injection wells, and θ_{in} [°] is the angle from the injection well between the mass at r_{in} and the axis intersecting the pumping and injection wells (see Figure 7-1).

Second, we reduce the dimensionality from two to one. Solute transport toward the pumping well as shown in Figure 7-1 would require solution of a system of integro-differential equations in r_{out}, θ_{out}, and t. Azimuthal averaging can eliminate θ_{out} from this transport problem (Zlotnik and Logan, 1996). Azimuthal averaging takes all concentrations at a distance r from the pumping well and averages them. In a formation with uniform thickness, advective porosity, and hydraulic conductivity, all mass at a given radial distance from the pumping well will experience the same velocity and similar dispersion as it moves toward the well. Therefore, all concentrations at a distance r from the pumping well can be averaged and transport simulated in one dimension rather than two. The azimuthally averaged concentration at the end of the injection period, time = t_o (beginning of convergent-flow-only period), is given by (Zlotnik and Logan, 1996):

$$C(r_{out}, t_o) = \frac{1}{2\pi}\int_{-\pi}^{\pi} c(r_{out}, \theta_{out}, t_o)\, d\theta_{out} \qquad \text{(7-8)}$$

We need not integrate Eq. 7-8 over the entire interval [$-\pi$, $+\pi$], but only over the interval where concentrations are non-zero. Azimuthally averaged concentrations are also obtained for the matrix. After the azimuthal averaging of concentrations, transport to the pumping well is modeled using Eqs. 7-1 through 7-5.

The ability of the multirate model to estimate the diffusion-rate coefficient distribution is limited by the ratio of diffusive to advective mass-transfer rates within the tracer-test system. The ratio of diffusive to advective mass transfer can be parameterized with the Damkohler number, *DaI*. For a one-dimensional flow system with first-order mass transfer, the type 1 Damkohler number is (Haggerty and Gorelick, 1995):

$$DaI = \alpha_f(\beta(\alpha_f) + 1)\frac{R_a L}{v} \qquad \text{(7-9a)}$$

where α_f [1/T] is the first-order mass-transfer coefficient, $\beta(\alpha_f)$ [-] is the capacity coefficient, L [L] is the length of the flow path, R_a [-] is the retardation coefficient in the advective porosity, and v [L/T] is the pore velocity of the water. In a system with diffusion, Eq. 7-9a must be modified. Several papers, starting with Glueckauf (1955), have suggested that diffusive mass transfer can be approximated by first-order mass transfer. For diffusion into layers, this linear driving-force approximation is made by setting α_f equal to $3\alpha_d$ (Goltz and Roberts, 1987). Therefore, we modify the Damkohler expression accordingly:

$$DaI = 3\alpha_d(\beta(\alpha_d) + 1)\frac{R_a L}{v} \qquad \text{(7-9b)}$$

Damkohler numbers near 1 indicate that the rate of diffusion is similar to the rate of advection. At a Damkohler number of 100, diffusion can be considered instantaneous relative to advection and the local equilibrium assumption (LEA) applies (Bahr and Rubin, 1987). Conversely, at a Damkohler number of 0.01, diffusion is negligible relative to advection and a single-porosity (ϕ_a) conceptualization of the transport problem will apply.

The Damkohler number can be examined across the distribution of mass-transfer rates in a radial flow system by considering the average velocity along a flow path from an arbitrary starting radius, r_o, to the extraction well radius, r_w. For a radial flow system at steady state, the average advective velocity along a flow path is the distance between the injection and pumping wells divided by the time it takes to pump one pore volume from the cylinder defined by r_o and the aquifer thickness, *b*. This time is expressed as the pore volume of the cylinder divided by the discharge rate at the pumping well, *Q*. After algebraic reduction, this temporally averaged velocity, $\bar{v}$, is:

$$\bar{v} = \frac{Q(r_o - r_w)}{\pi(r_o^2 - r_w^2)b\phi_a} \qquad (7\text{-}10)$$

This average flow path velocity is used in Eq. 7-9b to determine the Damkohler number across the distribution of mass-transfer rates. The Damkohler number is used below to determine the limits of diffusion coefficients that can be resolved by the MWCF tests and to examine the effect of a multirate model at scales larger than those of the tracer tests.

7.3 Results of MWCF Tracer Test Simulations

Two pumping-injection well pairs are analyzed and each well pair is analyzed at two different pumping rates. The H-11 and H-19 pathways (H-11b3 to b1 and H-19b7 to b0) were selected because high-quality data were available for tracer transported at both the high and low pumping rates. The H-19 data set selected is the same one that was evaluated in Chapter 5. Each pair of injection/withdrawal wells provides a full set of benzoic-acid tracer data for each of two different pumping rates. The different tracer tests will be referred to by the hydropad name and the relative pumping rate in the remainder of this chapter (e.g., "H-19 high"). The parameters that are assigned fixed values (i.e., not optimized)in the models are given in Table 7-1. All fluid and tracer injections and withdrawals were done across the full aquifer thickness; however, hydraulic testing has shown that flow within the upper portion of the Culebra is insignificant (Beauheim and Ruskauff, 1998). Therefore, all flow and transport is modeled as occurring in the lower 4.4 m of the Culebra. Further details regarding the physical setup and data collection of the tracer tests can be found in Chapter 3.

7.3.1 Experimental Data

The H-11 low-pumping-rate test (H-11 low) was run at a constant pumping rate for approximately 25 days after injection of the tracer. During this time period, 107 samples were collected and analyzed for concentration. For the higher pumping rate test (H-11 high), a total of 75 samples were collected over 14 days to define the breakthrough curve. These samples and the upper and lower limits of the 95% confidence intervals based on analytical error are shown in Figure 7-2. All BTC concentration data shown in this chapter are normalized by the injection concentration (C/C_o).

For the H-19 low-pumping-rate tracer test, 67 samples collected over 47 days were used in the parameter estimation. For the H-19 high-pumping-rate test, approximately 29 days of observed data were used in the modeling results presented here (total of 77 data points). The H-19 BTC's and the 95% confidence intervals based on analytical error are shown in Figure 7-3.

7.3.2 Parameter Estimation

Parameter estimation applied to the multirate-diffusion model discussed above was used to obtain an optimal fit of the model results to the observed data. The parameter estimation minimized the root mean square error (RMSE) between the log of the observed data and the log of the predicted concentrations. Errors are calculated on the logs of the concentrations in order to apply more weight to the late-time, low-concentration data where the effects of mass transfer are most significant. Four parameters were estimated: the mean *ln* diffusion-rate coefficient, μ_d; the standard deviation of the *ln* diffusion-rate coefficient distribution, σ_d; the advective porosity, ϕ_a; and the longitudinal dispersivity, α_L. The parametric expression of diffusion-rate coefficients used here is a lognormal distribution fully characterized by the mean and standard deviation. In addition to the four parameters, normalized sensitivity of the results to each estimated parameter is calculated.

Table 7-1. Fixed Parameters for MWCF Tracer Tests

Parameter	H-11[1] "low"	H-11[1] "high"	H-19[1] "high"	H-19[1] "low"
Number of Data (analyses)	107	75	77	67
Pumping Rate (m^3/s)	2.23×10^{-4}	3.76×10^{-4}	2.74×10^{-4}	1.57×10^{-4}
Tracer Injection Time (s)	1974	1998	960	1698
Tracer Injection Rate (m^3/s)	9.57×10^{-5}	9.5×10^{-5}	2.06×10^{-4}	1.17×10^{-4}
Chaser Injection Time (s)	3810	3840	780	1410
Chaser Injection Rate (m^3/s)	9.76×10^{-5}	9.71×10^{-5}	2.16×10^{-4}	1.19×10^{-4}
Diffusive Porosity	0.16	0.16	0.147	0.147
Tortuosity	0.11	0.11	0.09	0.09
Aquifer Thickness (m)	4.4	4.4	4.4	4.4
Aqueous Diffusion Coefficient (m^2/s) (benzoic acids)	7.9×10^{-10}	8.2×10^{-10}	8.2×10^{-10}	8.0×10^{-10}
Distance Between Wells (m)	20.9	20.9	12.2	12.2

1. H-11 data are for the H-11b3 to b1 pathway. The low and high pumping rate data are from the round 1 and round 2 injections, respectively. The H-19 data are for the H-19b7 to b0 pathway. The high and low pumping rate data are from the round 1 and round 3 injections, respectively. See Chapter 3 for additional details.

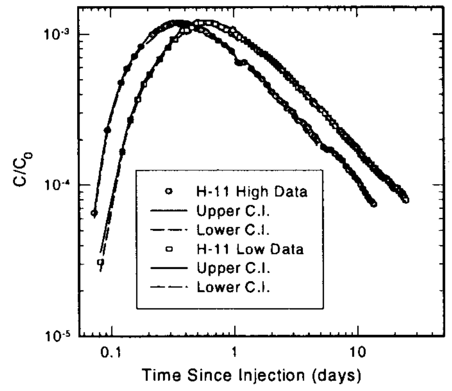

Figure 7-2. **Observed breakthrough curve data and the limits of the 95% confidence intervals for the two H-11b3 to b1 tracer tests.**

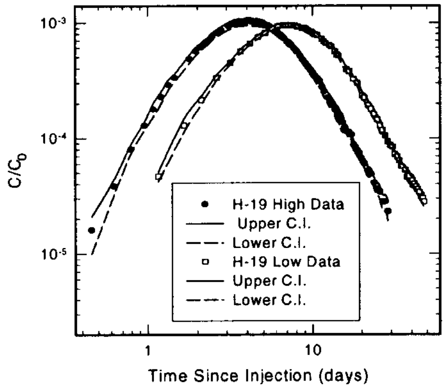

Figure 7-3. **Observed breakthrough curve data and the limits of the 95% confidence intervals for the two H-19b7 to b0 tracer tests.**

The inverse parameter-estimation model creates a matrix containing the sensitivity of concentration change with respect to each parameter for each observation time. The entries of this Jacobian may be normalized to allow comparison of parameter sensitivities through time and between different parameters (Harvey et al., 1996):

$$J_{ij} = \frac{p_j}{\sigma} \frac{\partial C_i}{\partial p_j} \qquad (7\text{-}11)$$

where J_{ij} is the normalized sensitivity of the modeled concentration at the ith time to the jth parameter, C_i is the ith component of the vector of normalized concentrations through time, p_j is the jth component of the vector of estimated parameters, and σ_d is the estimated standard deviation for the concentration observations. Here we assume that errors are uncorrelated and due to measurement error rather than model error and thus we use the RMSE in Eq. 7-11 as a measure of σ. The Jacobian is a useful instrument for investigating the sensitivity through time of the model to the estimated parameters (e.g., Wagner and Harvey, 1997), and gives insight into the correlation between estimated parameters.

The normalized sensitivities of the H-11 low test are shown as an example of normalized sensitivities in the MWCF tests (Figure 7-4). Examination of the normalized sensitivities shows that the model of the MWCF tests is relatively insensitive to the values of σ and α_L after the time of peak concentration (approximately 0.6 days for the H-11 low test). Beyond this time, the model is only sensitive to the mean diffusion-rate coefficient, μ_d, and ϕ_a (Figure 7-4).

The estimated parameter values and the RMSE statistic obtained with the multirate model are given for the H-11 and H-19 tests in Table 7-2. The 95% confidence intervals in Table 7-2 are approximated as +/- 2 standard deviations about the estimated value. For σ_d, ϕ_a, and α_L, the confidence interval is taken about the natural log of the estimated value as these three parameters are estimated in natural-log space within the parameter-estimation algorithm. Examination of Table 7-2 shows that the RMSE values are all relatively small, indicating that the models provide a good fit to the observed data. Figures 7-5 and 7-6 compare the model results to the observed data for the H-11 and H-19 data, respectively. From these figures, we see that the models approximate the data best at times after the peak concentration when diffusion of solute back out of the diffusive porosity into the advective porosity is the dominant mass-transfer process.

Additional modeling of the tracer tests was conducted and these results are presented in Appendix S. The H-19b7 data sets modeled in Appendix S have the first data point removed and thus the RMSE values in Appendix S are lower than those shown in Table 7-2. The results in Appendix S for the H-11b3 low pumping rate test show a smaller RMSE than the results in Table 7-3; however, the dispersivity estimated in the Appendix S results is considerably larger than that estimated in this chapter. These results highlight the fact that the model fits to the observed data are non-unique.

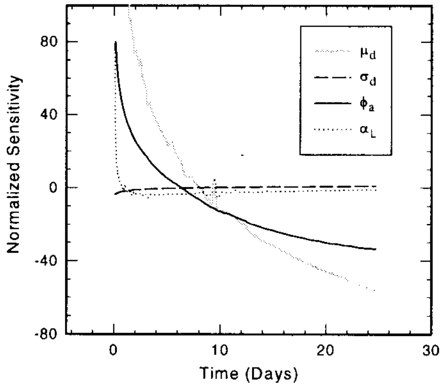

Figure 7-4. Normalized sensitivities of the BTC model to each of the four estimated parameters. Sensitivities from the H-11 low test are shown as an example.

Table 7-2. Multirate Parameter Estimation Results For MWCF Tracer Tests

Test	$\mu_d \pm 2\sigma$ range	σ_d $ln(\sigma_d \pm 2\sigma)$ range	ϕ_a $ln(\phi_a \pm 2\sigma)$ range	α_L(m) $ln(\alpha_L \pm 2\sigma)$ range	RMSE
H-11 Low n = 107	-17.7 ± 0.9 -18.6, -16.8	1.3 0.3 ± 0.7 0.7, 2.6	1.3×10^{-3} -6.6 ± 0.8 6.1×10^{-4}, 2.8×10^{-3}	3.4 1.2 ± 0.3 2.5, 4.5	0.09
H-11 High n = 75	-17.2 ± 1.3 -18.5, -15.9	1.1 0.1 ± 0.2 0.9, 1.4	6.2×10^{-4} -7.4 ± 0.6 3.4×10^{-4}, 1.0×10^{-3}	3.0 1.1 ± 2.6 0.2, 39.3	0.12
H-19 Low n = 67	-16.2 ± 0.6 -16.8, -15.6	5.5 1.7 ± 3.5 0.2, 180.2	3.7×10^{-3} -5.6 ± 0.2 2.6×10^{-3}, 5.7×10^{-3}	1.0 0.0 ± 0.9 0.4, 2.4	0.12
H-19 High n = 77	-15.2 ± 0.9 -16.1, -14.2	5.5 1.7 ± 2.5 0.4, 68.9	8.5×10^{-4} -7.1 ± 0.02 8.3×10^{-4}, 8.6×10^{-4}	1.1 9.5×10^{-2} ± 0.7 0.5, 2.2	0.13

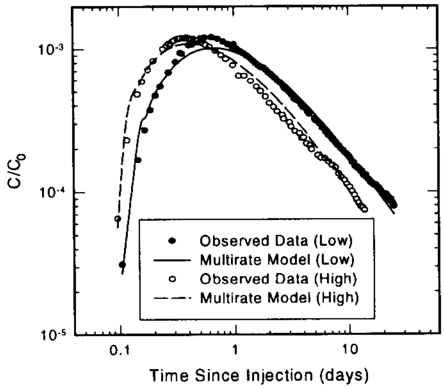

Figure 7-5. Multirate diffusion transport model fits to the H-11 data for both pumping rates.

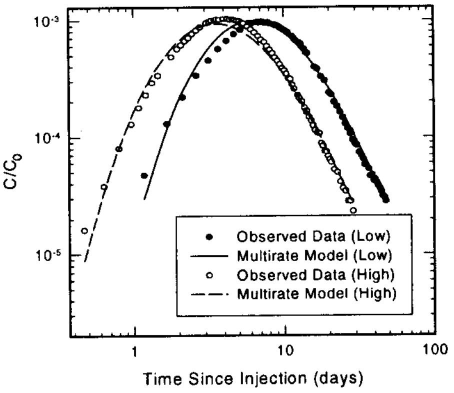

Figure 7-6. Multirate diffusion transport model fits to the H-19 data for both pumping rates.

7.3.3 Discussion of Results

The results shown in Figures 7-5 and 7-6 are based on estimated lognormal distributions of diffusion coefficients. For both hydropads, the analysis of the tracer test conducted at the lower pumping rate produces a lower estimate of the natural log of the mean diffusion rate (μ_d). The cumulative diffusive-porosity volume as a function of diffusion-rate coefficient as determined from the inverse parameter estimation using the multirate model is shown in Figure 7-7 for both pumping rates at both hydropads. Examination of Figure 7-7 shows that for the two hydropads, the estimated distribution of diffusion-rate coefficients is similar from one pumping rate

Table 7-3. Values of Parameters Estimated Using a Single-Rate MWCF Model

Test	μ_d	σ_d	ϕ_a	α_L (m)	ϕ_d	RMSE
H-11 Low n=107	-19.5	0.0	$8.2\text{x}10^{-04}$	2.44	0.16	0.18
H-19 Low n=67	-21.1	0.0	$5.7\text{x}10^{-02}$	2.4	0.094	0.16

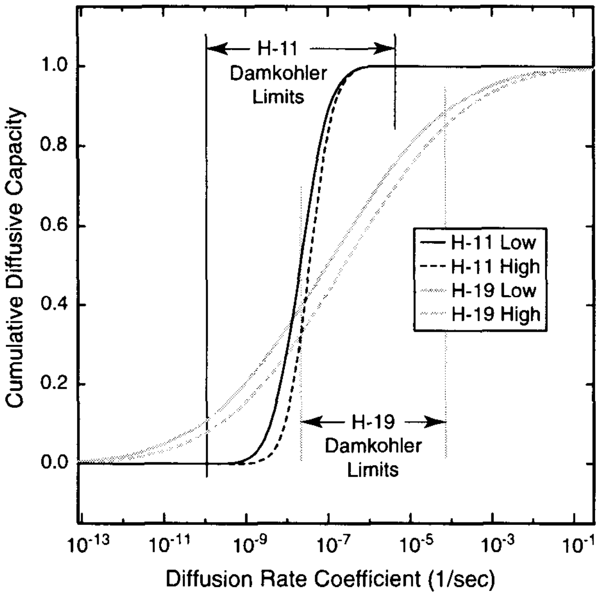

Figure 7-7. Cumulative distributions of diffusion-rate coefficients as estimated from the four two-well tests. The regions of each for which the Damkohler number is between 100 (right-hand side) and 0.01 (left-hand side) are indicated.

to the other. However, the estimated distributions for the H-11 and H-19 hydropads differ significantly. A similar result was observed in the evaluations of the SWIW tests (Chapter 6).

The portion of the lognormal distributions that can actually be resolved during the tests is determined by applying the Damkohler number limits of 0.01 and 100. Recall from Section 7.2 that a Damkohler number of 0.01 reflects negligible diffusion relative to advection (i.e., single porosity) and a value of 100 reflects instantaneous diffusion relative to advection (i.e., local equilibrium assumption applies). At the H-11 hydropad, roughly 99% of the diffusion-rate distribution lies within the 0.01 and 100 Damkohler number limits with just the slowest 1% of the rates lying below the 0.01 cutoff. At the H-19 hydropad, approximately 59% of the distribution lies within the Damkohler number limits as shown by the dotted line in Figure 7-7. Consequently, at the H-19 hydropad, approximately 29% of the estimated diffusion rates are so slow as to be negligible and approximately 12% of the rates are fast enough to appear instantaneous. The large confidence intervals about the estimates of σ_d shown in Table 7-2 for H-19 are due to the large proportion of the estimated mass-transfer coefficient distribution that lies outside the limits imposed by the Damkohler number. The distribution is effectively inestimable outside these limits and only has shape in those regions (Figure 7-7) because of the *a priori* assumption of a lognormal distribution.

Relatively larger confidence intervals are estimated for α_L from the H-11 high test. We believe that this imprecise estimate is caused by the rapid transport of the tracer to the pumping well (peak concentration is achieved in less than 9 hours after injection) and the insensitivity of the models to α_L beyond the time of peak concentration. Longer times to peak concentration in the H-11 low and H-19 tests allow for more precise determination of α_L.

The approximate consistency of the estimated, lognormal distributions of mass-transfer rates with field observations of the Culebra can be checked by determining the estimated matrix-block-size distribution. To do this, variability in the mass-transfer rates is assumed to be the result of matrix block size variations and tortuosity is held constant. The estimated matrix-block lengths are then compared to field observations. For one-dimensional diffusion paths into the matrix, the distance from the fracture/matrix interface to the center of the matrix block, l, (matrix-block half-length) can be calculated as:

$$l = \sqrt{\frac{D_o \tau}{\alpha_f}} \tag{7-12}$$

where D_o [L^2/T] is the aqueous diffusion coefficient, τ [-]is the tortuosity, and α_f [1/T] is the first-order mass-transfer coefficient. Using the values of D_o and τ in Table 7-1, the resulting distributions show that these tests were able to image, within the Damkohler limits, a range of half-block sizes from < 0.001 to 0.09 m at the H-11 hydropad and from 0.0004 to 0.06 m at the H-19 hydropad. These estimates of block size are consistent with the lower end of the range of block sizes observed in core and outcrop samples (Holt, 1997).

The observed BTC data show similar peak concentrations for both pumping rates. This behavior generally reflects single-porosity, as opposed to double-porosity, conditions, provided the difference in pumping rates is large enough to change the peak concentration significantly in a double-porosity medium. In a multirate system characterized by a lognormal distribution of diffusion coefficients, the change in peak height between different pumping rates decreases as σ_d increases. Using the parameters estimated at H-19 ($\sigma_d > 5.0$), numerical simulations show a constant peak height across pumping rates that change by up to one order of magnitude. Similar simulations using the parameters estimated at H-11 (σ_d near 1.0) show a change in peak concentration across the same range of pumping rates. We are currently evaluating different parametric and non-parametric, including bimodal, distributions of diffusion coefficients to understand better the observed similarity in peak concentrations across different pumping rates.

7.4 Alternative Conceptual Models

The multirate mass-transfer model provides reasonable matches to the observed MWCF test data considered in the analysis. Additionally, the multirate model is consistent with observed matrix-block sizes. However, the BTC's could result from either a single-porosity medium with a heterogeneous transmissivity field or from a conventional double-porosity medium. In Chapter 5, numerical simulations of the H-19 low test suggest that the data cannot be matched with a heterogeneous, single-porosity model. A mass-transfer process appears to be necessary to create the BTC tailing observed in the data. The conventional (single-rate) double-porosity model is tested here as a possible explanation for the observed MWCF results.

Prior to this work, only single-valued diffusion rates have been applied to the analysis of MWCF tracer tests conducted in double-porosity media. To compare the results of the multirate model to the single-rate (conventional double-porosity) approach, single-rate simulations were conducted using parameter estimation for the low-pumping-rate tracer test at each hydropad. This estimation procedure is the same as that used for the multirate model; however, σ_d is set to 0.0. In order to maintain consistency, these single-rate simulations were constrained to have the same total porosity ($\phi_a + \phi_d$) as used in the multirate modeling. This value of total porosity is based on the measurements of core porosity and the consideration that the vast majority of the total porosity in the Culebra is matrix porosity. Results of the single-rate matches to the observed data are given in Table 7-3 and Figures 7-8 and 7-9.

In general, the single rate of mass transfer is smaller (larger negative number) than the mean of the multirate distribution for both of the MWCF tests modeled. The estimated mass-transfer rate using the conventional double-porosity model results in matrix half-block sizes of 0.16 and 0.32 m at the H-11 and H-19 hydropads, respectively. For the H-19 test, the advective porosity estimated with a single-rate model is over an order of magnitude larger than that estimated with the multirate model (Table 7-3). As measured by the RMSE, the multirate model provides a better fit to the data than does the single-rate model for both the H-11 and H-19 tests. The RMSE is approximately a factor of two lower for the multirate model of the H-11 data; however, the improvement in the fit to the data is only marginal for the H-19 test.

The Damkohler numbers calculated with a single-rate model change in inverse correspondence to the change in average velocity between pumping rates. The Damkohler numbers estimated based on the single-rate model of the tests at the lower pumping rates are 4.4 x 10^{-2} and 4.1 x 10^{-3} for H-11 and H-19, respectively. For the length of time that these tracer tests were run, these low Damkohler numbers indicate that the single-rate model considers diffusion into the matrix to be extremely small to negligible. Conversely, the multirate model estimated relatively rapid to instantaneous rates for a significant fraction of the total porosity. In the H-11 models, fracture porosity does not increase significantly from the multirate results to the single-rate results. Results of the H-19 models show that the advective porosity estimated assuming single-rate diffusion is over an order of magnitude higher than the value estimated for multirate diffusion. In order to account for the instantaneous diffusion rates resolved by the multirate model, the single-rate model predicts a higher advective porosity relative to the multirate model. Over the length of the tracer test, a fraction of the matrix will reach equilibrium with the solute concentration in the advective porosity with solute due to "fast" diffusion rates. In the single-rate model, this process is accounted for by assigning that fraction to the advective porosity.

7.5 Uniqueness and Testing of the Estimated Models

A test of the robustness or validity of the estimated multirate transport model is to use the transport parameters estimated at one pumping rate to model the observed BTC at the other pumping rate. If the conceptual model of a continuous distribution of diffusion-rate coefficients holds, the change in pumping rate will shift the portion of the diffusion-rate coefficient distribution that the test is able to see (that region between seemingly infinite block size and LEA behavior). In the case of a continuous diffusion-rate-coefficient distribution, the corresponding distribution of Damkohler numbers can remain approximately constant with a change in pumping rate by activating a different portion of the diffusion-rate-coefficient distribution. However, if the single mass-transfer-rate model applies, no other rates can be shifted to and the single Damkohler number will change with changing pumping rates giving different transport results. If this change in *DaI* is significant, then matching the BTC using

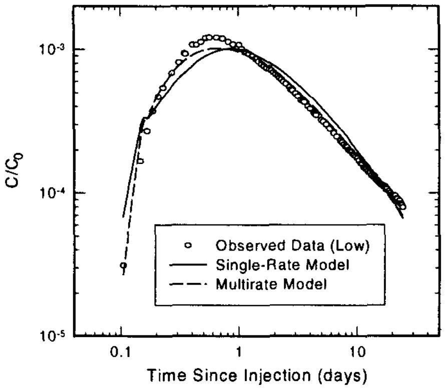

Figure 7-8. Single-rate model fit to the H-11 low data. The multirate model fit is shown for comparison.

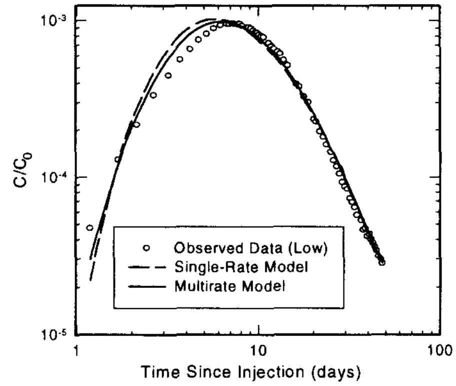

Figure 7-9. Single-rate model fit to the H-19 low data. The multirate model fit is shown for comparison.

transport parameters from tests at a different pumping rate will not be possible.

The observed data at the higher pumping rates are modeled using both the continuous distribution of diffusion rates estimated at the lower pumping rate and also using the single diffusion rate estimated at the lower pumping rate with the single-rate model. The results of these runs are shown with the observed data in Figures 7-10 and 7-11. The RMSE for the fits shown in Figure 7-10 (H-11 tracer test) are 0.26 and 0.30 for the single-rate and multirate models respectively. The RMSE values for the models shown in Figure 7-11 (H-19 tracer test) are 0.33 and 0.24 for the single-rate and multirate models respectively. In both cases, the parameter values for the single-rate simulation that best fit the data from the lower pumping rate test are capable of matching the data observed at the higher pumping rate as well as the multirate model. These results are not surprising given that the higher pumping rates lower the Damkohler number by roughly a factor of two. The calculated Damkohler numbers are already indicating negligible diffusion at the low pumping rate and the potential for diffusion is even less at a higher advection rate. These results suggest that a single-porosity model may be capable of matching the observed data. A number of single-porosity models were run and they are discussed in Appendix S. If a larger difference in pumping rates had been used in the field test, we might have been able to differentiate between the two models.

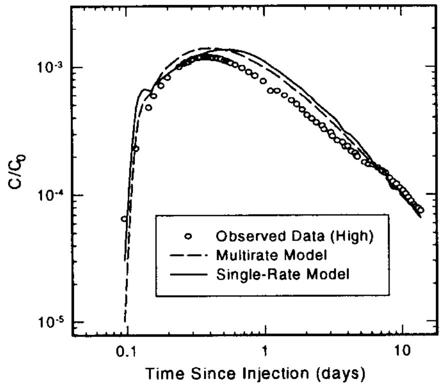

Figure 7-10. Model fits to the H-11 high tracer test data using both multirate and single-rate models estimated on the H-11 low tracer test data.

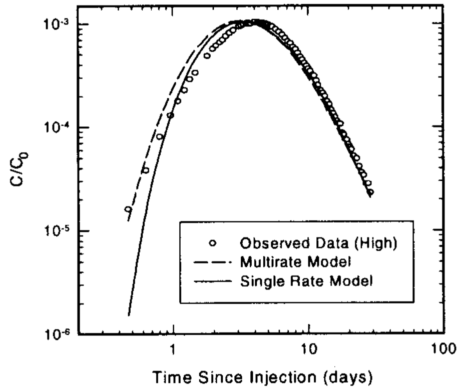

Figure 7-11. Model fits to the H-19 high tracer test data using both multirate and single-rate models estimated on the H-19 low tracer test data.

7.6 Comparison of SWIW and MWCF Test Results

Results of modeling the MWCF tests are compared to those of the SWIW tests with the goal of understanding the differences in the estimated parameter values in terms of the differences in the two tracer-test designs. We do not expect that the results of the different tests will be completely comparable because of the different test geometries and, to a large extent, non-overlapping volumes of aquifer being tested. Additionally, the MWCF tests are more sensitive to ϕ_a and α_L than are the SWIW tests. For example, the SWIW test is completely insensitive to the value of advective porosity (see Table 6-3), but ϕ_a is estimated with relatively tight confidence intervals by models of the MWCF tests (Table 7-2).

Comparison of Table 6-3 with Table 7-2 shows that the estimates of μ_d from the SWIW and MWCF data are similar at H-11 and quite different at H-19. At H-19, the estimates of the mean diffusion-rate coefficient by the SWIW model are approximately two orders of magnitude higher than those estimated by the MWCF model. One explanation for the large differences between the SWIW and MWCF tests at H-19 is the time available for diffusion. The normalized sensitivities (see Figure 7-4) indicate that, for times beyond the peak concentration, the main process affecting the BTC is diffusion back out of the diffusive porosity into the advective porosity. The advective porosity and mean diffusion-rate coefficient are correlated at times past the peak concentration (Figure 7-4). The elapsed time from beginning of tracer collection to peak concentration in the BTC is used as a representative time for diffusion to occur. At H-11, this representative time is approximately 0.87 days for the BTC's from the SWIW test and roughly 0.52 days for the MWCF BTC analyzed here (H-11b3 to b1 path). However, at H-19, this representative time for diffusion is almost an order of magnitude longer in the MWCF tests (4.05 to 6.94 days) than in the BTC's from the SWIW tests (approximately 0.87 days). The similar times for diffusive mass transfer at H-11 for both test types results in models that predict similar values for μ_d (see Table 7-2). The longer time for diffusion in the H-19 MWCF tests relative to the SWIW tests allows the tracer to sample slower diffusion rates, and these slower rates significantly decrease the estimated mean of the diffusion-rate coefficient distribution relative to the SWIW test.

7.7 Mass-Transfer Processes at Larger Scales

The final goal of determining mass-transfer rates within the Culebra, and many aquifers examined by tracer testing, is use of the estimated parameters in a solute-transport model for predictions of transport processes at larger spatial and temporal scales. These calculations may be performed on spatial scales of kilometers and temporal scales of hundreds to thousands of years. This raises the question of the effect a multirate mass-transfer process might have on the shape of a solute plume at various distances downgradient of the solute source relative to that predicted by a conventional double-porosity model.

At larger time and length scales, two differences between the single-rate and multirate model results estimated in this work must be considered: 1) single-rate models may predict a larger advective porosity than do the multirate models, and 2) slow rates in the tail of the multirate-diffusion-coefficient distribution may cause at least a fraction of the diffusive porosity to not reach equilibrium with the solute concentration in the advective porosity, even at very large times. The significance of these differences is analyzed by calculating the Damkohler number (Eq. 7-9b) at transport distances of 300 and 3000 m using the estimated distributions of diffusion-rate coefficients.

A specific discharge of 1 x 10^{-8} m/s is used with the multirate distributions estimated for the H-11 and H-19 low tracer tests to calculate a cumulative distribution of Damkohler numbers. For the estimated H-11 diffusion-coefficient distribution, the Damkohler numbers are all greater than 0.01 at both 300- and 3000-m transport distances. At a transport distance of 300 m, approximately 77% of the total matrix capacity has reached equilibrium with the solute concentration in the advective porosity ($DaI > 100$) and at 3000 m, more than 99% of the capacity has reached equilibrium. For this distribution, no fraction of the storage capacity lies in seemingly infinite matrix-block sizes ($DaI < 0.01$); while not at the equilibrium solute concentration, all matrix blocks would have a nonzero solute concentration at their centers. Equilibrium concentrations in such a large fraction of the matrix coupled with no extremely slow diffusion rates creates transport results that are indistinguishable from the single-rate model at both 300 and 3000 m. Given the estimated H-11 distribution of diffusion coefficients with the associated high Damkohler numbers, we could also conceptualize transport through the Culebra as occurring in a single-porosity system with an effective porosity of 77 or >99% of the total porosity ($\phi_a + \phi_d$) for the 300- and 3000-m transport distances, respectively.

The estimated diffusion-coefficient distribution from the H-19 tracer tests has a much broader σ_d

value. At a transport distance of 300 m, approximately 68% of the total matrix capacity has reached equilibrium with the solute concentration in the advective porosity ($DaI > 100$) and at 3000 m, approximately 81% of the capacity has reached equilibrium. The multirate distribution estimated at H-19 produces a fraction (<2%) of the total capacity with diffusion rates slow enough to appear as seemingly infinite matrix-block sizes at both the 300- and 3000-m transport distances. These extremely slow rates cannot occur in the single-rate model, and transport results are different for the H-19 single-rate and multirate parameters at both 300- and 3000-m transport distances. Because of the slow diffusion rates (and low Damkohler numbers), transport in the Culebra on the 300- or 3000-m scale cannot be accurately modeled, as parameterized using the H-19 tracer-test results, with a single-porosity conceptualization. The single-porosity model, in which solutes move through the entire (matrix) porosity, would probably provide a non-conservative (i.e., low) estimate of the cumulative release of solutes across a regulatory boundary.

7.8 Conclusions

The multirate-diffusion model developed previously (Haggerty and Gorelick, 1995) is extended to the case of a convergent-flow system with an injection at some distance from the pumping well. This model has been applied to results for single pathways from both the H-11 and H-19 MWCF tracer tests conducted in the Culebra dolomite at the WIPP site. Modeling of the observed data suggests that the parameters controlling diffusion are different at the two hydropads. For the pathway evaluated at the H-11 hydropad, the estimated values of α_L are greater than 15% of the length of the transport pathway, while for the pathway evaluated at the H-19 hydropad these values are less than 10% of the pathway length. At H-11, the confidence intervals on the estimated σ_d values are relatively tight while the confidence intervals on σ_d at H-19 are quite large and indicate that σ_d is inestimable at H-19. The confidence intervals on ϕ_a are narrow at both hydropads.

Results of this work indicate that evidence of multirate diffusion is best determined by the SWIW tracer test. In an SWIW test, the effects of flow-field heterogeneity are mitigated by reversal of the flow paths and the signature of multirate diffusion is easily detectable. In the case of the MWCF tracer tests, both single-rate and multirate models appear capable of describing the observed data equally well. The added effects of flow-field heterogeneity and correlation of the mean diffusion rate with the advective porosity in the MWCF tests make the interpretation of the diffusion process more ambiguous.

Parameters derived with data from an SWIW test are not necessarily transferable to an MWCF test. The fast end of the diffusion-rate distribution is better estimated with an SWIW test because of the insensitivity of that test to advective porosity. The SWIW tests could not be simulated with a single-rate model because the late-time slopes were significantly steeper than -1.5 (see Chapter 6). For an MWCF test, differentiation between very fast diffusion rates and advective porosity can be difficult. For example, the H-19 MWCF data can be simulated with a single-rate model using an increased advective porosity to account for the instantaneous diffusion.

At larger transport scales, the width of the estimated multirate-diffusion-coefficient distribution will dictate whether or not a single-ratemodel can accurately model the transport behavior for a given transport distance. Based on the parameters estimated in this work, a single-rate conceptualization may predict a smaller cumulative release across a regulatory boundary, relative to a multirate model, if the entire matrix reaches an equilibrium solute concentration. In this case, a single-porosity simulation should provide a cumulative release equal to that of the single-rate model. If very slow diffusion rates are present in the multirate model, a fraction of the matrix may not achieve equilibrium concentration and the cumulative releases across the regulatory boundary will be larger than in the single-rate or single-porosity models. Disequilibrium between solute concentrations in the fractures and in the matrix can also be maintained at larger scales with a single-rate model if a slower diffusion rate is chosen. At large transport scales, the fraction of the capacity associated with fast diffusion rates will have reached equilibrium. Whether this fraction of the total capacity is accounted for explicitly in the transport model, or just assigned as advective porosity, does not make a difference for the cases examined here.

7.9 References

Bahr, J.M., and J. Rubin. 1987. "Direct Comparison of Kinetic and Local Equilibrium Formulations for Solute Transport Affected by Surface Reactions," *Water Resources Research.* Vol. 23, no. 3, 438-452.

Beauheim, R.L., and G.J. Ruskauff. 1998. *Analysis of Hydraulic Tests of the Culebra and Magenta Dolomites and Dewey Lake Redbeds Conducted at the Waste Isolation Pilot Plant Site.* SAND98-0049. Albuquerque, NM: Sandia National Laboratories.

Cunningham, J.A., C.J. Werth, M. Reinhard, and P.V. Roberts. 1997. "Effects of Grain-Scale Mass Transfer on the Transport of Volatile Organics Through Sediments 1. Model Development," *Water Resources Research.* Vol. 33, no. 12, 2713-2726.

Glueckauf, E. 1955. "Theory of Chromatography, Part 10, Formulae for Diffusion into Spheres and their Application to Chromatography," *Transactions of the Faraday Society.* Vol. 51, 1540-1551.

Goltz, M.N., and P.V. Roberts. 1987. "Using the Method of Moments to Analyze Three-Dimensional Diffusion-Limited Solute Transport from Temporal and Spatial Perspectives," *Water Resources Research.* Vol. 23, no. 8, 1575-1585.

Guvanasen, V., and V.M. Guvanasen. 1987. "An Approximate Semianalytical Solution for Tracer Injection Tests in a Confined Aquifer with a Radially Converging Flow Field and Finite Volume of Tracer and Chase Fluid," *Water Resources Research.* Vol. 23, no. 8, 1607-1619.

Haggerty, R., S.W. Fleming, and S.A. McKenna. 2000. *STAMMT-R: Solute Transport and Mulitrate Mass Transfer in Radial Coordinates, Version 1.01.* SAND99-0164. Albuquerque, NM: Sandia National Laboratories.

Haggerty, R., and S.M. Gorelick. 1995. "Multiple-Rate Mass Transfer for Modeling Diffusion and Surface Reactions in Media with Pore-Scale Heterogeneity," *Water Resources Research.* Vol. 31, no. 10, 2383-2400.

Haggerty, R., and S.M. Gorelick. 1998. "Modeling Mass Transfer Processes in Soil Columns with Pore-Scale Heterogeneity," *Soil Science Society of America Journal.* Vol. 62, no. 1, 62-74.

Harvey, J.W., B.J. Wagner, and K.E. Bencala. 1996. "Evaluating the Reliability of the Stream Tracer Approach to Characterize Stream-Subsurface Water Exchange," *Water Resources Research.* Vol. 32, no. 8, 2441-2451.

Holt, R.M. 1997. *Conceptual Model for Transport Processes in the Culebra Dolomite Member, Rustler Formation.* SAND97-0194. Albuquerque, NM: Sandia National Laboratories.

Wagner, B.J., and J.W. Harvey. 1997. "Experimental Design for Estimating Parameters of Rate-Limited Mass Transfer: Analysis of Stream Tracer Studies," *Water Resources Research.* Vol. 33, no. 7, 1731-1741.

Zlotnik, V.A., and J.D. Logan. 1996. "Boundary Conditions for Convergent Radial Tracer Tests and Effect of Well Bore Mixing Volume," *Water Resources Research.* Vol. 32, no. 7, 2323-2328.

Chapter 8
Discussion and Conclusions

By Lucy C. Meigs[1], Richard L. Beauheim[2], and Toya L. Jones[3]

8.1 Introduction

In the event the WIPP repository is breached via human intrusion, the Culebra Dolomite Member of the Rustler Formation is the most likely geologic pathway to the accessible environment. Testing (geologic, hydraulic, and tracer) of the Culebra has been conducted as part of the overall assessment of the WIPP site. The tracer tests conducted in 1995 and 1996 at the H-19 and H-11 hydropads, as well as earlier tracer tests conducted at the H-2, H-3, H-4, H-6, and H-11 hydropads, provide valuable insight into transport processes within the Culebra dolomite. The data from the 1995-96 tests at H-11 and H-19 are of excellent quality and should be of significant value for improving our general understanding of transport processes in fractured permeable rocks. Interpretations of the tracer data have increased our understanding and improved our conceptualization of the Culebra.

Chapters 1, 2, and 3 and various appendices provide background information on the Culebra dolomite and the rationale for performing the 1995-96 tracer tests. Chapters 4 through 7 and Appendices P, R, and S discuss the numerical analyses that have been completed to date. The purpose of this chapter is to provide a summary of the information contained in this report and to integrate our current understanding of transport processes in the Culebra based on examination of the tracer-test data, the results of numerical simulations, and other information such as geologic data and interpretations of hydraulic tests. To provide a coherent explanation of all of the tracer-test data, additional work is clearly required.

The test details needed to perform additional interpretations of the WIPP tracer data are provided in this report. The tracer test data sets and input parameters for numerical simulations are presented and summarized in Appendices B and C. In addition, the electronic versions of the observed data are available to those interested in analyzing the tests in the Sandia WIPP Central Files ERMS #251278 or by contacting Lucy Meigs.

8.2 Summary of Geologic, Hydrologic, and Chemistry Information

At the WIPP site, the Culebra is located approximately 230 m below land surface and is underlain by a mudstone unit and overlain by an anhydrite unit (Holt and Powers, 1988). At the hydropad sites where tracer tests have been performed, the Culebra thickness varies between 7 and 8 m. On the basis of shaft descriptions (Holt and Powers, 1984; 1986; 1990), core descriptions (Holt and Powers, 1988; Holt, 1997), and borehole video logs, four distinct Culebra units (CU) can be identified (see Figure 2-1) in the subsurface across the entire WIPP area (Holt, 1997). The upper Culebra comprises CU-1 and the lower Culebra comprises CU-2, 3, and 4.

CU-1 consists primarily of well-indurated intercrystalline dolomite and is more massively bedded than the underlying units. CU-1 has an average thickness across the site area of approximately 3.0 m. The Culebra units below CU-1, especially CU-2 and 3, are typically more intensely fractured, have more vugs, and contain interbeds of poorly indurated dolomite. CU-4 is less intensely fractured than CU-2 and 3 and has more clearly defined bedding planes that are undulatory in nature. CU-2 and 3 combined have an average thickness of 2.8 m across the WIPP area and CU-4 has an average thickness of 1.6 m. (See Chapter 2 and Holt (1997) for additional details.)

---

[1] Sandia National Laboratories, Geohydrology Department, P.O. Box 5800, MS-0735, Albuquerque, NM 87185-0735. Email: lcmeigs@sandia.gov

[2] Sandia National Laboratories, Repository Performance and Certification Department, P.O. Box 5800, MS-1395, Albuquerque, NM 87185-1395.

[3] Duke Engineering & Services, Inc., 9111 Research Boulevard, Austin, TX 78758.

Over 100 Culebra core samples have been tested for permeability, porosity, and/or electrical-resistivity formation factor (Kelley and Saulnier, 1990; Holt, 1997). Horizontal permeabilities (parallel to bedding) have been found to range from 2×10^{-18} to 4×10^{-13} m^2, corresponding to hydraulic conductivities between approximately 10^{-11} and 10^{-6} m/s. The higher values are believed to reflect fractures in the core. The measured Culebra porosities range from 3 to 30%, with an average of 15% (ERMS #237228). Formation factors have been found to range from 12 to 407, with an average value of 108 (ERMS #237226). Calculated tortuosity values range from 0.02 to 0.33.

Hydraulic testing has shown that the transmissivity of the Culebra varies by six orders of magnitude in the vicinity of the WIPP site (see Figure 2-2). Beauheim and Holt (1990) suggest that much of the variation in transmissivity is due to variations in the relative percentages of open and filled fractures. Where transmissivity values are less than $\sim 4 \times 10^{-6}$ m^2/s, such as at the H-2 and H-4 hydropads, hydraulic tests can be best interpreted with a single-porosity (porous medium) conceptualization reflecting the absence of open, transmissive fractures. Where transmissivities are greater than $\sim 4 \times 10^{-6}$ m^2/s, such as at the H-3, H-6, H-11, and H-19 hydropads, a double-porosity conceptualization reflecting the interaction between open, transmissive fractures and less transmissive matrix best explains the data (Beauheim and Ruskauff, 1998). Hydraulic tests, tracer tests, and borehole observations at several locations suggest that significant vertical variations in hydraulic properties exist in the Culebra. At the tested locations, the upper Culebra has significantly lower permeability than the lower Culebra. See Chapter 2 and Appendix E for additional details.

Flow in the Culebra is generally to the south across the WIPP site (Crawley, 1988; Corbet and Knupp, 1996) with hydraulic gradients ranging from approximately 0.001 to 0.01 meters of fresh water per meter distance. Calculated Darcy velocities on the WIPP site range from approximately 1×10^{-11} to 2×10^{-9} m/s (LaVenue et al., 1990).

In the vicinity of the WIPP site, Culebra water is a moderate- to high-ionic-strength brine of predominantly sodium-chloride type composition (see Table 2-2). Brines at the H-11 and H-19 hydropads are characterized by ionic strengths of 1.8 to 2.2 molal and Mg/Ca molar ratios between approximately 1.3 and 1.4. Brines at the H-2, H-3, H-4, and H-6 hydropads have lower ionic strengths (0.3 to 1.1 molal) and lower Mg/Ca molar ratios (0.4 to 1.2) (Siegel and Anderholm, 1994). The density of the Culebra brine ranges between 1.01 and 1.09 g/cm^3 at the six tracer-test hydropads (Bodine et al., 1991; Randall et al., 1988).

8.3 Summary of Observations from Examination of Tracer-Test Data

Between 1980 and 1988, tracer testing was performed at the H-2, H-3, H-4, H-6, and H-11 hydropads (Figure 2-2). The tests at H-2 and H-4 showed slow transport, reflecting flow through a porous (rather than fractured) medium. The tests at H-3, H-6, and H-11, however, showed rapid initial tracer breakthrough along some flow paths followed by long "tails" of declining tracer concentrations. These tests were thought to reflect transport through fractures, with the tails caused by diffusion of tracer between the fractures and the adjacent rock matrix, a form of physical retardation. Due to criticism of interpretations of these tests that assumed matrix diffusion was the sole mechanism causing the observed physical retardation, additional tests were planned and conducted in 1995 and 1996 to obtain detailed and accurate data under carefully controlled conditions in order to test the validity of the double-porosity conceptual model for the Culebra.

The series of tracer tests performed at the H-11 and H-19 hydropads in 1995 and 1996 produced a detailed and accurate data base to evaluate advective and diffusive transport processes in the Culebra. These tests included single-well injection-withdrawal (SWIW) and multiwell convergent flow (MWCF) tests at both locations. The MWCF tests included repeated injections at different pumping rates and simultaneous injection of tracers with different aqueous diffusion coefficients. An objective for including these types of injections in the tests was to evaluate the applicability of describing the Culebra with a conventional (i.e., single-rate of diffusion) double-porosity conceptualization as has been proposed by previous investigations of WIPP tracer data (i.e., Jones et al., 1992). In addition, distinct tracers were injected into only the lower Culebra and only the upper Culebra at H-19. For the data collected during the 1995 and 1996 tests, the lack of significant data scatter and the tightness of the 95% confidence intervals on most data sets demonstrate the high quality of the tracer analyses (see Appendix C). Although MWCF tests previously conducted at the H-11, H-3, and H-6 hydropads provide some valuable insights, they are not of as high quality as the 1995-96 data.

The data from all of the SWIW tests conducted at the H-11 and H-19 hydropads show gradual mass recovery as would be anticipated if matrix diffusion is the dominant process. The late-time slopes of the data on log-log plots are shallower than was predicted by Tsang (1995) for a highly heterogeneous single-porosity system but are steeper than the -1.5 slope predicted by conventional double-porosity models with a single rate of diffusion. The late-time slopes of the two H-11 data sets and the three H-19 data sets are similar, indicating that a similar process is controlling the gradual mass recovery observed at both hydropads.

The breakthrough curves from the MWCF tests at the H-11 and H-19 hydropads show gradual mass recovery as would be expected with matrix diffusion. However, several characteristics of the observed data cannot be explained with a conventional double-porosity conceptualization. For instance, the breakthrough curves for two different pumping rates show a similar peak height. In a conventional double-porosity system with a single rate of diffusion, a lower pumping rate should lead to a lower peak concentration due to the lower velocity and the associated increased time for diffusion (unless matrix blocks are very small; see Appendix P). In addition, the peak heights should be different for tracers having different aqueous diffusion coefficients. The peak heights for iodide and benzoic acid from H-19 are not clearly different, in part due to the poor quality of the iodide data. However, the iodide data from H-11, which were obtained using an improved analytical technique, do show a lower peak height than the associated benzoic-acid data, consistent with a double-porosity conceptualization.

The extremely low mass recoveries for all tracers injected into the upper portion of the Culebra at H-19 indicate that most tracer transport takes place in the lower Culebra. This is consistent with both geologic and hydraulic data showing the transmissivity of the upper Culebra (CU-1) to be much lower than that of the lower Culebra (CU-2, 3, and 4).

Tracer-transport behavior at the H-19 hydropad differs from that at the H-3, H-6, and H-11 hydropads. The tracer-test results for the latter three hydropads can be characterized by one rapid transport path with a rapid rate of mass recovery and one or more slow transport path(s) with a slow rate of mass recovery. At the H-19 hydropad, however, none of the six transport paths showed tracer breakthrough as rapid as that observed for the fast paths at H-3, H-6, or H-11, and the differences in the mass-recovery rates for the six flow paths at H-19 are not as great as those for the two or three flow paths at the other three hydropads. These differences in transport behavior may be related to the Culebra transmissivity being about an order of magnitude lower at H-19 than at H-3, H-6, and H-11 (Table 2-1). If high Culebra transmissivities are the results of open fractures, the Culebra must have fewer highly transmissive open fractures at H-19 than at the other three hydropads. In addition, the contrast in fracture and matrix permeability is probably less at H-19 than at H-3, H-6, and H-11. This may allow significant advection to occur in relatively high-permeability portions of the matrix at the H-19 hydropad, such as vugs connected by microfractures or poorly cemented zones with high interparticle porosity, while advection is concentrated in fractures at the other three hydropads. The high advective porosities greater than reasonable limits on fracture porosity, such as 0.01, calculated for H-19 assuming plug flow transport (see Section 3.3.2.3) further suggest that advective transport may be taking place in more than just fractures. Increased matrix participation in advection would tend to slow breakthrough and reduce differences among flow paths, consistent with the observations from H-19.

The relatively greater concentration of advection within fractures at H-3, H-6, and H-11 compared to H-19 may explain why transport is more directionally dependent at those three hydropads. If the fractures important for advection have a preferred orientation, transport along flow paths (sub)parallel to that orientation may be rapid while transport along flow paths more transverse to that orientation might be delayed, due to increased matrix diffusion. Hydraulic anisotropy cannot be evaluated at H-3 and H-11 with the available data (Appendix E). At the H-6 hydropad, however, flow appears to be radial subject to an anisotropy factor of 1.6 (Beauheim and Ruskauff, 1998) and the pathway with the fastest recovery during the tracer test is aligned subparallel to the major axis of transmissivity defined from the anisotropy analysis. At the H-19 hydropad, anisotropy is poorly defined but is estimated at an insignificant factor of 1.2 (Beauheim and Ruskauff, 1998).

8.4 Summary of Numerical Simulations

A variety of different approaches have been used to evaluate the tracer-test data. Chapter 4 discusses the effects of heterogeneity in the hydraulic-conductivity field and plume drift due to a regional gradient on SWIW test results for a single-porosity system. Both heterogeneity and plume drift were found to decrease the slope of a SWIW tracer-recovery curve, but both must be large before confusion between a single-porosity and double-porosity system could potentially arise. Numerical simulations demonstrate that the recovery curves from the WIPP SWIW tests cannot be explained with a single-porosity model employing heterogeneity and plume drift, suggesting that the observed data cannot be explained without incorporating matrix diffusion.

Chapter 5 discusses single-porosity simulations of an observed breakthrough curve from the H-19b7 to H-19b0 pathway at the H-19 hydropad. This particular data set was selected because it exhibits one of the fastest mass recoveries of all the H-19 data sets and should, therefore, be easiest to simulate using a single-porosity model. The purpose of the simulations was to evaluate the role of heterogeneity in breakthrough-curve tailing. The tailing observed in the MWCF breakthrough-curve data could not be reproduced with heterogeneous, single-porosity numerical simulations, suggesting that matrix diffusion may be required. The simulations showed that breakthrough-curve tailing is not a strong function of the conceptual model of heterogeneity (i.e., maximum entropy or indicator) or of the relative correlation length, regardless of the value of advective porosity. The simulations presented in Chapter 5, as well as those in Chapter 4 and Jones et al. (1992), indicate that the Culebra tracer-test data cannot be explained with a single-porosity conceptualization.

Chapter 6 demonstrates that a double-porosity model with only a single rate of diffusion is unable to match the SWIW test data, but that a double-porosity model with a lognormal distribution of diffusion rates (STAMMT-R) can match the data. The STAMMT-R simulations show that the late-time slope of a recovery curve increases (becomes more negative) from -1.5 as the standard deviation of the diffusion-rate distribution (σ_d) increases from zero for a single rate of diffusion to values reflecting multiple rates of diffusion. Both the H-11 and H-19 SWIW data can be well matched with this model. In Appendix R, a piecewise-linear distribution of diffusion rates is shown to be able to match one of the H-11 SWIW data sets, providing further confidence that including multiple rates of diffusion is the key to matching the data. The similarity between the piecewise linear and the lognormal distributions for the H-11 data suggests that the lognormal distribution used for all of the STAMMT-R simulations is likely to be a good approximation of the actual distribution of rate coefficients for the Culebra.

Chapter 7 presents interpretations of MWCF tracer-test data from the H-19b7 to H-19b0 and H-11b3 to H-11b1 pathways using a double-porosity model (STAMMT-R) with single- and multirate diffusion. Unlike the simulations of the SWIW test data in Chapter 6, the simulations of the H-11b3 to H-11b1 and H-19b7 to H-19b0 data suggest that the multirate double-porosity model provides a fit to the data that is only marginally better, as measured by the RMSE, than that provided by the single-rate model (Tables 7-2 and

7-3). Results of this work indicate that evidence of multirate diffusion is best determined by the SWIW tracer test. In a SWIW test, the effects of flow-field heterogeneity are mitigated by reversal of the flow paths and the signature of multirate diffusion is easily detectable. This chapter also investigated the effects of multirate diffusion on transport on large spatial and temporal scales. If diffusion-rate distributions include even a few percent of rates that are so slow that some matrix blocks appear infinitely large at the scale of interest, then the cumulative mass transported to that distance will be larger than would be predicted using a single-rate model that would allow the entire matrix to become saturated with solute (see Chapter 7).

Additional double-porosity simulations of the MWCF data using the THEMM and SWIFT II codes that assume a single rate of diffusion are presented in Appendix P. Many of these simulations provide a reasonable fit to the data in linear space. However, in all cases, the conventional double-porosity model is unable to match the observed data from a single flow path for two different pumping rates using a single set of parameters.

Appendix S presents STAMMT-R double-porosity simulations of the MWCF data from the 1995-96 testing at H-11 and H-19 using both multiple and single rates of diffusion. Simulations are also presented for selected flow paths from the earlier testing at H-3, H-6, and H-11. The simulations show that almost all of the data are better fit with a multirate model than with a single-rate model. Unique parameter sets were defined for three of the H-19 pathways using the multirate model that could simulate the results of multiple tests along those pathways involving different pumping rates and/or tracers with different free-water diffusion coefficients. No unique parameter sets could be found using the single-rate model that could simulate different tracer-breakthrough curves along the same pathways.

The multirate simulations presented in Appendix S provided estimated diffusion-rate distributions that are widest for the pathways at H-19, narrower for the pathways at H-3 and H-11, and narrowest for the pathways at H-6 (Table S-4 and Figures S-26, S-27, and S-28). We suspect that as the distribution widens, advective transport shifts from being concentrated in a few fractures to occurring through more fractures and interparticle porosity and vugs. As expected, as the diffusion-rate distribution narrows, a single-rate model is better able to replicate the multirate model results.

In summary, numerous simulations have shown that single-porosity models cannot match either the SWIW or MWCF tracer-test data from the Culebra. Double-porosity models with a single rate of diffusion cannot match the SWIW test data, but can match the MWCF data from some pathways. However, attempts at finding unique parameter sets for the single-rate model that can adequately simulate multiple breakthrough curves along individual pathways have so far been unsuccessful. A double-porosity model with multiple rates of diffusion can match the SWIW test data and all of the MWCF test data. It can also match multiple breakthrough curves along individual pathways with unique parameter sets. Thus, the multirate-diffusion model appears to be the simplest model capable of explaining all the observed data.

Diffusion rates can only be inferred for those portions of the porosity involved in diffusion during the time span of the tracer-test data. Porosity in which diffusion occurs too rapidly to be represented in the data cannot be distinguished from advective porosity, while porosity involved in very slow diffusion may not affect the data at all on the time scale of the test. The overall test duration, the length of tracer-injection and pause periods, the pumping rate, and the fracture spacing (matrix-block length) all affect the portion of the porosity to which diffusion rates can be assigned. For those portions of the porosity not sampled during the tracer test, inferred diffusion rates are constrained by the model selected for the distribution (e.g., lognormal). Because a lognormal distribution of diffusion coefficients has been assumed *a priori*, our model fits a different distribution to every data set depending on the rates represented in the data. The mean rate will decrease as the test duration increases or pumping rate decreases and slower rates (bigger blocks) affect the data. Thus, the mean rates inferred from our SWIW tests decreased as the residence times of the tracers in the formation before pumping increased and the mean rates inferred from our MWCF tests decreased as the pumping rates decreased. The mean rates inferred from MWCF tests may also decrease as the pumping rate decreases because the faster rates become increasingly difficult to distinguish from advection. If this occurs, the inferred values of advective porosity should increase and this was, in fact, observed in most cases (see Table S-2).

The distributions of diffusion-rate coefficients inferred from the H-19 tracer tests, both SWIW and MWCF, are different from those inferred from tests at the other hydropads (see Figures 6-4, S-26, S-27, and S-28). The distributions for H-19 tend to be wider than those at the other hydropads, which probably reflects a greater degree of heterogeneity in porosity types and properties at H-19. Also, the mean diffusion-rate coefficients inferred from the fast pathways at the H-3, H-6, and H-11 hydropads are all significantly lower than those inferred from all of the H-19 pathways except for those from H-19b2, H-19b6, and, to a lesser extent, H-19b7 to H-19b0 (see Table 8-1). These lower mean diffusion rates, of course, imply larger mean matrix-block lengths for those fast pathways compared to those inferred for the H-19 pathways, with the same three exceptions (see Table S-2). Higher mean diffusion-rate coefficients and wider distributions were also inferred from the H-19 SWIW tests compared to the H-11 SWIW tests.

Figures 6-4 and 7-7 show that 10 to 20% of the diffusive porosity at H-19 may be indistinguishable from advective porosity on the scale of the tests because of rapid diffusion, while the same may be true for only 1% of the diffusive porosity at H-11. This difference could be caused by advection occurring in a greater proportion of the total porosity at H-19 than at H-11, so that a larger percentage of the diffusive porosity is in close proximity to the advective porosity (i.e., effectively the "matrix blocks" are smaller). At both H-11 and H-19, the values of advective porosity inferred from the multirate simulations of the MWCF tests increased as the pumping rate decreased, probably reflecting an increased amount of rapid diffusion. On the other end of the diffusion-rate distribution, 10 to 40% of the diffusive porosity at H-19 may have been associated with diffusion rates too low to be sampled during the various tests, while the same may be true for up to 15% of the diffusive porosity at H-11. These slower rates may be a result of fitting the data with a lognormal distribution and/or may represent other factors such as heterogeneity in porosity types and characteristics. Thus, the diffusion-rate distributions at H-11 and especially H-19 are probably not well defined over their entire ranges.

8.5 Evaluation and Revision of Conceptual Transport Model for the Fractured Culebra

Our original conceptual model for the Culebra is described in Section 3.2. We conceptualized the Culebra as a single-porosity (matrix-only, i.e. no significant advection in fractures) medium at some locations and as a double-porosity (fractured) medium at other locations. Our model for the fractured Culebra considered it to be a homogeneous, anisotropic, double-porosity medium in which matrix diffusion occurred at a single rate. The 1995-96 tracer-test results from H-11 and H-19 confirm that the Culebra cannot be represented by a single-porosity model (neither fracture-only nor matrix-only) at these locations, no matter how heterogeneous. Some form of physical retardation, which we infer to be matrix diffusion, is causing recovery- and breakthrough-curve tails to be prolonged beyond what could be produced by heterogeneity and plume drift in a single-porosity system. However, the data suggest that the simple conventional double-porosity conceptual model for transport in the fractured Culebra used to explain past tests (Jones et al., 1992) is overly simplistic. That is, the data are inconsistent with a double-porosity model with a single rate of diffusion. The SWIW recovery curves do not have late-time slopes of -1.5 and the peak heights from MWCF tests with different pumping rates are not distinctly different, both of which are obtained with a conventional (i.e., single-rate) double-porosity model.

These observations motivated a detailed reexamination of the Culebra geology (e.g., Holt, 1997). A double-porosity model with a single rate of diffusion is often used to represent a medium in which advection occurs in numerous discrete

Table 8-1. Summary of Inferred Multirate Diffusion Coefficients

Hydropad	SWIW Test Well	MWCF Injection Well	Test/Round or Tracer	ln Mean Diffusion-Rate Coefficient (μ_d)	Standard Deviation of ln Diffusion-Rate Coefficients (σ_d)
H-19	H-19b0		SWIW1/1	-11.9	6.87
	H-19b0		SWIW1/2	-10.1	2.56
	H-19b0		SWIW2/1	-10.9	5.83
		H-19b2	7-well/1	-16.58	5.53
		H-19b3	7-well/1	-13.01	3.12
		H-19b3	7-well/1-iodide	-12.99	2.80
		H-19b3	7-well/2	-13.09	4.69
		H-19b3	7-well/3	-13.02	3.24
		H-19b4	7-well/1	-13.13	3.28
		H-19b5	7-well/1	-11.57	0.55
		H-19b5	7-well/2	-12.89	0.28
		H-19b6	7-well/1	-17.21	4.87
		H-19b6	7-well/3	-17.36	4.34
		H-19b7	7-well/1	-14.95	4.27
		H-19b7	7-well/2	-16.15	6.47
		H-19b7	7-well/3	-15.95	5.17
		H-19b7	7-well/3-iodide	-15.65	4.96
H-11	H-11b1		SWIW/1	-15.8	3.55
	H-11b1		SWIW/2	-15.7	3.83
		H-11b2	1996/1	-14.30	4.50
		H-11b2	1996/2	-13.82	2.99
		H-11b2	1988	-15.98	1.54
		H-11b3	1996/1	-17.69	1.35
		H-11b3	1996/2	-17.19	1.12
		H-11b3	1996/2-iodide	-16.79	1.08
		H-11b3	1988	-16.36	0.83
H-3		H-3b1	1984	-19.67	1.40
H-6		H-6a	1981/1	-11.85	0.62
		H-6b	1981/1	-17.29	0.33
		H-6b	1981/2	-17.19	0.15

Note: SWIW data are from Table 6-3. MWCF data are from Table S-2.

fractures, based on an assumption that the numerous fractures provide fairly uniform access to all parts of a uniform matrix. Examination of Culebra core, however, does not support either an assumption that all parts of the matrix are uniformly accessed by fractures and other advective pathways or an assumption that the matrix itself is uniform. The descriptions of the variations in the porosity structures of the Culebra given in Holt (1997) suggest that diffusion within the matrix probably could not be accurately modeled using a single rate. In addition, recent static-diffusion tests conducted using X-ray absorption imaging demonstrate significant variation in diffusion rates within the Culebra matrix (Tidwell et al., 2000a and b).

We attempted to simulate the SWIW test data from H-11 and H-19 using the code STAMMT-R with both single and multiple rates of diffusion. The late-time slopes of the recovery curves could only be matched by multiple diffusion rates. Tracer data from the MWCF tests performed at the H-19, H-11, H-3, and H-6 hydropads were also analyzed using STAMMT-R assuming both single and multiple diffusion rates (see Appendix S and Chapter 7). The multirate results provide a closer match to the late-time data than do the single-rate results, and similar peak heights for different pumping rates could be produced by multiple rates of diffusion, but not by single rates. Thus, the only model that provides results consistent with both the SWIW and MWCF tracer-test data is a double-porosity model with multiple rates of diffusion.

8.6 Remaining Issues and Future Research Directions

While we believe that a double-porosity medium with multiple rates of diffusion is an appropriate conceptual model for the fractured Culebra, the best way of representing that model analytically or numerically remains to be determined. As formulated in STAMMT-R, the Culebra is assumed to be a homogeneous, isotropic, double-porosity medium. Heterogeneity is allowed only in diffusion rates. In actuality, the transport behavior that STAMMT-R tries to simulate by varying only the diffusion rate is probably also caused by small-scale (mm to m) heterogeneity in permeability (which leads to variations in fluid velocity). In addition, STAMMT-R assumes that diffusion rates have a lognormal distribution, whereas Appendix R shows that other distributions, such as piecewise linear, may also be possible. Thus, we know that STAMMT-R, like all models, is a simplified representation of reality. What remains to be determined is how the simplifying assumptions made in STAMMT-R affect the suitability of the inferred parameters for use in calculations of transport on other scales.

Without changing some of its underlying assumptions, STAMMT-R could be made more robust by expanding its data-fitting capabilities. STAMMT-R currently optimizes its match to a single data set in log-log space. However, different aspects of the data, such as the slope of the rising limb, time and value of peak concentration, and slope of the falling limb may display different sensitivities when plotted in different formats. Thus, STAMMT-R could be improved by allowing it to optimize to the same data presented in different ways simultaneously, and by allowing different types of diffusion-rate distributions. These types of enhancements might alleviate some of the difficulties encountered in matching different features in the data shown in Appendix S. It could be further enhanced by allowing simultaneous fitting to multiple data sets from the same or different pathways. This would allow tests that had been designed to "interrogate" different portions of the diffusion-rate distribution to be analyzed together, providing a more complete definition of the entire distribution. By adding anisotropy as a fitting parameter, STAMMT-R might be able to fit data sets from different pathways simultaneously and provide a single diffusion-rate distribution for an entire hydropad. Improved statistical evaluation of solution uniqueness is also desirable.

Other useful interpretive capabilities are beyond the scope of a one-dimensional analytical code such as STAMMT-R. Fitting tracer data from multiple pathways in a heterogeneous system simultaneously would require at least a numerical two-dimensional code to represent the required spatial variation. Numerical two- or three-dimensional codes would be able to include heterogeneity in permeability, as well as regional drift and a more detailed approximation of the initial distribution of tracer in the formation following tracer and chaser injection. Codes possessing these capabilities that have been used to simulate tracer-test data assuming a single rate of diffusion, such as THEMM and SWIFT II (Appendix P), could be modified to incorporate multiple rates of diffusion. However, parameter fitting is much more difficult for this type of numerical code than for an analytical code such as STAMMT-R.

Additional research is also needed to determine the relationships between diffusion rates and different geologic/sedimentologic features. The work of Tidwell et al. (2000a and b) using X-ray absorption to image diffusion in rock samples in the laboratory is an important development in this area. However, *in situ* fracture pathways are always difficult to capture in core, so one cannot be certain that all, or the most important, diffusive pathways have been evaluated in the laboratory.

Research is also needed to scale the information derived from small laboratory tests to the field tracer-test scale and then to scales of regulatory concern.

8.7 Conclusions

A series of tracer tests has been conducted in the Culebra dolomite at the WIPP site. The data, especially those from the tests performed in 1995-96, provide valuable insight into transport processes within the Culebra. Interpretations of the tracer tests in combination with geologic information, hydraulic-test information, and laboratory studies (e.g., Tidwell et al., 2000a and b) have resulted in a greatly improved conceptual model of transport processes within the Culebra.

At locations where the transmissivity of the Culebra is less than approximately 4 x 10^{-6} m^2/s, such as the H-2 and H-4 hydropads, we conceptualize the Culebra as a single-porosity medium in which advection occurs largely through the primary porosity of the dolomite matrix. What open fractures exist are either not sufficiently pervasive or high enough in permeability to provide the dominant advective pathways. At these single-porosity locations, heterogeneity within and among layers in the Culebra leads to variations in relatively slow transport rates.

At locations where the transmissivity of the Culebra is greater than approximately 4 x 10^{-6} m^2/s, we conceptualize the Culebra as a heterogeneous, layered, fractured medium with multiple rates of diffusion. The variations in diffusion rate can be attributed to both variations in fracture spacing (or the spacing of advective pathways) and matrix heterogeneity. Flow and transport appear to be concentrated in the lower Culebra. Where the Culebra is highly transmissive (>2 x 10^{-5} m^2/s), such as at the H-3, H-11, and H-6 hydropads, flow is predominantly through open fractures. Because the fracture transmissivity is significantly larger than that of the matrix, tracer accesses the matrix primarily through diffusion. At H-19, where the overall transmissivity is lower (7 x 10^{-6} m^2/s), the contrast between fracture permeability and the permeability of portions of the matrix is also lower. Therefore, at H-19 we conceptualize flow as occurring both in fractures and in high-permeability portions of the matrix (interparticle porosity and vugs connected by microfractures). At all locations, diffusion is the dominant transport process in the portions of the matrix that tracer does not access by flow.

Variations in fracture spacing and pore structure lead to diffusion occurring at a range of rates. Diffusion into most of the Culebra porosity occurs on the time and length scales of the tracer tests described herein, allowing us to estimate the parameters controlling that diffusion. A portion of the porosity, however, is accessed only over longer time scales and parameters describing that diffusion cannot be estimated from these tests. Nevertheless, that porosity could still be active in diffusion over the time scale at which transport of radionuclides off the WIPP site could possibly occur.

8.8 References

Beauheim, R.L., and R.M. Holt. 1990. "Hydrogeology of the WIPP Site," *Geological and Hydrological Studies of Evaporites in the Northern Delaware Basin for the Waste Isolation Pilot Plant (WIPP), New Mexico, Field Trip #14 Guidebook, November 1-4, 1990, Geological Society of America 1990 Annual Meeting.* Dallas, TX: Dallas Geological Society. 131-179.

Beauheim, R.L., and G.J. Ruskauff. 1998. *Analysis of Hydraulic Tests of the Culebra and Magenta Dolomites and Dewey Lake Redbeds Conducted at the Waste Isolation Pilot Plant Site.* SAND98-0049. Albuquerque, NM: Sandia National Laboratories.

Bodine, M.W., Jr., B.F. Jones, and S.J. Lambert. 1991. "Chapter 4. Normative Analysis of Groundwaters from the Rustler Formation Associated with the Waste Isolation Pilot Plant, Southeastern New Mexico," *Hydrogeochemical Studies of the Rustler Formation and Related Rocks in the Waste Isolation Pilot Plant Area, Southeastern New Mexico.* Eds. M.D. Siegel, S.J. Lambert, and K.L. Robinson. SAND88-0196. Albuquerque, NM: Sandia National Laboratories. 4-1 through 4-140.

Corbet, T.F., and P.M. Knupp. 1996. *The Role of Regional Groundwater Flow in the Hydrogeology of the Culebra Member of the Rustler Formation at the Waste Isolation Pilot Plant (WIPP), Southeastern New Mexico.* SAND96-2133. Albuquerque, NM: Sandia National Laboratories.

Crawley, M.E. 1988. *Hydrostatic Pressure and Fluid Density Distribution of the Culebra Dolomite Member of the Rustler Formation Near the Waste Isolation Pilot Plant, Southeastern New Mexico.* DOE/WIPP 88-030. Carlsbad, NM: Westinghouse Electric Corporation.

Holt, R.M. 1997. *Conceptual Model for Transport Processes in the Culebra Dolomite Member, Rustler Formation.* SAND97-0194. Albuquerque, NM: Sandia National Laboratories.

Holt, R.M., and D.W. Powers. 1984. *Geotechnical Activities in the Waste Handling Shaft, Waste Isolation Pilot Plant (WIPP) Project, Southeastern New Mexico.* WTSD-TME 038. Carlsbad, NM: U.S. Department of Energy, Waste Isolation Pilot Plant.

Holt, R.M., and D.W. Powers. 1986. *Geotechnical Activities in the Exhaust Shaft.* DOE-WIPP 86-008. Carlsbad, NM: U.S. Department of Energy.

Holt, R.M., and D.W. Powers. 1988. *Facies Variability and Post-Depositional Alteration Within the Rustler Formation in the Vicinity of the Waste Isolation Pilot Plant, Southeastern New Mexico.* DOE-WIPP 88-004. Carlsbad, NM: Westinghouse Electric Corporation.

Holt, R.M., and D.W. Powers. 1990. *Geologic Mapping of the Air Intake Shaft at the Waste Isolation Pilot Plant.* DOE-WIPP 90-051. Carlsbad, NM: Westinghouse Electric Corporation.

Jones, T.L., V.A. Kelley, J.F. Pickens, D.T. Upton, R.L. Beauheim, and P.B. Davies. 1992. *Integration of Interpretation Results of Tracer Tests Performed in the Culebra Dolomite at the Waste Isolation Pilot Plant Site.* SAND92-1579. Albuquerque, NM: Sandia National Laboratories.

Kelley, V.A., and G.J. Saulnier, Jr. 1990. *Core Analyses for Selected Samples from the Culebra Dolomite at the Waste Isolation Pilot Plant Site.* SAND90-7011. Albuquerque, NM: Sandia National Laboratories.

LaVenue, A.M., T.L. Cauffman, and J.F. Pickens. 1990. *Ground-Water Flow Modeling of the Culebra Dolomite, Volume I: Model Calibration.* SAND89-7068/1. Albuquerque, NM: Sandia National Laboratories.

Randall, W.S., M.E. Crawley, and M.L. Lyon. 1988. *1988 Annual Water Quality Data Report for the Waste Isolation Pilot Plant.* DOE-WIPP 88-006. Carlsbad, NM: Westinghouse Electric Corporation.

Siegel, M.D., and S.A. Anderholm. 1994. "Geochemical Evolution of Groundwater in the Culebra Dolomite Near the Waste Isolation Pilot Plant, Southeastern New Mexico, USA," *Geochimica et Cosmochimica Acta.* Vol. 58, no. 10, 2299-2323.

Tidwell, V.C., L.C. Meigs, C. Chocas, C.M. Boney, C. Frieiherr von Schwerin, and R. Haggerty. 2000a. Letter Report Static Diffusion Tests: Phase 1 Experiments. (Copy on file in the Sandia WIPP Central Files (SWCF) as ERMS #248941).

Tidwell, V.C., L.C. Meigs, T. Christian-Frear, and C.M. Boney. 2000b. "Effects of Spatially Heterogeneous Porosity on Matrix Diffusion as Investigated by X-ray Absorption Imaging," *Journal of Contaminant Hydrology.* Vol. 42, no. 2-4, 285-302.

Tsang, Y.W. 1995. "Study of Alternative Tracer Tests in Characterizing Transport in Fractured Rocks," *Geophysical Research Letters.* Vol. 22, no. 11, 1421-1424.

Appendix A
Sources of Information

By Lucy C. Meigs[1] and Toya L. Jones[2]

A.1 Introduction

This appendix summarizes the sources of information used for the simulations presented in this document. The information needed for the simulations includes the observed tracer data, to which the simulated results were matched, and values for simulation input parameters.

Simulations were conducted for the tracer tests performed at the H-3, H-6, H-11, and H-19 hydropads. Documentation, including test design, equipment configuration, sample collection, sample-analysis technique, and the observed data, can be found in Hydro Geo Chem (1985) and INTERA Technologies (1986) for the H-3 tracer test, in Hydro Geo Chem (1985) for the H-6 tracer test, and in Stensrud et al. (1990) for the 1988 tracer test at H-11.

Discussion of the tracer tests at H-19 and the 1996 tracer test at H-11 has not previously been published. The following sections identify the individual sources of information for these tests.

A.2 Test Design, Implementation, and Equipment

The 4-well tracer test performed at the H-19 hydropad was conducted under a Field Operations Plan (Saulnier and Beauheim, 1995). The 7-well tracer test performed at the H-19 hydropad and the 1996 tracer test performed at the H-11 hydropad were conducted under a Test Plan (Beauheim et al., 1995). Information regarding the borehole and test-tool configurations and sample collection can be found in ERMS #240460 for the H-19 4-well test and in ERMS #240462 for the 7-well test at H-19 and the 1996 test at H-11.

A.3 Observed Tracer Data

Samples collected during the tests were analyzed for the benzoic acids and iodide at the University of Nevada - Las Vegas. Sample-analysis results are documented in ERMS #237466 (general records), ERMS #237467 (1996 H-11 tracer test), ERMS #237468 (H-19 4-well test), and ERMS #237452 (H-19 7-well test). The analysis results were modified by Duke Engineering and Services (DE&S) to prepare them for numerical simulations (e.g., correcting the sample time to reflect the travel time in the Culebra rather than the travel time from surface injection to surface sample collection by adjusting for tracer travel up the withdrawal well and down the injection well). The adjusted data can be found in ERMS #237466. That records package not only contains the data for the H-19 tracer tests and the 1996 H-11 tracer test, but also the data for the H-3 and 1988 H-11 tracer tests and the interpreted data (see Appendix F) for the H-6 tracer tests. Plots of these data can be found in diagram (a) of the figures in Appendix C.

Calculations of the 95% confidence intervals were performed at the University of Nevada – Las Vegas on the H-19 tracer data and the tracer data from the 1996 test at H-11. Those calculations are documented in ERMS #237467 (1996 H-11 test), ERMS #237468 (H-19 4-well test), and ERMS #237452 (H-19 7-well test). Tracer-breakthrough data at corrected times for the confidence-interval data were prepared by DE&S and can be found in ERMS #251278. Plots of the confidence-interval data can be found in diagrams (b) through (f) of the figures in Appendix C.

---

[1] Sandia National Laboratories, Geohydrology Department, P.O. Box 5800, MS-0735, Albuquerque, NM 87185. Email: lcmeigs@sandia.gov.

[2] Duke Engineering & Services, Inc., 9111 Research Boulevard, Austin, TX 78758.

A.4 Input Parameters for Simulations

To simplify numerical simulations and to provide a common source of input-parameter values for all analysts evaluating the H-3, H-6, H-11 and H-19 tracer-test data, the Transport Input Parameter Sheets (TIPS) were prepared. The original version of the TIPS can be found in ERMS #237439 and an updated version of the TIPS can be found in ERMS #251279. Hard copies of a portion of the final TIPS can be found in Appendix B. The TIPS contain most of the input information used in the simulations in this report. DE&S and Sandia prepared the TIPS records packages which contain or reference all of the calculations and checking of calculations that were done to verify the input parameters. To clarify, the TIPS provide tabulated input parameters for simulations of the WIPP tracer-test data. They do not provide input parameters for larger scale simulations such as WIPP performance-assessment calculations.

A.5 Simulations Presented in This Document

The majority of the simulations presented in this report were performed under analysis plans AP-013 (McCord and Meigs, 1996) and AP-053 (Chocas et al., 1999). A records package (ERMS #251278) has been opened that will contain the documentation for most of the simulations, and associated calculations, presented in this document. The records for most of the simulations in Appendix P are in ERMS #237450.

A.6 References

Beauheim, R.L., L.C. Meigs, G.J. Saulnier, Jr., and W.A. Stensrud. 1995. "Culebra Transport Program Test Plan: Tracer Testing of the Culebra Dolomite Member of the Rustler Formation at the H-19 and H-11 Hydropads on the WIPP Site." Albuquerque, NM: Sandia National Laboratories. (Copy on file in the Sandia WIPP Central Files (SWCF) as ERMS #230156.)

Chocas, C., T. Corbet, L. Meigs, and M. Seigel. 1999. "Culebra Transport Technical Studies Analysis Plan for the Annual Sensitivity Analysis." AP-053, Revision 1. Albuquerque, NM: Sandia National Laboratories. (Copy on file in the SWCF as ERMS #506185.)

Hydro Geo Chem, Inc. 1985. *WIPP Hydrology Program, Waste Isolation Pilot Plant, SENM, Hydrologic Data Report #1*. SAND85-7206. Albuquerque, NM: Sandia National Laboratories.

INTERA Technologies, Inc. 1986. *WIPP Hydrology Program, Waste Isolation Pilot Plant, Southeastern New Mexico, Hydrologic Data Report #3*. SAND86-7109. Albuquerque, NM: Sandia National Laboratories.

McCord, J., and L. Meigs. 1996. "Analysis Plan for Determination of Physical Transport Parameters for the Culebra Dolomite Member of the Rustler Formation at the Waste Isolation Pilot Plant (WIPP) Site." AP-013, Revision 1. Albuquerque, NM: Sandia National Laboratories. (Copy on file in the SWCF as ERMS #237154.)

Saulnier, G.J., Jr., and R.L. Beauheim. 1995. "Appendix A: Culebra Transport Program Field Operations Plan: Well Construction and Preliminary Testing on the H-19 Hydropad at the WIPP Site." Albuquerque, NM: Sandia National Laboratories. (Copy on file in the SWCF as ERMS #220256.) Reprinted 1998. *Basic Data Report for Drillholes on the H-19 Hydropad (Waste Isolation Pilot Plant—WIPP)*. J.W. Mercer, D.L. Cole, and R.M. Holt. SAND98-0071. Albuquerque, NM: Sandia National Laboratories. A-3 through A-58.

Stensrud, W.A., M.A. Bame, K.D. Lantz, J.B. Palmer, and G.J. Saulnier, Jr. 1990. *WIPP Hydrology Program, Waste Isolation Pilot Plant, Southeastern New Mexico, Hydrologic Data Report #8*. SAND89-7056. Albuquerque, NM: Sandia National Laboratories.

Appendix B
Transport Input Parameter Spreadsheets (TIPS)

By Toya L. Jones[1]

B.1 Introduction

Transport Input Parameter Spreadsheets (TIPS) were generated for the WIPP tracer tests conducted at the H-19, H-11, H-6, and H-3 hydropads. For the H-6 tests, only the data determined to be reliable for interpretation, as discussed in Appendix F and Jones et al. (1992), are included in the TIPS. The purpose of the TIPS, which were created at a time when several analysts were interpreting the tracer-test data, is to provide a single, concise source for the input-parameter values needed for analyses of the data. (The TIPS do not provide input parameters for larger scale simulations such as WIPP performance-assessment calculations.) The TIPS will remain an important companion to the tracer-test data to ensure the use of consistent input in future interpretations of the data. We highly recommend that all future interpretations of the WIPP tracer-test data use the TIPS as the source for model-input parameters.

B.2 TIPS Contents

The TIPS are divided by:

- hydropad,
- parameter type (either fixed or injection-specific), and
- test or round of injection, if applicable.

The TIPS containing fixed parameters include:

- hydropad-specific parameters, the values of which are constant for all the test(s) conducted at that hydropad, such as well spacing, Culebra thickness, porosity, etc.;
- production-well parameters, such as production rate and time;
- tracer-injection start times for all injections; and
- the name of the Excel spreadsheets containing the raw tracer data.

Tracer and injection-well-specific parameters (e.g., tracer free-water diffusion coefficient, borehole volume, injection rates/times, etc.) are contained in the injection-specific TIPS. If more than one round of injections was performed during a test or more than one test was performed at the hydropad, the injection-specific parameter values for each round or test are contained in a separate TIPS. The injection-specific parameters for the H-6 tests are the one exception to this last statement, being included in the TIPS in the same spreadsheet. For instances when iodide and a benzoic acid were injected together, the injection-well-specific parameters are identical for both and are listed in the TIPS only once under the benzoic acid. Values for tracer-specific parameters are listed for both the iodide and the benzoic acid. A listing of the TIPS and their contents is given in Table B-1.

In addition to providing parameter values, the version of the TIPS in the Sandia WIPP Central Files (SWCF) identifies the sources for the data and calculations used to derive the values. The sources are either published information or WIPP records maintained in the SWCF. All WIPP records are referenced by an Electronic Records Management System (ERMS) number or a records number. The TIPS and all supporting documentation can be found in ERMS #237439 (version of the TIPS developed for the

---

[1] Duke Engineering & Services, Inc., 9111 Research Boulevard, Austin, TX 78758.
Email: tjones@dukeengineering.com

Table B-1. Transport Input Parameter Spreadsheets

Hydropad	Type Parameters	Test/Round
H-19	Fixed	All
H-19	Injection Specific	7-well Test Round 1 (SWIW and MWCF)
H-19	Injection Specific	7-well Test Round 2
H-19	Injection Specific	7-well Test Round 3
H-19	Injection Specific	4-well Test (SWIW and MWCF)
H-11	Fixed	All
H-11	Injection Specific	1996 Test Round 1 (SWIW and MWCF)
H-11	Injection Specific	1996 Test Round 2
H-11	Injection Specific	1988 Test
H-6	Fixed	All
H-6	Injection Specific	MWCF Tests #1 and #2
H-3	Fixed	All
H-3	Injection Specific	All

CCA calculations) and ERMS #251279 (final version of the TIPS). The main differences between the version of the TIPS developed for the CCA calculations and the final TIPS are:

- well radii were added to the final TIPS containing hydropad-specific parameters;
- a separate pumping rate was calculated for the SWIW tests and added to the final TIPS containing the hydropad-specific parameters;
- the calculated average pumping rates given in the TIPS containing the hydropad-specific parameters were updated for the final version;
- a listing of the spreadsheets containing the raw data and the confidence-interval data (see Appendix C) was added to the TIPS containing the hydropad-specific parameters for the final version;
- the system information and duration of test components information found in the TIPS containing the tracer and injection-well-specific parameters were updated for the final version; and
- a listing of the data files containing the raw data and the confidence-interval data was added to the TIPS containing the tracer and injection-well-specific parameters for the final version.

All parameters that changed or were added between the TIPS developed for the CCA calculations and the final TIPS are highlighted on the final versions of the TIPS. The parameter value changes between the two versions of the TIPS all appear to result in negligible to very minor changes in numerical-simulation results.

B.3 Hard Copy of TIPS

The remainder of this appendix contains a partial copy of the TIPS in the same order as they are listed in the Table B-1. The hard copies included here differ from the actual TIPS in that the sources for the data and calculations are not given here. As previously stated, the sources can be found in the records package for the final TIPS (ERMS #251279).

Table B-2. H-19 Fixed Parameters
Transport Input Parameter Sheet

Parameter	Value
Well Inner Radius (m)	
H-19b0 (Pumping Well)	0.113
H-19b2 (Injection Well)	0.077
H-19b3 (Injection Well)	0.076
H-19b4 (Injection Well)	0.076
H-19b5 (Injection Well)	0.075
H-19b6 (Injection Well)	0.076
H-19b7 (Injection Well)	0.076
Average Pumping Rate (a)	
4-Well Test - SWIW	
gpm	3.76
L/s	0.237
m^3/s	2.37E-04
4-Well Test - Convergent	
gpm	3.74
L/s	0.236
m^3/s	2.36E-04
7-Well Test - SWIW	
gpm	4.35
L/s	0.274
m^3/s	2.74E-04
7-Well Test - Round 1	
gpm	4.29
L/s	0.271
m^3/s	2.71E-04
7-Well Test - Round 2	
gpm	3.99
L/s	0.252
m^3/s	2.52E-04
7-Well Test - Round 3	
gpm	2.45
L/s	0.155
m^3/s	1.55E-04

Parameter	Value
Tracer Injection Start Times	
4-Well Test - SWIW	
H-19b0 (brine)	10:37 06/15/95
H-19b0 (2,4-DCBA)	10:45 06/15/95
H-19b0 (o-TFMBA)	12:52 06/15/95
4-Well Test - Convergent	
H-19b2 (2,3-DFBA)	19:41:10 06/19/95
H-19b3 (2,3,4,5-TFBA)	02:20 06/20/95
H-19b4 (2,6-DFBA)	21:20 06/19/95
7-Well Test - SWIW	
H-19b0 (2,4-DCBA)	11:32 12/14/95
7-Well Test - Round 1	
H-19b2 (2,3,4-TFBA)	17:49:50 12/22/95
H-19b3 (m-TFMBA & NaI)	10:44 12/22/95
H-19b4 (3,5-DFBA)	13:10:40 12/22/95
H-19b5u (2,3-DCBA)	17:28 12/20/95
H-19b5l (2,5-DCBA)	17:29 12/20/95
H-19b6 (2,5-DFBA)	16:48:25 12/21/95
H-19b7 (2,4-DFBA)	12:26 12/21/95
7-Well Test - Round 2	
H-19b3u (p-TFMBA)	12:26 01/19/96
H-19b3l (o-TFMBA)	12:26 01/19/96
H-19b5 (2,4-DCBA)	8:26:45 01/19/96
H-19b7u (PFBA)	09:36 01/20/96
H-19b7l (3,5-DCBA)	09:36 01/20/96
7-Well Test - Round 3	
H-19b3 (2,3,4,5-TFBA)	11:56:35 02/22/96
H-19b6 (2,4,6-TCBA)	09:15:27 02/22/96
H-19b7 (2,3,6-TFBA & NaI)	14:05:40 02/22/96

Table B-2. H-19 Fixed Parameters
Transport Input Parameter Sheet (continued)

Parameter	Value
Well Spacing at Culebra Depth (b)	
H-19b2 to H-19b0	
feet	82.3
meters	25.1
H-19b3 to H-19b0	
feet	36.2
meters	11.0
H-19b4 to H-19b0	
feet	73.3
meters	22.3
H-19b5 to H-19b0	
feet	45.5
meters	13.9
H-19b6 to H-19b0	
feet	65.1
meters	19.8
H-19b7 to H-19b0	
feet	39.9
meters	12.2
Culebra Thickness	
H-19b0	
feet	24.3
meters	7.4
H-19b2	
feet	24.4
meters	7.4
H-19b3	
feet	25
meters	7.6

Parameter	Value
Culebra Thickness (continued)	
H-19b4	
feet	23.5
meters	7.2
H-19b5	
feet	24.5
meters	7.5
H-19b6	
feet	24.8
meters	7.6
H-19b7	
feet	24.5
meters	7.5
Average Thickness	
Full Thickness (m)	7.4
Upper Zone - Unit 1	
feet	9.8
meters	3.0
Lower Zone - Units 2, 3,4 (m)	4.4
Hydropad Transmissivity (m^2/s)	6.8E-06
Hydraulic Conductivity (m/s)	
assuming full thickness	9.2E-07
assuming lower zone thickness	1.5E-06
Diffusive Tortuosity	0.091
Diffusive Porosity	0.147

(a) the uncertainty in the average pumping rate is estimated to be ±4%

(b) the uncertainty in the well spacing is estimated to be no more than ±1.5 m

Table B-3. H-19 Tracer/Chaser/System Parameters - SWIW and Round 1 Transport Input Parameter Sheet

Parameter	Value	Value	Value	Value	Value	Value	Value	Value	Value
INJECTION WELL	H-19b0	H-19b2	H-19b3	H-19b3	H-19b4	H-19b5u	H-19b5l	H-19b6	H-19b7
TEST TYPE	SWIW	Convergent	Convergent	Convergent	Convergent	Convergent	Convergent	Convergent	Convergent
INJECTION DATE	12/14/95	12/22/95	12/22/95	12/22/95	12/22/95	12/20/95	12/20/95	12/21/95	12/21/95
TRACER NAME	2,4-DCBA	2,3,4-TFBA	m-TFMBA (a)	Iodide (a)	3,5-DFBA	2,3-DCBA	2,5-DCBA	2,5-DFBA	2,4-DFBA
AQUEOUS DIFFUSION COEFFICIENT (m2/s) (b)	7.3E-10	8.0E-10	7.4E-10	18.0E-10	8.2E-10	7.3E-10	7.3E-10	8.2E-10	8.2E-10
TRACER INJECTION									
Calculated Mass Injected (kg)	4.995	1.653	1.884	2.003	1.677	1.684	1.970	1.884	1.489
Concentration (mg/L)	5974	8176	9517	11762	8462	11451	13489	9491	7580
Volume (c)									
liters	849	202	198	- (a)	198	147	149	199	198
cubic meters	0.849	0.202	0.198	-	0.198	0.147	0.149	0.199	0.198
Injection Time									
minutes	122.0	25.6	18.0	-	28.3	164.0	230.0	26.6	16.0
seconds	7320	1536	1080	-	1698	9840	13800	1596	960
Injection Rate (d)									
L/s	0.116	0.132	0.183	-	0.117	0.0149	0.0108	0.124	0.206
m^3/s	1.16E-04	1.32E-04	1.83E-04	-	1.17E-04	1.49E-05	1.08E-05	1.24E-04	2.06E-04
CHASER INJECTION									
Volume (c)									
liters	1697	154	173	- (a)	143	105 (e)	65 (e)	154	168
cubic meters	1.697	0.154	0.173	-	0.143	0	0	0.154	0.16848
Injection Time									
minutes	243.0	17.6	12.5	-	19.5	178.0	117.0	21.3	13.0
seconds	14580	1056	750	-	1170	10680	7020	1278	780
Injection Rate (d)									
L/s	0.116	0.146	0.231	-	0.122	0.00000	0.00000	0.121	0.216
m^3/s	1.16E-04	1.46E-04	2.31E-04	-	1.22E-04	9.83E-06	9.26E-06	1.21E-04	2.16E-04

Table B-3. H-19 Tracer/Chaser/System Parameters - SWIW and Round 1 Transport Input Parameter Sheet (continued)

Parameter	Value	Value	Value	Value	Value	Value	Value	Value	Value
INJECTION WELL	H-19b0	H-19b2	H-19b3	H-19b3	H-19b4	H-19b5u	H-19b5l	H-19b6	H-19b7
TRACER NAME	2,4-DCBA	2,3,4-TFBA	m-TFMBA	Iodide	3,5-DFBA	2,3-DCBA	2,5-DCBA	2,5-DFBA	2,4-DFBA
SYSTEM INFORMATION (f)									
Thickness									
Upper Zone									
feet	-	-	na	- (a)	-	8.36	na	-	na
meters	-	-	na	-	-	2.55	na	-	na
Lower Zone									
feet	14.12	-	na	-	-	na	15.05	-	na
meters	4.30	-	na	-	-	na	4.59	-	na
Full Zone									
feet	27.30	23.61	24.85	-	22.82	na	na	25.48	24.80
meters	8.32	7.20	7.57	-	6.96	na	na	7.77	7.56
Borehole Volume (L)									
Upper Zone	-	-	na	-	-	44.3	na	-	na
Lower Zone	149.9	-	na	-	-	na	82.6	-	na
Full Zone	337.3	132.8	137.8	-	126.4	na	na	140.5	135.4
Tool Volume									
Upper Zone									
gallons		-	na	-	-	7.19	na	-	na
liters		-	na	-	-	27.2	na	-	na
Lower Zone									
gallons	12.94	-	na	-	-	na	13.8	-	na
liters	48.96	-	na	-	-	na	52.1	-	na
Full Zone									
gallons	19.96	22.54	22.87	-	21.71	na	na	24.46	22.82
liters	75.54	85.32	86.55	-	82.19	na	na	92.57	86.37

Table B-3. H-19 Tracer/Chaser/System Parameters - SWIW and Round 1 Transport Input Parameter Sheet (continued)

Parameter	Value	Value	Value	Value	Value	Value	Value	Value	Value
INJECTION WELL	H-19b0	H-19b2	H-19b3	H-19b3	H-19b4	H-19b5u	H-19b5l	H-19b6	H-19b7
TRACER NAME	2,4-DCBA	2,3,4-TFBA	m-TFMBA	Iodide	3,5-DFBA	2,3-DCBA	2,5-DCBA	2,5-DFBA	2,4-DFBA

SYSTEM INFORMATION (continued)									
Downhole Volume (L) [(g)]									
Upper Zone	-	-	na	-	-	17.0	na	-	na
Lower Zone	100.9	-	na	-	-	na	30.6	-	na
Full Zone	261.8	47.48	51.25	-	44.21	na		47.93	49.03
Tubing Volume									
gallons	4.433	4.392	4.409	-	4.419	4.39	4.46	4.411	4.416
liters	16.78	16.62	16.69	-	16.73	16.6	16.9	16.70	16.71
Total System Vol. (L) [(h)]									
Upper Zone									
liters	-	-	na	-	-	33.7 [(d)]	na	-	na
cubic meters	-	-	na	-	-	3.37E-02	na	-	na
Lower Zone									
liters	117.7	-	na	-	-	na	47.4 [(d)]	-	na
cubic meters	1.177E-01	-	na	-	-	na	4.74E-02	-	na
Full Zone									
liters	na	64.10	67.93	-	60.94	na	na	64.63	65.75
cubic meters	na	6.410E-02	6.793E-02	-	6.094E-02	na	na	6.463E-02	6.575E-02

DURATION OF TEST COMPONENTS									
Total Injection Time [(i)]									
days	0.25	0.03	0.02	- [(a)]	0.03	0.24	0.24	0.03	0.02
hours	6.08	0.72	0.51	-	0.80	5.70	5.78	0.80	0.48
minutes	365.00	43.20	30.50	-	47.80	342.00	347.00	47.83	29.00
seconds	21900	2592	1830	-	2868	20520	20820	2870	1740
Pause Length for SWIW Test (j)									
days	0.74	-	-	-	-	-	-	-	-
hours	17.72	-	-	-	-	-	-	-	-
minutes	1063.34	-	-	-	-	-	-	-	-
seconds	63800	-	-	-	-	-	-	-	-

Table B-3. H-19 Tracer/Chaser/System Parameters - SWIW and Round 1 Transport Input Parameter Sheet (continued)

Parameter	Value	Value	Value	Value	Value	Value	Value	Value	Value
INJECTION WELL	H-19b0	H-19b2	H-19b3	H-19b3	H-19b4	H-19b5u	H-19b5l	H-19b6	H-19b7
TRACER NAME	2,4-DCBA	2,3,4-TFBA	m-TFMBA	Iodide	3,5-DFBA	2,3-DCBA	2,5-DCBA	2,5-DFBA	2,4-DFBA
DURATION OF TEST COMPONENTS (continued)									
Pumping Duration at Initial Rate of 0.27 L/s (k)									
days	33.31	26.02	26.32	-	26.20	27.80	27.78	27.05	27.25
hours	799.50	624.37	631.69	-	628.92	667.12	666.77	649.29	654.00
minutes	47970.00	37462.39	37901.45	-	37735.19	40027.44	40006.04	38957.40	39239.82
seconds	2878200	2247743	2274087	-	2264111	2401646	2400362	2337444	2354389
Pumping Duration at Second Rate of 0.25 L/s (l)									
days	32.74	32.74	32.74	-	32.74	32.74	32.74	32.74	32.74
hours	785.83	785.83	785.83	-	785.83	785.83	785.83	785.83	785.83
minutes	47150.00	47150.00	47150.00	-	47150.00	47150.00	47150.00	47150.00	47150.00
seconds	2829000	2829000	2829000	-	2829000	2829000	2829000	2829000	2829000
Pumping Duration at Final Rate of 0.16 L/s (m)									
days	51.94	51.94	51.94	-	51.94	51.94	51.94	51.94	51.94
hours	1246.67	1246.67	1246.67	-	1246.67	1246.67	1246.67	1246.67	1246.67
minutes	74800.00	74800.00	74800.00	-	74800.00	74800.00	74800.00	74800.00	74800.00
seconds	4488000	4488000	4488000	-	4488000	4488000	4488000	4488000	4488000
Total Duration of Test (n)									
days	118.99	110.73	111.03	-	110.93	112.72	112.71	111.77	111.96
hours	2855.81	2657.59	2664.72	-	2662.23	2705.32	2705.05	2682.60	2687.01
minutes	171348.34	159455.56	159882.95	-	159734.03	162319.44	162303.04	160955.98	161220.82
seconds	10280900	9567334	9592977	-	9584042	9739166	9738182	9657359	9673249
TRACER DATA FILES (o)									
Raw Data	H19S1Y21	H19N1Z12	H19N1Z12	H19N1Z12	H19N1Z12	H19N1Z12	H19N1Z12	H19N1Z12	H19N1Z12
Confidence Interval Data	RH19S1B0	RH19N1B2	RH19N1B3	RH19N1IO(p) RH19N1TI(q)	RH19N1B4	RH19N1U5	RH19N1L5	RH19N1B6	RH19N1B7

Table B-3. H-19 Tracer/Chaser/System Parameters - SWIW and Round 1 Transport Input Parameter Sheet (continued)

(a) m-TFMBA and NaI were injected into H-19b3 simultaneously followed by the injection of chaser fluid and, therefore, the chaser, system, and duration of test components information is identical for both tracers

(b) the aqueous diffusion coefficients were calculated using the Hayduk and Laudie method described by Tucker and Nelken (1982); this is the same method used by Benson and Bowman (1996) and Bowman and Gibbens (1992). Also see Walter (1982) and Skagus and Neretnicks (1986). This calculation is for low ionic strength water. Thus the actual aqueous diffusion coefficients may be lower than these calculated values (e.g., Carey et al., 1995). (The use of aqueous diffusion coefficients that are too high for numerical simulations will result in estimated matrix block lengths that are too large. This is conservative for estimates of parameters for WIPP.)

(c) the uncertainty in tracer and chaser volumes is estimated to be ±6% for the H-19b0 tracer and chaser and the H-19b7 chaser and ±4% for all other tracer and chaser volumes

(d) calculated as the injection volume divided by the injection time

(e) Due to a mix up in the field, the volumes of chaser to be injected into H-19b5u and H-19b5l were reversed; this resulted in a chaser of less than 2 times the total system volume for the H-19b5l injection

(f) in this section of the spreadsheet, "-" indicates that the tracer tool was not equipped to inject into that zone and "na" indicates that the tracer tool was equipped to inject into that zone but injection into that zone did not occur during this round of injections; the only exception is H-19b3 iodide were the "-" indicates that this information is not applicable because it is the same as for H-19b3 m-TFMBA

(g) calculated as the borehole volume minus the tool volume

(h) calculated as the downhole volume plus the tubing volume

(i) time for injection of tracer and chaser

(j) time from the end of chaser injection to the start of pumping minus the time for chaser to travel down the injection well

(k) for the SWIW test tracer, this is the time from the start of pumping to the slight pumping rate decrease (during which the withdrawal well was pumping at a rate of 0.27 L/s) for the round 1 tracers, this is the time from the end of chaser injection to the slight pumping rate decrease (during which the withdrawal well was pumping at a rate of 0.27 L/s) minus the time for chaser to travel down the injection well

(l) time from the slight pumping rate decrease to the major pumping rate reduction (during which the withdrawal well was pumping at a rate of 0.25 L/s)

(m) time from the major pumping rate reduction to the end of pumping (during which the withdrawal well was pumping at a rate of 0.16 L/s)

(n) total duration of the test from the start of injection to the end of pumping minus the time for chaser to travel down the injection well; includes the pause time for the SWIW test tracer

(o) all data files have the extension .DAT; for a description of raw data and confidence interval data see Appendix C

(p) this data file contains the IC and HPLC iodide data in separate columns

(q) this data file contains all of the iodide data from the two analysis methods (IC and HPLC) sorted together chronologically

Table B-4. H-19 Tracer/Chaser/System Parameters - Round 2 Transport Input Parameter Sheet

Parameter	Value	Value	Value	Value	Value
INJECTION WELL	H-19b3u	H-19b3l	H-19b5	H-19b7u	H-19b7l
INJECTION TYPE	Convergent	Convergent	Convergent	Convergent	Convergent
INJECTION DATE	01/19/96	01/19/96	01/19/96	01/20/96	01/20/96
TRACER NAME	p-TFMBA	o-TFMBA	2,4-DCBA	PFBA	3,5-DCBA
AQUEOUS DIFFUSION COEFFICIENT (m^2/s) (a)	7.4E-10	7.4E-10	7.3E-10	7.7E-10	7.3E-10
TRACER INJECTION					
Calculated Mass Injected (kg)	1.866	1.916	1.959	1.896	1.513
Concentration (mg/L)	14127	9694	9852	14511	7667
Volume (b)					
liters	132	198	199	131	197
cubic meters	0.132	0.198	0.199	0.131	0.197
Injection Time					
minutes	134.5	120.0	17.25	259.0	212.0
seconds	8070	7200	1035	15540	12720
Injection Rate (c)					
L/s	0.0164	0.0275	0.192	0.00841	0.0155
m^3/s	1.64E-05	2.75E-05	1.92E-04	8.41E-06	1.55E-05
CHASER INJECTION					
Volume (b)					
liters	69	143	169	64	139
cubic meters	0.069	0.143	0.169	0.064	0.139
Injection Time					
minutes	76.5	72.0	17.0	111.0	158.0
seconds	4590	4320	1020	6660	9480
Injection Rate (c)					
L/s	0.0151	0.0330	0.166	0.00965	0.0147
m^3/s	1.51E-05	3.30E-05	1.66E-04	9.65E-06	1.47E-05

Table B-4. H-19 Tracer/Chaser/System Parameters - Round 2 Transport Input Parameter Sheet (continued)

Parameter	Value	Value	Value	Value	Value
INJECTION WELL	H-19b3u	H-19b3l	H-19b5	H-19b7u	H-19b7l
TRACER NAME	p-TFMBA	o-TFMBA	2,4-DCBA	PFBA	3,5-DCBA
SYSTEM INFORMATION [(d)]					
Thickness					
Upper Zone					
feet	8.50	na	na	8.39	na
meters	2.59	na	na	2.56	na
Lower Zone					
feet	na	14.10	na	na	14.16
meters	na	4.30	na	na	4.32
Full Zone					
feet	na	na	25.66	na	na
meters	na	na	7.82	na	na
Borehole Volume (L)					
Upper Zone	47.2	na	na	45.0	na
Lower Zone	na	78.4	na	na	78.7
Full Zone	na	na	139.1	na	na
Tool Volume					
Upper Zone					
gallons	7.22	na	na	7.35	na
liters	27.3	na	na	27.8	na
Lower Zone					
gallons	na	13.1	na	na	12.9
liters	na	49.5	na	na	48.8
Full Zone					
gallons	na	na	23.56	na	na
liters	na	na	89.17	na	na
Downhole Volume (L) [(e)]					
Upper Zone	19.9	na	na	17.2	na
Lower Zone	na	28.9	na	na	29.9
Full Zone	na	na	49.93	na	na

Table B-4. H-19 Tracer/Chaser/System Parameters - Round 2 Transport Input Parameter Sheet (continued)

Parameter	Value	Value	Value	Value	Value
INJECTION WELL	H-19b3u	H-19b3l	H-19b5	H-19b7u	H-19b7l
TRACER NAME	p-TFMBA	o-TFMBA	2,4-DCBA	PFBA	3,5-DCBA

SYSTEM INFORMATION (d) (continued)					
Tubing Volume					
gallons	4.38	4.44	4.427	4.38	4.45
liters	16.6	16.8	16.76	16.6	16.8
Total System Vol. (L) (f)					
Upper Zone					
liters	36.5	na	na	33.8	na
cubic meters	3.65E-02	na	na	3.38E-02	na
Lower Zone					
liters	na	45.7	na	na	46.8
cubic meters	na	4.57E-02	na	na	4.68E-02
Full Zone					
liters	na	na	66.69	na	na
cubic meters	na	na	6.669E-02	na	na

DURATION OF TEST COMPONENTS					
Total Injection Time (g)					
days	0.15	0.13	0.02	0.26	0.26
hours	3.52	3.20	0.57	6.17	6.17
minutes	211.00	192.00	34.25	370.00	370.00
seconds	12660	11520	2055	22200	22200
Pumping Duration at Second Rate of 0.25 L/s (h)					
days	30.85	30.87	31.16	29.85	29.85
hours	740.40	740.94	747.75	716.34	716.47
minutes	44423.70	44456.22	44864.81	42980.48	42988.00
seconds	2665422	2667373	2691889	2578829	2579280

Table B-4. H-19 Tracer/Chaser/System Parameters - Round 2
Transport Input Parameter Sheet (continued)

Parameter	Value	Value	Value	Value	Value
INJECTION WELL	H-19b3u	H-19b3l	H-19b5	H-19b7u	H-19b7l
TRACER NAME	p-TFMBA	o-TFMBA	2,4-DCBA	PFBA	3,5-DCBA
DURATION OF TEST COMPONENTS (q) (continued)					
Pumping Duration at Final Rate of 0.16 L/s (i)					
days	51.94	51.94	51.94	51.94	51.94
hours	1246.67	1246.67	1246.67	1246.67	1246.67
minutes	74800.00	74800.00	74800.00	74800.00	74800.00
seconds	4488000	4488000	4488000	4488000	4488000
Total Duration of Test (j)					
days	82.94	82.95	83.12	82.05	82.05
hours	1990.58	1990.80	1994.98	1969.17	1969.30
minutes	119434.70	119448.22	119699.06	118150.48	118158.00
seconds	7166082	7166893	7181944	7089029	7089480
TRACER DATA FILES (k)					
Raw Data	H19N2Z12	H19N2Z12	H19N2Z12	H19N2Z12	H19N2Z12
Confidence Interval Data	RH19N2U3	RH19N2L3	RH19N2B5	RH19N2U7	RH19N2L7

(a) the aqueous diffusion coefficients were calculated using the Hayduk and Laudie method described by Tucker and Nelken (1982); this is the same method used by Benson and Bowman (1996) and Bowman and Gibbens (1992). Also see Walter (1982). This calculation is for low ionic strength water. Thus the actual aqueous diffusion coefficients may be lower than these calculated values (e.g., Carey et al., 1995). (The use of aqueous diffusion coefficients that are too high for numerical simulations will result in estimated matrix block lengths that are too large. This is conservative for estimates of parameters for WIPP.)

(b) the uncertainty in tracer and chaser volumes is estimated to be ±4%

(c) calculated as the injection volume divided by the injection time

(d) in this section of the spreadsheet "na" indicates that the tracer tool was equipped to inject into that zone but injection into that zone did not occur during this round of injections

(e) calculated as the borehole volume minus the tool volume

(f) calculated as the downhole volume plus the tubing volume

(g) time for injection of tracer and chaser

(h) time from the end of chaser injection to the major pumping rate reduction (during which the withdrawal well was pumping at its second rate of 0.25 L/s) minus the time for chaser to travel down the injection well

(i) time from the major pumping rate reduction to the end of pumping (during which the withdrawal well was pumping at a final rate of 0.16 L/s)

(j) total duration of the test from the start of injection to the end of pumping minus the time for chaser to travel down the injection well

(k) all data files have the extension .DAT; for a description of raw data and confidence interval data see Appendix C

Table B-5. H-19 Tracer/Chaser/System Parameters - Round 3

Transport Input Parameter Sheet

Parameter	Value	Value	Value	Value
INJECTION WELL	H-19b3	H-19b6	H-19b7	H-19b7
INJECTION TYPE	Convergent	Convergent	Convergent	Convergent
INJECTION DATE	02/22/96	02/22/96	02/22/96	02/22/96
TRACER NAME	2,3,4,5-TFBA	2,4,6-TCBA	2,3,6-TFBA (a)	Iodide (a)
AQUEOUS DIFFUSION COEFFICIENT (m^2/s) (b)	7.9E-10	6.8E-10	8.0E-10	18.0E-10

TRACER INJECTION				
Calculated Mass Injected (kg)	1.969	1.948	1.897	1.982
Concentration (mg/L)	9949	9872	9540	10610
Volume (c)				
liters	198	197	199	-(a)
cubic meters	0.198	0.197	0.199	-
Injection Time				
minutes	32.9	47.1	28.3	-
seconds	1974	2826	1698	-
Injection Rate (d)				
L/s	0.100	0.0698	0.117	-
m^3/s	1.00E-04	6.98E-05	1.17E-04	-

CHASER INJECTION				
Volume (c)				
liters	173	153	168	-(a)
cubic meters	0.173	0.153	0.168	-
Injection Time				
minutes	25.0	37.3	23.5	-
seconds	1500	2238	1410	-
Injection Rate (d)				
L/s	0.115	0.0684	0.119	-
m^3/s	1.15E-04	6.84E-05	1.19E-04	-

Table B-5. H-19 Tracer/Chaser/System Parameters - Round 3 Transport Input Parameter Sheet (continued)

Parameter	Value	Value	Value	Value
INJECTION WELL	H-19b3	H-19b6	H-19b7	H-19b7
TRACER NAME	2,3,4,5-TFBA	2,4,6-TCBA	2,3,6-TFBA	Iodide
SYSTEM INFORMATION [e]				
Thickness (Full Zone)				
feet	24.85	25.48	24.80	-[a]
meters	7.57	7.77	7.56	-
Borehole Volume (Full Zone) (L)	137.8	140.5	135.4	-
Tool Volume (Full Zone)				
gallons	22.87	24.46	22.82	-
liters	86.55	92.57	86.37	-
Downhole Volume (Full Zone) (L) [f]	51.25	47.93	49.03	-
Tubing Volume				
gallons	4.409	4.411	4.416	-
liters	16.69	16.70	16.71	-
Total System Volume (Full Zone) [g]				
liters	67.93	64.63	65.75	-
cubic meters	6.793E-02	6.463E-02	6.575E-02	-
DURATION OF TEST COMPONENTS				
Total Injection Time [h]				
days	0.04	0.06	0.04	-[a]
hours	0.97	1.41	0.86	-
minutes	57.90	84.40	51.80	-
seconds	3474	5064	3108	-
Pumping Duration at Final Rate of 0.16 L/s [i]				
days	48.94	49.03	48.85	-
hours	1174.49	1176.67	1172.45	-
minutes	70469.37	70600.26	70346.73	-
seconds	4228162	4236016	4220804	-
Total Duration of Test [j]				
days	48.98	49.09	48.89	-
hours	1175.45	1178.08	1173.31	-
minutes	70527.28	70684.64	70398.56	-
seconds	4231637	4241078	4223914	-

Table B-5. H-19 Tracer/Chaser/System Parameters - Round 3 Transport Input Parameter Sheet (continued)

Parameter	Value	Value	Value	Value
INJECTION WELL	H-19b3	H-19b6	H-19b7	H-19b7
TRACER NAME	2,3,4,5-TFBA	2,4,6-TCBA	2,3,6-TFBA	Iodide

TRACER DATA FILES (k)				
Raw Data	H19N3Z12	H19N3Z12	H19N3Z12	H19N3Z12
Confidence Interval Data	RH19N3B3	RH19N3B6	RH19N3B7	RH19N3HP (l) RH19N3IC (m) RH19N3TI (n)

(a) 2,3,6-TFBA and NaI were injected into H-19b7 simultaneously followed by the injection of chaser fluid and, therefore, the chaser, system, and duration of test components information is identical for both tracers

(b) the aqueous diffusion coefficients were calculated using the Hayduk and Laudie method described by Tucker and Nelken (1982); this is the same method used by Benson and Bowman (1996) and Bowman and Gibbens (1992). Also see Walter (1982) and Skagus and Neretnicks (1986). This calculation is for low ionic strength water. Thus the actual diffusion coefficients that are aqueous diffusion coefficients may be lower than these calculated values (e.g., Carey et al., 1995). (The use of aqueous diffusion coefficients too high for numerical simulations will result in estimated matrix block lengths that are too large. This is conservative for estimates of parameters for WIPP.)

(c) the uncertainty in the tracer and chaser volumes is estimated to be ±4%

(d) calculated as the injection volume divided by the injection time

(e) the injections for Round 3 were only into the full thickness of the Culebra; no upper or lower zone injections were performed

(f) calculated as the borehole volume minus the tool volume

(g) calculated as the downhole volume plus the tubing volume

(h) time for injection of tracer and chaser

(i) time from the end of chaser injection to the end of pumping (during which the withdrawal well was pumping at its final rate of 0.16 L/s) minus the time for chaser to travel down the injection well

(j) total duration of the test from the start of injection to the end of pumping minus the time for chaser to travel down the injection well

(k) all data files have the extension .DAT; for a description of raw data and confidence interval data see Appendix C

(l) iodide data from HPLC analysis method

(m) iodide data from IC analysis method

(n) iodide data from the two analysis methods (IC and HPLC) sorted together chronologically

Table B-6. H-19 Tracer/Chaser/System Parameters - 1995 4-Well Test Transport Input Parameter Sheet

Parameter	Value	Value	Value	Value	Value	Value
INJECTION WELL	H-19b0	H-19b0	H-19b0	H-19b2	H-19b3	H-19b4
INJECTION TYPE	SWIW	SWIW	SWIW	Convergent	Convergent	Convergent
INJECTION DATE	06/15/95	06/15/95	06/15/95	06/19/95	06/20/95	06/19/95
TRACER NAME	brine (a)	2,4-DCBA (a)	o-TFMBA (a)	2,3-DFBA	2,3,4,5-TFBA	2,6-DFBA
AQUEOUS DIFFUSION COEFFICIENT (m^2/s) (b)	na	7.3E-10	7.4E-10	8.2E-10	7.9E-10	8.2E-10

TRACER INJECTION						
Calculated Mass Injected (kg)	na	4.9	1.9	1.795	2.015	1.870
Concentration (mg/L)	na	4938	1906	7303	7769	7060
Volume (c)						
liters	76	997	1005	246	259	265
cubic meters	0.076	0.997	1.005	0.246	0.259	0.265
Injection Time (d)						
minutes	8.0	127.0	132.5	36.8	28.0	33.4
seconds	480	7620	7950	2208	1680	2004
Injection Rate (e)						
L/s	0.158	0.131	0.126	0.111	0.154	0.132
m^3/s	1.58E-04	1.31E-04	1.26E-04	1.11E-04	1.54E-04	1.32E-04

CHASER INJECTION						
Volume (c) (f)						
liters	-	2020	1015	246	206	255
cubic meters	-	2.020	1.015	0.246	0.206	0.255
Injection Time (d)						
minutes	-	263.0	130.5	36.5	25.0	39.0
seconds	-	15780	7830	2190	1500	2340
Injection Rate (e)						
L/s	-	0.128	0.130	0.112	0.137	0.109
m^3/s	-	1.28E-04	1.30E-04	1.12E-04	1.37E-04	1.09E-04

Table B-6. H-19 Tracer/Chaser/System Parameters - 1995 4-Well Test
Transport Input Parameter Sheet (continued)

Parameter	Value	Value	Value	Value	Value	Value
INJECTION WELL	H-19b0	H-19b0	H-19b0	H-19b2	H-19b3	H-19b4
TRACER NAME	brine	2,4-DCBA	o-TFMBA	2,3-DFBA	2,3,4,5-TFBA	2,6-DFBA

SYSTEM INFORMATION						
Thickness (m) (g)	-	-(a)	7.41	7.86	9.08	7.44
Borehole Volume (L)	-	-	271.20	140.80	158.06	134.24
Tool Volume (L)	-	-	165.40	61.50	68.81	58.20
Downhole Volume (L) (h)	-	-	105.80	79.30	89.25	76.04
Tubing Volume						
gallons	-	-	4.518	4.958	4.420	4.605
liters	-	-	17.10	18.77	16.73	17.43
Total System Vol. (L) (i)						
liters	-	-	122.90	98.07	105.98	93.47
cubic meters	-	-	0.1229	0.0981	0.1060	0.0935

DURATION OF TEST COMPONENTS						
Total Injection Time (j)						
days	-	0.27	0.18	0.05	0.04	0.05
hours	-	6.50	4.38	1.22	0.88	1.21
minutes	-	390.00	263.00	73.30	53.00	72.40
seconds	-	23400	15780	4398	3180	4344
Pause Length for SWIW Test (k)						
days	-	0.73	0.73	-	-	-
hours	-	17.60	17.60	-	-	-
minutes	-	1056.03	1056.03	-	-	-
seconds	-	63362	63362	-	-	-
Pumping Duration (l)						
days	-	41.83	41.83	38.41	38.15	38.35
hours	-	1004.00	1004.00	921.95	915.66	920.32
minutes	-	60240.00	60240.00	55316.81	54939.54	55219.10
seconds	-	3614400	3614400	3319009	3296372	3313146
Total Test Duration (m)						
days	-	42.84	42.75	38.47	38.19	38.40
hours	-	1028.10	1025.98	923.17	916.54	921.53
minutes	-	61686.03	61559.03	55390.14	54992.54	55291.52
seconds	-	3701162	3693542	3323408	3299552	3317491

Table B-6. H-19 Tracer/Chaser/System Parameters - 1995 4-Well Test Transport Input Parameter Sheet (continued)

Parameter	Value	Value	Value	Value	Value	Value
INJECTION WELL	H-19b0	H-19b0	H-19b0	H-19b2	H-19b3	H-19b4
TRACER NAME	brine	2,4-DCBA	o-TFMBA	2,3-DFBA	2,3,4,5-TFBA	2,6-DFBA

TRACER DATA FILES (n)						
Raw Data		H194SY22	H194SY22	H194CY22	H194CY22	H194CY22
Confidence Interval Data		RH194ST1	RH194ST2	RH194CB2	RH194CB3	RH194CB4

(a) the single-well test in H-19b0 consisted of four injections; a slug of Culebra water followed by tracer slug 1 consisting of 2,4-DCBA solution followed by tracer slug 2 consisting of o-TFMBA solution followed by a chaser slug of Culebra water; therefore, system information is identical for all injections into H-19b0

(b) the aqueous diffusion coefficients were calculated using the Hayduk and Laudie method described by Tucker and Nelken (1982); this is the same method used by Benson and Bowman (1996) and Bowman and Gibbens (1992). Also see Walter (1982). This calculation is for low ionic strength water. Thus the actual aqueous diffusion coefficients may be lower than these calculated values (e.g., Carey et al., 1995). (The use of aqueous diffusion coefficients that are too high for numerical simulations will result in estimated matrix block lengths that are too large. This is conservative for estimates of parameters for WIPP.)

(c) the uncertainty in the volumes is estimated to be ±6%

(d) calculated from the injection start and stop times reported in the H-19 Field Logbook

(e) calculated as the injection volume divided by the injection time

(f) for the first tracer slug (2,4-DCBA), the chaser volume includes the injected volume of tracer slug 2 (o-TFMBA) and the injected volume of untraced Culebra water; for the second tracer injected, the chaser volume includes the injected volume of untraced Culebra water

(g) thickness from the bottom of the packer seal to the shale basket for H-19b2, H-19b3, and H-19b4 and the thickness of the Culebra for H-19b0

(h) calculated as the borehole volume minus the tool volume

(i) calculated as the downhole volume plus the tubing volume

(j) time for injection of tracer(s) and chaser; for the SWIW test, the second tracer was considered part of the chaser for the first tracer

(k) time from the end of chaser injection to the start of pumping minus the time for chaser to travel down the injection well

(l) time from the start of pumping to the end of pumping for the SWIW tracers and the time from the end of chaser injection to the end of pumping minus the time for chaser to travel down the injection well for the convergent flow tracers

(m) total duration of the test from the start of injection to the end of pumping minus the time for chaser to travel down the injection well; includes the pause time for the SWIW tracers

(n) all data files have the extension .DAT; for a description of raw data and confidence interval data see Appendix C

Table B-7. H-11 Fixed Parameters Transport Input Parameter Sheet

Parameter	Value
Well Inner Radius (m)	
H-11b1 (Pumping Well)	0.065
H-11b2 (Injection Well)	0.069
H-11b3 (Injection Well)	0.091
H-11b4 (Injection Well)	0.060
Average Pumping Rate (a)	
1988 Test	
gpm	6.0
L/s	0.38
m^3/s	3.8E-04
1996 Test - SWIW	
gpm	3.55
L/s	0.224
m^3/s	2.24E-04
1996 Test - Initial Rate	
gpm	3.53
L/s	0.223
m^3/s	2.23E-04
1996 Test - Increased Rate	
gpm	5.96
L/s	0.376
m^3/s	3.76E-04
Tracer Injection Start Times	
1988 Test	
H-11b2 (PFBA)	11:00 05/14/88
H-11b3 (m-TFMBA)	13:30 05/14/88
H-11b4 (o-TFMBA)	16:00 05/14/88
1996 Test - SWIW	
H-11b1 (2,4-DCBA)	09:41 02/06/96
H-11b1 (3,4-DFBA)	11:57 02/06/96
1996 Test - Round 1	
H-11b2 (2,6-DFBA)	09:57:40 02/15/96
H-11b3 (2,3,4,5-TFBA)	14:17:38 02/15/96
1996 Test - Round 2	
H-11b2 (p-TFMBA)	15:03:40 03/14/96
H-11b3 (2,5-DFBA & NaI)	15:42 03/13/96

Parameter	Value
Well Spacing (b)	
H-11b2 to H-11b1	
feet	70.4
meters	21.5
H-11b3 to H-11b1	
feet	68.5
meters	20.9
H-11b4 to H-11b1	
feet	140.8
meters	42.9
Culebra Thickness	
H-11b1	
feet	> 21
meters	> 6.4
H-11b2	
feet	> or = 23.0
meters	> or = 7.0
H-11b3	
feet	> or = 23.8
meters	> or = 7.3
H-11b4	
feet	24.9
meters	7.6
Average Thickness	
Full Thickness (m)	7.4
Upper Zone - Unit 1	
feet	9.8
meters	3.0
Lower Zone - Units 2, 3, 4 (m)	4.4
Hydropad Transmissivity (m2/s)	4.70E-05
Hydraulic Conductivity (m/s)	
assuming full thickness	6.35E-06
assuming lower zone thickness	1.07E-05
Diffusive Tortuosity	0.11
Diffusive Porosity	0.16

(a) the uncertainty in the average pumping rate is -0.0025 to +0.0075 L/s for the 1988 test and is estimated to be ±4% for the 1996 test

(b) the uncertainty in the well spacing is estimated to be no more than ±1.5 m

Table B-8. H-11 Tracer/Chaser/System Parameters - SWIW and Round 1 Transport Input Parameter Sheet

Parameter	Value	Value	Value	Value
INJECTION WELL	H-11b1	H-11b1	H-11b2	H-11b3
TEST TYPE	SWIW	SWIW	Convergent	Convergent
INJECTION DATE	02/06/96	02/06/96	02/15/96	02/15/96
TRACER NAME	2,4-DCBA (a)	3,4-DFBA (a)	2,6-DFBA	2,3,4,5-TFBA
AQUEOUS DIFFUSION COEFFICIENT (m^2/s) (b)	7.3E-10	8.2E-10	8.2E-10	7.9E-10

TRACER INJECTION				
Calculated Mass Injected (kg)	8.035	5.050	1.962	2.049
Concentration (mg/L)	8071	5020	10381	10851
Volume (c)				
liters	996	1010	189	189
cubic meters	0.996	1.010	0.189	0.189
Injection Time				
minutes	136.0	133.0	46.2	32.9
seconds	8160	7980	2772	1974
Injection Rate (d)				
L/s	0.122	0.127	0.0682	0.0957
m^3/s	1.22E-04	1.27E-04	6.82E-05	9.57E-05

CHASER INJECTION				
Volume (c) (e)				
liters	1920	910	213	372
cubic meters	1.920	0.910	0.213	0.372
Injection Time (f)				
minutes	257.0	124.0	59.2	63.5
seconds	15420	7440	3552	3810
Injection Rate (d)				
L/s	0.125	0.122	0.0600	0.0976
m^3/s	1.25E-04	1.22E-04	6.00E-05	9.76E-05

SYSTEM INFORMATION				
Thickness (g)				
feet	- (a)	25.22	28.67	24.23
meters	-	7.69	8.74	7.39
Borehole Volume (L)	-	107	141.3	196.9
Tool Volume				
gallons	-	12.6	16.99	15.05
liters	-	47.8	64.31	56.95

Table B-8. H-11 Tracer/Chaser/System Parameters - SWIW and Round 1 Transport Input Parameter Sheet (continued)

Parameter	Value	Value	Value	Value
INJECTION WELL	H-11b1	H-11b1	H-11b2	H-11b3
TRACER NAME	2,4-DCBA	3,4-DFBA	2,6-DFBA	2,3,4,5-TFBA
SYSTEM INFORMATION (continued)				
Downhole Volume (L) [(h)]	-	59.2	76.99	140.0
Tubing Volume				
gallons	-	4.31	4.359	4.315
liters	-	16.3	16.50	16.33
Total System Vol. (L) [(i)]				
liters	-	75.6	93.49	156.3
cubic meters	-	7.56E-02	9.349E-02	1.563E-01
DURATION OF TEST COMPONENTS				
Total Injection Time [(j)]				
days	0.27	0.18	0.07	0.07
hours	6.55	4.28	1.76	1.61
minutes	393.00	257.00	105.30	96.40
seconds	23580	15420	6318	5784
Pause Length for SWIW Test [(k)]				
days	0.74	0.74	-	-
hours	17.66	17.66	-	-
minutes	1059.74	1059.74	-	-
seconds	63584	63584	-	-
Pumping Duration at Initial Rateof 0.22 L/s [(l)]				
days	33.21	33.21	25.13	24.95
hours	797.00	797.00	603.03	598.85
minutes	47820.00	47820.00	36181.73	35931.26
seconds	2869200	2869200	2170904	2155876
Pumping Duration at Increased Rate of 0.38 L/s [(m)]				
days	15.70	15.70	15.70	15.70
hours	376.72	376.72	376.72	376.72
minutes	22603.00	22603.00	22603.00	22603.00
seconds	1356180	1356180	1356180	1356180
Total Test Duration [(n)]				
days	49.91	49.82	40.90	40.72
hours	1197.93	1195.66	981.50	977.18
minutes	71875.74	71739.74	58890.06	58630.63
seconds	4312544	4304384	3533404	3517838

Table B-8. H-11 Tracer/Chaser/System Parameters - SWIW and Round 1 Transport Input Parameter Sheet (continued)

Parameter	Value	Value	Value	Value
INJECTION WELL	H-11b1	H-11b1	H-11b2	H-11b3
TRACER NAME	2,4-DCBA	3,4-DFBA	2,6-DFBA	2,3,4,5-TFBA

TRACER DATA FILES (o)				
Raw Data	H11S1Y15	H11S1Y15	H11N1Y15	H11N1Y15
Confidence Interval Data	RH11S1T1	RH11S1T2	RH11N1B2	RH11N1B3

(a) the single-well test in H-11b1 consisted of three injections; tracer slug 1 consisting of 2,4-DCBA solution followed by tracer slug 2 consisting of 3,4-DFBA solution followed by a chaser slug consisting of Culebra water; therefore, the system information is identical for both tracers

(b) the aqueous diffusion coefficients were calculated using the Hayduk and Laudie method described by Tucker and Nelken (1982); this is the same method used by Benson and Bowman (1996) and Bowman and Gibbens (1992). Also see Walter (1982). This calculation is for low ionic strength water. Thus the actual aqueous diffusion coefficients may be lower than these calculated values (e.g., Carey et al., 1995). (The use of aqueous diffusion coefficients that are too high for numerical simulations will result in estimated matrix block lengths that are too large. This is conservative for estimates of parameters for WIPP.)

(c) the uncertainty in the volumes is estimated to be ±4%

(d) calculated as the injection volume divided by the injection time

(e) for the first tracer injected during the SWIW test, the chaser volume includes the volume of the second tracer injected and the volume of untraced Culebra water injected

(f) for the first tracer injected during the SWIW test, the chaser injection time includes the time to inject the second tracer and the time to inject the untraced Culebra water

(g) the thickness from the bottom packer seal to the base of Culebra for H-11b1 and the thickness from the bottom packer seal to the shale basket for H-11b2 and H-11b3

(h) calculated as the borehole volume minus the tool volume

(i) calculated as the downhole volume plus the tubing volume

(j) time for injection of tracer(s) and chaser; for the SWIW test, the second tracer was considered part of the chaser for the first tracer

(k) time from the end of chaser injection to the start of pumping minus the time for chaser to travel down the injection well

(l) for the SWIW test tracers, this is the time from the start of pumping to the pumping rate increase on 3/11/96 (during which the withdrawal well was pumping at its initial rate of 0.22 L/s); for the round 1 tracers, this is the time from the end of chaser injection to the pumping rate increase on 3/11/96 (during which the withdrawal well was pumping at its initial rate of 0.22 L/s) minus the time for chaser to travel down the injection well

(m) time from the pumping rate increase on 03/11/96 to the end of pumping on 03/27/96 (during which the withdrawal well was pumping at it final rate of 0.38 L/s)

(n) total duration of the test from the start of injection to the end of pumping minus the time for chaser to travel down the injection well; includes the pause time for the SWIW test tracers

(o) all data files have the extension .DAT; for a description of raw data and confidence interval data see Appendix C

Table B-9. H-11 Tracer/Chaser/System Parameters - Round 2
Transport Input Parameter Sheet

Parameters	Value	Value	Value
INJECTION WELL	H-11b2	H-11b3	H-11b3
TEST TYPE	Convergent Flow	Convergent Flow	Convergent Flow
INJECTION DATE	03/14/96	03/13/96	03/13/96
TRACER NAME	p-TFMBA	2,5-DFBA (a)	Iodide (a)
AQUEOUS DIFFUSION COEFFICIENT (m^2/s) (b)	7.4E-10	8.2E-10	18.0E-10

TRACER INJECTION			
Calculated Mass Injected (kg) (c)	2.024	1.959	1.972
Concentration (mg/L)	10779	10300	10872
Volume (d)			
liters	189	190	- (a)
cubic meters	0.189	0.190	-
Injection Time			
minutes	43.5	33.3	-
seconds	2610	1998	-
Injection Rate (e)			
L/s	0.0723	0.0952	-
m^3/s	7.23E-05	9.52E-05	-

CHASER INJECTION			
Volume (d)			
liters	213	373	- (a)
cubic meters	0.213	0.373	-
Injection Time			
minutes	56.8	64.0	-
seconds	3408	3840	-
Injection Rate (e)			
L/s	0.0624	0.0971	-
m^3/s	6.24E-05	9.71E-05	-

Table B-9. H-11 Tracer/Chaser/System Parameters - Round 2 Transport Input Parameter Sheet (continued)

Parameters	Value	Value	Value
INJECTION WELL	H-11b2	H-11b3	H-11b3
TRACER NAME	p-TFMBA	2,5-DFBA	Iodide

SYSTEM INFORMATION			
Thickness			
feet	28.67	24.23	- (a)
meters	8.74	7.39	-
Borehole Volume (L)	141.3	196.9	-
Tool Volume			
gallons	16.99	15.05	-
liters	64.31	56.95	-
Downhole Volume (L) (f)	76.99	140.0	-
Tubing Volume			
gallons	4.359	4.315	-
liters	16.50	16.33	-
Total System Volume (L) (g)			
liters	93.49	156.3	-
cubic meters	9.349E-02	1.563E-01	-

DURATION OF TEST COMPONENTS			
Total Injection Time (h)			
days	0.07	0.07	- (a)
hours	1.67	1.62	-
minutes	100.30	97.30	-
seconds	6018	5838	-
Pumping Duration at Increased Rate (0.38 L/s) (i)			
days	12.61	13.59	-
hours	302.74	326.15	-
minutes	18164.31	19568.85	-
seconds	1089858.6	1174131	-
Total Test Duration (j)			
days	12.68	13.66	-
hours	304.41	327.77	-
minutes	18264.64	19666.18	-
seconds	1095878.4	1179970.8	-

Table B-9. H-11 Tracer/Chaser/System Parameters - Round 2 Transport Input Parameter Sheet (continued)

Parameters	Value	Value	Value
INJECTION WELL	H-11b2	H-11b3	H-11b3
TRACER NAME	p-TFMBA	2,5-DFBA	Iodide

TRACER DATA FILES [k]			
Raw Data	H11N2Y15	H11N2Y15	H11N2Y15
Confidence Interval Data	RH11N2B2	RH11N2B3	RH11N2IO

(a) 2,5-DFBA and NaI were injected into H-11b3 simultaneously followed by the injection of chaser fluid and, therefore, the chaser, system, and test component information is identical for both tracers

(b) the aqueous diffusion coefficients were calculated using the Hayduk and Laudie method described by Tucker and Nelken (1982); this is the same method used by Benson and Bowman (1996) and Bowman and Gibbens (1992). Also see Walter (1982) and Skagus and Neretnicks (1986). This calculation is for low ionic strength water. Thus the actual diffusion coefficients that are aqueous diffusion coefficients may be lower than these calculated values (e.g., Carey et al., 1995). (The use of aqueous diffusion coefficients too high for numerical simulations will result in estimated matrix block lengths that are too large. This is conservative for estimates of parameters for WIPP.)

(c) the source of the mass calculations is spreadsheet MASSINJ.XLS found in ERMS # 237439

(d) the uncertainty in the injected volumes is estimated to be ±4%

(e) calculated as the injection volume divided by the injection time

(f) calculated as the borehole volume minus the tool volume

(g) calculated as the downhole volume plus the tubing volume

(h) time for injection of tracer(s) and chaser

(i) time from the end of chaser injection to the end of pumping on 03/27/96 minus the time for chaser to travel down the injection well

(j) total duration of the test from the start of injection to the end of pumping minus the time for chaser to travel down the injection well

(k) all data files have the extension .DAT; for a description of raw data and confidence interval data see Appendix C

Table B-10. H-11 Tracer/Chaser/System Parameters - 1988 Test Transport Input Parameter Sheet

Parameter	Value	Value	Value
INJECTION WELL	H-11b2	H-11b3	H-11b4
INJECTION TYPE	Convergent Flow	Convergent Flow	Convergent Flow
INJECTION DATE	05/14/88	05/14/88	05/14/88
TRACER NAME	PFBA	m-TFMBA	o-TFMBA
AQUEOUS DIFFUSION COEFFICIENT (m^2/s) (a)	7.7E-10	7.4E-10	7.4E-10

TRACER INJECTION			
Calculated Mass Injected (kg)	1.991	1.891	2.889
Concentration (g/L)	12.5	10.0	15.8
Volume			
liters	189	189	189
cubic meters	0.189	0.189	0.189
Injection Time			
minutes	43	32	24
seconds	2580	1920	1440
Injection Rate (b)			
L/s	0.0731	0.0985	0.131
m^3/s	7.31E-05	9.85E-05	1.31E-04

CHASER INJECTION			
Volume			
liters	188	373	187
cubic meters	0.188	0.373	0.187
Injection Time			
minutes	51	62	39
seconds	3060	3720	2340
Injection Rate (b)			
L/s	0.0613	0.100	0.0801
m^3/s	6.13E-05	1.00E-04	8.01E-05

Table B-10. H-11 Tracer/Chaser/System Parameters - 1988 Test Transport Input Parameter Sheet (continued)

Parameter	Value	Value	Value
INJECTION WELL	H-11b2	H-11b3	H-11b4
TRACER NAME	PFBA	m-TFMBA	o-TFMBA
SYSTEM INFORMATION			
Tubing Volume (L)	12	12	12
Downhole Volume (L) (c)	49	138	32
Total System Volume			
liters	61	150	44
cubic meters	0.061	0.150	0.044
DURATION OF TEST COMPONENTS			
Total Injection Time (d)			
days	0.07	0.07	0.04
hours	1.57	1.57	1.05
minutes	94	94	63
seconds	5640	5640	3780
Pumping Duration (e)			
days	53.84	53.74	53.66
hours	1292.27	1289.71	1287.85
minutes	77536.08	77382.50	77271.17
seconds	4652165	4642950	4636270
Total Test Duration (f)			
days	53.91	53.80	53.70
hours	1293.83	1291.28	1288.90
minutes	77630.08	77476.50	77334.17
seconds	4657805	4648590	4640050
TRACER DATA FILES (g)			
Raw Data	H1188Y15	H1188Y15	H1188Y15
Confidence Interval Data	RH1188B2	RH1188B3	RH1188B4

Table B-10. H-11 Tracer/Chaser/System Parameters - 1988 Test Transport Input Parameter Sheet (continued)

(a) the aqueous diffusion coefficients were calculated using the Hayduk and Laudie method described by Tucker and Nelken (1982); this is the same method used by Benson and Bowman (1996) and Bowman and Gibbens (1992). Also see Walter (1982). This calculation is for low ionic strength water. Thus the actual aqueous diffusion coefficients may be lower than these calculated values (e.g., Carey et al., 1995). (The use of aqueous diffusion coefficients that are too high for numerical simulations will result in estimated matrix block lengths that are too large. This is conservative for estimates of parameters for WIPP.)

(b) calculated as the injection volume divided by the injection time

(c) calculated as the total system volume minus the tubing volume

(d) time for injection of tracer and chaser

(e) time from the end of chaser injection to the end of pumping minus the time for chaser to travel down the injection well

(f) total duration of the test from the start of injection to the end of pumping minus the time for chaser to travel down the injection well

(g) all data files have the extension .DAT; for a description of raw data and confidence interval data see Appendix C

Table B-11. H-6 Fixed Parameters
Transport Input Parameter Sheet

Parameter	Value
Well Inner Radius (m)	
H-6a (Injection Well)	0.0603
H-6b (Injection Well)	0.0603
H-6c (Pumping Well)	0.0629
Average Pumping Rate	
gpm	16.5
L/s	1.04
m^3/s	1.04E-03
Tracer Injection Start Times	
H-6a Test #1 (m-TFMBA)	17:36 08/23/81
H-6b Test #1 (PFBA)	17:36 08/23/81
H-6b Test #2 (p-FB)	13:00 09/02/81
Well Spacing	
H-6a to H-6c	
feet	98.09
meters	29.90
H-6b to H-6c	
feet	98.00
meters	29.87

Parameter	Value
Culebra Thickness (m)	
H-6a	
feet	23
meters	7.0
H-6b	
feet	23
meters	7.0
H-6c	
feet	23
meters	7.0
Average Thickness for Model	
Full Thickness (m)	7.0
Upper Zone - Unit 1	
feet	9.8
meters	3.0
Lower Zone - Units 2, 3,4 (m)	4.0
Hydropad Transmissivity (m^2/s)	4.00E-05
Hydraulic Conductivity (m/s)	
assuming full thickness	5.71E-06
assuming lower zone thickness	1.00E-05
Diffusive Tortuosity	0.11
Diffusive Porosity	0.15

Table B-12. H-6 1981 Tests #1 and #2 Tracer/Chaser/System Parameters Transport Input Parameter Sheet

Parameter	Value	Value	Value
INJECTION WELL	H-6a	H-6b	H-6b
INJECTION TYPE	Convergent	Convergent	Convergent
TEST NUMBER	Test #1	Test #1	Test #2
INJECTION DATE	08/23/81	08/23/81	09/02/81
TRACER NAME	m-TFMBA	PFBA	p-FB
AQUEOUS DIFFUSION COEFFICIENT (m^2/s)	7.4E-10 (a)	7.7E-10 (a)	9.3E-10

TRACER INJECTION			
Mass (g)	953	894	569
Concentration (mg/L)	9530	8940	5690
Volume			
liters	100	100	100
cubic meters	0.100	0.100	0.100
Injection Time			
minutes	10	10	13
seconds	600	600	780
Injection Rate (b)			
L/s	0.167	0.167	0.128
m^3/s	1.67E-04	1.67E-04	1.28E-04

CHASER INJECTION			
Volume			
liters	100	100	100
cubic meters	0.100	0.100	0.100
Injection Time			
minutes	19	19	13
seconds	1140	1140	780
Injection Rate (b)			
L/s	0.0877	0.0877	0.128
m^3/s	8.77E-05	8.77E-05	1.28E-04

Table B-12. H-6 1981 Tests #1 and #2 Tracer/Chaser/System Parameters Transport Input Parameter Sheet (continued)

Parameter	Value	Value	Value
INJECTION WELL	H-6a	H-6b (Test #1)	H-6b (Test #2)
TRACER NAME	m-TFMBA	PFBA	p-FB

SYSTEM INFORMATION			
Tool Volume (L) [(c)]	0	0	0
Tubing Volume (L)	13	14	14
Downhole Volume (L)	94	80	80
Total System Vol. (L) [(d)]			
liters	108	94	94
cubic meters	1.08E-01	9.4E-02	9.4E-02

DURATION OF TEST COMPONENTS			
Total Injection Time [(e)]			
days	0.02	0.02	0.02
hours	0.48	0.48	0.43
minutes	29	29	26
seconds	1740	1740	1560
Pumping Duration [(f)]			
days	18.53	18.53	8.73
hours	444.73	444.75	209.45
minutes	26683.60	26684.74	12566.97
seconds	1601016	1601084	754018
Total Test Duration [(g)]			
days	18.55	18.55	8.75
hours	445.21	445.23	209.88
minutes	26712.60	26713.74	12592.97
seconds	1602756	1602824	755578

TRACER DATA FILES [(h)]			
Raw Data	H6810624	H6810624	H6810624
Confidence Interval Data	RH681A1	RH681B1	RH681B2

Table B-12. H-6 1981 Tests #1 and #2 Tracer/Chaser/System Parameters Transport Input Parameter Sheet (continued)

(a) the aqueous diffusion coefficients were calculated using the Hayduk and Laudie method described by Tucker and Nelken (1982); this is the same method used by Benson and Bowman (1996) and Bowman and Gibbens (1992). Also see Walter (1982). This calculation is for low ionic strength water. Thus the actual aqueous diffusion coefficients may be lower than these calculated values (e.g., Carey et al., 1995). (The use of aqueous diffusion coefficients that are too high for numerical simulations will result in estimated matrix block lengths that are too large. This is conservative for estimates of parameters for WIPP.)

(b) calculated as the injection volume divided by the injection time

(c) no tool was used for injection of tracers during H-6 convergent flow tracer tests #1 and #2 (Hydrogeochem, 1985)

(d) calculated as tubing volume plus downhole volume

(e) time for injection of tracer and chaser

(f) time from the end of chaser injection to the end of pumping minus the time for chaser to travel down the injection well

(g) total duration of the test from the start of tracer injection to the end of pumping minus the time for chaser to travel down the injection well

(h) all data files have the extension .DAT; for a description of raw data and confidence interval data see Appendix C

Table B-13. H-3 Fixed Parameters Transport Input Parameter Sheet

Parameter	Value
Well Inner Radius (m)	
H-3b1 (Injection Well)	0.0752
H-3b2 (Injection Well)	0.0603
H-3b3 (Pumping Well)	0.0603
Average Pumping Rate	
Anisotropy Test	
gpm	4.0
L/s	0.25
m^3/s	2.5E-04
Tracer Test	
gpm	3.0
L/s	0.19
m^3/s	1.9E-04
Tracer Injection Start Times	
H-3b1 (m-TFMBA)	13:55 05/09/84
H-3b2 (PFBA)	12:45 05/09/84
Well Spacing	
H-3b1 to H-3b3	
feet	100.6
meters	30.66
H-3b2 to H-3b3	
feet	87.9
meters	26.79

Parameter	Value
Culebra Thickness (m)	
H-3b1	
feet	24
meters	7.3
H-3b2	
feet	24
meters	7.3
H-3b3	
feet	23
meters	7.0
Average Thickness for Model	
Full Thickness (m)	7.2
Upper Zone - Unit 1	
feet	9.8
meters	3.0
Lower Zone - Units 2, 3,4 (m)	4.2
Hydropad Transmissivity (m^2/s)	2.5E-06
Hydraulic Conductivity (m/s)	
assuming full thickness	3.47E-07
assuming lower zone thickness	5.95E-07
Diffusive Tortuosity	0.11
Diffusive Porosity	0.20

Table B-14. H-3 1984 Test Tracer/Chaser/System Parameters
Transport Input Parameter Sheet

Parameter	Value	Value
INJECTION WELL	H-3b1	H-3b2
INJECTION TYPE	Convergent	Convergent
INJECTION DATE	05/09/84	05/09/84
TRACER NAME	m-TFMBA	PFBA
AQUEOUS DIFFUSION COEFFICIENT (m^2/s) (a)	7.4E-10	7.7E-10

TRACER INJECTION		
Mass (kg)	1	1
Concentration (mg/L)	13210	26420
Volume		
gallons	20	10
liters	75.7	37.85
cubic meters	0.076	0.038
Injection Time (b)		
minutes	20	10
seconds	1200	600
Injection Rate (c)		
L/s	0.0631	0.0631
m^3/s	6.31E-05	6.31E-05

CHASER INJECTION		
Volume		
gallons	80	50
liters	303	189
cubic meters	0.303	0.189
Injection Time (d)		
minutes	75	50
seconds	4500	3000
Injection Rate (c)		
L/s	0.07	0.06
m^3/s	6.73E-05	6.31E-05

Table B-14. H-3 1984 Test Tracer/Chaser/System Parameters Transport Input Parameter Sheet (continued)

Parameter	Value	Value
INJECTION WELL	H-3b1	H-3b2
TRACER NAME	m-TFMBA	PFBA
SYSTEM INFORMATION		
Tool Volume (L) (e)	0	0
Tubing Volume (L)	12	15
Downhole Volume (L)	258	98
Total System Volume (f)		
liters	270	113
cubic meters	2.70E-01	1.13E-01
DURATION OF TEST COMPONENTS		
Total Injection Time (g)		
days	0.07	0.04
hours	1.58	1.00
minutes	95	60
seconds	5700	3600
Pumping Duration (h)		
days	33.83	33.92
hours	812.01	814.02
minutes	48720.43	48841.22
seconds	2923226	2930473
Total Test Duration (i)		
days	33.90	33.96
hours	813.59	815.02
minutes	48815.43	48901.22
seconds	2928926	2934073
TRACER DATA FILES (j)		
Raw Data	H3840903	H3840903
Confidence Interval Data	RH384B1	RH384B2

Table B-14. H-3 1984 Test Tracer/Chaser/System Parameters Transport Input Parameter Sheet (continued)

(a) the aqueous diffusion coefficients were calculated using the Hayduk and Laudie method described by Tucker and Nelken (1982); this is the same method used by Benson and Bowman (1996) and Bowman and Gibbens (1992). Also see Walter (1982). This calculation is for low ionic strength water. Thus the actual aqueous diffusion coefficients may be lower than these calculated values (e.g., Carey et al., 1995). (The use of aqueous diffusion coefficients that are too high for numerical simulations will result in estimated matrix block lengths that are too large. This is conservative for estimates of parameters for WIPP.)

(b) calculated as the total injection time times the ratio of the tracer volume to total volume

(c) calculated as the injection volume divided by the injection time

(d) calculated as the total injection time times the ratio of the chaser volume to total volume

(e) no tool was used for injection of tracers during the H-3 tracer test

(f) calculated as tubing volume plus downhole volume

(g) time for injection of tracer and chaser

(h) time from the end of chaser injection to the end of pumping minus the time for chaser to travel down the injection well

(i) total duration of the test from the start of tracer injection to the end of pumping minus the time for chaser to travel down the injection well

(j) all data files have the extension .DAT; for a description of raw data and confidence interval data see Appendix C

B.4 References for Text and TIPS

Benson, C.F., and R.S. Bowman. 1996. "Erratum: Tri- and Tetrafluorobenzoates as Nonreactive Tracers in Soil and Groundwater," *Soil Science Society of America Journal.* Vol. 60, no. 6, 1780.

Bowman, R.S., and J.F. Gibbens. 1992. "Difluorobenzoates as Nonreactive Tracers in Soil and Ground Water," *Ground Water.* Vol. 30, no. 1, 8-14.

Carey, A.E., S.W. Wheatcraft, R.J. Glass, and J.P. O'Rourke. 1995. "Non-Fickian Ionic Diffusion Across High-Concentration Gradients," *Water Resources Research.* Vol. 31, no. 9, 2213-2218.

Hydro Geo Chem, Inc. 1985. *WIPP Hydrology Program, Waste Isolation Pilot Plant, SENM, Hydrologic Data Report #1.* SAND85-7206. Albuquerque, NM: Sandia National Laboratories. 12, 150-153.

Jones, T.L., V.A. Kelley, J.F. Pickens, D.T. Upton, R.L. Beauheim, and P.B. Davies. 1992. *Integration of Interpretation Results of Tracer Tests Performed in the Culebra Dolomite at the Waste Isolation Pilot Plant Site.* SAND92-1579. Albuquerque, NM: Sandia National Laboratories.

Lerman, A. 1979. *Geochemical Processes: Water and Sediment Environments.* New York, NY: John Wiley & Sons.

Skagius, K., and I. Neretnieks. 1986. "Porosities and Diffusivities of Some Nonsorbing Species in Crystalline Rocks," *Water Resources Research.* Vol. 22, no. 3, 389-398.

Tucker, W.A., and L.H. Nelken. 1982. "Diffusion Coefficients in Air and Water," *Handbook of Chemical Property Estimation Methods: Environmental Behavior of Organic Compounds.* W.J. Lyman, W.R. Reehl, and D.H. Rosenblatt. New York, NY: McGraw-Hill Book Co. 17-1 through 17-25.

Walter, G.R. 1982. *Theoretical and Experimental Determination of Matrix Diffusion and Related Solute Transport Properties of Fractured Tuffs from the Nevada Test Site.* LA-9471-MS. Los Alamos, NM: Los Alamos National Laboratories.

Appendix C
WIPP Tracer-Test Data

By Toya L. Jones[1], Irene M. Farnham[2],
Lucy C. Meigs[3], and Joanna B. Ogintz[1,4]

C.1 Introduction

The purpose of this appendix is to present the observed data for the WIPP tracer tests. Tracer testing at the WIPP can be divided into two eras: testing at the H-2, H-3, H-4, H-6, and H-11 hydropads during the 1980's and testing at the H-11 and H-19 hydropads in 1995-1996. This appendix does not contain all of the WIPP tracer data. Rather, only the data from the 1980's tests that are considered interpretable based on an extensive review of the tracer tests and all of the data collected during the 1995-1996 tests are included. A discussion of which 1980's data are considered interpretable can be found in Appendix F and Jones et al. (1992).

Samples collected during the 1995-1996 tests were analyzed for the benzoic acids and iodide at the University of Nevada - Las Vegas. Sample analysis results are documented in ERMS #237466 (general records), ERMS #237467 (1996 H-11 tracer test), ERMS #237468 (H-19 4-well test), and ERMS #237452 (H-19 7-well test). The analysis results were modified by Duke Engineering and Services (DE&S) to prepare them for numerical simulations (e.g., correcting the sample time to reflect the travel time in the Culebra rather than the travel time from surface injection to surface sample collection by adjusting for tracer travel up the withdrawal well and down the injection well). The adjusted data can be found in ERMS #237466. That records package not only contains the data for the H-19 tracer tests and the 1996 H-11 tracer test, but also the data for the H-3 and 1988 H-11 tracer tests and the interpreted data (see Appendix F) for the H-6 tracer tests. Plots of these data can be found in diagram (a) of the attached figures.

Calculations of the 95% confidence intervals were performed at the University of Nevada – Las Vegas on the H-19 tracer data and the tracer data from the 1996 test at H-11. Those calculations are documented in ERMS #237467 (1996 H-11 test), ERMS #237468 (H-19 4-well test), and ERMS #237452 (H-19 7-well test). Tracer-breakthrough data at corrected times for the confidence-interval data were prepared by DE&S and can be found in ERMS #251278. Plots of the confidence-interval data can be found in diagrams (b) through (f) of the attached figures.

In addition to plots of the data (see Section C.2), this appendix discusses calculation of the 95% confidence intervals for the measured tracer concentrations for both the recovered fluid and the injectate for the tests conducted at H-11 and H-19 during 1995-1996 (see Section C.3), and presents and discusses a table containing summary information about the data and the theoretical plug-flow advective porosity calculated from the data (see Section C.4).

C.2 Data Plots

The majority of this appendix is made up of plots of the WIPP tracer data. Each data set is presented individually in the following six ways:

1. tracer concentration (mg/L) versus time since injection (days) plotted linear-linear;

---

[1] Duke Engineering & Services, Inc., 9111 Research Boulevard, Austin, TX 78758.
Email: tjones@dukeengineering.com.

[2] University of Nevada at Las Vegas, Harry Reid Center for Environmental Studies, 4505 Maryland Parkway, Las Vegas, NV 89154-4009.

[3] Sandia National Laboratories, Geohydrology Department, P.O. Box 5800, MS-0735, Albuquerque, NM 87185-0735.

[4] Now at Stormwater Management, 2035 NE Columbia Boulevard, Portland, OR 97211.

2. normalized tracer concentration (C/C_o) versus time since injection (days) plotted linear-linear;
3. normalized tracer concentration (C/C_o) versus time since injection (days) plotted log-log;
4. normalized tracer concentration (C/C_o) versus cumulative volume pumped (L) plotted log-log;
5. normalized cumulative mass (M/M_o) versus cumulative volume pumped (L) plotted linear-linear;
6. one minus normalized cumulative mass ($1-M/M_o$) versus time since injection (days) plotted log-log.

The data plotted in diagram (a) are the raw data taken from the tracer data spreadsheets (records package ERMS #237466). The data plotted in diagrams (b) through (f) are the confidence-interval data taken from the confidence-interval spreadsheets (records package ERMS #251278). The differences between the raw data and the confidence-interval data are:

- the correction factor used to convert the times from surface injection to surface sample collection to times of travel in the Culebra (i.e., travel times in the Culebra are the surface times minus the times for the tracer to travel down the injection well and up the pumping well); and
- multiple analyses of a single sample and duplicate samples for a single sample time are averaged in the confidence-interval data but are included individually in the raw data.

For the 1995-1996 tests at the H-11 and H-19 hydropads, the 95%-confidence-interval calculations on the measured data were used to develop confidence-interval bounds which are plotted as small dots on plots (b) through (f). The following section discusses how those bounds were calculated. Confidence-interval bounds could not be determined for the data collected during the H-3, H-6, and H-11 tracer tests conducted in the 1980's because confidence-interval calculations were not made on those data.

C.3 Calculation of Confidence Intervals for 1995-1996 Data

Confidence intervals were calculated for the measured tracer concentrations using the method described in Skoog and West (1986). Replicate analyses of a sample are required for calculating confidence intervals. Because replicate analyses were performed only on selected samples, confidence intervals were calculated based on the replicate samples and then applied to the samples with single measurements. Replicates included several analyses of the same field sample on the same or different dates and analyses of blind or labeled field duplicates.

Confidence intervals vary depending on the concentration of the analyte. The observed tracer-breakthrough curves span a large range of concentrations and, therefore, were divided into subsets. The range of tracer concentrations within each of the subsets did not exceed an order of magnitude. The 95% confidence limits, CL, for each subset were calculated as:

$$CL\,for\,\mu = \bar{x} \pm \frac{z\sigma}{\sqrt{N}} \qquad \text{(C-1)}$$

where $\bar{x}$ is the mean concentration of the replicate analysis, z is 1.96 for the 95% confidence interval, σ is the standard deviation of all replicate analyses included in the subset, and N is the number of replicate measurements included in the mean.

The standard deviation (σ) was calculated using the pooled estimate of the standard deviation for each subset of samples. The pooled estimate of the standard deviation (s_{pooled}) was calculated as:

$$s_{pooled} = \sqrt{\frac{\sum_{j=1}^{K} \sum_{i=1}^{L} \left[\left(x_i - \bar{x}_j \right)^2 \right]_j}{N-K}} \qquad \text{(C-2)}$$

where K is the number of samples with replicate analyses, L is the number of replicate analyses of a given sample, and N is the total number of replicate measurements included in the subset. Each individual measurement (i) within the group of replicate analyses (j) is represented as x_i and the mean of the group of replicates is $\bar{x}_j$.

Confidence intervals for the injectate samples were calculated as described in Equation C-1. In most cases, replicate analyses were only performed on one sample and the standard deviation (σ) is reduced to the sample standard deviation (s).

The 95% confidence interval for the quotient C_i/C_o, where C_o is the initial tracer (injectate) concentration and C_i is the mean tracer concentration, was desired. Confidence limits for C_i/C_o were calculated using the propagation of errors in quotients as:

$$CL\,for\,\frac{C_i}{C_o} = \frac{C_i}{C_o} \pm \frac{C_i}{C_o}\sqrt{\left(\frac{L_o}{C_o}\right)^2 + \left(\frac{L_i}{C_i}\right)^2} \qquad \text{(C-3)}$$

with

$$L_o = \frac{z\sigma_{C_o}}{\sqrt{N}} \quad and \quad L_i = \frac{z\sigma_{C_i}}{\sqrt{N}} \qquad \text{(C-4)}$$

where L_o is the half length of the confidence interval for the injectate and L_i is the half length of the confidence interval for the samples.

For the plots of normalized tracer concentration (diagrams (b) through (d)), the upper confidence-interval bound was calculated as the measured C/C_o + the half length of the 95% confidence interval for the measured value and the lower confidence-interval bound was calculated as the measured C/C_o – the 95% confidence interval for the measured value.

The normalized cumulative mass was calculated by summing the normalized incremental masses. The normalized incremental mass, M_I, is the amount of normalized mass recovered between two samples and was calculated as:

$$M_I = \frac{V_I\left(\frac{C}{C_o}\right)}{V_o} \qquad \text{(C-5)}$$

where V_I is the incremental volume pumped between the two sample times of interest and V_o is the volume of injected tracer. In one instance (H-19b7, round 1 injection), the calculated normalized cumulative mass is slightly greater than 1.0 at the end of the test. This is attributed to a slight error in one of the parameters used to calculate the normalized mass. For the normalized cumulative mass, the upper confidence-interval bound was calculated by replacing C_o in Equation C-5 with C_o+CI_{Co} and the lower confidence-interval bound was calculated by replacing C_o in Equation C-5 with C_o-CI_{Co} where CI_{Co} is the 95% confidence interval for the injectate. In some cases, the confidence-interval bounds for the normalized-cumulative-mass data become wide. This occurs when total mass recovery is high and/or when the 95% confidence interval for the injectate concentration is large.

C.4 Table of Calculations

Also included in this appendix are two tables that summarize information about the observed data for the multiwell convergent-flow tracer tests. The tables also include the advective porosity calculated for each data set based on the theoretical direct plug-flow travel time between the injection well and the pumping well (see Section 3.3.2.3 for more details) and all parameter values required for that calculation. These tables were developed by DE&S. Table C-1 contains the summary information and calculations for the observed data from the H-19 hydropad and Table C-2 contains the summary information and calculations for the observed data from the H-3, H-6, and H-11 hydropads. Due to low mass recovery, the data sets for the injections into the upper Culebra at the H-19 hydropad are not included in Table C-1.

The summary information contained in the tables includes:

- the time to the peak concentration in days and seconds;
- the normalized tracer concentration at the peak;
- the volume of fluid pumped at the time of the peak concentration in liters;

- the normalized cumulative mass at the peak;
- the time to 50% mass recovery in days;
- the volume of fluid pumped at 50% mass recovery in liters;
- the time to 90% mass recovery in days;
- the volume of fluid pumped at 90% mass recovery in liters;
- the total time to the last sample collected in days;
- the total volume of fluid pumped to the time of the last sample in liters;
- the total mass recovered;
- the total mass recovered plus the confidence interval; and
- the total mass recovered minus the confidence interval.

All of this information was taken from the confidence-interval spreadsheets (records package ERMS #251278).

For each data set, the names of the raw data file used to create diagram (a) and the confidence-interval data file used to create diagrams (b) through (f) are listed in the last two columns of the tables.

A value for advective porosity was calculated from each data set base on the theoretical direct plug-flow travel time between the injection and pumping wells. This initial estimate of the advective porosity, ϕ_A, can be calculated using the relationship:

$$\phi_A = \frac{Qt_p}{\pi r^2 b} \tag{C-6}$$

where Q is the pumping rate, t_p is the time to the peak concentration, r is the distance between the injection and pumping wells, and b is the thickness of the permeable medium. The values for Q, t_p, r, and b used in the calculations are given in the tables. A discussion of the relationship between the calculated advective porosities for the different flow paths at a single hydropad and from hydropad to hydropad can be found in Section 3.3.2.3 of the main body of this document.

C.5 References

Jones, T.L., V.A. Kelley, J.F. Pickens, D.T. Upton, R.L. Beauheim, and P.B. Davies. 1992. *Integration of Interpretation Results of Tracer Tests Performed in the Culebra Dolomite at the Waste Isolation Pilot Plant Site.* SAND92-1579. Albuquerque, NM: Sandia National Laboratories.

Skoog, D.A., and D.M. West. 1986. *Analytical Chemistry: An Introduction.* 4th ed. Philadelphia, PA: Saunders College Pub.

This page intentionally left blank.

Table C-1. H-19 Summary Information and Calculations

	Q (L/s)	Q (m³/s)	t_p (days)	t_p (seconds)	r (m)	b (m)	phi_A	Average phi_A (pathway)	Normalized conc. at t_p	Volume pumped at t_p (L)	Cl Data M/Mo at t_p *
SOURCE OF DATA:	*(1)*		*(2)*		*(1)*	*(1)*	*(3)*	*(4)*	*(2)*	*(2)*	*(2)*
H-19b2 to H-19b0 path											
preliminary test	0.236	0.000236	23.98	2071945	25.1	4.4	0.056		0.000326	490678.2	0.2432
round 1 injection	0.271	0.000271	17.59	1519672	25.1	4.4	0.047	**0.052**	0.000278	417375.9	0.2390
H-19b3 to H-19b0 path											
preliminary test	0.236	0.000236	7.87	680143	11.0	4.4	0.096		0.000644	163593.5	0.2214
round 1 injection - acid	0.271	0.000271	5.48	473817	11.0	4.4	0.077		0.000703	132306.8	0.2575
round 1 injection - IC	0.271	0.000271	5.48	473817	11.0	4.4	0.077		0.000669	132306.8	0.2205
round 1 injection - HPLC	0.271	0.000271	5.48	473817	11.0	4.4	0.077		0.000671	-	-
round 2 lower injection	0.252	0.000252	5.19	448632	11.0	4.4	0.068		0.000784	114869.8	0.2248
round 3 injection	0.155	0.000155	9.21	795589	11.0	4.4	0.074	**0.078**	0.000714	125036.9	0.2152
H-19b4 to H-19b0 path											
preliminary test	0.236	0.000236	24.37	2105721	22.3	4.4	0.072		0.000248	499074.1	0.1724
round 1 injection	0.271	0.000271	21.71	1876116	22.3	4.4	0.074	**0.073**	0.000198	520134.7	0.2175
H-19b5 to H-19b0 path											
round 1 lower injection	0.271	0.000271	14.00	1209972	13.9	4.4	0.123		0.000207	333756.1	0.2155
round 2 injection	0.252	0.000252	17.91	1547746	13.9	4.4	0.146	**0.134**	0.000227	395445.1	0.2390
H-19b6 to H-19b0 path											
round 1 injection	0.271	0.000271	7.23	624656	19.8	4.4	0.031		0.000468	173184.0	0.2021
round 3 injection	0.155	0.000155	13.23	1143198	19.8	4.4	0.033	**0.032**	0.000456	181659.7	0.2112
H-19b7 to H-19b0 path											
round 1 injection	0.271	0.000271	4.00	345328	12.2	4.4	0.045		0.001026	96510.7	0.2684
round 2 lower injection	0.252	0.000252	4.13	357178	12.2	4.4	0.044		0.000893	91815.7	0.2116
round 3 injection - acid	0.155	0.000155	7.12	614815	12.2	4.4	0.046		0.000961	97063.4	0.2494
round 3 injection - IC	0.155	0.000155	7.68	663175	12.2	4.4	0.050		0.000908	104066.3	0.2520
round 3 injection - HPLC	0.155	0.000155	7.87	679615	12.2	4.4	0.051	**0.047**	0.000933	107014.4	0.2550

SOURCES:

(1) Source is transport input parameter sheets (Appendix B)

(2) Source is confidence interval data set listed in the last column of second page of Table C-1

(3) Advective porosity (phi_A) is calculated using equation on second page of Table C-1

(4) Average advective porosity is calculated as the average for each path

(5) These values are calculated by interpolating values from the confidence interval data sets listed on second page of Table C-1

* = Confidence Interval Data, Cumulative Normalized Mass at Time of Peak Concentration.

Table C-1. H-19 Summary Information and Calculations (continued)

	(5) Time to 50% mass recovery (days)	(5) Vol pumped at 50% mass recovery (L)	(5) Time to 90% mass recovery (days)	(5) Vol pumped at 90% mass recovery (L)	(2) Total time (last sample) (days)	(2) Total volume pumped (L)	(2) Total mass recovered (%)	(2) Total mass recovered + conf.int. (%)	(2) Total mass recovered - conf.int. (%)	Confidence interval data set
H-19b2 to H-19b0 path										
preliminary test	34.82	716371.9	-	-	37.44	763484.7	0.544	0.520	0.570	rh194cb2.dat
round 1 injection	26.92	639546.2	-	-	103.52	1921755.2	0.876	0.851	0.903	rh19n1b2.dat
H-19b3 to H-19b0 path										
preliminary test	16.05	330708.7	-	-	37.17	757867.4	0.686	0.662	0.710	rh194cb3.dat
round 1 injection - acid	9.17	218499.5	-	-	103.81	1928694.5	0.882	0.837	0.932	rh19n1b3.dat
round 1 injection - IC	10.10	242769.7	-	-	62.78	1379111.0	0.804	-	-	rh19n1io.dat
round 1 injection - HPLC	-	-	-	-	-	-	-	-	-	rh19n1io.dat
round 2 lower injection	8.50	194028.6	-	-	81.79	1355227.2	0.888	0.866	0.912	rh19n2l3.dat
round 3 injection	15.68	216222.7	-	-	47.81	640210.4	0.804	0.777	0.833	rh19n3b3.dat
H-19b4 to H-19b0 path										
preliminary test	-	-	-	-	37.38	762110.3	0.411	0.380	0.448	rh194cb4.dat
round 1 injection	36.79	854907.7	-	-	103.71	1926278.1	0.839	0.682	1.090	rh19n1b4.dat
H-19b5 to H-19b0 path										
round 1 lower injection	24.19	578208.1	-	-	105.50	1968137.4	0.839	0.768	0.926	rh19n1l5.dat
round 2 injection	29.03	642836.8	-	-	81.97	1359054.6	0.828	0.775	0.887	rh19n2b5.dat
H-19b6 to H-19b0 path										
round 1 injection	14.06	334721.3	-	-	104.56	1946152.5	0.877	0.865	0.889	rh19n1b6.dat
round 3 injection	25.51	348008.2	-	-	47.92	641684.2	0.740	0.715	0.768	rh19n3b6.dat
H-19b7 to H-19b0 path										
round 1 injection	6.03	145101.4	15.32	364641.9	104.74	1950447.3	1.027	0.960	1.105	rh19n1b7.dat
round 2 lower injection	7.25	164186.7	78.40	1314639.9	80.90	1335765.3	0.901	0.855	0.952	rh19n2l7.dat
round 3 injection - acid	11.45	155715.3	44.35	600793.8	47.72	639020.9	0.906	0.881	0.932	rh19n3b7.dat
round 3 injection - IC	12.02	165280.9	-	-	47.72	639020.9	0.881	0.772	1.025	rh19n3ic.dat
round 3 injection - HPLC	12.48	170094.5	-	-	46.90	628139.9	0.858	0.849	0.867	rh19n3hp.dat

phi_A=Qxt_p/pixr^{2}xb

Q = pumping rate
t_p = time to peak concentration
r = well spacing
b = formation thickness

Table C-2. H-3, H-6, H-11 Summary Information and Calculations

SOURCE OF DATA:	(1)		(2)		(1)	(1)	(3)	(4)	(2)	(2)	(2)
	Q (L/s)	Q (m³/s)	t_p (days)	t_p (seconds)	r (m)	b (m)	phi_A	Average phi_A (pathway)	Normalized conc. at t_p	Volume pumped at t_p (L)	Cl Data M/Mo * at t_p
H-3 HYDROPAD											
H-3b1 to H-3b3 path	0.190	0.000190	2.53	218659	30.7	4.2	0.003	**0.003**	0.000256	42229.2	0.0466
H-3b2 to H-3b3 path	0.190	0.000190	23.01	1988080	26.8	4.2	0.040	**0.040**	0.000017	409883.1	0.0963
H-6 HYDROPAD											
H-6a to H-6c	1.040	0.001040	12.30	1062828	29.9	4.0	0.098	**0.098**	0.000022	1109085.5	0.1103
H-6b to H-6c - test 1	1.040	0.001040	0.67	57865	29.9	4.0	0.005		0.000339	66106.9	0.1129
H-6b to H-6c - test 2	1.040	0.001040	0.71	61426	29.9	4.0	0.006	**0.006**	0.000314	65754.8	0.1100
H-11 HYDROPAD											
H-11b2 to H-11b1 path											
1988 test	0.380	0.000380	5.53	477394	21.5	4.4	0.028		0.000118	189617.8	0.0776
round 1 injection	0.223	0.000223	12.22	1055938	21.5	4.4	0.037		0.000107	238692.0	0.0874
round 2 injection	0.376	0.000376	7.66	661554	21.5	4.4	0.039	**0.035**	0.000124	257317.2	0.1186
H-11b3 to H-11b1 path											
1988 test	0.380	0.000380	0.35	30671	20.9	4.4	0.002		0.000797	11997.0	0.0272
round 1 injection	0.223	0.000223	0.62	53844	20.9	4.4	0.002		0.001197	12810.1	0.0515
round 2 injection	0.376	0.000376	0.36	31508	20.9	4.4	0.002		0.001186	12016.3	0.0443
round 2 injection - iodide	0.376	0.000376	0.39	33308	20.9	4.4	0.002	**0.002**	0.000908	12693.1	0.0325
H-11b4 to H-11b1 path											
1988 test	0.380	0.000380	21.32	1842080	42.9	4.4	0.028	**0.028**	0.000044	716406.3	0.1016

SOURCES:

(1) Source is transport input parameter sheets (Appendix B)
(2) Source is confidence interval data set listed in the last column of second page of Table C-2
(3) Advective porosity (phi_A) is calculated using equation on second page of Table C-2
(4) Average advective porosity is calculated as the average for each path
(5) These values are calculated by interpolating values from the confidence interval data sets listed on second page of Table C-2

* = Confidence Interval Data, Cumulative Normalized Mass at Time of Peak Concentration.

Table C-2. H-3, H-6, H-11 Summary Information and Calculations (continued)

	(5) Time to 50% mass recovery (days)	(5) Vol pumped at 50% mass recovery (L)	(5) Time to 90% mass recovery (days)	(5) Vol pumped at 90% mass recovery (L)	(2) Total time (last sample) (days)	(2) Total volume pumped (L)	(2) Total mass recovered (%)	(2) Total mass recovered + conf.int. (%)	(2) Total mass recovered - conf.int. (%)	Confidence interval data set
H-3 HYDROPAD										
H-3b1 to H-3b3 path	23.88	427943.2	-	-	32.70	536761.2	0.554	-	-	rh384b1.dat
H-3b2 to H-3b3 path	-	-	-	-	32.76	537791.1	0.146	-	-	rh384b2.dat
H-6 HYDROPAD										
H-6a to H-6c	-	-	-	-	18.51	1663197.5	0.200	-	-	rh681a1.dat
H-6b to H-6c - test 1	3.15	292347.2	-	-	18.51	1663234.9	0.794	-	-	rh681b1.dat
H-6b to H-6c - test 2	3.80	347368.5	-	-	8.70	781794.8	0.628	-	-	rh681b2.dat
H-11 HYDROPAD										
H-11b2 to H-11b1 path										
1988 test	45.86	1522049.8	-	-	53.89	1769429.8	0.529	-	-	rh1188b2.dat
round 1 injection	-	-	-	-	40.87	994743.3	0.403	0.401	0.405	rh11n1b2.dat
round 2 injection	-	-	-	-	12.67	411627.6	0.211	0.209	0.214	rh11n2b2.dat
H-11b3 to H-11b1 path										
1988 test	14.63	496754.4	-	-	53.79	1765887.0	0.770	-	-	rh118b3.dat
round 1 injection	14.67	285821.5	-	-	40.69	991223.5	0.740	0.724	0.756	rh11n1b3.dat
round 2 injection	9.31	310379.7	-	-	13.64	443194.3	0.564	0.555	0.572	rh11n2b3.dat
round 2 injection - iodide	11.68	387782.3	-	-	13.64	443194.3	0.527	0.526	0.528	rh11n2io.dat
H-11b4 to H-11b1 path										
1988 test	-	-	-	-	53.69	1762698.3	0.290	-	-	rh1188b4.dat

phi_A=Q×t_p/pi×r^{2}×b

Q = pumping rate
t_p = time to peak concentration
r = well spacing
b = formation thickness

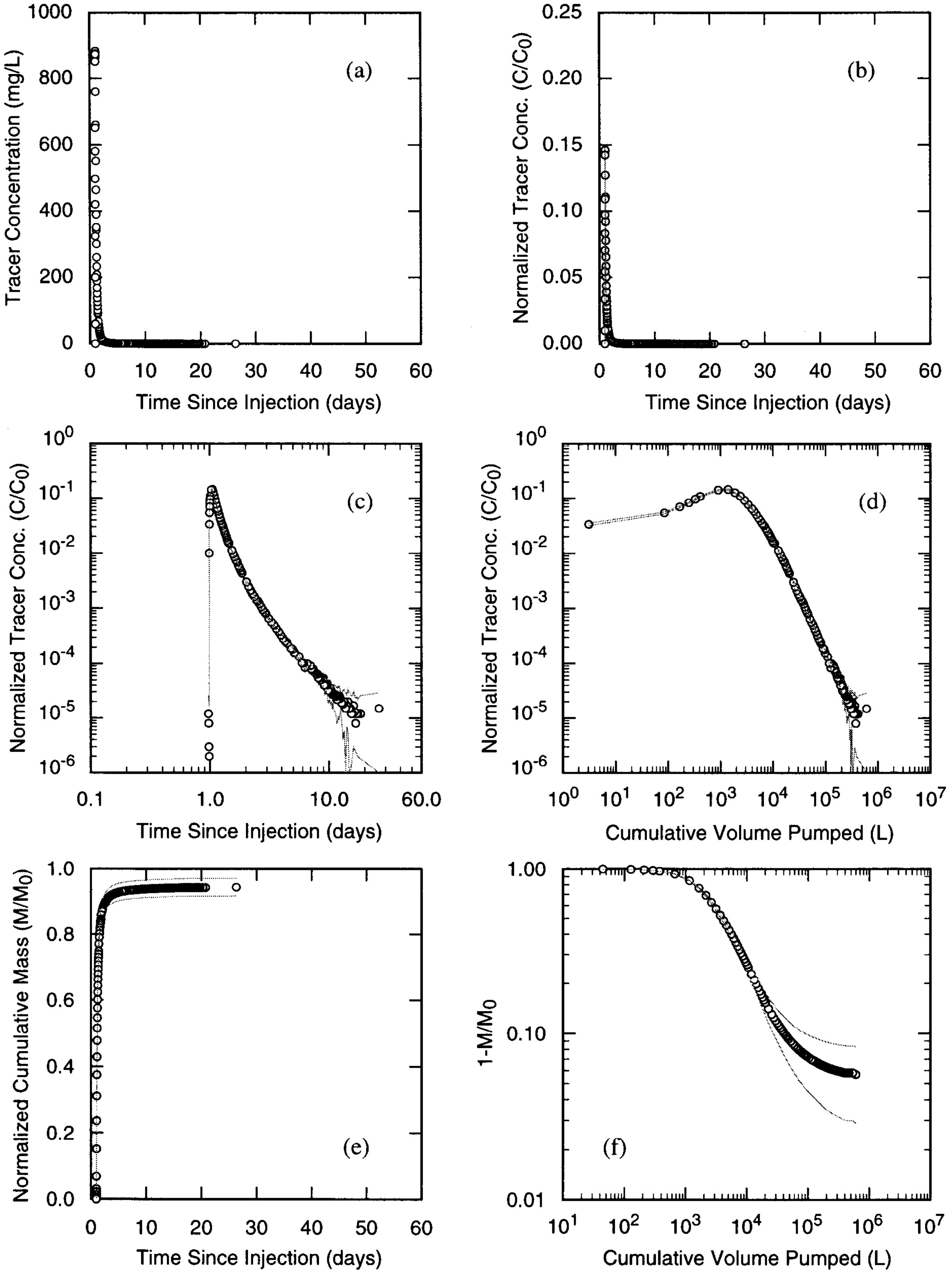

TRI-6115-916-0

Figure C-1. 2,4-DCBA data from H-19b0, 7-well test—SWIW Test 2 (Q=0.27 L/s), lower Culebra injection.

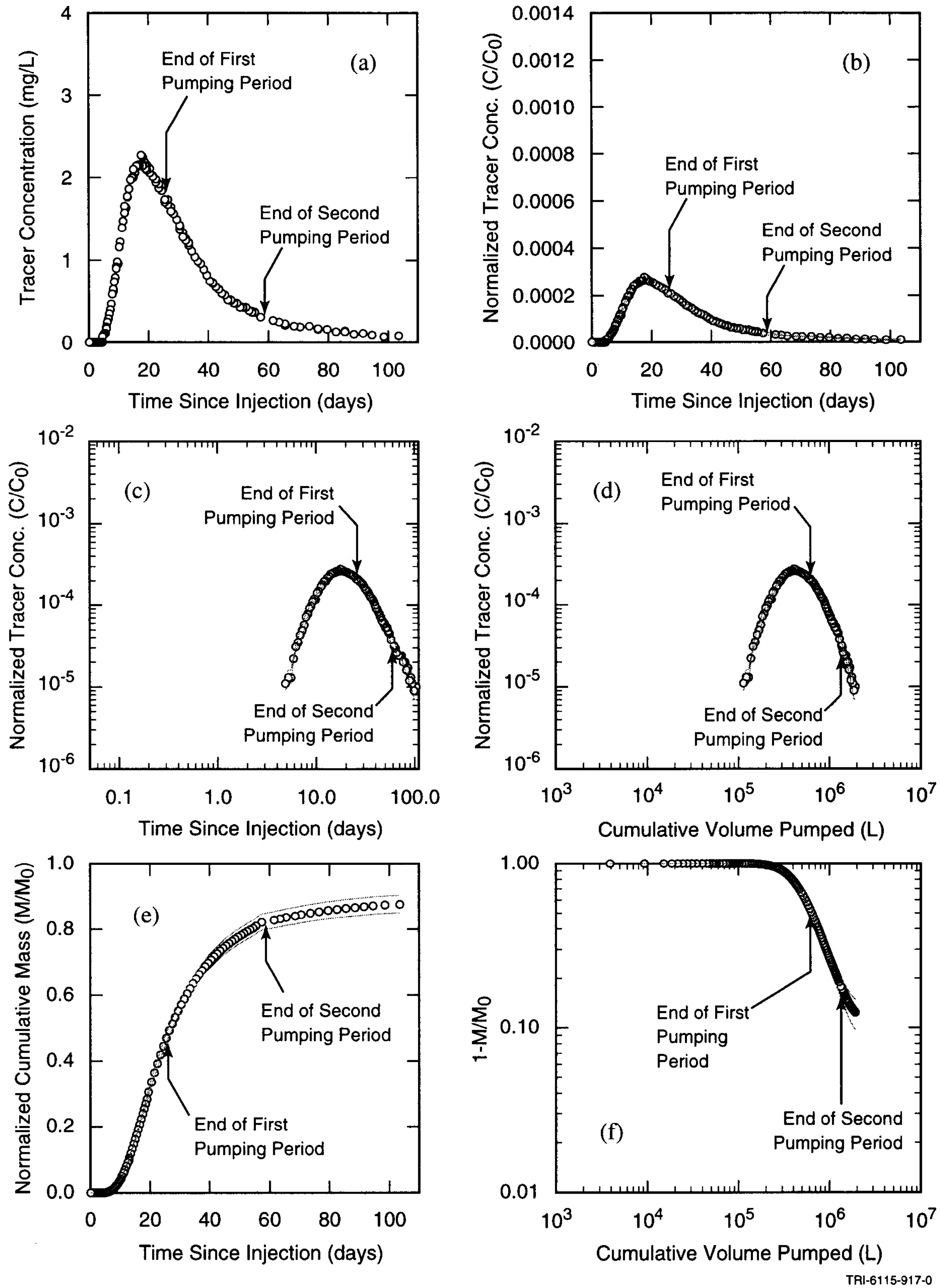

TRI-6115-917-0

Figure C-2. 2,3,4-TFBA data from H-19b2 to H-19b0 pathway, H-19 7-well test, round 1 (Q=0.27 L/s), full Culebra injection.

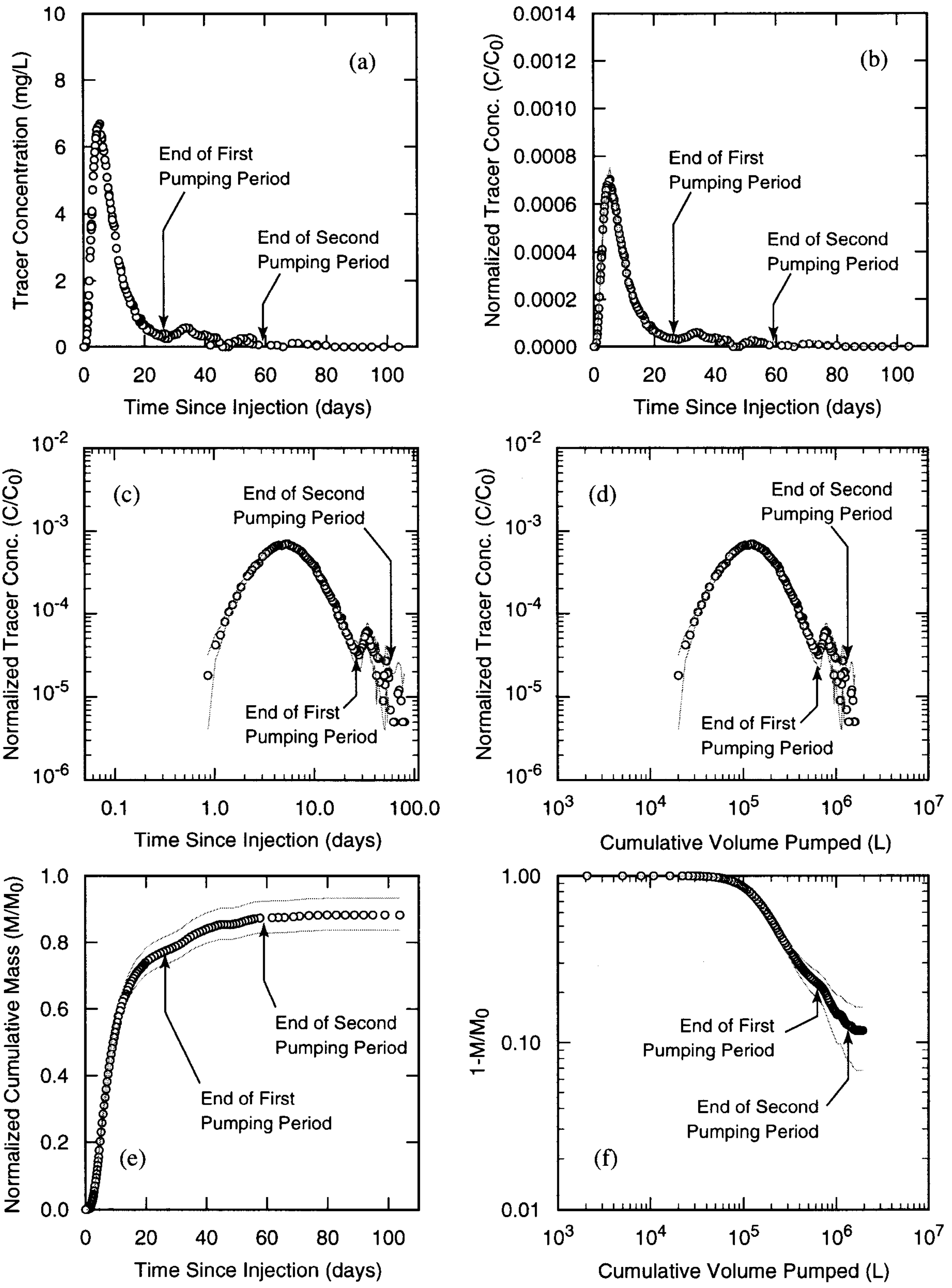

Figure C-3. **m-TFMBA data from H-19b3 to H-19b0 pathway, H-19 7-well test, round 1 (Q=0.27 L/s), full Culebra injection.**

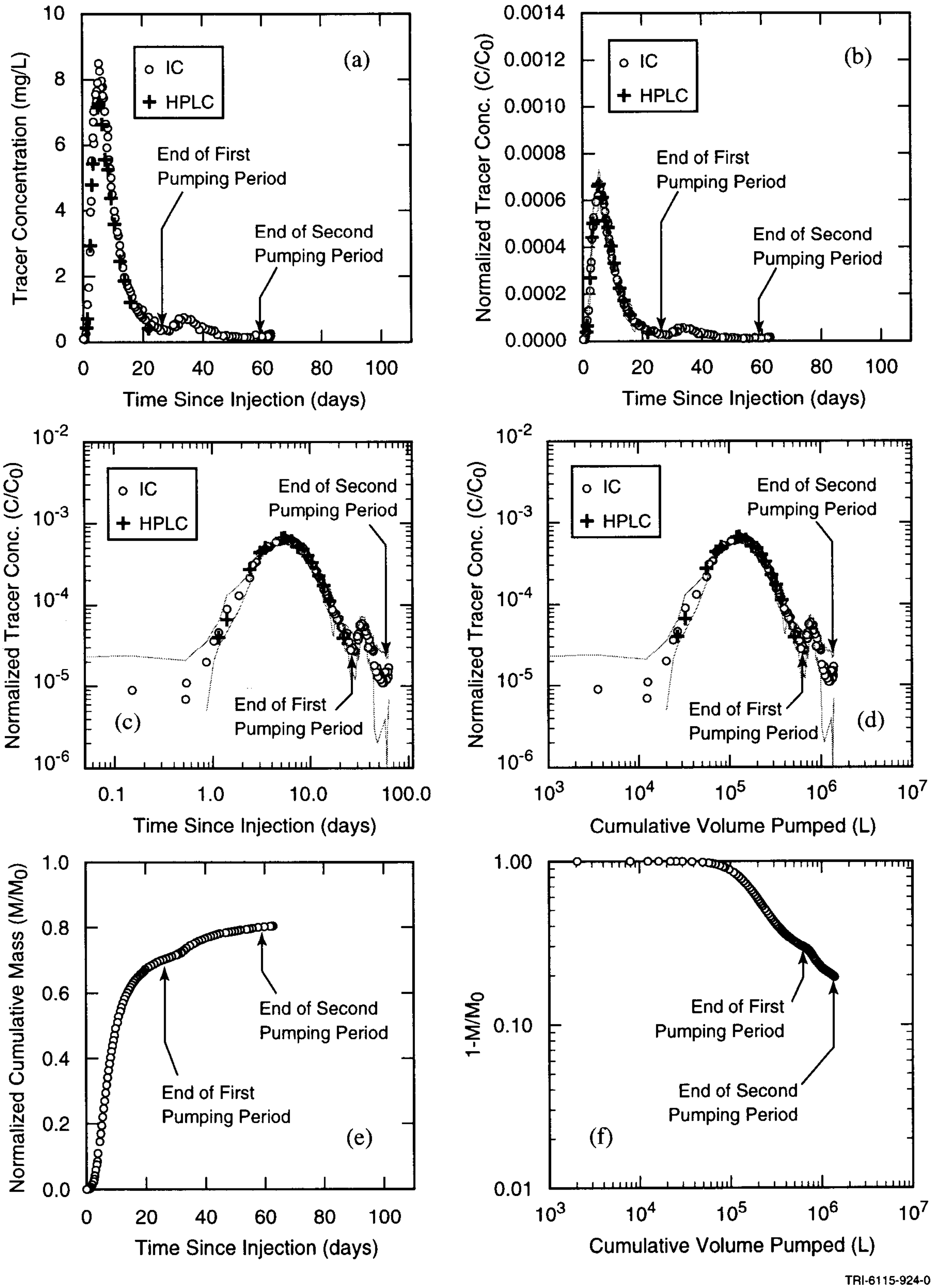

Figure C-4. Iodide data from H-19b3 to H-19b0 pathway, H-19 7-well test, round 1 (Q=0.27 L/s), full Culebra injection analyzed using both an ion chromatograph (IC) and a high performance liquid chomatograph (HPLC) .

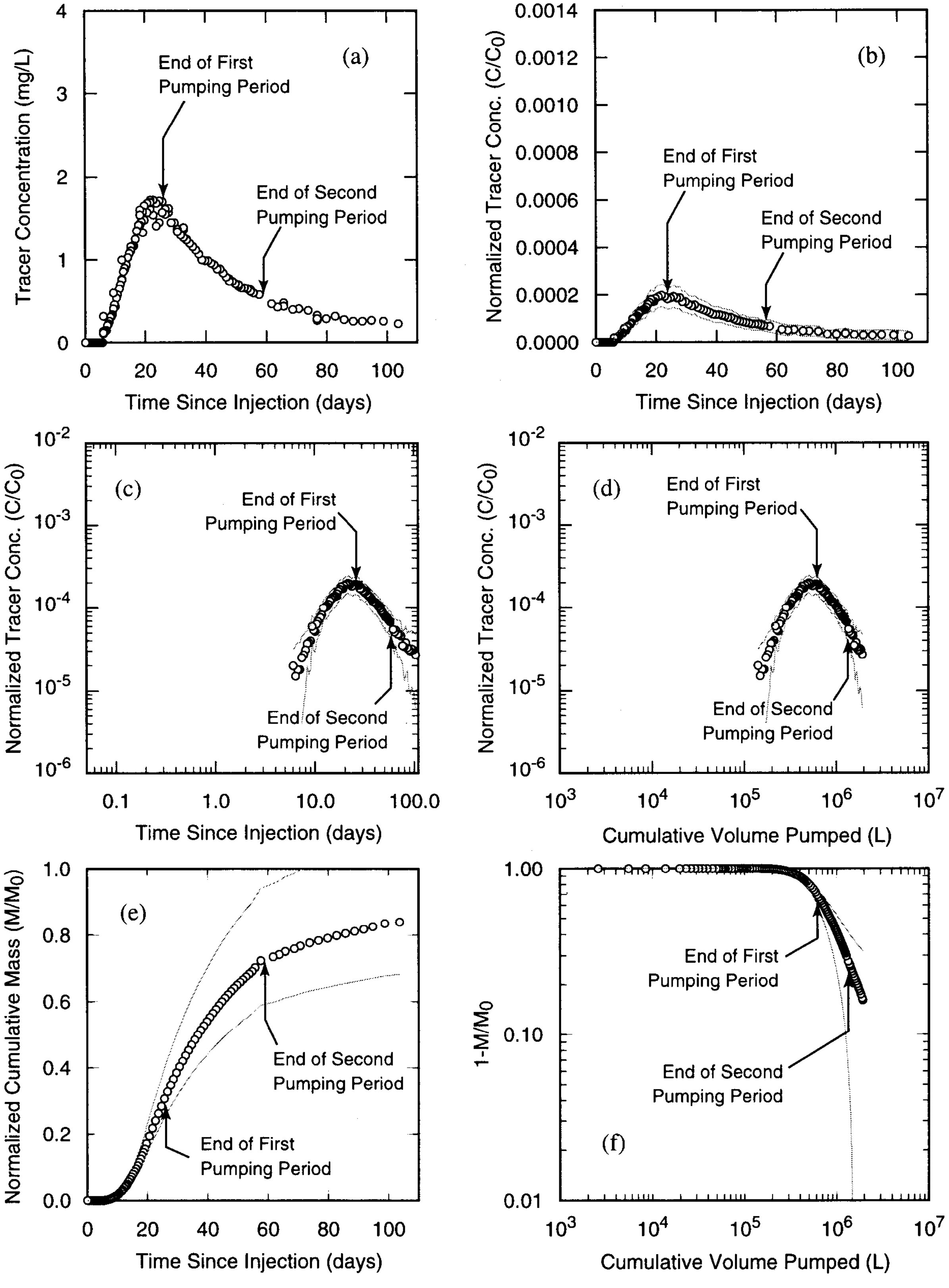

Figure C-5. **3,5-DFBA data from H-19b4 to H-19b0 pathway, H-19 7-well test, round 1 (Q=0.27 L/s), full Culebra injection.**

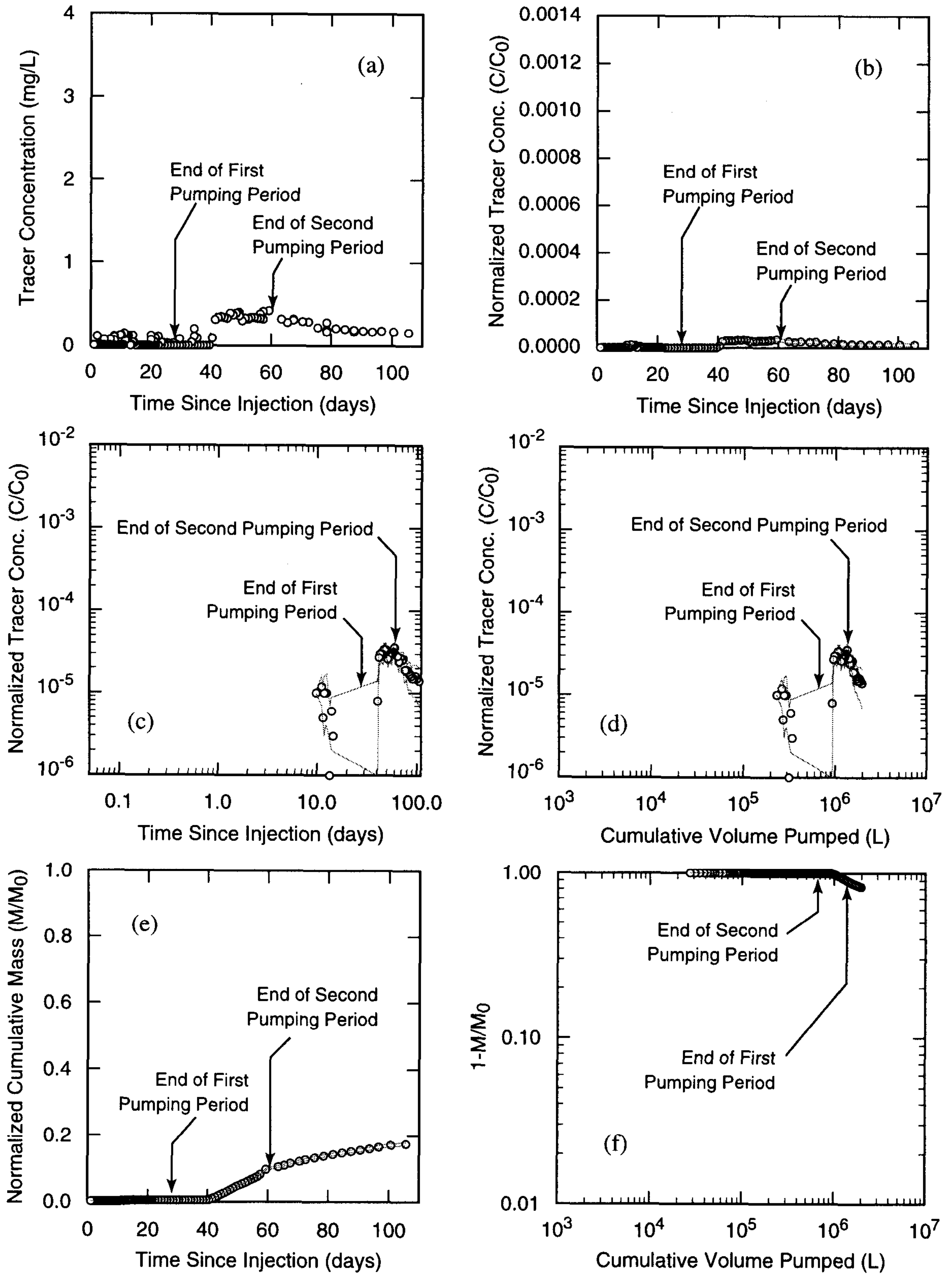

TRI-6115-920-0

Figure C-6. 2,3-DCBA data from H-19b5 to H-19b0 pathway, H-19 7-well test, round 1 (Q=0.27 L/s), upper Culebra injection.

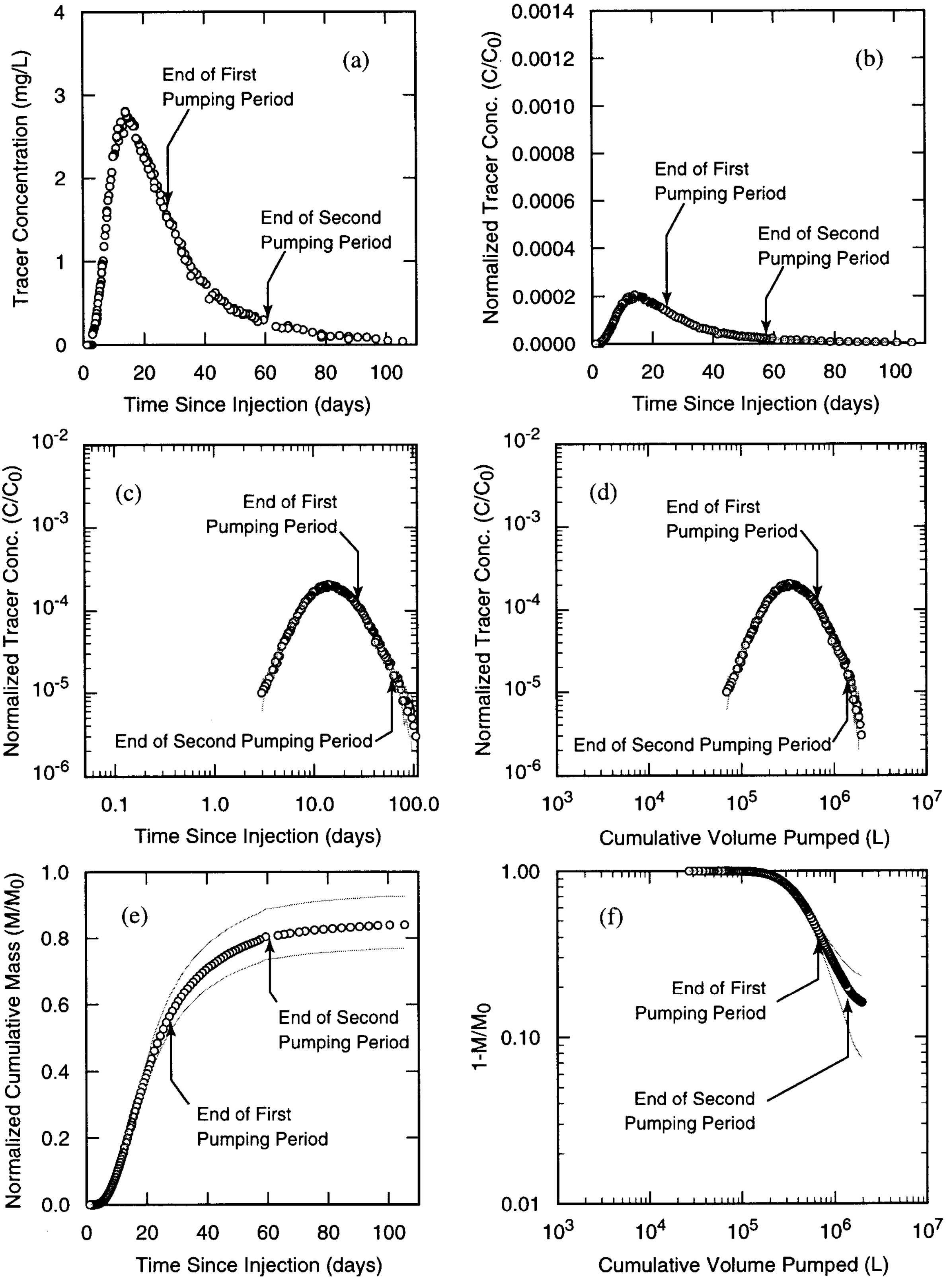

TRI-6115-921-0

Figure C-7. **2,5-DCBA data from H-19b5 to H-19b0 pathway, H-19 7-well test, round 1 (Q=0.27 L/s), lower Culebra injection.**

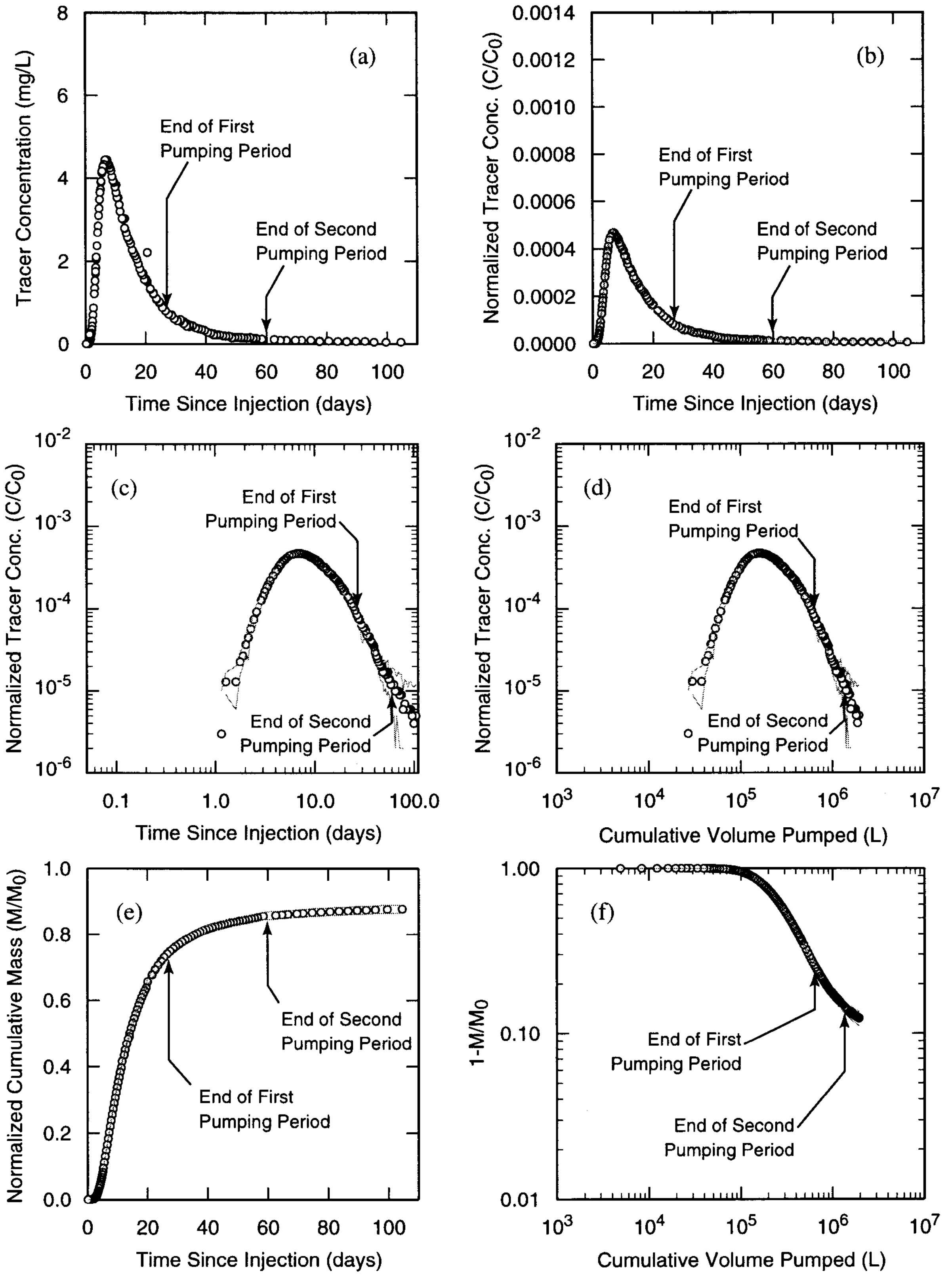

TRI-6115-922-0

Figure C-8. 2,5-DFBA data from H-19b6 to H-19b0 pathway, H-19 7-well test, round 1 (Q=0.27 L/s), full Culebra injection.

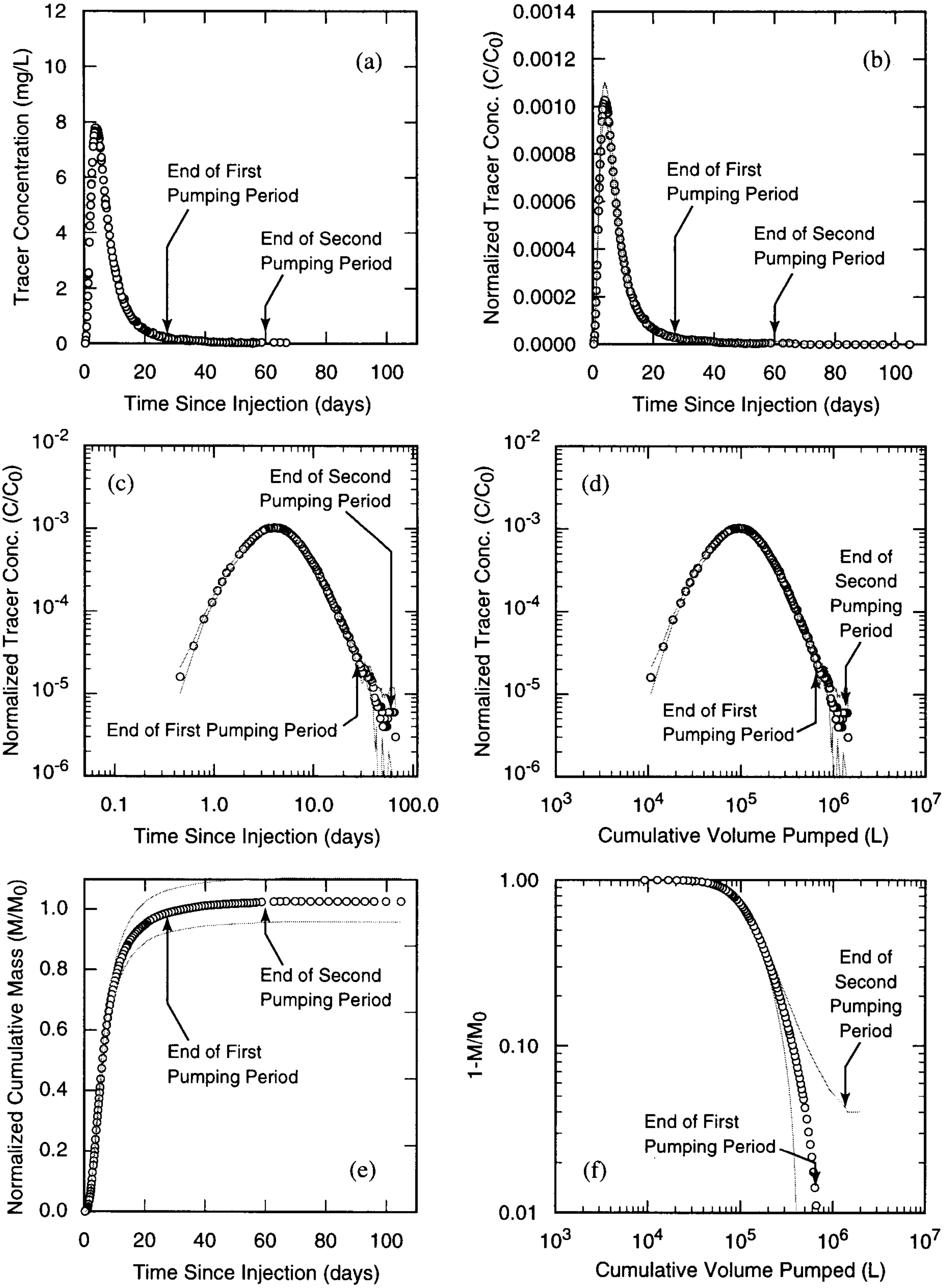

TRI-6115-923-0

Figure C-9. 2,4-DFBA data from H-19b7 to H-19b0 pathway, H-19 7-well test, round 1 (Q=0.27 L/s), full Culebra injection.

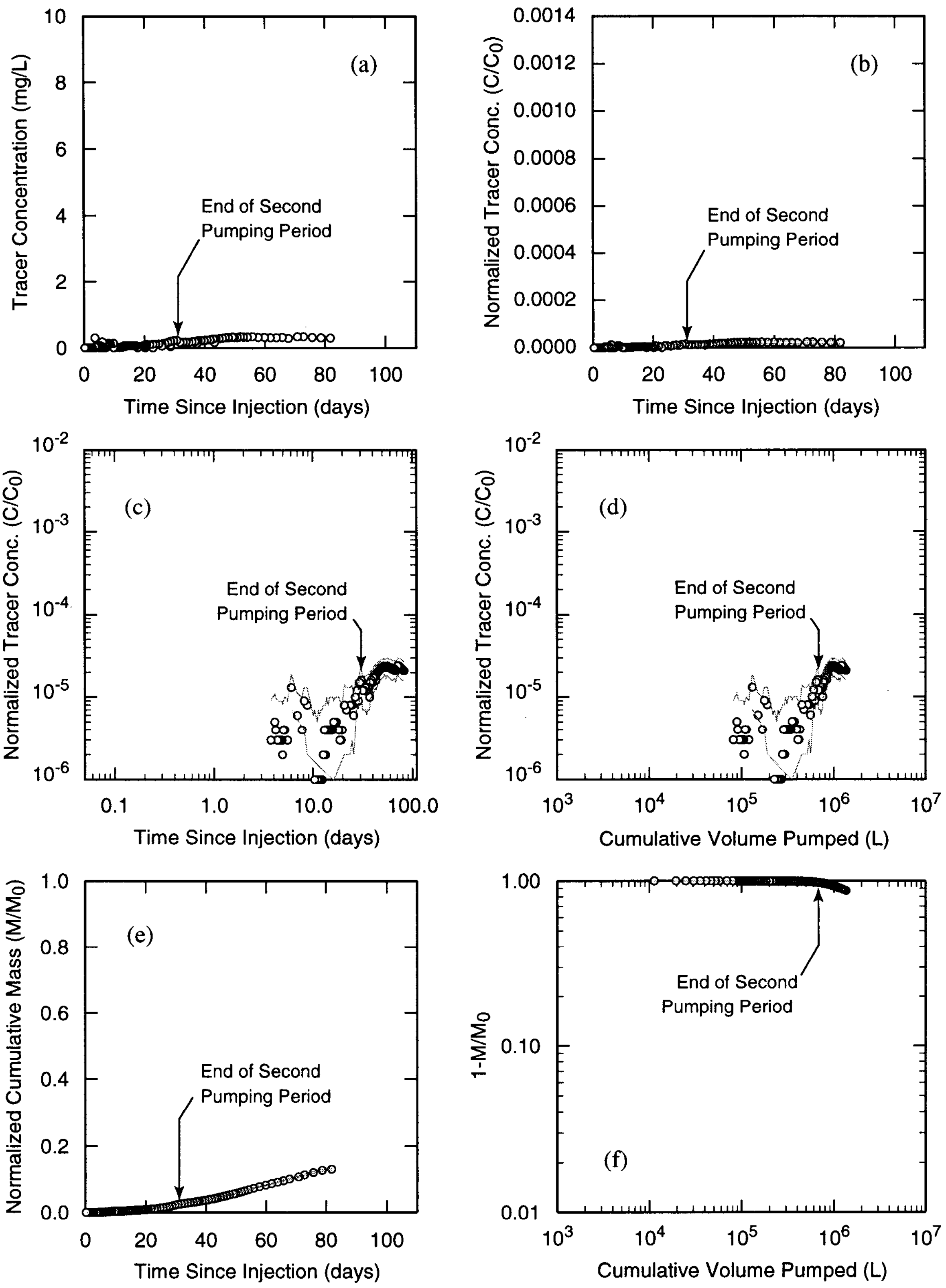

Figure C-10. p-TFMBA data from H-19b3 to H-19b0 pathway, H-19 7-well test, round 2 (Q=0.25 L/s), upper Culebra injection.

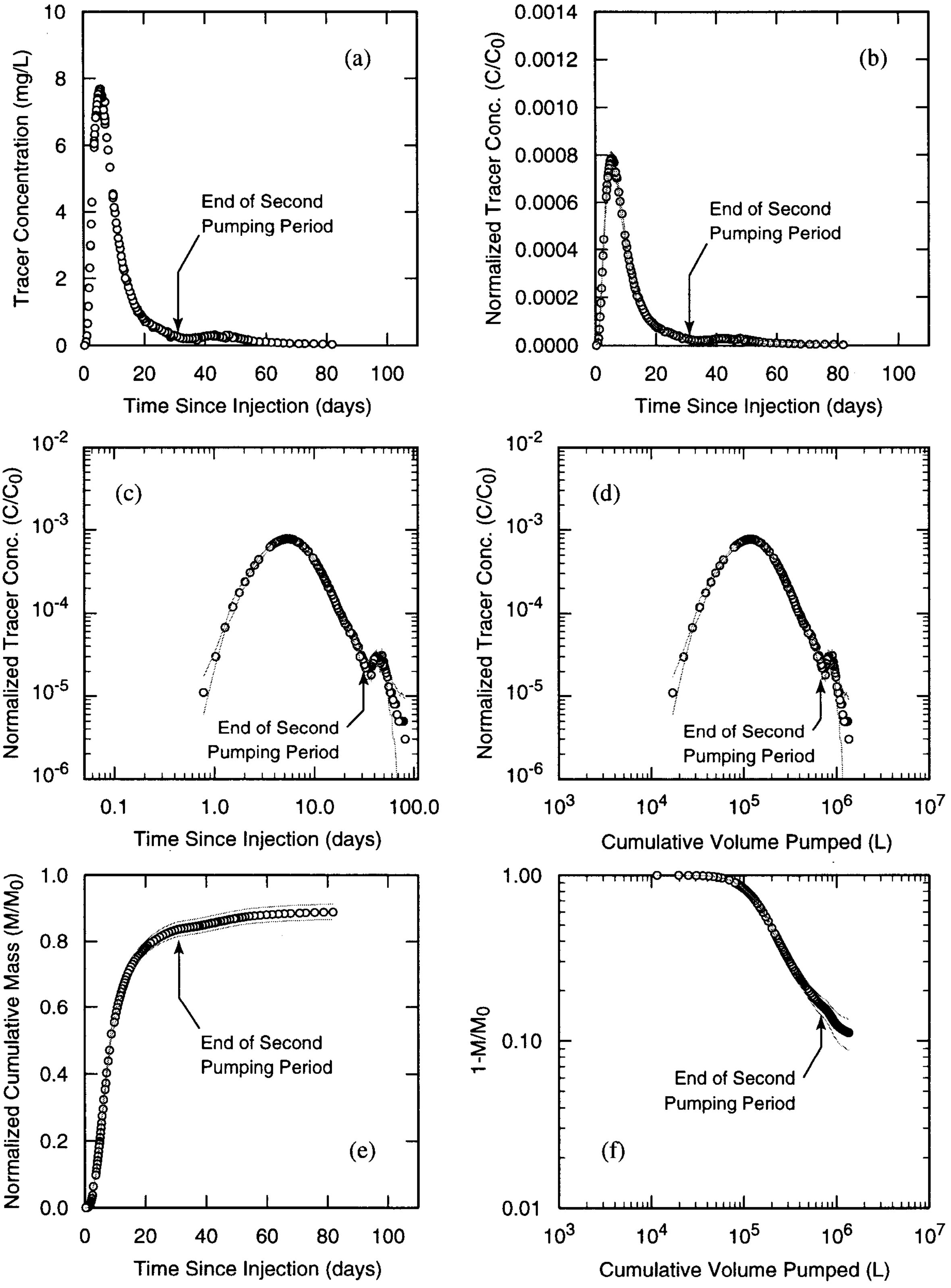

Figure C-11. o-TFMBA data from H-19b3 to H-19b0 pathway, H-19 7-well test, round 2 (Q=0.25 L/s), lower Culebra injection.

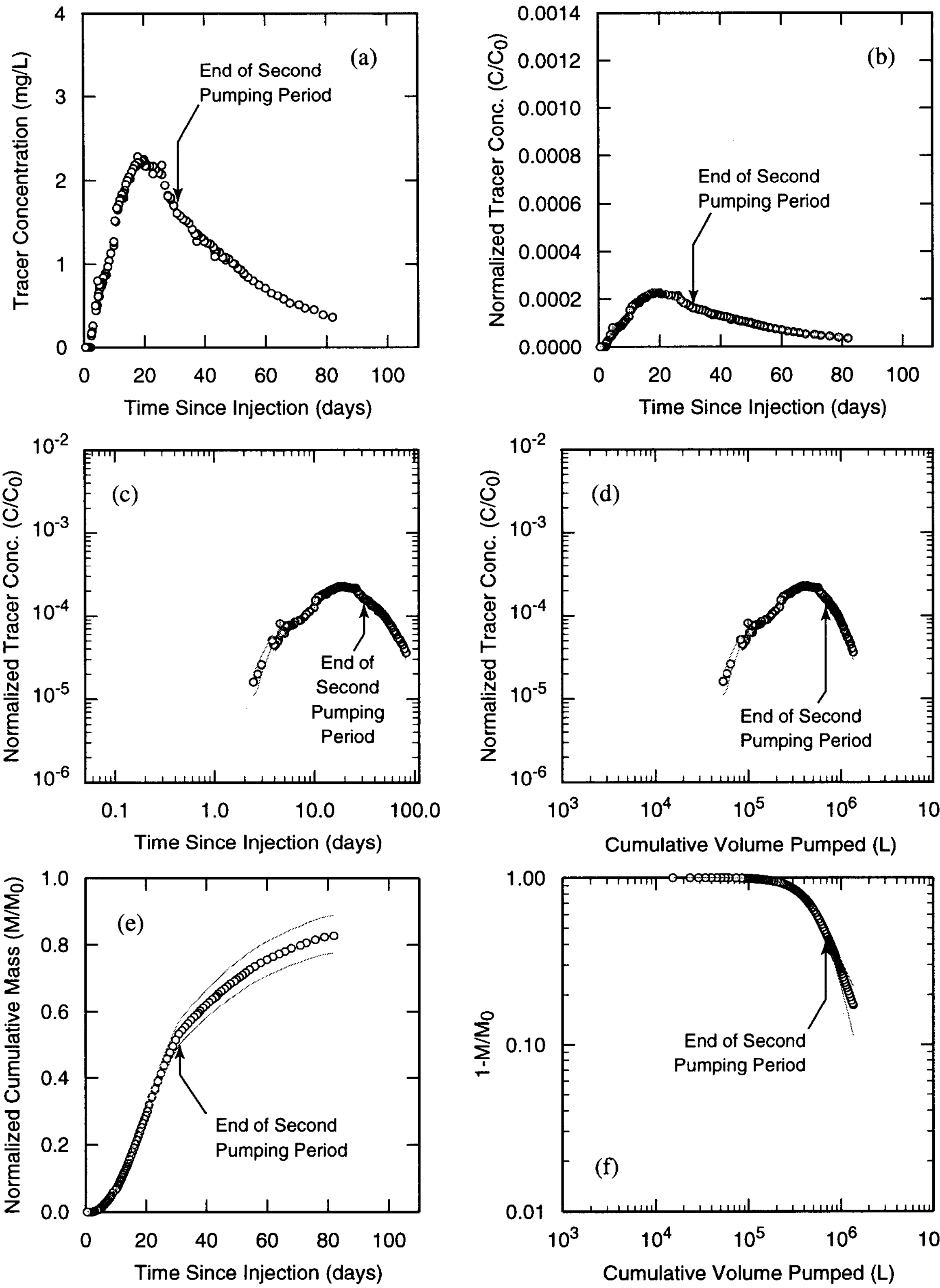

TRI-6115-928-0

Figure C-12. 2,4-DCBA data from H-19b5 to H-19b0 pathway, H-19 7-well test, round 2 (Q=0.25 L/s), full Culebra injection.

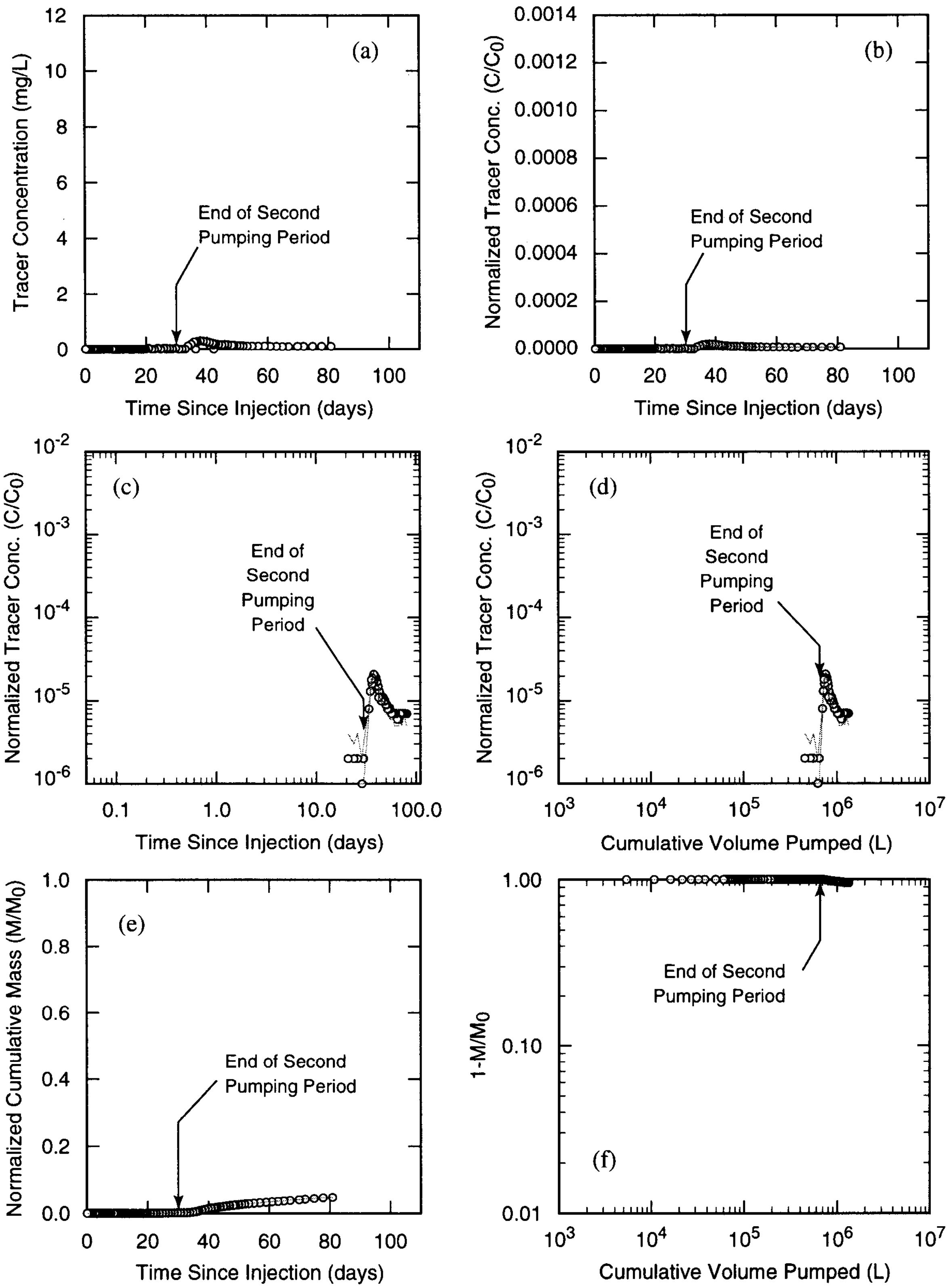

TRI-6115-929-0

Figure C-13. PFBA data from H-19b7 to H-19b0 pathway, H-19 7-well test, round 2 (Q=0.25 L/s), upper Culebra injection.

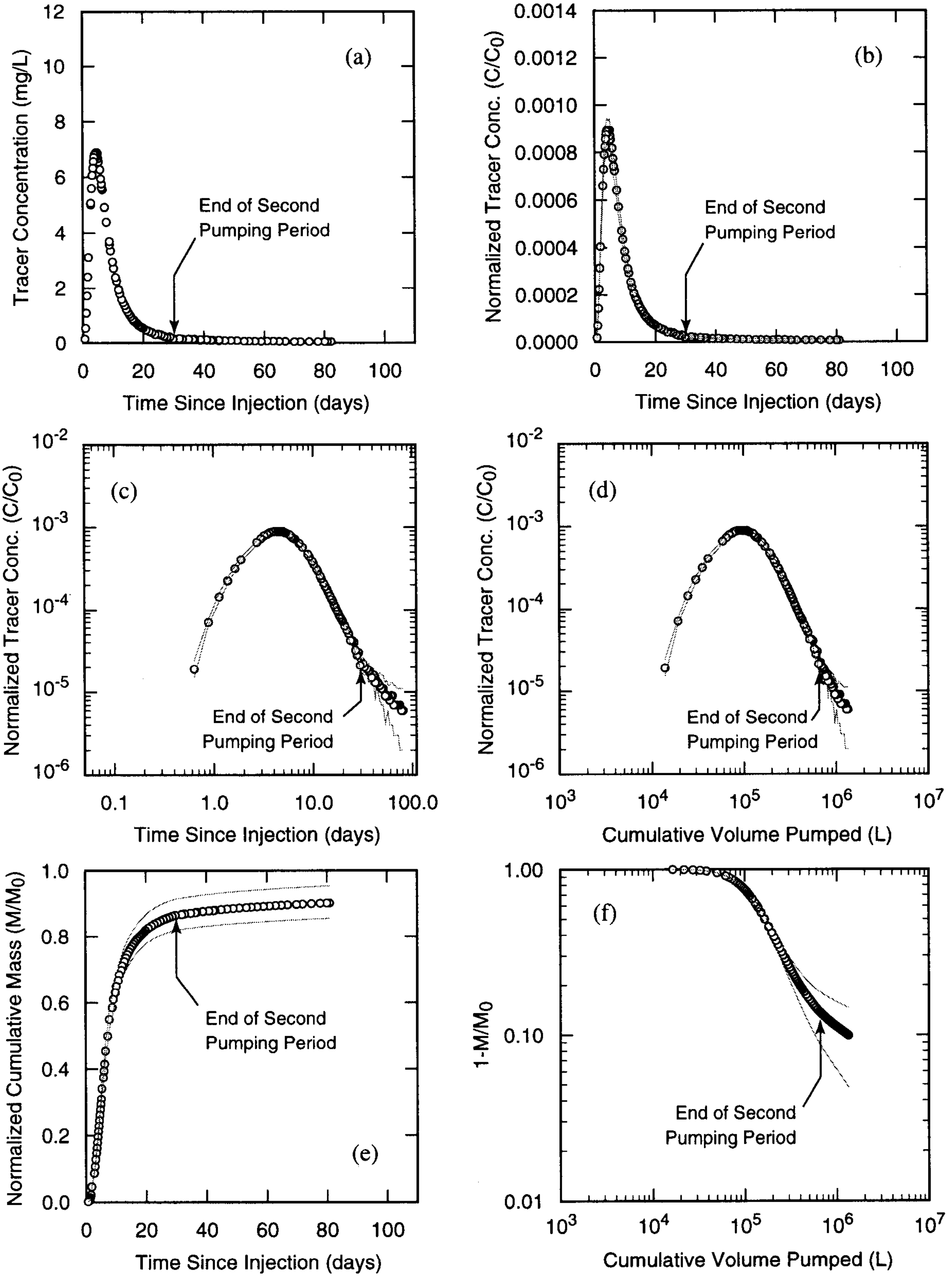

TRI-6115-930-0

Figure C-14. 3,5-DCBA data from H-19b7 to H-19b0 pathway, H-19 7-well test, round 2 (Q=0.25 L/s), lower Culebra injection.

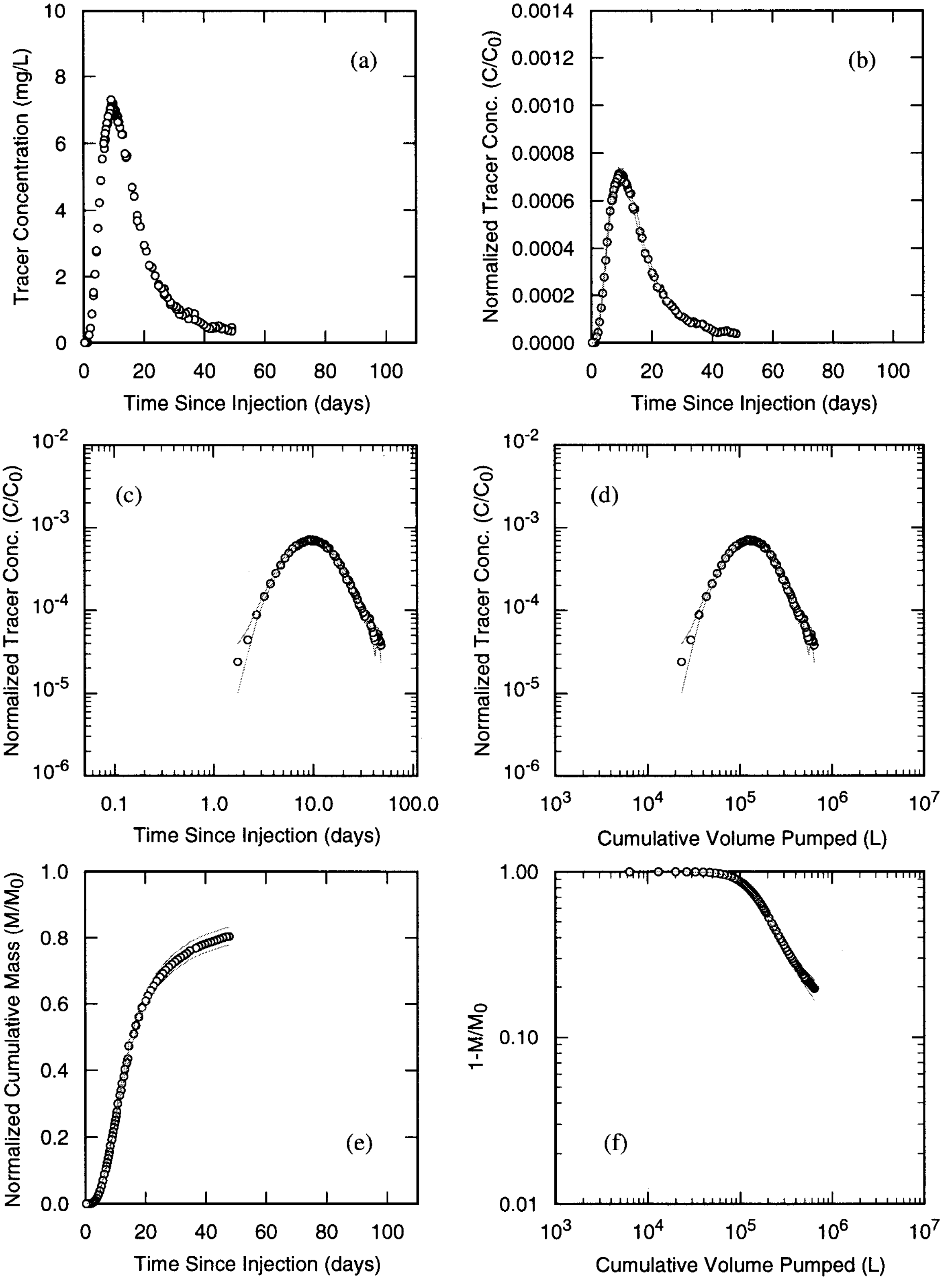

Figure C-15. 2,3,4,5-TFBA data from H-19b3 to H-19b0 pathway, H-19 7-well test, round 3 (Q=0.16 L/s), full Culebra injection.

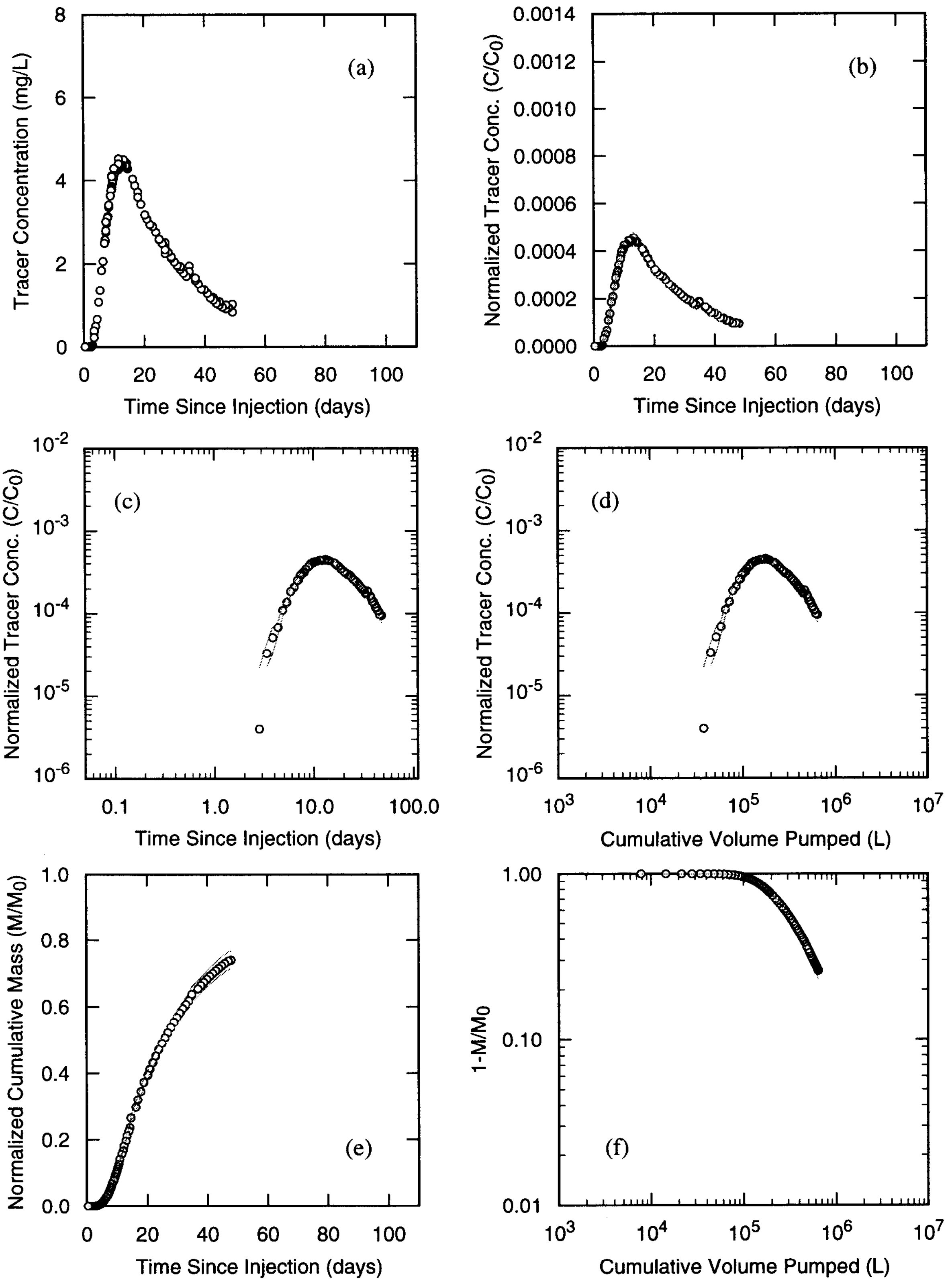

TRI-6115-932-0

Figure C-16. **2,4,6-TCBA data from H-19b6 to H-19b0 pathway, H-19 7-well test, round 3 (Q=0.16 L/s), full Culebra injection.**

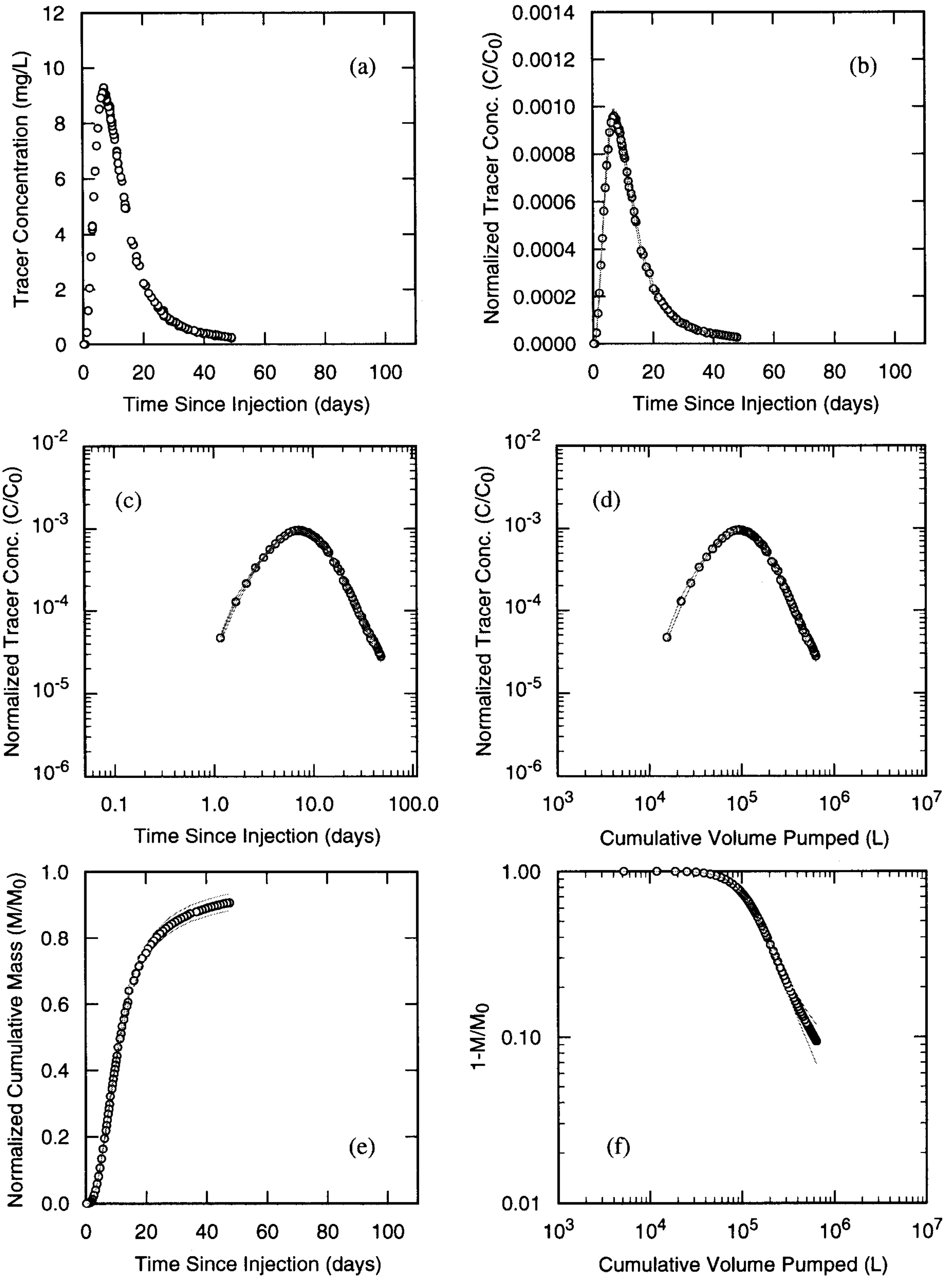

Figure C-17. 2,3,6-TFBA data from H-19b7 to H-19b0 pathway, H-19 7-well test, round 3 (Q=0.16 L/s), full Culebra injection.

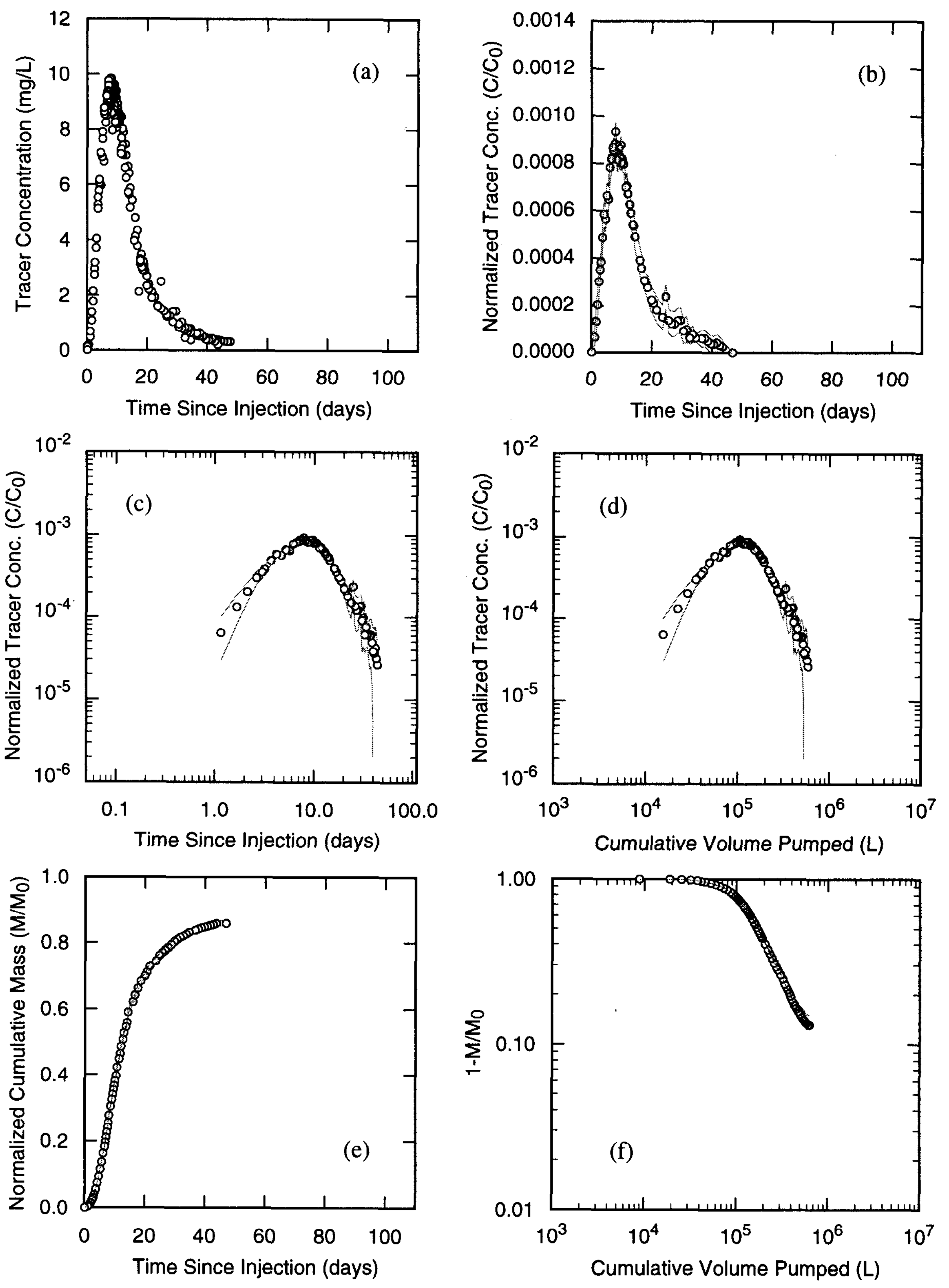

TRI-6115-934-0

Figure C-18. Iodide data from H-19b7 to H-19b0 pathway, H-19 7-well test, round 3 (Q=0.16 L/s), full Culebra injection analyzed using a high performance liquid chomatograph.

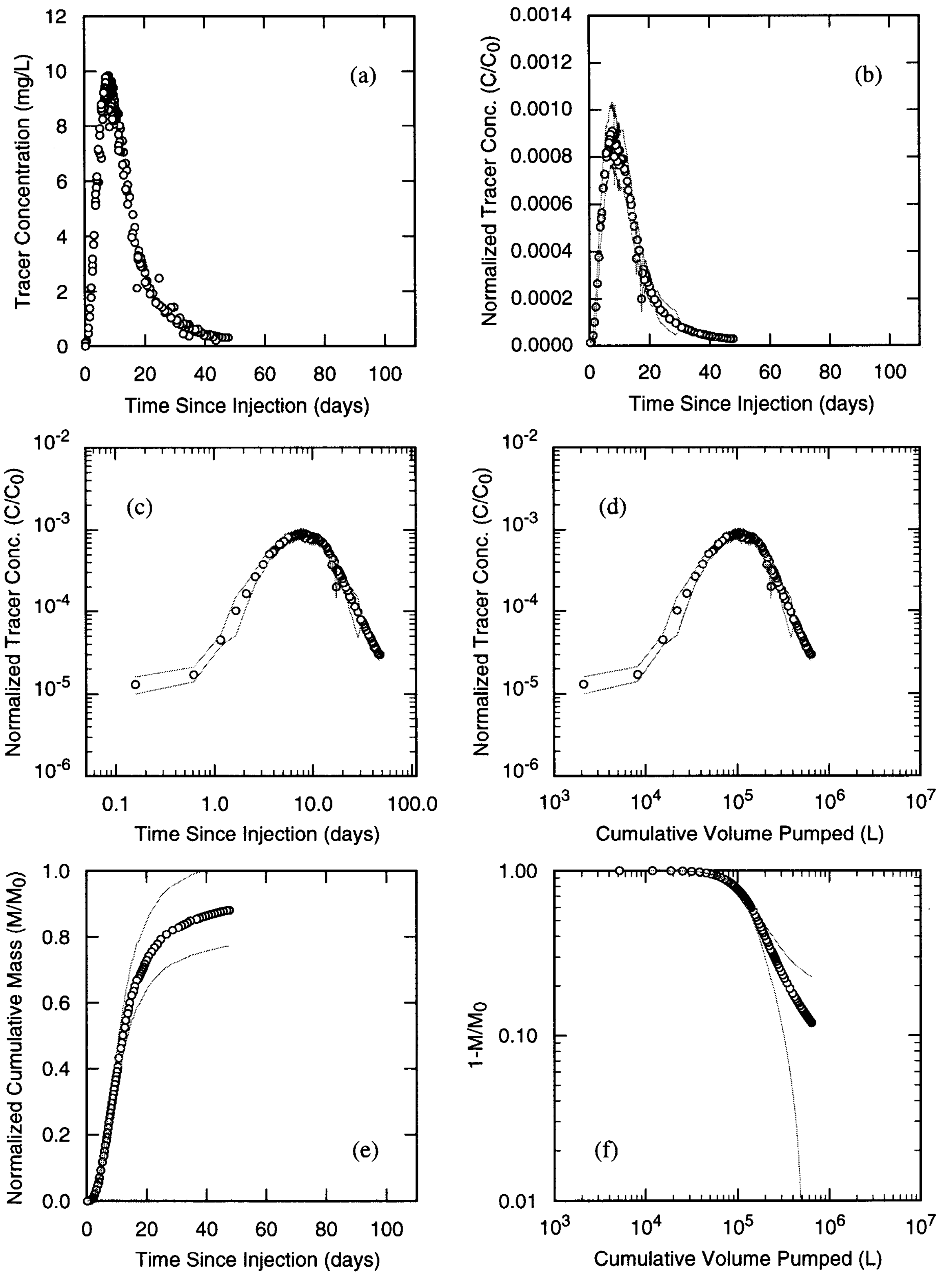

Figure C-19. Iodide data from H-19b7 to H-19b0 pathway, H-19 7-well test, round 3 (Q=0.16 L/s), full Culebra injection analyzed using an ion chromatograph.

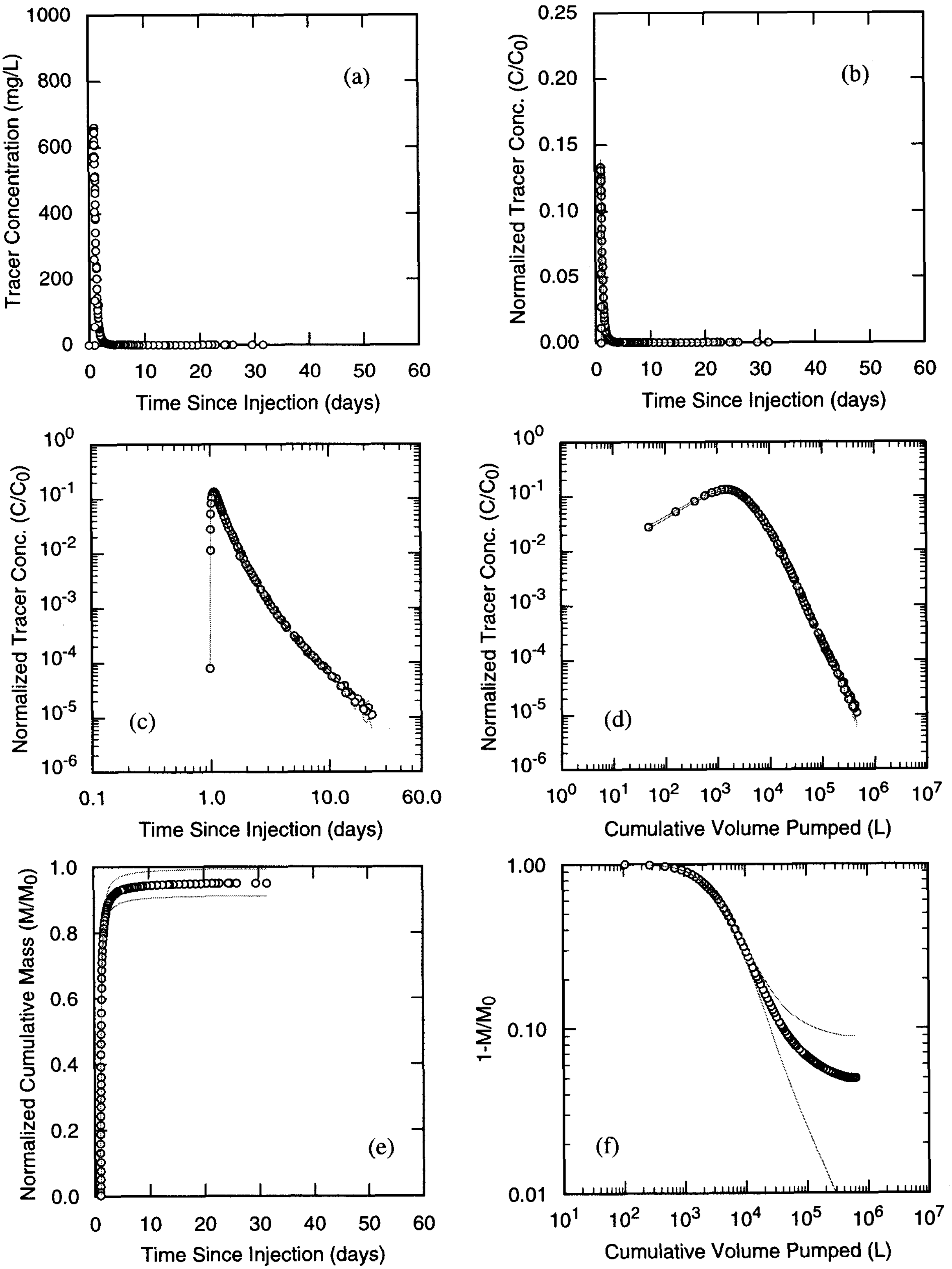

TRI-6115-553-0

Figure C-20. 2,4-DCBA data (Tracer 1) from H-19b0, 4-well test—SWIW Test 1 (Q=0.24 L/s), full Culebra injection.

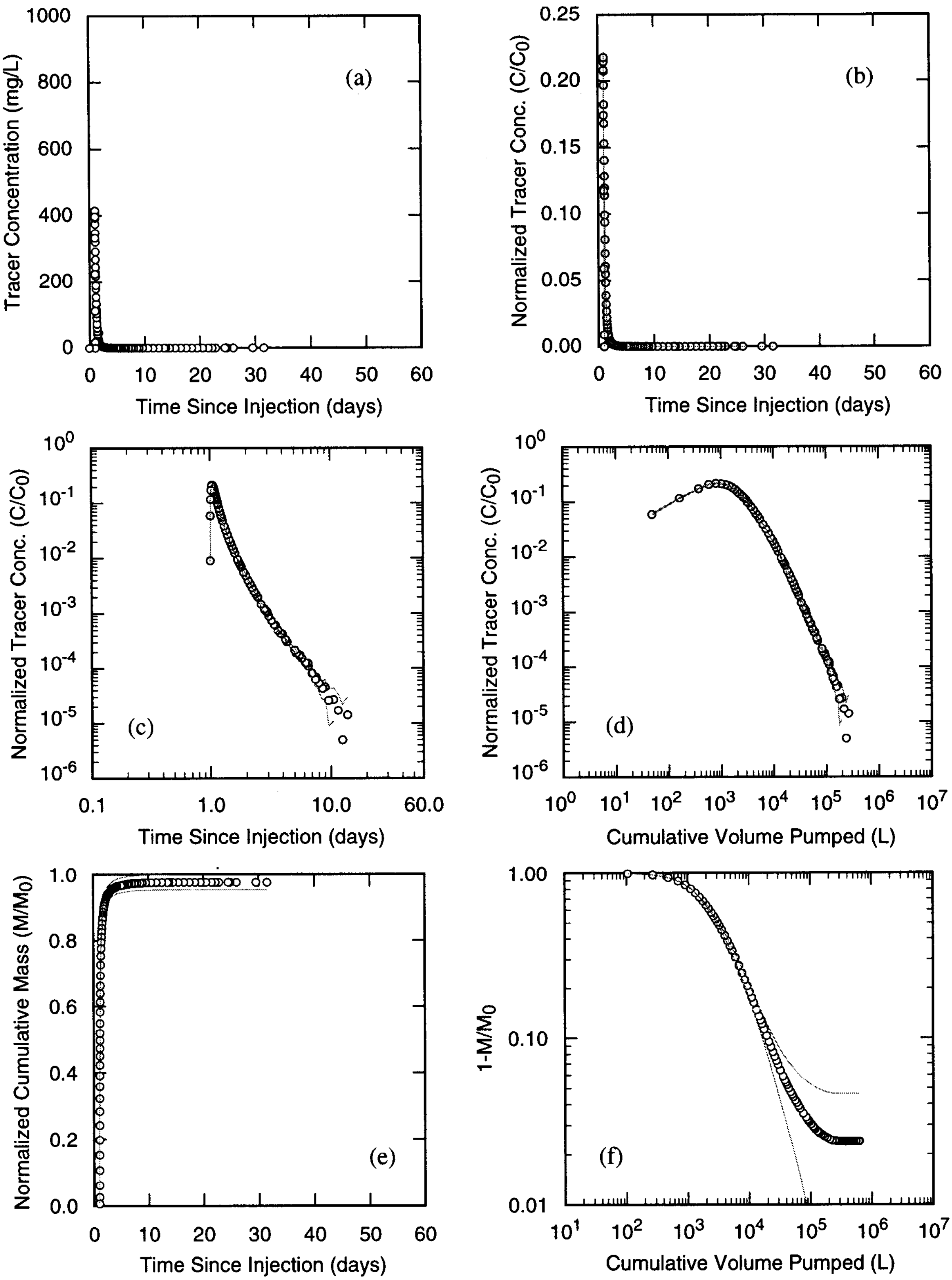

TRI-6115-554-0

Figure C-21. **o-TFMBA data (Tracer 2) from H-19b0, 4-well test—SWIW Test 1 (Q=0.24 L/s), full Culebra injection.**

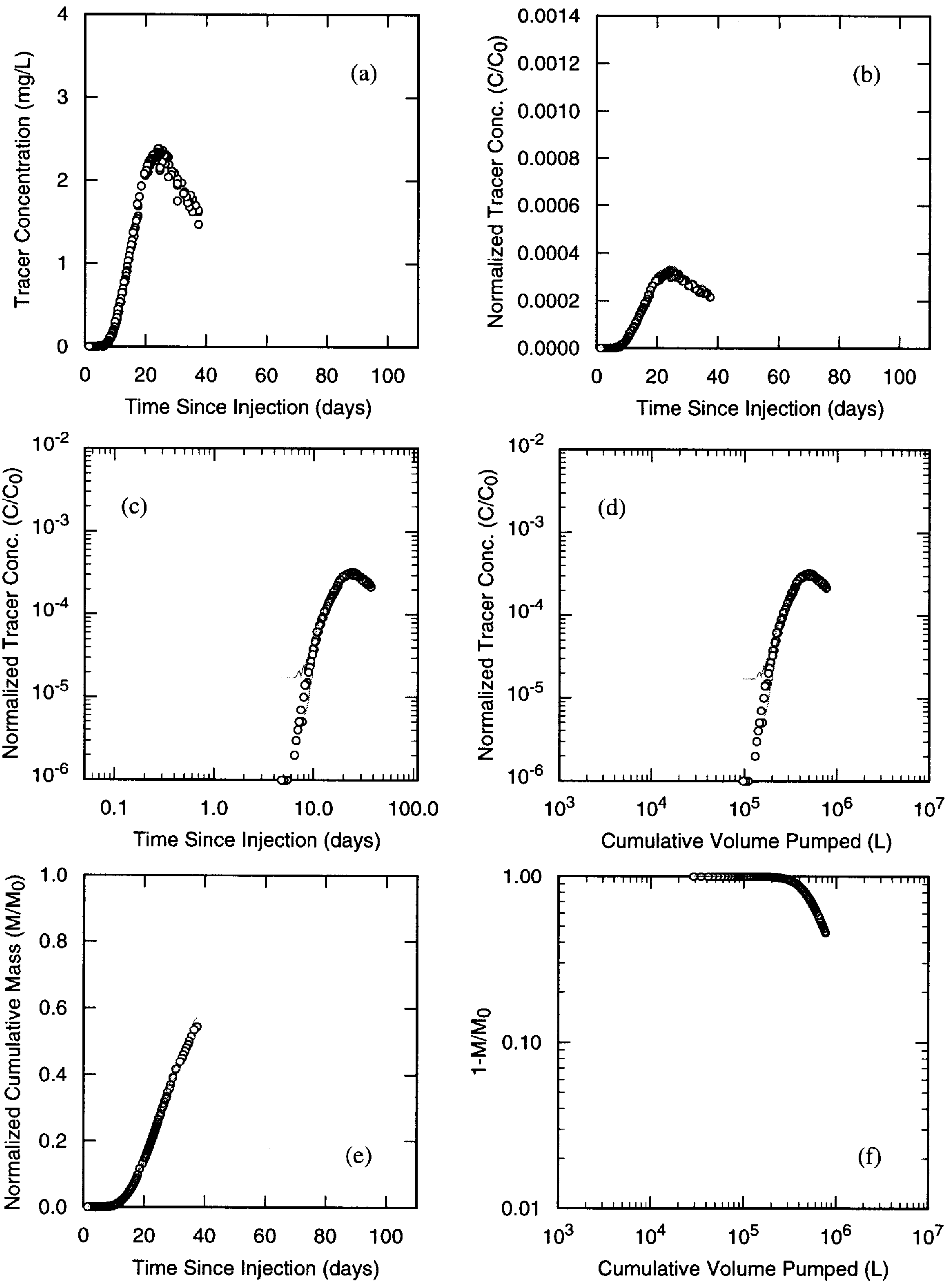

TRI-6115-937-0

Figure C-22. 2,3-DFBA data from H-19b2 to H-19b0 pathway, H-19 4-well test (Q=0.24 L/s).

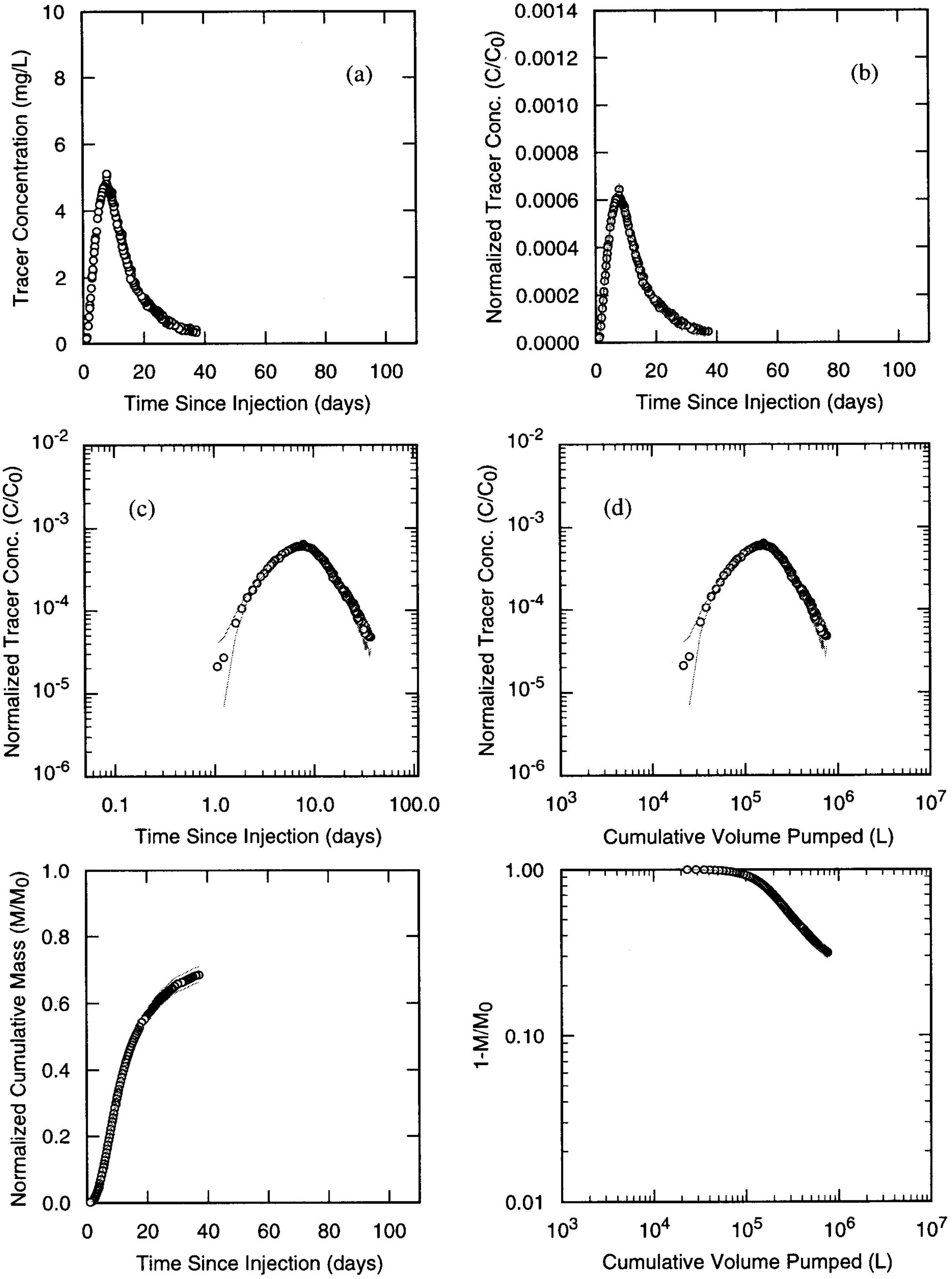

TRI-6115-938-0

Figure C-23. 2,3,4,5-TFBA data from H-19b3 to H-19b0 pathway, H-19 4-well test (Q=0.24 L/s).

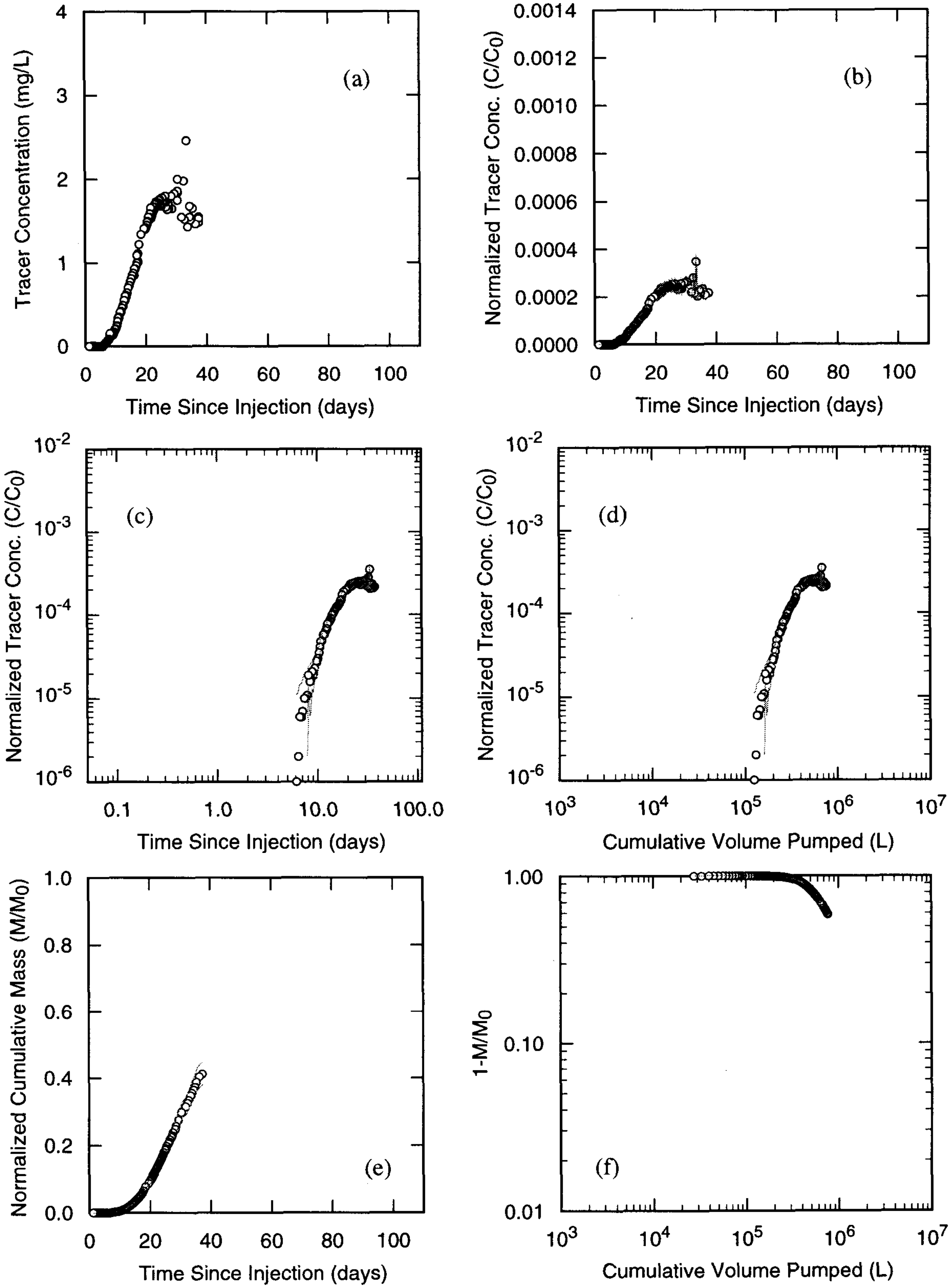

TRI-6115-939-0

Figure C-24. **2,6-DFBA data from H-19b4 to H-19b0 pathway, H-19 4-well test (Q=0.24 L/s).**

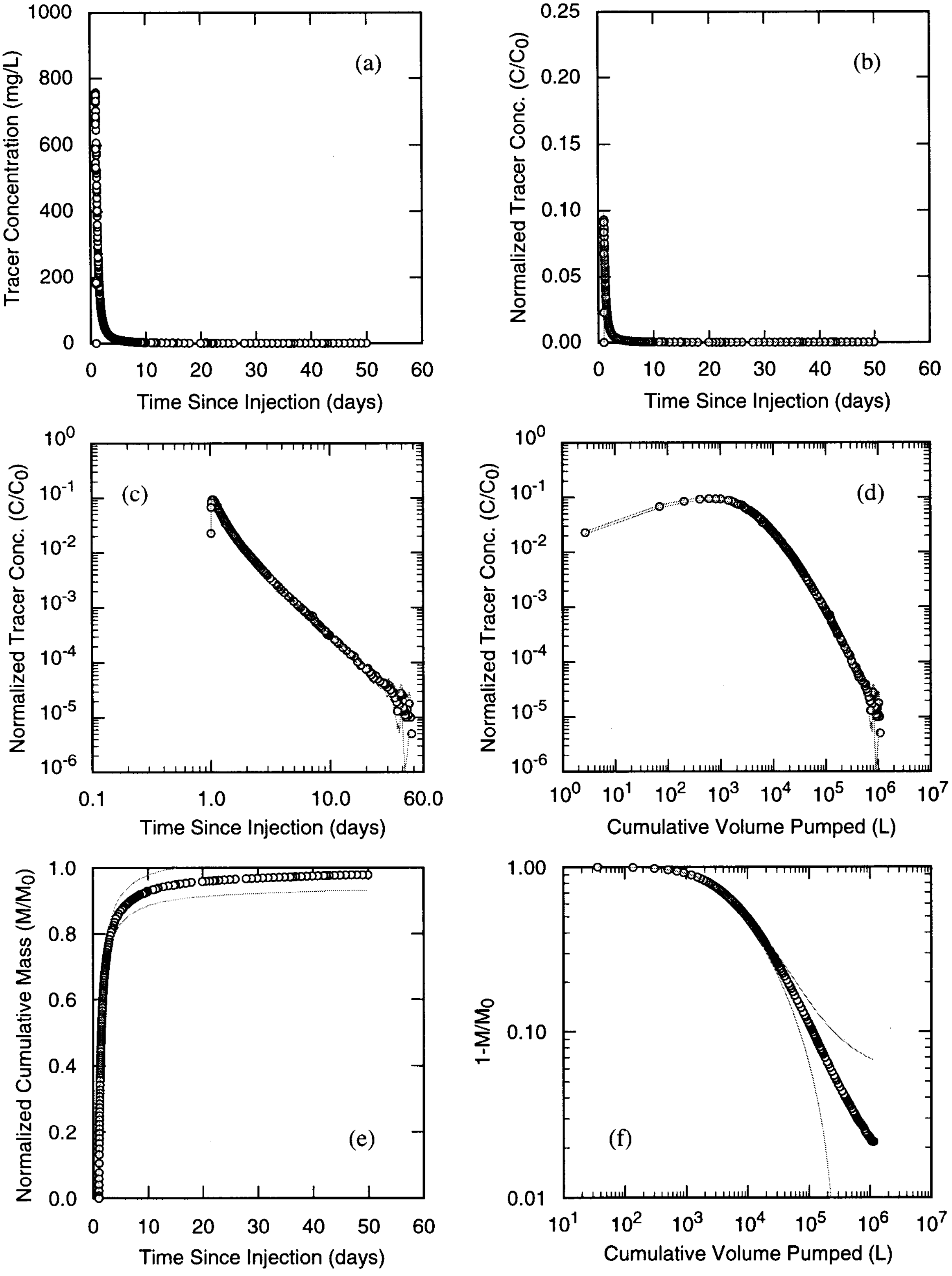

TRI-6115-546-0

Figure C-25. 2,4-DCBA data (Tracer 1) from H-11b1—SWIW test (Q=0.22 L/s).

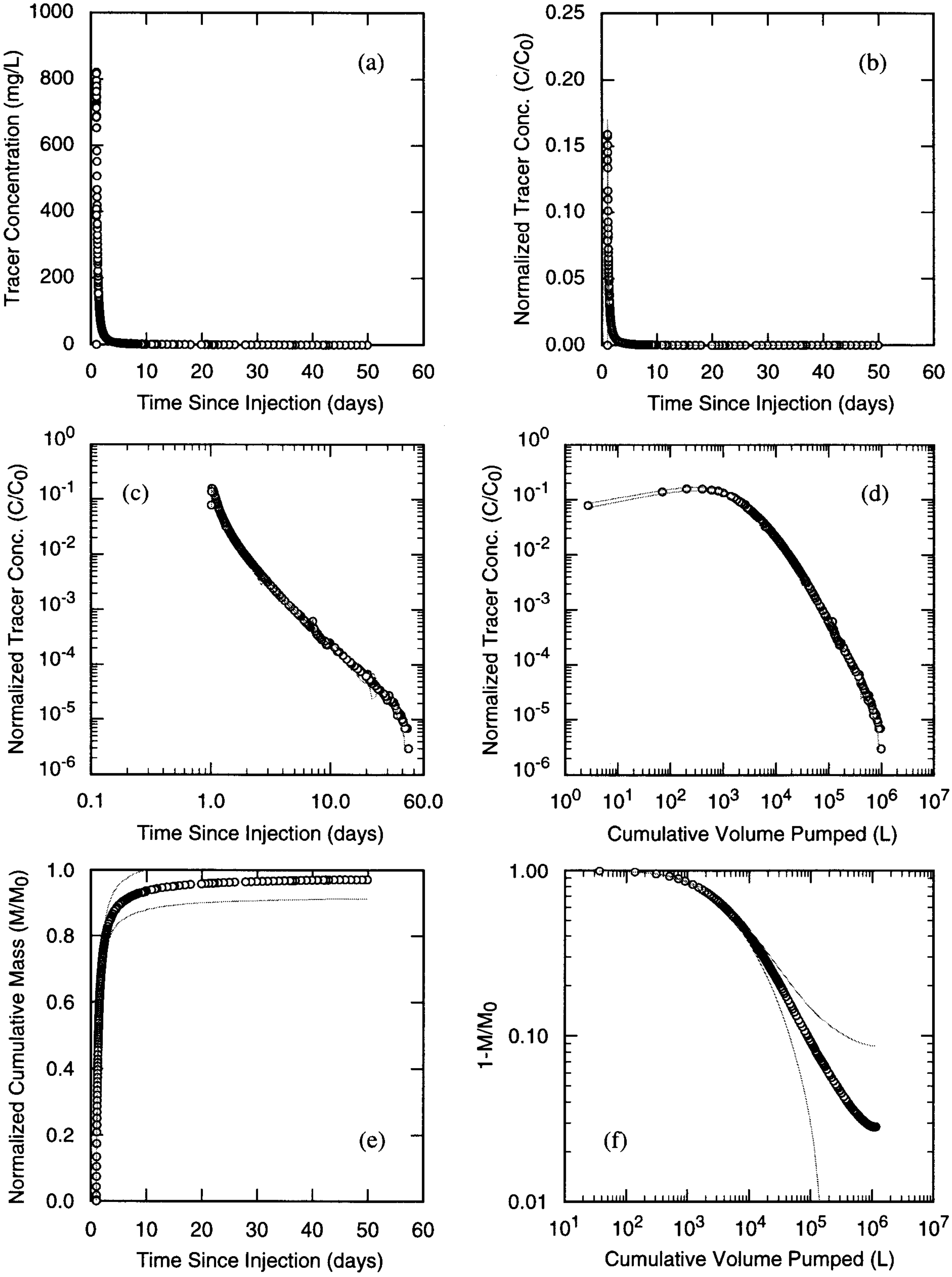

Figure C-26. 3,4-DFBA data (Tracer 2) from H-11b1—SWIW Test (Q=0.22 L/s).

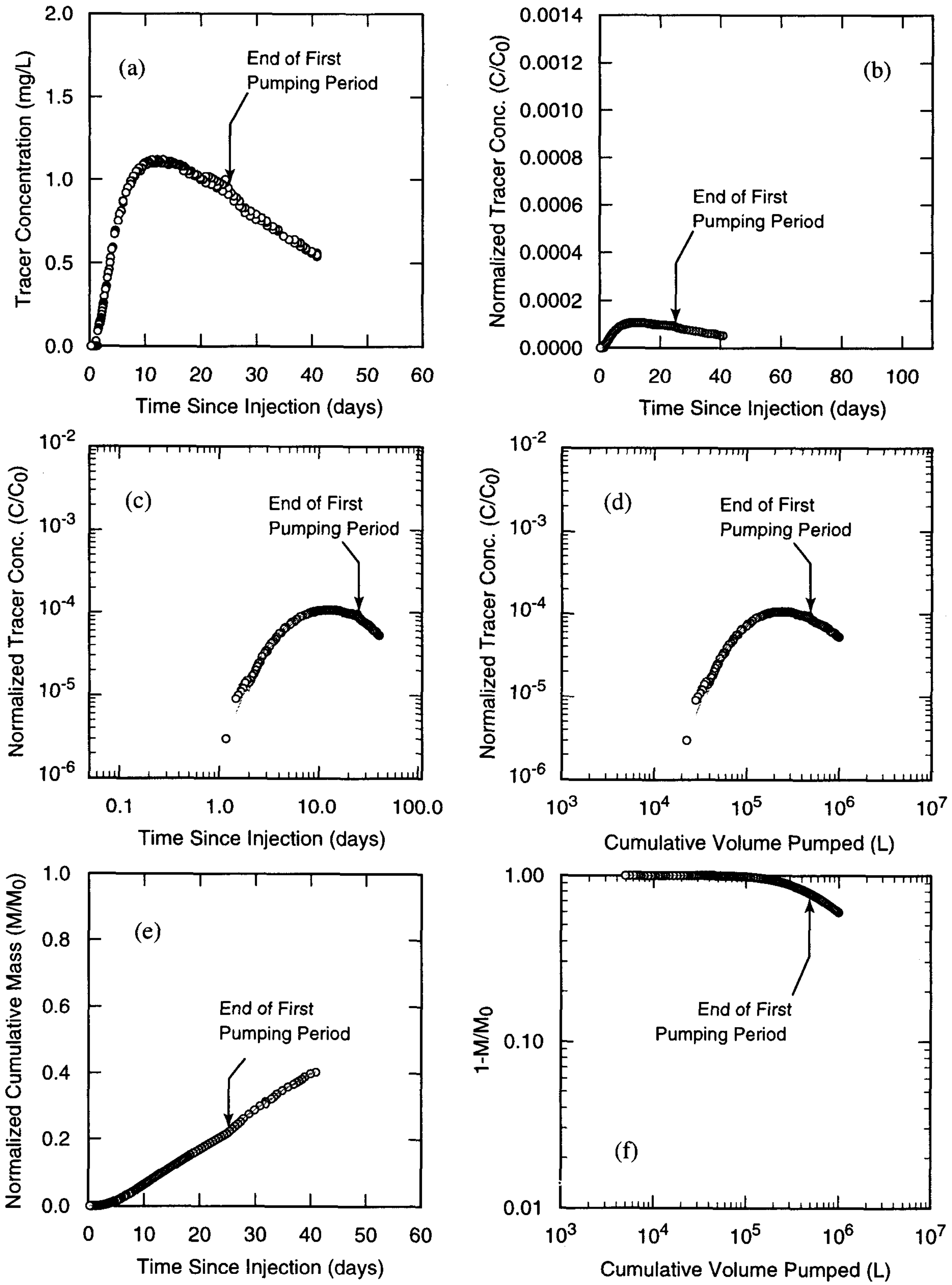

TRI-6115-548-0

Figure C-27. 2,6-DFBA data from H-11b2 to H-11b1 pathway, H-11 1996 test, round 1 (Q=0.22 L/s).

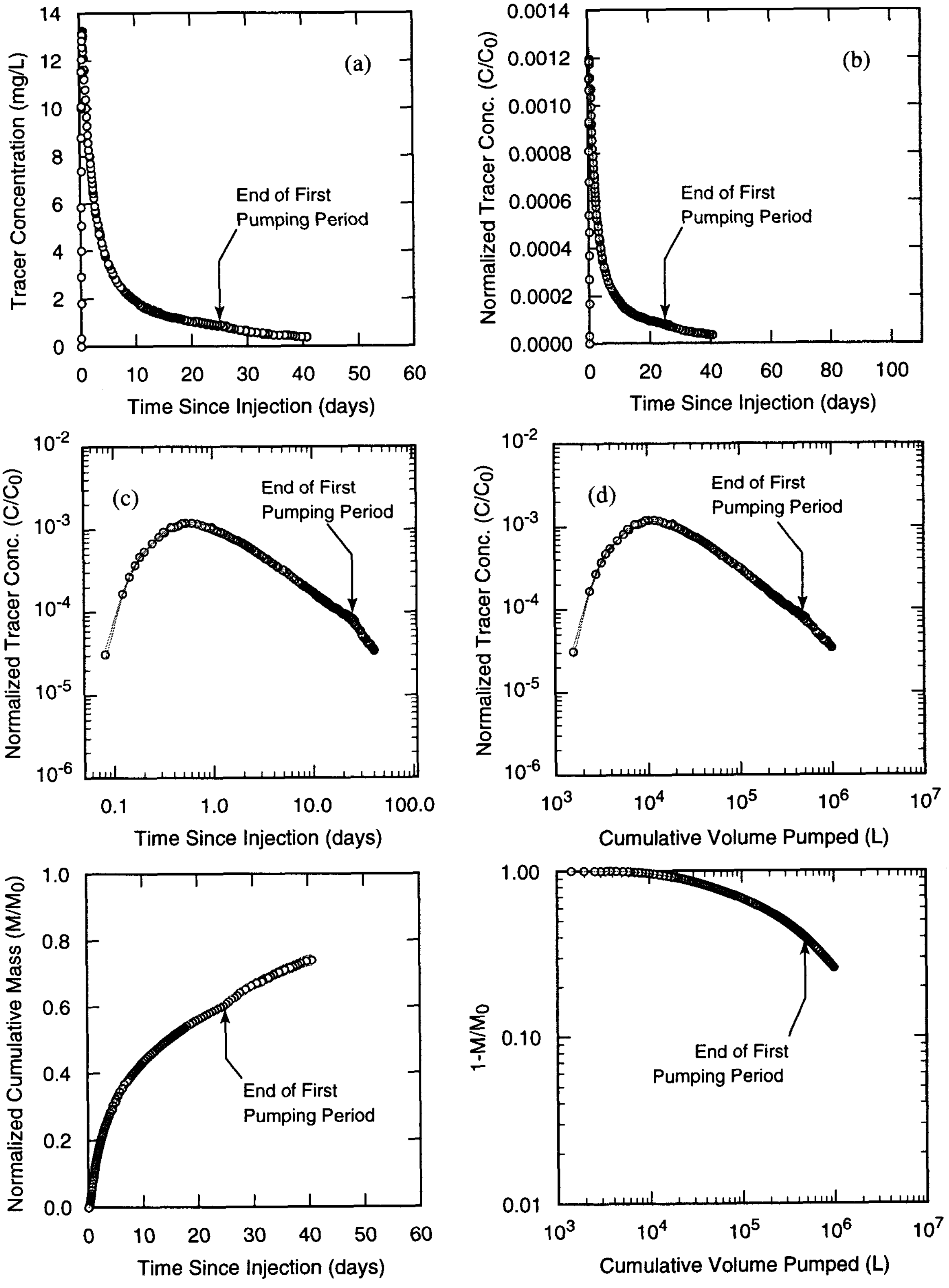

Figure C-28. 2,3,4,5-TFBA data from H-11b3 to H-11b1 pathway, H-11 1996 test, round 1 (Q=0.22 L/s).

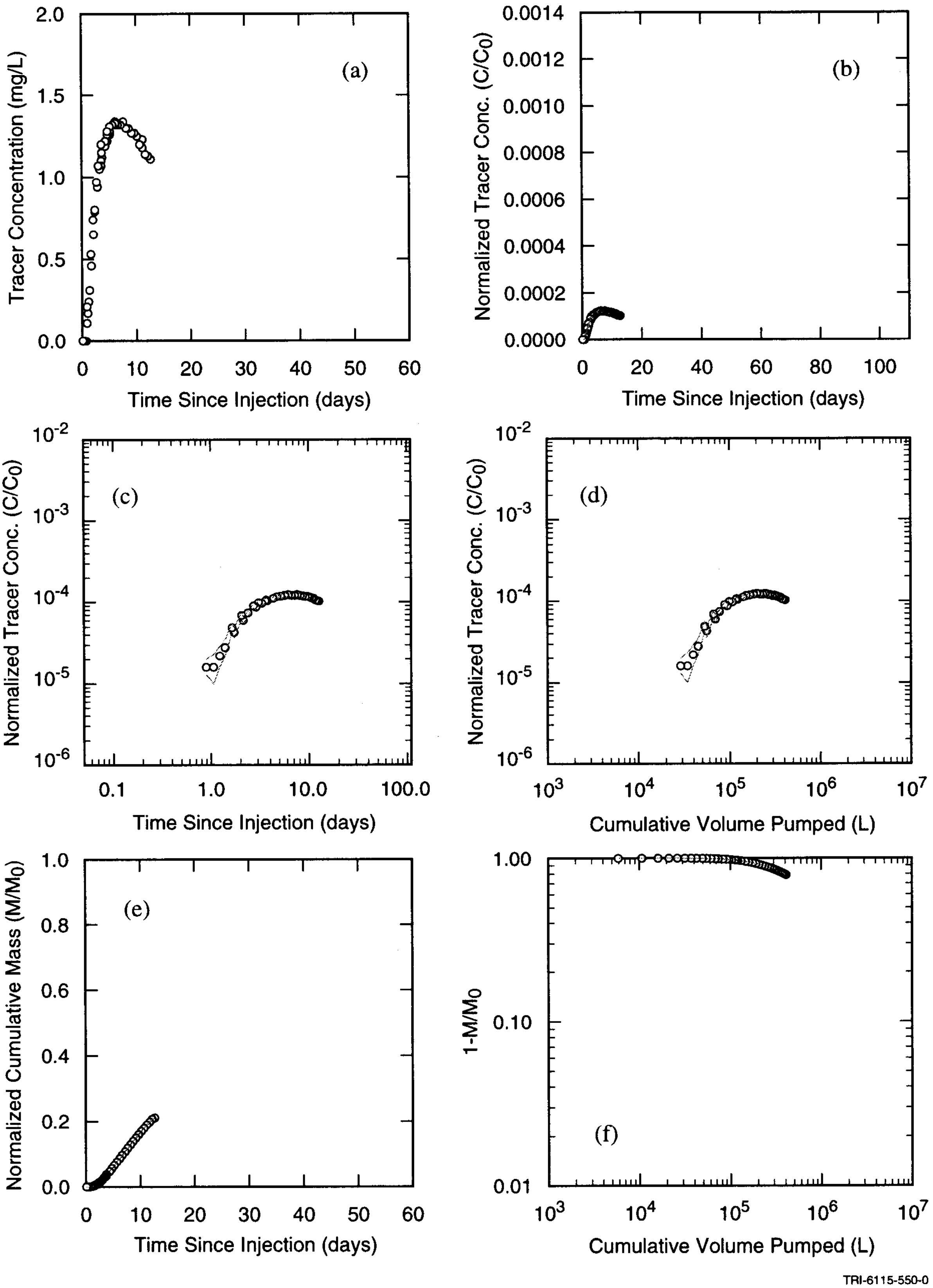

Figure C-29. p-TFMBA, data from H-11b2 to H-11b1 pathway, H-11 1996 test, round 2 (Q=0.38 L/s).

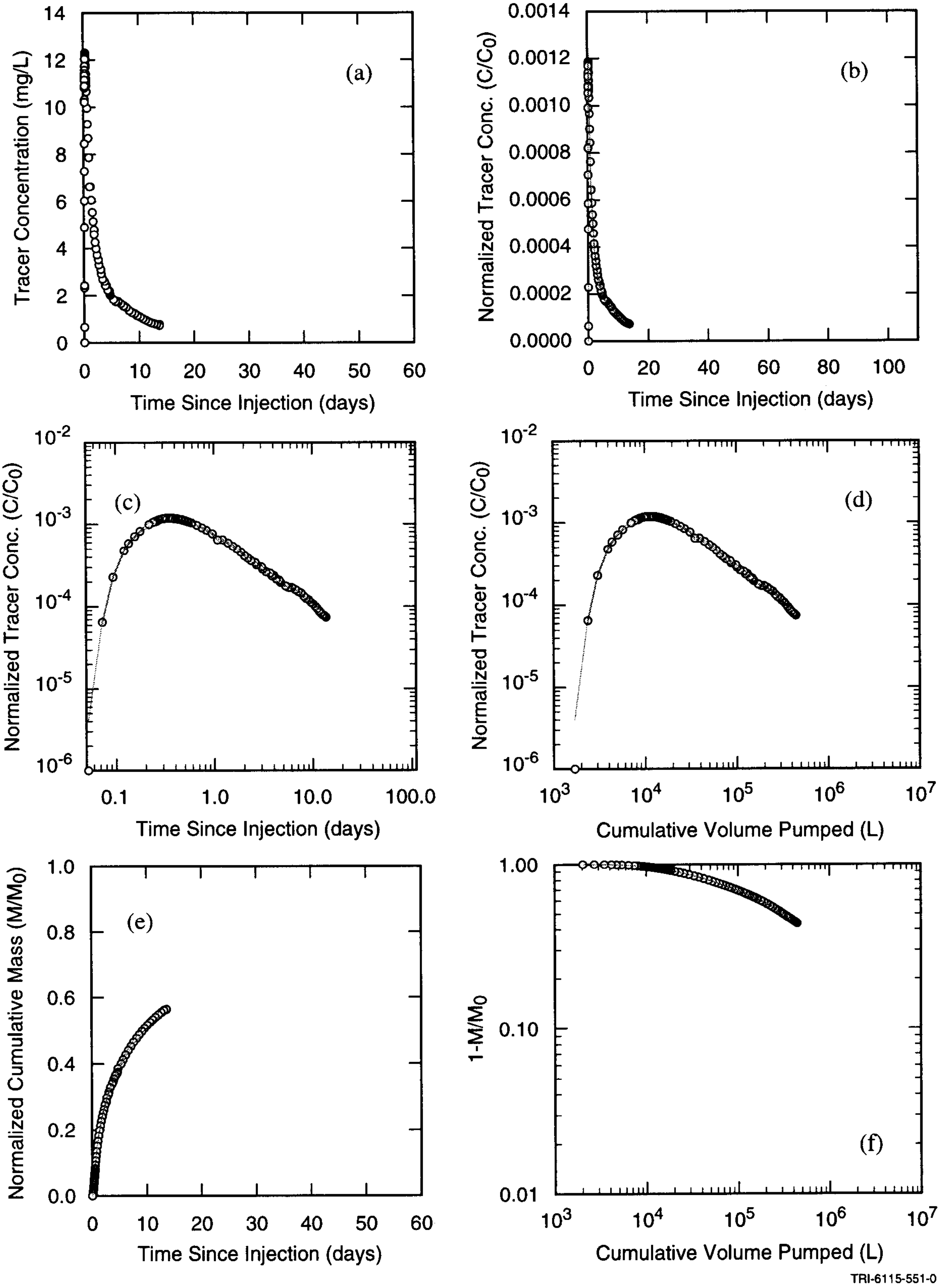

Figure C-30. **2,5-DFBA data from H-11b3 to H-11b1 pathway, H-11 1996 test, round 2 (Q=0.38 L/s).**

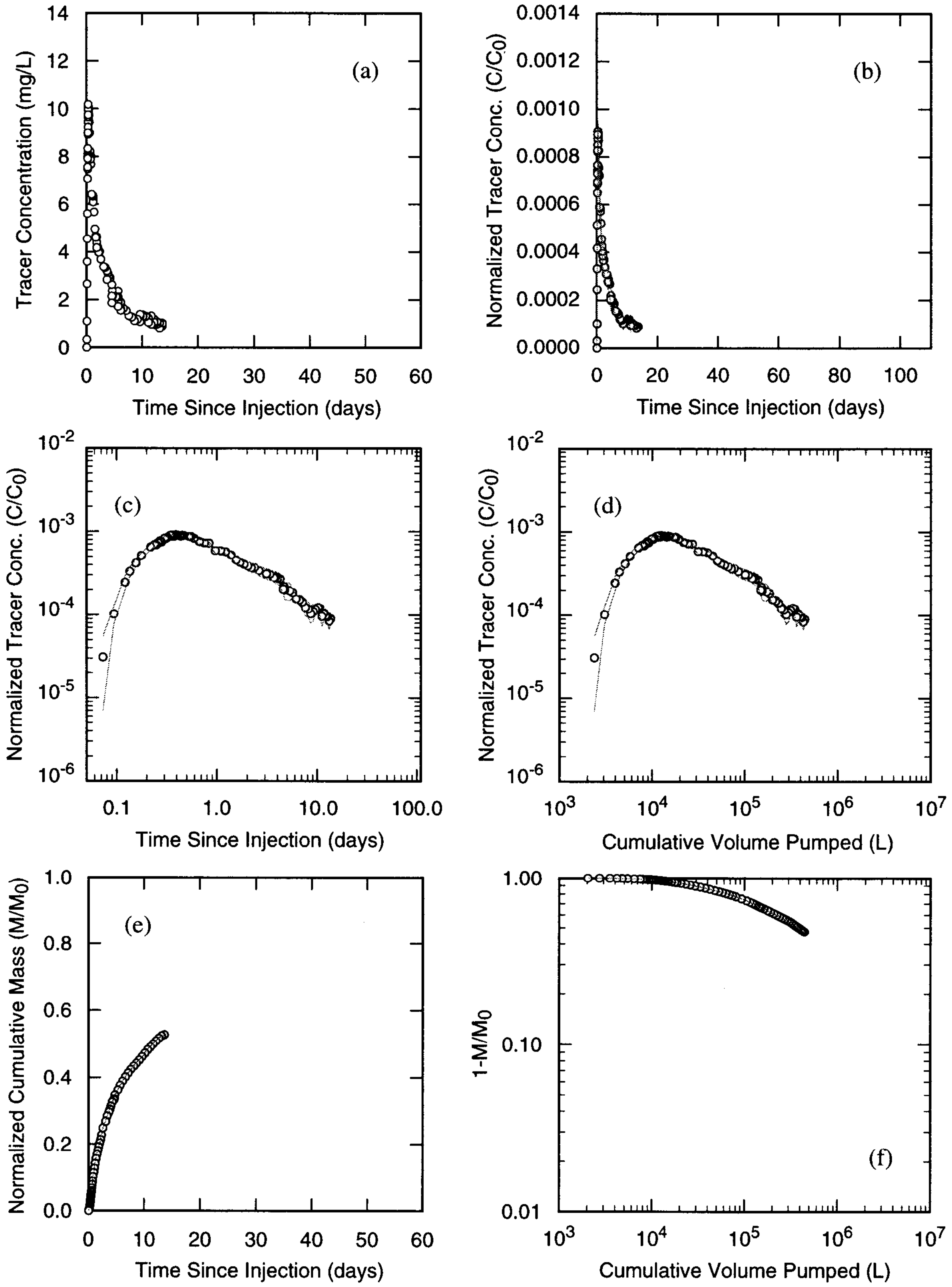

TRI-6115-552-0

Figure C-31. **Iodide data from H-11b3 to H-11b1 pathway, H-11 1996 test, round 2 (Q=0.38 L/s) analyzed using a high performance liquid chomatograph.**

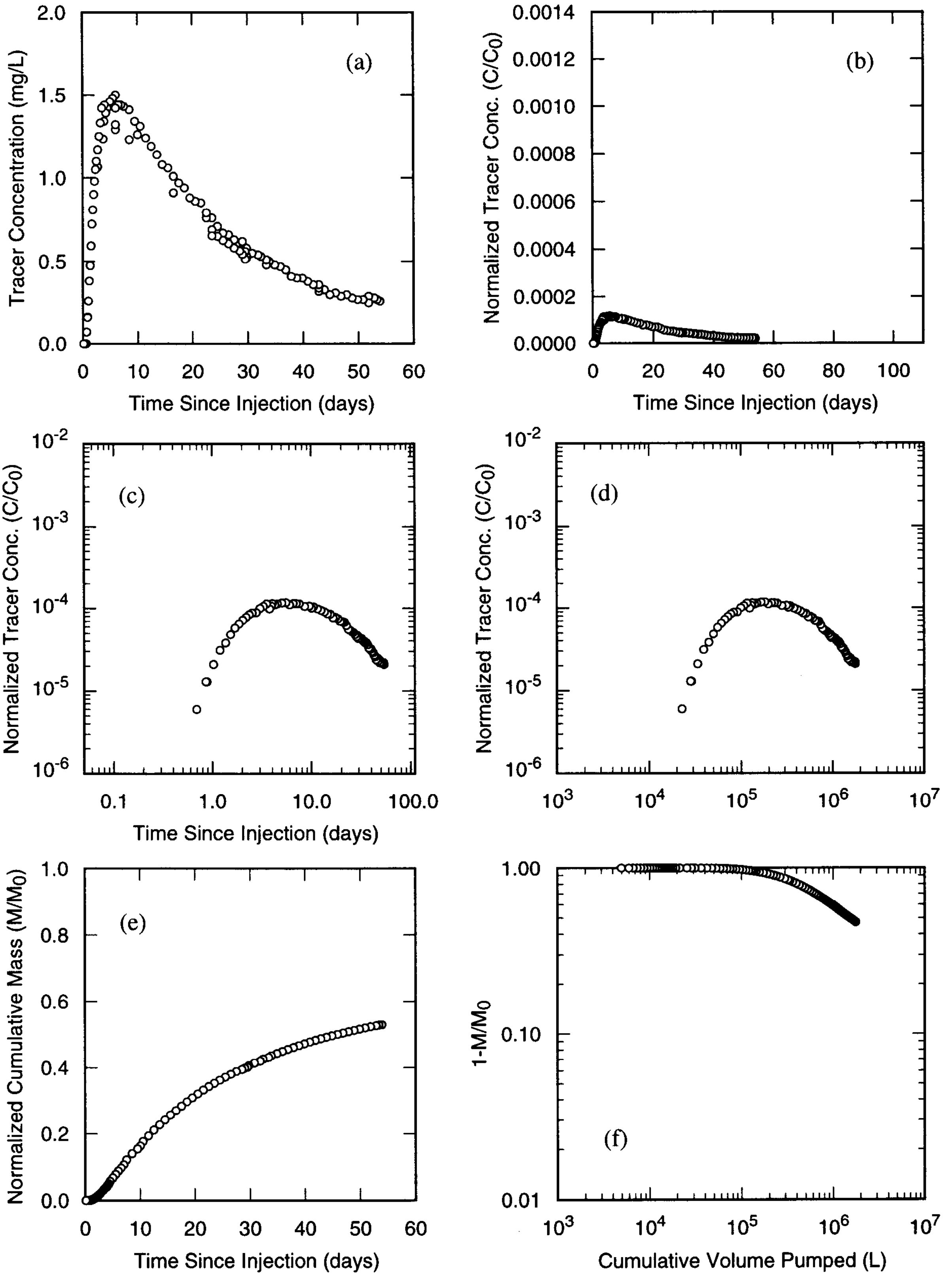

TRI-6115-543-0

Figure C-32. PFBA data from H-11b2 to H-11b1 pathway, H-11 1988 test (Q=0.38 L/s).

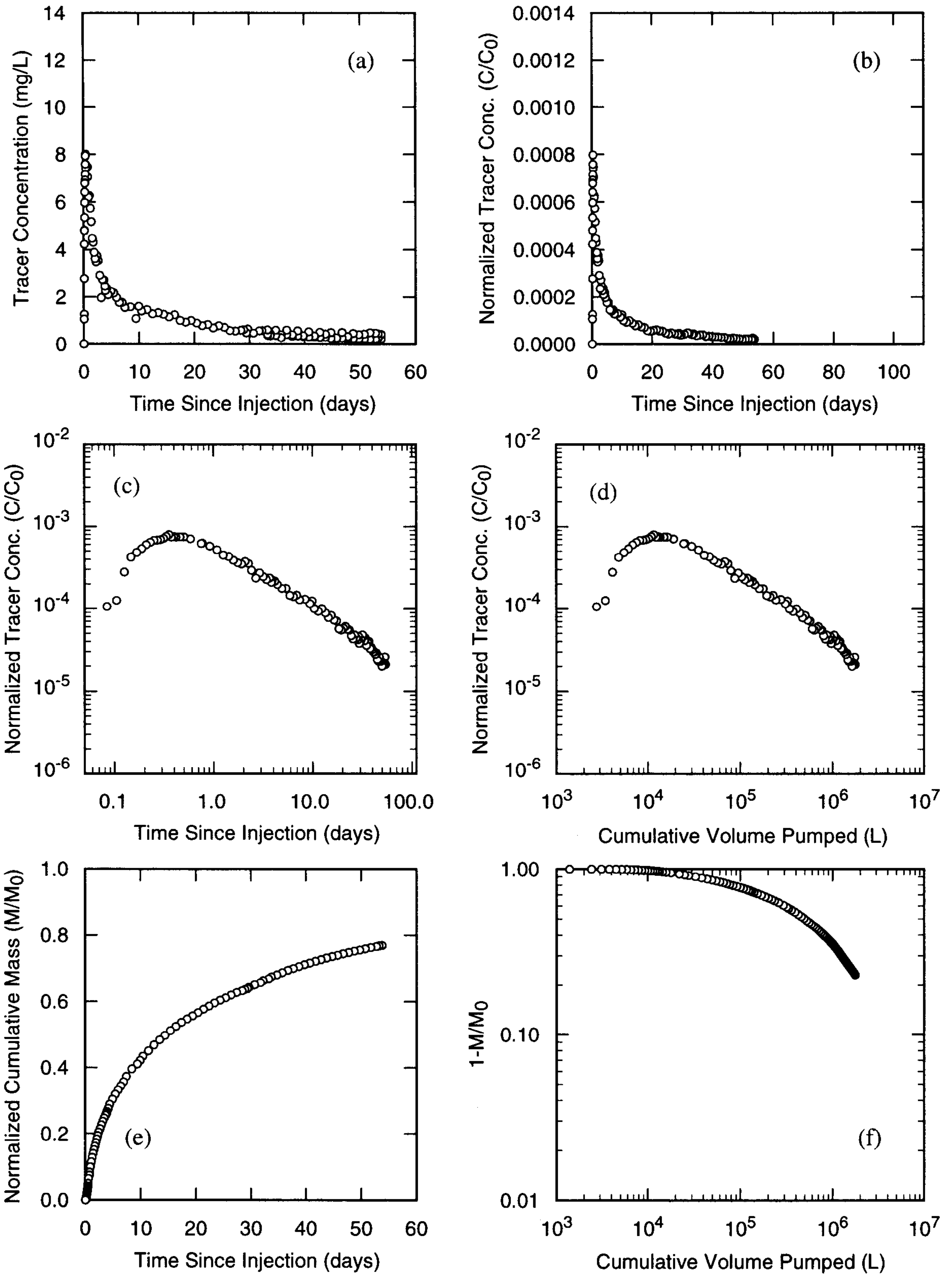

Figure C-33. m-TFMBA data from H-11b3 to H-11b1 pathway, H-11 1988 test (Q=0.38 L/s).

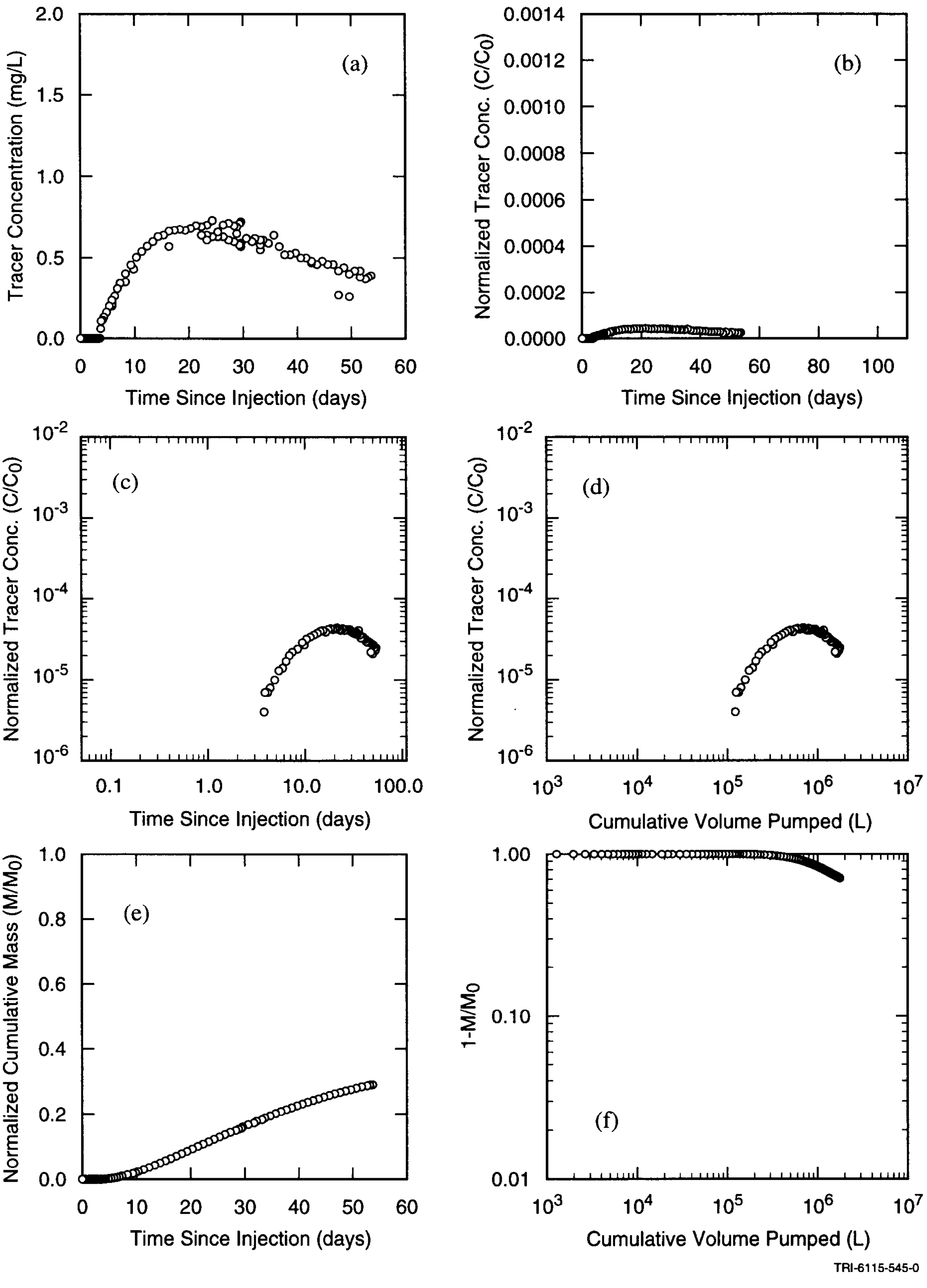

Figure C-34. o-TFMBA data from H-11b4 to H-11b1 pathway, H-11 1988 test (Q=0.38 L/s).

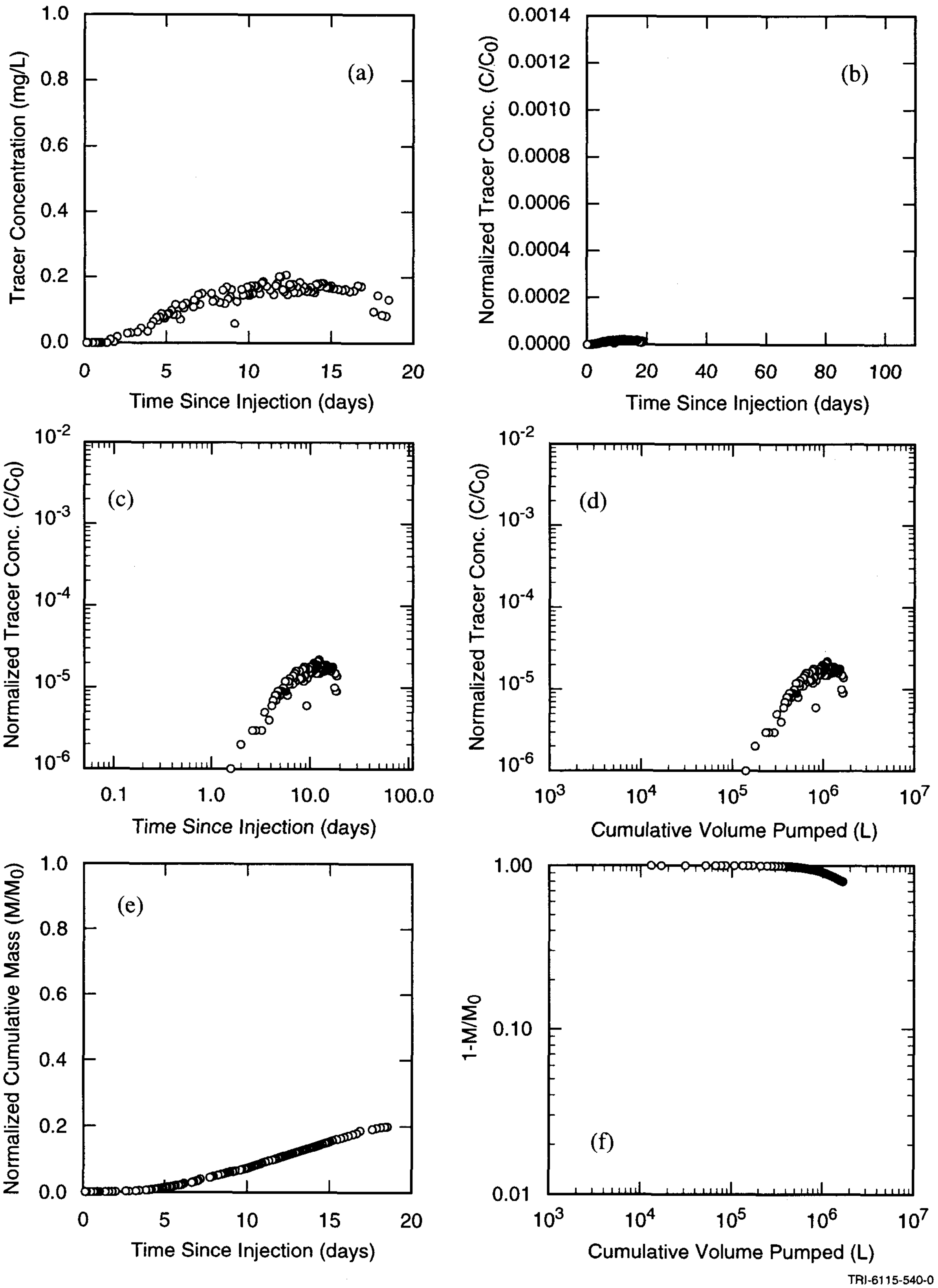

Figure C-35. m-TFMBA data from H-6a to H-6c pathway, H-6 1981 test 1 (Q=1.04 L/s).

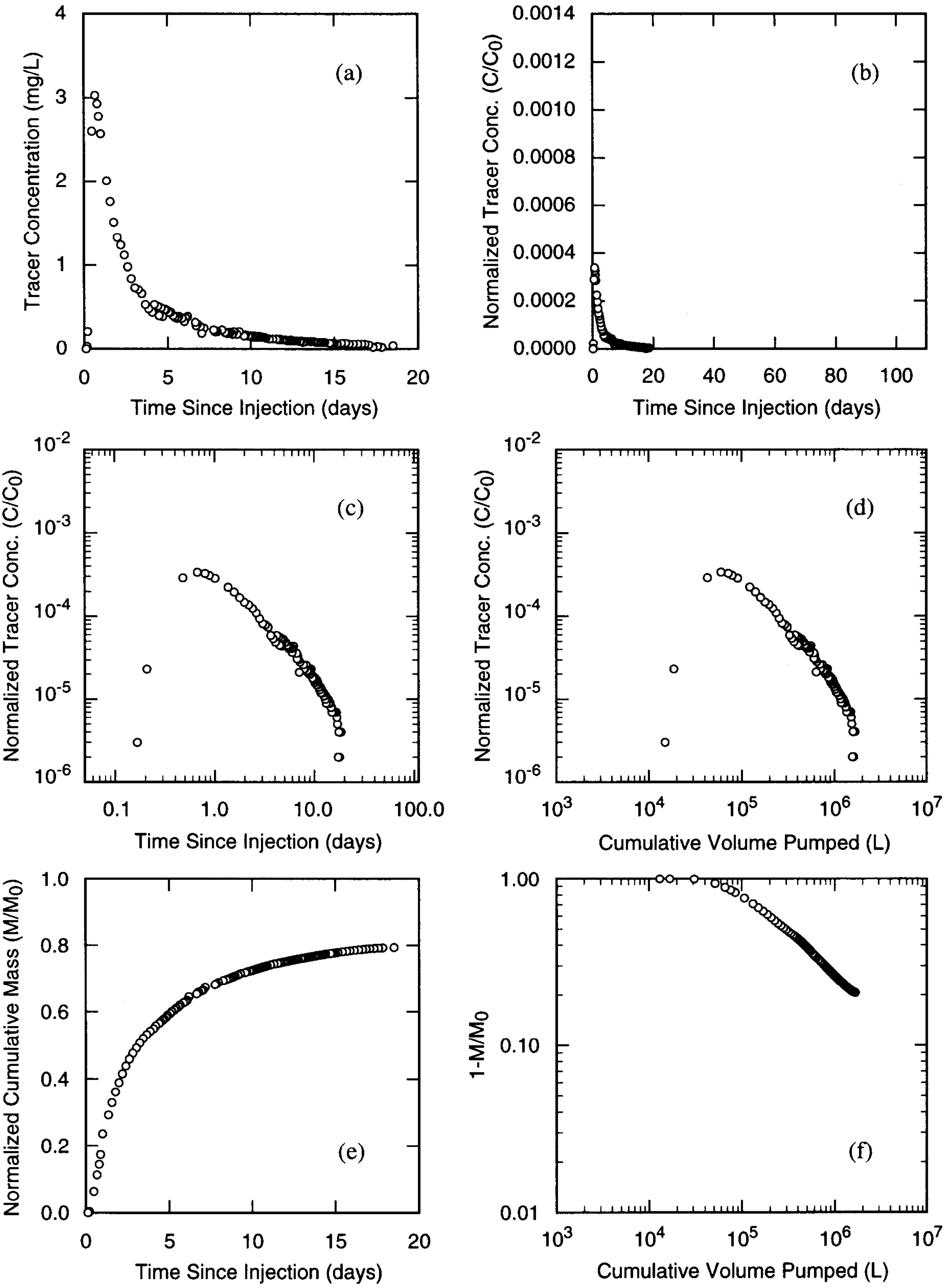

TRI-6115-541-0

Figure C-36. PFBA data from H-6b to H-6c pathway, H-6 1981 test 1 (Q=1.04 L/s).

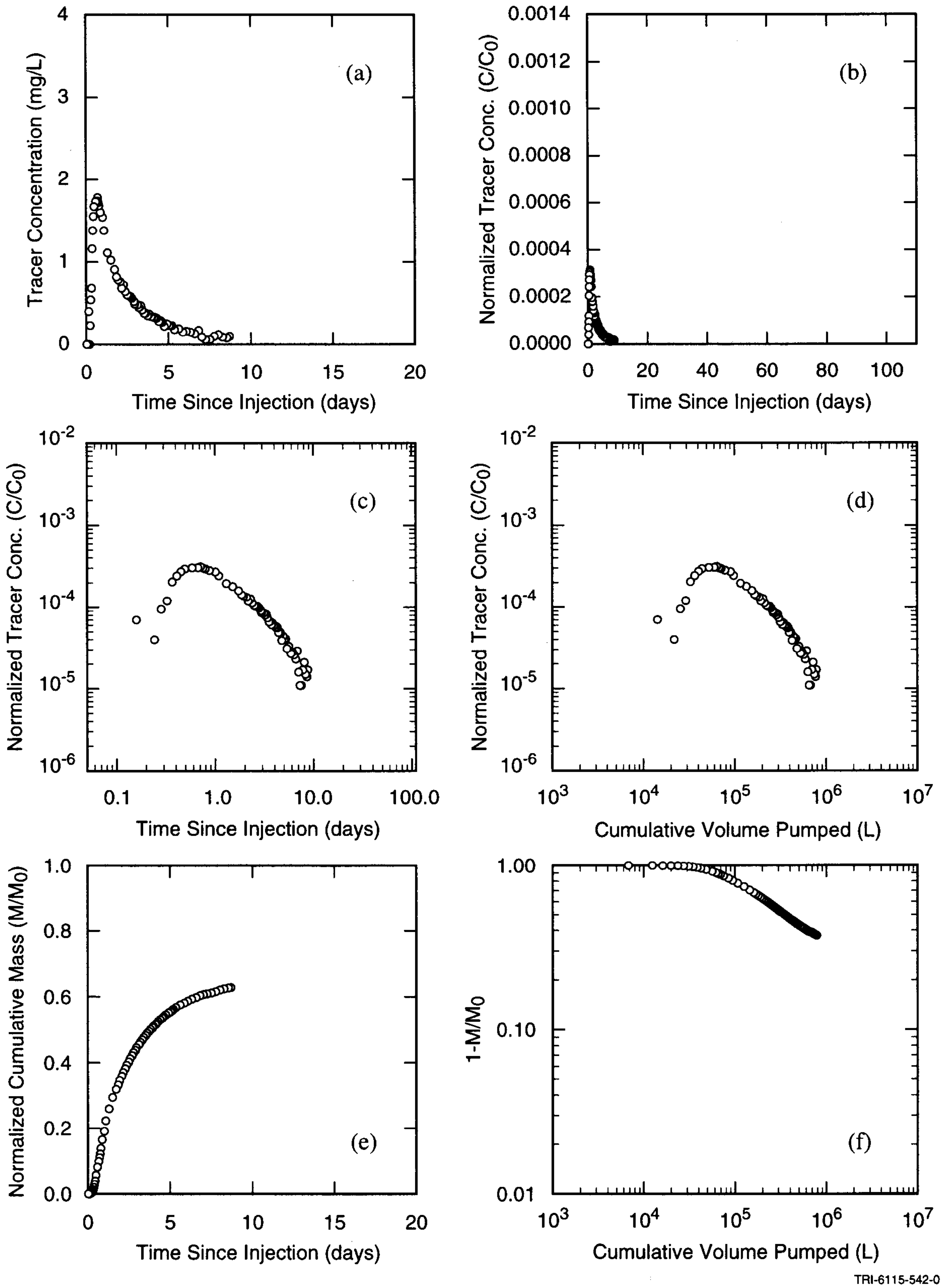

Figure C-37. p-FB data from H-6b to H-6c pathway, H-6 1981 test 2 (Q=1.04 L/s).

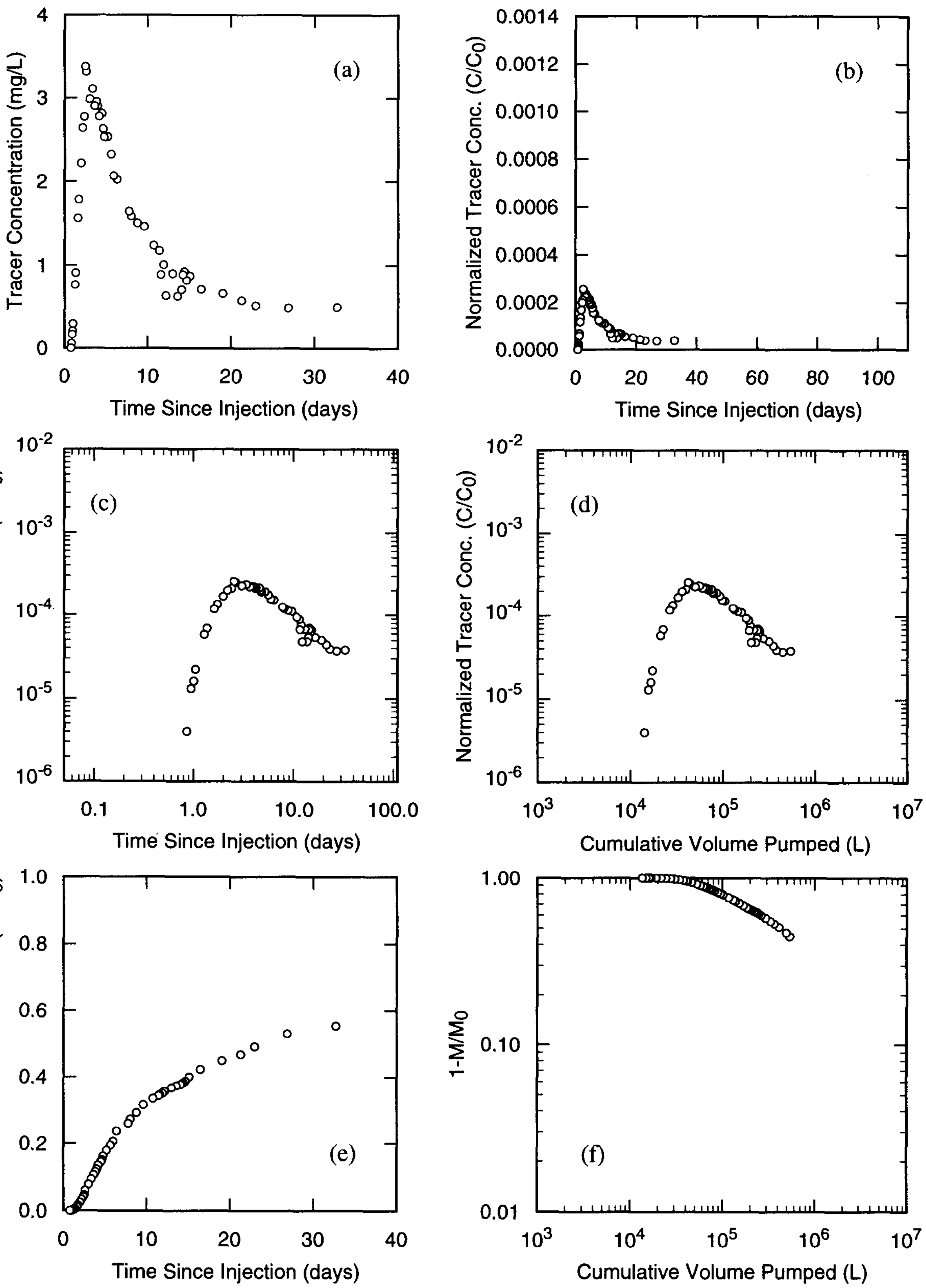

TRI-6115-538-0

Figure C-38. m-TFMBA data from H-3b1 to H-3b3 pathway, H-3 1984 test (Q=0.19 L/s).

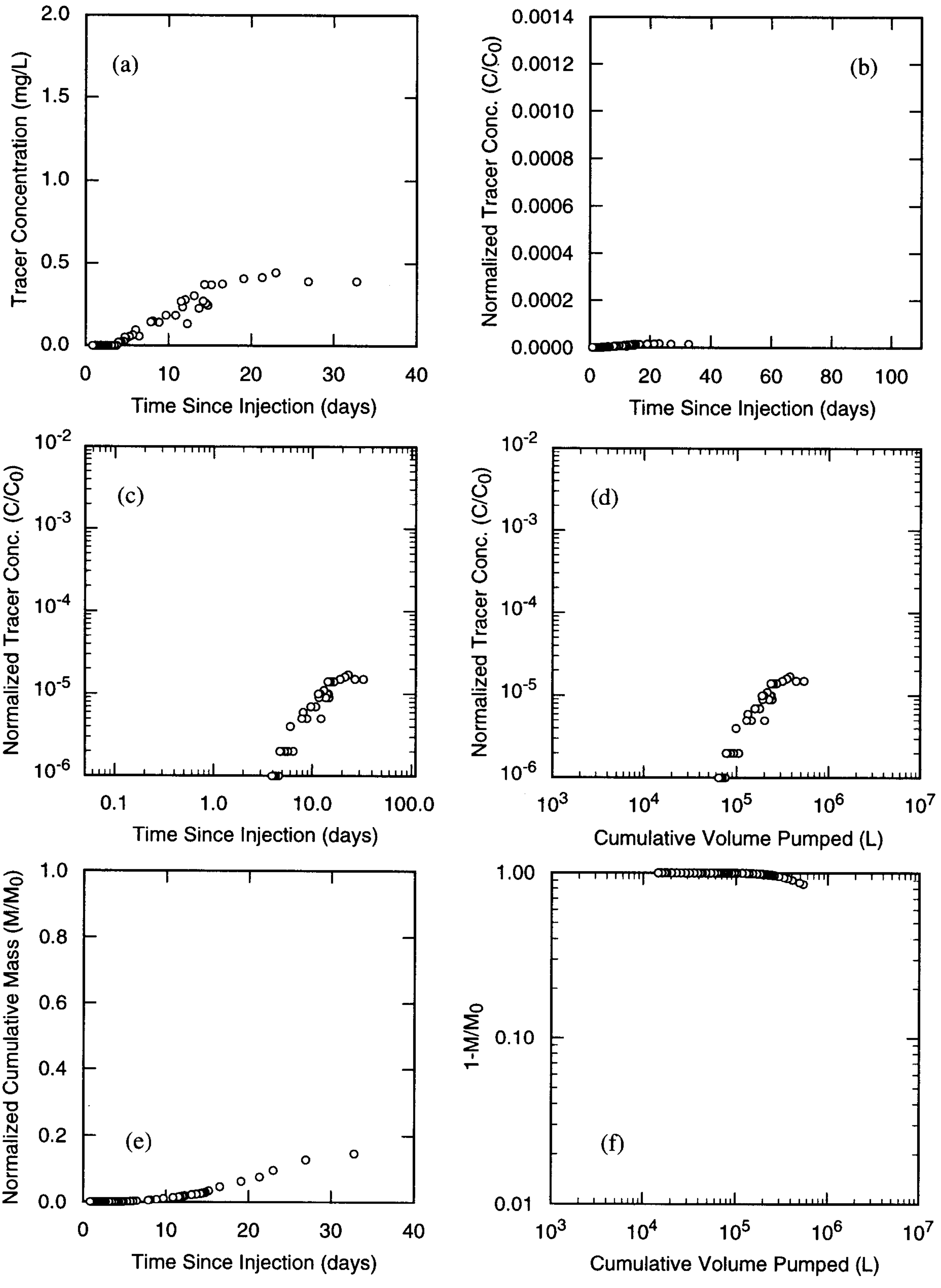

Figure C-39. **PFBA data from H-3b2 to H-3b3 pathway, H-3 1984 test (Q=0.19 L/s).**

Appendix D
Well Configurations, Test Equipment, and Hydraulic Data

By Richard L. Beauheim[1]

D.1 Introduction

This appendix describes the configurations of the wells at the H-19 and H-11 hydropads and the equipment used during the tracer tests, and also includes annotated plots of the pressure and flow-rate data collected during the tests. Dimensions, capacities, etc. of the various pieces of equipment are given in the manufacturer's specified units and/or the units given in the original records (usually English foot-pound units), with conversions provided to SI units. The use of brand names in this report is for identification purposes only and does not imply endorsement of specific products by Sandia National Laboratories.

D.2 Well Configurations

The wells at the H-19 and H-11 hydropads are all cased from ground surface to the lower Tamarisk Member of the Rustler Formation. They are open holes through the Culebra, as they originally were through the upper portion of the Los Medanos Member below the Culebra. Before the 1995-96 tracer tests, PVC liners were placed in the bottom of all wells except H-19b0 and H-11b4 to prevent sloughing of the Los Medanos Member. Additional details are provided below.

D.2.1 H-19 Hydropad

Well-construction details for the H-19 wells are shown in Figures D-1 through D-3 and discussed by Mercer et al. (1998). H-19b0 is cased with 8.42-inch (21.4-cm) I.D. fiberglass casing and is an approximately 8-inch (20.3-cm) open hole through the Culebra. The other six wells at the H-19 hydropad are cased with 6.38-inch (16.2-cm) I.D. fiberglass casing and are 5.88-inch (14.9-cm) open holes through the Culebra. To stop sloughing of clay from the Los Medanos Member into the holes, 20-ft (6.1-m) lengths of 5.5-inch (14.0-cm) O.D. PVC pipe were set in the bottom of all of the wells except for H-19b0.

D.2.2 H-11 Hydropad

Well-construction details for the H-11 wells are shown in Figure D-4 and discussed by Beauheim and Ruskauff (1998). The wells are cased with 4.95-inch (12.6-cm) I.D. steel casing and are 4.75-inch (12.1-cm) open holes through the Culebra. H-11b3, however, was accidentally reamed from its intended diameter of 4.75 inches (12.1 cm) to 7.875 inches (20.0 cm) over the Culebra interval from 733.4 to 749.3 ft (223.5 to 228.4 m) bgs. As a result of this reaming, the fluid volume contained within the Culebra interval of H-11b3 is larger than that in any of the other H-11 wells. To stop sloughing of clay from the Los Medanos Member into the holes, 20-ft (6.1-m) lengths of 4.5-inch (11.4-cm) O.D. PVC pipe were set in the bottom of all of the wells except for H-11b4.

D.3 Test Equipment

The equipment used at the surface for tracer injection was similar for all of the tests. Tracers were mixed with Culebra brine in 300-gallon (1,135-L) polyethylene tanks. Cole-Parmer magnetic-drive circulation pumps were used to keep the tracer solutions evenly mixed prior to injection. Separate tanks were used to hold tracer solutions and chaser fluid. Flow lines from the tanks were connected to a common tee so that

---

[1] Sandia National Laboratories, Repository Performance and Certification Department, P.O. Box 5800, MS-1395, Albuquerque, NM 87185-1395. Email: rlbeauh@sandia.gov.

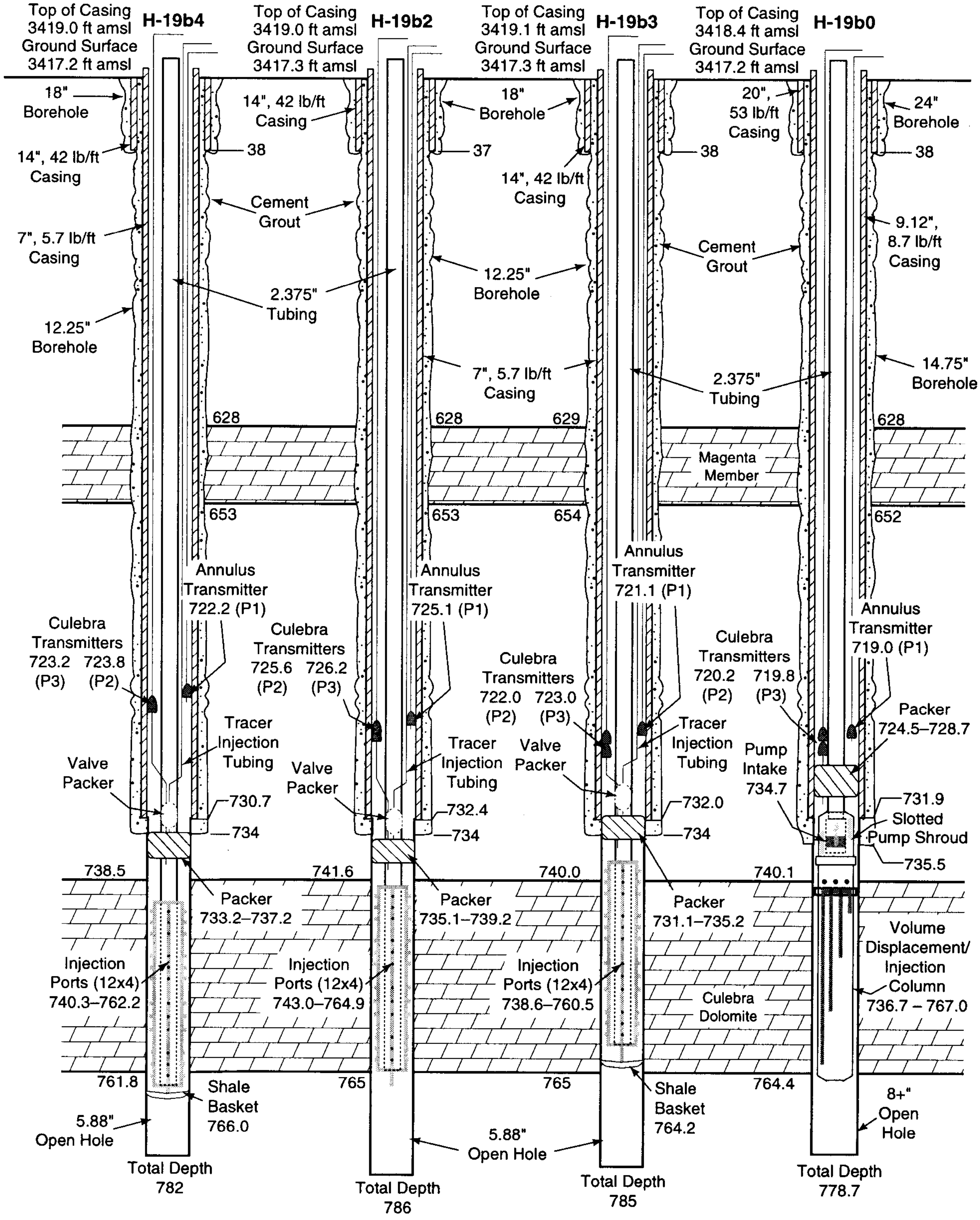
Top of Casing 3419.0 ft amsl
H-19b4
Ground Surface 3417.2 ft amsl
18" Borehole
14", 42 lb/ft Casing
7", 5.7 lb/ft Casing
12.25" Borehole
38
628
653
Annulus Transmitter 722.2 (P1)
Culebra Transmitters 723.2 723.8 (P3) (P2)
Tracer Injection Tubing
Valve Packer
730.7
734
738.5
Packer 733.2–737.2
Injection Ports (12x4) 740.3–762.2
761.8
Shale Basket 766.0
5.88" Open Hole
Total Depth 782
Top of Casing 3419.0 ft amsl
H-19b2
Ground Surface 3417.3 ft amsl
14", 42 lb/ft Casing
Cement Grout
2.375" Tubing
37
628
653
Annulus Transmitter 725.1 (P1)
Culebra Transmitters 725.6 726.2 (P2) (P3)
Tracer Injection Tubing
Valve Packer
732.4
734
741.6
Packer 735.1–739.2
Injection Ports (12x4) 743.0–764.9
765
5.88" Open Hole
Total Depth 786
Top of Casing 3419.1 ft amsl
H-19b3
Ground Surface 3417.3 ft amsl
18" Borehole
14", 42 lb/ft Casing
12.25" Borehole
7", 5.7 lb/ft Casing
38
629
654
Annulus Transmitter 721.1 (P1)
Culebra Transmitters 722.0 723.0 (P2) (P3)
Tracer Injection Tubing
Valve Packer
732.0
734
740.0
Packer 731.1–735.2
Injection Ports (12x4) 738.6–760.5
765
Shale Basket 764.2
Total Depth 785
Top of Casing 3418.4 ft amsl
H-19b0
Ground Surface 3417.2 ft amsl
20", 53 lb/ft Casing
24" Borehole
38
Cement Grout
2.375" Tubing
9.12", 8.7 lb/ft Casing
14.75" Borehole
628
Magenta Member
652
Annulus Transmitter 719.0 (P1)
Culebra Transmitters 720.2 719.8 (P2) (P3)
Packer 724.5–728.7
Pump Intake 734.7
731.9
Slotted Pump Shroud
735.5
740.1
Volume Displacement/ Injection Column 736.7 – 767.0
Culebra Dolomite
764.4
8+" Open Hole
Total Depth 778.7

Notes:
All depths in feet below ground surface
Drawing not to scale

TRI-6115-914-0

Figure D-1. Configurations of H-19b0, H-19b2, H-19b3, and H-19b4 during the 1995 4-well tracer test.

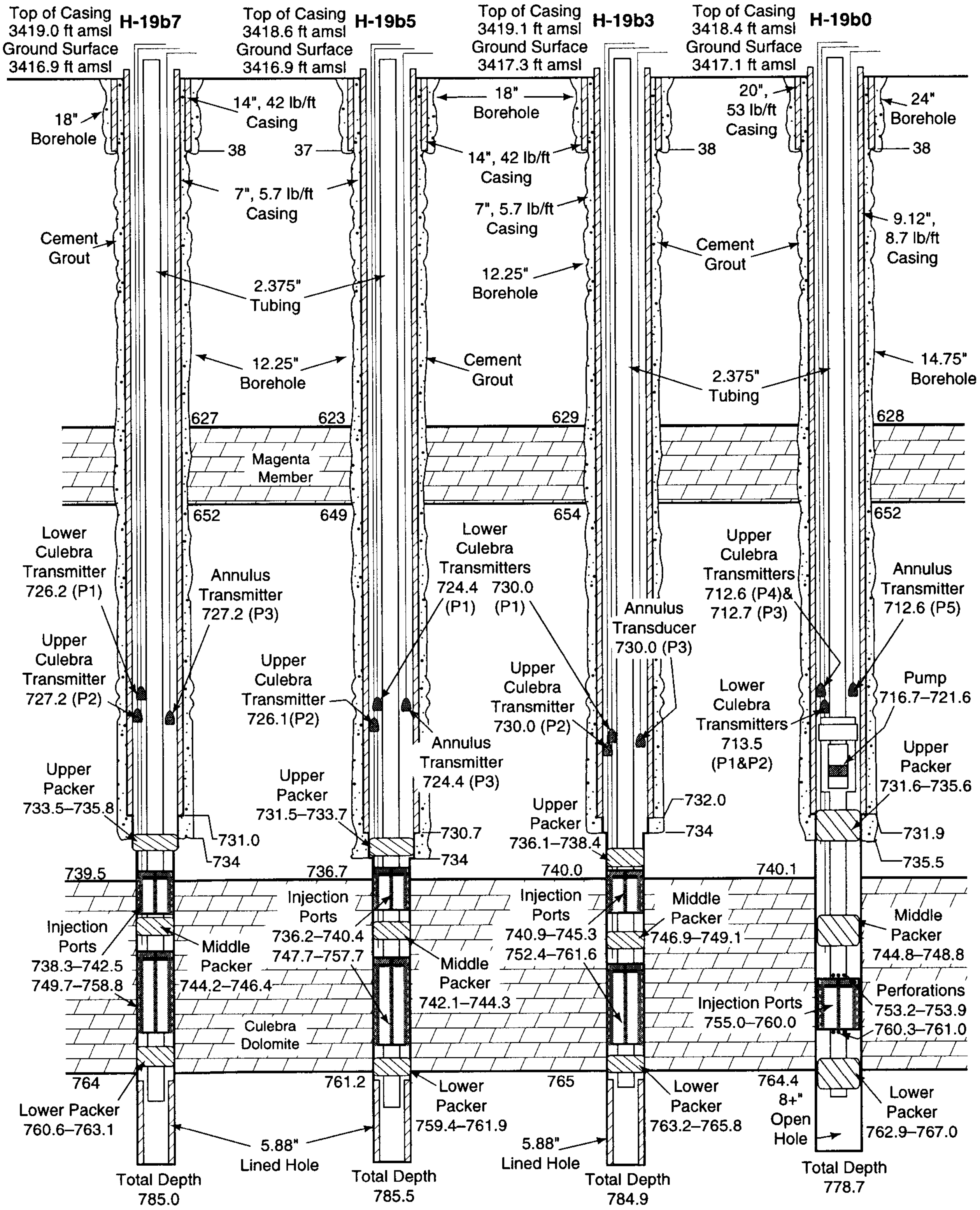

Top of Casing 3419.0 ft amsl
H-19b7
Ground Surface 3416.9 ft amsl
Top of Casing 3418.6 ft amsl
H-19b5
Ground Surface 3416.9 ft amsl
Top of Casing 3419.1 ft amsl
H-19b3
Ground Surface 3417.3 ft amsl
Top of Casing 3418.4 ft amsl
H-19b0
Ground Surface 3417.1 ft amsl
18" Borehole
14", 42 lb/ft Casing
38
37
18" Borehole
14", 42 lb/ft Casing
38
20", 53 lb/ft Casing
24" Borehole
38
7", 5.7 lb/ft Casing
7", 5.7 lb/ft Casing
Cement Grout
2.375" Tubing
12.25" Borehole
Cement Grout
9.12", 8.7 lb/ft Casing
12.25" Borehole
Cement Grout
2.375" Tubing
14.75" Borehole
627
623
629
628
Magenta Member
652
649
654
652
Lower Culebra Transmitter 726.2 (P1)
Annulus Transmitter 727.2 (P3)
Upper Culebra Transmitter 727.2 (P2)
Lower Culebra Transmitters 724.4 730.0 (P1) (P1)
Upper Culebra Transmitter 726.1(P2)
Annulus Transmitter 724.4 (P3)
Annulus Transducer 730.0 (P3)
Upper Culebra Transmitter 730.0 (P2)
Upper Culebra Transmitters 712.6 (P4)& 712.7 (P3)
Annulus Transmitter 712.6 (P5)
Lower Culebra Transmitters 713.5 (P1&P2)
Pump 716.7–721.6
Upper Packer 733.5–735.8
731.0
734
Upper Packer 731.5–733.7
730.7
734
Upper Packer 736.1–738.4
732.0
734
Upper Packer 731.6–735.6
731.9
735.5
739.5
736.7
740.0
740.1
Injection Ports 738.3–742.5 749.7–758.8
Middle Packer 744.2–746.4
Injection Ports 736.2–740.4 747.7–757.7
Middle Packer 742.1–744.3
Injection Ports 740.9–745.3 752.4–761.6
Middle Packer 746.9–749.1
Middle Packer 744.8–748.8
Perforations 753.2–753.9 760.3–761.0
Injection Ports 755.0–760.0
Culebra Dolomite
764
761.2
765
764.4
Lower Packer 760.6–763.1
Lower Packer 759.4–761.9
Lower Packer 763.2–765.8
Lower Packer 762.9–767.0
5.88" Lined Hole
5.88" Lined Hole
8+" Open Hole
Total Depth 785.0
Total Depth 785.5
Total Depth 784.9
Total Depth 778.7

Notes:
All depths in feet below ground surface
Drawing not to scale

TRI-6115-789-1

Figure D-2. Configurations of H-19b0, H-19b3, H-19b5, and H-19b7 during the 1995-96 7-well tracer test.

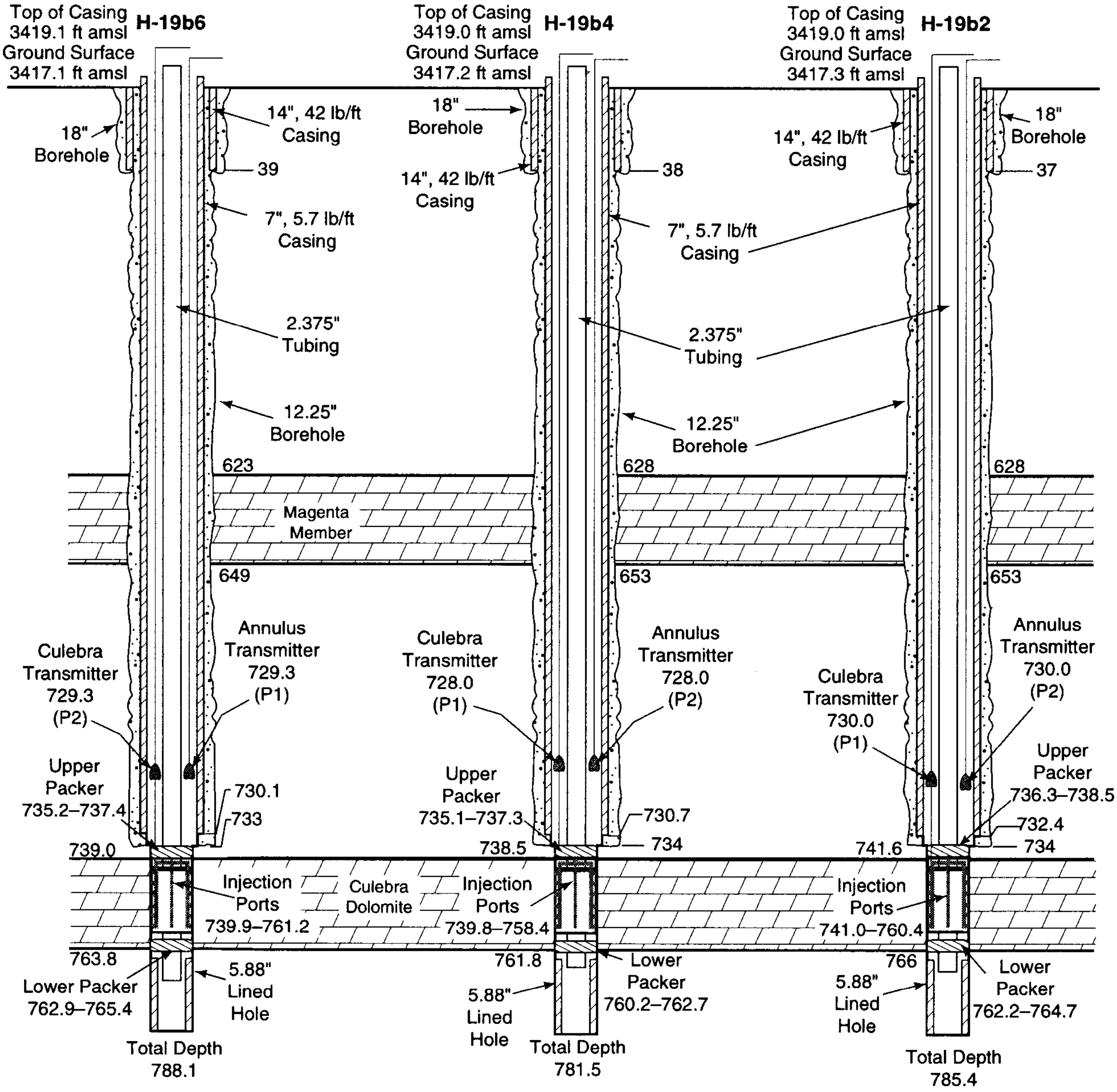
Top of Casing
3419.1 ft amsl
H-19b6
Ground Surface
3417.1 ft amsl
18" Borehole
14", 42 lb/ft Casing
39
7", 5.7 lb/ft Casing
2.375" Tubing
12.25" Borehole
623
Magenta Member
649
Culebra Transmitter
729.3
(P2)
Annulus Transmitter
729.3
(P1)
Upper Packer
735.2–737.4
730.1
733
739.0
Injection Ports
739.9–761.2
763.8
Lower Packer
762.9–765.4
5.88" Lined Hole
Total Depth
788.1
Top of Casing
3419.0 ft amsl
H-19b4
Ground Surface
3417.2 ft amsl
18" Borehole
14", 42 lb/ft Casing
38
7", 5.7 lb/ft Casing
2.375" Tubing
12.25" Borehole
628
653
Culebra Transmitter
728.0
(P1)
Annulus Transmitter
728.0
(P2)
Upper Packer
735.1–737.3
730.7
734
738.5
Culebra Dolomite
Injection Ports
739.8–758.4
761.8
Lower Packer
760.2–762.7
5.88" Lined Hole
Total Depth
781.5
Top of Casing
3419.0 ft amsl
H-19b2
Ground Surface
3417.3 ft amsl
14", 42 lb/ft Casing
18" Borehole
37
628
653
Culebra Transmitter
730.0
(P1)
Annulus Transmitter
730.0
(P2)
Upper Packer
736.3–738.5
732.4
734
741.6
Injection Ports
741.0–760.4
766
5.88" Lined Hole
Lower Packer
762.2–764.7
Total Depth
785.4

Notes:
All depths in feet below ground surface
Drawing not to scale

TRI-6115-790-1

Figure D-3. Configurations of H-19b2, H-19b4, and H-19b6 during the 1995-96 7-well tracer test.

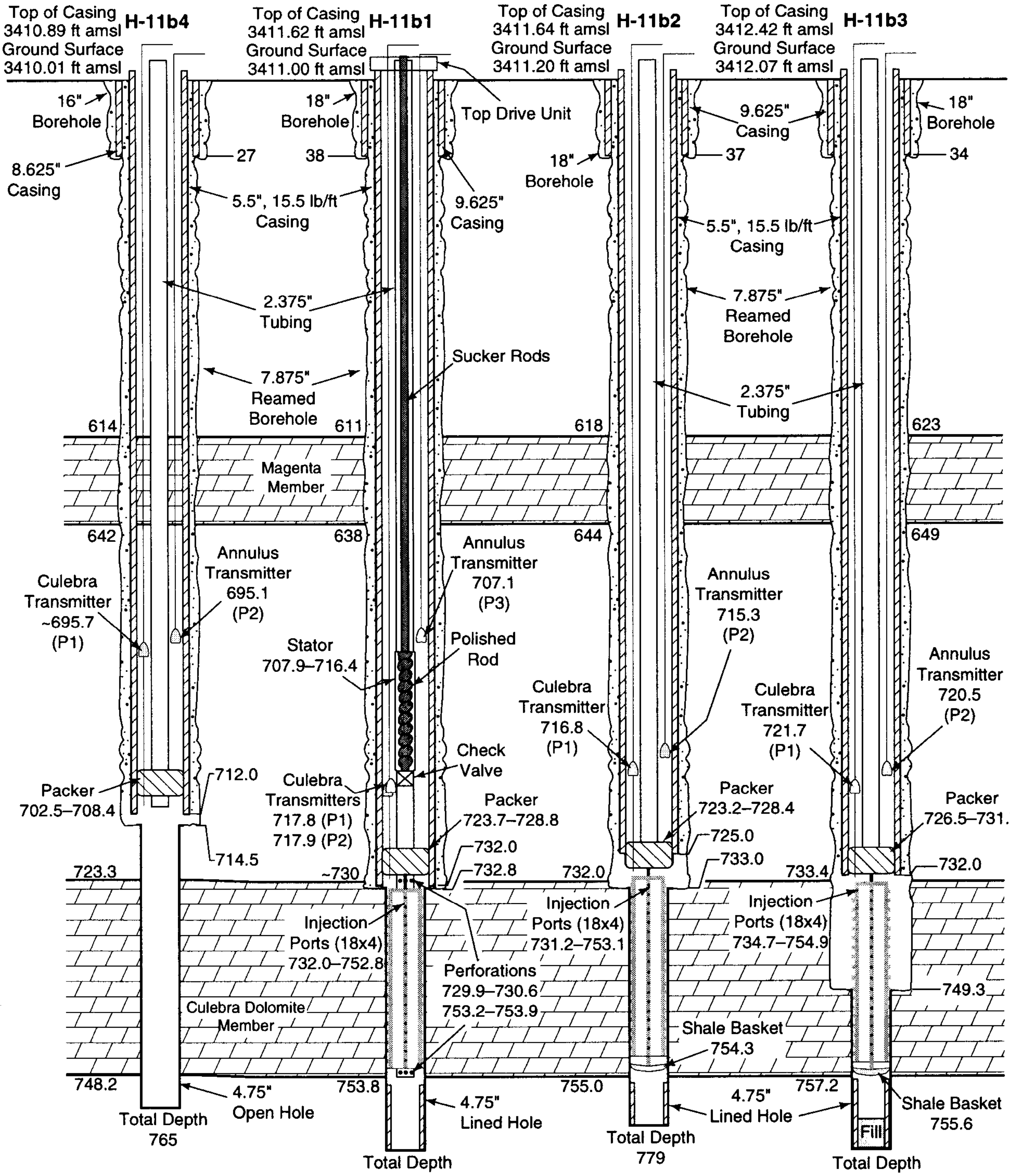
Top of Casing
3410.89 ft amsl
H-11b4
Ground Surface
3410.01 ft amsl
Top of Casing
3411.62 ft amsl
H-11b1
Ground Surface
3411.00 ft amsl
Top of Casing
3411.64 ft amsl
H-11b2
Ground Surface
3411.20 ft amsl
Top of Casing
3412.42 ft amsl
H-11b3
Ground Surface
3412.07 ft amsl
16" Borehole
8.625" Casing
27
18" Borehole
38
Top Drive Unit
9.625" Casing
5.5", 15.5 lb/ft Casing
18" Borehole
9.625" Casing
37
18" Borehole
34
5.5", 15.5 lb/ft Casing
2.375" Tubing
7.875" Reamed Borehole
Sucker Rods
7.875" Reamed Borehole
2.375" Tubing
614
611
618
623
Magenta Member
642
638
644
649
Culebra Transmitter ~695.7 (P1)
Annulus Transmitter 695.1 (P2)
Annulus Transmitter 707.1 (P3)
Annulus Transmitter 715.3 (P2)
Annulus Transmitter 720.5 (P2)
Stator 707.9–716.4
Polished Rod
Culebra Transmitter 716.8 (P1)
Culebra Transmitter 721.7 (P1)
Check Valve
Packer 702.5–708.4
712.0
714.5
Culebra Transmitters 717.8 (P1) 717.9 (P2)
Packer 723.7–728.8
Packer 723.2–728.4
Packer 726.5–731.7
732.0
732.8
725.0
733.0
732.0
723.3
~730
732.0
733.4
Injection Ports (18x4) 732.0–752.8
Injection Ports (18x4) 731.2–753.1
Injection Ports (18x4) 734.7–754.9
Perforations 729.9–730.6 753.2–753.9
749.3
Culebra Dolomite Member
Shale Basket 754.3
748.2
753.8
755.0
757.2
4.75" Open Hole
4.75" Lined Hole
4.75" Lined Hole
Shale Basket 755.6
Fill
Total Depth 765
Total Depth 785
Total Depth 779
Total Depth 787

Notes:
All depths in feet below ground surface
Drawing not to scale

TRI-6115-677-1

Figure D-4. Configurations of H-11b1, H-11b2, H-11b3, and H-11b4 during the 1996 tracer test.

injection could be readily switched from one tank to another by opening and closing a pair of valves. A Cole-Parmer centrifugal magnetic-drive pump was used to drive the injection, while the rate was controlled manually using a Blue-White 0-5 gpm (0-0.3 L/s) rotameter to estimate the rate and a valve to increase or decrease the rate. After each tracer was injected, a calculated volume of chaser fluid (Culebra brine) was injected to displace all of the tracer solution out of the wellbore into the Culebra. For the H-11 test, 5 gallons (18.9 L) of Culebra brine were also injected in each well in advance of the tracer solutions to allow the injection rate to be adjusted before injecting the tracers. Tracer and chaser volumes and injection rates are summarized in Tables 3-2 and 3-3 for the single-well and multi-well tracer tests, respectively, carried out at the H-19 and H-11 hydropads.

A data-acquisition system (DAS) was used for each test to collect pressure and flow-rate data and, in some instances, to control the pumping rate. Druck PTX 161/D 0-300 psig (0-2.1 MPa) pressure transmitters were used to monitor pressures in the wells during the tests. For each test, the DAS channels for each well were given P# designations, in which the P stands for pressure and the number represents a particular transmitter. As shown on the well-configuration diagrams, all transmitters were physically located in the well annulus above the packer(s) isolating the Culebra. Stainless steel "feedthrough" tubing that passed through the packers was used to connect the transmitters to the appropriate intervals for monitoring.

D.3.1 H-19 Four-Well Tracer Test

The downhole equipment in H-19b0 for the four-well tracer test consisted of a 5.5-inch (14.0-cm) Baski packer, a submersible pump contained within a slotted shroud, and a tracer-injection/volume-displacement tool (Figures D-1 and D-5). The tracer-injection/volume-displacement tool consisted of a sealed 9.23-m length of 6.625-inch (16.83-cm) O.D. schedule 40 pipe to which were affixed four stainless steel injection lines. Each of the injection lines was a different diameter (O.D.'s of 0.125, 0.1875, 0.25, and 0.375 inches [3.175, 4.763, 6.35, and 9.525 mm]). The injection lines terminated at different depths, with the larger lines going to greater depths, so that tracer was injected uniformly at four locations within the Culebra. Tracer and chaser solutions traveled down from the surface through a 0.5-inch (1.27-cm) O.D. nylon line alongside the 2.375-inch (6.03-cm) discharge tubing. Just above the packer, the injection tubing entered a feedthrough plug to pass through the packer, and then went through the pump shroud to an injection manifold where the tracer was split among the four injection lines.

The downhole equipment in H-19b2, H-19b3, and H-19b4 consisted of 5.375-inch (13.65-cm) Baker packers above tracer-injection/volume-displacement tools (Figures D-1 and D-6). A smaller diameter (1.5-inch [3.8-cm]) Tigre Tierra packer "valve" was attached to two feedthrough plugs (see Jones et al., 1992, Figure 10-8, Detail A) and placed in a pup joint above the Baker packer to control the injection of tracers. When the packer valve was inflated, the 0.5-inch (1.27-cm) O.D. tracer-injection tubing was isolated from the test interval. When the packer valve was deflated, tracer could flow into the test interval. The tracer-injection/volume-displacement tools had been used previously for the 1988 H-11 tracer test (Stensrud et al., 1990) and consisted of 8.25-m lengths of 4-inch (10.2-cm) O.D. tubing through which 12 sets of 4 injection ports were drilled. The sets of injection ports were spaced two feet (61 cm) apart and each port was 0.75 inches (1.9 cm) in diameter. Shale baskets (rubber gaskets that block off the hole) were installed at the bottom of these tools in H-19b3 and H-19b4 to minimize tracer interaction with the stagnant water at the bottom of the wells.

The DAS and DAS software (BASys 1.A0) used for the H-19 four-well test were supplied by Baker Oil Tools. Three pressure transmitters were installed in each of the wells for the test. One transmitter (channel designated P1) monitored the pressure in the well annulus above the packer isolating the Culebra. A second transmitter (P2) monitored the pressure in the tracer-injection tubing in H-19b2, H-19b3, and H-19b4, which was the same as the Culebra pressure after the

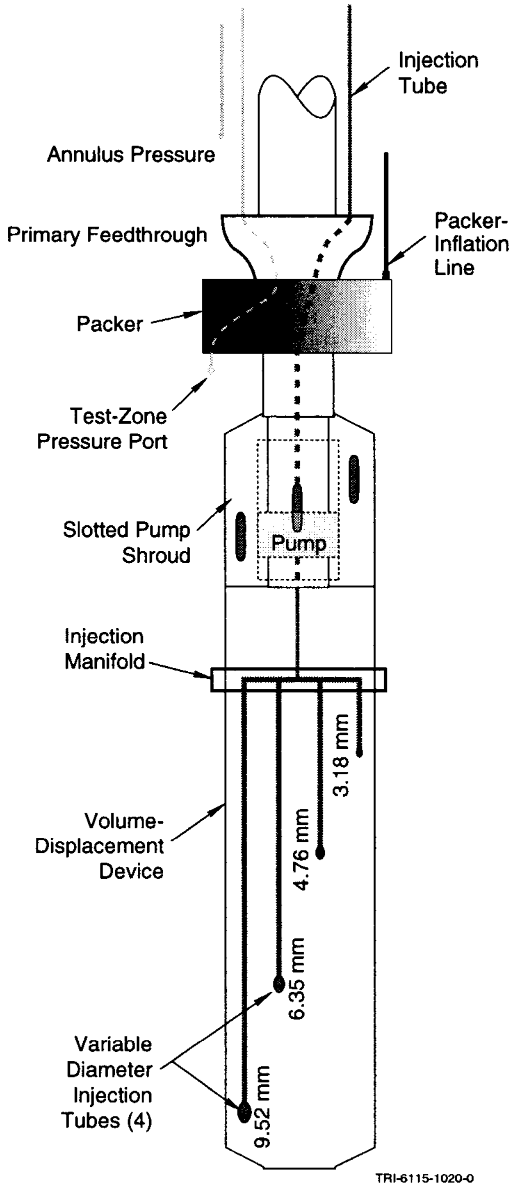
Injection Tube
Annulus Pressure
Primary Feedthrough
Packer-Inflation Line
Packer
Test-Zone Pressure Port
Slotted Pump Shroud
Pump
Injection Manifold
3.18 mm
Volume-Displacement Device
4.76 mm
6.35 mm
Variable Diameter Injection Tubes (4)
9.52 mm
TRI-6115-1020-0

Figure D-5. Downhole equipment in H-19b0 during the 1995 4-well tracer test.

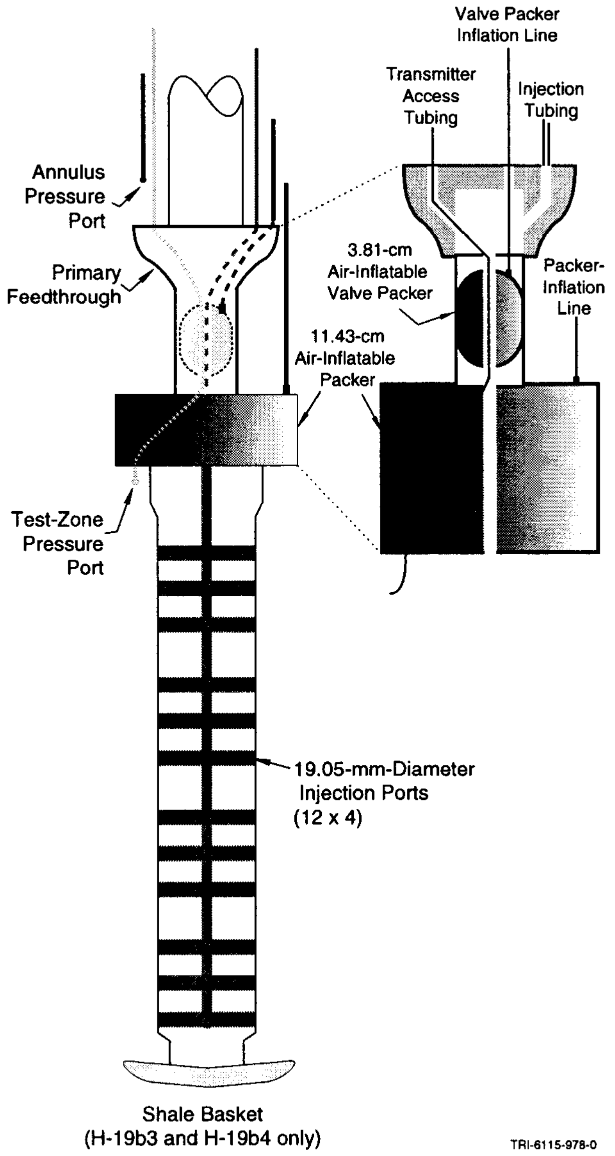
Valve Packer Inflation Line
Transmitter Access Tubing
Injection Tubing
Annulus Pressure Port
Primary Feedthrough
3.81-cm Air-Inflatable Valve Packer
Packer-Inflation Line
11.43-cm Air-Inflatable Packer
Test-Zone Pressure Port
19.05-mm-Diameter Injection Ports (12 x 4)
Shale Basket (H-19b3 and H-19b4 only)
TRI-6115-978-0

Figure D-6. Downhole equipment in H-19b2, H-19b3, and H-19b4 during the 1995 4-well tracer test.

valve packer was deflated. The P2 transmitter monitored the Culebra pressure in H-19b0. The third transmitter (P3) monitored the pressure in the Culebra. The cables from two of the transmitters in H-19b3 were inadvertently reversed while wiring the DAS, causing the Culebra transmitter signal to be sent to the channel designated P2 while the signal from the transmitter attached to the tracer-injection line went to the channel designated P3.

D.3.2 H-19 Seven-Well Tracer Test

The equipment located at the surface for the H-19 seven-well tracer test included an Endress & Hauser Promag 30A digital flow meter to measure the flow rate, a Honeywell Electro-Pneumatic Valve Positioner to open or close a valve to achieve the desired flow rate, a Bailey, Fischer & Porter Process Control Station to process the flow meter out put and send the appropriate signal to the valve positioner, and other data-acquisition equipment supplied by Baker Oil Tools. Baker also supplied the BASys 1.A0 software used for data acquisition. A Druck PTX 620 0-17 psia (0-117 kPa) pressure transmitter was used to monitor barometric pressure during the test.

H-19b0, the pumping well, was instrumented with a tool string that included three Baker packers. The upper and lower packers isolated the Culebra from the well casing and Los Medanos Member, respectively, while the middle packer divided the Culebra into upper and lower parts. A tracer-injection tool was installed in the lower portion of the Culebra along with perforated pup joints of 2.625-inch (6.7-cm) tubing. A 1.5-h.p. Goulds pump was installed in a pump shroud located above the top packer and drew water through the perforations in the 2.625-inch (6.7-cm) tubing. Five pressure transmitters were installed in the well, two to measure the pressure in the lower Culebra (P1 and P2), two for the upper Culebra (P3 and P4), and one for the annulus above the packers (P5). The configuration of the equipment in H-19b0 is shown in Figures D-2 and D-7.

H-19b3, H-19b5, and H-19b7 each were instrumented with tool strings containing three TAM packers. The packers isolated upper and lower Culebra intervals similar to those isolated in H-19b0. Tracer-injection tools were installed in each of the isolated intervals, allowing tracers to be injected independently into the upper and lower Culebra (Figure D-8). The tracer-injection tools in the upper Culebra consisted of an injection manifold and 3.9-inch (9.91-cm) O.D. tubing with four sets of four injection ports spaced approximately 14 inches (35.6 cm) apart along the length of the tool. The 0.5-inch (1.27-cm) O.D. tracer-injection line from the surface fed into the injection manifold, which split the tracer solution among the four sets of injection ports. The injection ports increased in diameter from 0.096 inches (2.44 mm) at the top set to 0.154 inches (3.01 mm) at the bottom set. (The increased diameter compensated for the increased head that had to be overcome with depth.) The tracer-injection tools in the lower Culebra had nine sets of four injection ports spaced approximately 14 inches (35.6 cm) apart. The injection ports increased in diameter from 0.041 inches (1.04 mm) at the top set to 0.120 inches (3.05 mm) at the bottom set. Three pressure transmitters were installed in each well to measure pressures in the lower Culebra (P1), upper Culebra (P2), and annulus above the packers (P3). The configurations of the equipment in H-19b3, H-19b5, and H-19b7 are shown in Figure D-2.

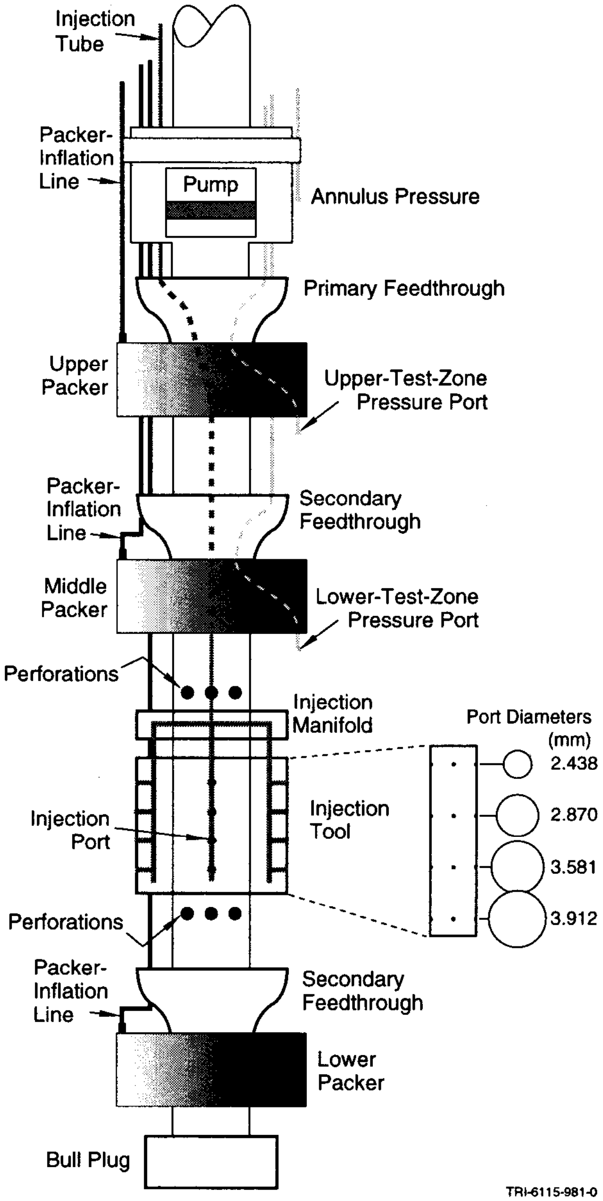
Injection Tube
Packer-Inflation Line
Pump
Annulus Pressure
Primary Feedthrough
Upper Packer
Upper-Test-Zone Pressure Port
Packer-Inflation Line
Secondary Feedthrough
Middle Packer
Lower-Test-Zone Pressure Port
Perforations
Injection Manifold
Port Diameters (mm)
2.438
2.870
3.581
3.912
Injection Port
Injection Tool
Perforations
Packer-Inflation Line
Secondary Feedthrough
Lower Packer
Bull Plug
TRI-6115-981-0

Figure D-7. Downhole equipment in H-19b0 during the 1995-96 7-well tracer test.

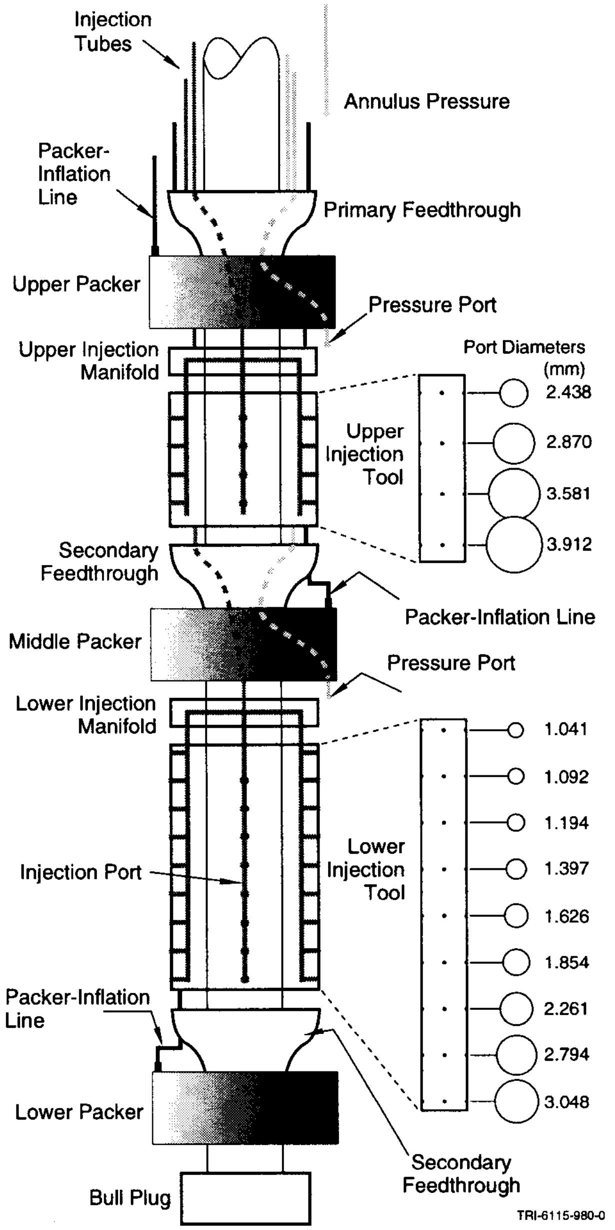
Injection Tubes
Annulus Pressure
Packer-Inflation Line
Primary Feedthrough
Upper Packer
Pressure Port
Upper Injection Manifold
Port Diameters (mm)
2.438
Upper Injection Tool
2.870
3.581
3.912
Secondary Feedthrough
Packer-Inflation Line
Middle Packer
Pressure Port
Lower Injection Manifold
1.041
1.092
1.194
Lower Injection Tool
Injection Port
1.397
1.626
1.854
Packer-Inflation Line
2.261
2.794
Lower Packer
3.048
Secondary Feedthrough
Bull Plug
TRI-6115-980-0

Figure D-8. Downhole equipment in H-19b3, H-19b5, and H-19b7 during the 1995-96 7-well tracer test.

H-19b2, H-19b4, and H-19b6 each were instrumented with tool strings containing two TAM packers. The packers isolated the entire Culebra from the Los Medanos Member below and well casing above. Tracer-injection tools were installed in the isolated Culebra intervals. The tracer-injection tools consisted of an injection manifold and 3.9-inch (9.91-cm) O.D. tubing with 18 sets of four injection ports spaced approximately 14 inches (35.6 cm) apart along the length of the tool. The injection ports increased in diameter from 0.022 inches (0.56 mm) at the top set to 0.120 inches (3.05 mm) at the bottom set (Figure D-9). Two pressure transmitters were installed in each well to measure pressures in the Culebra (P1) and annulus above the packers (P2). The cables from the transmitters in H-19b6 were inadvertently reversed while wiring the DAS,causing the Culebra transmitter signal to be

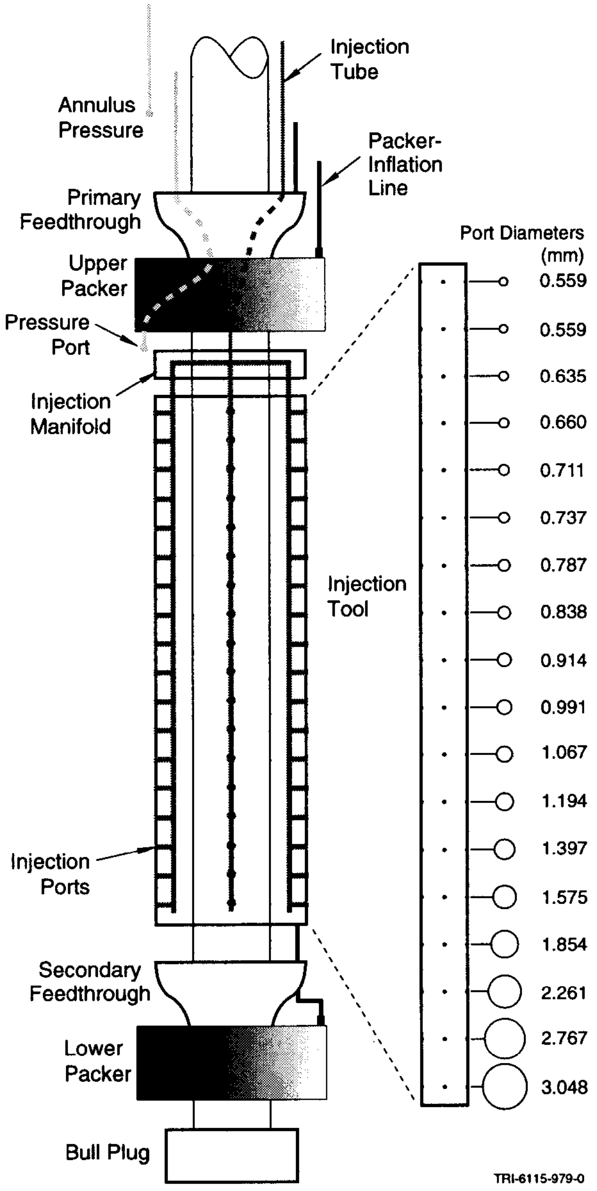
Injection Tube
Annulus Pressure
Packer-Inflation Line
Primary Feedthrough
Port Diameters (mm)
Upper Packer
0.559
Pressure Port
0.559
0.635
Injection Manifold
0.660
0.711
0.737
0.787
Injection Tool
0.838
0.914
0.991
1.067
1.194
1.397
Injection Ports
1.575
1.854
Secondary Feedthrough
2.261
Lower Packer
2.767
3.048
Bull Plug
TRI-6115-979-0

Figure D-9. Downhole rquipment in H-19b2, H-19b4, and H-19b6 during the 1995-96 7-well tracer test.

sent to the channel designated P2 while the annulustransmitter signal went to the channel designated P1. The configurations of the equipment in H-19b2, H-19b4, and H-19b6 are shown in Figure D-3.

D.3.3 H-11 Tracer Test

A Griffin Progressing Cavity Pump with a top drive was installed in well H-11b1 for the H-11 tracer test (Figure D-4). The pump drew water from the Culebra through perforations in the pipe above and below the tracer-injection assembly installed in H-11b1. A Baldor Series 15H Inverter Control was used to control the pump speed and maintain a constant flow rate. An Endress & Hauser Promag 30A digital flow meter was used to measure flow during the pumping period preceding tracer injection. Discharge thereafter was measured using a Precision totalizing flow meter and by the timed filling of a volumetrically calibrated standpipe. The DAS for the H-11 test consisted of a Gateway 2000 486/33 computer for system control, an HP-3497A data acquisi tion/control unit, an HP-3456A DVM, an Electronic Development Corporation (EDC) 501J programmable voltage standard, and Kepco PCX21-1MAT 0-40 VDC power supplies. In H-11b1, two pressure transmitters (channels P1 and P2) were used to monitor the Culebra pressure and one transmitter (channel P3) was used to monitor the annulus pressure. In H-11b2, H-11b3, and H-11b4, one transmitter (channel P1) monitored the Culebra pressure while another transmitter (channel P2) monitored the annulus pressure. The DAS software used for the test was PERM5 version 1.01 (ERMS#220443).

Tracer-injection assemblies were installed within the Culebra intervals of H-11b1, H-11b2, and H-11b3 below packers (Figure D-4). The tracer-injection assemblies consisted of injection manifolds situated above 4-inch (10.2-cm) pipe with 18 sets of four injection ports located 90° apart circumferentially around the tool (Figure D-10). Tracer and chaser were delivered to each manifold through 0.5-inch (1.27-cm) O.D. tubing. The sets of ports were spaced approximately 35.6 cm apart along the lengths of the tools in H-11b1 and H-11b3, and 39.4 cm apart along the length of the tool in H-11b2. The ports increased in diameter from 0.024 inches (0.61 mm) to 0.140 inches (3.56 mm) with depth to achieve a uniform distribution of tracer in the wellbore. Shale baskets were set at the base of the Culebra in H-11b2 and H-11b3 to minimize interaction between the tracers and the stagnant water at the bottom of the wells. A PIP was used to isolate the Culebra in H-11b4.

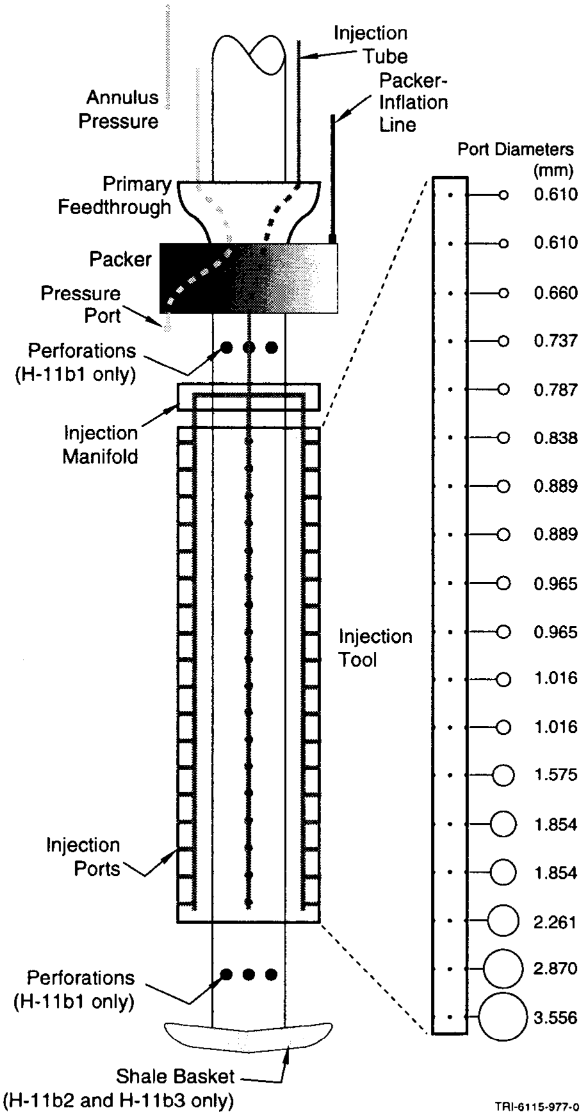
Annulus Pressure
Injection Tube
Packer-Inflation Line
Port Diameters (mm)
0.610
0.610
0.660
0.737
0.787
0.838
0.889
0.889
0.965
0.965
1.016
1.016
1.575
1.854
1.854
2.261
2.870
3.556
Primary Feedthrough
Packer
Pressure Port
Perforations (H-11b1 only)
Injection Manifold
Injection Tool
Injection Ports
Perforations (H-11b1 only)
Shale Basket (H-11b2 and H-11b3 only)
TRI-6115-977-0

Figure D-10. Downhole equipment in H-11b1, H-11b2, and H-11b3 during the 1996 tracer test.

D.4 Hydraulic Data

The pressures shown on the following plots have been compensated to reflect the pressure 229 m BGS, the approximate midpoint of the Culebra. For each transmitter, the compensation was performed by adding the pressure exerted by the column of water between the transmitter and the datum to the pressure measured by the transmitter. This additional pressure was calculated assuming a fluid density of 1066 kg/m^3.

D.4.1 H-19 Four-Well Tracer Test

Figure D-11 shows the pumping rates measured by a totalizing flow meter, calibrated standpipe, and the electronic flow meter connected to the DAS, annotated to show various events that occurred during the H-19 four-well tracer test. The electronic flow meter was in operation only during the last approximately 19 days of the test. Pumping began at 11:00 on 16 June 1995 and ended at 07:00 on 28 July 1995. The flow rate decreased by approximately 0.02 L/s over the first 13 days of pumping, but was more stable for the remainder of the test. The flow rate averaged approximately 0.24 L/s over the entire test.

Figures D-12 through D-23 show the pressures monitored in the H-19 wells during the four-well test. The test tools were installed in the wells with the tracer-injection lines filled to the surface with Culebra brine. Thus, the initial pressures in the tracer-injection lines were typically beyond the calibrated maximum values of the pressure transmitters (300 psig [2.1 MPa]).

Figure D-12 shows the pressure measured in the H-19b0 well annulus above the packer isolating the Culebra. The pressure was relatively stable for approximately the first nine days of pumping, but then increased by approximately 0.39 MPa over the next 33 days. This pressure increase represents a volume of approximately 1,240 L of Culebra brine added to the annulus, most likely from one or more small leaks in the discharge line from the pump to the surface. Figures D-13 and D-14 show the pressures measured in the Culebra

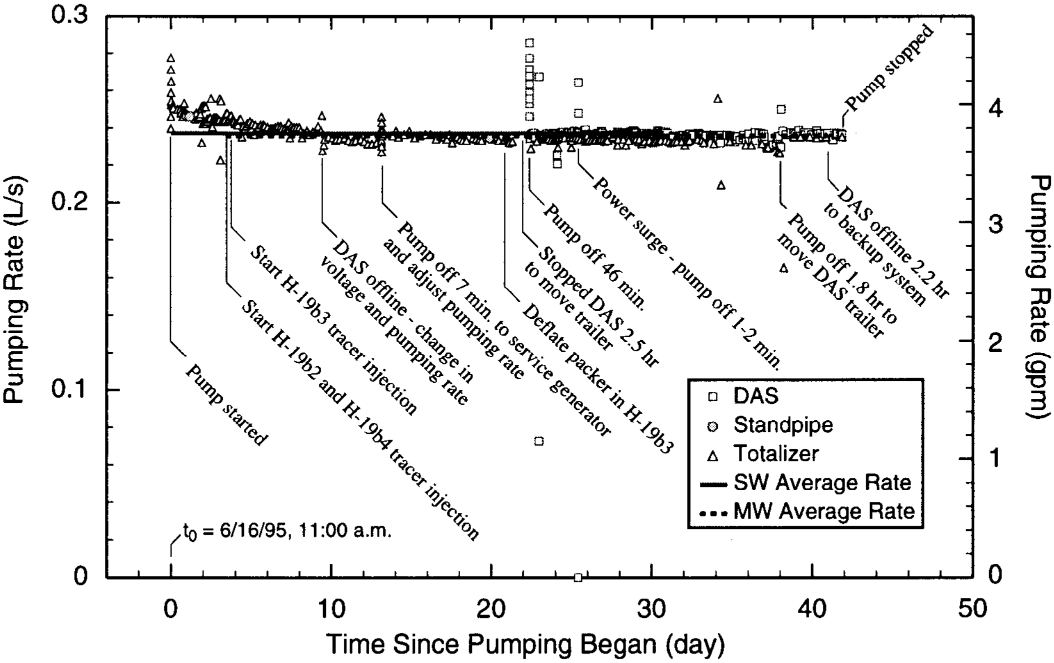

TRI-6115-974-0

Figure D-11. Flow-rate data during the 1995 H-19 4-well tracer test.

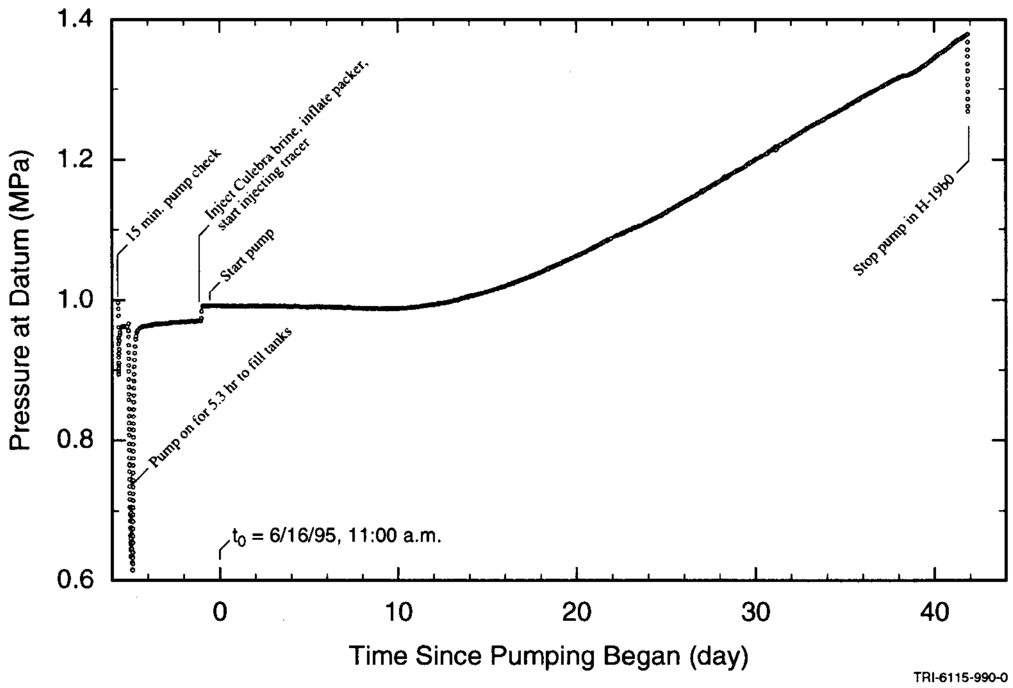

Figure D-12. H-19b0 annulus pressure (P1) during the 1995 4-well tracer test.

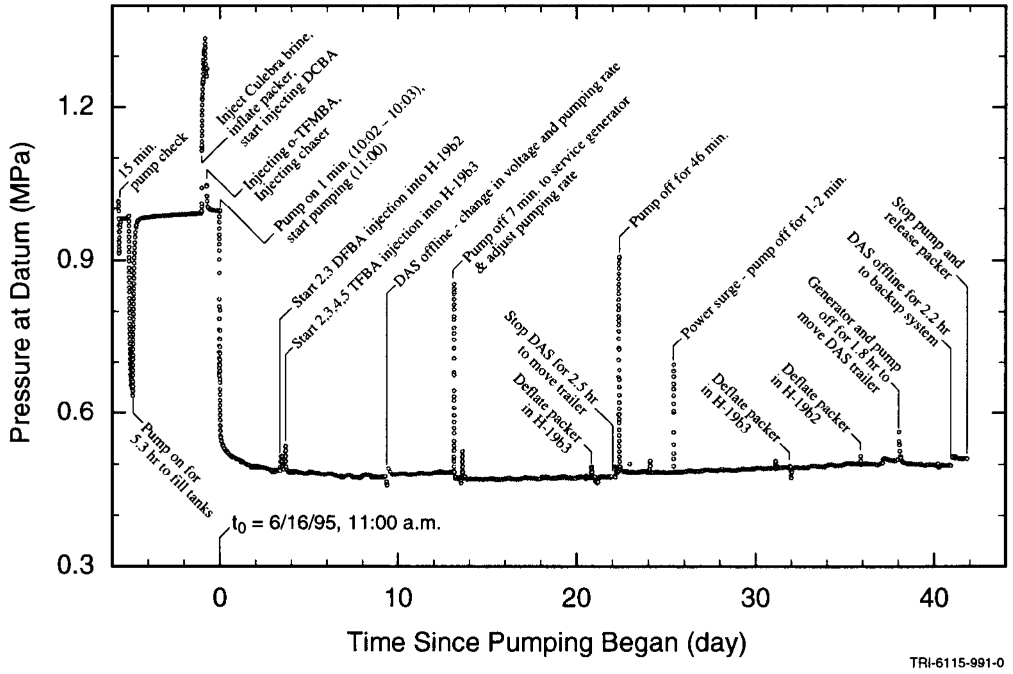

Figure D-13. H-19b0 Culebra pressure (P2) during the 1995 4-well tracer test.

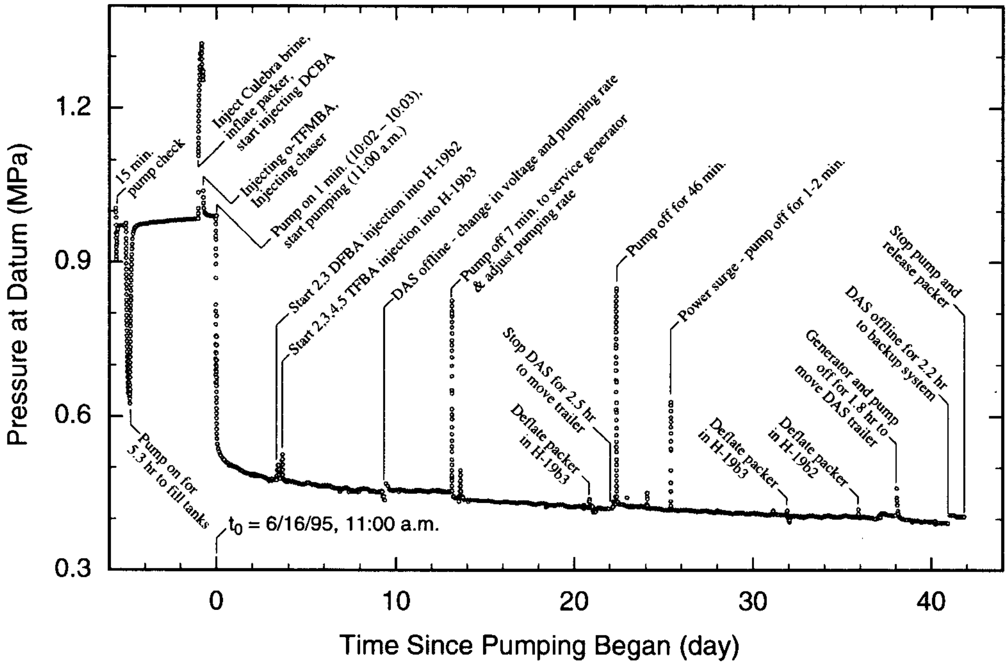

TRI-6115-992-0

Figure D-14. H-19b0 Culebra pressure (P3) during the 1995 4-well tracer test.

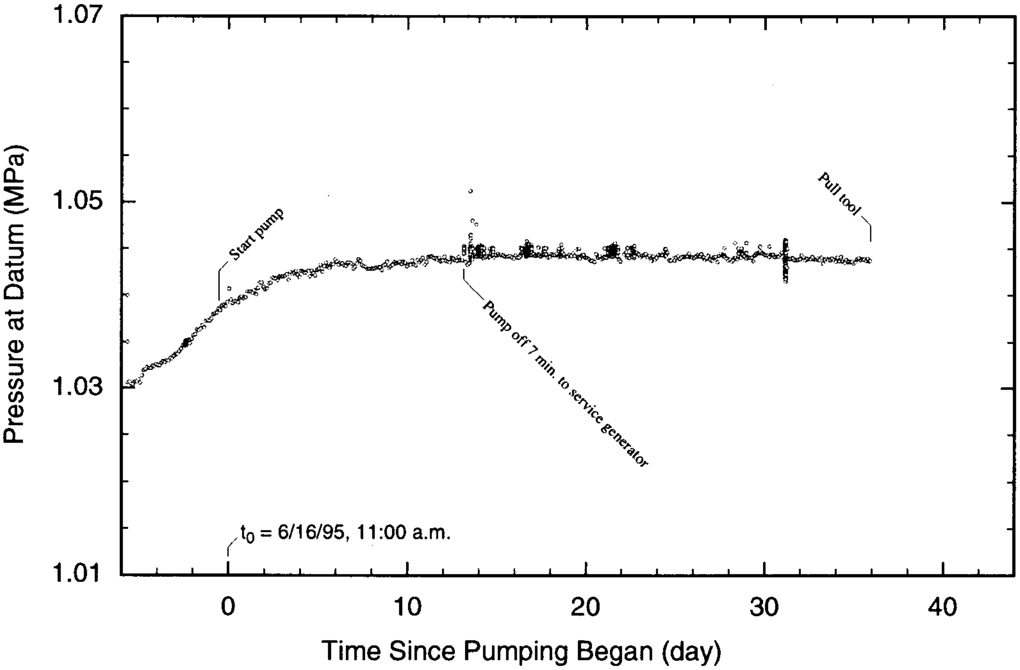

TRI-6115-993-0

Figure D-15. H-19b2 annulus pressure (P1) during the 1995 4-well tracer test.

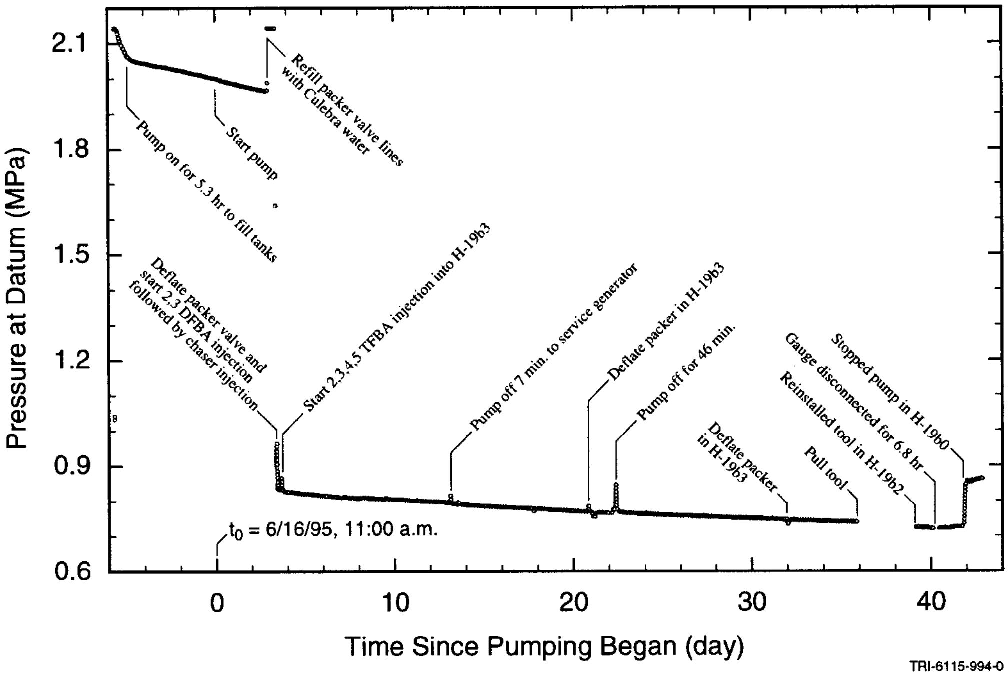

TRI-6115-994-0

Figure D-16. H-19b2 tracer-injection-line pressure (P2) during the 1995 4-well tracer test.

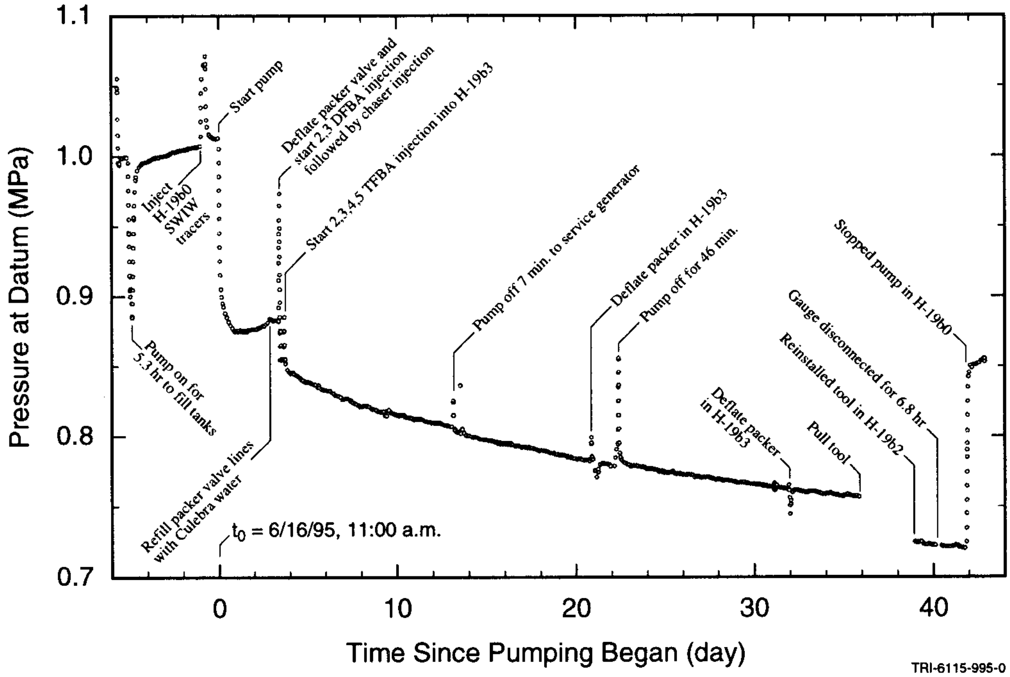

TRI-6115-995-0

Figure D-17. H-19b2 Culebra pressure (P3) during the 1995 4-well tracer test.

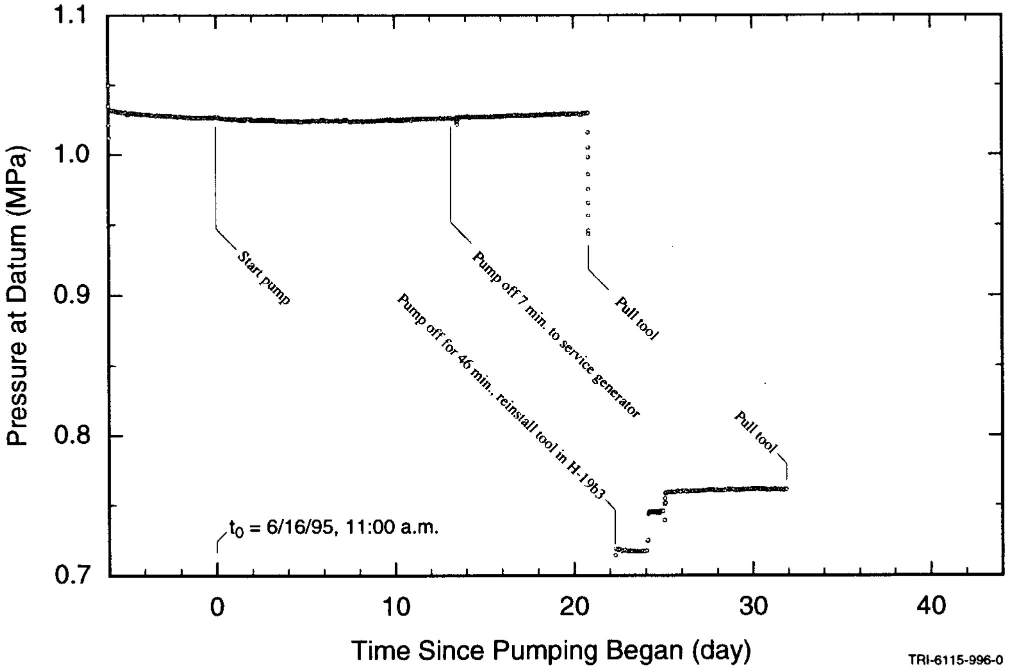

Figure D-18. H-19b3 annulus pressure (P1) during the 1995 4-well tracer test.

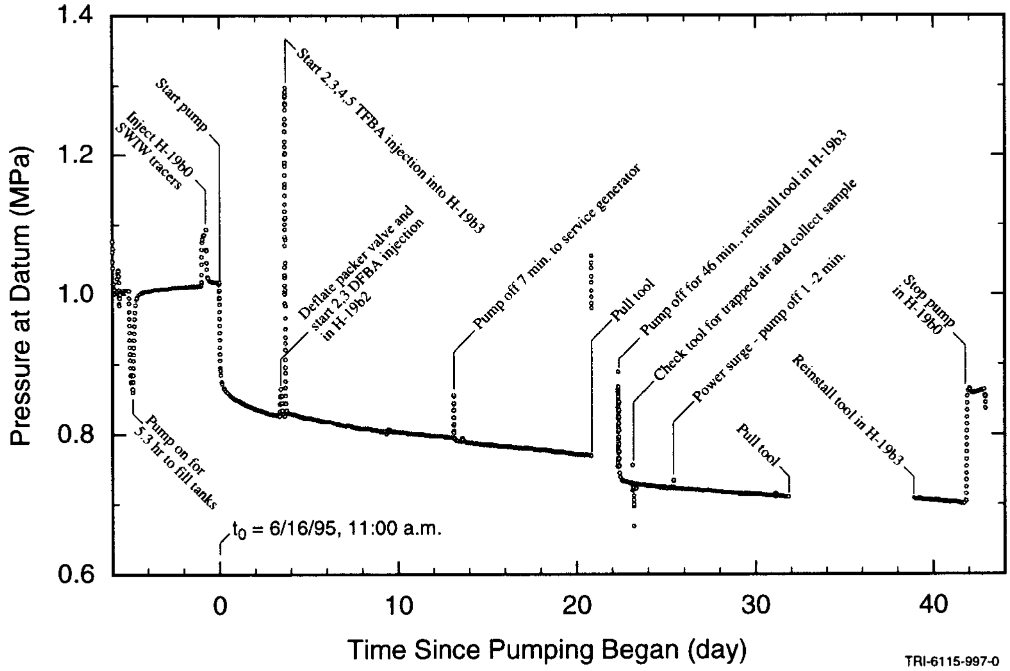

Figure D-19. H-19b3 Culebra pressure (P2) during the 1995 4-well tracer test.

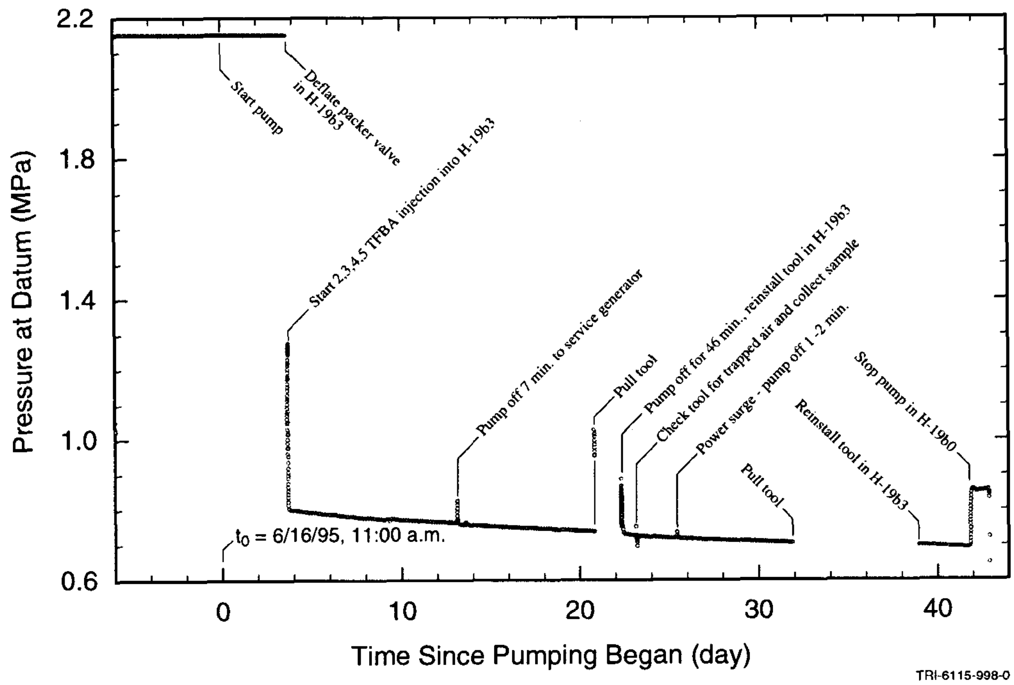

Figure D-20. H-19b3 tracer-injection-line pressure (P3) during the 1995 4-well tracer test.

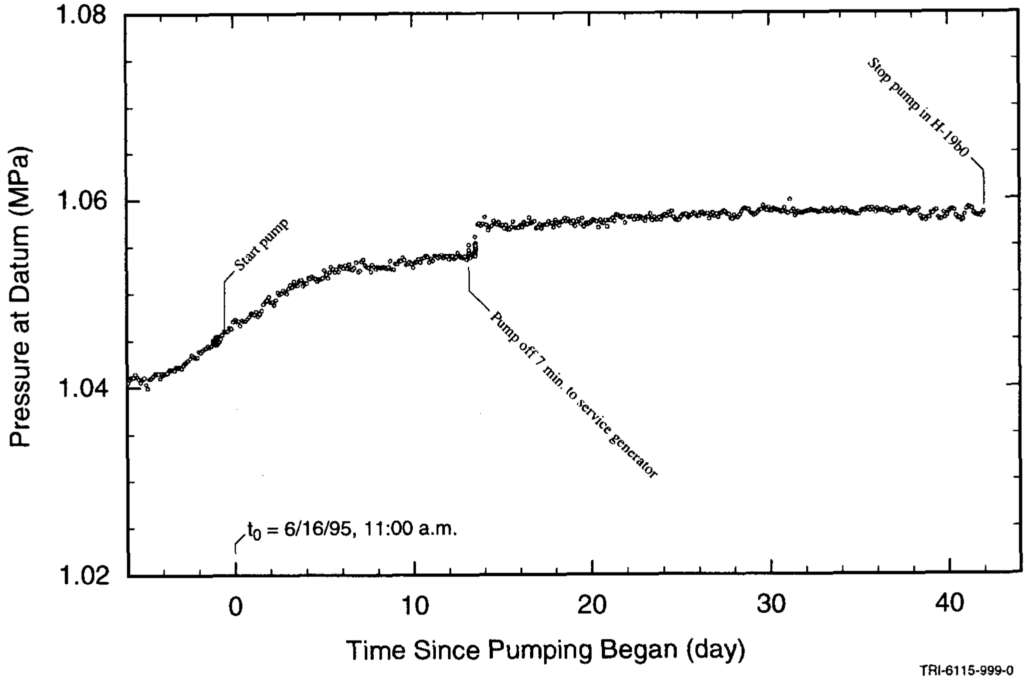

Figure D-21. H-19b4 annulus pressure (P1) during the 1995 4-well tracer test.

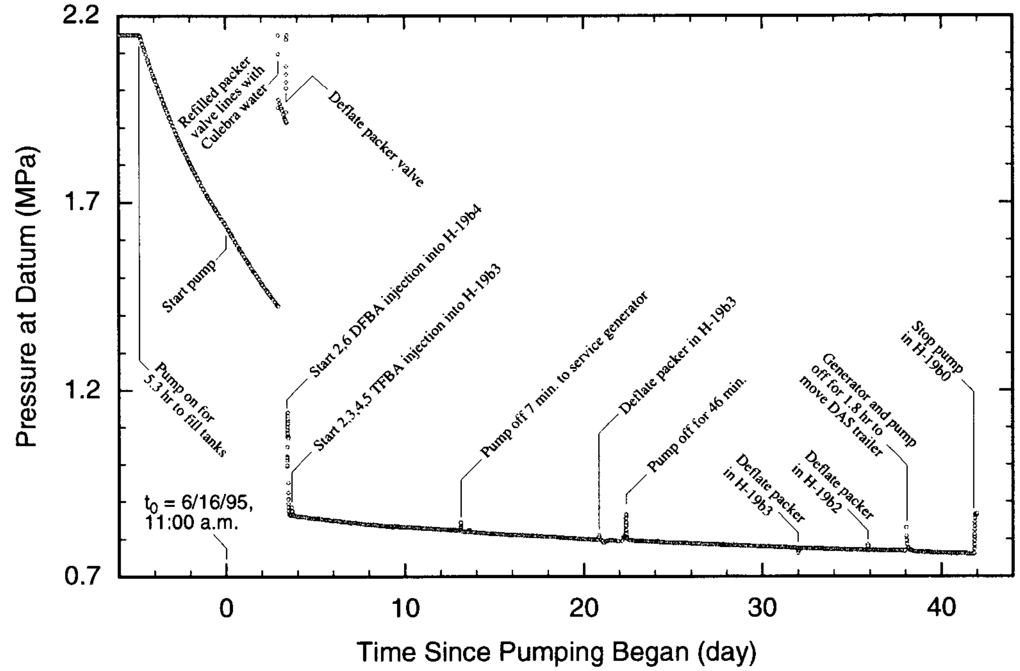

TRI-6115-1000-0

Figure D-22. H-19b4 tracer-injection-line pressure (P2) during the 1995 4-well tracer test.

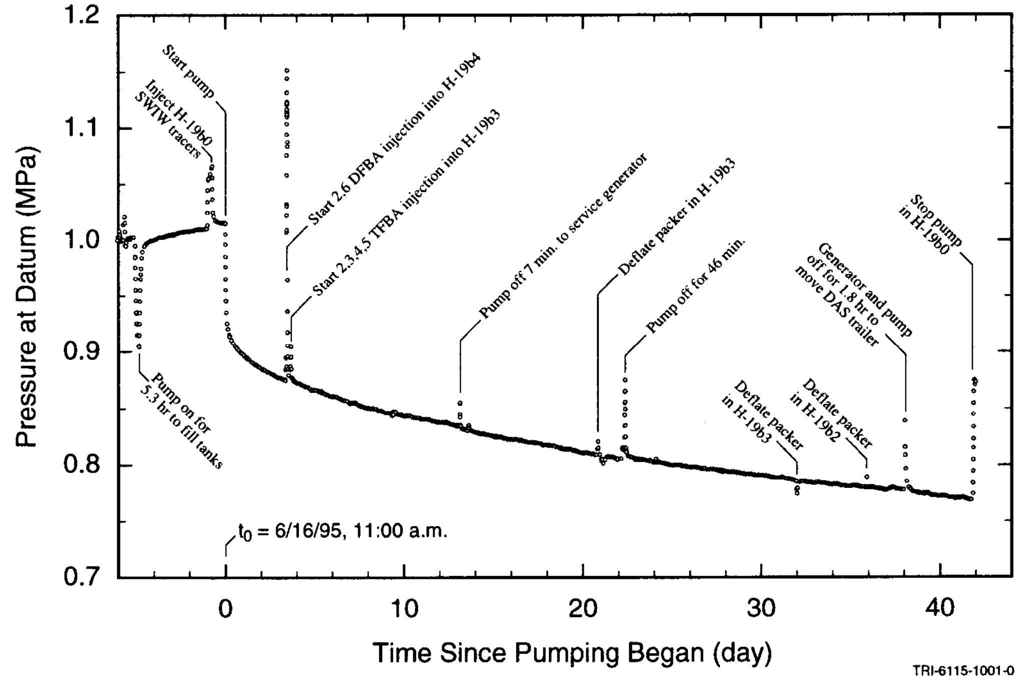

TRI-6115-1001-0

Figure D-23. H-19b4 Culebra pressure (P3) during the 1995 4-well tracer test.

in H-19b0. The two plots should be identical but, for some reason, the P2 transmitter showed a slight upward trend in pressure after the first several days of pumping rather than the expected downward trend shown by the P3 transmitter. We believe that this represents a malfunction in the P2 transmitter. Tracer injections in the other H-19 wells, brief pump stoppages, and test-tool replacements in the other wells are clearly evident in the pressures observed in H-19b0.

Figures D-15, D-16, and D-17 show the annulus, tracer-injection-line, and Culebra pressures, respectively, in H-19b2. Before pumping began, the annulus pressure was rising while the pressure in the tracer-injection line was decreasing, indicating a possible leak. After pumping began, the rate of pressure increase in the annulus slowed, but at the same time the Culebra pressure began to show evidence of a leak. After the packer valve was deflated for the tracer injection in H-19b2, the pressures in the Culebra and tracer-injection line equilibrated and the annulus pressure was stable for the duration of the test. The test tool was removed from H-19b2 on 22 July 1995. Two pressure transmitters were reinstalled on 25 July 1995 to monitor the Culebra pressure for the duration of the test.

Figures D-18, D-19, and D-20 show the annulus, Culebra, and tracer-injection-line pressures, respectively, in H-19b3. The annulus pressure dropped very slightly up until the time of tracer injection into H-19b3, and was then either stable or rose slightly for the remainder of the test. The other transmitters showed no evidence of any problems during the test. The test tool was removed from H-19b3 on 7 July 1995 so that a prototype passive-injection tool could be installed and tested. That tool was installed on 8 July 1995 and removed on 18 July 1995. Two pressure transmitters were reinstalled in the well on 25 July 1995 to monitor the Culebra pressure for the duration of the test.

Figures D-21, D-22, and D-23 show the annulus, tracer-injection-line, and Culebra pressures, respectively, in H-19b4. Before tracer injection, the annulus pressure was rising while the pressure in the tracer-injection line was decreasing, indicating a possible leak. After the packer valve was deflated for the tracer injection in H-19b4, the annulus pressure increased more slowly for a few days before stabilizing for the duration of the test. The other transmitters showed no evidence of any problems during the test.

D.4.2 H-19 Seven-Well Tracer Test

Figure D-24 shows the pumping rates measured by the totalizing flow meter, calibrated standpipe, and electronic flow meter during the H-19 seven-well tracer test. Pumping began at 11:30 on 15 December 1995 and ended at 11:30 on 11 April 1996. The design pumping rate for the first and second rounds of tracer injection was approximately 0.28 L/s. The pump proved unable to sustain this rate, however, and the rate slowly decreased to approximately 0.27 L/s over the first 33 days of pumping. When the pump was restarted after being off for approximately one hour on 17 January 1996, the pumping rate was only slightly above 0.25 L/s. This rate was then maintained until 19 February 1996, when it was reduced to slightly more than 0.15 L/s for the third round of tracer injections. At various times during the test, the electronic flow-control system did not function properly, but instead produced systematic oscillations in the pumping rate. These oscillations became particularly pronounced after the pumping rate was reduced for the third round of tracer injections. Fortunately, the average pumping rates during the three tracer-injection rounds were little affected by these short-term oscillations.

Figures D-25, D-26, and D-27 show the lower Culebra (P2), upper Culebra (P4), and annulus (P5) pressures, respectively, in H-19b0. The packer separating the upper and lower Culebra was deflated 5 to 11 minutes after pumping began; after that time, all of the Culebra pressure transmitters were monitoring the same thing. As shown on Figures D-25 and D-26, the Culebra pressure in H-19b0 was affected by many events during the test, such as pump stoppages, tracer injections, and problems with the flow controller. All of these events had little effect on the overall pressure trend, however. The annulus pressure decreased by approximately 0.02 MPa over the

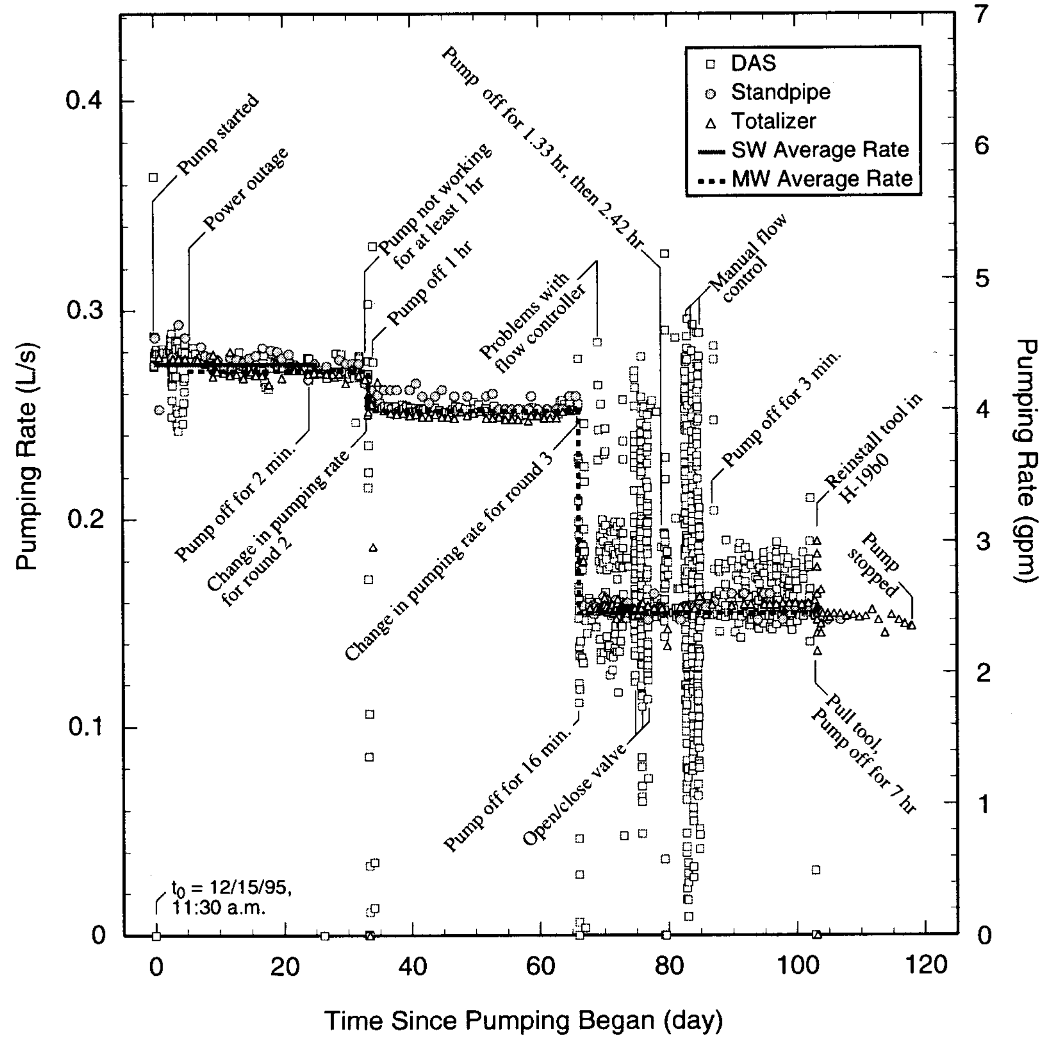

TRI-6115-975-0

Figure D-24. Flow-rate data during the 1995-96 H-19 7-well tracer test.

first 103 days of pumping (Figure D-27). This could possibly represent leakage of approximately 60 L of water past the upper packer into the test zone. This amount of leakage over 103 days would have had an insignificant effect on either pressures or tracer concentrations in the test zone.

Figures D-28 and D-29 show the Culebra (P1) and annulus (P2) pressures, respectively, in H-19b2. The Culebra pressure shows the effects of some of the pump stoppages and tracer injections, but had little response to the high-frequency pumping-rate fluctuations. The annulus pressure increased by less than 0.005 MPa over the course of the test.

Figures D-30, D-31, and D-32 show the lower Culebra (P1), upper Culebra (P2), and annulus (P3) pressures, respectively, in H-19b3. The packer dividing the Culebra into upper and lower parts in H-19b3 was inflated when testing began and was deflated on 20 December 1995. It was inflated again on 16 January 1996 and deflated for the last time on 21 February 1996. Therefore, at all other times, the lower and upper Culebra pressure transmitters (P1 and P2) were measuring the same thing. The Culebra pressures show the effects of some of the pump stoppages and tracer injections, but had little response to the high-frequency pumping-rate fluctuations. The annulus

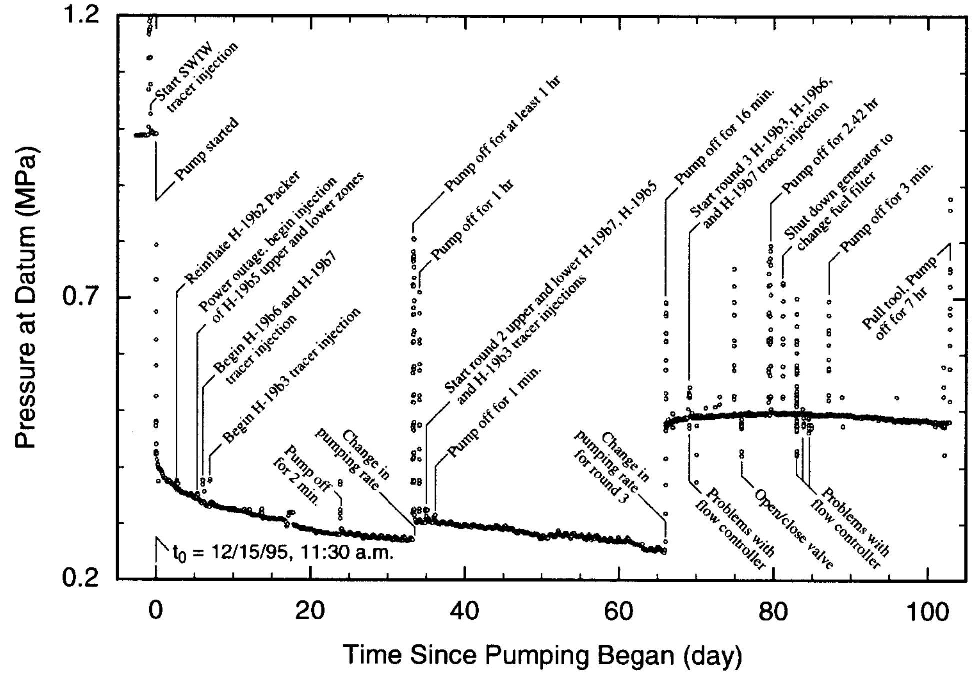

TRI-6115-1002-0

Figure D-25. H-19b0 lower Culebra pressure (P2) during the 1995-96 7-well tracer test.

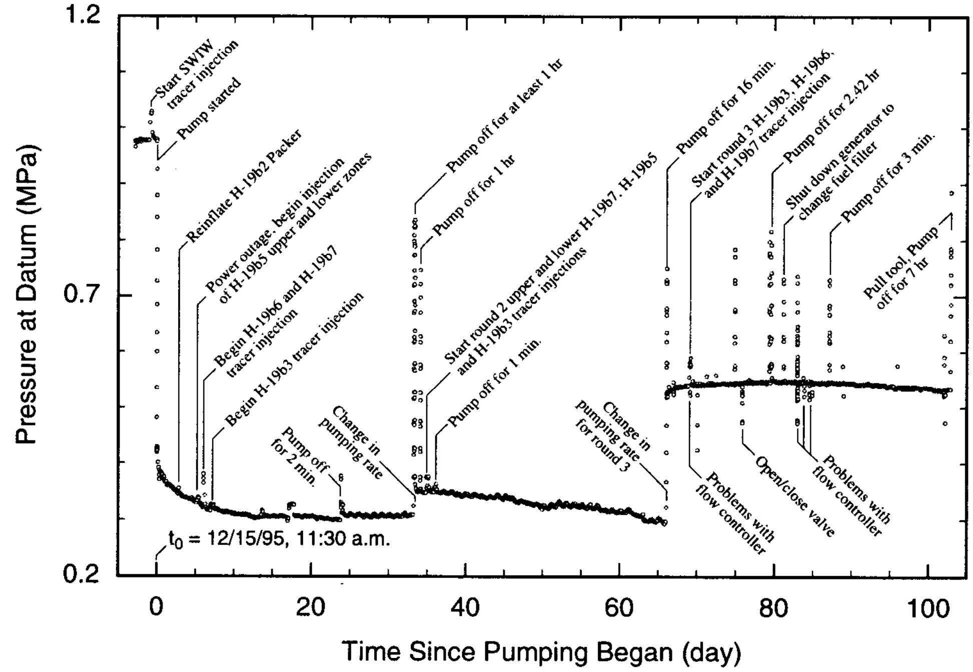

TRI-6115-1003-0

Figure D-26. H-19b0 upper Culebra pressure (P4) during the 1995-96 7-well tracer test.

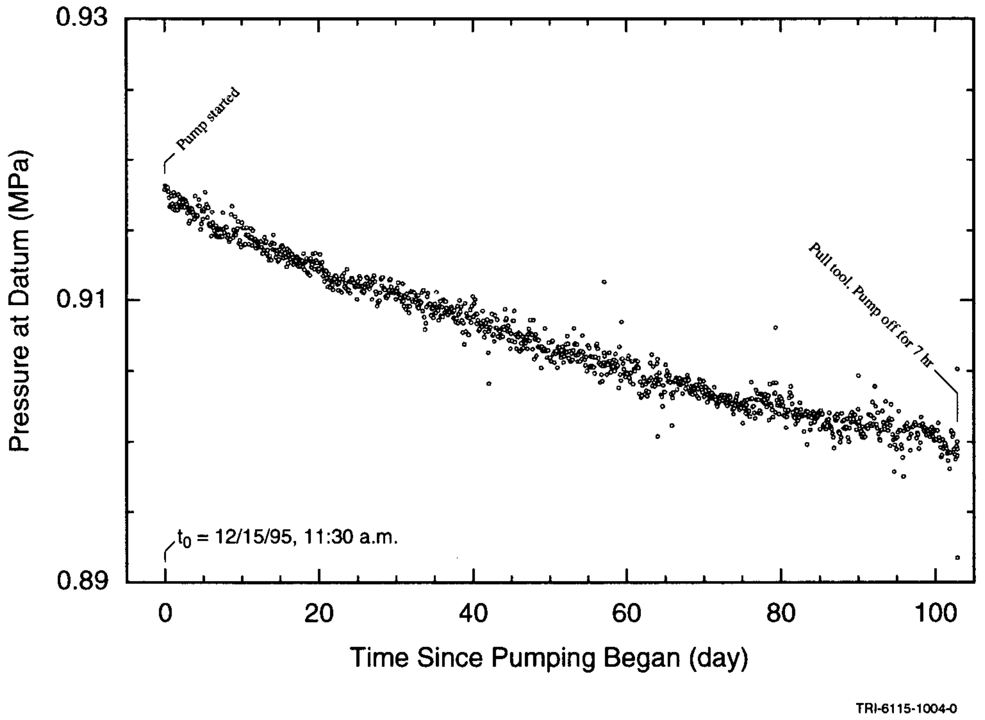

Figure D-27. H-19b0 annulus pressure (P5) during the 1995-96 7-well tracer test.

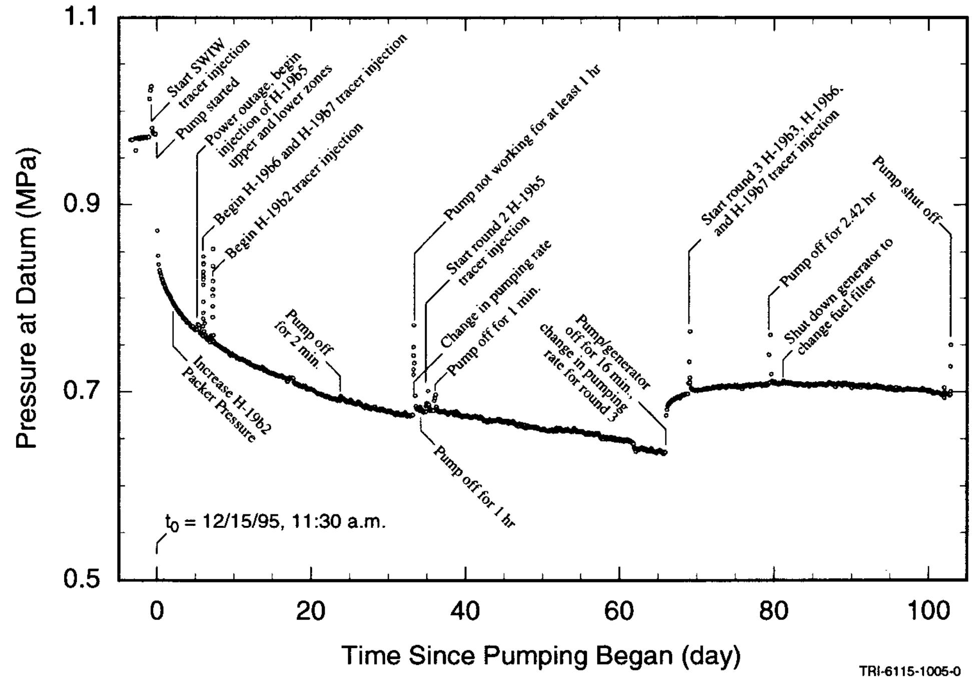

Figure D-28. H-19b2 Culebra pressure (P1) during the 1995-96 7-well tracer test.

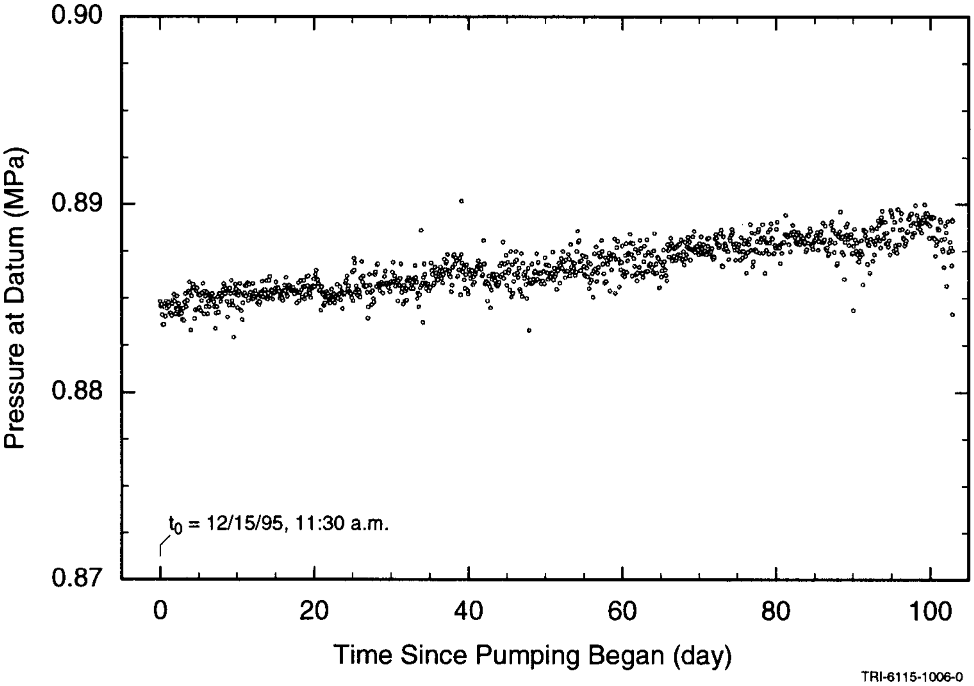

Figure D-29. H-19b2 annulus pressure (P2) during the 1995-96 7-well tracer test.

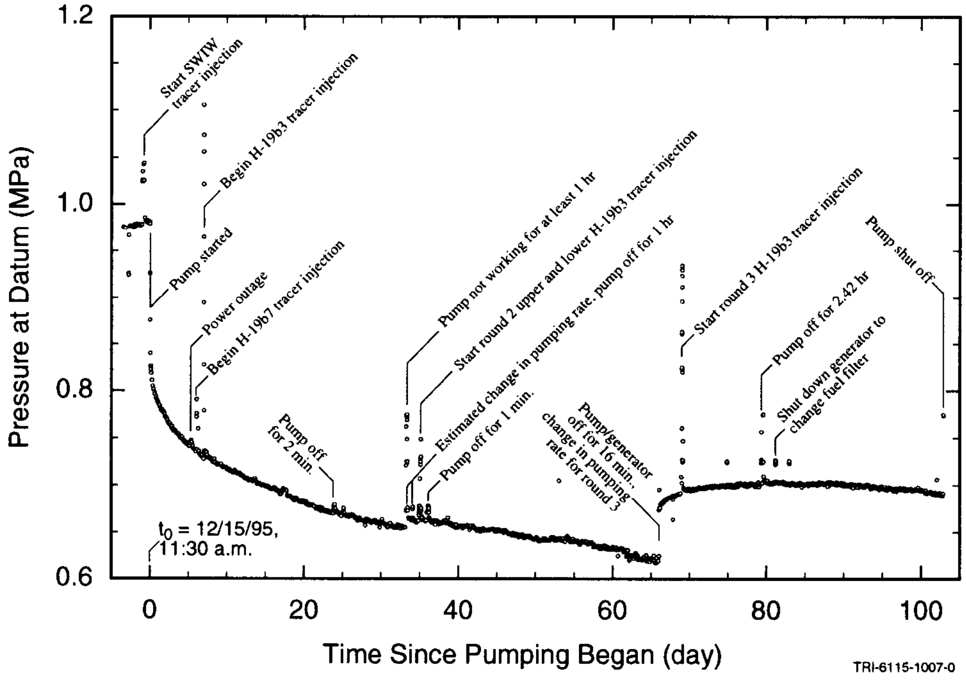

Figure D-30. H-19b3 lower Culebra pressure (P1) during the 1995-96 7-well tracer test.

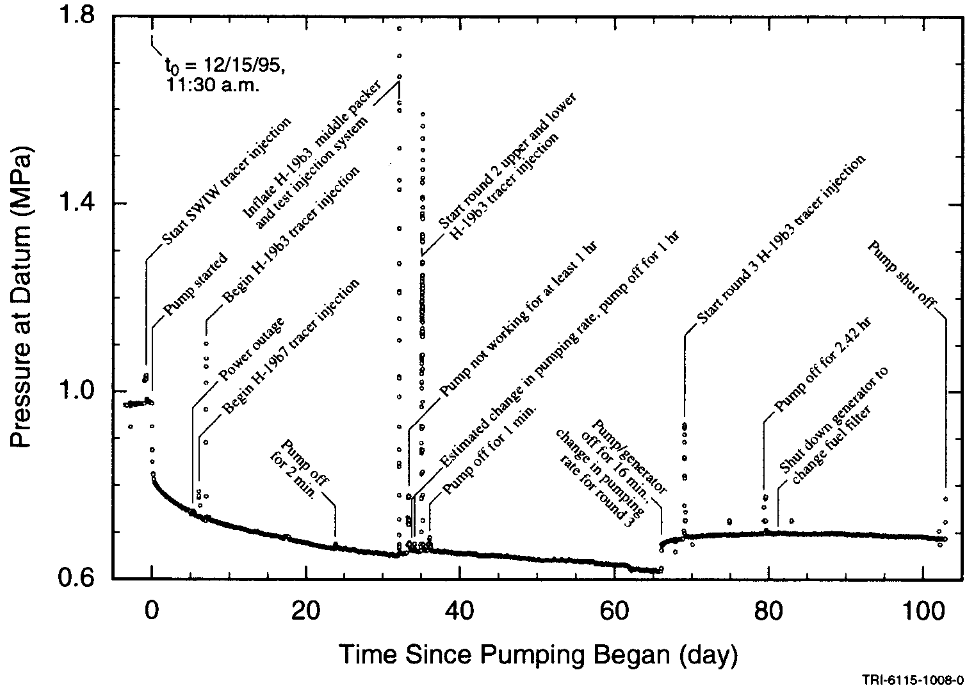

Figure D-31. H-19b3 upper Culebra pressure (P2) during the 1995-96 7-well tracer test.

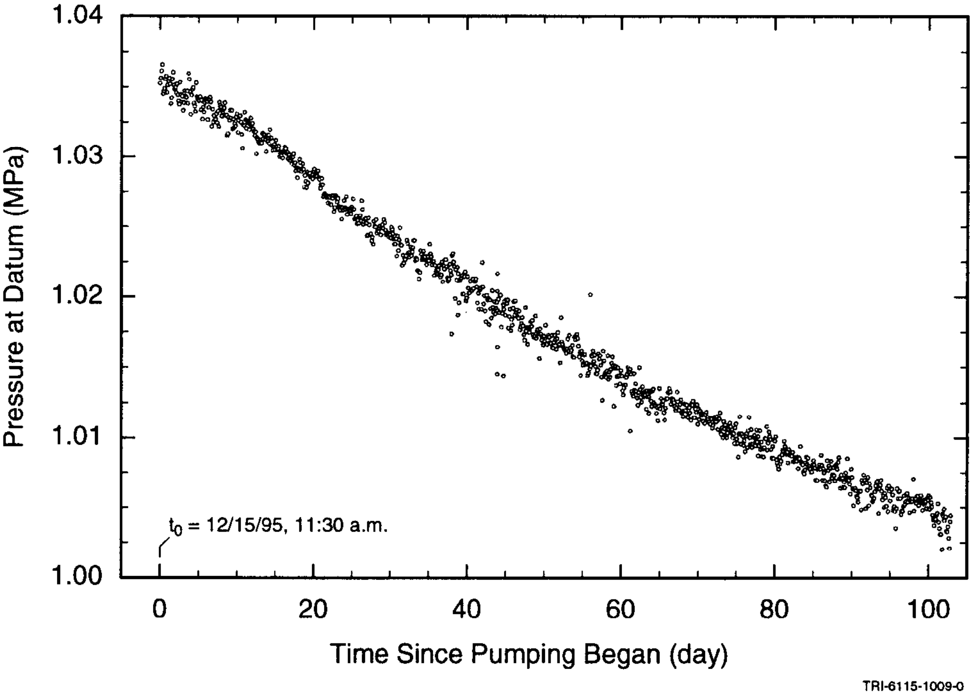

Figure D-32. H-19b3 annulus pressure (P3) during the 1995-96 7-well tracer test.

pressure decreased by approximately 0.03 MPa over the course of the test, corresponding to a possible leakage of approximately 50 L into the test zone. This amount of leakage over 103 days would have had no significant effect on any test parameter.

Figures D-33 and D-34 show the Culebra (P1) and annulus (P2) pressures, respectively, in H-19b4. The Culebra pressure shows the effects of some of the pump stoppages and tracer injections, but had little response to the high-frequency pumping-rate fluctuations. The annulus pressure decreased by nearly 0.05 MPa over the first approximately 33 days of pumping, and by approximately 0.01 MPa over the next 70 days. These pressure decreases correspond to potential leakages of approximately 80 and 20 L, respectively, which would have had no significant effect on test responses.

Figures D-35, D-36, and D-37 show the lower Culebra (P1), upper Culebra (P2), and annulus (P3) pressures, respectively, in H-19b5. The packer dividing the Culebra into upper and lower parts in H-19b5 was inflated when testing began and was deflated on 16 January 1996. Thereafter, the lower and upper Culebra pressure transmitters (P1 and P2) were measuring the same thing. The upper Culebra transmitter (Figure D-36) had a noisy signal at different times for an unknown reason; the noise does not appear to correlate with flow-rate fluctuations at H-19b0 and was not shown by the lower Culebra transmitter when both transmitters were measuring the same thing. The annulus pressure (Figure D-37) decreased by nearly 0.14 MPa over the first approximately 40 days of pumping, and by approximately 0.01 MPa over the next 63 days. These pressure decreases correspond to potential leakages of approximately 230 and 20 L, respectively. Most of the leakage occurred while the packer separating the upper and lower Culebra was inflated. Beauheim and Ruskauff (1998) discuss the effects of this leakage on the pressure responses observed in the upper Culebra during the first five days of pumping. The leakage might have accelerated transport in the upper Culebra from H-19b5 to H-19b0 slightly, but the tracer breakthrough was too low to interpret in any case.

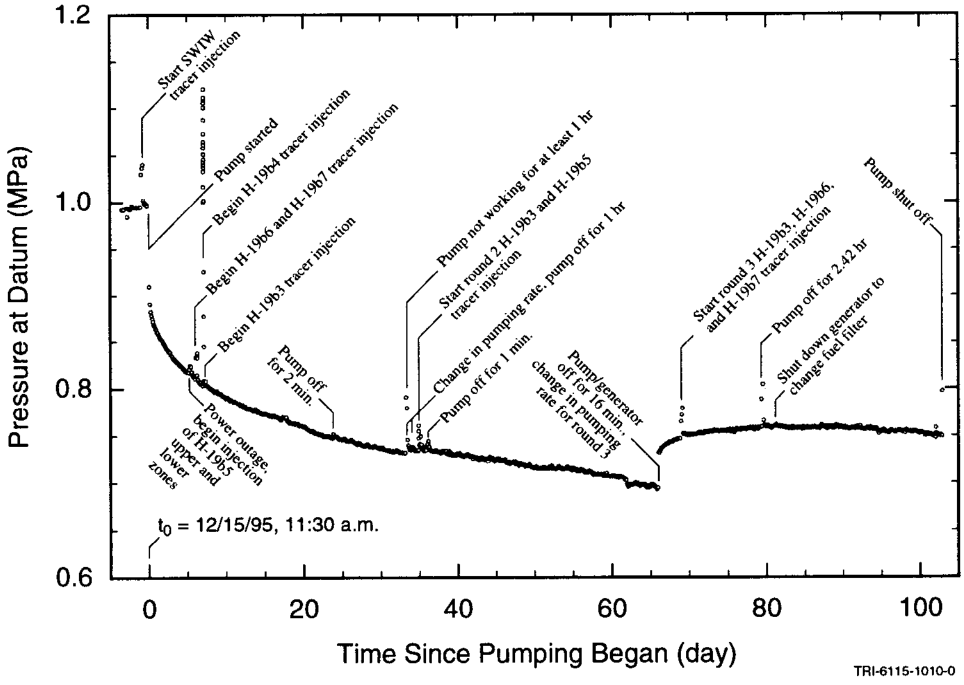

Figure D-33. H-19b4 Culebra pressure (P1) during the 1995-96 7-well tracer test.

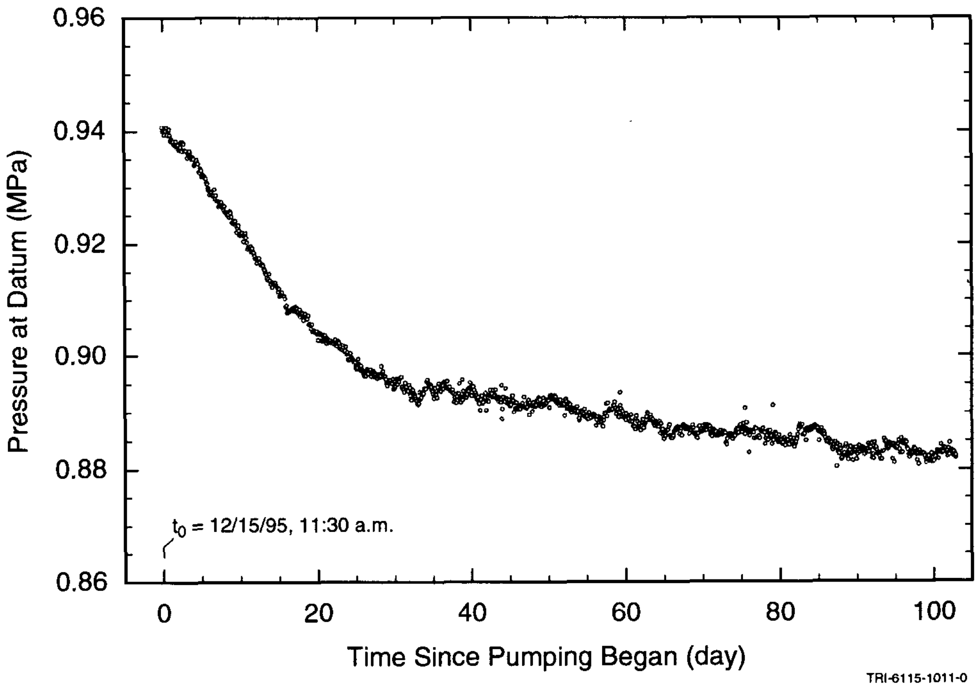

Figure D-34. H-19b4 annulus pressure (P2) during the 1995-96 7-well tracer test.

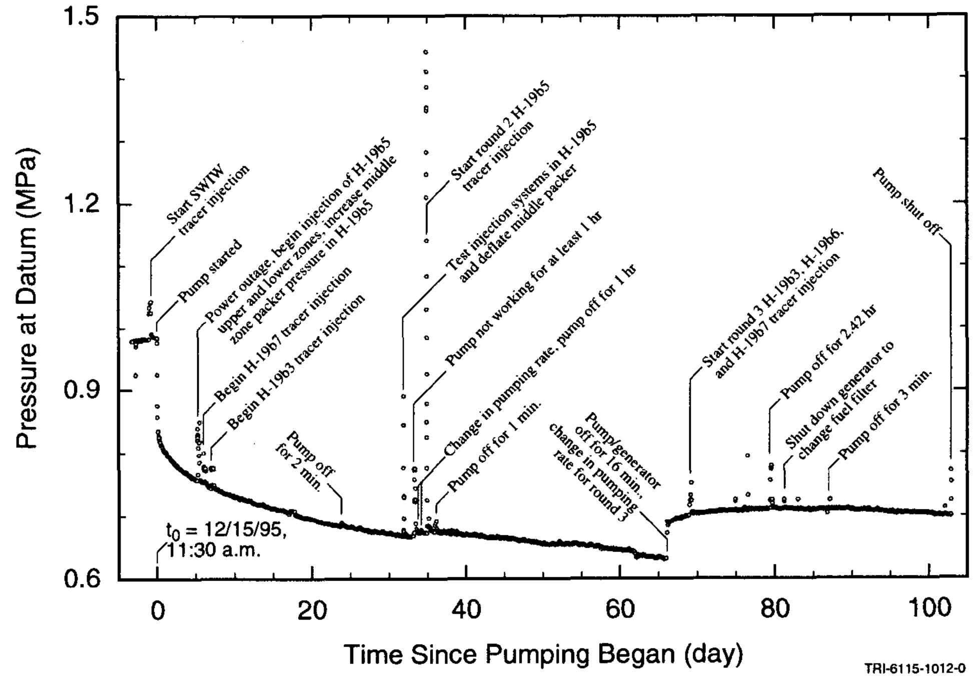

Figure D-35. H-19b5 lower Culebra pressure (P1) during the 1995-96 7-well tracer test.

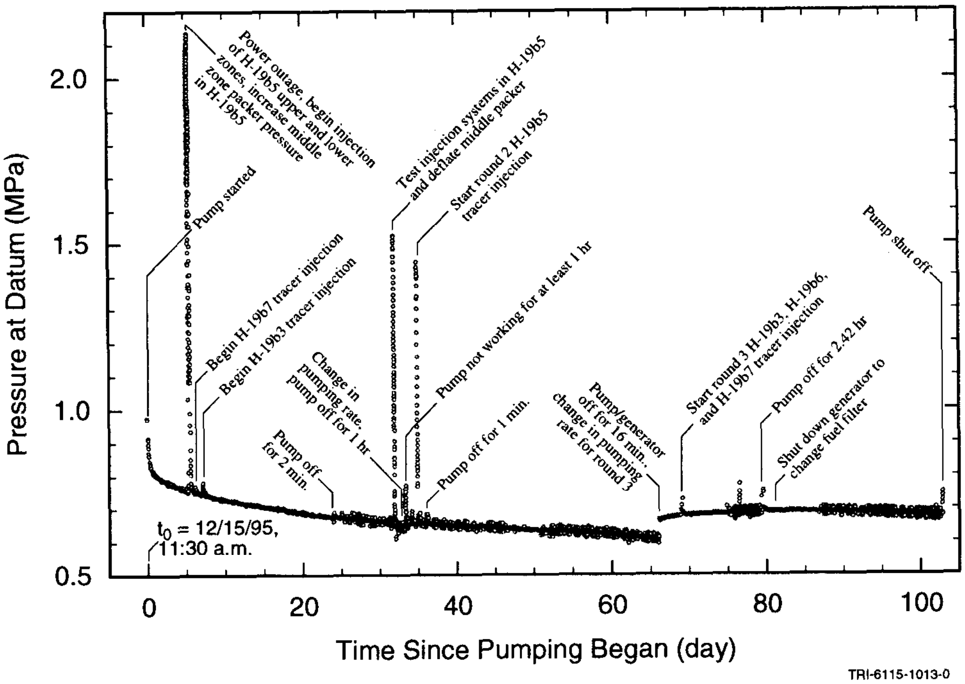

Figure D-36. H-19b5 upper Culebra pressure (P2) during the 1995-96 7-well tracer test.

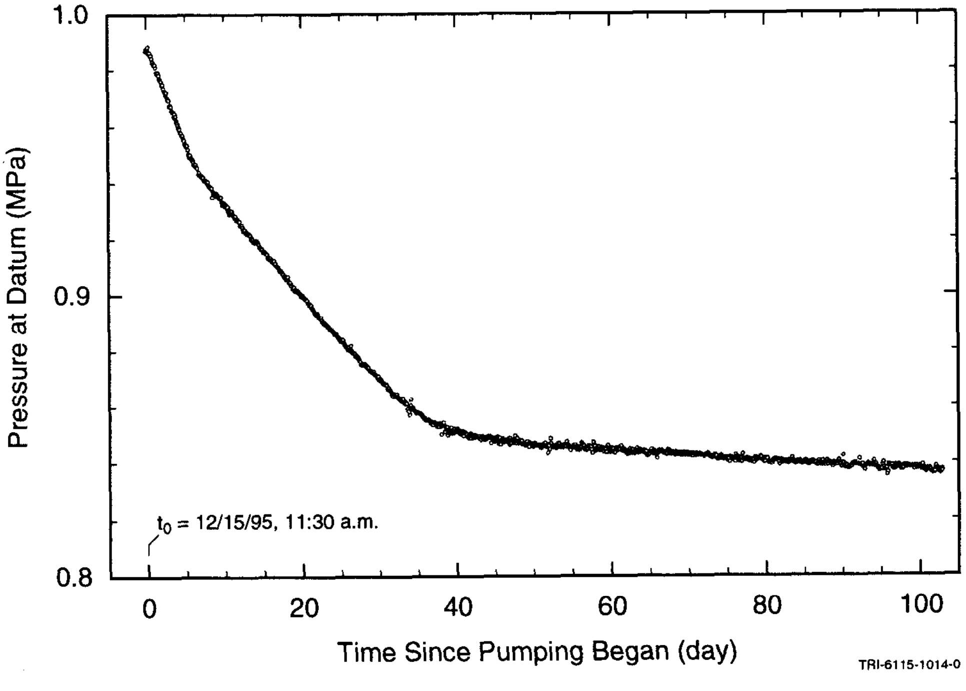

Figure D-37. H-19b5 annulus pressure (P3) during the 1995-96 7-well tracer test.

Figures D-38 and D-39 show the Culebra (P2) and annulus (P1) pressures, respectively, in H-19b6. The Culebra pressure shows the effects of some of the pump stoppages and tracer injections, but had little response to the high-frequency pumping-rate fluctuations. The annulus pressure decreased by approximately 0.05 MPa over 103 days of pumping, corresponding to potential leakage of approximately 90 L, which would have had no significant effect on test responses.

Figures D-40, D-41, and D-42 show the lower Culebra (P1), upper Culebra (P2), and annulus (P3) pressures, respectively, in H-19b7. The packer dividing the Culebra into upper and lower parts in H-19b7 was inflated when testing began and was deflated on 20 December 1995. It was inflated again on 16 January 1996 and deflated for the last time on 21 February 1996. Therefore, at all other times, the lower and upper Culebra pressure transmitters (P1 and P2) were measuring the same thing. All of the H-19b7 pressure transmitters shared the fluctuations seen in the H-19b0 pumping rate. Why the annulus transmitter showed the fluctuations is unknown; the fluctuations may simply represent electronic noise in the DAS rather than actual changing flow rates and pressures. The annulus pressure in H-19b7 decreased by less than 0.01 MPa over 103 days of pumping, which corresponds to leakage of less than 20 L.

D.4.3 H-11 Tracer Test

Figure D-43 shows the flow rates measured during the H-11 tracer test with various instruments. The plot is annotated to show the times of different events that occurred during the test. Pumping began at 10:00 on 7 February 1996 and ended at 07:43 on 27 March 1996. The pumping rate over the first 33.2 days of pumping averaged 0.22 L/s. The pumping rate was increased to approximately 0.38 L/s on 11 March 1996 for the second round of tracer injections. Information on the tracer injections (times, volumes, etc.) is contained in Tables 3-2 and 3-3.

Figures D-44 through D-47 show the pressures measured by the Culebra pressure transmitters in H-11b1 (P1 only), H-11b2, H-11b3, and H-11b4, respectively. The plots are annotated to show when events such as tracer injections and pump

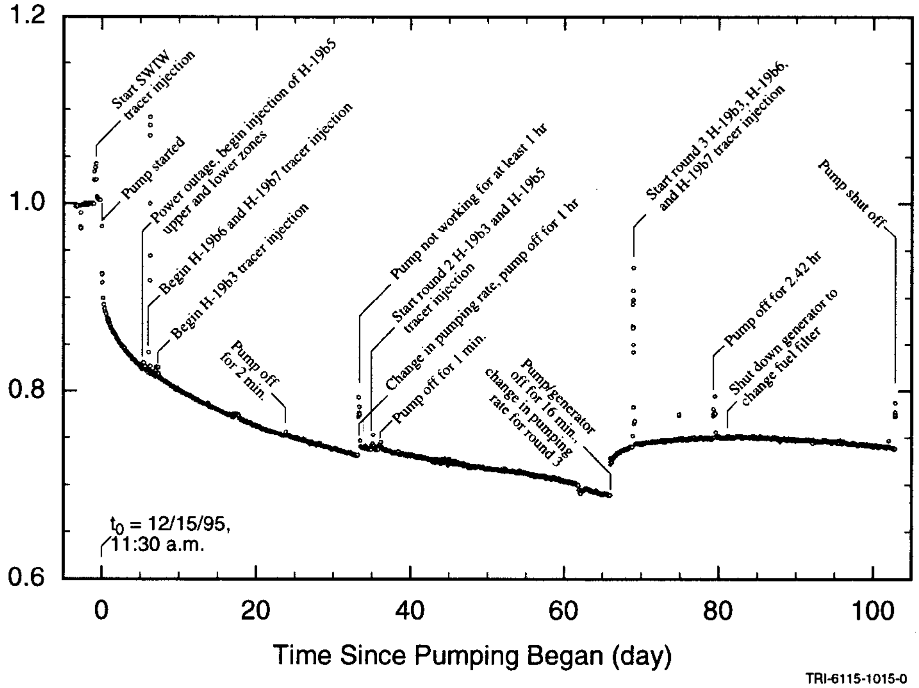

Figure D-38. H-19b6 Culebra pressure (P2) during the 1995-96 7-well tracer test.

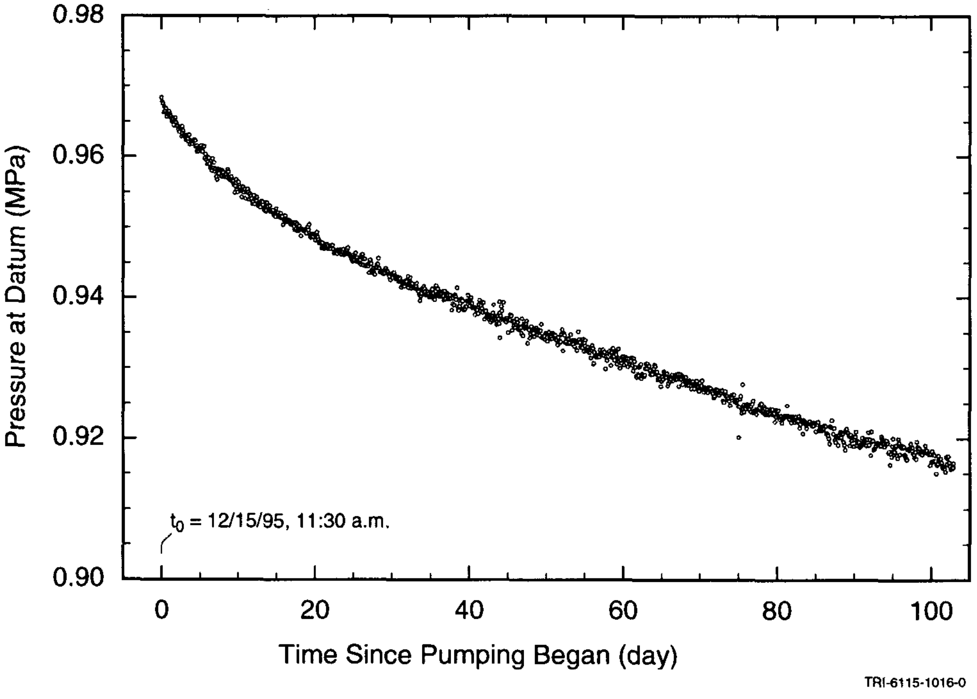

Figure D-39. H-19b6 annulus pressure (P1) during the 1995-96 7-well tracer test.

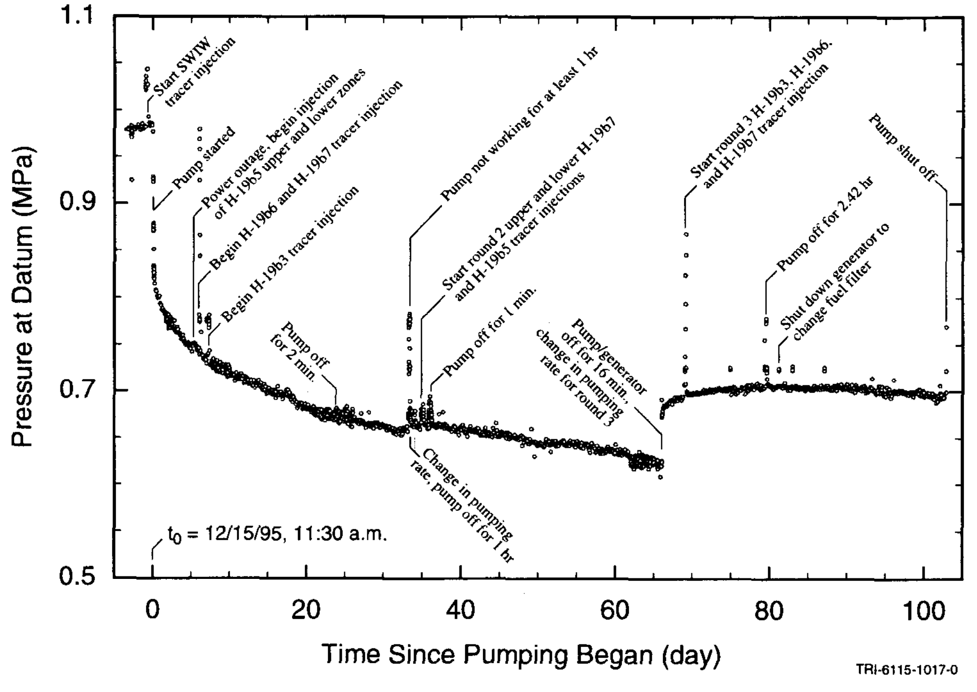

Figure D-40. H-19b7 lower Culebra pressure (P1) during the 1995-96 7-well tracer test.

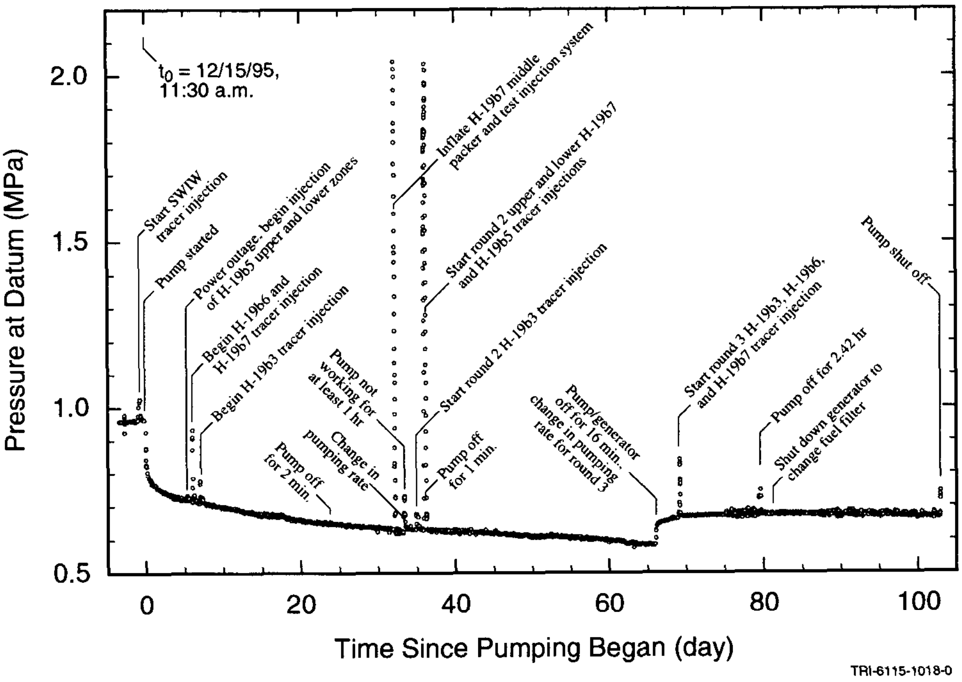

Figure D-41. H-19b7 upper Culebra pressure (P2) during the 1995-96 7-well tracer test.

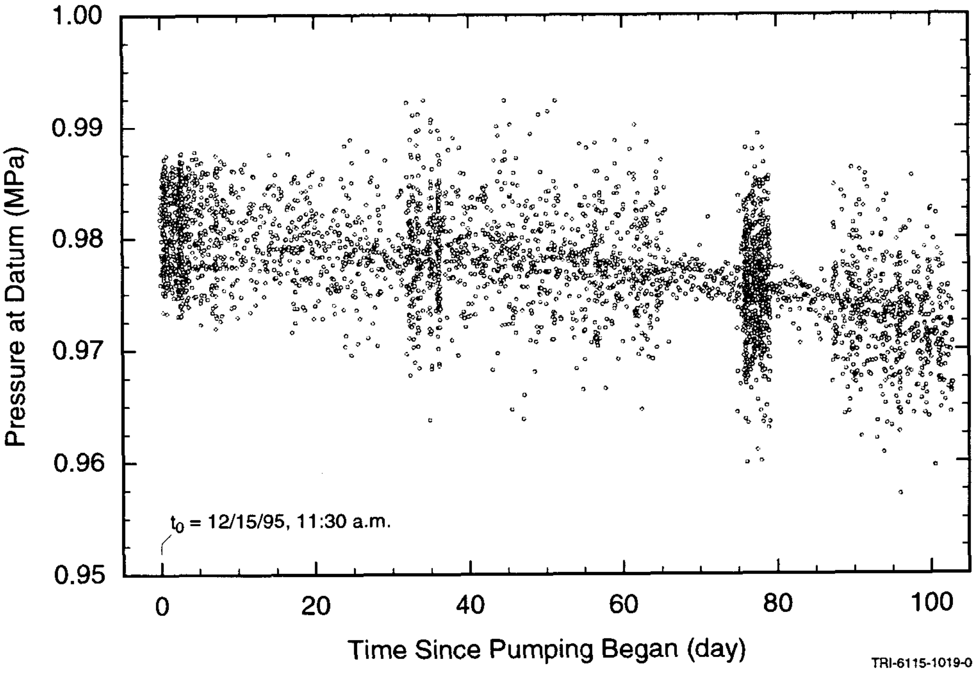

Figure D-42. H-19b7 annulus pressure (P3) during the 1995-96 7-well tracer test.

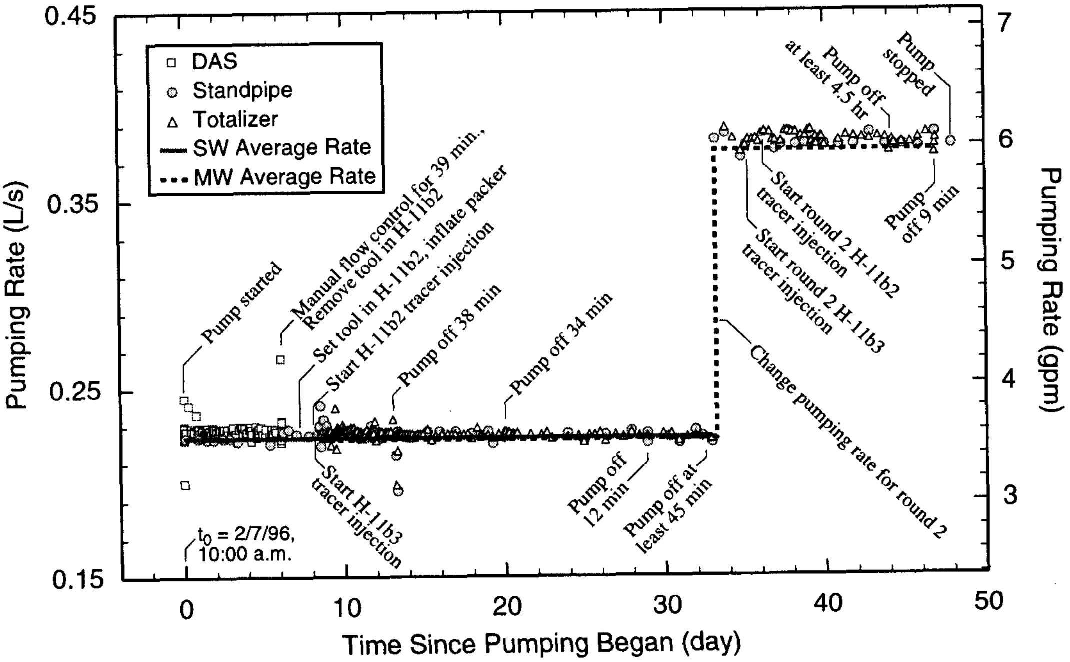

TRI-6115-973-0

Figure D-43. Flow-rate data during the 1996 H-11 tracer test.

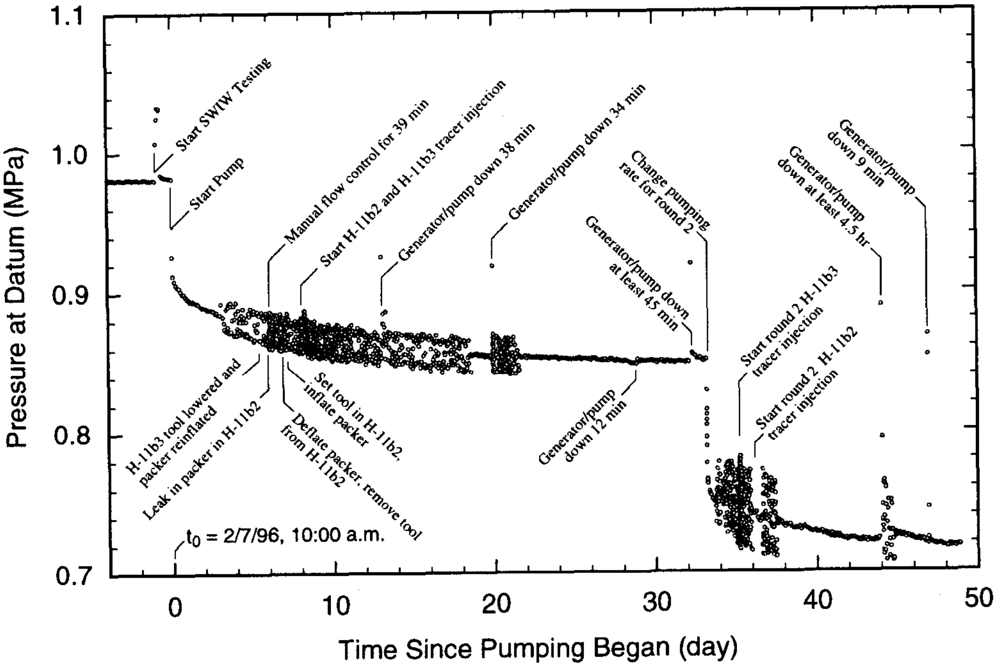

TRI-6115-982-0

Figure D-44. H-11b1 Culebra pressure (P1) during the 1996 tracer test.

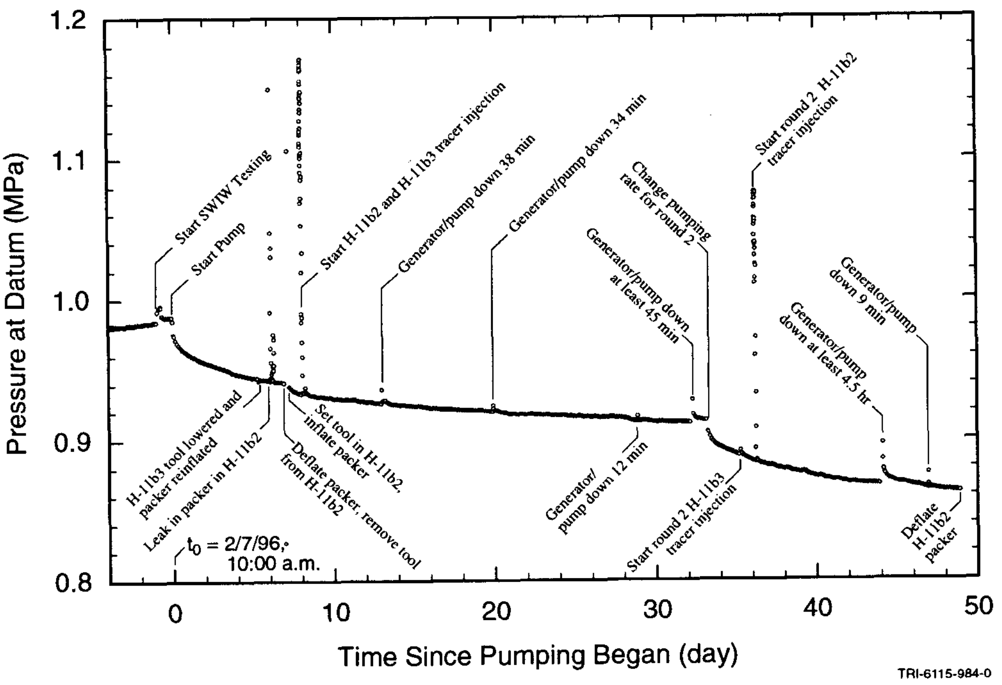

Figure D-45. H-11b2 Culebra pressure (P1) during the 1996 tracer test.

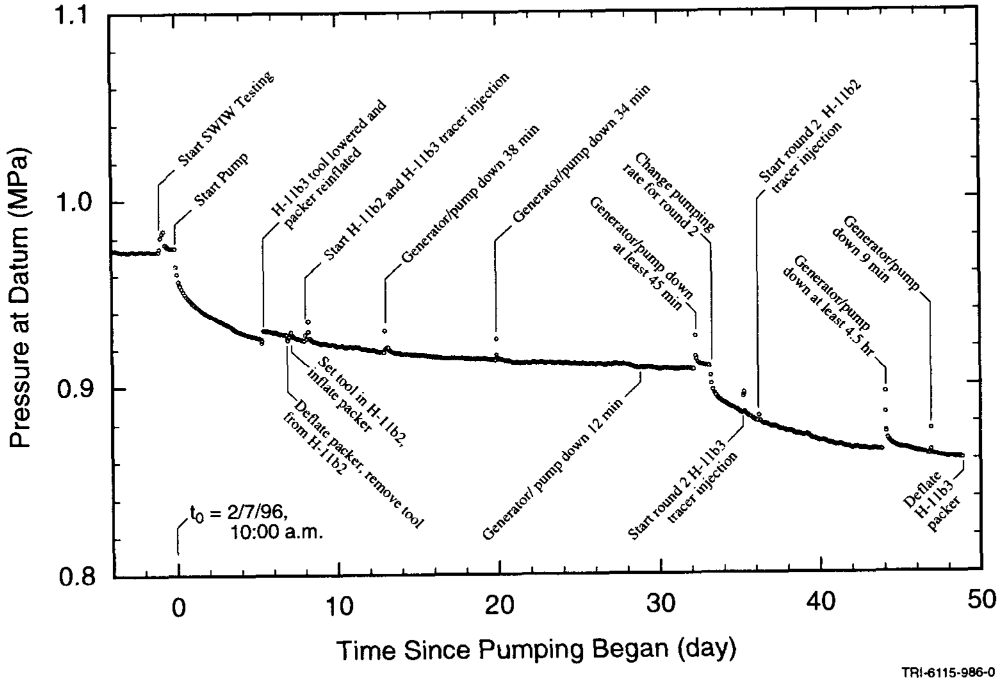

Figure D-46. H-11b3 Culebra pressure (P1) during the 1996 tracer test.

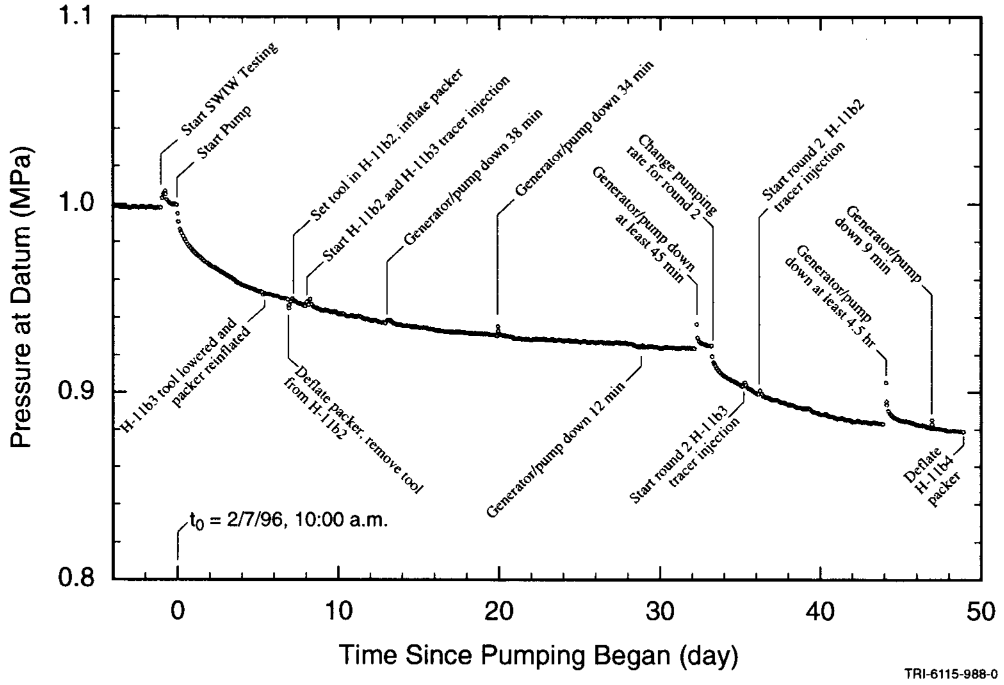

Figure D-47. H-11b4 Culebra pressure (P1) during the 1996 tracer test.

stoppages occurred. The pressure signal from the pumping well, H-11b1 (Figure D-44), was noisy at times for an unknown reason not associated with fluctuations in the pumping rate.

Figures D-48 through D-51 show the pressures measured in the well annulus above the packer isolating the Culebra in H-11b1, H-11b2, H-11b3, and H-11b4, respectively. The pressure in the H-11b1 annulus dropped by approximately 0.02 MPa during the first 43 days of (Figure D-48). On 21 March 1996, the H-11b1 annulus pressure began to rise, and was nearly 0.10 MPa higher by the end of the test six days later. Most likely, this rise reflects a small leak in the discharge line. The packer in H-11b2 began losing pressure after approximately six days of pumping. Consequently, the tool was removed, the packer was replaced, and the tool was reinstalled slightly deeper than before on 14 February 1996. The pressure in the H-11b2 annulus increased by less than 0.01 MPa every time the pump stopped (Figure D-49). After the pump was turned back on, the pressure declined slowly until the next stoppage, but the net effect was a rise of less than 0.01 MPa over the course of the test. The annulus pressure in H-11b3 decreased by approximately 0.10 MPa over the first five days of pumping (Figure D-50). After the tool in H-11b3 was repositioned on 12 February 1996, the annulus pressure decreased by less than 0.02 MPa over the remainder of the test. The H-11b4 annulus pressure decreased by approximately 0.01 MPa over the course of the test (Figure D-51). Both the H-11b3 and H-11b4 annulus pressures rose by less than 0.01 MPa in response to the pump stoppages on 10 March 1996 and 22 March 1996.

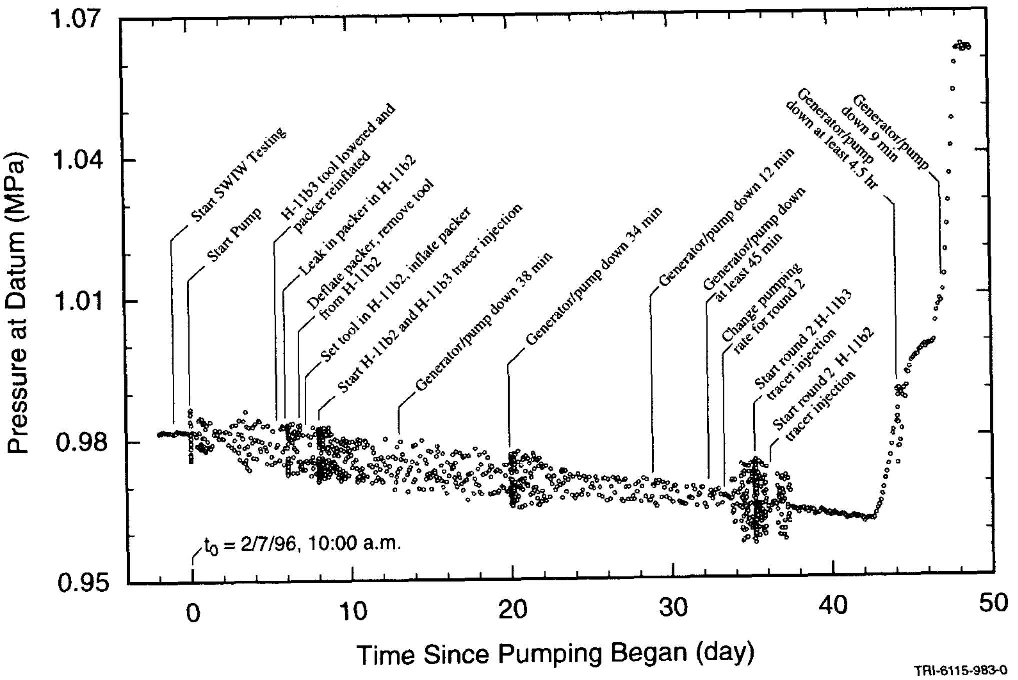

TRI-6115-983-0

Figure D-48. H-11b1 annulus pressure (P3) during the 1996 tracer test.

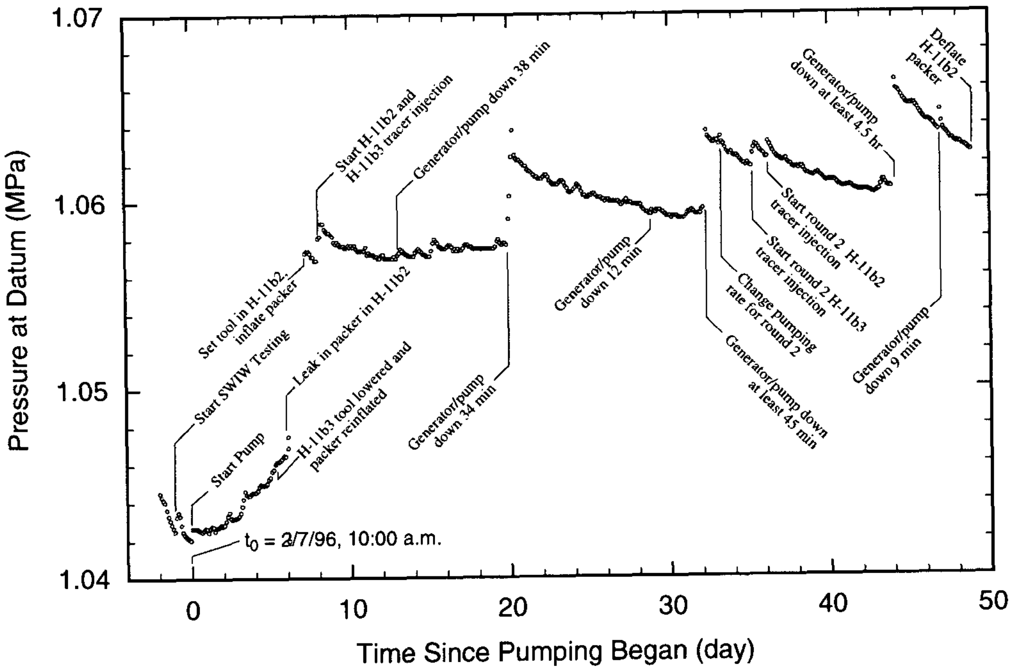

TRI-6115-985-0

Figure D-49. H-11b2 annulus pressure (P2) during the 1996 tracer test.

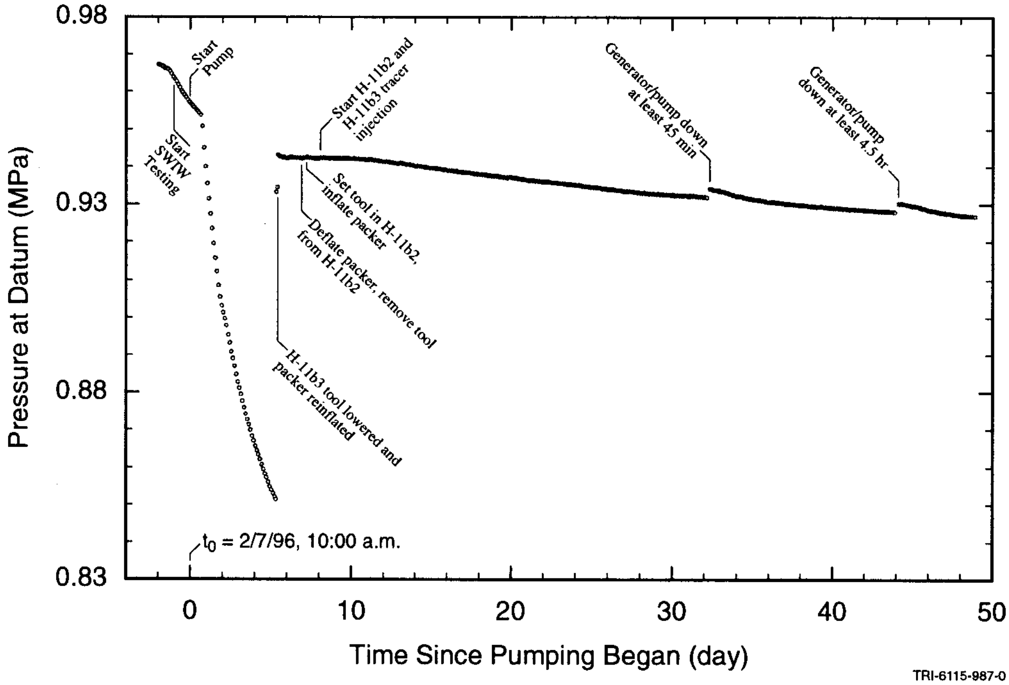

TRI-6115-987-0

Figure D-50. H-11b3 annulus pressure (P2) during the 1996 tracer test.

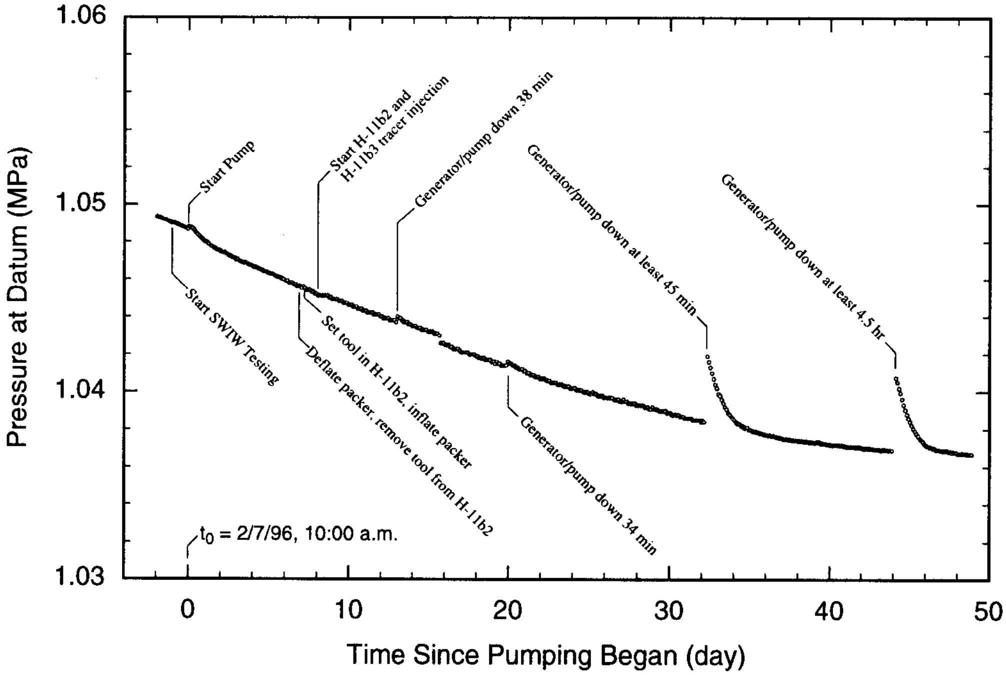

TRI-6115-989-0

Figure D-51. H-11b4 annulus pressure (P2) during the 1996 tracer test.

D.5 References

Beauheim, R.L., and G.J. Ruskauff. 1998. *Analysis of Hydraulic Tests of the Culebra and Magenta Dolomites and Dewey Lake Redbeds Conducted at the Waste Isolation Pilot Plant Site.* SAND98-0049. Albuquerque, NM: Sandia National Laboratories.

Jones, T.L., V.A. Kelley, J.F. Pickens, D.T. Upton, R.L. Beauheim, and P.B. Davies. 1992. *Integration of Interpretation Results of Tracer Tests Performed in the Culebra Dolomite at the Waste Isolation Pilot Plant Site.* SAND92-1579. Albuquerque, NM: Sandia National Laboratories.

Mercer, J.W., D.L. Cole, and R.M. Holt. 1998. *Basic Data Report for Drillholes on the H-19 Hydropad (Waste Isolation Pilot Plant – WIPP).* SAND98-0071. Albuquerque, NM: Sandia National Laboratories.

Stensrud, W.A., M.A. Bame, K.D. Lantz, J.B. Palmer, and G.J. Saulnier, Jr. 1990. *WIPP Hydrology Program, Waste Isolation Pilot Plant, Southeastern New Mexico, Hydrologic Data Report #8.* SAND89-7056. Albuquerque, NM: Sandia National Laboratories.

This page intentionally left blank.

Appendix E
Summary of Hydraulic Tests Performed at Tracer-Test Sites

By Richard L. Beauheim[1]

E.1 Introduction

A variety of hydraulic tests have been conducted at all of the hydropads where tracer tests have been performed (see Figure 2-2 in Chapter 2). This appendix summarizes those hydraulic tests. The test results included in the discussion are those relevant either to interpretations of the tracer-test results or to differences in transport behavior along different flow paths or at different hydropads.

E.2 H-2 Hydropad

Figure F-1 in Appendix F shows the present-day layout of wells at the H-2 hydropad. In 1981, a pumping test was performed using H-2c as the pumping well and H-2b1 as an observation well. At that time, these were the only wells on the hydropad completed to the Culebra. For the test, H-2c was pumped for 71 hr at an average rate of 0.016 L/s. Beauheim and Ruskauff (1998) interpreted the data from this test. They found that the Culebra behaved hydraulically like a single-porosity medium at H-2 with a transmissivity of 5.9×10^{-7} m^2/s and a storativity of 1.5×10^{-5}.

E.3 H-3 Hydropad

Figure F-2 in Appendix F shows the layout of wells at the H-3 hydropad. Shortly after the well casing in H-3b1 was perforated across the Culebra (204.8 to 211.5 m bgs) in March 1977, a tracer survey was conducted in the well (Mercer and Orr, 1979). A tracer solution containing radioactive iodine-131 was injected into the well at a rate of approximately 0.50 L/s. The survey indicated that approximately 36% of the solution entered the Culebra between 208.5 and 210.9 m bgs and the remaining 64% entered between 210.9 and 211.8 m bgs. No inflow was detected in the upper half of the Culebra (204.8 to 208.5 m bgs).

In 1984, SNL pumped H-3b3 for three 1-hr tests, one 13-hr test, and approximately 50 days for a convergent-flow tracer test (INTERA Technologies, 1986). In 1985, H-3b2 was pumped for 62 days at a rate of 0.30 L/s (INTERA Technologies, 1986). All three wells on the H-3 hydropad were monitored during all of the tests. The first and third 1-hr tests at H-3b3 were conducted at variable pumping rates that averaged 0.45 and 0.41 L/s, respectively. Recoveries from these tests were monitored for 20.5 and 17.5 hr, respectively, and provided the only data that could be readily interpreted. Because of their short duration, the 1-hr pumping tests also provide the information most representative of conditions in the immediate vicinity of the H-3 hydropad. All of the well responses to the 1-hr tests showed clear double-porosity responses, with a mean transmissivity of 2.1×10^{-5} m^2/s. With only two observation wells, neither anisotropy nor the true storativity could be determined. The geometric-mean storativity, however, is 4.8×10^{-5}. H-3b3 had an interpreted skin value of approximately -4, representative of fractures intersecting the wellbore.

For the 13-hr pumping test in H-3b3, as well as the later tracer test and 1985 test in H-3b2, a packer was used to isolate the Culebra interval in the pumping well. Use of a packer in this manner greatly reduces wellbore storage, and allows the pressure transient caused by pumping to propagate more quickly. Using packers in the H-3 pumping wells significantly changed the character of the responses in both the pumping and observation wells. The double-porosity effects became less distinct and no-flow-boundary-type effects, probably caused by heterogeneity, appeared as the pressure transients propagated beyond the hydropad. Using the interpretations of the 1-hr tests as a guide, we were able to simulate the recovery from the 13-hr test using a similar double-porosity model and transmissivity, with the addition of two no-flow boundaries.

---

[1] Sandia National Laboratories, Repository Performance and Certification Department, P.O.Box 5800, MS1395, Albuquerque, NM 87185-1395. Email: rlbeauh@sandia.gov.

Prior to injecting tracers for the 1984 tracer test, H-3b3 was pumped for 330 hr at a rate of 0.25 L/s to establish a converging flow field on the hydropad. Beauheim (1987a) attempted to interpret the data from this test and from the 1985 test in H-3b2 using a double-porosity model. However, he lacked interpretations of the earlier 1-hr tests to guide his analyses, and was unable to define unique parameter sets. Qualitatively, the responses to these two tests appear very similar to the responses to the 13-hr test. Beauheim (1987a) noted that H-3b1 was more sensitive to minor flow-rate fluctuations in H-3b3 than was H-3b2, even though it is farther from H-3b3 (30.7 m) than is H-3b2 (26.8 m). From this, Beauheim (1987a) concluded that H-3b1 and H-3b3 might be better connected by fractures than are H-3b2 and H-3b3.

H-3b2 and H-3b3 were completed open-hole through the Culebra (Hydro Geo Chem, Inc., 1985), whereas H-3b1 was cased and perforated across the Culebra (Mercer and Orr, 1979). Because of this difference in completion techniques, tracer injection into H-3b1 might be more difficult, requiring higher pressures, than injection into H-3b2 or H-3b3. The vertical distribution of tracer within the Culebra might also be different in H-3b1 because access to the Culebra is limited to the perforation locations.

E.4 H-4 Hydropad

Figure F-3 in Appendix F shows the layout of wells at the H-4 hydropad. Slug tests of the Culebra were performed by the U.S. Geological Survey (USGS) in H-4b in 1978 (Mercer et al., 1981) and by Sandia National Laboratories (SNL) in H-4c in 1986 (Stensrud et al., 1987). Data from both tests were well matched by type curves developed from analytical solutions for slug tests in single-porosity media. Mercer et al. (1981) estimated a transmissivity of 9.7 x 10^{-7} m^2/s for the Culebra at H-4b, and Beauheim (1987b) estimated a transmissivity of 7.0 x 10^{-7} m^2/s for the Culebra at H-4c.

E.5 H-6 Hydropad

In 1981, SNL performed one pumping test in H-6b and two pumping tests in H-6c (Hydro Geo Chem, Inc., 1985). All three H-6 wells were completed to the Culebra and monitored during these tests. The H-6b pumping test involved pumping for 48 hr at a rate of 1.45 L/s. The H-6c pumping tests entailed pumping at 1.19 L/s for over 33 hr, and at 1.04 L/s for over 148 hr. See Figure F-4 in Appendix F for the layout of wells at H-6.

Beauheim and Ruskauff (1998) interpreted the 1981 tests, finding clear indications of double-porosity conditions at the hydropad. They estimated a mean transmissivity of 4.0 x 10^{-5} m^2/s and a storativity of 1.8 x 10^{-4}. They also determined that transmissivity is weakly anisotropic at the H-6 hydropad, with the ratio of maximum to minimum transmissivity being approximately 1.6. The major axis of transmissivity is oriented N13°W, while the minor axis is oriented N77°E. All other things being equal, transport would be expected to be most rapid along the major axis of transmissivity.

H-6a and H-6b were completed open-hole through the Culebra, whereas H-6c was cased and perforated across the Culebra (Hydro Geo Chem, Inc., 1985). Because of this difference in completion techniques, H-6b and H-6c appear to have different skins. Beauheim and Ruskauff (1998) estimated a skin factor of -5.1 to -5.5 for H-6b, reflecting fractures intersecting the wellbore, but a positive skin of 1.2 for H-6c, indicating an impeded connection between the well and the Culebra. This implies that tracer injection into H-6c might be more difficult, requiring higher pressures, than injection into H-6a or H-6b. The vertical distribution of tracer within the Culebra might also be different in H-6c because access to the Culebra is limited to the perforation locations.

E.6 H-11 Hydropad

Well locations on the H-11 hydropad are shown in Figure 3-1 in the main body of this report. All of the wells were completed open-hole through the Culebra. Including the pumping for the 1996 tracer test, seven pumping tests have been performed at H-11. In 1984, H-11b1, H-11b2, and H-11b3 were each pumped for 12 to 21 hr at rates ranging from 0.14 to 0.26 L/s (Saulnier et al., 1987). H-11b3 was pumped again in four episodes totalling 17.4 days out of a 23.3-day period in 1985 (INTERA Technologies and Hydro Geo Chem, 1985). Average pumping rates during the four episodes ranged from 0.31 to 0.34 L/s. Saulnier (1987) interpreted the 1984-85 tests using a double-porosity model, and concluded that the average transmissivity was 2.6 x 10^{-5} m^2/s. However, the test data were of generally poor quality and no clear-cut stabilization of the pressure-derivative was ever achieved.

H-11b4 was pumped for 50 hr at a rate of 0.38 L/s shortly after it was drilled in 1988. Beauheim (1989) interpreted this test using a double-porosity model and found the transmissivity to be 4.5 x 10^{-5} m^2/s. Again, however, stabilization of the pressure-derivative was not achieved. The continued rise in the pressure-derivative observed during the test was modeled as the effect of two no-flow boundaries at different distances from H-11b4.

Beauheim (1989) used a similar double-porosity model with two no-flow boundaries to simulate the responses observed during the H-11 multipad pumping test. This test was also conducted in 1988, and entailed pumping H-11b1 for 62 days at an average rate of 0.38 L/s. Beauheim (1989) estimated a transmissivity value of 2.9 x 10^{-5} m^2/s from those data with no stabilization of the pressure-derivative. Derivative stabilization was achieved during the recovery period of this test beginning approximately 200 to 300 hr after pumping ceased and continuing for the next 1000 hr. This stabilization occurred after the rise in the pressure-derivative ascribed to the no-flow boundaries. Considering that well DOE-1, located 1200 m from the H-11 hydropad, responded to the H-11 pumping in only two hours (Beauheim, 1989), a transmissivity estimated from the stabilization observed after several hundred hours clearly represents properties far beyond the H-11 hydropad.

Beauheim and Ruskauff (1998) interpreted the data from the first 5.3 days of pumping for the 1996 tracer test at H-11, during which the pumping rate averaged 0.23 L/s. They used a double-porosity model with parallel (channel) no-flow boundaries to simulate the continued rise in the pressure-derivative observed during the test. They estimated a transmissivity value of 4.7 x 10^{-5} m^2/s, although no stabilization of the pressure-derivative was observed.

Beauheim and Ruskauff (1998) noted that the 1996 pumping data could be interpreted just as well using a single-porosity model as using a double-porosity model, with the single-porosity model providing transmissivity estimates between 9 x 10^{-5} and 1 x 10^{-4} m^2/s. The primary motivation for selecting a double-porosity model came from the results of slug tests conducted in H-11b4 in 1988 (Beauheim, 1989), which could not be simulated with a single-porosity model, as well as the requirement of a double-porosity model to interpret the 1988 H-11 tracer test (Jones et al., 1992).

H-11b2 appears to be more poorly connected to the Culebra than the other wells on the H-11 hydropad. When pumped in 1984, H-11b2 showed a much lower efficiency (i.e., higher drawdown per unit pumping rate) than either H-11b1 or H-11b3 (Saulnier, 1987). H-11b2 was originally to have been the pumping well for the 1988 H-11 tracer tests, but well-development efforts were unsuccessful in improving its connection to the Culebra, so H-11b1 was used instead (Stensrud et al., 1990). Pressures in H-11b2 also increased much more in response to tracer injection, both in 1988 and 1996, than pressures in the other H-11 injection wells (compare Figures D-45 and D-46). We do not know if the Culebra fractures intersecting H-11b2 were somehow plugged during drilling or if H-11b2 happened to be drilled into a relatively unfractured area of Culebra, but, in either case, H-11b2 seems to be not as well connected to the fracture system on the H-11 hydropad as the other three wells there.

E.7 H-19 Hydropad

Extensive hydraulic testing was performed at H-19 in preparation for the 1995-96 tracer tests. Well-development pumping ranging in duration from 26 to 124 hr was conducted in each of the wells on the hydropad. Beauheim and Ruskauff (1998) interpreted a transmissivity of 6.4 x 10^{-6} m^2/s from the well-development pumping of H-19b2 using a double-porosity model. They also interpreted the hydraulic data from the first 117 hr of pumping for the H-19 7-well tracer test. Again using a double-porosity model, they calculated a mean transmissivity of 6.8 x 10^{-6} m^2/s and a storativity of 4.9 x 10^{-5}. Beauheim and Ruskauff (1998) found anisotropy on the hydropad to be weak, with a ratio of maximum to minimum transmissivity of only 1.2. The major axis of transmissivity is oriented N8°W and the minor axis is oriented N82°E.

Hydrophysical logging was conducted in three of the wells at the H-19 hydropad: H-19b0, H-19b2, and H-19b4. In all three wells, flow was found to be concentrated in the lower ~4 m of the Culebra, with significant variability within that section. No measurable flow was detected in the upper ~3 m of the Culebra.

Tests were also performed pumping from upper and lower intervals of the Culebra in H-19b0 and H-19b4 using a sinusoidal rate, while monitoring responses in upper and lower intervals of the other wells on the hydropad. These tests showed that the lower Culebra is much more permeable than the upper Culebra, and that vertical connectivity within the Culebra is poor over at least the northwestern portion of the hydropad. No extreme heterogeneity was observed in the lower Culebra such as might be caused by fractures having highly preferred orientations with poor cross-connections. The data from the observation wells in the lower Culebra show that response amplitudes decreased and lag times increased with distance from the pumping well (with only a few minor exceptions), regardless of the orientation of the observation well with respect to the pumping well.

E.8 Single- and Double-Porosity

The tests discussed above, as well as those performed in other WIPP wells (e.g., Beauheim, 1987b; Beauheim et al., 1991), have shown that the hydraulic responses of the Culebra can best be represented by a single-porosity model at some locations and by a double-porosity model at others. At locations where the Culebra transmissivity is ≤ 2 x 10^{-6} m^2/s, such as H-1, H-2, H-4, P-17, WQSP-5, and D-268 (see Figure 1-3), single-porosity models simulate hydraulic-test data well. At locations where the Culebra transmissivity is ≥ 6 x 10^{-6} m^2/s, such as H-3, H-6, H-11, and H-19, a double-porosity model is required to match hydraulic-test data. Thus, a transmissivity of ~4 x 10^{-6} m^2/s appears to represent the threshold at which fractures begin to dominate Culebra hydraulic responses. This is not to say that the Culebra does not contain any hydraulically active fractures at lower values of transmissivity, just that the fractures are not significantly more transmissive or more prevalent than the higher transmissivity portions of the matrix.

E.9 References

Beauheim, R.L. 1987a. *Analysis of Pumping Tests of the Culebra Dolomite Conducted at the H-3 Hydropad at the Waste Isolation Pilot Plant (WIPP) Site.* SAND86-2311. Albuquerque, NM: Sandia National Laboratories.

Beauheim, R.L. 1987b. *Interpretations of Single-Well Hydraulic Tests Conducted At and Near the Waste Isolation Pilot Plant (WIPP) Site, 1983-1987.* SAND87-0039. Albuquerque, NM: Sandia National Laboratories.

Beauheim, R.L. 1989. *Interpretation of H-11b4 Hydraulic Tests and the H-11 Multipad Pumping Test of the Culebra Dolomite at the Waste Isolation Pilot Plant (WIPP) Site.* SAND89-0536. Albuquerque, NM: Sandia National Laboratories.

Beauheim, R.L., and G.J. Ruskauff. 1998. *Analysis of Hydraulic Tests of the Culebra and Magenta Dolomites and Dewey Lake Redbeds Conducted at the Waste Isolation Pilot Plant Site.* SAND98-0049. Albuquerque, NM: Sandia National Laboratories.

Beauheim, R.L., T.F. Dale, and J.F. Pickens. 1991. *Interpretations of Single-Well Hydraulic Tests of the Rustler Formation Conducted in the Vicinity of the Waste Isolation Pilot Plant Site, 1988-1989.* SAND89-0869. Albuquerque, NM: Sandia National Laboratories.

Hydro Geo Chem, Inc. 1985. *WIPP Hydrology Program, Waste Isolation Pilot Plant, SENM, Hydrologic Data Report #1.* SAND85-7206. Albuquerque, NM: Sandia National Laboratories.

INTERA Technologies, Inc. 1986. *WIPP Hydrology Program, Waste Isolation Pilot Plant, Southeastern New Mexico, Hydrologic Data Report #3.* SAND86-7109. Albuquerque, NM: Sandia National Laboratories.

INTERA Technologies, Inc., and Hydro Geo Chem, Inc. 1985. *WIPP Hydrology Program, Waste Isolation Pilot Plant, Southeastern New Mexico, Hydrologic Data Report #2.* SAND85-7263. Albuquerque, NM: Sandia National Laboratories.

Jones, T.L., V.A. Kelley, J.F. Pickens, D.T. Upton, R.L. Beauheim, and P.B. Davies. 1992. *Integration of Interpretation Results of Tracer Tests Performed in the Culebra Dolomite at the Waste Isolation Pilot Plant Site.* SAND92-1579. Albuquerque, NM: Sandia National Laboratories.

Mercer, J.W., and B.R. Orr. 1979. *Interim Data Report on the Geohydrology of the Proposed Waste Isolation Pilot Plant Site, Southeast New Mexico.* Water-Resources Investigations Report 79-98. Albuquerque, NM: U.S. Geological Survey.

Mercer, J.W., P. Davis, K.F. Dennehy, and C.L. Goetz. 1981. *Results of Hydrologic Tests and Water-Chemistry Analyses, Wells H-4A, H-4B, and H-4C at the Proposed Waste Isolation Pilot Plant Site, Southeastern New Mexico.* Water-Resources Investigations 81-36. Albuquerque, NM: U.S. Geological Survey.

Saulnier, G.J., Jr. 1987. *Analysis of Pumping Tests of the Culebra Dolomite Conducted at the H-11 Hydropad at the Waste Isolation Pilot Plant (WIPP) Site.* SAND87-7124. Albuquerque, NM: Sandia National Laboratories.

Saulnier, G.J., Jr., G.A. Freeze, and W.A. Stensrud. 1987. *WIPP Hydrology Program, Waste Isolation Pilot Plant, Southeastern New Mexico, Hydrologic Data Report #4.* SAND86-7166. Albuquerque, NM: Sandia National Laboratories.

Stensrud, W.A., M.A. Bame, K.D. Lantz, A.M. LaVenue, J.B. Palmer, and G.J. Saulnier, Jr. 1987. *WIPP Hydrology Program, Waste Isolation Pilot Plant, Southeastern New Mexico, Hydrologic Data Report #5.* SAND87-7125. Albuquerque, NM: Sandia National Laboratories.

Stensrud, W.A., M.A. Bame, K.D. Lantz, J.B. Palmer, and G.J. Saulnier, Jr. 1990. *WIPP Hydrology Program, Waste Isolation Pilot Plant, Southeastern New Mexico, Hydrologic Data Report #8.* SAND89-7056. Albuquerque, NM: Sandia National Laboratories.

This page intentionally left blank.

Appendix F
Summary of Tracer Testing in the Culebra During the 1980s

By Toya L. Jones[1] and Timothy F. Dale[1]

F.1 Introduction

This appendix contains a brief discussion of the tracer tests performed in the Culebra dolomite at the WIPP site during the 1980's. Locations for these tests were the H-2, H-3, H-4, H-6, and H-11 hydropads (see Figure 2-2 in Chapter 2). Table 3-1 in Chapter 3 summarizes the types of tests conducted at each hydropad and lists references which contain detailed descriptions and interpretations of the tests. In addition to describing the tests, this appendix also discusses the observed data and their suitability for interpretation. The majority of the discussion presented here was taken from Jones et al. (1992).

Two types of tracer tests were performed in the Culebra during the 1980's: two-well recirculating (TWR) tests at the H-2 and H-6 hydropads and multiwell convergent-flow (MWCF) tests at the H-3, H-4, H-6, and H-11 hydropads. The TWR tracer tests entailed withdrawing fluid from one well, adding tracer to the fluid, and injecting the now-traced fluid into a second well in a continuous recirculation loop. Because the tracer was recirculated between two wells, the formation was tested along the flow paths developed between those two wells. MWCF tracer tests were conducted at hydropads containing three or more wells. The tests involved pumping one well until a steady-state flow field was established and then injecting traced fluid followed by untraced fluid (chaser) into the other wells at the hydropad. Because the tracers were injected into several wells and recovered from a different well, the formation was tested along well-to-well flow paths at the hydropad.

F.2 Tracer Testing at the H-2 Hydropad

Two TWR tracer tests performed at the H-2 hydropad (see Figure 2-2) between February 1980 and April 1981 were the first multiwell tracer tests conducted at the WIPP site. At the time of the tracer tests, the H-2 hydropad consisted of three wells, H-2a, H-2b (later renamed and hereafter called H-2b1), and H-2c, with only H-2b1 and H-2c completed to the Culebra. Figure F-1 shows the current configuration of the H-2 hydropad.

The first recirculating test was conducted between February 1980 and June 1980 using two anionic tracers (benzoate and pentafluorobenzoate (PFB)) and three halocarbon tracers (CCl_4, $CFCl_3$, and CF_2Cl_2). H-2b1 was configured as the extraction well and H-2c as the injection well. The second recirculating test was conducted between July 1980 and April 1981 using the tracers thiocyanate (SCN) and difluorochlorobromomethane (BCF). The second test reversed the flow direction between the two wells by withdrawing from H-2c and injecting into H-2b1.

During testing, the Culebra within both wellbores was isolated with the use of production-injection packers. A pump jack was used to withdraw fluid from the production well. The produced fluids were transferred to the injection well through a pipe train connecting the two wells. Tracer mass was injected at a constant rate into the fluid stream at the top of the injection well. Fluid samples were collected at the pumping head on the production well. The samples to be analyzed for anionic tracers or volatile tracers were stored in 30-mL plastic scintillation counting bottles or

---

[1] Duke Engineering & Services, Inc., 9111 Research Boulevard, Austin, TX 78758.
Email: tjones@dukeengineering.com.

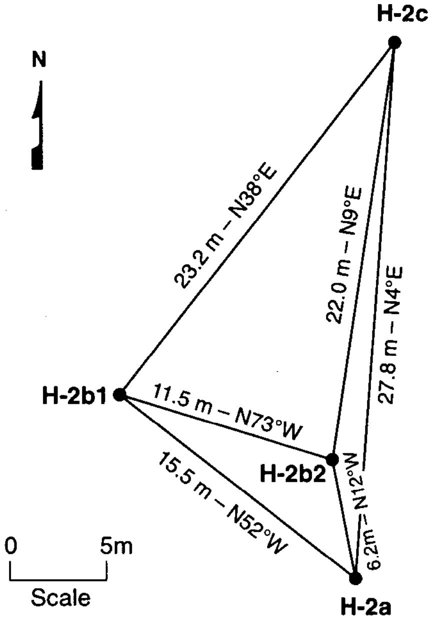

Notes:
The Culebra interval was completed in wells H-2a and H-2b2 in 1983.

H-2b1 is also referred to as H-2b.

The borehole deviation survey did not extend to the center of the Culebra dolomite in borehole H-2b2.

Figure F-1. Plan view of the wells at the H-2 hydropad showing distances between wells at the center of the Culebra.

30-mL glass melt-seal vials, respectively. High-performance liquid chromatography (HPLC) with ultraviolet detection was used to analyze samples for anionic tracer concentrations. Volatile tracer samples were qualitatively analyzed at the site, but no laboratory analyses were conducted. A description of the performance of the tests, including equipment configurations, test methods, and test results, is presented in Hydro Geo Chem (1985).

Pumping for test #1 was initiated on February 13, 1980. Tracer injection began on February 22, 1980, but was prematurely terminated two days later as a result of equipment failure. The recirculation process continued intermittent until pumping was terminated on June 18, 1980. No tracers were detected in the collected samples at the time the test was terminated and, therefore, tracer-breakthrough curves do not exist for test #1. Test #2 was initiated on July 7, 1980 with the start of pumping. Injection of tracers into the recirculating fluid occurred from July 10, 1980 until August 7, 1980. Fluid recirculation continued for another eight months until pumping was terminated on April 7, 1981.

Samples collected during test #2 were analyzed for SCN, which was injected as part of test #2, and also for PFB, which had been injected into H-2c (the withdrawal well for test #2) during test #1. No data are published for BCF, which was also injected during test #2. Plots of the PFB and SCN data can be found in Figures 6-7 and 6-8, respectively, in Jones et al. (1992). A numerical analysis of the SCN data assuming a one-dimensional, single-porosity, homogeneous, porous medium is presented in Hydro Geo Chem (1986). Due to the equipment problems encountered during test #1 and the reversed roles of the pumping and injection wells, the operating conditions are considered too uncertain and complex to warrant analysis of the PFB data. Stetzenbach and Stetzenbach (1986) (which can be found in Appendix A of Jones et al., 1992) believe that "thiocyanate is not a good long-term tracer because of the chemisorption problems." In addition, field notes by Hydro Geo Chem state that SCN shows signs of degradation in time periods of days to tens of days in laboratory stability tests. Based on these observations, we consider the concentration results for SCN to be unreliable and uninterpretable due to the long duration required for SCN breakthrough (74 days for first arrival and 171 days for peak concentration). Calculations by Jones et al. (1992) to estimate plug-flow travel times between wells from the H-2 data suggest that transport through fractures is not important and a single-porosity conceptualization (where the advective porosity is equal to the total porosity) for the Culebra at the H-2 hydropad is most representative.

F.3 Tracer Testing at the H-3 Hydropad

A MWCF tracer test was performed at the H-3 hydropad (see Figure 2-2) from May to June 1984. The H-3 hydropad consists of three wells arranged in an approximate equilateral triangle (Figure F-2). The tracer-withdrawal (pumping) well was H-3b3 and the tracer-injection wells were H-3b1 and H-3b2.

Packers were used in each borehole to isolate the Culebra during the test. A submersible pump was installed beneath the packer in H-3b3. The tracers were mixed in separate tanks on the surface and gear pumping delivered the respective tracers downhole through 0.5-inch (1.27-cm) polyethylene tubing. Water samples from H-3b3 were taken from the pump discharge line using an automatic sampler. Manual samples were collected when the automatic sampler malfunctioned. After collection, the samples were transferred to 50-mL polyethylene bottles for shipment to the laboratory for analysis. The fluid samples were analyzed by HPLC using analytical techniques described in Hydro Geo Chem (1985) and Stetzenbach et al. (1982). Full details of the performance and results of the H-3 tracer test are reported in Hydro Geo Chem (1985) and INTERA Technologies (1986).

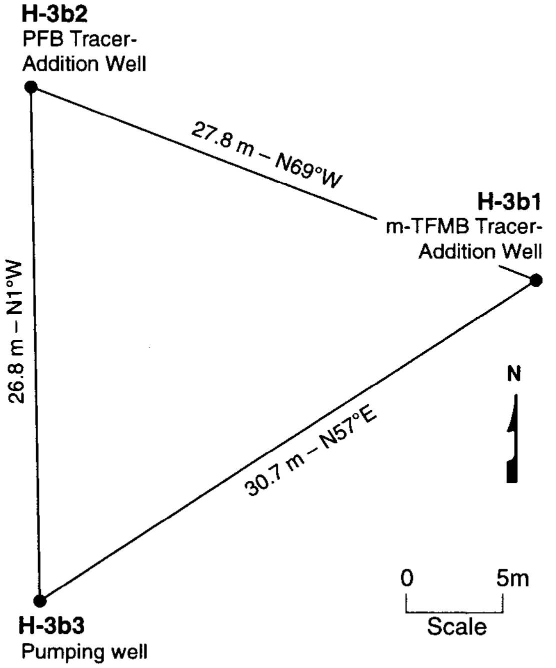

Note:
The borehole deviation survey did not extend to the center of the Culebra dolomite in boreholes H-3b2 and H-3b3.

Figure F-2. Plan view of the wells at the H-3 hydropad showing distances between wells at the center of the Culebra.

Pumping from H-3b3 began on April 23, 1984 at a rate of approximately 0.25 L/s. The rate was reduced to 0.19 L/s on May 7, 1984 in preparation for the tracer test. Tracer injection occurred on May 9, 1984 with the injection of meta-trifluoromethylbenzoate (m-TFMB) into H-3b1 and pentafluorobenzoate (PFB) into H-3b2, followed by a slug of formation fluid to displace the tracer out of the borehole and into the formation. Total injection times of 1 hr, 35 min and 1 hr were recorded at H-3b1 and H-3b2, respectively. The convergent flow field was maintained until the test was terminated on June 12, 1984.

The m-TFMB and PFB tracer-breakthrough curves demonstrate significantly different behavior as illustrated in Figures C-38 and C-39 found in Appendix C. Kelley and Pickens (1986) present an analysis of the tracer test assuming fracture flow within a dual-porosity system. They attribute the difference in the observed breakthrough data for the two flow paths to heterogeneity in the rock characteristics. Jones et al. (1992) reanalyzed the results of the H-3 tracer test using a similar conceptual approach with updated transport parameter constants (e.g., diffusive tortuosity and porosity) for the Culebra. They also interpreted the results assuming that the observed differences in the breakthrough curves are due to anisotropy in the horizontal transmissivity field. Both Kelley and Pickens (1986) and Jones et al. (1992) conclude that the H-3 tracer data are best matched using a double-porosity conceptualization for the Culebra. Additional interpretations of the H-3 data are presented in Appendices P and S of this document.

F.4 Tracer Testing at the H-4 Hydropad

A long-term (approximately 722-day) MWCF tracer test was performed at the H-4 hydropad (see Figure 2-2) from October 1982 to October 1984. The H-4 hydropad consists of three wells arranged in an approximate equilateral triangle (Figure F-3). The pumping and tracer-recovery well was H-4c and the tracer-injection wells were H-4a and H-4b.

Feedthrough packer assemblies were utilized to isolate the Culebra in H-4a and H-4b. Tracers were injected under gravity-feed conditions into the isolated interval via the feedthrough ports on the packers. The tracers m-TFMB and SCN were simultaneously injected into H-4b over a 27-min period on October 27, 1982, and the tracers PFB and para-fluorobenzoate (p-FB) were simultaneously injected into H-4a over a 30-min period on November 5, 1982. A volume of formation fluid was then fed into both wells to force the tracers out of the borehole and into the formation.

The pumped interval in H-4a was isolated with a bridge plug installed in the casing below the Culebra. Access to the Culebra was through perforated casing. A pump jack was installed on H-4c for fluid withdrawal. Fluid samples were collected from the discharge line using an automated sampler or manual sampling techniques until the test was terminated on October 15, 1984. All samples were transferred to 50-mL polyethylene bottles for shipment to the lab. The samples were analyzed for tracer by HPLC using the analytical techniques described in Hydro Geo Chem (1985) and Stetzenbach et al. (1982). Full details of the performance and the results obtained during the H-4 hydropad tracer test are reported in Hydro Geo Chem (1985) and plots of the observed tracer-breakthrough curves can be found in Figures 8-6 and 8-7 in Jones et al. (1992).

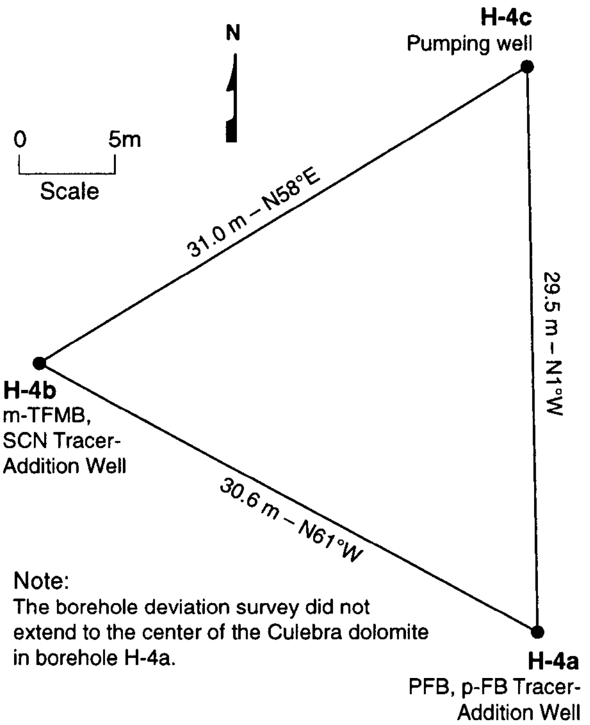

Note:
The borehole deviation survey did not extend to the center of the Culebra dolomite in borehole H-4a.

Figure F-3. Plan view of the wells at the H-4 hydropad showing distances between wells at the center of the Culebra.

After pumping for approximately 230 days (October 24, 1982 to June 10, 1983), no tracers had been detected at H-4c. As a result, the pumping rate was doubled from 1.7×10^{-2} to 3.3×10^{-2} L/s. Tracer breakthrough was finally observed 262 days after injection for m-TFMB, 270 days after injection for SCN, 390 days after injection for p-FB, and 501 days after injection for PFB. All tracer-breakthrough curves were very erratic with poorly defined peaks (see figures in Jones et al., 1992). Tracer mass recoveries were low, with 37% recovery for m-TFMB, 0.2% for SCN, 3.5% for p-FB, and 2.2% for PFB. Although m-TFMB and SCN were both injected into the same well, the maximum concentration for m-TFMB was a factor of about 1800 greater than the maximum concentration for SCN, suggesting substantial degradation of SCN during transport.

Kelley and Pickens (1986) concluded that an analysis of the PFB and SCN data could yield no information toward characterization of transport parameters at the H-4 hydropad, but they do present an analysis of the m-TFMB and p-FB breakthrough data from the H-4 tracer test. Due to the erratic nature of the breakthrough curves, the low mass recoveries, and the long duration of the test, Jones et al. (1992) considered all of the H-4 data too uncertain for further analysis. We agree with the Jones et al. (1992) conclusion regarding the interpretability of the H-4 data. Therefore, no analyses of the tracer-breakthrough curves from the H-4 test were conducted for this document. Based on the lack of open fractures in core samples, the long travel times for the tracer test, and the single-porosity behavior indicated by hydraulic testing, the Culebra is conceptualized as a single-porosity system (where the advective porosity is equal to the total porosity) at the H-4 hydropad.

F.5 Tracer Testing at the H-6 Hydropad

A total of seven tracer tests have been conducted at the H-6 hydropad (see Figure 2-2). A series of five MWCF tests was performed between August 1981 and November 1982 and two TWR tests were performed from April to July 1983. The H-6 hydropad contains three wells arranged approximately in an equilateral triangle (Figure F-4). Detailed information regarding these seven tests is contained in Hydro Geo Chem (1985).

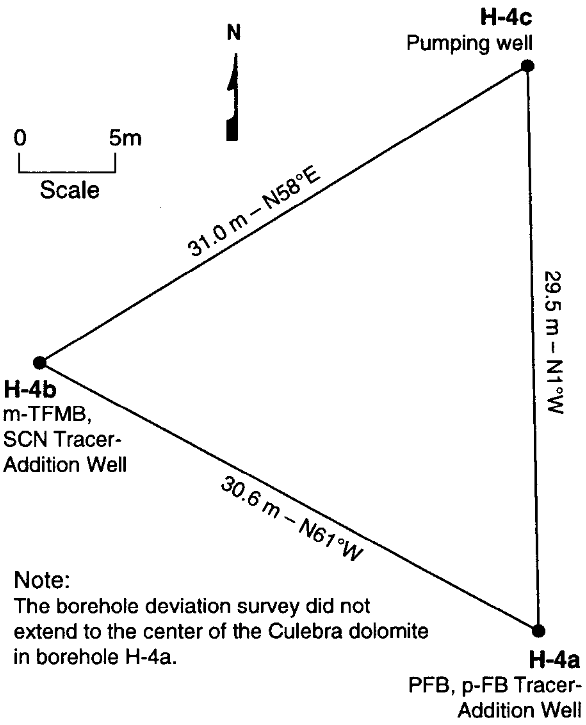

Note:
The borehole deviation survey did not extend to the center of the Culebra dolomite in borehole H-4a.

Figure F-4. Plan view of the wells at the H-6 hydropad showing distances between wells at the center of the Culebra.

F.5.1 Multiwell Convergent-Flow Tracer Tests

The purpose of conducting the series of MWCF tracer tests was to evaluate Culebra properties (effective porosity and dispersivity) along different travel paths for several pumping conditions (Hydro Geo Chem, 1985). The injection wells, tracers injected, injection dates, pumping well, and pumping rates for the five MWCF tests at H-6 are summarized in Table F-1.

For the first four tests, the pumping well was H-6c. Pumping for tests #1 and #2, at a rate of approximately 1.04 L/s, began on August 19, 1981 and ended on September 11, 1981. For test #1, m-TFMB and ortho-fluorobenzoate (o-FB) were simultaneously injected into H-6a and PFB and meta-fluorobenzoate (m-FB) were simultaneously injected into H-6b via gravity feed on August 23, 1981. A chaser of formation fluid designed to flush the tracers into the formation was injected immediately following injection of the tracers. Test #2 was initiated on September 2, 1981 with the injection of p-FB, and a subsequent chaser of formation fluid, into H-6b. The tracer-breakthrough curves for tests #1 and #2 can be found in Figures 9-6 and 9-7, respectively, in Jones et al. (1992) and in Figures C-35, C-36, and C-37 found in Appendix C.

For tests #3 and #4, H-6c was pumped at a rate of approximately 0.50 L/s beginning on September 30, 1982 and ending on October 15, 1982. For test #3, p-FB was injected in H-6b on September 30, 1982. Test #4 consisted of the simultaneous injection of PFB and SCN into H-6b on October 5, 1982. For both tests #3 and #4, tracer injection was followed by injection of a chaser, although the volumes of chaser were not sufficient to flush all of the tracers out of the boreholes. The tracer-breakthrough curves for tests #3 and #4 can be found in Figures 9-8 and 9-9, respectively, in Jones et al. (1992).

For test #5, H-6b was pumped at a rate of approximately 1.01 L/s from October 24, 1982 to November 29, 1982. SCN and m-TFMB were simultaneously injected into H-6a on October 27, 1982 and p-FB was injected into H-6c on

Table F-1. Summary of Tracer Injections and Pumping for the H-6 MWCF Tracer Tests

MWCF Test #	H-6a	H-6b	H-6c
1	m-TFMB and o-FB injection on 08/23/81	PFB and m-FB injection on 08/23/81	pumping at 1.04 L/s
2	--	p-FB injection on 09/02/81	pumping at 1.04 L/s
3	--	p-FB injection on 09/30/82	pumping at 0.5 L/s
4	--	PFB and SCN injection on 10/05/82	pumping at 0.5 L/s
5	m-TFMB and SCN injection on 10/27/82	pumping at 1.01 L/s	p-FB injection on 11/05/82

November 5, 1982. Both injections were followed by chaser volumes large enough to displace all of the tracers from the boreholes. The tracer-breakthrough curves for test #5 can be found in Figure 9-10 in Jones et al. (1992).

Jones et al. (1992) examined the test conditions and observed data for the H-6 MWCF tests to evaluate the suitability of the data for analysis. They concluded that:

- the results for tests #3 and #4 are unreliable due to the insufficient chaser volume injected and the associated high uncertainty in the initial tracer mass in the Culebra;
- the results for test #5 are unreliable because the tracers injected during that test had previously been injected at the hydropad and a high potential existed for recovery of previously injected tracer mass; and
- the conditions for tests #1 and #2 provided the best opportunity for obtaining meaningful interpreted results; however, only the PFB and m-TFMB data from test #1 warrant analysis because laboratory suitability tests suggest that the other two tracers injected during test #1 (o-FB and m-FB) show signs of degradation in time periods of days to tens of days per field notes by Hydro Geo Chem.

Jones et al. (1992) present interpretations of the m-TFMB and PFB data from test #1 and the p-FB data from test #2. They conclude that these data are best matched using a double-porosity conceptualization for the Culebra. Additional analyses of these data are presented in Appendices P and S of this document. Like Jones et al. (1992), we do not consider the remaining data from the H-6 MWCF tracer tests to be reliable for analysis.

F.5.2 Two-Well Recirculating Tracer Tests

The first TWR test at the H-6 hydropad was conducted between H-6b and H-6c. Pumping of H-6b began on April 15, 1983. The tracers SCN and PFB were simultaneously injected into H-6c over a 2-hr, 32-min period on April 19, 1983. The second test was conducted between wells H-6b and H-6a. Pumping of H-6b began on June 17, 1983. The tracers p-FB and m-TFMB were simultaneously injected into H-6a over a 4-hr, 37-min period on June 22, 1983. The tracer-breakthrough curves for the TWR tests can be found in Figures 9-3 and 9-4 in Jones et al. (1992). Jones et al. (1992) concluded that a defensible analysis of the TWR data could not be performed due to the previous injection of all four tracers at the H-6 hydropad during the preceding MWCF tests. No analysis of the H-6 TWR data was conducted for this document.

F.6 Tracer Testing in 1988 at the H-11 Hydropad

A four-well MWCF tracer test was conducted at the H-11 hydropad (see Figure 2-2) between May and July 1988. The H-11 hydropad consists of four wells. Wells H-11b1, H-11b2, and H-11b3 are arranged in a triangular pattern with approximately 22-m sides and H-11b4 is located approximately 43 m to the west of the triangle (see Figure 3-1). A complete description of this test is given in Stensrud et al. (1990).

For this test, H-11b1 was pumped at an average rate of 0.38 L/s from May 5, 1988 until July 7, 1988. An inflatable packer was installed in the casing above the Culebra to isolate the test interval. Fluid was removed from the well using a submersible pump installed beneath the packer and slightly above the top of the Culebra. The fluid samples manually collected from the H-11b1 discharge line were stored in 4-oz. (118.3-mL) bottles capped with aluminum foil and sealed. HPLC methods were used to analyze the samples for tracer concentrations. A complete description of the tracer-analysis technique is given in Stensrud et al. (1990).

Inflatable packers were also installed in the casing above the Culebra to isolate the test interval in the three injection wells. A perforated injection tool was installed across each injection interval to enable uniform tracer distribution. The tracer and chaser volumes for each well were contained in separate tanks and injected under gravity-feed conditions. All tracers were injected on May 14, 1988. Tracer injections were immediately followed by injection of a chaser of formation fluid designed to displace the tracer out of the borehole and into the Culebra. PFB and chaser were injected in H-11b2 over a 1-hr, 34-min period, m-TFMB and chaser were injected into H-11b3 over a 1-hr, 34-min period, and ortho-trifluoromethylbenzoate (o-TFMB) and chaser were injected into H-11b4 over a 1-hr, 3-min period.

The three tracer-breakthrough curves demonstrated significantly different behavior as illustrated in Figures C-32, C-33, and C-34 found in Appendix C. Interpretations of this test given in Jones et al. (1992) indicate that the data are best matched using a double-porosity conceptualization for the Culebra. Additional interpretations of this test are presented in Appendices P and S of this document.

F.7 References

Hydro Geo Chem, Inc. 1985. *WIPP Hydrology Program, Waste Isolation Pilot Plant, SENM, Hydrologic Data Report #1.* SAND85-7206. Albuquerque, NM: Sandia National Laboratories.

Hydro Geo Chem, Inc. 1986. *Two-Well Recirculation Tracer Tests at the H-2 Hydropad, Waste Isolation Pilot Plant (WIPP), Southeastern New Mexico.* SAND86-7092. Albuquerque, NM: Sandia National Laboratories.

INTERA Technologies, Inc. 1986. *WIPP Hydrology Program, Waste Isolation Pilot Plant, Southeastern New Mexico, Hydrologic Data Report #3.* SAND86-7109. Albuquerque, NM: Sandia National Laboratories.

Jones, T.L., V.A. Kelley, J.F. Pickens, D.T. Upton, R.L. Beauheim, and P.B. Davies. 1992. *Integration of Interpretation Results of Tracer Tests Performed in the Culebra Dolomite at the Waste Isolation Pilot Plant Site.* SAND92-1579. Albuquerque, NM: Sandia National Laboratories.

Kelley, V.A., and J.F. Pickens. 1986. *Interpretation of the Convergent-Flow Tracer Tests Conducted in the Culebra Dolomite at the H-3 and H-4 Hydropads at the Waste Isolation Pilot Plant (WIPP) Site.* SAND86-7161. Albuquerque, NM: Sandia National Laboratories.

Stensrud, W.A., M.A. Bame, K.D. Lantz, J.B. Palmer, and G.J. Saulnier, Jr. 1990. *WIPP Hydrology Program, Waste Isolation Pilot Plant, Southeastern New Mexico, Hydrologic Data Report #8.* SAND89-7056. Albuquerque, NM: Sandia National Laboratories.

Stetzenbach, K.J., and L.D. Stetzenbach. 1986. "Appendix A: Review of Chemical and Biological Activity of Fluorinated Acids Used as Tracers," *Integration of Interpretation Results of Tracer Tests Performed in the Culebra Dolomite at the Waste Isolation Pilot Plant Site.* T.L. Jones, V.A. Kelley, J.F. Pickens, D.T. Upton, R.L. Beauheim, and P.B. Davies. SAND92-1579. Albuquerque, NM: Sandia National Laboratories. A-1 through A-22.

Stetzenbach, K.J., S.L. Jensen, and G.M. Thompson. 1982. "Trace Enrichment of Fluorinated Organic Acids Used as Ground-Water Tracers by Liquid Chromatography," *Environmental Science and Technology.* Vol. 16, no. 5, 250-254.

Appendix G
Design of H-19 Well Layout

By Richard L. Beauheim[1]

G.1 Introduction

Designing the locations of wells to be used for a multiwell convergent-flow (MWCF) tracer test depends on the objectives of the test. If a test has a single objective, such as understanding scale effects or characterizing heterogeneity, designing the well layout is a straightforward matter. When a test has multiple objectives, however, and the number of potential wells is limited, the design becomes more complex and may require compromises. The logic used to site the wells at the H-19 hydropad to meet multiple objectives is described below.

G.2 Test Objectives and Design Considerations

The objectives of the H-19 MWCF tracer test included identifying the extent to which heterogeneity, anisotropy, and the scale of testing affected flow and transport in the Culebra while testing the largest scale feasible (Beauheim et al., 1995). Figure G-1 shows well layouts that might result from trying to meet these objectives individually. Figure G-1a shows a well layout designed to address heterogeneity. Its key feature is the existence of multiple pairs of flow paths that are

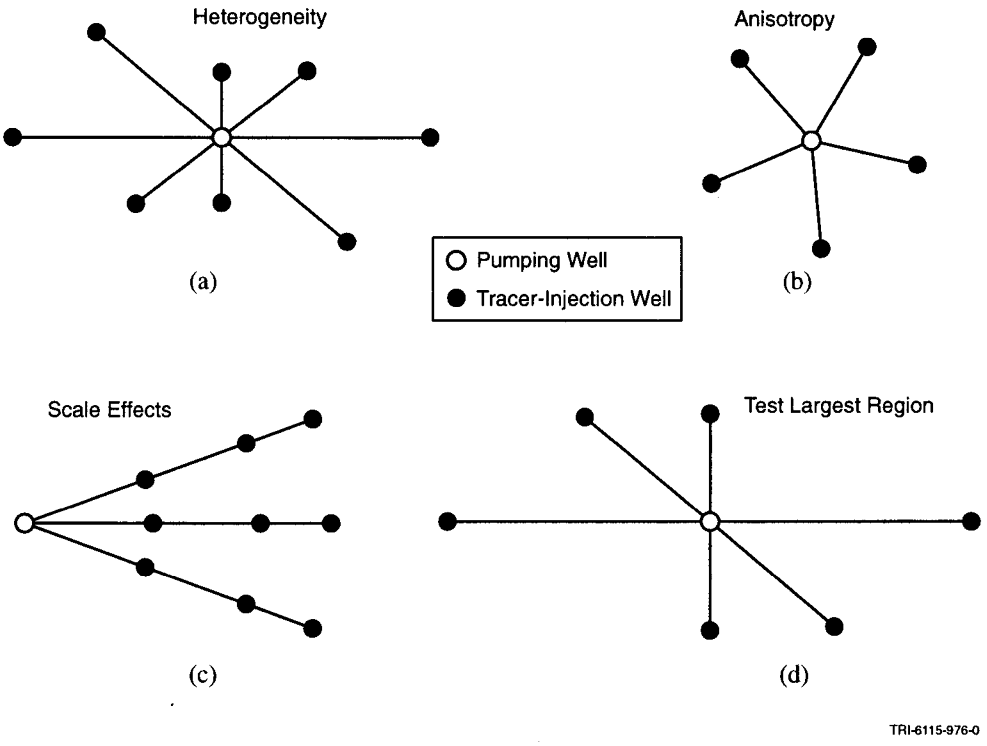

Figure G-1. Well layouts designed to meet specific tracer-test objectives.

---

[1] Sandia National Laboratories, Repository Performance and Certification Department, P.O. Box 5800, MS1395, Albuquerque, NM 87185-1395. Email: rlbeauh@sandia.gov.

identical in orientation and length but offset in space. In a homogeneous system, tracer-breakthrough data from the two members of such a pair would be identical. In a heterogeneous system, the degree to which the data are different provides a measure of the heterogeneity.

Figure G-1b shows a well layout designed to address anisotropy. Here, the flow paths are all of the same length but have different orientations. In an isotropic (and homogeneous) system, the tracer-breakthrough data for transport along each flow path would be identical. The amount and pattern of variation observed in an anisotropic system would reflect the magnitude and directionality of the anisotropy.

Figure G-1c shows a well layout designed to address scale effects. The key feature here is the existence of wells at different distances along individual flow paths. The differences in tracer-breakthrough data observed for the wells along a particular flow path represent the effects of transport scale.

Finally, Figure G-1d shows a well layout designed to maximize the volume of aquifer tested. In this layout, wells are placed as far from the pumping well in each direction as possible and still provide interpretable data during a test of some given duration. Note that this design requires some prior knowledge of what the maximum testable distance might be.

G.3 Preliminary Design of H-19 Well Layout

Given an unlimited budget and time, all of the objectives discussed above could be met simultaneously by simply installing a large number of wells and testing for as long as necessary. For the H-19 testing program, however, neither the budget nor time available were unlimited. We therefore designed a well layout plan that had well installation implemented in two phases, with a preliminary tracer test to be conducted after the first phase of installations was complete to aid in designing the well locations for the second phase of installations (Saulnier and Beauheim, 1998). The first phase consisted of a minimal anisotropic configuration (Figure G-2a) of a central pumping well (H-19b1) surrounded by three tracer-injection wells (H-19b2, H-19b3, and H-19b4) oriented 120° apart, with each well located 50 ft (15.2 m) from the pumping well. The 50-ft (15.2-m)

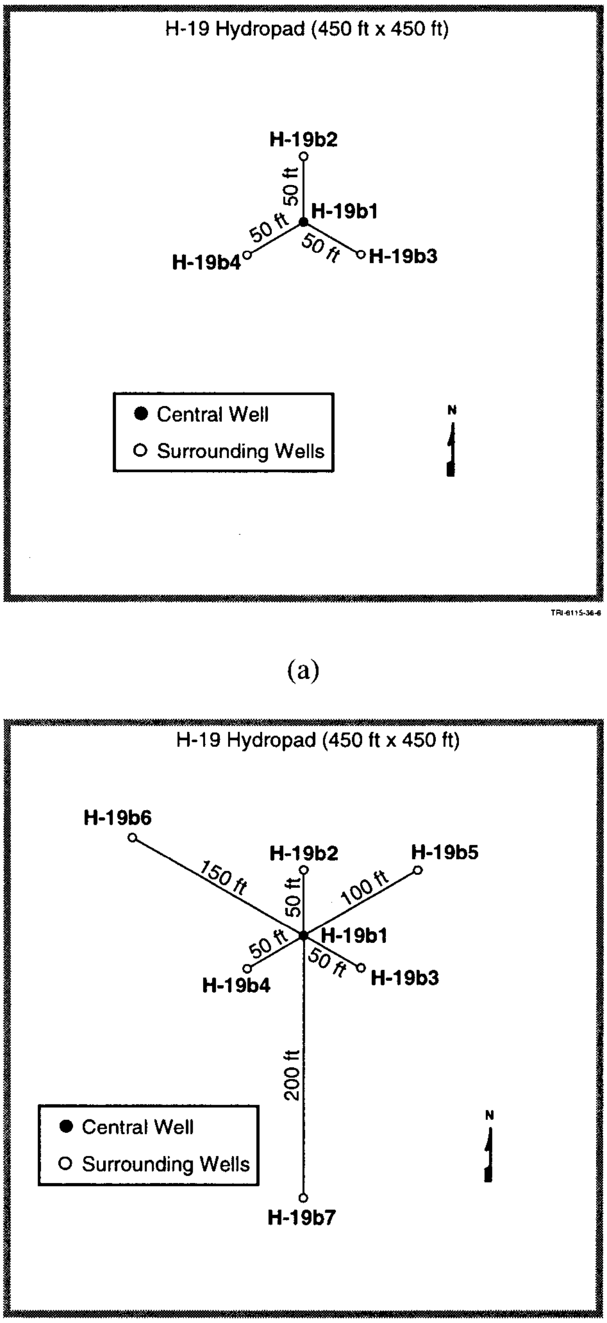

(a)

(b)

Figure G-2. Preliminary design of H-19 well layout.

spacing was selected based on experience from previous successful tracer tests at the H-3, H-6, and H-11 hydropads where well spacings ranged from approximately 70 to 140 ft (21 to 43 m) and on a desire to perform the preliminary tracer test in approximately one month.

The second phase of well construction was to begin after data were available from the preliminary tracer test. H-19b5 was to be constructed 100 ft (30.5 m) from the central pumping well diametrically opposed to the well into which the slowest arriving tracer was injected. H-19b7 was to be drilled diametrically opposed to the well into which the fastest arriving tracer was injected at the greatest distance considered feasible for later tracer testing taking anticipated tracer dilution and detection capabilities into consideration. H-19b6 was to be drilled diametrically opposed to the last of the original three injection wells at a distance from the pumping well intermediate between that of H-19b5 and that of H-19b7.

Figure G-2b shows an example of what the final well layout may have looked like if everything had proceeded according to the plan. The desired information on anisotropy would be provided primarily by the three inner injection wells, all located the same distance from H-19b1. Information on scale effects and heterogeneity would now be lumped, as testing would be performed along spatially shifted flow paths having the same orientation but different lengths (c.f., H-19b2 to H-19b1 and H-19b7 to H-19b1 in Figure G-2b). This configuration would also allow testing of a region nearly as large as possible.

G.4 Final Design of H-19 Well Layout

Once well construction began, a number of events occurred that led to the final well layout at H-19 being considerably different from the idealized layout shown in Figure G-2b. First, drill collars and a bit were lost in H-19b1, leading to the abandonment of that hole (Mercer et al., 1998). A replacement hole, H-19b0, was placed 50 ft (15.2 m) due south and the location for H-19b2 was shifted 150 ft (45.7 m) to the south to allow the staked locations for H-19b3 and H-19b4 to be preserved while also preserving the symmetry of the original design (Beauheim, 1998a). Second, after the first four wells were completed and before the preliminary tracer test was conducted, deviation surveys were performed to determine well positions at the depth of the Culebra for comparison to the orginal design locations. These surveys revealed severe deviations, much greater than the approximately 4-ft (1.3-m) average observed in other wells drilled at the WIPP site. Deviations of the four wells ranged from 10.1 to 26.9 ft (3.1 to 8.2 m), all in different directions, destroying the hoped-for symmetry of the locations. As shown in Figure G-3, H-19b2, H-19b3, and H-19b4 were located 82.3, 36.2, and 73.3 ft (25.1, 11.0, and 22.3 m) from H-19b0, respectively, at the depth of the Culebra instead of the desired 50 ft (15.2 m).

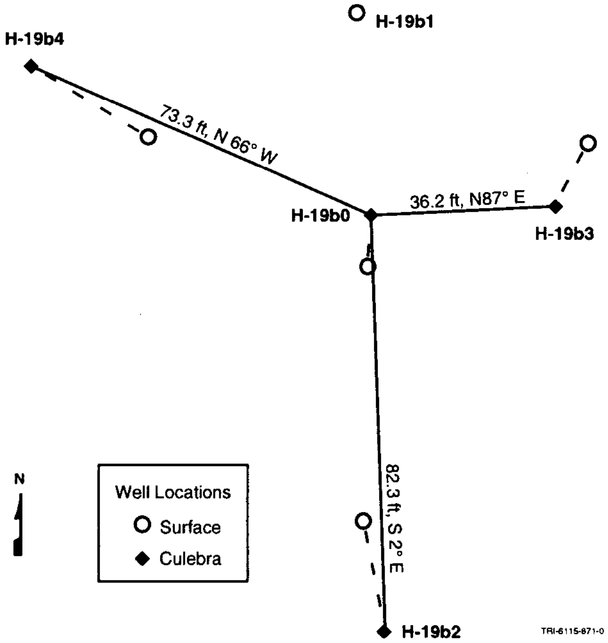

Figure G-3. Designed and deviated locations of first four H-19 wells.

To avoid excessive drilling rig standby charges, a new location was selected for H-19b5 before results were available from the preliminary tracer test (Beauheim, 1998b). The location selected was 50 ft (15.2 m) from the Culebra location of H-19b0 along a ray intermediate between those connecting H-19b2 and H-19b4 to H-19b0. This location was selected because it filled a gap in both area and orientation of wells. Because the Culebra intervals of H-19b2 and H-19b4 were both further from H-19b0 than desired, H-19b5 was located closer to H-19b0 than was originally planned. After drilling was completed, H-19b5 was found to have deviated 12.0 ft (3.6 m) to the north, so that its final distance from H-19b0 at the Culebra was only 45.5 ft (13.9 m) (Figure G-4).

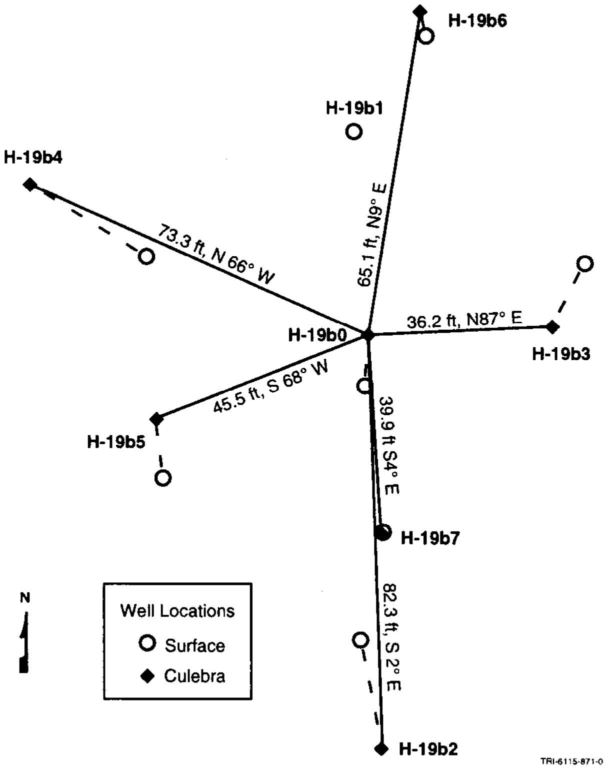

Figure G-4. Final layout of H-19 wells.

Preliminary data from the H-19 preliminary tracer test suggested that transport was more rapid in the north-south direction (H-19b2 to H-19b0) than in the east-west (H-19b3 to H-19b0) or northwest-southeast (H-19b4 to H-19b0) directions. Inasmuch as the largest areal gap in coverage on the H-19 hydropad after the first five wells were drilled was the northern area between H-19b3 and H-19b4, we decided to place H-19b6 north of H-19b0 (Beauheim, 1998c). The exact location selected was 60 ft (18.3 m) from H-19b0 along a ray bisecting the angle formed by H-19b3, H-19b0, and H-19b4. H-19b6 was placed closer to H-19b0 than either H-19b2 or H-19b4 because the preliminary tracer test data suggested transport at H-19 was not as rapid as at other hydropads tested and a closer location would provide better data. After drilling was completed, H-19b6 was found to have deviated 5.0 ft (1.5 m) to the north, so that its final distance from H-19b0 at the Culebra was 65.1 ft (19.8 m) (Figure G-4).

Preliminary model simulations of the H-19 preliminary test data suggested that the H-19b2 to H-19b0 path was the fastest pathway tested. To investigate scale effects and heterogeneity, we wanted to place another well along this path, approximately halfway between H-19b2 and H-19b0. Because of uncertainty as to how the hole might deviate, we decided to start H-19b7 slightly to the east of the line connecting H-19b2 and H-19b0 (Beauheim, 1998d). From this location, if the hole deviated to the west, it would go toward the desired location. If the hole deviated to the east, it would go into a region where information was lacking and would, therefore, be valuable. In the end, the hole deviated only 0.6 ft (0.2 m) to the southwest, very close to the desired position (Figure G-4).

G.5 Summary

The actual layout of wells on the H-19 hydropad differs considerably from the original design for two principal reasons. First, unanticipated hole deviations affected the Culebra locations of the first four wells, destroying the hoped-for symmetry and significantly altering the designed distances between wells. Second, the preliminary four-well tracer test showed transport to be slower at H-19 than at other tested locations, so the last three wells were placed closer to H-19b0 than had been originally planned. Despite these unexpected occurrences, the final locations of the H-19 wells still allowed us to collect desired data on anisotropy, heterogeneity, and scale effects, as well as test over a region as large as practicable. The flexibility provided by the planned two-phase approach to well siting, with a preliminary test between phases, allowed us to compensate for the deviations of the first four wells and optimize the locations of the last three wells for the final seven-well tracer test.

G.6 References

Beauheim, R. 1998a. "Appendix A: Deviation from Field Operations Plan: Well Construction and Preliminary Testing on the H-19 Hydropad at the WIPP Site," *Basic Data Report for Drillholes on the H-19 Hydropad (Waste Isolation Pilot Plant–WIPP).* J.W. Mercer, D.L. Cole, and R.M. Holt. SAND98-0071. Albuquerque, NM: Sandia National Laboratories. A-59 to A-60.

Beauheim, R. 1998b. "Appendix A: Location and Drilling of Well H-19b5," *Basic Data Report for Drillholes on the H-19 Hydropad (Waste Isolation Pilot Plant–WIPP).* J.W. Mercer, D.L. Cole, and R.M. Holt. SAND98-0071. Albuquerque, NM: Sandia National Laboratories. A-71 to A-72.

Beauheim, R. 1998c. "Appendix A: Location and Drilling of Well H-19b6," *Basic Data Report for Drillholes on the H-19 Hydropad (Waste Isolation Pilot Plant–WIPP).* J.W. Mercer, D.L. Cole, and R.M. Holt. SAND98-0071. Albuquerque, NM: Sandia National Laboratories. A-73 to A-74.

Beauheim, R. 1998d. "Appendix A: Location and Drilling of Well H-19b7," *Basic Data Report for Drillholes on the H-19 Hydropad (Waste Isolation Pilot Plant–WIPP).* J.W. Mercer, D.L. Cole, and R.M. Holt. SAND98-0071. Albuquerque, NM: Sandia National Laboratories. A-75 to A-76.

Beauheim, R.L., L.C. Meigs, G.J. Saulnier, Jr., and W.A. Stensrud. 1995. "Culebra Transport Program Test Plan: Tracer Testing of the Culebra Dolomite Member of the Rustler Formation at the H-19 and H-11 Hydropads on the WIPP Site." Albuquerque, NM: Sandia National Laboratories. (Copy on file in the Sandia WIPP Central Files (SWCF) as ERMS #230156.)

Mercer, J.W., D.L. Cole, and R.M. Holt. 1998. *Basic Data Report for Drillholes on the H-19 Hydropad (Waste Isolation Pilot Plant–WIPP).* SAND98-0071. Albuquerque, NM: Sandia National Laboratories.

Saulnier, G.J., Jr., and R.L. Beauheim. 1998. "Appendix A: Culebra Transport Program Field Operations Plan: Well Construction and Preliminary Testing on the H-19 Hydropad at the WIPP Site," *Basic Data Report for Drillholes on the H-19 Hydropad (Waste Isolation Pilot Plant–WIPP).* J.W. Mercer, D.L. Cole, and R.M. Holt. SAND98-0071. Albuquerque, NM: Sandia National Laboratories. A-3 to A-58.

This page intentionally left blank.

Appendix H
Evaluation of Tracers Used for the WIPP Tracer Tests

By Irene M. Farnham[1], Lucy C. Meigs[2], Martha E. Dominguez[1], Kazumasa Lindley[1], Jeanette M. Daniels[1], and Klaus J. Stetzenbach[1]

Abstract

Tracer tests used to characterize groundwater flow near the Waste Isolation Pilot Plant (WIPP) site in New Mexico demonstrate the usefulness of the fluoro- and chlorobenzoates as groundwater tracers. Eighteen separate tracers were used for a series of single-well injection-withdrawal and multiwell convergent-flow tests. Another tracer test recently completed near the proposed site of the high-level waste repository at Yucca Mountain (YM) in Nevada also consisted of multiple tracer injections into each of three wells. These tests required a large number of tracers that both behave conservatively in the tested environments and can be chromatographically separated in order to quantify each one accurately. In addition, due to extreme dilution of tracers between the injection and pumping wells, tracers soluble at concentrations up to six orders of magnitude above the analytical quantitation limit were required.

The conservative nature of the benzoate tracers used in the WIPP and YM field tests is demonstrated through batch testing in both dolomite from the WIPP site and volcanic tuff from the YM site. Relative solubilities for each benzoate compound investigated were rated based on the ability to achieve concentrations necessary for the injectate solutions (2 to 100 g/L). Detection limits in the low μg/L levels were observed for individual tracers and separation of 20 of the 24 potential tracers was achieved using reversed-phase liquid chromatography.

H.1 Introduction

Understanding and predicting the behavior of solutes in the subsurface is frequently critical for effective environmental management. Field tracer tests can provide valuable information on transport processes, including transport pathways, advection rates, dispersion, diffusion, and sorption. In general, conservative groundwater tracers should not sorb to the aquifer material, should be stable for the duration of the tracer test, be nontoxic, and should have solubilities several orders of magnitude higher than the analytical detection limit. Low background levels of the tracer are also required to insure accurate interpretation of the results. Most aquifer materials are negatively charged. As a result, anions generally make the best tracers because they are less susceptible to adsorption or ion-exchange processes on natural aquifer materials (Davis et al., 1980). Inorganic ions such as chloride, bromide, and iodide are commonly used as tracers. Numerous organic compounds also have been used to trace groundwater movement, including fluorescent organic dyes such as fluorescein and rhodamine. The advantages of using fluorescent dyes are their relatively low cost, large detection range, and ease of rapid field analysis (Boulding, 1995). However, most of the organic dyes sorb to aquifer materials and are readily degraded by microbes under many conditions (Sabatini and Austin, 1991). Optical brighteners (additives to laundry detergents) are also used as tracers, but they have drawbacks similar to those for the organic dyes (Jones, 1991). Due to sorption and degradation problems, dyes and optical brighteners appear best suited for non-

---

[1] University of Nevada at Las Vegas, Harry Reid Center for Environmental Studies, 4505 Maryland Parkway, Las Vegas, NV 89154-4009. Email: farnham@nevada.edu.

[2] Sandia National Laboratories, Geohydrology Department, P.O. Box 5800, MS-0735, Albuquerque, NM 87185-0735.

quantitative studies such as flow-path definition in karst aquifers.

A class of organic anionic compounds showing excellent tracer characteristics is the halogenated benzoates. An important attribute of these compounds is the availability of numerous isomers that can be separated chromatographically, thus allowing for the analysis of numerous tracer compounds within one sample. This attribute enables the design of elaborate tracer tests with numerous tracers injected into several wells. The fluorinated and chlorinated benzoates have pK_a values of less than four and, consequently, are anionic and soluble at most groundwater pHs. Solubilities as high as 100 g/L have been achieved for some of these compounds. The halogenated benzoates absorb in the ultraviolet region and can be detected at low µg/L levels (Bowman, 1984). Lower detection limits can be achieved using concentration-enhancement techniques (Stetzenbach et al., 1982). The high solubility and low detection limits for these compounds enable their use in tests where high levels of dilution are anticipated. The fluorobenzoates also may be preferred over bromide for mimicking transport of organic contaminants because they are frequently more similar in size to the contaminants than bromide (Brusseau, 1993).

The conservative nature of many of the fluorinated benzoates has been previously demonstrated (Bowman, 1984; Benson and Bowman, 1994; Bowman and Gibbens, 1992). The fluorobenzoates have been used to characterize aquifer properties (Jones et al., 1992; Boggs et al., 1992) as well as to provide insight into the fate of agrichemicals in soils (Pearson et al., 1996a and b; Beck et al., 1995). The use of the chlorinated benzoates as groundwater tracers has not previously been explored.

Although extensive research has been conducted on the toxicity of benzoic acid, very little information on the halogenated benzoic acids is available. Benzoic acid is used in numerous food products (Kilgore and Li, 1980) and is also found naturally in most berries at concentrations as high as 500 mg/L (Budvari, 1989). Benzoic acid is rapidly metabolized and excreted (Neal, 1980; Stewart and Stolman, 1960, p. 113). In a study with humans, 96% of a 20-g dose was eliminated as its metabolite, hippuric acid, within 12 hours (Stewart and Stolman, 1960, p. 113). The halogenated analogues are also metabolized and excreted, but are excreted as the free acids at significantly higher rates (Caldwell, 1978). The lethal dose to 50% of the population (LD50) for benzoic acid, based on a study using white rats (Hager and Starkey, 1943), was calculated to be 1.714 ± 0.037 g/kg. The LD50s for fluoro-, chloro-, bromo-, and iodo-substituted acids determined in the same study were 1.542 ± 0.107, 0.838 ± 0.033, 0.812 ± 0.042, and 0.786 ± 0.037 g/kg, respectively. While the toxicity of benzoic acid and its p-fluoro substituted derivative did not differ significantly, the latter three halogenated acids are twice as toxic. These limited data, therefore, suggest that the toxicity of the chlorobenzoate tracers may be greater than that of the fluorobenzoate tracers.

The purpose of this appendix is to provide a detailed overview of the physical characteristics of both the fluorinated and chlorinated benzoates and evaluate their suitability as groundwater tracers. This research was conducted to determine the feasibility of using a suite of benzoate tracers for extensive field tracer-test studies in the Culebra dolomite at the Waste Isolation Pilot Plant (WIPP) site and in volcanic tuff at the Yucca Mountain (YM) site. This appendix provides a summary of: 1) previous laboratory and field studies by others; 2) batch tests conducted to evaluate stability and potential sorption; 3) studies of solubility and minimum detection limits; and 4) the results of a tracer test at the WIPP site, where a total of eighteen separate tracers was used for a series of single-well injection-withdrawal (SWIW) and multi-well convergent-flow tests (MWCF). For additional details on the batch tests conducted on Culebra dolomite samples, see ERMS #237453.

H.2 Background

The halogenated benzoates consist of the parent benzoate structure (Figure H-1a) with the positions labeled 2 to 6 substituted with two to five fluorines or chlorines. For instance, 2,4,6-trifluorobenzoate (2,4,6-TFBA) consists of

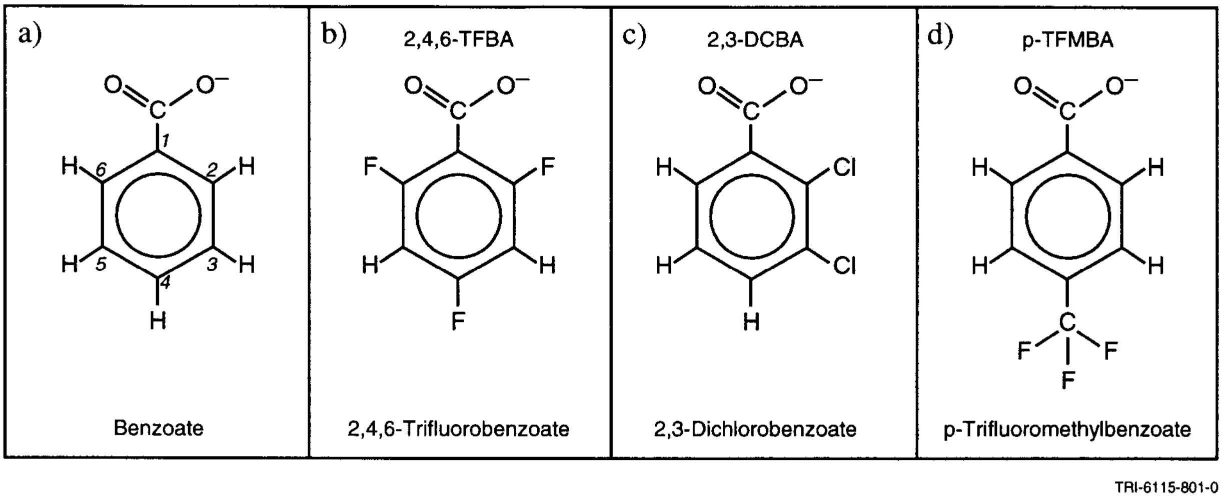

Figure H-1. Acronyms, structures, and chemical names of benzoate and selected halogenated benzoates included in this study.

the parent benzoate with fluorine substituted for hydrogen in the 2, 4, and 6 positions (Figure H-1b). 2,3-dichlorobenzoate (2,3-DCBA) consists of the ring structure with chlorine substituted for hydrogen in the 2 and 3 positions (Figure H-1c). A single CF_3 is substituted for one of the ring hydrogens in the triflouromethylbenzoates (Figure H-1d). The CF_3 group substitution for o-(trifluoromethyl)benzoate (o-TFMBA), m-(trifluoromethyl)benzoate (m-TFMBA), and p-(trifluoromethyl)benzoate (p-TFMBA) is in the 2, 3, and 4 positions, respectively. The protinated (free-acid) form is referred to as a benzoic acid, whereas the anionic, water-soluble form is referred to as a benzoate. These terms are often used interchangeably.

Early studies have shown that the monofluorinated benzoates do not have the stability required for use as groundwater tracers (Bentley, 1983; Thompson and Stetzenbach, 1980). An increased stability is observed for the multiple-substituted fluorinated benzoates (Barackman, 1986; McCray et al., 1985). The use of the polyfluorobenzoates as groundwater tracers has been evaluated in many hydrological environments. Tables H-1 and H-2 summarize most of the studies which have been conducted to evaluate the polyfluorobenzoates as groundwater tracers. The sorptive nature of these compounds can vary depending on the clay content and organic-carbon fraction of the aquifer material, as well as the pH of the groundwater.

No sorption of the fluorobenzoates was observed when batch tested over 28 to 85 days in Bluepoint sand with low organic carbon fraction (0.001 - 0.002) and an approximately neutral pH (7.5). Solute breakthrough curves using these conditions were indistinguishable from those of Br^- in laboratory column tests (Bowman and Gibbens, 1992; Benson and Bowman, 1994). The compounds 2,3-difluorobenzoate (2,3-DFBA), 2,5-DFBA, 3,4-DFBA, and 3,5-DFBA also behaved like Br^-, at the 95% confidence limit, in aquifer and vadose-zone tracer tests (Bowman and Gibbens, 1992). 2,6-DFBA, pentafluorobenzoate (PFBA), m-TFMBA, and o-TFMBA were applied to a field soil and monitored over 69 days in soil water at depths of 1.0 and 1.8 m. All of these compounds, with the exception of m-TFMBA, behaved similar to Br^- (Bowman, 1984). Some FBAs did show a decrease in concentration over time when exposed to soils with a larger organic-carbon fraction (0.02). The decrease in the solution concentration was greater for the FBAs with a higher pK_a (weaker acids) and for the more acidic (pH 6.6), higher organic-carbon content soil (Benson and Bowman, 1994). Howard (1997) and Jaynes (1994) observed a similar relationship between sorption and tracer pK_a; more sorption for higher pK_a values. Of the tracers included in the study, the tracer with the lowest pK_a, 2,6-DFBA, showed no measurable sorption in batch experiments using fractured shale saprolite from the Oak Ridge Reservation and synthetic groundwater at a pH of 4.6 (Howard, 1997). In a column transport

Table H-1. Lab and Field Studies Using Benzoate Tracers

Study No.[(a)]	Reference	Type Test	Material Type	Clay Content (%)	Organic-Carbon Fraction	pH	Observed Sorption	Comment (Estimated K_d in mL/g)
I	this report	Field/Batch	Fractured dolomite (Culebra)			7.8	No	
II	Reimus and Haga (1999)	Field	Volcanic tuff				No	
III	Umari et al. (1998)	Field	Volcanic tuff (Prow Pass)				No	
IV	Seaman (1998)	Column	Quartz sand (acid washed)			5	No	
V	Seaman (1998)	Column	Soil (Orangeburg)	8.6	0.0072	5.46	Variable	
VI	Seaman (1998)	Column	Sediment (Barnwell)	4.6	<detection limit	5.18	Yes	
VII	Fahy (1997)	Field	Volcanic tuff (Bullfrog)				No	
VIII	Howard (1997)	Batch/Column	Fractured shale saprolite		0.0005	5.2 (column test) 4.5 to 4.7 (batch test)	Variable	sorption correlated to pK_a
IX	Howard (1997)	Batch/Column	Fractured shale saprolite		0.0005	>6.8	No	
X	Wilson and Linderfelt (1995)	Field	Sand (Borden)			6.8 to 8.0[(b)]	No	
XI	Benson and Bowman (1994)	Batch/Column	Fine sand (Bluepoint)		0.001	7.5	No	
XII	Benson and Bowman (1994)	Batch	Silty loam (Naff)		0.021	6.6	Yes	(K_d =0.05 to 0.34)
XIII	Benson and Bowman (1994)	Batch	Silty clay loam (Bearden)		0.020	7.1	Variable	(K_d =0.01 to 010)
XIV	Benson and Bowman (1994)	Column	Dune sand (97% silica sand)		0.0001	7.5	No	
XV	Jaynes (1994)	Batch/Column	Clarion soil	24.7	0.029	7.2	Variable	
XVI	Jaynes (1994)	Column	Silty clay loam (Okoboji)	37.2	0.050	6.2	Yes	
XVII	Bowman and Gibbens (1992)	Batch/Column	Fine sand (Bluepoint)		0.0002	7.5	No	
XVIII	Bowman and Gibbens (1992)	Batch	Silty clay loam (Bearden)		0.035	7.2	No	
XIX	Boggs et al. (1992); Boggs and Adams (1992)	Column/Field	Sand and gravel			4.3 to 5.2	Yes	possible anionic sorption (K_d = 0.002 for 2,6-DFBA, 0.019 for PFBA, and 0.025 for o-TFMBA)
XX	Jones et al. (1992)	Field	Fractured dolomite (Culebra)					
XXI	Bowman (1984)	Batch	Loamy sand subsoil		0.0005	7.4	No	
XXII	Bowman (1984)	Column	Carrizo Series soil	2.5	0.015	7.2	No	
XXIII	Bowman (1984)	Field	Avondale silty clay loam	21-42	0.0097	7.9	Variable	degradation or sorption of m-TFMBA was observed

(a) used for cross-referencing with Table H-2
(b) Nicholson et al. (1983)

experiment conducted under similar conditions (pH 5.2), 2,6-DFBA behaved as conservatively as bromide, but retardation of both 2,5- and 3,5-DFBA was observed (Howard, 1997). Batch tests performed by Jaynes (1994) using soils with a pH of 7.2, an organic fraction of 0.029, and a clay fraction of 0.247 showed significant decreases in concentration over a 60-day period for five of the six tracers tested (2,6-DFBA, m-TFMBA, o-TFMBA, 3,5-DFBA, and 2,5-DFBA) and a negligible change in concentration for one tracer (PFBA). 3,4-DFBA, 3,5-DFBA, and m-TFMBA appeared to interact more strongly with the soil than the other tracer tested as indicated by low recoveries at early times. Column leaching experiments were also performed using this soil and a second soil having a pH of 6.2, an organic-carbon fraction of 0.050,

Table H-2. Measured and Calculated Parameters Relevant to the Selection of Halogenated Benzoates for Field Tracer Tests

Compound	Aqueous Diffusion Coefficient (cm^2/s) $^{(a)}$	pK_a		MDL (μg/mL)	Solubility Rating	Cost$^{(i)}$ (\$/kg)	Batch Test Results		Column Studies (Results relative to bromide or tritium*)		Field Tests
		calculated $^{(c)}$	measured				No Sorption	Sorption	Similar Behavior	Increased Retardation	
2,3-DFBA	8.2×10^{-6}	2.93	3.29^{d}, 3.10^{f}	2	2	1500	I, XVII, XVIII	VIII	XVII		I, X
2,4-DFBA	8.2×10^{-6}	3.21	3.58^{d}, 3.44^{e}	1	3	1000	I, IX	VIII			I
2,5-DFBA	8.2×10^{-6}	2.93	3.30^{d}, 3.10^{f}	1	2	1300	I, XVII, XVIII	XV	IX, XVII	VIII, XV, XVI	I
2,6-DFBA	8.2×10^{-6}	2.34	2.85^{d}, 2.24^{e}	5	1	310	I, VIII, XXI	XV	IV*, V*, VIII, IX, XV, XXII	VI*, XVI, XIX*	I, II, VII, X, XIX, XXIII
3,4-DFBA	8.2×10^{-6}	3.80	3.83^{d}, 3.79^{f}	1	4	1500	I, XVII, XVIII	VIII, XV	IV*, IX, XVII	V*, VI*, VIII, XV, XVI	I, X
3,5-DFBA	8.2×10^{-6}	3.52	3.59^{d}, 3.52^{f}	1	3	1025	I, XVII, XVIII	XV	XVII	XV, XVI	X
2,3,4-TFBA	8.0×10^{-6}	2.87	3.30^{d}	3	4	3200	I, XI	XII, XIII	XI, XIV		I
2,3,6-TFBA	8.0×10^{-6}	2.00	2.82^{d}	20	2	5000	I, XI, XIII	XII	XI, XIV		I
2,4,5-TFBA	8.0×10^{-6}	2.87	3.28^{d}	2	4	1600	I, XI, XIII	XII	XI, XIV		III
2,4,6-TFBA	8.0×10^{-6}	2.28	2.83^{d}	7	3	5000	I				
3,4,5-TFBA	8.0×10^{-6}	3.46	3.54^{d}	12	2	2000	I, XI	XII, XIII	IV*, XI, XIV	V*, VI*	
2,3,4,5-TeFBA	7.9×10^{-6}	2.53	3.08^{d}	5	2	910	I, XI	XII, XIII	IV*, XI, XIV	V*, VI*	I, III
2,3,5,6-TeFBA	7.9×10^{-6}	1.66	2.71^{d}	16	2		I, XI, XII, XIII, XV		XI, XV, XIV		
PFBA	7.7×10^{-6}, $7.2 \times 10^{-6(b)}$	1.60	1.73^{b}, 2.72^{d}, 1.48^{f}, 1.74^{g}, 1.49^{h}	12	1	375	I, VIII, XXI, XV		XV, XXII	XVI, XIX*	I, II, III, VII, X, XIX, XX, XXIII
o-TFMBA	7.4×10^{-6}	NA		4	2	1000	I, XXI	XV	XXII, XV	XVI, XIX*	I, X, XIX, XX, XXIII
m-TFMBA	7.4×10^{-6}, $7.2 \times 10^{-6(b)}$	3.74	3.79^{b}, 3.9^{g}	3	2	785	I, XXI	XV	XXII	XV, XVI	I, X, XX, XXIII
p-TFMBA	7.4×10^{-6}	3.67		2	2	495	I				I
2,3-DCBA	7.3×10^{-6}	2.55	2.63^{h}	2	2	2000	I				I
2,4-DCBA	7.3×10^{-6}	2.68	2.76^{h}	2	2	70	I				I
2,5-DCBA	7.3×10^{-6}	2.55		3	4	650	I				I
2,6-DCBA	7.3×10^{-6}	1.64	1.75^{h}	6	1	500	I				I
3,4-DCBA	7.3×10^{-6}	3.59	3.64^{h}		5	380					
3,5-DCBA	7.3×10^{-6}	3.46	3.51^{h}		4	2000	I				I
2,3,5-TCBA	6.8×10^{-6}	2.18		2							
2,4,6-TCBA	6.8×10^{-6}	1.40		3	3		I				I

[a] Estimated with the Hayduk and Laudie method (Tucker and Nelken, 1982)
[b] Measured by Walter (1982)
[c] Calculated using the Hammett Equation (Perrin et al., 1981)
[d] Measured by Benson and Bowman (1994)
[e] Measured by Strong et al. (1982)
[f] Measured by Strong et al. (1987)
[g] Stetzenbach et al. (1982)
[h] Estimated by Bijloo and Rekker (1984)
[i] Oakwood Research Chemical (ORC in West Columbia, SC). The citing of ORC is not an endorsement of their products. Prices will vary.
NA - The parameter required for the calculation of the pKa was not available

and a clay fraction of 0.372. A significant loss of mass was observed for m-TFMBA and 3,5-DFBA. These tracers, along with 3,4-DFBA, also experienced retardation with respect to Br^-. A laboratory soil column study performed by Boggs and Adams (1992) to investigate a declining mass-balance trend observed during a natural-gradient field test showed that approximately 20% of bromide and 10% of the three fluorobenzoates (PFBA, 2,6-DFBA, and o-TFMBA) were adsorbed during the field experiment. In this test, a low pH (4.8) along with the presence of iron oxides and kaolinite in the alluvial aquifer produced geochemical conditions conducive to adsorption of anionic tracers. K_d values for bromide, PFBA, 2,6-DFBA, and o-TFMBA were calculated to be 0.041, 0.019, 0.002, and 0.025 mL/g, respectively.

H.3 Methodology

H.3.1 Materials and Chemical Analysis

All halogenated benzoates used for the laboratory studies were purchased from Aldrich Chemical Company, Inc. (Milwaukee, WI). Chemical purities were $\geq$97%. Bulk tracers used for field testing were purchased from Fluorochem (Old Glossop, England). The benzoic acids evaluated in this study are listed in Table H-3.

All analyses were performed using reversed-phase high-performance liquid chromatography with ultraviolet (UV) detection. Two instruments were used: a SpectraPhysics SP8800-010 high-performance liquid chromatograph (HPLC) equipped with a SpectraPhysics SP8880 autosampler, and a SpectraSYSTEM UV3000 Detector or a SpectraSYSTEM P2000 HPLC equipped with a SpectraSYSTEM AS1000 autosampler and SpectraSYSTEM UV1000 detector. The analytical column used for the majority of the work was a SUPELCOSIL LC-18 column (15 cm x 4.6 mm) with a 5-μm particle size (Supelco, Chromatographic Products, Bellefonte, PA). The mobile phase for all analyses consisted of methanol (HPLC Grade, Burdick & Jackson) and potassium phosphate buffer (0.05 M KH_2PO_4 adjusted to a pH of 2.7 with H_3PO_4). The flowrate and percentage of each solvent in the mobile phase depended on the particular tracers present in the mixture (see Appendix I). A detection wavelength of 230 nm was used for sample analyses.

H.3.2 Batch Experiments

Batch experiments were performed to evaluate the stability and sorptive character of each benzoate compound in an environment that simulated the tested aquifer at each site. Crushed dolomite and volcanic tuff were used to represent the WIPP and YM sites, respectively. The batch samples consist of 250 g of ground rock and a 250-mL solution consisting of several of the tracer compounds in water for the YM test. The amount of ground rock and the volume of the tracer solutions varied for the WIPP batch tests (see Table H-3). A blank sample containing only ground rock and water with no tracer and a control sample containing only the tracer solution but no rock were also prepared. Aliquots were periodically removed, over a period of approximately 60 to 90 days, for HPLC analysis of benzoic-acid concentrations.

Seven sets of batch-test mixtures, consisting of crushed Culebra dolomite (primarily dolomite with trace quantities of other minerals such as clays) and several fluoro- or chlorobenzoates in Culebra brine at concentrations between 2.5 and 25 mg/L, were prepared in triplicate. The fluoro- and chlorobenzoates included in each of the eight sets and their concentrations are listed in Table H-3. The combination of compounds in each set was selected based on the ease with which the different benzoates could be separated chromatographically. Crushed dolomite with a mesh size of 300 – 400 was used for the majority of the batch tests. One batch test (set 4) was performed using two mesh sizes (28 and 400) to test whether the mesh size of the dolomite had any impact on sorption of the tracers. Duplicate batch-test samples were prepared using each of the two mesh sizes. Batch samples were mixed every week by shaking them for approximately 2 hr using a Lab Line Orbit shaker. Samples were removed from the batch mixtures on approximately days 0, 7, 30, 60, and 90 of the experiment. An extraction was performed on the majority of these samples to transfer the benzoates from the brine of the Culebra to deionized (DI) water, which is more compatible with the HPLC system. Two liquid/liquid extractions were performed. Samples were first acidified to a pH of less than 2 with concentrated H_3PO_4. Next, the benzoates were extracted into ethyl acetate and then into 1% Na_2CO_3 in DI water. The solution was then neutralized using concentrated H_3PO_4. One of the benzoates not included in the batch samples was used as a surrogate compound. A known quantity of the surrogate compound was added to the sample prior to extraction and used to determine the efficiency of the extraction procedure. Due to methods improvements, two sets of batch tests (containing 2,3,4-TFBA, 2,4,5-TFBA, 2,4,6-TFBA, m-TFMBA, p-TFMBA, 3,5-DCBA, and

Table H-3. Experimental Conditions for the WIPP Batch Tests

Compound	Batch Test Set	Mass of Solid Phase (g)	Solution Volume (mL)	Initial Concentration of Solute (mg/L)	Sample Preparation Method
2,3-DFBA	1	125	125	5	Extraction
2,4-DFBA	2	125	250	2	Extraction
2,5-DFBA	3	125	250	5.	Extraction
2,6-DFBA	1	125	125	5	Extraction
3,4-DFBA	1	125	125	5	Extraction
3,5-DFBA	2	125	250	5	Extraction
2,3,4-TFBA	5	250	250	26	1:10 Dilution
2,3,6 -TFBA	3	125	250	5	Extraction
2,4,5 -TFBA	6	250	250	25	1:10 Dilution
2,4,6 -TFBA	6	250	250	25	1:10 Dilution
3,4,5 -TFBA	2	125	250	10	Extraction
2,3,4,5-TeFBA	1	125	125	5	Extraction
2,3,5,6-TeFBA	2	125	250	5	Extraction
PFBA	3	125	250	2	Extraction
o-TFMBA	3	125	250	5	Extraction
m-TFMBA	6	250	250	26	1:10 Dilution
p-TFMBA	5	250	250	26	1:10 Dilution
2,3-DCBA	4	125	125	2	Extraction
2,4-DCBA	4	125	125	5	Extraction
2,4-DCBA	5	250	250	26	1:10 Dilution
2,5-DCBA	4	123	125	2	Extraction
2,6-DCBA	4	125	125	2	Extraction
3,5-DCBA	5	250	250	25	1:10 Dilution
2,4,6-TCBA	7	125	125	2	Direct Analysis
Iodide	7	125	125	15	1:100 Dilution

2,4-DCBA) were not extracted; each sample was instead diluted 1:10 with DI water prior to HPLC analysis. The batch test containing 2,4,6-TCBA was also not extracted; each sample was analyzed directly with no dilution.

Nine samples were prepared for the YM batch tests using three different solutions and three different rocks. The three solutions contained four to eight fluorobenzoates at approximately 5 mg/L in water. The chlorobenzoates were not considered for these tests. The water used for preparation of the batch samples was collected from a well (J-13) located near the YM site. Water from J-13 is of drinking-water quality and chemically similar to the water at the location of the field testing. No extraction was required. The specific benzoates used for each solution were selected based on the ease with which they could be chromatographically separated from one another. Three types of crushed YM volcanic tuff were used for the rock component. The tuff material was Bullfrog Tuff, a crystal-rich, pumiceous, rhyolitic (silica-rich) tuff that underlies the Topopah Spring tuff in Yucca Mountain. The tuffs are referred to as light, medium, and dark and are classified as follows: un-welded "light" tuff, which is lightweight, porous, and easily broken; moderately-welded "medium" tuff, which is semi-porous, and contains some dense areas of collapsed pumice fragments; and the densely welded "dark" tuff which is hard, very dense and vitrophyric in nature, and can be classified as an obsidian. The Bullfrog Tuff contains 10 to 20% phenocrysts of sanidine (30 to 40%), plagioclase (20 to 40%), resorbed quartz (20 to 40%), biotite (1 to 5%), and 1 to 3% hornblende (Maldonado and Hausback, 1990). The samples were vigorously shaken and an approximately 2-mL sample was taken and filtered using 13-mm, 0.45-µm syringe filters (Whatman) into a vial for HPLC analysis. Samples were taken over a 60-day period at approximately 0, 1, 5, 10, 20, 30, and 60 days.

Iodide was also batch tested in both the dolomite and the YM tuff. The batch test samples were prepared as described for those of the fluoro- and chlorobenzoates with a few exceptions. The amount of ground dolomite and the volume of the tracer solution in the Culebra brine are listed in

Table H-3. The concentration of iodide in the solution was 20 mg/L. The samples were taken over a 90-day period and were diluted 1:100 prior to analysis. The YM batch test samples differed only in the concentration of the iodide solution in J-13 water. The concentration of iodide was 0.20 mg/L rather than the concentration of 5 mg/L used for the fluorobenzoates.

H.3.3 Determination of Physical Properties

Negative log acid dissociation constants (pK_as) were calculated from the molecular structures of the tracers using the Hammett equation (Perrin et al., 1981). For the ionization of substituted benzoic acids in water at 25°C, the Hammett equation is reduced to:

$$pK_a = 4.20 - (\sum \sigma) \qquad \text{(H-1)}$$

where 4.20 is the pK_a of the unsubstituted benzoic acid, and σ represents the contribution that each of the fluoro- or chloro- substituents makes to the acid strengthening or weakening of the benzoic acid. When fluorides are substituted in positions 2 or 6, 3 or 5, or position 4; σ = 0.93, 0.34, and 0.06, respectively. For chloride-substituted benzoic acids, σ = 1.28, 0.37, and 0.24 when substitutions are in positions 2 or 6, 3 or 5, or position 4, respectively. For the trifluoromethylbenzoates (TFMBA), σ = 0.46 and 0.53 for $-CF_3$ substitutions in positions 3 and 4, respectively.

Diffusion coefficients were estimated using the Hayduk and Laudie method (Tucker and Nelken, 1982). The diffusion coefficients were calculated for the anionic, water-soluble form (Table H-2). Diffusion coefficients for the free-acid form of the fluorobenzoates are also reported by Benson and Bowman (1996).

Rather than measuring solubilities for these compounds, laboratory studies were conducted to determine methods for achieving the highly concentrated injectate solutions required for each tracer test. Methods to dissolve the tracers at concentrations up to 100 g/L were examined in the J-13 water. For these studies, 0.5 g of tracer was placed in 5 mL of J-13 water and the pH was increased until the tracer was completely dissolved. Increasing the pH insured that the tracer was in the anionic, water-soluble form. Frequently, a pH significantly higher than the pK_a was required to reach dissolution. Once the tracer was dissolved, the pH was reduced with acid while maintaining tracer dissolution. The tracer concentrations in the injectate solutions for the tests conducted at the WIPP site ranged from 2 to 16 g/L. The concentrations varied depending on both the particular tracer test and the maximum solubility of the benzoate tracer compounds. Dissolution of a small number of compounds in the Culebra brine could not be achieved by solely increasing the pH. For those compounds, the tracer was first dissolved in a small amount of methanol and then brought to volume with the Culebra brine (see Appendix J).

The method detection limit (MDL) is defined as "the minimum concentration of a substance that can be identified, measured, and reported with 99% confidence that the analyte concentration is greater than zero" (Glaser et al., 1981). The MDL was determined for each compound individually; standard solutions were prepared containing 0.01 to 0.05 mg/L benzoic acid in DI water. Standard solution concentrations were designed to be two to five times higher than the estimated MDL. Seven replicates of each standard solution were analyzed and the detection limit (DL) was calculated as:

$$DL = ts \qquad \text{(H-2)}$$

where t is the student's t value for a one-tailed test at the 99% confidence level and s is the standard deviation of the replicate analysis (Glaser et al., 1981). The MDL is dependent on the retention time (i.e., the time that the compound is retained on the column) and, therefore, the methanol and KH_2PO_4 composition of the mobile phase (see Section H.3.1) was set so that similar retention times for each compound were observed. The LC-18 column at a flowrate of 1 mL/minute and a 100-µL injection loop was used. Consistent with the analyses described in this study, a detection wavelength of 230 nm was used for detection-limit determinations (see Section H.3.1).

H.3.4 Field Tests

Chapter 3 presents details of the 1995-96 tracer tests at the H-11 and H-19 hydropads. Eighteen different halogenated benzoates were used for these tests. A total of 21 injections of halogenated benzoates and two injections of iodide were made during the SWIW and MWCF tracer tests at the H-19 hydropad. The 1996 SWIW and MWCF tracer tests at the H-11 hydropad resulted in a total of six injections of halogenated benzoates and one injection of iodide.

H.4 Results

H.4.1 Benzoate Analysis

A chromatogram illustrating the ability to separate 20 of the 24 potential tracers is shown in Figure H-2. 3,4-DCBA was not included in the analyses as originally planned because low solubility prohibited its use in field testing. Separation for 2,3-DCBA / 3,4-DFBA (see Appendix I) and 2,4,6-TCBA / 2,4-DFBA was later achieved by varying the HPLC mobile-phase conditions, thus allowing the use of all of these compounds in the same test. Separation of the fluorobenzoate pairs 2,3,5,6-TeFBA / 2,3,6-TFBA and 3,4-DFBA / 3,5-DFBA could not be improved by varying any conditions. Therefore, these combinations of compounds should not be used for the same test.

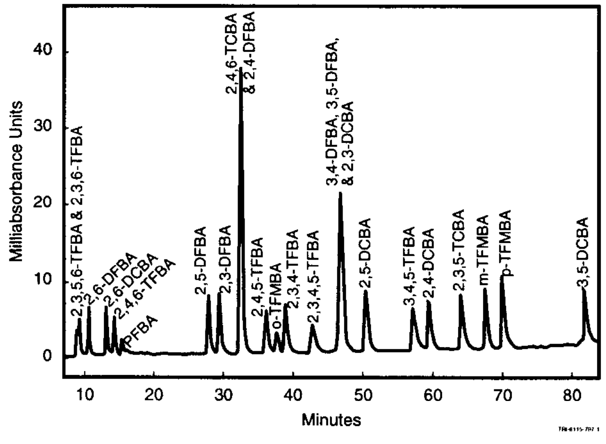

Figure H-2. Chromatogram of 20-µL injection of halogenated benzoates (5 mg/L). (95% potassium phosphate buffer: 5% methanol to 35% potassium phosphate buffer : 65% methanol over 100 minutes; Flowrate =1.4 mL/min).

Generally, the quantitation of 20 compounds in one sample is not required. The chromatogram shown in Figure H-2 can, therefore, be used to select tracers based on optimal chromatographic separation. Better chromatographic separation provides more flexibility in altering the chromatographic conditions to eliminate any interferences. Once tracer selection is made, the analytical conditions can be optimized by adjusting the methanol, the KH_2PO_4 composition, and the flowrate. Organic compounds elute more rapidly off of a reversed-phase LC column as the proportion of the organic solvent is increased. This results in shorter run times, which in turn results in sharper and more symmetrical chromatographic peaks. Minimizing the run time is not only time efficient but may also improve the sensitivity for these compounds. Background interferences are another consideration in tracer selection. The early-eluting compounds (2,3,5,6-TeFBA, 2,3,6-TFBA, 2,4,6-TFBA, and 2,6-DFBA) can often be difficult to separate from interferences. These compounds are not retained strongly on this HPLC column even with mobile-phase adjustments. Therefore, manipulating chromatographic conditions enough to provide accurate quantitation is often impossible. Background interference problems were observed for 2,6-DFBA in the YM batch test and are also reported by Boggs and Adams (1992) and Bowman (1984).

H.4.2 Batch Experiments

The results of the batch experiments for both the dolomite and the tuffs are shown in Figures H-3 through H-7. The compounds are plotted in these figures based on similar structure rather than on how they were combined in the batch tests. Data are plotted as the relative concentration (the concentration of the tracer in the batch sample divided by the concentration of the tracer prior to addition to the rock) versus time. The measured concentration of the tracer in the control sample, at T=0, was used as the concentration of tracer prior to addition to the rock. The average of the triplicate analyses of the dolomite samples is shown. The results for the three tuffs were quite similar; the percent relative standard deviations were well below 2% in most cases. Only the results for the dark tuff are shown in the figures. A high variability was observed in many of the batch-test results for the dolomite, primarily due to the extraction of the benzoates from the Culebra brine. The extraction was performed on 16 of the 24 benzoates tested (see Table H-3). The surrogate, added to evaluate extraction reproducibility, indicated that the recoveries for the three sets of batch tests that were extracted were: 95% ± 2%, 92% ± 2%, and 88% ± 2%. Most noteworthy of these results is the high precision of the extraction; although recoveries are less than 100%, the standard deviations are 2%, which indicates relatively high reproducibility in the extraction procedure. The less than 100% recovery is corrected for by using the relative recoveries; both concentrations reported in the relative recoveries reflect the loss in tracer due to the extraction.

No significant sorption or degradation is observed for the difluorobenzoates in either the dolomite or tuff (Figure H-3). The relative recoveries in dolomite (Figure H-3a) ranged from 0.93 to 1.07 (0.99 ± 0.04). An outlier is observed for 2,5-DFBA at day 30. This was probably due to slight measurement error because this anomaly was also observed for the control sample. The relative recoveries in the tuff ranged from 0.99 to 1.03 (1.01 ± 0.01). An interference was present in the 1- to 30-day tuff samples so that 2,6-DFBA could not be quantified. This interference was not present in the 0- and 60-day samples and, therefore, only these results for 2,6-DFBA are shown in Figure H-3b.

Similar relative recoveries are observed for the trifluorobenzoates (Figure H-4). No measurable sorption was observed for the TFBAs in the tuff (see Figure H-4b); the relative recoveries ranged from 0.97 to 1.05 (1.01 ± 0.02). The relative recoveries for 2,3,6-TFBA (1.07 ± 0.03) are significantly higher than for the other TFBAs (0.97 ± 0.02) in the dolomite. The relative concentrations for all of the benzoates (2,3,6-TFBA, 2,5-DFBA, o-TFMBA, and PFBA) included in the third set of dolomite batch-test samples (see Table H-3) were consistently greater than one (1.06 ± 0.04). This is probably due to an error in the measurement of the concentrations of these compounds in the control sample at T=0. The measured concentrations of all tracers in the control sample were lower at T=0 than from all subsequent analyses. The general trend of the results for the control sample is consistent with the general trend for the dolomite test sample. Although greater than one, the relative recoveries are consistent over the 90- day period (Figures H-4a and H-5a), indicating no significant degradation or sorption of any of these compounds.

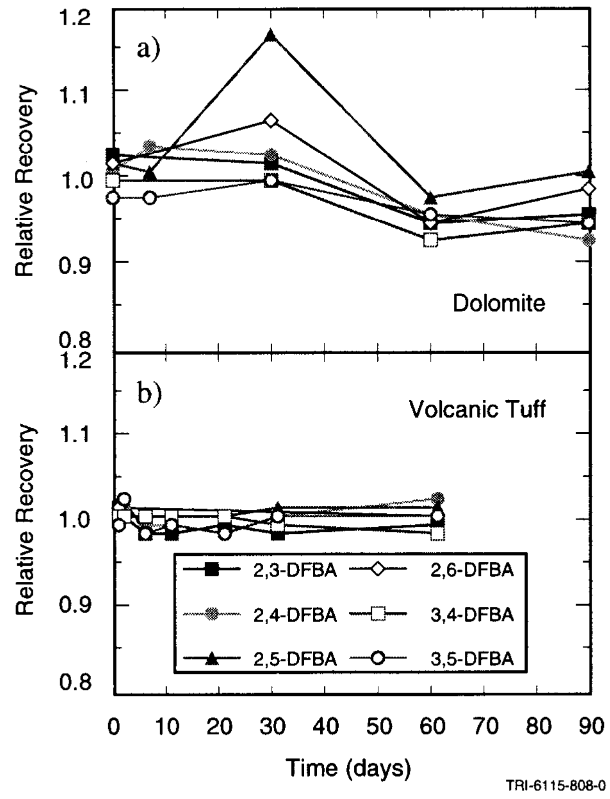

Figure H-3. **Results of batch tests for difluorobenzoates in (a) dolomite and (b) volcanic tuff.**

The results of the TeFBAs, TFMBAs, and PFBA in dolomite are also shown in Figure H-5a. The relative recoveries for these compounds range from 0.95 to 1.09 (1.00 ± 0.03). The TeFBAs,

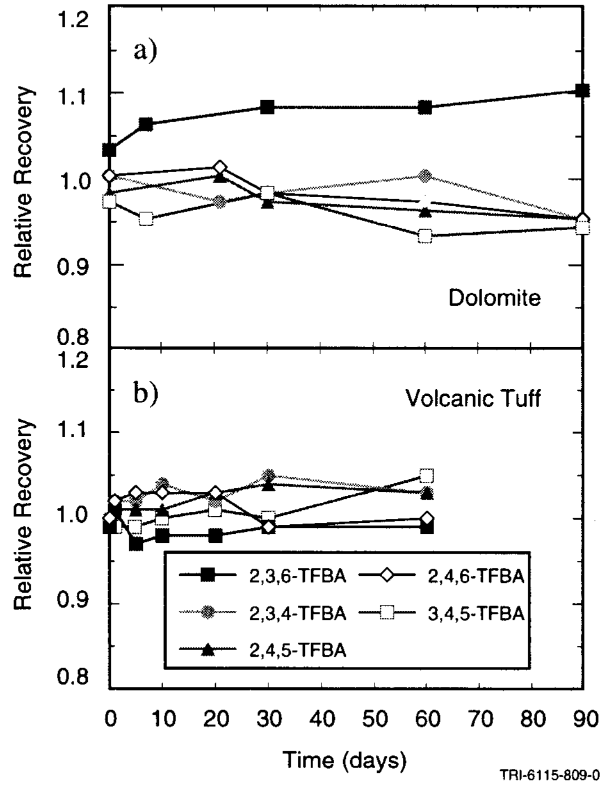

Figure H-4. Results of batch tests for trifluorobenzoates in (a) dolomite and (b) volcanic tuff.

TFMBAs, and PFBA in tuff are shown in Figure H-5b. The relative recoveries for these compounds range from 0. 96 to 1.02 (1.00 ± 0.01).

The chlorinated benzoates were batch tested only in the dolomite (Figure H-6). The relative recoveries for the DCBAs ranged from 0.92 to 1.01 (0.96 ± 0.02). 2,4-DCBA was batch tested twice. The two tests were identical except that the samples were extracted prior to HPLC analysis for one test and diluted 1:10 with DI water prior to HPLC analysis for the other test. The relative recovery for the test with extraction was 0.94 ± 0.02 and for the test with dilution was 0.98 ± 0.02. These results suggest that the lower recoveries observed for the dichlorobenzoates may be due to the extraction. The measured concentrations of 2,4,6-TCBA in the batch test and control samples at t=0 were anomalously high. All subsequent analyses of 2,4,6-TCBA in the batch test and control samples resulted in measured concentrations (1.98±0.01 ppm) quite similar to the prepared

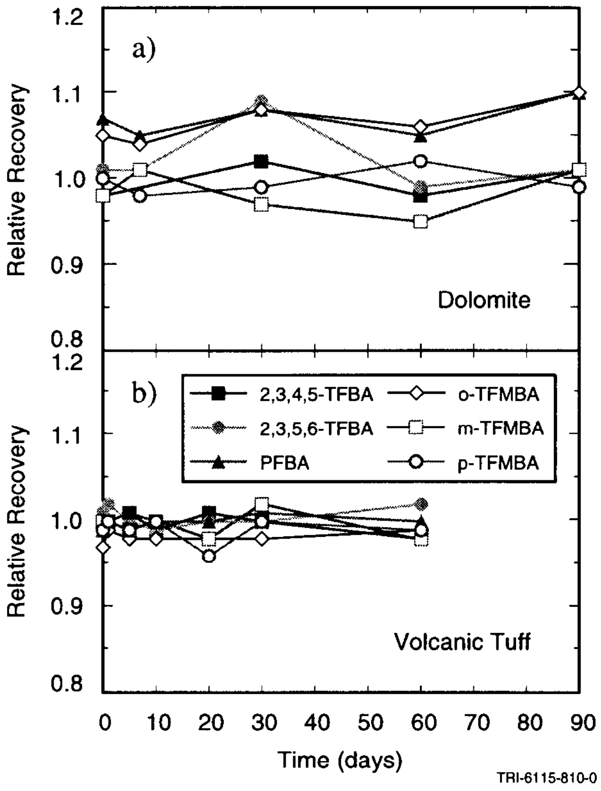

Figure H-5. Results of batch tests for tetrafluorobenzoates, pentafluorobenzoate, and trifluoromethylbenzoates in (a) dolomite and (b) volcanic tuff.

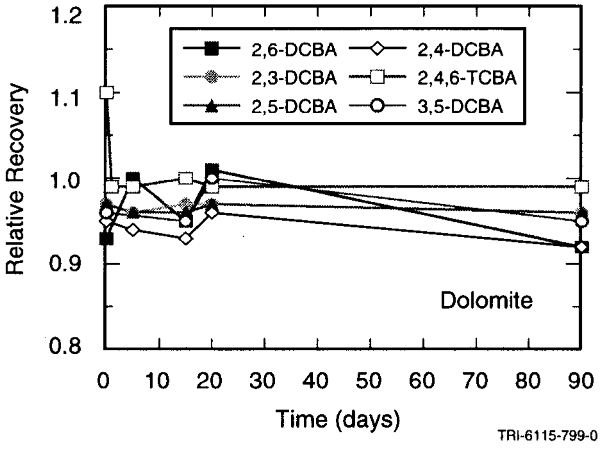

Figure H-6. Results of batch tests for chlorobenzoates in dolomite.

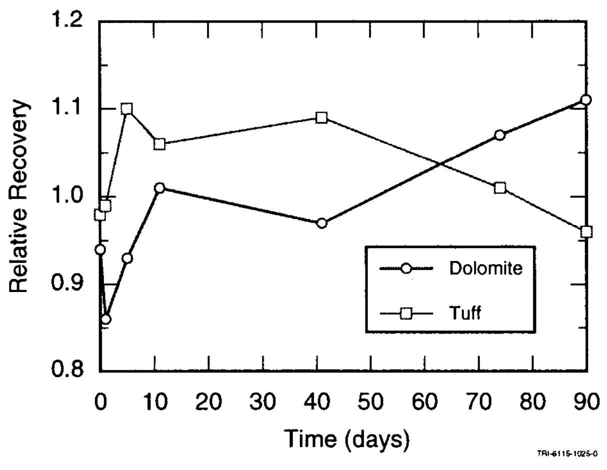

Figure H-7. Results of batch tests for iodide in dolomite and volcanic tuff.

concentration (2 ppm). Because these samples were analyzed directly, with no extraction, no loss of tracer occurred due to sample preparation. The recoveries for 2,4,6-TCBA in Figure H-6 are therefore plotted relative to the prepared concentration (2 ppm) rather than the measured concentration in the control at t=0. No significant sorption of 2,4,6-TCBA to the dolomite was observed.

The use of two different mesh sizes (28 and 400) of ground dolomite to prepare the batch-test samples did not appear to have any significant impact on the amount of sorption. The differences between the measured concentrations of each dichlorobenzoate tracer in the batch samples with different mesh sizes did not exceed the measurement variability.

The relative concentrations of iodide in both the dolomite and tuff batch samples over a 90-day period are shown in Figure H-7. A matrix effect was observed for the iodide in the Culebra brine. To eliminate this effect, all batch samples were diluted 1:100 in deionized water. The low concentration of iodide (0.2 ppm) caused some variability in quantification. This variability is observed in Figure H-7. The relative recoveries of iodide ranged from 0.86 to 1.11 (0.99±0.08) in the dolomite and from 0.96 to 1.10 (1.03±0.05) in the tuff.

In summary, the batch tests showed no measurable sorption to dolomite or tuff during the 60- to 90-day batch tests. In addition, no evidence of degradation of the benzoic acids or iodide was observed during the tests.

H.4.3 Physical Properties

Calculated and literature values for the pK_as are listed in Table H-2. The σ parameter required to calculate the pK_a for o-TFMBA was not available and, therefore, a pK_a could not be calculated for this compound. The pK_a is decreased as the number of halogens substituted on the ring is increased. Substitution on the 2 and 6 positions has the greatest acid-strengthening, pK_a-lowering, effect. Also, the pK_as for the chlorinated benzoic acids are lower in general than for the fluorinated benzoic acids. Although the pK_a values reported by Benson and Bowman (1994) are generally greater than those calculated using the Hammett equation, the trends are quite consistent. The pK_as for all compounds are less than four and, therefore, these compounds are all anionic at a pH of 6 or greater.

The solubility of the compounds investigated is greatly dependent on the properties of the water in which they are to be dissolved. The solubilities were much greater in the J-13 water than in the Culebra brine. An increased pH well above the tracer's pK_a value was required to achieve the desired concentrations for all injectate solutions. A concentration of 100 g/L was achieved in the J-13 water by increasing the pH to 14. The WIPP tests required injectate concentrations ranging from 2 to 16 g/L, depending on the type of test. The relative solubilities of these compounds were given a rating of 1 to 5 based on the following results. These ratings are listed in Table H-2. PFBA was the only tracer able to dissolve at a concentration of 100 g/L in the Culebra brine. 2,6-DFBA and 2,6-DCBA were the second-most soluble tracers; concentrations of 50 g/L were obtained through the addition of solid sodium hydroxide. These three tracers were, therefore, rated as the most soluble (1). Once the tracer was dissolved, the pH was decreased while still maintaining dissolution. The least soluble tracers were

3,4-DFBA, 2,4,5-TFBA, 2,5-DCBA, and 3,4-DCBA. The first three in this list required the addition of methanol and 1 M sodium hydroxide to first dissolve the tracer, after which Culebra brine was added to volume. One-percent solutions for 3,4-DFBA, 2,4,5-TFBA, and 2,5-DCBA (rated 4) were achieved using this method. 3,4-DCBA was not soluble at the 1% level using any of these methods. This tracer was, therefore, given a solubility rating of 5. All other tracers were soluble at least at the 1% level through either the addition of solid sodium hydroxide (rated 2) or a 1 M solution of sodium hydroxide in DI water (rated 3). The solid sodium hydroxide was preferred so that the pH adjustment was achieved in the brine with no addition of DI water. See Appendix J for additional information on tracer mixing.

The method detection limit (MDL) is dependent on the time that the compound is retained on the analytical column. In order to compare detection limits accurately, HPLC mobile-phase conditions were used that resulted in similar retention times for all compounds. The MDLs, listed in Table H-2, will increase with the higher retention times required for separation of mixtures. The detection limits may be improved with the use of acetonitrile rather than methanol in the mobile phase and a detection wavelength of 205 nm (see Appendix I).

H.4.4 Field Test

Figure H-8 shows all of the data from the 1995-96 SWIW and MWCF tracer tests conducted at the H-19 hydropad. This figure illustrates that, for any one sample collected from the pumping well, significant numbers of benzoate tracers were detected and chromatographically separated. More detailed plots of individual data sets can be found in Appendix C. A few of the tests were carried out for a long enough period of time that close to 100% of the mass was recovered. This indicates that significant irreversible sorption could not have occurred.

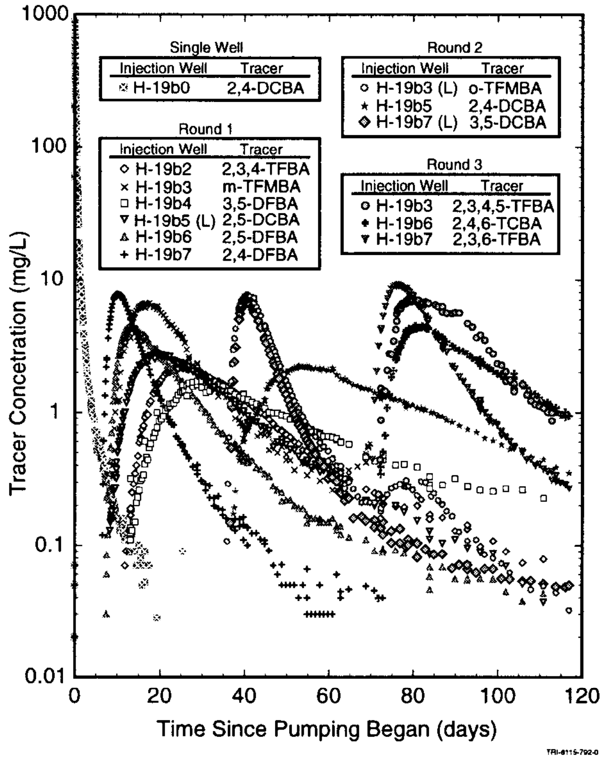

Figure H-8. Breakthrough curves for tracers used at H-19 at WIPP. Not shown are the tracers used in the less transmissive zone (2,3-DCBA, PFBA, p-TFMBA) and the tracers used in the preliminary test (2,6-DFBA, 2,3-DFBA, 2,3,4,5-Te FBA and 2,6-DCBA).

H.5 Conclusions

The fluorinated and chlorinated benzoic acids are excellent conservative tracers in environments with near neutral pH, low organic content, and small amounts of clay materials, such as the Culebra dolomite at WIPP and the Bullfrog tuff at YM. No other tracer compounds are available that could provide for the extensive testing using multiple tracers that has taken place at these sites. Although these compounds possess the necessary properties of a conservative tracer in these environments, their performance is greatly dependent on the conditions of the field testing. Adsorption of the halogenated benzoates may occur when the groundwater is acidic and when high amounts of clay or a high percentage of organic material is present. In these environments, sorption has been shown to be correlated to the tracer pK_a. Use of the tracers with a lower pKa (e.g., PFBA or 2,6-DFBA) may then become more desirable. In order to determine the potential of these tracers to sorb, laboratory studies should always be performed prior to tracer selection.

Once the conservative behavior of the tracers is established, several other properties should be considered when selecting tracers for field testing. The ability of the analytical method to separate the tracers from background interferences is essential to insure accurate quantitation. This is often difficult for those compounds that are not strongly retained on the LC column (2,6-DFBA, 2,3,5,6-TFBA, 2,3,6-TFBA, and 2,4,6-TFBA). When high concentrations are required, use of the highly soluble tracers PFBA, 2,6-DFBA, and 2,6-DCBA may be advantageous. The higher reported toxicity of the chlorinated benzoates may also make the fluorinated benzoates preferable. Because of the high solubility, low sorption potential, and low cost of PFBA and 2,6-DFBA, these compounds are considered the best of the halogenated benzoate tracers.

H.6 References

Barackman, M.L. 1986. “Diverging Flow Tracer Tests in Fractured Granite; Equipment Design and Data Collection.” M.S. thesis. Tucson, AZ: University of Arizona.

Beck, A.J., V. Lam, D.E. Henderson, K.J. Beven, G.L. Harris, K.R. Howse, A.E. Johnston, and K.C. Jones. 1995. “Movement of Water and the Herbicides Atrazine and Isoproturon Through a Large Structured Clay Soil Core,” *Journal of Contaminant Hydrology*. Vol. 19, no. 3, 237–260.

Benson, C.F., and R.S. Bowman. 1994. “Tri- and Tetrafluorobenzoates as Nonreactive Tracers in Soil and Groundwater,” *Soil Science Society of America Journal*. Vol. 58, no. 4, 1123-1129.

Benson, C.F., and R.S. Bowman. 1996. “Erratum: Tri- and Tetrafluorobenzoates as Nonreactive Tracers in Soil and Groundwater,” *Soil Science Society of America Journal*. Vol. 60, no. 6, 1780.

Bentley, H.W. 1983. “Development and Testing of Groundwater Tracers at the Waste Isolation Pilot Plant (WIPP Site), New Mexico,” *Eos Transactions, American Geophysical Union*. Vol. 64, no. 45, 714.

Bijloo, G.J., and R.F. Rekker. 1984. "Some Critical Remarks Concerning the Inductive Parameter σ_I Part III: Parametrization of the Ortho Effect in Benzoic Acids and Phenols," *Quantitative Structure-Activity Relationships in Pharmacology, Chemistry and Biology*. Vol. 3, no. 3, 91-96.

Boggs, J.M., and E.E. Adams. 1992. “Field Study of Dispersion in a Heterogeneous Aquifer 4. Investigation of Adsorption and Sampling Bias,” *Water Resources Research*. Vol. 28, no. 12, 3325-3336.

Boggs, J.M., S.C. Young, L.M. Beard, L.W. Gelhar, K.R. Rehfeldt, and E.E. Adams. 1992. “Field Study of Dispersion in a Heterogeneous Aquifer 1. Overview and Site Description,” *Water Resources Research*. Vol. 28, no. 12, 3281-3291.

Boulding, J.R. 1995. “Soil and Ground Water Tracers,” *Practical Handbook of Soil, Vadose-Zone, and Ground-Water Contamination: Assessment, Prevention, and Remediation*. Boca Raton, FL: Lewis Publishers. 439-491.

Bowman, R.S. 1984. “Analysis of Soil Extracts for Inorganic and Organic Tracer Anions via High-Performance Liquid Chromatography,” *Journal of Chromatography*. Vol. 285, no. 3, 467-477.

Bowman, R.S., and J.F. Gibbens. 1992. “Difluorobenzoates as Nonreactive Tracers in Soil and Ground Water,” *Ground Water*. Vol. 30, no. 1, 8-14.

Brusseau, M.L. 1993. “The Influence of Solute Size, Pore Water Velocity, and Intraparticle

Porosity on Solute Dispersion and Transport in Soil," *Water Resources Research.* Vol. 29, no. 4, 1071-1080.

Budavari, S., ed. 1989. *The Merck Index: An Encyclopedia of Chemicals, Drugs, and Biologicals.* 11th ed. Rahway, NJ: Merck. 170.

Caldwell, J. 1978. "Structure-Metabolism Relationships in the Amino Acid Conjugations," *Conjugation Reactions in Drug Biotransformation.* Ed. A. Aitio. New York, NY: American Elsevier Publishing Company. 111-121.

Davis, S.N., G.M. Thompson, H.W. Bentley, and G. Stiles. 1980. "Ground-Water Tracers - A Short Review," *Ground Water.* Vol. 18, no. 1, 14-23.

Fahy, M.F. 1997. "Dual-Porosity Analysis of Conservative Tracer Testing in Saturated Volcanic Rocks at Yucca Mountain in Nye County, Nevada," *International Journal of Rock Mechanics and Mining Sciences.* Vol. 34, no. 3/4, 486.

Glaser, J.A., D.L. Foerst, G.D. McKee, S.A. Quave, and W.L. Budde. 1981. "Trace Analyses for Wastewaters," *Environmental Science and Technology.* Vol. 15, no. 12, 1426–1435.

Hager, G.P., and E.B. Starkey. 1943. "Studies on the Mechanism of the Antifungal Action of Benzoate," *Journal of American Pharmaceutical Association.* Vol. 32, 44-49.

Howard, K.M. 1997. "Behavior of Fluorobenzoic Acid Groundwater Tracers in a Highly Fractured Shale Saprolite." M.S. thesis. Knoxville, TN: The University of Tennessee, Knoxville.

Jaynes, D.B. 1994. "Evaluation of Fluorobenzoate Tracers in Surface Soils," *Ground Water.* Vol. 32, no. 4, 532-538.

Jones, T.L. 1991. "The Detection and Evaluation of Fluorescent Brighteners as Organic Tracers in Alkaline Groundwaters." M.S. thesis. Las Vegas, NV: University of Nevada, Department of Chemistry.

Jones, T.L., V.A. Kelley, J.F. Pickens, D.T. Upton, R.L. Beauheim, and P.B. Davies. 1992. *Integration of Interpretation Results of Tracer Tests Performed in the Culebra Dolomite at the Waste Isolation Pilot Plant Site.* SAND92-1579. Albuquerque, NM: Sandia National Laboratories.

Kilgore, W.W., and M-Y. Li. 1980. "Food Additives and Contaminants," *Casarett and Doull's Toxicology: The Basic Science of Poisons.* 2nd ed. Eds. J. Doull, C.D. Klaassen, and M.O. Amdur. New York, NY: Macmillan. 593-607.

Maldonado, F., and B.P. Hausback. 1990. *Geologic Map of the Northeast Quarter of the Bullfrog 15-Minute Quadrangle, Nye County, Nevada.* Miscellaneous Investigations Series, Map I-2049. Denver, CO: U.S. Geological Survey.

McCray, J.G., E.A. Nowatzki, K.J. Stetzenbach, and G. Armstrong. 1985. *Low-Level Nuclear Waste Shallow Land Burial Trench Isolation. Final Report October 1981-September 1984.* NUREG/CR-4194. Tucson, AZ: University of Arizona for U.S. Nuclear Regulatory Commission, Washington, DC.

Neal, R.A. 1980. "Metabolism of Toxic Substances," *Casarett and Doull's Toxicology: The Basic Science of Poisons.* 2nd ed. Eds. J. Doull, C.D. Klaassen, and M.O. Amdur. New York, NY: Macmillan. 56–69.

Nicholson, R.V., J.A. Cherry, and E.J. Reardon. 1983. "Migration of Contaminants in Groundwater at a Landfill: A Case Study. 6. Hydrogeochemistry," *Journal of Hydrology.* Vol. 63, no. 1-2, 131-176.

Pearson, R.J., W.P. Inskeep, J.M. Wraith, S.D. Comfort, and H.M. Gaber. 1996a. "Observed and Simulated Solute Transport Under Varying Water Regimes: I. Bromide and Pentafluorobenzoic Acid," *Journal of Environmental Quality.* Vol. 25, no. 4, 646-653.

Pearson, R.J., W.P. Inskeep, J.M. Wraith, H.M. Gaber, and S.D. Comfort. 1996b. "Observed and Simulated Solute Transport Under Varying Water Regimes: II. 2,6-Difluorobenzoic Acid and Dicamba," *Journal of Environmental Quality.* Vol. 25, no. 4, 654-661.

Perrin, D.D., B. Dempsey, and E.P. Serjeant. 1981. *pK_a Prediction for Organic Acids and Bases.* New York, NY: Chapman and Hall.

Reimus, P.W., and M.J. Haga. 1999. *Analysis of Tracer Responses in the BULLION Forced-Gradient Experiment at Pahute Mesa, Nevada.* LA-13615-MS. Los Alamos, NM: Los Alamos National Laboratory.

Sabatini, D.A., and T.A. Austin. 1991. "Characteristics of Rhodamine WT and Fluorescein as Adsorbing Ground-Water Tracers," *Ground Water.* Vol. 29, no. 3, 341-349.

Seaman, J.C. 1998. "Retardation of Fluorobenzoate Tracers in Highly Weathered Soil and Groundwater Systems," *Soil Science Society of America Journal.* Vol. 62, no. 2, 354-361.

Stetzenbach, K.J., S.L. Jensen, and G.M. Thompson. 1982. "Trace Enrichment of Fluorinated Organic Acids Used as Ground-Water Tracers by Liquid Chromatography," *Environmental Science & Technology.* Vol. 16, no. 5, 250-254.

Stewart, C.P., and A. Stolman, eds. 1960. *Toxicology: Mechanisms and Analytical Methods.* New York, NY: Academic Press. Vol. 1, 113.

Strong, L.E., C. Van Waes, and K.H. Doolittle, II. 1982. "Ionization of Five Aqueous Fluorobenzoic Acids: Conductance and Thermodynamics," *Journal of Solution Chemistry.* Vol. 11, no. 4, 237-258.

Strong, L.E., C.L. Brummel, and P. Lindower. 1987. "Thermodynamics of the Ionization of our Difluorobenzoic and Pentafluorobenzoic Acids in Water," *Journal of Solution Chemistry.* Vol. 16, no. 2, 105-124.

Thompson, G.M., and K.J. Stetzenbach. 1980. *Assessment and Advances in Tracer Technology, A Topical Report to the Nuclear Regulatory Commission.* Tucson, AZ: Department of Hydrology and Water Resources, University of Arizona. (Copy on file in the Sandia WIPP Central Files (SWCF) as ERMS #208069.)

Tucker, W.A., and L.H. Nelken. 1982. "Diffusion Coefficients in Air and Water," *Handbook of Chemical Property Estimation Methods: Environmental Behavior of Organic Compounds.* Eds. W.J. Lyman, W.F. Reehl, and D.H. Rosenblatt. New York, NY: McGraw-Hill. 17-1 through 17-25.

Umari, A.M.J., M.F. Fahy, and J.D. Earle. 1998. "Appendix B: Tracer Tests in the Prow Pass Tuff, June to September 1998, Yucca Mountain, Nye County, Nevada," *Results and Interpretations of Hydraulic and Tracer Testing in the Prow Pass Tuff at the C-holes.* P.W. Reimus, A. Adams, M.J. Haga, A. Humphrey, T. Callahan, I. Anghel, and D. Counce. Yucca Mountain Project Milestone SP32E7M4. Los Alamos, NM: Los Alamos National Laboratory. (Unpublished Draft Milestone in the SWCF as ERMS #509444.)

Walter, G.R. 1982. *Theoretical and Experimental Determination of Matrix Diffusion and Related Solute Transport Properties of Fractured Tuffs from the Nevada Test Site.* LA-9471-MS. Los Alamos, NM: Los Alamos National Laboratory.

Wilson, J.L., and W.R. Linderfelt. 1995. "Field Tracer Experiment Design Problems at the Borden Site," *Proceedings from the 2nd Tracer Workshop, University of Texas at Austin, November 14-15, 1994.* IFE/KR/E-95/002. Eds. T. Bjørnstad and G.A. Pope. Kjeller, Norway: Institute for Energy Technology. 11-21.

This page intentionally left blank.

Appendix I
Liquid Chromatographic Separations of Fluoro- and Chlorobenzoates Used as Groundwater Tracers

By Irene M. Farnham[1], Jeanette M. Daniels[1], Martha E. Dominguez[1], Kazumasa Lindley[1], Klaus J. Stetzenbach[1], and Lucy C. Meigs[2]

Abstract

New reversed-phase high-performance liquid chromatographic (RP-HPLC) conditions were developed to obtain separation of 20 halogenated benzoates. The availability of the large number of fluoro- and chlorobenzoates along with the methodology for their simultaneous analysis make them excellent candidates for use as groundwater tracers. These compounds are especially useful for complex tracer tests that use multiple tracers in multiple wells, such as those performed at the H-19 hydropad at the Waste Isolation Pilot Plant (WIPP) site in New Mexico. A total of 18 separate halogenated benzoate tracers, along with iodide, were used for a series of single-well injection-withdrawal (SWIW) and multiwell convergent-flow (MWCF) tests. All samples were collected from a single well. Consequently, the samples contained tracers injected during all phases of the test up to the sample time.

Separation methodologies for these compounds in brine were developed using SUPELCOSIL LC-18 and LC-abz columns. Data quality is clearly improved when samples are analyzed within a short period of time, assuring minimal variability in chromatographic conditions. In small tests, selecting a subset of samples and re-analyzing over a short period of time allows for quantification using a minimum number of calibration curves and optimal conditions for the analyses.

I.1 Introduction

Halogenated benzoates have been used as groundwater tracers in many hydrological environments (Bowman, 1984; Bowman and Gibbens, 1992; Benson and Bowman, 1994; Jaynes, 1994). These compounds generally do not sorb to aquifer materials and are quite stable in groundwater, making them desirable for use as groundwater tracers. Also, solubilities of up to 100,000 mg/L in water and detection limits in the low μg/L levels have been achieved for these compounds (Appendix H and Bowman, 1984), allowing the use of these tracers for tests where high levels of dilution are anticipated. The primary advantage of the halogenated benzoic acids as groundwater tracers is the availability of the numerous isomers that can potentially be separated chromatographically. The ability to analyze several tracer compounds within one sample allows for the design of tracer tests with numerous tracer injections into several wells. The amount of information that can be extracted from a tracer test is greatly dependent on the quality of the analytical data. Methods to separate and analyze all of the tracers used in a given test are, therefore, crucial.

Several chromatographic techniques have been used for the analysis of halogenated benzoic acids. These compounds are readily analyzed using reversed-phase high-performance liquid chromatography (RP-HPLC) with a mobile phase of

---

[1] University of Nevada at Las Vegas, Harry Reid Center for Environmental Studies, 4505 Maryland Parkway, Las Vegas, NV 89154-4009. Email: farnham@nevada.edu.

[2] Sandia National Laboratories, Geohydrology Department, P.O. Box 5800, MS-0735, Albuquerque, NM 87185-0735.

phosphate buffer and methanol (Stetzenbach et al., 1982). With RP-HPLC, most of the inorganic ions often present at high background levels in the groundwater samples are not retained on the column and, therefore, do not interfere with the halogenated benzoates. This allows for the direct injection of groundwater samples containing high concentrations of salts (e.g., brine solutions). The greatest number of halogenated benzoic acids successfully separated in a single HPLC analysis prior to the work reported here was achieved by Elrod et al. (1993). Twelve halogenated benzoates, which are key intermediates or impurities in the synthesis of fluoroquinoline antibacterial agents, were separated using RP-HPLC with an ion-pair reagent (Elrod et al., 1993). Anion-exchange HPLC conditions have been developed that provided for the separation of three suites of benzoates: 1) six tri- and tetra-substituted benzoates (Benson and Bowman, 1994); 2) four difluorobenzoates (DFBAs) (Bowman and Gibbens, 1992); and 3) m-trifluoromethyl benzoic acid (m-TFMBA), pentafluorobenzoic acid (PFBA), o-trifluoromethyl benzoic acid (o-TFMBA), and 2,6-difluorobenzoic acid (2,6-DFBA), along with bromide, iodide, and thiocyanate (Bowman, 1984). Simultaneous analysis of all benzoates in the three suites was not achieved. Analysis of o-TFMBA, 2,6-DFBA, and PFBA was achieved with a run time of less than five minutes using ion chromatography (Pearson et al., 1992). Although gas chromatographic methods for a few of these compounds are available, a solvent exchange followed by derivitization is required to analyze water samples (Edgell et al., 1993; Han, 1998).

In this study, the current methodology for analysis of halogenated benzoates by HPLC was expanded in support of the 1995-96 tracer tests conducted at the H-19 hydropad at the WIPP Site (see Chapter 3 for a detailed description of this test). For these tests, 21 tracer injections, using 18 different halogenated benzoates, were performed in a total of seven wells in six phases (the SWIW and MWCF injection for the 4-well test and the SWIW and three rounds of MWCF injections for the 7-well test). The halogenated benzoates are the only tracers that can support testing that requires such a large number of tracers. Water samples were collected from a central pumping well and contain tracers injected during all phases of the test up to the sample time. A particular challenge of this tracer test was the high dissolved solids content of the native Culebra groundwater, which is a sodium-chloride brine solution with sodium and chloride concentrations exceeding 10,000 mg/L. In the Culebra water, sulfate concentrations exceed 4,000 mg/L, calcium and magnesium are present at approximately 1,000 mg/L levels, and bromide concentrations are approximately 30 mg/L. New chromatographic techniques were, therefore, required for the analysis of the benzoates in brine.

RP-HPLC appears to offer the best selectivity for these compounds (Elrod et al., 1993) and was, therefore, used for this study. This technique also allows for the direct injection of brine solutions. RP-HPLC conditions were developed that provide for the separation of 20 of the 24 commercially available halogenated benzoic acids. Separation methods were also developed to optimize quantification of the tracers injected during each phase of the test. This involved maximizing the separation of each tracer in the shortest possible run time while minimizing interferences from previously injected tracers.

In addition to optimizing separation of the tracers used for a given portion of the test, optimizing sensitivity is important. Dilutions of several orders of magnitude often occur between the injection well and the sampling well. Maximizing sensitivity may then become crucial to quantify the tracer compounds accurately. The detection wavelength is important when optimizing sensitivity. Bowman (1984) demonstrated that significantly higher sensitivity is observed using a detection wavelength of 205 nm when compared to higher wavelengths. He selected this wavelength to maximize the response of the halogenated benzoates, bromide, and iodide while minimizing the response of chloride, nitrate, and nitrite using a mobile phase of potassium dihydrogen phosphate (KH_2PO_4) buffer and 10% acetonitrile. Increasing the injection volume may result in higher sensitivity for these compounds (Bowman, 1984), but may also result in much broader chromatographic peaks. Consequently, this peak broadening may negate any advantage in sensitivity gained by increasing the injection volume.

This appendix describes the methodology used for analyzing the groundwater tracer samples collected during the 7-well test at the H-19 hydropad, discusses a portion of the test results, and makes recommendations regarding future testing.

I.2 Experimental Information

I.2.1 Instrumentation

All analyses were performed using a Spectra-Physics SP8800-010 HPLC with a SpectraPhysics SP8880 autosampler and a SpectraSYSTEM UV3000 Detector, or a SpectraSYSTEM P2000 HPLC with a SpectraSYSTEM AS1000 autosampler and SpectraSYSTEM UV1000 detector. The analytical column used for the majority of the work was a SUPELCOSIL LC-18 column (Supelco, Chromatographic Products, Bellefonte, PA). A second column, SUPELCOSIL LC-abz column was also used. Both columns are silica-based reversed-phase columns (15 cm x 4.6 mm) with 5-µm particle size. The mobile phase for all analyses consisted of either methanol (HPLC Grade, Burdick & Jackson) or acetonitrile (HPLC Grade, Burdick & Jackson) and 0.05-M KH_2PO_4 (Ultrapure, J.T. Baker) adjusted to a pH of 2.7 with H_3PO_4. The injection volume varied from 20 µL to 100 µL. A detection wavelength of 230 nm was used for sample analyses.

I.2.2 Chemicals

The halogenated benzoates used for the laboratory studies were purchased from Aldrich Chemical Company, Inc. (Milwaukee, WI). Chemical purities were $\geq$97% according to the manufacturer. Bulk tracers used for field testing were purchased from Fluorochem (Old Glossop, England).

I.2.3 Quality Assurance / Quality Control

All aspects of data collection and analysis were performed under stringent QA/QC requirements. Because standards traceable to the National Institute of Standards and Technology (NIST) are not available for the halogenated benzoates, the calibration standards for these compounds were prepared from the bulk chemical used to prepare the tracer-injectate solutions. The tracer concentrations in each of the field samples (C) as well as in the injectate solutions (C_o) were quantified based on these standards. Breakthrough curves were then generated from the field data as a plot of C/C_o or C as a function of time. In most cases, the instruments used for the analyses were calibrated daily using three to five calibration standards. The concentrations of the calibration standards were generally 0.1, 0.5, 1, 5, and 10 mg/L. The linear correlation coefficients for all calibrations were at least 0.995. A minimum of one in twenty samples was analyzed in duplicate. The duplicate concentrations agreed within ±20% except when near the detection limit. Calibration check standards were also frequently analyzed to insure that the instrument response did not drift during the analysis period. One criterion of the analysis that proved difficult to meet was that the response for the middle concentration standard agree with the response for the initial calibration (the first analysis of the suite of tracers) to within 10%. This criterion was used to ensure consistent chromatography throughout the analysis period as well as stability of the calibration standards. Blind duplicate samples were also analyzed. The blind duplicates were identified as either a blind sample or were given a fictitious sample identification.

I.3 Results and Discussion

I.3.1 Chromatographic Separation – Preliminary Studies

RP-HPLC conditions that provide separation of 20 of the 24 commercially available halogenated benzoate tracer compounds were developed for the LC-18 column. A chromatogram of a standard mix containing 24 of the commercially available compounds at 5 mg/L is shown in Figure I-1. Although co-elution of tracer compounds is observed in four cases, the potential to separate 20 of these compounds is apparent. Due to the difficulty of

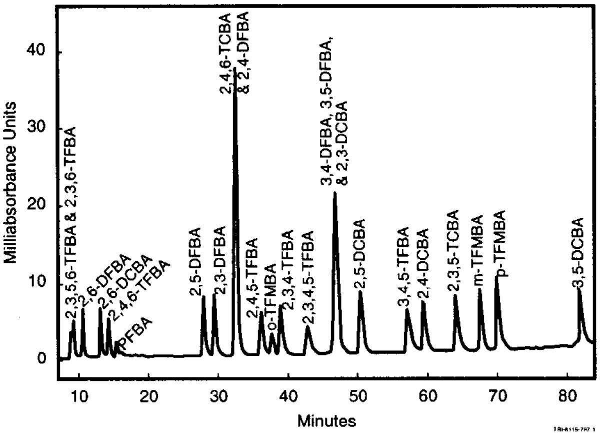

Figure I-1. Chromatogram demonstrating the ability to separate 20 benzoate tracers using the LC-18 column. (95% KH_2PO_4: 5% methanol to 35% KH_2PO_4: 65% methanol over 100 minutes. Flowrate = 1.4 mL/min, Injection volume = 10 μL)

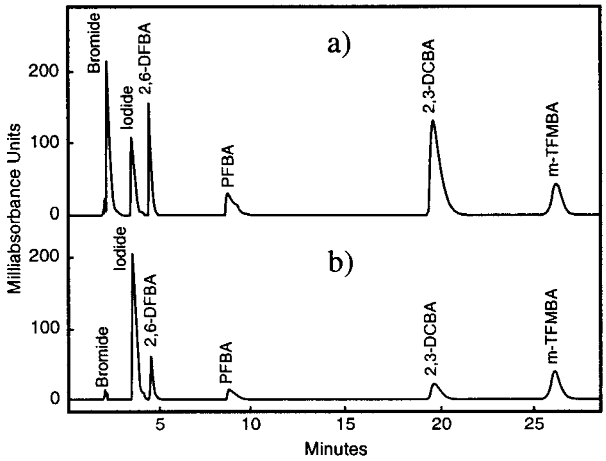

Figure I-2. Chromatogram demonstrating the ability to analyze selected benzoate tracers, bromide, and iodide simultaneously using the LC-abz column and detection wavelengths of a) 205 nm and b) 230 nm. (30% acetonitrile and 70% KH_2PO_4. Flowrate = 1 mL/min, Injection volume = 100 μL)

chromatographic separation, the following combinations of tracers should not be used in the same tracer test if possible: 2,3,5,6-TeFBA and 2,3,6-TFBA; 2,4,6-TCBA and 2,4-DFBA; and 2,3-DCBA, 3,4-DFBA, and 3,5-DFBA.

Lower selectivity, which limits the number of benzoates that can be analyzed simultaneously, was observed for the LC-abz column when compared to the LC-18 column. The LC-abz column is designed specifically for acids and bases (Supelco, 1991). A unique deactivation technique used for preparation of the LC-abz column gives it a different elution order and longer retention times for the halogenated benzoates. In addition to the longer retention of the benzoates, some inorganic anions are also retained on this column allowing for the simultaneous analysis of iodide, bromide, and the benzoates. Though bromide analysis on this column has not been substantially evaluated, successful analysis of iodide has been achieved (Figure C-31). Two chromatograms obtained with the LC-abz column for a 5-mg/L standard mix containing bromide, iodide, and four benzoates (2,6-DFBA, 2,3-DCBA, m-TFMBA, and PFBA) using detection wavelengths of 205 and 230 nm are shown in Figure I-2. In agreement with Bowman (1984), a substantial increase in sensitivity is observed for 2,3-DCBA, 2,6-DFBA, PFBA, and bromide when the detection wavelength is decreased from 230 to 205 nm (Figure I-2). In fact, bromide was not detected at a wavelength of 230 nm. Use of a detection wavelength of 230 nm may, therefore, be preferred when high concentrations of bromide are present in the background (e.g., brine solutions). Only slight improvement in sensitivity is observed for m-TFMBA when the wavelength is decreased from 230 to 205 nm. The sensitivity of iodide is greater with a detection wavelength of 230 nm.

The optimal detection wavelength is dependent on the mobile phase. An acetonitrile mobile phase was used to generate the chromatogram in Figure I-2. The ultraviolet (UV) cut-off wavelength for acetonitrile is 190 nm and, therefore, low UV absorbence is observed at the 205-nm wavelength. Because the cutoff wavelength of methanol is 205 nm, substantial background noise is observed at a detection wavelength of 205 nm when methanol is used in the mobile phase. Noise is further increased with mobile-phase mixing and gradient conditions. For this reason, a higher detection wavelength (e.g., 230 nm) is required when methanol is used as the mobile phase.

I.3.2 Field Studies

For the H-19 tracer tests, a primary requirement for the analysis methodology was the ability to separate all of the halogenated benzoate tracers used for all phases of testing. The emphasis of chromatographic method development was on optimizing separation and not sensitivity. The LC-18 column and a mobile phase consisting of methanol and 0.05-M KH_2PO_4 (pH 2.7) were, therefore, used for the majority of the sample analyses. Not only does the LC-18 column offer excellent selectivity (Figure I-1), but most of the inorganic anions are not retained on this column. Potential interferences from the brine solutions are, therefore, reduced. Although sensitivity for the halogenated benzoates is greater at a detection wavelength of 205 nm, use of a higher wavelength (230 nm) was necessary to allow for methanol in the mobile phase.

Separate chromatographic conditions were developed for the tracers used in each of the phases of the field test. The proportions of methanol and the KH_2PO_4 buffer solution varied depending on the suite of tracers being analyzed. The selection of tracers for use during each test phase was based primarily on the availability of tracers at the time of the scheduled injection rather than on the best analytical properties. In some cases, tracers that were difficult to separate chromatographically were included in the same round of injections. The performance of the benzoate tracers is demonstrated through the evaluation of both the chromatography used to separate the tracers in each of the phases of the field tests and also the resulting breakthrough curves.

I.3.2.1 SWIW and Round 1 of the H-19 7-Well Test

A total of eight tracers (2,5-DFBA, 2,4-DFBA, 2,3,4-TFBA, 2,3-DCBA, 3,5-DFBA, 2,5-DCBA, 2,4-DCBA, and m-TFMBA) were used for the SWIW and Round 1 injections of the H-19 7-well test (see Chapter 3 and Figure H-7 for additional details regarding this test). For the SWIW test, 2,4-DCBA was injected into H-19b0 and then withdrawn from H-19b0 after approximately 18 hr. The concentration of this tracer peaked at approximately 900 mg/L and decreased to below its detection limit after approximately 15 days. The other tracers were injected into each of six outer wells and withdrawn from the central sampling well (H-19b0) as part of the MWCF test. In one well, the upper (lower transmissivity) and lower (higher transmissivity) Culebra were packed off and separate injections were made into each zone. The tracer 2,3-DCBA was injected into the zone of lower transmissivity (upper Culebra). The concentration of this tracer never exceeded 0.4 mg/L in the sampling well.

Determining chromatographic conditions for this suite of tracers was particularly difficult due to the presence of the two often co-eluting compounds 2,3-DCBA and 3,5-DFBA. Three tracers (2,3-DFBA, 2,6-DFBA, and 2,3,4,5-TFBA) were present in the samples from the previously conducted 4-well tracer test and, therefore, separation from these compounds was also required. A chromatogram of a sample collected nine days after the injection of most tracers is shown in Figure I-3a. The highly concentrated ions in the brine water elute much earlier than the benzoates using this LC-18 column (see Figure I-3a).

Near real-time sample analysis was required in order to determine when the next round of injections should begin. Samples were, therefore, analyzed as soon as possible following collection. This was primarily important from the time of tracer injection to the time at which the peak concentration was observed at the withdrawal well. During this time, samples were collected frequently and analyzed in sets consisting of only a few days worth of samples. Once the tracer concentration reached its peak at the pumping well, sampling frequency was decreased and samples collected over a period of a week to several weeks were then analyzed together in sets. New calibration curves were generated for quantification of each set of samples. Because of this, tracers were quantified using many different calibration curves. Excellent reproducibility of the chromatogram, shown in Figure I-3a, was observed over time. The percent relative standard deviations (%RSD) for the peak areas of each compound in the 5-mg/L calibration standard over a 10-month period are as follows: 2,5-DFBA (3%), 2,4-DFBA (0.6%), 2,3,4-TFBA (1.5%), 2,3-DCBA (18%), 3,5-DFBA (7%), 2,5-DCBA (5%), 2,4-DCBA (4%), and m-TFMBA (4%). A higher %RSD was observed for the three compounds that are least separated (2,3-DCBA, 3,5-DFBA, and 2,5-DCBA).

The quality of separation in the chromatogram is also reflected in the corresponding breakthrough curves (Figure I-3b). These curves summarize the results from the analyses of approximately 130 samples (including duplicate and blind duplicate samples) collected over 105 days. Very smooth breakthrough curves are observed for the two tracers with the best chromatographic separation (2,4-DFBA and 2,5-DFBA). Some noise is present in the peak of the breakthrough curve for 2,3,4-TFBA. This noise is the result of one day's analyses when 2,3,4-TFBA concentrations for all samples analyzed were approximately 2 to 5% greater than those measured in previous analyses. Increased noise was also observed for 3,5-DFBA due to the difficulty of separating the higher concentrations (5 mg/L and 10 mg/L) of 2,3-DCBA and 3,5-DFBA in the calibration standards (Figure I-3a). Separation of these two compounds in the field samples was not as difficult due to the low concentrations observed for 2,3-DCBA (not plotted in Figure I-3b due to low recovery). Unfortunately, the behavior of 2,3-DCBA, which was injected into the upper Culebra (low transmissivity) was not known prior to the test (see Chapter 3). Preparation of calibration standards that reflected this difference in concentration between these two compounds would have been preferable. Ideally, rather than using calibration standards that contain the same concentration of each of the tracers, standards would be prepared that bracket the actual concentrations of the tracers in the samples. For instance, the highest concentration calibration standard may contain 0.5 mg/L 2,3-DCBA, 2 mg/L 3,5-DFBA, and 3 mg/L 2,5-DCBA instead of the same 5 mg/L of each. Similar chromatography between the calibration standards and the samples would, therefore, have been achieved.

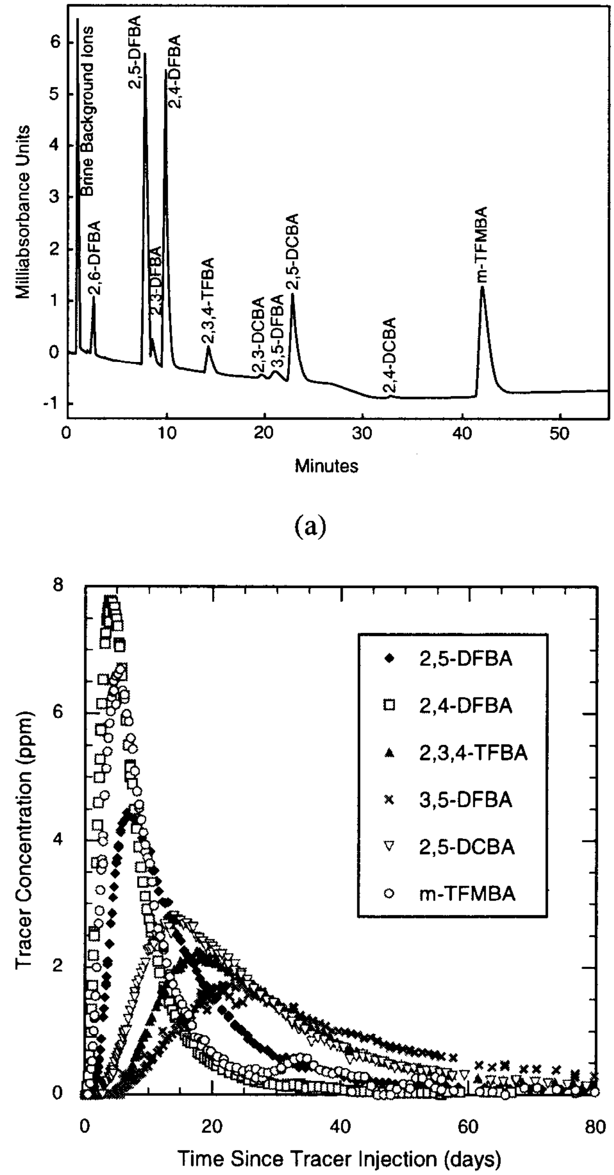

(a)

(b)

Figure I-3. (a) Chromatogram for a well sample containing the tracers injected during Round 1 of the H-19 7-well test. (75% KH_2PO_4: 25% methanol to 70% KH_2PO_4: 30% methanol over 25 minutes (held for 2 minutes) and then to 65% KH_2PO_4: 35% methanol over 3 minutes (held for 25 minutes). Flowrate = 2 mL/min, injection volume = 20 μL. (b) Breakthrough curves summarizing the results for Round 1 of the H-19 7-well tracer test.

Data quality is further demonstrated by the results of the blind duplicate analyses. The concentrations of each tracer in eight sets of field samples and the equivalent blind duplicates are listed in Table I-1. For each tracer, the concentrations measured in the samples are shown in the first row (a) and those for the blind duplicate are shown in the second row (b). The concentrations of the tracers in the blind duplicates generally agree to within less than 5% with the samples. Larger percent differences are observed for the tracers that are not chromatographically resolved, or are present at low concentrations.

I.3.2.2 Round 2 of the H-19 7-Well Test

Five additional tracers (PFBA, o-TFMBA, 2,4-DCBA, p-TFMBA, and 3,5-DCBA) were injected during Round 2 of the test once the concentrations of most of the tracers injected during Round 1 had decreased significantly from their peak value (see Figure H-7). The concentration of 2,4-DCBA injected for the SWIW test had fallen below the detection limit prior to the start of injection for Round 2 and, therefore, it was re-used. Tracers used for previous MWCF tests were still present at levels up to 1.6 mg/L. The HPLC conditions were optimized to provide the most rapid run time while maintaining the best separation possible for the five tracers. A 5-mg/L standard containing each of these tracers in the brine was prepared and analyzed with each set of samples. Chromatograms of the 5-mg/L standard in both the brine and in deionized (DI) water are shown in Figure I-4a. Although the retention times of the later eluting compounds are slightly shifted, the responses for the standards in brine and DI water are quite similar. Low percent differences in the peak areas (1 to 3%) for each tracer were observed between the two sample matrices (brine versus DI water). This shows that no significant matrix effect is observed for these tracers in brine water. Separation of the benzoates from the high concentration of background ions in the brine water is also demonstrated in Figure I-4a.

The breakthrough curves resulting from the analysis of approximately 100 samples (including duplicates, and blind duplicates) are shown in Figure I-4b. The smoothness of these breakthrough curves demonstrates the high precision of the analytical measurements. The %RSDs for the peak areas of each compound in the 5-mg/L calibration standard over an 8-month period are as follows: PFBA (4.3%), o-TFMBA (3.2%), 2,4-DCBA (2.0%), p-TFMBA (2.6 %), and 3,5-DCBA (6.5%). A higher variability was observed in the chromatographic response for the later eluting compound (3,5-DCBA) due to the poor chromatographic behavior of this compound using these mobile-phase conditions. This variability, which can be seen in the observed breakthrough curve (Figure I-4b), resulted in difficulties meeting the QA requirements (20% agreement

Table I-1. Tracer Concentrations in (a) Samples and (b) Blind Duplicates

Tracer	1	2	3	4	5	6	7	8
2,5-DFBA (a)	0.06, 0.23	1.75	2.10, 2.05	4.17	4.44, 4.39, 4.41	3.65	2.80, 2.79	1.67, 1.70
(b)	0.08	1.71	2.05	4.13	4.41	3.83	3.03	1.71
2,4-DFBA (a)	2.56, 2.51	7.60	7.78, 7.45	6.71	5.00, 5.02, 5.19	2.56	1.44, 1.45	0.57, 0.55
(b)	2.50	7.52	7.60	6.59	5.15	2.63	1.61	0.58
2,3,4-TFBA (a)	<DL, <DL	<DL	<DL, <DL	<DL	0.17, 0.18, 0.19	0.90	1.57, 1.57	2.14, 2.25
(b)	<DL	<DL	<DL	0.07	0.17	0.92	1.65	2.16
2,3-DCBA (a)	<DL	<DL	<DL, 0.07	<DL	0.06, 0.10, <DL	0.14	0.04, 0.03	0.07, <DL
(b)	<DL	<DL	<DL	0.07	0.11	0.13	0.12	0.12
3,5-DFBA (a)	<DL, <DL	<DL	<DL, <DL	<DL	0.12, 0.14, 0.11	0.41	0.76, 0.77	1.54, 1.42
(b)	<DL	<DL	<DL	<DL	0.32	0.60	1.00	1.60
2,5-DCBA (a)	<DL, <DL	0.34	0.42, 0.37	1.01	1.59, 1.53,1.61	2.50	2.80, 2.79	2.24, 2.33
(b)	<DL	0.27	0.32	0.99	1.53	2.49	2.81	2.24
m-TFMBA (a)	<DL, <DL	3.63	4.08, 3.99	6.59	6.25, 6.24, 6.22	3.83	2.28, 2.32	0.83, 0.81
(b)	<DL	3.54	3.64	6.14	6.29	3.93	2.35	0.76

between duplicates and 10% agreement between each of the calibrations and the initial calibration). A subset of the samples was, therefore, re-analyzed for 3,5-DCBA using HPLC conditions that resulted in the elution of this compound at approximately four minutes (see Figure I-5). Because these later analyses were accomplished in three days, only three calibrations were required. The %RSD for the 5-mg/L calibration standard of the three calibrations (two injections each) was only 1.2% compared to the 6.5%RSD previously observed. Although an asymmetric chromatographic peak was observed for the HPLC conditions used for the re-analyses (Figure I-5a), excellent reproducibility in multiple measurements of the same sample was observed due to the very similar chromatographic conditions used to quantify this compound in all samples. The resulting breakthrough curve for the re-analysis of 3,5-DCBA is shown in Figure I-5b.

I.4 Conclusions

RP-HPLC with UV detection is effective for the analysis of the chloro- and fluorobenzoates as groundwater tracers in brine solutions. Two reversed-phase columns (LC-18 and LC-abz) were evaluated. The LC-18 column was used for maximum selectivity. Twenty of the 24 commercially available benzoate tracers can be separated using this column (Figure I-1). Most of the inorganic ions present in the brine solution are not retained on this column (Figures I-3a and 4a), thus reducing potential background interferences. Although a lower selectivity is observed for the LC-abz column, this column may be used for the simultaneous analysis of selected benzoate tracers along with iodide and possibly bromide.

The quality of the breakthrough curves is quite dependent on the ability to baseline-resolve each of the tracers used for a given round of injections. The shape of the tracer-breakthrough curves is difficult to predict prior to field testing. Frequent collection of samples is, therefore, required for accurate definition of the breakthrough curves. The tracer-breakthrough curves observed for the H-19 tracer tests generally increased rapidly until the concentrations reached a maximum, and then

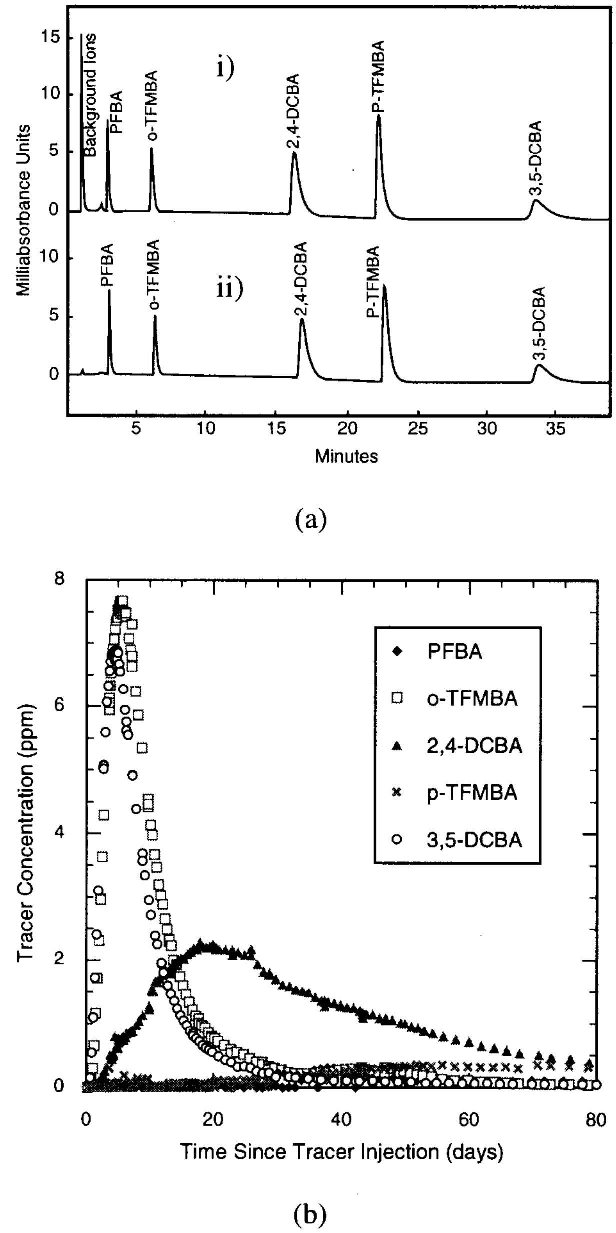

Figure I-4. **(a) Chromatogram for the 5-mg/L calibration standard containing the tracers injected during Round 2 of the H-19 7-well tracer test in Culebra brine (*i*) and DI water (*ii*). (60% KH_2PO_4: 40% methanol to 70% KH_2PO_4: 30%; methanol (held for 13 minutes) to 50% KH_2PO_4: 50% methanol over 7 minutes (held for 25 minutes). Flowrate = 1.5 mL/min, Injection volume = 20 μL).**
(b) Breakthrough curves summarizing the results for Round 2 of the H-19 7-well tracer test.

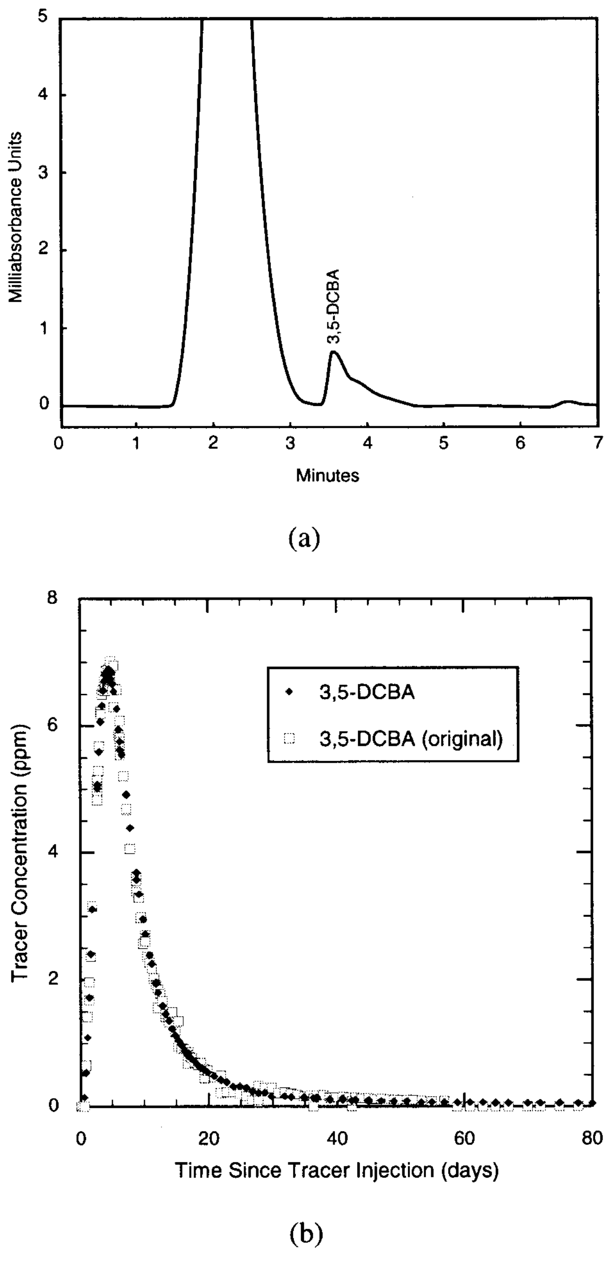

Figure I-5. (a) Chromatogram for a well sample containing the tracers injected during Round 2 of the H-19 7-well tracer test with conditions optimized for early elution of 3,5-DCBA. (25% KH_2PO_4: 75% methanol for 7 minutes. Flowrate = 1 mL/min, Injection volume = 20 μL). (b) Breakthrough curve summarizing the results of re-analysis of field samples for 3,5-DCBA.

slowly decreased in concentration. Sampling at time intervals too large may result in inaccurate measurement of the peak concentration of the breakthrough curves. Sampling too frequently may result in an overload of samples that are difficult to analyze in real time. A large number of analyses also requires quantification based on many different calibration curves. Variability between different calibration curves may result in slight differences in the measured concentrations. These differences may result in shifts in the breakthrough curve for each separate day of sample analysis. Substantial noise in the final breakthrough curve may then be observed. Data quality is clearly improved when samples are analyzed within a short period of time, assuring minimal variability in chromatographic conditions. Selecting a subset of samples and re-analyzing over a short period of time may be preferable. This not only allows quantification using a minimum number of calibration curves, but also allows for the use of optimal conditions for the analyses. For instance, the highest concentration calibration standards can be prepared to reflect the maximum concentrations observed (peak of the breakthrough curve) for each of the tracers. This ensures similar chromatography between the calibration standards and the samples. This is increasingly important when several tracers are used and chromatographic separations are not optimal.

Analytical sensitivity was not the primary issue for the analysis of the samples from the H-19 tracer tests, although large dilutions of tracers occurred between the injection wells and the sampling well, resulting in extremely low tracer concentrations in the samples. Adequate sensitivity was observed using a detection wavelength of 230 nm. Use of this wavelength also resulted in decreased background effects from the brine. The ability to separate all of the tracers used for testing was most crucial.

Using a detection wavelength of 205 nm offers superior sensitivity for many of these tracers when acetonitrile instead of methanol is used as the mobile phase (Figure I-2). When tracer concentrations are extremely low and maximizing sensitivity is the main concern, use of the more costly acetonitrile may be required. Again, optimal

HPLC conditions are dependent on the number of tracers and the particular tracers used. Thorough laboratory evaluation of potential tracers is recommended prior to tracer selection.

I.5 References

Benson, C.F., and R.S. Bowman. 1994. "Tri- and Tetrafluorobenzoates as Nonreactive Tracers in Soil and Groundwater," *Soil Science Society of America Journal.* Vol. 58, no. 4, 1123-1129.

Bowman, R.S. 1984. "Analysis of Soil Extracts for Inorganic and Organic Tracer Anions via High-Performance Liquid Chromatography," *Journal of Chromatography.* Vol. 285, no. 3, 467-477.

Bowman, R.S., and J.F. Gibbens. 1992. "Difluorobenzoates as Nonreactive Tracers in Soil and Ground Water," *Ground Water.* Vol. 30, no. 1, 8-14.

Edgell, K.W., E.J. Erb, R.J. Wesselman, and J.E. Longbottom. 1993. "Gas Chromatographic/Electron Capture Detection Method for Determination of Chlorinated Acids in Water: Collaborative Study," *Journal of AOAC (Association of Official Analytical Chemists) International.* Vol. 76, no. 5, 1098-1112.

Elrod, L., Jr., S.G. Spanton, M. Cirovic, D.I. Shaffer, T.G. Golich, C.L. Linton, D.R. Vievia, P. Kalaritis, and H. Schmand. 1993. "Determination of 2-Chloro-4, 5-Difluorobenzoic Acid and Related Impurities by Liquid Chromatography," *Analytica Chimica Acta.* Vol. 280, no. 1, 85-92.

Han, C. 1998. "Determination of Ground-Water Tracer 2,6-Difluorobenzoic Acid by GC/MS." M.S. thesis. Las Vegas, NV: University of Nevada, Department of Chemistry.

Jaynes, D.B. 1994. "Evaluation of Fluorobenzoate Tracers in Surface Soils," *Ground Water.* Vol. 32, no. 4, 532-538.

Pearson, R.J., S.D. Comfort, and W.P. Inskeep. 1992. "Analysis of Fluorobenzoate Tracers by Ion Chromatography," *Soil Science Society of America Journal.* Vol. 56, no. 6, 1794-1796.

Stetzenbach, K.J., S.L. Jensen, and G.M. Thompson. 1982. "Trace Enrichment of Fluorinated Organic Acids Used as Ground-Water Tracers by Liquid Chromatography," *Environmental Science & Technology.* Vol. 16, no. 5, 250-254.

Supelco, Inc. 1991. "Analyze Acids, Bases, and Zwitterions with Our New SUPELCOSIL™ LC-ABZ HPLC Column," *Biotext, The Supelco Quarterly Inquiry Into the Life Sciences.* Vol. 2, no. 2, 2-4.

Appendix J
Tracer-Mixing Methodology

By Irene Farnham[1]and Kazumasa Lindley[1]

The 1996-96 tracer testing at the H-19 and H-11 hydropads utilized 18 different benzoic-acid tracers. In this appendix, the methodologies used to achieve dissolution of these tracers in the Culebra brine for preparation of the injectate solutions are briefly described. For additional details on the exact methodologies used, see the Field Logbooks in ERMS #240460 and 240462.

In order for a tracer test to be successful, the concentration of the injectate solutions must be high enough to allow for dilution that will occur as the tracer travels between the injection well and pumping/sampling well. Tracer concentrations in the sampling well must also be high enough to insure adequate definition of the breakthrough curve. Optimally, the concentration of the tracer at the peak of the breakthrough curve should be several orders of magnitude higher than the analytical detection limit. Determination of the tracer-injectate concentration needed for a test is, therefore, dependent on: 1) the anticipated dilution, 2) the volume of tracer solution injected, 3) the analytical detection limit for the tracer, and 4) the solubility of the tracer.

The tracer concentrations in the injectate solutions for the 1995-96 WIPP tests ranged from 2 to 15 g/L. The concentrations varied depending on both the tracer test and the maximum solubility of the particular benzoate tracer used. Injectate solutions of varying concentrations were prepared for the multiwell convergent-flow (MWCF) and single-well injection-withdrawal (SWIW) tests. Tracer-injectate concentrations of 10 g/L were prepared for the majority of the MWCF tracer tests. In general, these tracer-injectate solutions consisted of 2 kg of tracer in a total volume of 200 L. The tracer-injectate concentrations for the SWIW tracer tests ranged from 2 to 8 g/L with up to 8 kg of tracer dissolved in 1,000 L of brine.

The benzoate tracers are soluble in water in their anionic forms. The addition of a base (e.g., sodium hydroxide (NaOH) or potassium hydroxide (KOH)) is, therefore, often required to increase the pH of the solution to achieve tracer dissolution. Approximate stoichiometric amounts of base to tracer (viz. 1 mole base: 1 mole tracer) are recommended. The formula weights (FW) of the tracers range from 158.1 g/mole (DFBA) to 212.1 g/mole (PFBA). The formula weight for NaOH is 40.0 g/mole. Therefore, to dissolve 1 kg of a difluorobenzoic acid (6.32 moles), 253.0 g of NaOH (6.32 moles) is added. The base and tracer should be added incrementally, dissolving portions of each until dissolution of the desired quantity of tracer is achieved. Once the tracer is dissolved, the pH of the solution can generally be decreased to its original value without precipitating the tracer. HCl is used to lower the pH. KOH, NaOH, and hydrochloric acid (HCl) are caustic. Addition of KOH and NaOH may increase the temperature of the solution and, therefore, they should be added slowly while monitoring the temperature of the solution. HCl vapor causes damage to lungs, so a respirator and laboratory apparel are required when using this compound.

The solubilities of the benzoic-acid tracers in the high-ionic-strength brine of the Culebra were much lower than observed in most other waters. Consequently, extreme conditions (e.g., high pH or dissolution in alcohol prior to the addition of the brine) were often required to dissolve these compounds. Another difficulty encountered while preparing the injectate solutions was the formation of a precipitate as the pH was increased. The presence of the precipitate often made it difficult to observe dissolution of the tracer. Once the pH of the solution was lowered to its original value, the precipitate dissolved.

---

[1] University of Nevada at Las Vegas, Harry Reid Center for Environmental Studies, 4505 Maryland Parkway, Las Vegas, NV 89154-4009. Email: farnham@nevada.edu.

Laboratory-scale experiments using gram levels of the benzoates were performed to develop procedures for dissolving the tracers in brine without significantly changing the brine's background chemistry. In general, the amount of base required to dissolve the tracers in the laboratory exceeded that predicted by stoichiometric calculations. Dissolution of the tracers in the laboratory experiments also did not perfectly coincide with the dissolution observed in the field for the large quantities of tracer used in the injectate solutions. Nevertheless, laboratory studies are recommended when dissolving tracers in high-ionic-strength waters.

In most cases, a concentrated injectate solution was prepared in a 55-gallon (208-L) drum a few days before the scheduled tracer injection. Once the tracer was in solution, concentrated HCl was added in approximately 100-mL increments to adjust the pH to a value close to that for Culebra brine (between 7 and 8). The pH of the tracer solution was measured using litmus paper. Just prior to injection, the concentrated solution was added to Culebra brine in a 300-gallon (1,135-L) polyethylene container to obtain the desired injectate concentration and volume. The containers were equipped with circulation systems used to ensure uniform tracer concentration during injection. The following three methods were used to prepare the concentrated tracer solutions for the H-19 and H-11 tracer tests.

Method I

Solid NaOH or KOH and tracer were dissolved directly in the brine. Only the most soluble tracers were dissolved using this method. The following example demonstrates tracer dissolution using Method I. For 2,6-DFBA, 2 kg of tracer were added to 51 L of Culebra brine in a 55-gallon (208-L) drum. Six hundred grams of NaOH were then slowly added while mixing the solution. Once the tracer and NaOH had dissolved, a total of 190 mL of HCl was added in small increments until the desired pH was achieved ($7 < pH < 8$). Prior to injection, the concentrated solution and 138 L of Culebra brine were mixed in a 300-gallon (1,135-L) tank. The pH was again checked and found to be below 7. Two hundred milliliters of 1M NaOH were then added to increase the pH to between 7 and 8. 2,6-DFBA is one of the most soluble benzoate tracers. Tracers that were less soluble (e.g., 2,3-DFBA) were more difficult to dissolve using this method. After rigorously stirring the concentrated mixture, solid tracer remained in the bottom of the 55-gallon (208-L) drum. In order to achieve dissolution of this tracer, the solution was decanted, the solid materials were physically broken up, and additional brine was added. The pH was then increased to above 11 with the addition of 700 g of KOH. A small amount of solid was still present. The concentrated solution was then decanted into a 300-gallon (1,135-L) tank containing brine.

Method II

Tracers that were not soluble in the brine through direct addition of base were first dissolved in a 1M NaOH or KOH solution prepared in deionized (DI) water. Once the tracer was dissolved, brine was added. For example, the 2,4-DCBA injectate for the H-11 SWIW test was prepared by adding 8 kg of tracer to 60 L of 1M NaOH. This solution was mixed until tracer dissolution was achieved. The injectate solution was prepared by transferring the concentrated tracer solution to a 300-gallon (1,135-L) tank and adding 200 gallons (757 L) of Culebra brine in 50-gallon (189-L) portions. A total of 1,300 mL of concentrated HCl was then added in portions varying in volume from 40 to 300 mL to achieve a pH of 7.7.

Method III

Tracers that could not be dissolved through pH adjustment alone were first dissolved in a small volume of alcohol (either methanol (MeOH) or ethanol (EtOH)). A volume of 1M NaOH solution was then added to the tracer and alcohol mixture to maintain an elevated pH during subsequent addition of Culebra brine. The following example illustrates tracer dissolution using this method. For 2,5-DCBA, 2 kg of tracer were dissolved in 8 L of methanol. Once all tracer had dissolved, 10 L of 1M NaOH solution were added to maintain an elevated pH. Next, 51 L of Culebra brine were added. The concentrated solution was then poured into a 300-gallon (1,135-L) tank containing 68 L of Culebra brine. To reduce the pH, 250 mL of concentrated HCl were added to the tank. Addition of the acid reduced the pH to 4.5 which was too low. The pH was increased to an acceptable value by adding 123 g of NaOH.

The methods used for preparation of the tracer-injectate solutions are summarized in Table J-1. Listed in Table J-2 are the quantities of each component used to make the injectate solutions. Although not all tracers are included, Table J-2 contains a representative set of all methods described above.

Table J-1. Methods Used to Prepare Tracer-Injectate Solutions

Method I	Method II	Method III
2,3-Difluorobenzoate	2,4-Difluorobenzoate	2,5-Dichlorobenzoate
2,6-Difluorobenzoate	3,5-Difluorobenzoate	2,3-Dichlorobenzoate
2,3,6-Trifluorobenzoate	2,5-Difluorobenzoate	3,5-Dichlorobenzoate
o-Trifluoromethylbenzoate	2,3,4-Trifluorobenzoate	2,4,6-Trichlorobenzoate
2,3,4,5-Tetrafluorobenzoate	Pentafluorobenzoate	3,4-Difluorobenzate
	p-Trifluoromethylbenzoate	
	m-Trifluoromethylbenzoate	
	2,4-Dichlorobenzoate	

Table J-2. Injectate-Solution Compositions

Tracer	Test	Tracer Mass (kg)	NaOH (g)	1M NaOH (L)	MeOH (L)	HCl (L)	DI (L)	Brine (L) (Approx.)
2,4-DCBA	H-11-SW	8.09		60		1.30		937
3,4-DFBA	H-11-SW	5.06		44	10	0.80		959
2,6-DFBA	H-11-MW	2.02	600	0.2		0.19		189
2,3,4,5-TFBA	H-11-MW	2.07	600			0.37		189
p-TFMBA	H-19-MW	1.99		19		1.06	4.5	110
2,5-DCBA	H-19-MW	1.99	123	10	8	0.25		132
2,5-DFBA	H-19-MW	1.99	300	19.5		1.50		181
m-TFMBA + iodide (NaI)	H-19-MW	1.99 2.40		15		0.62		185
2,4-DFBA	H-19 MW	2.00		14		0.44		186

This page intentionally left blank.

Appendix K

Development of Late-Time Slopes on Log-Log Breakthrough Curves After a Pulse-Type Injection for the Case of Infinite Matrix Blocks

By Roy Haggerty[1]

The late-time behavior of a breakthrough curve is of particular importance to matrix diffusion. Because the behavior of the peak at early time is dominated by advection and dispersion, most of the information about matrix diffusion in a breakthrough curve is found in the tail. The slope of the tail of the breakthrough curve contains information about the type of mass transfer (e.g., single-rate or multirate diffusion, or first-order sorption) while the relative concentration contains information about the relative volume of the advective and diffusive porosity.

In this appendix, we show that late-time concentration goes as $t^{-3/2}$ in the presence of advection and infinite matrix diffusion, where "late time" is defined as time much greater than the time-to-peak. Alternatively, one might say that the late-time concentration goes as $t^{-3/2}$ before $t = l^2/D_a$, where l is the half-thickness of the matrix block and D_a is the apparent diffusivity. Clearly, when l is very large, we expect an asymptotic slope of -3/2 when graphed as log (c) vs. log (t). Note, however, that such a late-time behavior can only be expected if all matrix blocks are large; if any matrix blocks are small, then the late-time behavior can be expected to deviate from the -3/2 behavior.

Such late-time behavior is well-known in the statistical physics literature (e.g., Bouchaud and Georges, 1990) and is used in a number of applications there. Within the groundwater literature, the late-time behavior has been derived by Heer and Hadermann (1994). The $t^{-3/2}$ behavior can also be seen in the context of full solutions in papers such as Neretnieks (1980) and Hadermann and Heer (1996). We present an alternate derivation here.

Consider a set of fractures running through a rock. A constant concentration of solute is injected into the fracture system and its breakthrough curve is measured down gradient. The solution for this breakthrough curve is given by Neretnieks and Rasmuson (1984) if we assume that (1) the effects of hydrodynamic dispersion can be ignored; and (2) the fractures are separated sufficiently such that solute diffusing from one fracture never comes in contact with solute diffusing from another fracture over the time scale of the experiment (i.e., the assumption of "infinite" matrix blocks). This solution is:

$$\frac{c}{c_0} = \operatorname{erfc}\left[\frac{a_s D_a^{1/2} t_w}{2\left(t - t_w\right)^{1/2}}\right] \qquad \text{(K-1)}$$

where c/c_0 is the normalized breakthrough concentration; a_s $[L^{-1}]$ is the specific surface area (ratio of fracture surface area to fracture volume); D_a $[L^2/T]$ is the apparent diffusion coefficient of the rock matrix; t_w $[T]$ is the residence time from the point of injection to the point of measurement in the absence of matrix diffusion; and t $[T]$ is time from injection.

Using the principle of superposition, the breakthrough curve after a pulse injection of duration t_{inj} $[T]$ is given by:

---

[1] Oregon State University, Department of Geosciences, 104 Wilkinson Hall, Corvallis, OR 97331-5506.
Email: haggertr@geo.orst.edu.

$$\frac{c}{c_0} = \operatorname{erfc}\left[\frac{a_s D_a^{1/2} t_w}{2\left(t - t_w\right)^{1/2}}\right] - \operatorname{erfc}\left[\frac{a_s D_a^{1/2} t_w}{2\left(t - t_{inj} - t_w\right)^{1/2}}\right] \qquad \text{(K-2)}$$

We are interested in the late-time slope of this breakthrough concentration when graphed as ln (c/c_0) vs. ln (t). We can express this by taking the natural log of both sides and making the following substitutions:

$$t \equiv e^{\ln t} \qquad \text{(K-3a)}$$

$$\frac{a_s D_a^{1/2}}{2} \equiv \sqrt{\alpha_s} \qquad \text{(K-3b)}$$

Equation K-2 can now be rewritten in double-log format:

$$\ln\left(\frac{c}{c_o}\right) = \ln\left\{\operatorname{erfc}\left[\frac{\sqrt{\alpha_s}\,t_w}{\left(e^{\ln t} - t_w\right)^{1/2}}\right] - \operatorname{erfc}\left[\frac{\sqrt{\alpha_s}\,t_w}{\left(e^{\ln t} - t_{inj} - t_w\right)^{1/2}}\right]\right\}$$

(K-4)

Now we are able to find the slope of the double-log breakthrough curve by taking the derivative of Equation K-4 with respect to ln (t):

$$\frac{d\left[\ln\left(\frac{c}{c_o}\right)\right]}{d(\ln t)} = \frac{\alpha_s^{1/2} t_w}{\pi^{1/2}} \times$$

$$\left\{\frac{\left(e^{\ln t} - t_w\right)^{-3/2}\exp\left(\ln t - \frac{t_w^2\alpha_s}{e^{\ln t} - t_w}\right) - \left(e^{\ln t} - t_{inj} - t_w\right)^{-3/2}}{\operatorname{erf}\left[\alpha_s^{1/2} t_w\left(e^{\ln t} - t_{inj} - t_w\right)^{-1/2}\right] - \operatorname{erf}\left[\alpha_s^{1/2} t_w\left(e^{\ln t} - t_w\right)^{-1/2}\right]} \times\right.$$

$$\left.\frac{\exp\left(\ln t - \frac{t_w^2\alpha_s}{e^{\ln t} - t_{inj} - t_w}\right)}{1}\right\}$$

(K-5)

This expression can be simplified to:

$$\frac{d\left[\ln\left(\frac{c}{c_o}\right)\right]}{d(\ln t)} = \frac{\alpha_s^{1/2} t_w t}{\pi^{1/2}} \times$$

$$\left\{\frac{\left(t - t_w\right)^{-3/2}\exp\left(-\frac{t_w^2\alpha_s}{t - t_w}\right) - \left(t - t_{inj} - t_w\right)^{-3/2}\exp\left(-\frac{t_w^2\alpha_s}{t - t_{inj} - t_w}\right)}{\operatorname{erf}\left[\alpha_s^{1/2} t_w\left(t - t_{inj} - t_w\right)^{-1/2}\right] - \operatorname{erf}\left[\alpha_s^{1/2} t_w\left(t - t_w\right)^{-1/2}\right]}\right\}$$

(K-6)

As the value of t gets large (i.e., for $t\text{-}t_w\text{-}t_{inj} >> t_w^{\,2}\alpha_s$), Equation K-6 goes to -3/2. This can be shown by taking the following steps. First, we eliminate the terms in Equation K-6 that go to 1 for large t. At the same time, let us replace $t\text{-}t_w$ by t^*:

$$\lim_{t^* \to \infty} \frac{d\left[\ln\left(\frac{c}{c_o}\right)\right]}{d(\ln t)} = \frac{\alpha_s^{1/2} t_w\left(t^* - t_w\right)}{\pi^{1/2}} \times$$

$$\left\{\frac{t^{*\,-3/2} - \left(t^* - t_{inj}\right)^{-3/2}}{\operatorname{erf}\left[\alpha_s^{1/2} t_w\left(t^* - t_{inj}\right)^{-1/2}\right] - \operatorname{erf}\left[\alpha_s^{1/2} t_w t^{*\,-1/2}\right]}\right\}$$

(K-7)

This equation is of the form (0-0)/(0-0) for large t^* and, therefore, we need to estimate the difference between the first and second terms in the numerator and denominator. Both the numerator and denominator are of the form $f\left(t^*\right) - f\left(t^* - t_{inj}\right)$, which can be represented using the Taylor series:

$$f(t^*) - f\left(t^* \text{-} t_{inj}\right) = t_{inj} f'(t^*) - \frac{t_{inj}^2}{2!} f''(t^*) + \frac{t_{inj}^3}{3!} f'''(t^*) \cdots \qquad \text{(K-8)}$$

As t* gets large, all but the first term can be neglected because the higher order derivatives go to zero much faster than the first derivative in both the numerator and denominator. Therefore,

$$\lim_{t^* \to \infty} \frac{d\left[\ln\left(\frac{c}{c_0}\right)\right]}{d(\ln t)} = \frac{\alpha_s^{1/2} t_w (t^* - t_w)}{\pi^{1/2}} \times$$

$$\left\{ \frac{t_{inj} \frac{d\left(t^{*\,-3/2}\right)}{dt^*}}{-t_{inj} \frac{d\left[\operatorname{erf}\left(\alpha_s^{1/2} t_w t^{*\,-1/2}\right)\right]}{dt^*}} \right\} = \frac{\alpha_s^{1/2} t_w (t^* - t_w)}{\pi^{1/2}} \times$$

$$\left\{ \frac{-\frac{3}{2} t^{*\,-5/2} t_{inj}}{\alpha_s^{1/2} t_w \pi^{-1/2} \exp\left(-\frac{\alpha_s t_w^2}{t^*}\right) t^{*\,-3/2} t_{inj}} \right\} = -\frac{3}{2} \tag{K-9}$$

From this, we can see that the late-time slope will be -3/2.

The evidence for expected late-time tracer-breakthrough curves proportional to $t^{-3/2}$ has been developed numerically by Tsang (1995) and in the context of experimental data by Hadermann and Heer (1996). Derivation of the -3/2 late-time slope after injection of a Dirac pulse is given by Heer and Hadermann (1994). A related result from the literature of statistical physics (e.g., Bouchaud and Georges, 1990) is that the probability of first return, P_1, for a particle undergoing random motion along an infinite line is:

$$P_1(t) \sim t^{-3/2} \tag{K-10}$$

Probability is analogous to concentration and, therefore, this is precisely the same as the case of a molecule that finds itself within a one- dimensional immobile zone of infinite length. The concentration at late time at the exit from the immobile zone is proportional to $t^{-3/2}$; equivalently, the late-time double-log slope is -3/2. We can assume that once a molecule comes back to the exit, it is taken away by fluid. Therefore, this result is the same as that in Equation K-9.

References

Bouchaud, J-P., and A. Georges. 1990. "Anomalous Diffusion in Disordered Media: Statistical Mechanisms, Models and Physical Applications," *Physics Reports*. Vol. 195, no. 4-5, 127-293.

Hadermann, J., and W. Heer. 1996. "The Grimsel (Switzerland) Migration Experiment: Integrating Field Experiments, Laboratory Investigations and Modelling," *Journal of Contaminant Hydrology*. Vol. 21, no. 1-4, 87-100.

Heer, W., and J. Hadermann. 1994. *Grimsel Test Site: Modelling Radionuclide Migration Field Experiments*. PSI-Bericht No. 94-13. Würenlingen, Switzerland: Paul Scherrer Institut.

Neretnieks, I. 1980. "Diffusion in the Rock Matrix: An Important Factor in Radionuclide Retardation?," *Journal of Geophysical Research*. Vol. 85, no. B8, 4379-4397.

Neretnieks, I., and A. Rasmuson. 1984. "An Approach to Modelling Radionuclide Migration in a Medium with Strongly Varying Velocity and Block Sizes Along the Flow Path," *Water Resources Research*. Vol. 20, no. 12, 1823-1836.

Tsang, Y.W. 1995. "Study of Alternative Tracer Tests in Characterizing Transport in Fractured Rocks," *Geophysical Research Letters*. Vol. 22, no. 11, 1421-1424.

This page intentionally left blank.

Appendix L
Calculation of the Standard Deviation of the Natural Log of Transmissivity (σ ln T) for WIPP-Specific Data

By Toya L. Jones[1] and Susan J. Altman[2]

Chapter 4 of this report discusses simulations of the single-well injection-withdrawal (SWIW) tracer tests conducted in the Culebra at the WIPP site. Those simulations assumed that the horizontal transmissivity in the Culebra is heterogeneous. Generation of the heterogeneous transmissivity fields for the simulations required a value for the standard deviation of the natural log of the transmissivity (σ ln T). In order to evaluate an appropriate σ ln T value for use, the natural logs of transmissivity values determined from Culebra hydraulic tests conducted within and surrounding the WIPP site were taken and the standard deviation of those log values was calculated. The calculation of σ ln T was made for two sets of data: (1) transmissivity values determined for locations within the WIPP-site boundary and (2) all transmissivity values determined for locations within and surrounding the WIPP site.

The source of the transmissivity values was the Culebra transmissivity database contained in records package ERMS #235406. Table L-1 summarizes the locations at which transmissivity values have been estimated for the Culebra, the estimated transmissivity value, the natural log of the transmissivity value, and statistical information regarding the transmissivity values including the standard deviation. For locations at which a transmissivity value was estimated for several wells and/or from several hydraulic tests, the value given in Table L-1 is the arithmetic average value for the hydropad or well as given in the database. The statistical information was obtained using Microsoft Excel, a commercial off-the-shelf program. The transmissivity database contains values for 44 locations within and surrounding the WIPP site. The standard deviation of the natural log of those transmissivities is 3.3. The standard deviation of the natural log of the 25 transmissivity values for locations within the WIPP site boundary is 2.1. See Chapter 4 for the application of these σ ln T values to the heterogeneous simulations of the SWIW tracer tests.

References

Beauheim, R.L. 1986. *Hydraulic-Test Interpretations for Well DOE-2 at the Waste Isolation Pilot Plant (WIPP) Site.* SAND86-1364. Albuquerque, NM: Sandia National Laboratories.

Beauheim, R.L. 1987a. *Interpretations of Single-Well Hydraulic Tests Conducted At and Near the Waste Isolation Pilot Plant (WIPP) Site, 1983-1987.* SAND87-0039. Albuquerque, NM: Sandia National Laboratories.

Beauheim, R.L. 1987b. *Analysis of Pumping Tests of the Culebra Dolomite Conducted at the H-3 Hydropad at the Waste Isolation Pilot Plant (WIPP) Site.* SAND86-2311. Albuquerque, NM: Sandia National Laboratories.

Beauheim, R.L. 1987c. *Interpretation of the WIPP-13 Multipad Pumping Test of the Culebra Dolomite at the Waste Isolation Pilot Plant (WIPP) Site.* SAND87-2456. Albuquerque, NM: Sandia National Laboratories.

Beauheim, R.L. 1989. *Interpretation of H-11b4 Hydraulic Tests and the H-11 Multipad*

---

[1] Duke Engineering & Services, Inc., 9111 Research Boulevard, Austin, TX 78758. Email: tjones@dukeengineering.com.

[2] Sandia National Laboratories, Geohydrology Department, P.O. Box 5800, MS-0735, Albuquerque, NM 87185-0735.

Pumping Test of the Culebra Dolomite at the Waste Isolation Pilot Plant (WIPP) Site. SAND89-0536. Albuquerque, NM: Sandia National Laboratories.

Beauheim, R.L., and G.J. Ruskauff. 1998. *Analysis of Hydraulic Tests of the Culebra and Magenta Dolomites and Dewey Lake Redbeds Conducted at the Waste Isolation Pilot Plant Site.* SAND98-0049. Albuquerque, NM: Sandia National Laboratories.

Beauheim, R.L., T.F. Dale, J.F. Pickens. 1991. *Interpretations of Single-Well Hydraulic Tests of the Rustler Formation Conducted in the Vicinity of the Waste Isolation Pilot Plant Site, 1988-1989.* SAND89-0869. Albuquerque, NM: Sandia National Laboratories.

Cooper, J.B. 1962. *Ground-Water Investigations of the Project Gnome Area, Eddy and Lea Counties, New Mexico.* Trace Elements Investigations Report TEI-802. Albuquerque, NM: U.S. Geological Society.

Cooper, J.B., and V.M. Glanzman. 1971. *Geohydrology of Project Gnome Site, Eddy County, New Mexico.* U.S. Geological Survey Professional Paper 712-A. Washington, DC: United States Government Printing Office.

Dennehy, K.F., and J.W. Mercer. 1982. *Results of Hydrologic Tests and Water-Chemistry Analyses, Wells H-5a, H-5b, and H-5c at the Proposed Waste Isolation Pilot Plant Site, Southeastern New Mexico.* Water-Resources Investigations Report 82-19. Albuquerque, NM: U.S. Geological Society.

Mercer, J.W., P. Davis, K.F. Dennehy, and C.L. Goetz. 1981. *Results of Hydrologic Tests and Water-Chemistry Analyses, Wells H-4A, H-4B, and H-4C at the Proposed Waste Isolation Pilot Plant Site, Southeastern New Mexico.* Water-Resources Investigations 81-36. Albuquerque, NM: U.S. Geological Society.

Table L-1. Culebra Transmissivities and Calculated σ ln T Values

Hydropad/Well	Average Transmissivity(1) (m^2/s)	ln T – All Locations (m^2/s)	ln T – Locations Within WIPP Boundary (m^2/s)	Reference(s) for Interpretations Yielding Individual Values(2)
H-1	9.4 x 10^{-7}	-13.9	-13.9	Beauheim (1987a)
H-2	5.9 x 10^{-7}	-14.3	-14.3	Beauheim and Ruskauff (1998)
H-3	2.5 x 10^{-6} (3)	-12.9	-12.9	Beauheim (1987b)
H-4(4)	8.3 x 10^{-7}	-14.0		Mercer et al. (1981); Beauheim (1987a)
H-5	2.2 x 10^{-7}	-15.3	-15.3	Dennehy and Mercer (1982)
H-6	4.0 x 10^{-5}	-10.1	-10.1	Beauheim and Ruskauff (1998)
H-7(4)	1.5 x 10^{-3}	-6.5		Beauheim and Ruskauff (1998)
H-8(4)	8.8 x 10^{-6}	-11.6		Beauheim (1987a)
H-9(4)	1.1 x 10^{-4}	-9.1		Beauheim and Ruskauff (1998)
H-10(4)	4.4 x 10^{-8}	-16.9		Beauheim and Ruskauff (1998)
H-11	4.7 x 10^{-5}	-10.0	-10.0	Beauheim (1989); Beauheim and Ruskauff (1998)
H-12(4)	1.9 x 10^{-7}	-15.5		Beauheim (1987a)
H-14	3.3 x 10^{-7}	-14.9	-14.9	Beauheim (1987a)
H-15	1.4 x 10^{-7}	-15.8	-15.8	Beauheim (1987a)
H-16	8.6 x 10^{-7}	-14.0	-14.0	Beauheim (1987a)
H-17(4)	2.3 x 10^{-7}	-15.3		Beauheim (1987a)
H-18	2.2 x 10^{-6}	-13.0	-13.0	Beauheim (1987a); Beauheim et al. (1991)
H-19	6.8 x 10^{-6}	-11.9	-11.9	Beauheim and Ruskauff (1998)
DOE-1	1.2 x 10^{-5}	-11.3	-11.3	Beauheim (1987a)
DOE-2(4)	9.6 x 10^{-5}	-9.3		Beauheim (1986)
P-14(4)	5.4 x 10^{-4} (5)	-7.5		Beauheim and Ruskauff (1998)
P-15	9.8 x 10^{-8}	-16.1	-16.1	Beauheim (1987a)
P-17(4)	1.1 x 10^{-6}	-13.7		Beauheim (1987a)
P-18(4)	7.5 x 10^{-11}	-23.3		Beauheim (1987a)
WIPP-12	1.1 x 10^{-7}	-16.0	-16.0	Beauheim (1987a)
WIPP-13	7.4 x 10^{-5}	-9.5	-9.5	Beauheim (1987c)
WIPP-18	3.2 x 10^{-7}	-15.0	-15.0	Beauheim (1987a)
WIPP-19	6.5 x 10^{-7}	-14.2	-14.2	Beauheim (1987a)
WIPP-21	2.7 x 10^{-7}	-15.1	-15.1	Beauheim (1987a)
WIPP-22	4.0 x 10^{-7}	-14.7	-14.7	Beauheim (1987a)
WIPP-25(4)	(6)			
WIPP-26(4)	(6)			
WIPP-27(4)	5.1 x 10^{-4}	-7.6		Beauheim and Ruskauff (1998)

Table L-1. Culebra Transmissivities and Calculated σ ln T Values (continued)

Hydropad/Well	Average Transmissivity(1) (m^2/s)	ln T – All Locations (m^2/s)	ln T – Locations Within WIPP Boundary (m^2/s)	Reference(s) for Interpretations Yielding Individual Values(2)
WIPP-28(4)	2.8×10^{-4}	-8.2		Beauheim and Ruskauff (1998)
WIPP-29(4)	(6)			
WIPP-30(4)	1.9×10^{-7}	-15.5		Beauheim (1987a)
ERDA-9	4.9×10^{-7}	-14.5	-14.5	Beauheim (1987a)
CabinBaby(4)	3.0×10^{-7}	-15.0		Beauheim (1987a)
Engle(4)	4.6×10^{-5}	-10.0		Beauheim (1987a)
USGS-1(4)	5.5×10^{-4}	-7.5		Cooper (1962); Cooper and Glanzman (1971)
D-268(4)	2.2×10^{-6}	-13.0		Beauheim et al. (1991)
AEC-7(4)	1.7×10^{-7}	-15.6		Beauheim et al. (1991)
WQSP-1	3.0×10^{-5}	-10.4	-10.4	Beauheim and Ruskauff (1998)
WQSP-2	2.0×10^{-5}	-10.8	-10.8	Beauheim and Ruskauff (1998)
WQSP-3(4)	(6)			
WQSP-4	1.4×10^{-5}	-11.2	-11.2	Beauheim and Ruskauff (1998)
WQSP-5	1.3×10^{-6}	-13.6	-13.6	Beauheim and Ruskauff (1998)
WQSP-6	2.7×10^{-7}	-15.1	-15.1	Beauheim and Ruskauff (1998)
STATISTICAL INFORMATION				
Number of Values		44	25	
Minimum Value		-23.3	-16.1	
Maximum Value		-6.5	-9.5	
Mean of Values		-12.9	-13.4	
Median of Values		-13.8	-14.0	
Standard Deviation of Values		3.3	2.1	
Variance of Values		10.6	4.4	

(1) Average transmissivity value for well or hydropad as given in the Culebra transmissivity database (records package ERMS #235406).

(2) Reference(s) containing interpretations and estimate transmissivity values for individual hydraulic tests at the well or hydropad.

(3) This value has been superseded by the value in Tables 2-1 and 8-1.

(4) Well or hydropad is located outside of the WIPP-site boundary.

(5) Value is not the well average value but rather the value determined from the single-porosity interpretation of test PUMPING-R (1P)

(6) No interpreted transmissivity value is available.

Appendix M
Comparison of Results for an SWIW Tracer Test Using the Numerical Codes SWIFT II and THEMM

By Toya L. Jones[1] and Susan J. Altman[2]

M.1 Introduction

The majority of the single-porosity simulations of the SWIW tracer tests presented in Chapter 4 were conducted using the numerical code THEMM. Due to a limitation with THEMM, the double-porosity simulations presented in that chapter were conducted using the numerical code SWIFT II. The purpose of the double-porosity simulations was to compare them to single-porosity simulations. The method of simulating transport with SWIFT II results in some numerical spreading that is not experienced with THEMM. Consequently, the THEMM single-porosity simulations could not be compared to the SWIFT II double-porosity simulations. In order to allow for direct comparison, several single-porosity simulations were rerun using SWIFT II. The purpose of this appendix is to compare the differences in SWIFT II and THEMM results for single-porosity simulations with identical model input.

M.2 Model Setup and Input

The model consisted of a 4.4-m-thick layer extending 634 m in both the x- and y-directions. The central 120 m x 120 m area was heterogeneous with each grid block assigned a different transmissivity value. The remaining portion of the model was homogeneous and assigned a transmissivity equal to the geometric mean value for the heterogeneous region. The model grid blocks were 0.5 m x 0.5 m in the heterogeneous region and increased from 0.5 m to 128 m in the homogeneous region with the largest grid blocks located at the model's outer edge. Solute transport occurred only within the heterogeneous region. Constant-head boundary conditions were set on the four sides of the model domain such that a gradient was induced from the top to the bottom (north to south). The average of the head values assigned at the top and bottom was assigned to the lateral boundaries. Simulations confirmed that these lateral boundaries were far enough from the inner region to not affect plume dimensions. For the THEMM simulations, an internal, constant-rate, source/sink term was specified to represent the injection/withdrawal well (located at 60 m, 80 m). For the SWIFT II simulations, the injection/withdrawal well was explicitly incorporated into the simulations using a model well located at 60 m, 80 m. A constant injection rate was assigned during injection, a zero rate during the resting phase, and a constant extraction rate during the withdrawal phase. A transmissivity value ten times greater than the maximum transmissivity of the entire field was assigned to the grid block containing the well to represent the increased conductivity of the well. Because the grid block containing the well was small compared to the size and movement of the plume, the increased transmissivity did not significantly affect plume movement.

The input parameter values including injection rates and times, pumping rate, regional gradient, etc., for the code comparison are summarized in Table M-1. Values for the parameters were determined based on the first tracer injected during the Culebra SWIW tracer test performed at the H-11 hydropad. The comparison was performed for two realizations of the heterogeneous transmissivity field. These fields correspond to the fields in the sensitivity study discussed in Chapter 4 that produced the most rapid and slowest tracer recovery.

---

[1] Duke Engineering & Services, Inc., 9111 Research Boulevard, Austin, TX 78758.
Email: tjones@dukeengineering.com.

[2] Sandia National Laboratories, Geohydrology Department, P.O. Box 5800, MS-0735, Albuquerque, NM 87185-0735.

Table M-1. Input parameters for the comparison of THEMM and SWIFT II

Parameter	Values
Mean transmissivity (T) (m^2/s)	5.1×10^{-5}
Standard deviation of ln T ($\sigma \ln T$)	1.76
Correlation Length λ (m)	15
Transmissivity distribution	Gaussian
Culebra thickness (b) (m)	4.4
Longitudinal and Transverse Dispersivity (m)	0.0
Porosity (ϕ)	1×10^{-3}
Injection rate (m^3/s)	1.24×10^{-4}
Pumping rate (m^3/s)	2.23×10^{-4}
Mass of tracer injected (kg)	8.035
Tracer-injection duration (s)	8160
Chaser-injection duration (s)	15420
Resting-phase duration (s)	63583
Regional gradient (dh/dl)	0.011

M.3 Results

Simulation results for the two codes are shown in Figure M-1. For both transmissivity fields, the THEMM results show more rapid recovery and more distinct fluctuations in the tracer-recovery and mass-recovery curves than the SWIFT II results. These differences are believed to be due to the occurrence of some numerical dispersion in the SWIFT II simulations.

THEMM does not allow input of a longitudinal dispersivity but rather assumes a value of zero. Direct input of a value for longitudinal dispersivity is required by SWIFT II. For this application, a value of zero was assigned and, therefore, the longitudinal dispersivity for both the THEMM and the SWIFT II simulations was zero. However, because of the nature of the finite-difference approximations used in SWIFT II, the effective dispersivity in the SWIFT II simulations was greater than zero due to numerical dispersion. With SWIFT II, which is a finite-difference code, calculations are performed at grid-block centers and they represent grid-block average values. Therefore, if SWIFT II calculates tracer movement into an adjacent grid block during a timestep, the tracer mass is smeared across the entire grid block regardless of the calculated distance of transport into the grid block. That is, if the code calculates tracer will move 0.05 m into a grid block, the code will smear the tracer mass an extra 0.45 m so that it extends across the entire 0.5-m grid-block width. This extra smearing is numerical dispersion. The effect of dispersion (whether numerical or real) is to spread out tracer in the direction of flow. That spreading results in smoother tracer-recovery and mass-recovery curves and causes a reduction in the mass-recovery rate.

Transport in the THEMM code is performed using a particle-tracking method. With this method, numerical dispersion does not occur because the location at which concentrations are calculated does not rely on a grid structure. In addition, numerical dispersion is minimized because particles are not allowed to diffuse across stream tubes. Because the THEMM simulations do not have numerical dispersion, mass recovery is faster and the lack of tracer spreading in the flow direction results in sharp slope changes in the simulated tracer-recovery and mass-recovery curves.

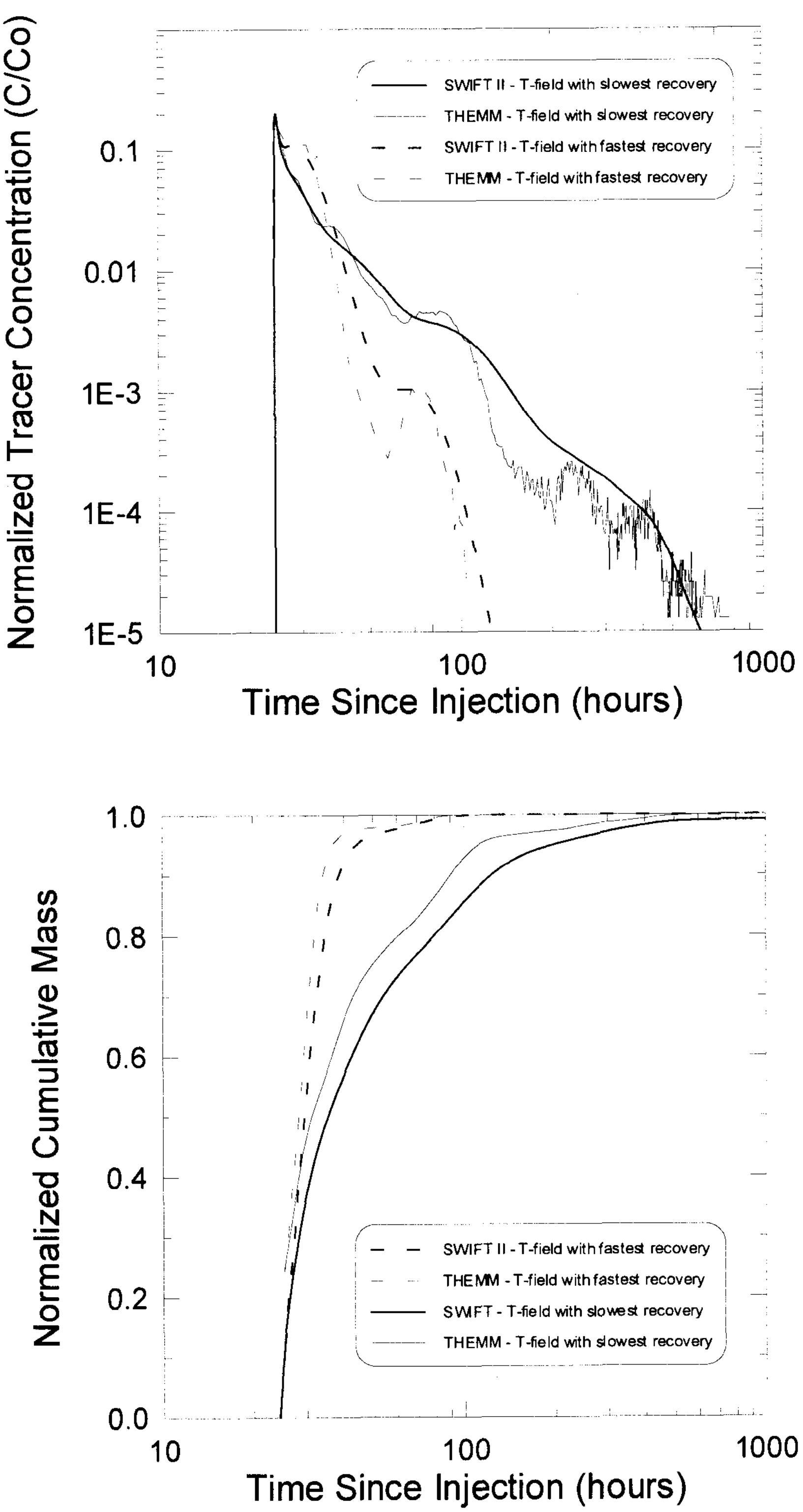

Figure M-1. **Comparison of (a) tracer-breakthrough curves and (b) mass-recovery curves for THEMM and SWIFT II simulations.**

This page intentionally left blank.

Appendix N
Calculation of Diffusion of Tracer Trapped in the Borehole During Injection

By Toya L. Jones[1] and Lucy C. Meigs[2]

N.1 Introduction

A series of tracer tests was conducted in the Culebra dolomite at the WIPP site between June 1995 and April 1996. The tests consisted of both single-well injection-withdrawal (SWIW) tracer tests and multiwell convergent-flow (MWCF) tracer tests performed at two sites. The primary function of the SWIW tracer tests was to determine whether matrix diffusion within the formation dominated the behavior of the tracer-recovery curves. The effect of matrix diffusion is to reduce the late-time slope of the observed recovery data relative to that produced by a SWIW tracer test conducted in a single-porosity medium.

The entire mass of tracer may not exit the injection well during the injection phase of a tracer test. If the portion of the borehole lying below the test interval is not isolated in some way (e.g., by a packer or a shale basket), some potential exists for tracer to get trapped in the bottom of the borehole during injection. This tracer could then diffuse back into the test interval during the remainder of the test (i.e., during the pause and withdrawal phases of a SWIW test and during the withdrawal phase of a MWCF test), affecting the shape of the tracer-recovery/breakthrough curve. The purpose of the calculations presented here is to determine whether or not the effects of diffusion of tracer trapped in the bottom of a borehole could be confused with matrix-diffusion effects from a double-porosity medium.

The data observed for the five tracers used during the three SWIW tracer tests at the WIPP site show late-time slopes that are significantly shallower than those for a single-porosity medium and steeper than those for a conventional double-porosity medium (i.e., one with a single matrix-diffusion rate) (see Chapter 6). An investigation was conducted to determine whether the observed late-time slopes could have been affected by the diffusion of tracer trapped in the borehole after injection. Although the SWIW tests incorporated equipment configurations and injection strategies designed to maximize tracer displacement from the borehole into the formation, this exercise was conducted to eliminate uncertainty regarding the processes controlling the shallow slopes of the observed data. This investigation was not intended to yield realistic results based on actual borehole conditions, but rather to provide maximum estimates of the potential for mass to be recovered during pumping as a result of the molecular diffusion of trapped tracer. That is, the study was designed to show that, with very conservative assumptions regarding conditions in the borehole, the mass recovered due to diffusion from the bottom of the hole is insignificant.

The study was conducted for conditions during SWIW tests for two reasons. First, because the same well is used for both injection and withdrawal, tracer diffusing from the bottom of the borehole goes directly into the fluid pumped from the recovery well. For MWCF tests, once the tracer diffuses back into the test interval from the bottom of the injection well, it must then travel through the formation to the recovery well. Travel over this extra distance, which is not a factor for the SWIW tests, results in additional dilution of the tracer. Second, for the tests at H-19, the borehole used for the SWIW test has a larger diameter than the injection wells used for the MWCF tests and, therefore, has a larger surface area across which diffusion could occur. Therefore, if the calculations show that diffusion of trapped tracer is insignificant for SWIW tests, it is even less of a factor for MWCF tests. In addition, a main objective of the SWIW tests was to demonstrate matrix diffusion within the Culebra. Therefore, we wish to show that no mechanism other than matrix diffusion caused the gradual mass recovery observed in the data.

---

[1] Duke Engineering & Services, Inc., 9111 Research Boulevard, Austin, TX 78758.
Email: tjones@dukeengineering.com.

[2] Sandia National Laboratories, Geohydrology Department, P.O. Box 5800, MS-0735, Albuquerque, NM 87185-0735.

N.2 Molecular Diffusion in a Borehole

We assumed that the bottom of the injection wells for the SWIW tests could be represented as a semi-infinite fluid with a constant initial concentration and a zero-concentration boundary located at the base of the test interval. The one-dimensional analytical solution describing molecular diffusion for this type of system is:

$$C(x,t) = C_o erf\left[\frac{x}{2(D't)^{1/2}}\right] \tag{N-1}$$

where C is the concentration at location x and time t [M/L^3], C_o is the initial concentration [M/L^3], x is the distance below the zero-concentration boundary [L], D' is the molecular diffusivity (the free-water diffusion coefficient times the medium tortuosity) [L^2/T], and t is the time of interest [T]. The initial conditions for Equation N-1 are:

$C(x>0,t=0)$ = constant (C_o)

$C(x=0,t=0)$ = zero

and the boundary condition is:

$C(x=0,t>0)$ = zero.

Use of Equation N-1 to calculate diffusion of trapped tracer has the following inherent assumptions:

- the tracer trapped in the bottom of the borehole acts as an infinite source;
- the concentration in the test interval during the time over which diffusion occurs is zero; and
- interaction between fluid in the test interval and the trapped tracer is by diffusion only.

These first two assumptions do not take into account the fact that (1) the borehole actually has a finite depth, thus limiting the amount of tracer that could be trapped and subsequently diffuse back into the test interval and (2) the concentration in the test interval is actually non-zero due to tracer recovery from the formation. Therefore, the calculations using Equation N-1 overestimate diffusion. For the calculations, all fluid below the zero-concentration boundary (i.e., the base of the test interval) was assumed to have an initial tracer concentration equal to that of the injectate.

The reduction in the concentration of the trapped tracer as a function of distance below the zero-concentration boundary due to diffusion across the boundary was calculated at various times using Equation N-1. For each time, concentrations were calculated at equally spaced distances below the boundary until no change in concentration with distance was observed. The cumulative mass, M, of tracer that had diffused across the boundary (i.e., into the test interval) by each time was then calculated using:

$$M = \sum_{i=0}^{nx} A(C_o - C_i)\Delta x \tag{N-2}$$

where A is the surface area for diffusion [L^2], C_o is the initial concentration of the trapped tracer [M/L^3], C_i is the concentration of the trapped tracer as calculated with Equation N-1 [M/L^3], Δx is the depth increment for the normalized-concentration calculations [L], and nx is the total distance below the boundary over which normalized concentrations were calculated [L]. This latter distance varied from 0.34 to 0.49 m.

The surface area available for diffusion was assumed to be the cross-sectional area of the borehole and the initial concentration was assumed to be equal to the tracer injectate concentration. These assumptions result in maximum estimates of mass added to the test interval due to diffusion because (1) the first assumption ignores the reduction in the surface area available for diffusion due to the presence of the injection tool and (2) the second assumption ignores any reduction in the tracer concentration during injection. Dividing the mass determined using Equation N-2 by the mass of tracer injected during the SWIW test gives the normalized mass. These calculations yield normalized mass contributed to the test interval as a function of time due to diffusion of trapped tracer. All parameters used for the calculations are summarized in Table N-1.

The mass in the test interval due to molecular diffusion and the observed mass recovery were compared in terms of an incremental normalized mass flux. The equation used to calculate this flux for both the calculated diffusion and the observed data is:

$$F_m = \frac{NM_2 - NM_1}{t_2 - t_1} \qquad \text{(N-3)}$$

where F_m is the incremental normalized mass flux [T^{-1}], NM is the normalized mass, and t is time [T].

Incremental normalized mass fluxes for the observed tracer data and the diffusion calculations are shown on Figure N-1. For all SWIW tracers, the mass fluxes due to molecular diffusion are less than the observed mass fluxes at all times. In addition, with one exception, the slopes of the mass fluxes calculated for molecular diffusion are shallower than the slopes of the observed mass fluxes at all times. The exception to this observation is for the tracer 2,4-DCBA injected into H-19b0 during the 7-well test. For this tracer, the slope of the observed data is similar to that calculated for diffusion at the very end of the test. However, molecular diffusion of trapped tracer is not considered to have had any influence on the observed recovery curve for this tracer due to the configuration of equipment in the borehole. For the SWIW test during which this tracer was injected, the bottom of the borehole was isolated by a packer placed slightly above the base of the Culebra. Therefore, no stagnant space existed in the borehole in which tracer could have been trapped.

The total amounts of mass calculated to be in the test interval due to diffusion of trapped tracer are summarized in Table N-1 along with the percentage of diffused mass relative to the injected mass. This table shows that the diffused mass ranges from 3.9 x 10^{-3} to 1.1 x 10^{-2} kg and the percentage ranges from 0.08 to 0.22%. These percentages are very small and indicate that the diffusion of trapped tracer from the bottom of the borehole into the test interval will have a negligible effect on observed data.

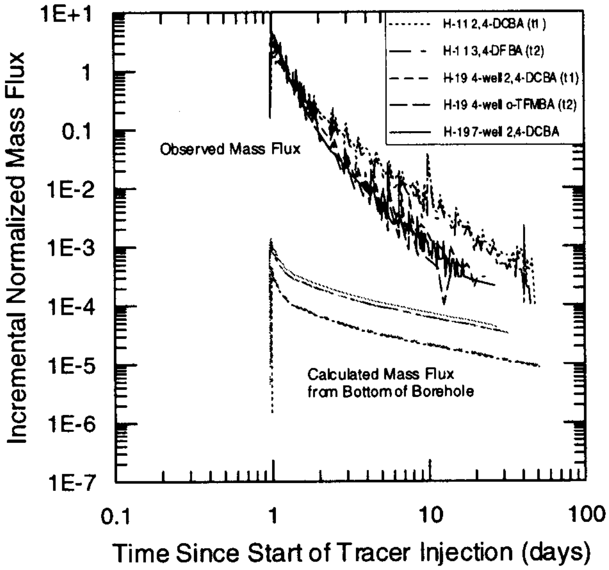

Figure N-1. Normalized mass fluxes for the observed tracer data and the diffusion calculations.

N.3 Summary and Conclusions

An investigation was conducted to determine how the diffusion of tracer trapped in the bottom of the borehole during injection could affect observed SWIW tracer data. This investigation did not attempt to determine a realistic estimate of the degree of molecular diffusion that may have occurred in the boreholes used for the SWIW tracer tests. Rather, assumptions regarding the analytic solution and the parameter values used for the calculations ensured a maximum estimate of the additional mass that could have been introduced into the test interval by diffusion of trapped tracer. The comparison between the calculated and observed values shows that, even with conservative assumptions that result in maximizing the calculated diffusion, the mass fluxes calculated for diffusion are not consistent with the observed mass fluxes in either magnitude or slope. In addition, the mass potentially returned to the test interval by diffusion from the bottom of the borehole is an insignificant percentage of the total injected mass. These results indicate that molecular diffusion within the borehole had an insignificant, if any, effect on the shape of the observed mass-recovery curves for the WIPP SWIW tracer tests.

Diffusion of tracer trapped in the injection well would have a greater effect on SWIW data than on MWCF data because diffused tracer is immediately recovered from the withdrawal well for SWIW tests, whereas tracer must migrate through the formation before being recovered for MWCF tests. In addition, for tests at the H-19 hydropad, more diffusion could occur in the borehole used for the SWIW test because of its larger diameter relative to that of the injection wells used in the MWCF test. Therefore, because the results for conditions during SWIW tests show that diffusion of trapped tracer does not affect observed tracer recovery, the same conclusion can be made for the MWCF tests.

Table N-1. Parameter Values and Results for the Borehole Diffusion Calculations

Hydropad	H-11		H-19		
Test(1)			4-Well Test		7-Well Test
Tracer Number (2)	Tracer 1	Tracer 2	Tracer 1	Tracer 2	
Tracer Name	2,4-DCBA	3,4-DFBA	2,4-DCBA	o-TFMBA	2,4-DCBA
INPUT PARAMETERS AND VALUES					
Length of Test (hr)	1200	1200	768	768	624
Injected Mass (kg)	8.035	5.05	4.9	1.9	4.995
Injectate Concentration (mg/L)	8071	5020	4938	1906	5974
Tortuosity	1	1	1	1	1
Surface Area (m^2)	0.0132	0.0132	0.0398	0.0398	0.0398
Free-Water Diffusion Coefficient (m^2/s)	7.3×10^{-10}	8.2×10^{-10}	7.3×10^{-10}	7.4×10^{-10}	7.3×10^{-10}
Δx for Calculations (m)	0.002	0.002	0.002	0.002	0.002
Total Distance (m)	0.468	0.492	0.368	0.372	0.336
Times for Calculations	(3)	(3)	(4)	(4)	(5)
CALCULATION RESULTS					
Diffused Mass (kg) (6)	6.65×10^{-3}	4.52×10^{-3}	9.61×10^{-3}	3.89×10^{-3}	1.11×10^{-2}
Percentage of Injected Mass (%) (7)	0.08	0.09	0.20	0.20	0.22

(1) given if more than one SWIW test was performed at the hydropad
(2) given if more than one tracer was injected during the SWIW test
(3) calculations using Equations N-1 and N-2 were performed for times of 0.01, 0.05, 0.075, 0.1, 0.2, 0.3, 0.4, 0.5, 0.6, 0.7, 0.8, 0.9, 1, 2, 3, 4, 5, 6, 7, 8, 9, 10, 15, 20, 30, 40, 50, 60, 70, 80, 90, 100, 125, 150, 175, 200, 250, 300, 400, 500, 600, 700, 800, 900, 1000, 1100, and 1200 hr
(4) calculations using Equations N-1 and N-2 were performed for times of 0.01, 0.05, 0.075, 0.1, 0.2, 0.3, 0.4, 0.5, 0.6, 0.7, 0.8, 0.9, 1, 2, 3, 4, 5, 6, 7, 8, 9, 10, 15, 20, 30, 40, 50, 60, 70, 80, 90, 100, 125, 150, 175, 200, 250, 300, 400, 500, 600, 700, and 744 hr
(5) calculations using Equations N-1 and N-2 were performed for times of 0.01, 0.05, 0.075, 0.1, 0.2, 0.3, 0.4, 0.5, 0.6, 0.7, 0.8, 0.9, 1, 2, 3, 4, 5, 6, 7, 8, 9, 10, 15, 20, 30, 40, 50, 60, 70, 80, 90, 100, 125, 150, 175, 200, 250, 300, 400, 500, 600, and 644 hr
(6) calculated using Equations N-1 and N-2
(7) calculated as the diffused mass divided by the injected mass times 100

Appendix O

Effects of Sorption on Tracer Breakthrough for an SWIW Test

By Toya L. Jones[1] and Susan J. Altman[2]

O.1 Introduction

A series of tracer tests was conducted in the Culebra dolomite at the WIPP site between June 1995 and April 1996. The tests consisted of both single-well injection-withdrawal (SWIW) and multiwell convergent-flow (MWCF) tracer tests performed at two sites. The primary function of the SWIW tracer tests was to determine whether matrix diffusion within the formation dominated the behavior of the tracer-recovery curves. The effect of matrix diffusion is to reduce the late-time slope on a log-log plot of the observed recovery data relative to that produced by a SWIW tracer test conducted in a single-porosity medium.

Log-log plots of the data observed for the five tracers used during the three SWIW tracer tests at the WIPP site show late-time slopes that are significantly shallower than those for a single-porosity medium and steeper than those for a conventional double-porosity medium (i.e., one with a single matrix-diffusion rate). An investigation was conducted to determine whether the observed late-time slopes could have been affected by the sorption of tracer to aquifer material. Single-porosity simulations were conducted using the numerical code SWIFT II to evaluate the effect of linear sorption on model-generated tracer-breakthrough curves in a heterogeneous system with a regional gradient. Although batch tests of the tracers used in the SWIW tests show no sorption within measurement error (see Appendix H), this study was conducted to eliminate uncertainty regarding the processes controlling the shapes of the observed tracer-recovery curves.

O.2 Code Description

SWIFT II (Sandia Waste-Isolation Flow and Transport code) is a fully transient, three-dimensional, finite-difference code that solves the coupled equations for single-phase flow and transport in porous and fractured geologic media. SWIFT II is capable of simulating fluid flow, heat transport, dominant-species miscible displacement, and trace-species miscible displacement. The first three processes are coupled via fluid density and viscosity and together they provide the velocity field required in the third and fourth processes. SWIFT II treats density, viscosity, porosity, and enthalpy as functions of pressure, temperature, and dominant-species concentration. SWIFT II can be used in a transient or steady-state mode. It is capable of modeling confined or unconfined (including partially saturated) flow systems and heterogeneous and/or anisotropic conditions. Either cylindrical or Cartesian coordinate systems can be modeled with SWIFT II. A complete discussion of the theory and implementation of SWIFT II and the basic limitations of the methodology can be found in Reeves et al. (1986a). A guide to the SWIFT II input data is provided by Reeves et al. (1986b). Comparison of the results from SWIFT II to analytical solutions appear in Finley and Reeves (1981), Reeves et al. (1987), and Ward et al. (1984).

For this application, SWIFT II was used to solve the steady-state fluid-flow and transient radionuclide-transport equations in heterogeneous single-porosity media using a Cartesian coordinate system. The equation describing steady-state flow applicable to this application is (Reeves et al., 1986a):

---

[1] Duke Engineering & Services, Inc., 9111 Research Boulevard, Austin, TX 78758. Email: tjones@dukeengineering.com.

[2] Sandia National Laboratories, Geohydrology Department, P.O. Box 5800, MS-0735, Albuquerque, NM 87185-0735.

$$0 = -\nabla \cdot \left[\frac{\rho k}{\mu} (\rho g \nabla z - \nabla p) \right] - q \qquad \text{(O-1)}$$

where ρ is fluid density, k is the hydraulic-conductivity tensor for the system, μ is fluid viscosity, g is the gravitational constant, z is the vertical coordinate, p is pressure, and q is fluid flux sources (-) or sinks (+).

The equation used to describe transient radionuclide transport in a single-porosity system incorporating sorption is (Reeves et al., 1986a):

$$\frac{\delta}{\delta t}\left[\phi\rho C + (1-\phi)\rho_s W\right] =$$
$$-\nabla \cdot \left[\frac{\rho C k}{\mu} (\rho g \nabla z - \nabla p) \right] - \nabla \cdot \left[\rho(D + D_M) \cdot \nabla C\right] - Cq - q_r$$
$$\text{(O-2)}$$

where t is time, ϕ is porosity, C is the concentration of the radionuclide, ρ_s is the grain density, W is the solid-phase concentration of the radionuclide, D is the dispersion/diffusion tensor for the radionuclide, D_M is the molecular diffusion coefficient for the radionuclide, and q_r is the source(+)/sink(-) term for the radionuclide. Equations O-1 and O-2 are coupled via porosity, fluid density, fluid viscosity, fluid enthalpy, fluid internal energy, and rock internal energy relationships. The solid-phase concentration of the radionuclide is assumed to be given by a nonlinear Freundlich equilibrium isotherm (Reeves et al., 1986a):

$$W = \kappa (\rho C)^{\eta} \qquad \text{(O-3)}$$

where κ is the sorption coefficient and η is the sorption exponent. For this application, sorption was assumed to be linear by assigning a value of one to the sorption exponent. For linear sorption as assumed here, the sorption coefficient in Equation O-3 is equal to the distribution coefficient, K_d. A complete discussion of the implementation of Equations O-1 through O-3 is provided in Reeves et al. (1986a).

O.3 Model Conceptualization and Input Parameters

The transmissive portion of the Culebra was assumed to be homogeneous in the vertical direction (two-dimensional approximation) and isotropic in the horizontal direction, and was considered to be a confined layer because it is underlain by mudstone with an expected permeability orders of magnitude lower than that of the Culebra (Beauheim, 1987) and overlain by a significantly less permeable portion of the Culebra. Based on extensive hydraulic testing conducted at five hydropads at the WIPP site, including H-11 (Beauheim and Ruskauff, 1998), the Culebra fractures appear to have a high-enough density and be well-enough connected to be reasonably approximated by a heterogeneous stochastic continuum for advective transport.

The model consisted of a single layer. The central area of the model domain was heterogeneous with each grid block assigned a different transmissivity value. The remaining portion of the model domain was homogeneous and assigned a transmissivity equal to the geometric mean value for the heterogeneous region. The model grid blocks were a constant dimension in the heterogeneous region and geometrically increased in the homogeneous region with the largest grid blocks located at the model's outer edge. Solute transport occurred only within the heterogeneous region. The heterogeneous transmissivity field was created using a sequential simulation algorithm as described in Deutsch and Journel (1998). Generation of the transmissivity field utilized a spherical model of spatial correlation with isotropic correlation lengths and no nugget effect.

Constant-head boundary conditions were set on the four sides of the model domain such that a gradient was induced from the top to the bottom (north to south). The average of the head values assigned at the top and bottom was assigned to the lateral boundaries. Simulations confirmed that these lateral boundaries were far enough from the inner region to not affect plume dimensions. The injection/withdrawal well was explicitly incorporated into the simulation using a model well. A constant injection rate was assigned during injection, a zero rate during the resting phase, and a constant extraction rate during the withdrawal phase. A transmissivity value ten times greater than the maximum transmissivity of the entire field was assigned to the grid block containing the well to represent the increased conductivity of the well. Because the grid block containing the well was small compared to the size and movement of the plume, the increased transmissivity did not significantly affect plume movement.

Four simulations were conducted for this study, each using a different value for the distribution coefficient, K_d. One simulation assumed a K_d value of zero to show the effects of no sorption and the other three simulations assumed non-zero K_d values. A discussion of the relationship between the results of the batch-test experiments and the estimated K_d can be found in records package ERMS #237453. This study looked only at the effects of linear sorption. The parameter values for the simulations (Table O-1) were based on the injection of 2,4-DCBA during the SWIW test performed at the H-11 hydropad. Because the plume sizes were smaller for the simulations with sorption than for the simulation without sorption, the size of the modeled region, the grid-block size in the heterogeneous region, and the correlation length for generation of the heterogeneous transmissivity field were smaller for the simulations with sorption (see Table O-1).

Table O-1. Parameter Values Used for the Simulations

Parameter	Simulations with Sorption	Simulation without Sorption
Total Model Dimension (m)	126.8 x 126.8	634 x 634
Heterogeneous Region Dimension (m)	24 x 24	120 x 120
Grid-Block Size in Heterogeneous Region (m)	0.1 x 0.1	0.5 x 0.5
x,y Location of Well Within Heterogeneous Region (m)	12, 16	60, 80
Thickness (m)	4.4	4.4
Porosity	4.0×10^{-4}	4.0×10^{-4}
Mean Transmissivity (T) (m^2/s)	5.1×10^{-5}	5.1×10^{-5}
Standard Deviation of ln T ($\sigma \ln T$)	1.76	1.76
Correlation Length (λ) (m)	0.5	15
Transmissivity Distribution	Gaussian	Gaussian
Grain Density (kg/m^3)	2820	2820
Distribution Coefficient (K_d) (cm^3/g)	0.1, 0.01, and 0.001	0.0
Injection Rate (m^3/s)	1.24×10^{-4}	1.24×10^{-4}
Pumping Rate (m^3/s)	2.23×10^{-4}	2.23×10^{-4}
Mass Injected (kg)	8.035	8.035
Tracer-Injection Duration (s)	8160	8160
Chaser-Injection Duration (s)	15420	15420
Resting-Pause Duration (s)	63583	63583
Regional Gradient (dh/dl)	0.011	0.011

Batch tests with crushed Culebra dolomite showed no measurable sorption of 2,4-DCBA within measurement error. If we take into account the measurement error, the maximum potential K_d for 2,4-DCBA was calculated to be less than 0.1 cm^3/g (ERMS #237453). The simulations used values of 0.1, 0.01, and 0.001 cm^3/g to test the sensitivity of the model results to the assumed K_d.

0.4 Results

Figure O-1 shows the tracer-recovery and mass-recovery curves for the simulated results and the observed data. For the simulations with a non-zero K_d, the tracer-recovery curves show that the peak concentration and duration of the rising limb decrease as the magnitude of the K_d increases (Figure O-1a). For the simulation with the highest K_d, the maximum concentration occurs immediately upon the start of pumping and the tracer-recovery curve has no rising limb. The peak concentration decreases as the value for K_d increases because the fraction of tracer adsorbed to the aquifer material increases and the fraction of tracer present in the fluid decreases. The mass-recovery curves show that mass is recovered quickest for the simulation with the lowest K_d and slowest for the simulation with the highest K_d (Figure O-1b).

The falling-limb slope is shallower and mass recovery is slower for the simulation without sorption than for the two sorption simulations with the smallest K_d's. For the simulations with sorption, plume drift during the resting phase due to the regional gradient is negligible. Consequently, the injection and withdrawal pathways are identical and the tracer-recovery curves have the same general characteristics as for a single-porosity system without drift. For the simulation without sorption, however, the regional gradient causes the plume to drift significantly during the resting phase. As a result, the withdrawal paths differ from the injection pathways and tracer recovery is slowed. If no regional gradient is present, the rate of mass recovery for the simulation with no sorption is faster than for the simulations with sorption.

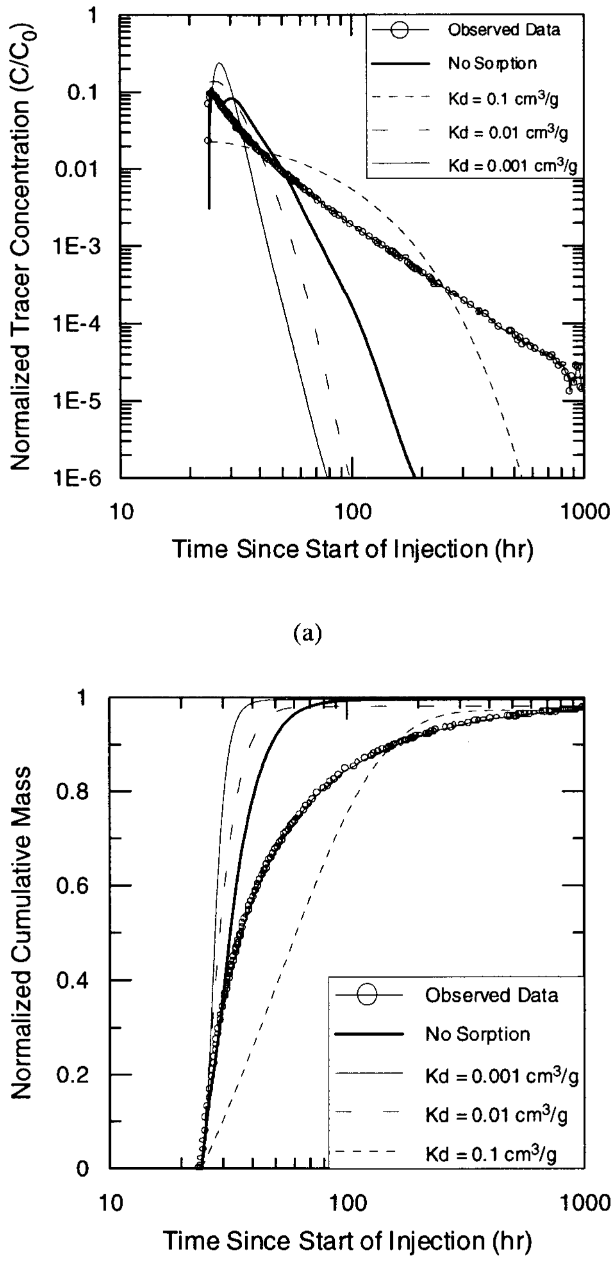

(a)

(b)

Figure O-1. Tracer-recovery curves (a) and mass-recovery curves (b) for the simulations to determine the effects of sorption.

Although sorption can reduce the rate of mass recovery, the characteristics of the tracer-recovery curves for the simulations incorporating sorption are not consistent with the characteristics of the observed tracer-recovery curve. The slope of the falling limb of the observed data is intermediate between the falling-limb slopes for the simulations with the two largest K_d values for approximately 200 hr, after which the simulated curves show much higher slopes. Also, the observed data have a much better defined rising limb and peak concentration than the simulated curves with the two largest K_d values.

O.5 Summary and Conclusions

An investigation was conducted to determine how sorption of tracer to aquifer material could affect observed SWIW tracer data in a heterogeneous, single-porosity system with a regional gradient. A comparison of the simulated results and the observed data indicates that the characteristics of the tracer-recovery curves for the simulations with sorption are inconsistent with the characteristics of the observed data. For simulations that include sorption and have a well-defined peak, the slope of the falling limb is much steeper than the slope of the observed data. Simulations that include sorption and have an initially shallow falling-limb slope do not have a rising limb on the tracer-recovery curve, which is inconsistent with the observed data. In all cases, simulations that include sorption show much steeper late-time log-log slopes than were observed during the WIPP tests.

Simulations that include sorption can have faster mass recovery than simulations without sorption if a regional gradient is present. The regional gradient will cause the plume to drift during the resting phase for a non-sorbing tracer and thus reduce the rate of mass recovery. However, sorbed tracers will not drift significantly during the resting phase in the presence of a regional gradient. If the effects of sorption for a sorbing tracer are less than the effects of drift for a non-sorbing tracer, tracer recovery will be quicker for the sorbing tracer.

O.6 References

Beauheim, R.L. 1987. *Interpretations of Single-Well Hydraulic Tests Conducted At and Near the Waste Isolation Pilot Plant (WIPP) Site, 1983-1987.* SAND87-0039. Albuquerque, NM: Sandia National Laboratories.

Beauheim, R.L., and G.J. Ruskauff. 1998. *Analysis of Hydraulic Tests of the Culebra and Magenta Dolomites and Dewey Lake Redbeds Conducted at the Waste Isolation Pilot Plant Site.* SAND98-0049. Albuquerque, NM: Sandia National Laboratories.

Deutsch, C.V., and A.G. Journel. 1998. *GSLIB: Geostatistical Software Library and User's Guide.* 2nd ed. New York, NY: Oxford University Press.

Finley, N.C., and M. Reeves. 1981. *SWIFT Self-Teaching Curriculum: Illustrative Problems to Supplement the User's Manual for the Sandia Waste-Isolation Flow and Transport Model (SWIFT).* SAND81-0410, NUREG/CR-1968. Albuquerque, NM: Sandia National Laboratories.

Reeves, M., D.S. Ward, N.D. Johns, and R.M. Cranwell. 1986a. *Theory and Implementation for SWIFT II, The Sandia Waste-Isolation Flow and Transport Model for Fractured Media, Release 4.84.* SAND83-1159, NUREG/CR-3328. Albuquerque, NM: Sandia National Laboratories.

Reeves, M., D.S. Ward, N.D. Johns, and R.M. Cranwell. 1986b. *Data Input Guide for SWIFT II, The Sandia Waste-Isolation Flow and Transport Model for Fractured Media, Release 4.84.* SAND83-0242, NUREG/CR-3925. Albuquerque, NM: Sandia National Laboratories.

Reeves, M., D.S. Ward, P.A. Davis, and E.J. Bonano. 1987. *SWIFT II Self-Teaching Curriculum: Illustrative Problems for the Sandia Waste-Isolation Flow and Transport Model for Fractured Media.* SAND84-1586 Revision, NUREG/CR-3925. Albuquerque, NM: Sandia National Laboratories.

Ward, D.S., M. Reeves, and L.E. Duda. 1984. *Verification and Field Comparison of the Sandia Waste-Isolation Flow and Transport Model (SWIFT).* SAND83-1154, NUREG/CR-3316. Albuquerque, NM: Sandia National Laboratories.

This page intentionally left blank.

Appendix P
Double-Porosity Single-Rate Interpretations of Multiwell Convergent-Flow Tracer-Test Data

By Toya L. Jones[1], Joanna Ogintz[1,2], Susan J. Altman[3], Sean A. McKenna[3], and Lucy C. Meigs[3]

P.1 Introduction

As discussed in Chapter 1, groundwater flow in the Culebra is considered the primary means of offsite transport of radionuclides released from the WIPP repository through human intrusion. The potential importance of this offsite pathway has motivated the design and implementation of conservative tracer tests to characterize the solute-transport properties of the Culebra. Tracer tests have been performed at the H-2, H-3, H-4, H-6, H-11, and H-19 hydropads (see Figure 2-2). The types of tests that have been conducted include two-well recirculating tracer tests, multiwell convergent-flow (MWCF) tracer tests, and single-well injection-withdrawal (SWIW) tracer tests (see Table 3-1). A brief discussion of the tracer tests conducted in the 1980s at H-2, H-3, H-4, H-6, and H-11 can be found in Appendix F. The 1995-96 tests performed at the H-11 and H-19 hydropads are discussed in Chapter 3.

A main objective for conducting the SWIW tests was to demonstrate matrix diffusion within the Culebra (see Chapter 3). Because these tests inject tracer into and withdraw tracer from a single well (see Section 3.1), several important transport parameters can not be determined through interpretation of SWIW test results (e.g., advective porosity, dispersivity). MWCF tracer tests were conducted at hydropads containing three or more wells. These tests involved pumping one well until an effectively steady-state flow field was established and then injecting traced fluid followed by untraced fluid (chaser) into the other wells at the hydropad. Because tracers were injected into several wells and recovered from a single different well, the formation was tested along well-to-well flow paths at the hydropad. Due to the one-directional nature of the transport, transport parameters that can not be determined from SWIW test results should be estimable through interpretation of results from MWCF tracer tests.

At the time that the WIPP Compliance Certification Application (CCA) (US DOE, 1996) was developed, several of the tracer-breakthrough curves from the MWCF tracer tests were interpreted using a conventional double-porosity model (i.e., a double-porosity model that assumes a single rate of diffusion). The objective of the interpretations was to estimate values for transport parameters that can not be determined from core measurements and/or interpretation of hydraulic-test results (e.g., advective porosity, matrix-block length, dispersivity). The purpose of this appendix is to present the results of the MWCF interpretations that provided a reasonable fit to the observed data using a conventional (i.e. single-rate) double-porosity model. Previous interpretations by Jones et al. (1992), that assumed a homogeneous transmissivity for the Culebra, have come under criticism because they attribute all tailing in the observed data to physical retardation by matrix diffusion rather than allowing for some additional tracer spreading due to heterogeneity. As a result, the analyses presented here considered both ho-

---

[1] Duke Engineering & Services, Inc., 9111 Research Boulevard, Austin, TX 78758.
Email: tjones@dukeengineering.com.

[2] Now at Stormwater Management, 2035 NE Columbia Boulevard, Portland, OR 97211.

[3] Sandia National Laboratories, Geohydrology Department, P.O. Box 5800, MS-0735, Albuquerque, NM 87185-0735.

mogeneous and heterogeneous transmissivity fields in order to address the concern that some of the spreading observed in the tracer-breakthrough curves may be caused by heterogeneous flow rather than diffusion from the fractures to the matrix. The heterogeneous analyses used the THEMM (Transport in Heterogeneous Media with Matrix diffusion) code and the homogeneous analyses used the SWIFT II (Sandia Waste-Isolation Flow and Transport) code.

P.2 Model Conceptualization

For these simulations, we conceptualized the Culebra as having two porosities and modeled the system with a conventional double-porosity continuum model. We conceptualized one porosity as advective porosity (fractures and, for some pathways, the transmissive portions of the matrix) where advection is the dominant process and the other porosity as diffusive porosity (the portion of the matrix where advection does not dominate) where diffusion is the dominant process. An inherent assumption with conventional double-porosity models is that the fractures can be represented by a uniform fracture network and the matrix is homogeneous. The Culebra was modeled as a single layer with homogeneous transport parameters along each well-to-well flow path (e.g., advective porosity, matrix-block length, matrix porosity, and tortuosity). The thickness of the single layer was set equal to that of the lower Culebra, which is underlain by mudstone with an expected permeability orders of magnitude lower than that of the Culebra (Beauheim, 1987) and overlain by a significantly less permeable portion of the Culebra. Given the short time scale of the tracer tests, diffusion into the upper portion of the Culebra was assumed to be negligible. The heterogeneous interpretations assumed that the Culebra can be represented with a spatially correlated, random, heterogeneous hydraulic-conductivity field.

P.3 Code Descriptions and Numerical Implementations

The following sections contain a brief description of THEMM and SWIFT II and describe how the conceptual model of the Culebra was numerically implemented by the two codes.

P.3.1 THEMM

The THEMM computer code models flow through a heterogeneous advective continuum using a finite-difference solution to the steady-state groundwater-flow equation, which is based on mass-balance principles and Darcy's law (Hale and Tsang, 1996). No advective flow occurs in the diffusive continuum. Solution of the flow equation yields a steady-state head field, and a discretized non-uniform velocity field subsequently is computed by multiplying gradients in the head field by the heterogeneous hydraulic-conductivity field. Transient advective transport in the advective continuum is simulated by a particle-tracking method, with matrix diffusion incorporated using a grid-block residence-time adjustment. The residence-time adjustment is based on a numerical solution to a differential equation describing single-rate Fickian diffusion into the matrix with an assumed spherical matrix-block geometry. For a detailed description of the THEMM code, see Hale and Tsang (1996).

The THEMM interpretations of the MWCF data simulated each tracer flow path independently using a Cartesian grid. The pumping well was located at the center of the model region and the tracer-injection well was located at the appropriate distance from the pumping well to within one-half the grid-block dimension. The model boundaries consisted of constant heads. The boundaries were located a large distance from the pumping and injection wells by adding ten rows and columns of grid blocks having geometrically increasing sizes and a homogeneous hydraulic conductivity outside the finely gridded computational domain with the heterogeneous hydraulic-conductivity field within which all transport occurred. This extended grid with distant constant-head boundaries essentially represented flow in an infinite aquifer. In an effort to account for uncertainty in the heterogeneity of the Culebra, several realizations of the hydraulic-conductivity field were generated. Steady-state flow fields were calculated for the tracer-injection period, chaser-injection period, and the period from the end of injection to the end of pumping. These flow fields were created for each tracer flow path analyzed and each realization of the heterogeneous hydraulic-conductivity field. Transient advective transport was then calculated for each steady-state flow field.

Heterogeneous interpretations of selected tracer results from the H-3 and H-19 hydropad were conducted. All of the THEMM analyses used unconditioned random hydraulic-conductivity fields. The heterogeneous hydraulic-conductivity field used for the H-19 simulations was generated using a turning bands algorithm. An exponential covariance model assuming a mean hydraulic conductivity of 4.1 x 10^{-6} m/s, a log-Gaussian distribution for the hydraulic conductivity, a ln K variance of about 3.10, and a correlation length of 0.733 m was used to create the hydraulic-conductivity field. For the H-3 simulations, the heterogeneous hydraulic-conductivity fields were generated using a Fast Fourier Transform (FFT) algorithm for log-Gaussian correlated random fields (Gutjahr et al., 1996). A Mizell-A covariance model was used to generate all fields assuming a mean hydraulic conductivity of 6.1 x 10^{-7} m/s, a ln K variance of 0.75, and an isotropic covariance structure correlated over a distance of 3 m in both the x- and y-directions. The parameters used to generate the heterogeneous hydraulic-conductivity fields are summarized in Table P-1.

P.3.2 SWIFT II

SWIFT II is a fully transient, three-dimensional, finite-difference code that solves the coupled equations for single-phase flow and transport in porous and fractured (double-porosity) geologic media. The processes that SWIFT II is capable of simulating include fluid flow, heat transport, dominant-species miscible displacement (brine), and trace-species miscible displacement (radionuclide chains or other contaminants). The first three processes are coupled via porosity, fluid density, viscosity, and enthalpy. Together they provide the Darcy-velocity field required to model solute transport. SWIFT II can be used in a transient or steady-state mode. The model can be used with either Cartesian or cylindrical coordinate systems. The SWIFT II model used for the interpretations presented here assumed transient fluid flow and brine transport in a homogeneous double-porosity medium using a Cartesian coordinate system.

The transient equations for fluid flow and brine transport in the advective porosity are obtained by combining the appropriate continuity and constitutive relations. The approach used by SWIFT II to treat an advective porosity-diffusive porosity system is similar to that used by Bear and Braester (1972), Huyakorn et al. (1983), Pruess and Narasimhan (1982), Tang et al. (1981), Grisak and Pickens (1980), Streltsova-Adams (1978), and Rasmuson et al. (1982). For double-porosity applications, SWIFT II solves two sets of equations, one for the processes in the advective porosity and the other for the processes in the diffusive porosity. The equations describing flow and transport in the advective porosity are identical to the equations for the diffusive porosity, except for sink/source terms representing exchange processes with the diffusive porosity.

The only means for large-scale movement provided by SWIFT II in a double-porosity system is within the advective porosity. The storage for the double-porosity system is provided by the diffusive porosity. Interaction between the advective porosity and diffusive porosity is by diffusion only. The diffusive porosity is assumed to be one-dimensional in a direction orthogonal to the movement in the advective porosity. The geometry of the diffusive porosity can be either parallel slabs characterized with prismatic grid blocks or cubes characterized with prismatic or spherical grid blocks. Cubic geometry was used for this application. A reflective no-flow boundary is assumed for the interior boundary of the diffusive porosity. The advective porosity/diffusive porosity interface provides a source to the diffusive porosity that is identical to the loss from the advective porosity to within a geometrical scaling factor.

Table P-1. Summary of Parameters Used to Generate the Heterogeneous Hydraulic-Conductivity Fields

Parameter	H-19 Simulations	H-3 Simulations
Algorithm[(1)]	Turning Bands	Fast Fourier Transform[(2)]
Hydraulic-Conductivity Distribution	log-Gaussian	log-Gaussian
Type Covariance Model Used	Exponential	Mizell-A
Mean Hydraulic Conductivity (m/s)	4.1 x 10^{-6}	6.1 x 10^{-7}
Natural Log Hydraulic Conductivity (ln K) variance (m/s)	3.10	0.75
Correlation Length (m)	0.733	3.0
Type Correlation	unconditional	unconditional

(1) Gives the algorithm used to generate the heterogeneous hydraulic-conductivity fields.
(2) Gutjahr et al. (1996)

A compete discussion of the theory and implementation of SWIFT II and the basic limitations of the methodology can be found in Reeves et al. (1986a). A guide to the input data is provided by Reeves et al. (1986b). Comparisons of the results from SWIFT II to analytical solutions appear in Finley and Reeves (1981), Reeves et al. (1987), and Ward et al. (1984).

The SWIFT II simulations assumed the Culebra is a double-porosity medium and the entire model region, with the exception of the grid block containing the pumping well, was assigned double-porosity parameters. Each tracer flow path was simulated independently using a Cartesian grid. The pumping well was located at the left edge of the model and the injection well was located at the appropriate radial distance from the pumping well. The model grid extended a short distance beyond the location of the injection well. Carter-Tracy boundary conditions (Reeves et al., 1986a) were applied at the outer edge of the grid and embedded the modeled region into an infinite aquifer.

Using a Cartesian grid allowed for adequate discretization in the vicinity of both the tracer-injection well and the pumping well. However, Cartesian grids do not allow for the development of radial flow fields as are formed during the tracer test (radially converging toward the pumping well and radially diverging around the tracer-injection well during injection). To account for the difference between the x- and y-direction flow in the Cartesian grid and the radial flow during the tracer tests, specific flow and transport parameters in SWIFT II were modified such that the two-dimensional Cartesian flow field was converted to a radially symmetric flow field. The parameters modified were the transmissibilities, Darcy velocities, dispersion terms, and pore volumes. A pre-processor to SWIFT II was used to calculate the modifications. In general, the modifications were developed based on the difference between the cross-sectional area of the interface between grid blocks defined by the x, y, and z dimensions in a Cartesian grid and the cross-sectional area of the interface between grid blocks defined by the r, theta, and z dimensions in a radial grid. The modifications converted the x- and y-flow directions in the rectangular-shaped Cartesian grid into radial flow directions in a pie-slice-shaped grid with the production well located at the point of the pie slice. A complete description of how the modifications were calculated and implemented can be found in analysis package ERMS #237450.

Because the underlying Cartesian grid contained more than one grid block in the y-direction, which is converted to the theta direction, the point of the pie slice representing the location of the production well consisted of more than one grid block. To account for the actual production well correctly, model production wells were placed in each of the grid blocks making up the point of the pie slice. The production rate for each well was a fraction of the actual pumping rate with the magnitude of that fraction a function of the angular width of the theta (or y-direction) grid block containing the model well. Calculation of the modified pumping rates can also be found in analysis package ERMS #237450.

Simulation of each tracer injection consisted of a transient flow solution followed by a transient flow and transport solution. The initial transient flow solution consisted of pumping at the withdrawal well for several days in order to establish an approximately steady-state flow field. This established the initial pressure conditions for the simulation of tracer transport. After the steady-state flow field was established, tracer was injected and both transient flow and transient migration were simulated.

The data from the H-3, H-6, and 1988 H-11 tracer tests were previously analyzed by Jones et al. (1992) using SWIFT II. However, the model conceptualization and treatment of the source term for their analysis differs significantly from that used for the analyses presented here. The Jones et al. (1992) simulations used a radial-transport conceptualization (implemented with a radial grid) based on the assumption that the lateral concentration differences in the convergent-flow field need not be preserved at the pumping well. They also considered the tracer-injection phase independently from tracer transport between the injection and pumping wells by calculating tracer concentrations immediately after injection in a preprocessing step that ignored tracer diffusion into the matrix and tracer transport toward the pumping well during injection. Those concentrations were then input into SWIFT II as initial conditions. Jones et al. (1992) state that this treatment of the source is supported by the relatively short time period during which tracer injection occurs compared to the length of time required for the peak tracer concentration to reach the pumping well.

The implementation used in the present application is considered an improvement over the work by Jones et al. (1992) for two main reasons. First, the model conceptualization considered here includes the diffusion of tracer into the matrix and the transport of tracer from the injection well to the pumping well during the period of tracer and chaser injection by explicitly modeling the injection period. This change is considered an improvement because the time to reach peak concentration is not always short relative to the time for tracer injection. For the H-11b3 to H-11b1 flow path, the length of the injection period was as high as 18% of the time to reach peak concentration in the pumping well. Second, the present model considers only the more transmissive lower portion of the Culebra rather than the full Culebra thickness. This improvement is warranted due to the results of the 1995-96 tracer test at H-19 that showed essentially no transport within the upper Culebra (see Section 3.2.2).

For the H-3, H-6, and H-11 hydropads, the observed tracer data are dramatically different for the different flow paths tested. At each location, rapid tracer transport occurred along one flow path and slow tracer transport occurred along the other path(s). The Jones et al. (1992) analyses used two approaches to account for the differences in the observed tracer-breakthrough curves. Their first approach assumed that the differences are due to different rock characteristics along the different flow paths and their second approach assumed that the differences are due to anisotropy in the horizontal transmissivity field. The approach used to describe the differences between the different flow paths for the interpretations presented here is consistent with the first approach of Jones et al. (1992).

P.4 Interpretation Methodology

In general, the interpretation methodology consisted of attempting to calibrate the model results to the observed tracer data. For this process, most of the transport-related parameters required as input for the simulations were assigned fixed values based on field measurements, core measurements, and literature data. The fixed parameters are the Culebra effective thickness, the well spacing, the pumping rate, the injection rate and time, the free-water diffusion coefficient, the diffusive porosity, and the diffusive tortuosity. The sources for the fixed parameter values used in the simulations (Table P-2) were the Tracer Input Parameter Sheets (TIPS) found in Appendix B. In some cases, the value used in a simulation differed slightly from the value given in the TIPS due to conducting the simulations prior to finalization of the TIPS. A summary of the deviations between the simulation values and the TIPS values and the effect on simulation results, which in general was insignificant, can be found in analysis package ERMS #237450.

Interpretations of the tracer data were conducted using both "best-estimate" and "stressed" values for the fixed parameters. The best-estimate values were taken from the actual TIPS tables and the stressed values were generally calculated from the parameter uncertainties given in the TIPS footnotes. The objective of using both types of parameters was to evaluate the effects of increasing or decreasing diffusion on interpretation results.

Two important parameters for tracer transport during MWCF tests cannot be measured on core samples, determined from hydraulic-test results, or found in the literature. They are the advective porosity and matrix-block length. Consequently, values for these two parameters were determined through the analyses by using them as fitting parameters in the calibration process. The calibration process consisted of running the model numerous times until the closest match between the simulated and observed data was obtained. Determination of the closest match was based on visual inspection of the results plotted as linear normalized concentration versus linear time.

A review of the literature for various tracer-test scales and contaminant-plume sizes (e.g., Lallemand-Barrès and Peaudecerf, 1978; Pickens and Grisak, 1981; Gelhar et al., 1985) suggested that the magnitude of dispersivity increases with increasing scale of the tracer test or contaminant plume. The flow-path lengths for the interpreted tracer data range from 11.0 to 42.9 m. Because the lengths of the flow paths are different, the dispersivity for each flow path will also be different. Dispersivity can not be measured in the field and, because it is a transport parameter, cannot be inferred from hydraulic tests. Therefore, the interpretations with the homogeneous model (SWIFT II) also used dispersivity as a fitting parameter. The heterogeneous model (THEMM) assumes that dispersivity is captured in the heterogeneity of the flow field and, therefore, does not include it as an input parameter.

In summary, for each attempted calibration, the values for the fixed parameters remained constant and the values for the fitting parameters were varied until the simulated data matched the observed data based on visual inspection of linear normalized concentration plotted versus linear time. Calibration of the simulated breakthrough curves to the observed breakthrough curves with the heterogeneous model was achieved by adjusting the advective porosity and matrix-block length and, with the homogeneous model, by adjusting the advective porosity, matrix-block length, and dispersivity. The interpreted values for the fitting parameters are summarized in Table P-3.

P.5 Results

MWCF tracer data from the H-3, H-6, H-11, and H-19 hydropads were interpreted using a conventional double-porosity model. The purpose of this section is to present the results of those interpretations for which a reasonable fit to the observed data was obtained. In addition, instances where the data could not be fit with our conceptual model are also identified. As stated in Section P.4, the interpretations consisted of calibrating the numerical model to the observed data by adjusting the advective porosity, matrix-block length, and dispersivity (for the homogeneous model only). Model calibration was determined by visual inspection of the degree of agreement between the simulated and observed data plotted as linear normalized concentration versus linear time.

An increase in the advective porosity results in a corresponding decrease in the velocity within the advective porosity under the same pumping rate. As advective porosity increases, the tracer residence time in the formation is increased, allowing for greater diffusive losses to the diffusive porosity that results in delaying mass breakthrough and the peak-arrival time and decreasing the peak concentration. The opposite effects occur when the advective porosity is decreased. In addition, the size of the tracer plume (doughnut) increases with decreasing advective porosity, which in turn increases the effective surface area for diffusion.

Table P-2. Summary of Values Used for the Fixed Parameters

Pumping Rate (L/s)	Well Spacing (m)	Thickness (m)	Free-Water Diffusion Coefficient (m^2/s)	Tortuosity	Diffusive Porosity	Tracer Injection Rate (L/s)	Tracer Injection Time (s)	Chaser Injection Rate (L/s)	Chaser Injection Time (s)	Percent Mass	Type Hydraulic-Conductivity Field and Parameters(1)
H-19 HYDROPAD											
H-19b3 – 7-Well Test Round 1 (m-TFMBA injected 12/22/95)											
0.27	11.0	4.4	7.4x10^{-10}	0.09	0.15	0.183	1080	0.231	750	100	HOMO/B
0.27	11.0	4.4	7.9x10^{-10}	0.11	0.15	0.183	1080	0.231	750	100	HETERO/B
H-19b5 – 7-Well Test Round 2 (2,4-DCBA injected 01/19/96)											
0.25	13.9	4.4	7.3x10^{-10}	0.09	0.15	0.192	1035	0.166	1020	100	HOMO/B
0.24	12.4	4.1	8.8x10^{-10}	0.09	0.25	0.192	1035	0.166	1020	100	HOMO/S(2)
H-19b7 – 7-Well Test Round 1 (2,4-DFBA injected 12/21/95)											
0.27	12.2	4.4	8.2x10^{-10}	0.09	0.15	0.206	960	0.216	780	100	HOMO/B
H-19b7 – 7-Well Test Round 3 (2,3,6-TFBA injected 02/22/96)											
0.16	12.2	4.4	8.0x10^{-10}	0.09	0.15	0.117	1698	0.119	1410	100	HOMO/B

H-11 HYDROPAD											
H-11b2 – 1988 Test (PFBA injected 05/14/88)											
0.38	21.5	4.4	7.7x10^{-10}	0.11	0.16	0.0731	2580	0.0613	3060	100	HOMO/B
0.40	20.0	4.1	5.9x10^{-10}	0.11	0.16	0.0731	2580	0.0613	3060	100	HOMO/S(2)
H-11b2 – 1996 Test Round 2 (p-TFMBA injected 03/14/96)											
0.38	21.5	4.4	7.4x10^{-10}	0.11	0.16	0.0723	2610	0.0624	3408	100	HOMO/B
H-11b3 – 1988 Test (m-TFMBA injected 05/14/88)											
0.38	20.9	4.4	7.4x10^{-10}	0.11	0.16	0.0985	1920	0.100	3720	100	HOMO/B
H-11b3 – 1996 Test Round 1 (2,3,4,5-TFBA injected 02/15/96)											
0.22	20.9	4.4	7.9x10^{-10}	0.11	0.16	0.0957	1974	0.0976	3810	100	HOMO/B
H-11b3 – 1996 Test Round 2 (2,5-DFBA injected 03/13/96)											
0.38	20.9	4.4	8.2x10^{-10}	0.11	0.16	0.0952	1998	0.0971	3840	100	HOMO/B
0.38	20.9	4.4	8.2x10^{-10}	0.11	0.16	0.0952	1998	0.0971	3840	90	HOMO/S(2)
H-11b4 – 1988 Test (o-TFMBA injected 05/14/88)											
0.38	42.9	4.4	7.4x10^{-10}	0.11	0.16	0.131	1440	0.0801	2340	100	HOMO/B

H-3 HYDROPAD											
H-3b1 (m-TFMBA injected 05/09/84)											
0.19	30.7	4.2	7.4x10^{-10}	0.11	0.20	0.0667	1140	0.0664	4560	100	HETERO/B
0.19	30.7	4.2	7.4x10^{-10}	0.11	0.20	0.0631	1200	0.070	4500	100	HOMO/B

Table P-2. Summary of Values Used for the Fixed Parameters (continued)

Pumping Rate (L/s)	Well Spacing (m)	Thickness (m)	Free-Water Diffusion Coefficient (m^2/s)	Tortuosity	Diffusive Porosity	Tracer Injection Rate (L/s)	Tracer Injection Time (s)	Chaser Injection Rate (L/s)	Chaser Injection Time (s)	Percent Mass	Type Hydraulic-Conductivity Field and Parameters(1)
0.18	32.2	7.2	8.9×10^{-10}	0.11	0.25	0.0667	1140	0.0664	4560	90	HETERO/S (2)
0.18	32.2	4.2	8.9×10^{-10}	0.11	0.25	0.0631	1200	0.070	4500	100	HOMO/S(2)
0.18	32.2	4.2	8.9×10^{-10}	0.11	0.25	0.0631	1200	0.070	4500	90	HOMO/S(2)
0.18	32.2	7.2	8.9×10^{-10}	0.11	0.25	0.0631	1200	0.070	4500	100	HOMO/S(2)
0.20	29.2	4.2	5.9×10^{-10}	0.11	0.25	0.0631	1200	0.070	4500	100	HOMO/S(2)

H-6 HYDROPAD											
H-6a – Test #1 (m-TFMBA injected 08/23/81)											
1.04	29.9	4.0	7.4×10^{-10}	0.11	0.15	0.167	600	0.0877	1140	100	HOMO/B
H-6b – Test #1 (PFBA injected 08/23/81)											
1.04	29.9	4.0	7.7×10^{-10}	0.11	0.15	0.167	600	0.0877	1140	100	HOMO/B
H-6b – Test #2 (p-FB injected 09/02/81)											
1.04	29.9	4.0	9.3×10^{-10}	0.11	0.15	0.128	780	0.128	780	100	HOMO/B

(1) HOMO indicates that a homogeneous hydraulic-conductivity field was assumed and HETERO indicates that a heterogeneous hydraulic-conductivity field was assumed. B indicates best-estimate values for fixed parameters were used and S indicates stressed values for fixed parameters were used.

(2) Stressed values calculated based on:

- a well-spacing uncertainty of ±1.5 m
- a minimum thickness equal to the full thickness minus the thickness of CU-1 (3.0 m) and a maximum thickness equal to the full Culebra thickness
- a free-water diffusion coefficient uncertainty of ± 20 percent
- a porosity uncertainty of about ± 10 percent or the use of the maximum well-averaged value for the entire WIPP site area
- a pumping rate uncertainty of ± 4 percent
- a percent mass uncertainty of -10 percent

Table P-3. Summary of Interpreted Values for Fitting Parameters

Injection Well	Tracer	Test and/or Round	Code	Type Permeability Field (1)	Type Fixed Parameters (2)	Advective Porosity	Matrix-Block Length (m)	Dispersivity (m)
H-19 HYDROPAD								
H-19b3	m-TFMBA	7-Well (Round 1)	SWIFT II	Homogeneous	Best-estimate	0.075	0.083	1.10
			THEMM	Heterogeneous	Best-estimate	0.06	0.15	-
H-19b5	2,4-DCBA	7-Well (Round 2)	SWIFT II	Homogeneous	Best-estimate	0.11	0.030	1.39
				Homogeneous	Stressed	0.07	0.034	1.24
H-19b7	2,4-DFBA	7-Well (Round 1)	SWIFT II	Homogeneous	Best-estimate	0.0476	0.118	0.61
	2,3,6-TFBA	7-Well (Round 3)	SWIFT II	Homogeneous	Best-estimate	0.0476	0.172	0.61
H-11 HYDROPAD								
H-11b2	PFBA	1988	SWIFT II	Homogeneous	Best-estimate	4.5 x 10^{-4}	0.059	2.15
				Homogeneous	Stressed	5.0 x 10^{-5}	0.034	4.00
	p-TFMBA	1996 (Round 2)	SWIFT II	Homogeneous	Best-estimate	4.5 x 10^{-4}	0.060	2.15
H-11b3	m-TFMBA	1988	SWIFT II	Homogeneous	Best-estimate	1.0 x 10^{-4}	0.194	1.50
	2,3,4,5-TFBA	1996 (Round 1)	SWIFT II	Homogeneous	Best-estimate	1.7 x 10^{-4}	0.353	1.25
	2,5-DFBA	1996 (Round 2)	SWIFT II	Homogeneous	Best-estimate	1.7 x 10^{-4}	0.260	1.36
				Homogeneous	Stressed	1.7 x 10^{-4}	0.272	1.36
H-11b4	o-TFMBA	1988	SWIFT II	Homogeneous	Best-estimate	1.0 x 10^{-4}	0.150	1.50
H-3 HYDROPAD								
H-3b1	m-TFMBA	1984	SWIFT II	Homogeneous	Best-estimate	2.0 x 10^{-3} (4)	0.634 (4)	1.61
				Homogeneous	Best-estimate	1.0 x 10^{-3} (5)	0.634 (5)	1.61
				Homogeneous	Stressed	8.93x10^{-4} to 6.93x10^{-3} (4)	0.863 to 0.903 (4)	1.61 to 5.83
				Homogeneous	Stressed	5.2x10^{-4} to 8.93x10^{-4} (5)	0.963 to 1.753 (5)	1.61
			THEMM	Realization #1(3)	Best-estimate	10^{-4} to 10^{-3}	0.65 to 0.75	-
				Realization #2(3)	Best-estimate	5.0x10^{-5} to 10^{-3}	0.55 to 0.75	-
				Realization #1	Stressed	10^{-4}	1.1	-
				Realization #2	Stressed	10^{-4}	1.1	-
				Realization #3	Stressed	8.0x10^{-4}	1.2	-
H-6 HYDROPAD								
H-6a	m-TFMBA	1981 Test # 1	SWIFT II	Homogeneous	Best-estimate	No fit (6)	No fit (6)	No fit (6)
H-6b	PFBA	1981 Test # 1	SWIFT II	Homogeneous	Best-estimate	2.63x10^{-3}	0.194	1.50
	p-FBA	1981 Test # 2	SWIFT II	Homogeneous	Best-estimate	2.63x10^{-3}	0.203	1.50

(1) Gives whether a heterogeneous or homogeneous hydraulic-conductivity field was used for the interpretation; for heterogeneous fields, the realization number for the field is also given.

(2) Gives whether best-estimate or stressed values for the fixed parameters were used for the interpretation.

(3) Data were successfully matched with a range of advective porosity and/or matrix-block length values.

(4) Matched to third-highest data point.

(5) Matched to two highest data points.

(6) A fit to the observed data could not be obtained.

The sensitivity of the simulated results to changes in the advective porosity is greatest for the pathways dominated by advective transport (i.e., the pathways with rapid tracer breakthrough such as H-11b3 to H-11b1) and less for the pathways dominated by diffusive transport (i.e., the pathways with slow tracer breakthrough such as H-11b2 to H-11b1). The effects of varying advective porosity are illustrated in Figure P-1 as discussed below.

As the matrix-block length decreases, the matrix surface area to volume ratio increases and, for a given advective porosity, the number of fractures increases, resulting in a decrease in the fracture aperture. Both of these effects result in greater diffusion of solute from the advective porosity to the diffusive porosity. As a result, the peak concentration is reduced, the peak-arrival time is delayed, and tailing of the breakthrough curve is increased. The opposite is true for an increase in the matrix-block length. The sensitivity of changes in the matrix-block length is greatest for pathways with the least fracture/matrix interaction (i.e., pathways dominated by advective transport). The effects of varying the matrix-block length are illustrated in Figure P-1 as discussed below.

P.5.1 Results for MWCF Tracer Data from the H-19 Hydropad

The well configuration for the H-19 hydropad is shown in Figure 3-2. The MWCF tracer tests conducted at this hydropad are described in Chapter 3. Reasonable matches to the observed data are presented for the Round 1 injection of m-TFMBA into H-19b3, the Round 2 injection of 2,4-DCBA into H-19b5, and the Round 1 injection of 2,4-DFBA and Round 3 injection of 2,3,6-TFBA into H-19b7. No attempt was made to match the remaining data from the H-19 hydropad.

Figure P-1 shows the simulated results that best match the observed data for the H-19b3 Round 1 injection assuming a homogeneous hydraulic conductivity. The model results overpredict the time to tracer breakthrough and the amount of tailing at the end of the test. From about the middle of the rising limb to about the middle of the falling limb, close agreement between the simulated and observed data was achieved. In general, the observed tracer-breakthrough curve can be matched reasonably well using a conventional double-porosity model. At the end of the test, the total amount of mass recovered is 5% higher for the model results than for the observed data. Figure P-1 also shows the sensitivity of the model results to changes in the advective porosity and matrix-block length. As discussed above, decreasing the matrix-block length increased the amount of diffusion, which resulted in decreasing the peak concentration and delaying peak arrival (compare the solid black and dashed curves in Figure P-1), and decreasing the advective porosity decreased the travel time, which decreased the amount of diffusion resulting in a higher peak concentration and an earlier peak-arrival time (compare the gray and dashed curves in Figure P-1).

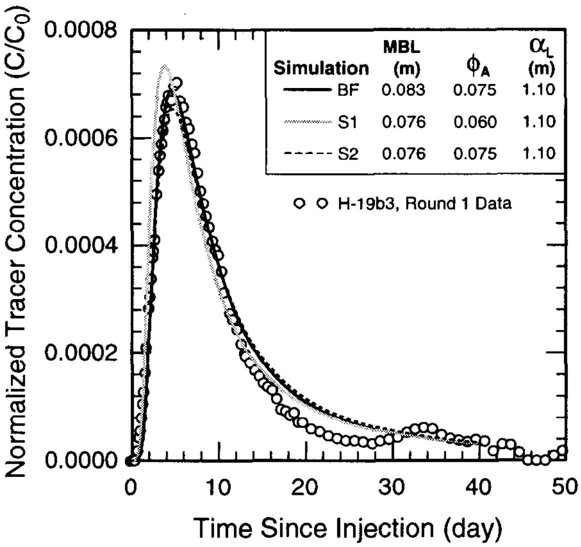

Figure P-1. Observed and simulated tracer-breakthrough curves for the H-19b3 Round 1 data. Simulations show the best fit to the observed data (black curve) and the sensitivity of the simulated results to the advective porosity and matrix-block length. All simulations assumed best-estimate values for the fixed parameters and a homogeneous hydraulic-conductivity field.

Results from simulations of the H-19b3 Round 1 data assuming a heterogeneous hydraulic-conductivity field are shown in Figure P-2. This figure shows best-fit simulated results using both a conventional double-porosity model and a single-porosity model. The simulated results using the single-porosity model match the observed peak-arrival time well but overpredict the magnitude of the peak concentration by a factor of about 2.4, underpredict the width of the peak, and underpredict the amount of tailing. These results indicate that the observed data can not be matched using a single-porosity model. The results from the conventional double-porosity model provide a reasonable match to the observed data. This model slightly overpredicts the time to tracer breakthrough and overpredicts the slope of the rising limb, but matches the remainder of the observed curve well. Total mass recovery at the end of the test is about 3% less for the simulated data than for the observed data.

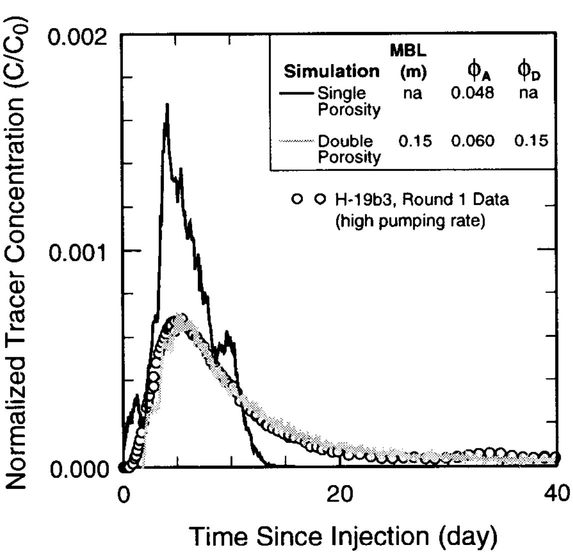

Figure P-2. Observed and simulated tracer-breakthrough curves for the H-19b3 Round 1 data. Simulations show best fits to the observed data using single- and double-porosity models. All simulations assumed best-estimate values for the fixed parameters and a heterogeneous hydraulic-conductivity field.

The advective porosity and matrix-block length determined by the heterogeneous interpretation are slightly lower and about a factor of 1.8 greater, respectively, than the values determined by the homogeneous interpretation (Table P-3). The heterogeneous model required a higher matrix-block length than did the homogeneous model indicating that less diffusion was needed to match the data. This suggests that some of the tracer spreading that occurred during the test could have been caused by heterogeneous flow rather than diffusion from the advective porosity to the diffusive porosity.

Tracer was injected into the full Culebra thickness at H-19b3 during Round 1 and Round 3 of the H-19 7-well tracer test. The withdrawal rates for these two rounds of the test were different; the pumping rate was about 0.27 L/s during Round 1 and about 0.16 L/s during Round 3. As shown on Figure 3-9, the observed peak concentrations are very similar for these data and the observed peak-arrival time is later for the data transported while the pumping rate was lower.

Figure P-3 compares results of conventional double-porosity simulations for two pumping rates for a range of matrix-block lengths. The comparison shows that the relationship between the peak-arrival time and peak height for the two pumping rates is a function of the assumed matrix-block length. For all block lengths considered, the time to peak arrival is always longer for the lower pumping rate and the difference between the peak-arrival times for the same matrix-block length but different pumping rates increases as the matrix-block length decreases. The effect of pumping rate on the difference in peak height for simulations with the same matrix-block length but different pumping rates, however, is not consistent. For the larger matrix-block lengths, the peak height is lower for the lower pumping rate, but for the smaller values of matrix-block length, the peak height is higher for the lower pumping rate. The matrix-block-length value defining the point at which the peak concentration stops decreasing and starts increasing with a lower pumping rate is not unique, but rather a function of the specific system tested and the pumping rates used.

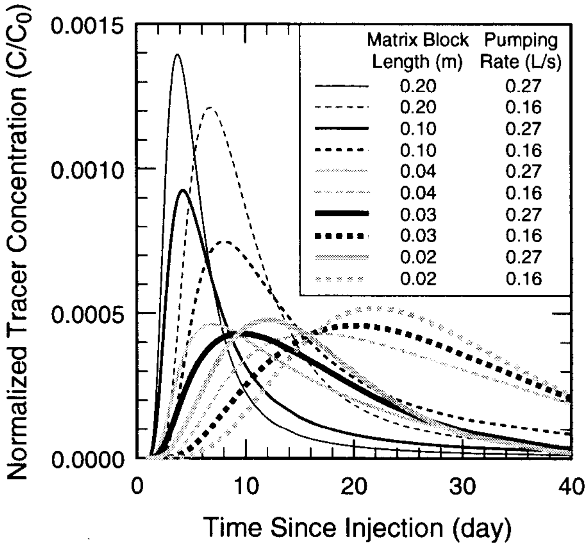

Figure P-3. **Sensitivity of the simulated results from a conventional double-porosity model to a reduction in the pumping rate as a function of the matrix-block length.**

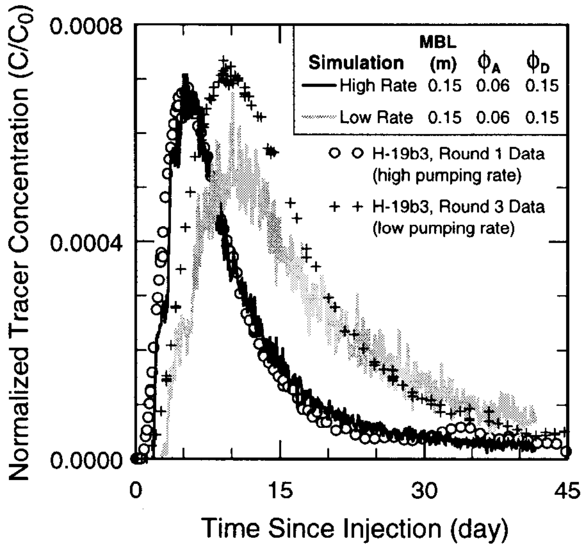

Figure P-4. **Observed and simulated tracer-breakthrough curves for the H-19b3 Round 1 and Round 3 data. Simulations show the best fit to the Round 1 data (black curve), and the prediction of the Round 3 data using the parameters determined from calibration to the Round 1 data (gray curve). All simulations assumed best-estimate values for the fixed parameters and a heterogeneous hydraulic-conductivity field.**

The Round 3 injection into H-19b3 was simulated using the advective porosity and matrix-block length determined from calibration to the Round 1 data using the heterogeneous model. Consistent with the comparison shown in Figure P-3, that simulation yielded a lower peak concentration than the Round 1 simulation due to the lower pumping rate (Figure P-4). These results suggest that the data from the Round 1 and Round 3 injections into H-19b3 are inconsistent with a conventional double-porosity model.

The simulated results that best match the observed tracer-breakthrough curve for the H-19b5 Round 2 injection assuming a homogeneous hydraulic-conductivity field are shown in Figure P-5. Results for simulations using both best-estimate (black curve) and stressed (gray curve) values for the fixed parameters are shown on this figure. Stressing of the parameters was designed to maximize diffusion. Both of the simulated curves overpredict the width of the peak and underpredict the degree of tailing. The time of tracer breakthrough is best matched with the simulation assuming stressed values for the fixed parameters and overpredicted by the simulation using best-estimate values for the fixed parameters. Both simulated curves match a portion of the rising limb of the observed curve, but not the entire rising limb, and provide a good match to the observed peak concentration. Although neither simulated curve matches the overall shape of the observed curve exactly, they both provide a reasonable match to the data. Total mass recovery for the two simulations is almost identical to that observed.

The observed data from the Round 1 injection into H-19b7 were interpreted assuming a homogeneous hydraulic-conductivity field. Figure P-6 shows the results of the best-fit simulation using best-estimate values for the fixed parameters. Notice that two sets of observed data are plotted on this figure. One set (open circles) corresponds to the final data and the other set (plus signs) corresponds to the data available at the time the

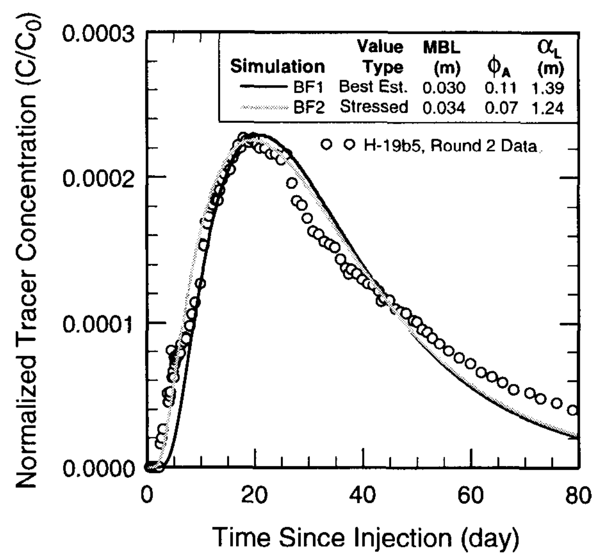

Figure P-5. Observed and simulated tracer-breakthrough curves for the H-19b5 Round 2 data. Simulations show the best fits to the observed data assuming both best-estimate (black curve) and stressed (gray curve) values for the fixed parameters. All simulations assumed a homogeneous hydraulic-conductivity field.

simulation was performed. The difference between the two sets of observed data is the analyzed value for the injectate concentration used to calculate the normalized concentration. The simulation overpredicts the time to tracer breakthrough, the slope of the rising limb, and the time to peak concentration. Mass recovery is lower for the simulated results than for the observed data at all times throughout the test. When compared to the final data, the model predicts total mass recovery about 9% lower than what was observed.

As for H-19b3, tracer was injected across the full Culebra interval in H-19b7 during Rounds 1 and 3 of the 7-well tracer test, and the observed peak concentrations from those two injections were very similar, although the pumping rate was different during the two rounds (0.27 versus 0.16 L/s). Figure P-7 shows the simulated results for the Round 3 injection (black curve) using the advective porosity and matrix-block length obtained from calibration to the Round 1 data. The

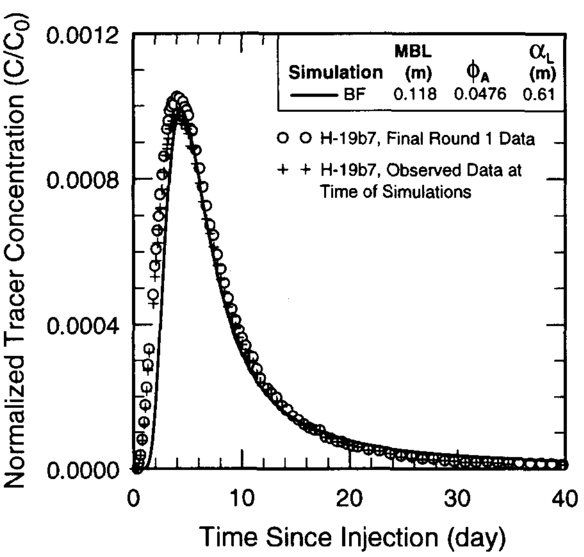

Figure P-6. Observed and simulated tracer-breakthrough curves for the H-19b7 Round 1 data. Two sets of observed data are shown; one set is the final data (open circles) and the other set is the data at the time of the simulation (plus signs). The simulation shows the best fit to the observed data assuming best-estimate values for the fixed parameters and a homogeneous hydraulic-conductivity field.

model predicts a lower peak concentration and slightly longer time to peak arrival than were observed, the same results as were obtained for the H-19b3 data using the heterogeneous model. In order to match the observed Round 3 peak height and arrival time, a matrix-block length about 1.5 times larger than that needed to match the Round 1 data was required (gray curve on Figure P-7). Because the peak concentrations are nearly the same but the residence times in the formation were different due to different advective velocities, interpretation of the tracer data for the lower pumping rate (longer residence time) required a higher matrix-block length (i.e., less diffusion) to match the peak concentration. The inability of the conventional double-porosity model to match the similar peak heights for different pumping rates indicates that it is inconsistent with the physical system tested. Simulations discussed in Chapter 7 and Appendix S suggest that a model including

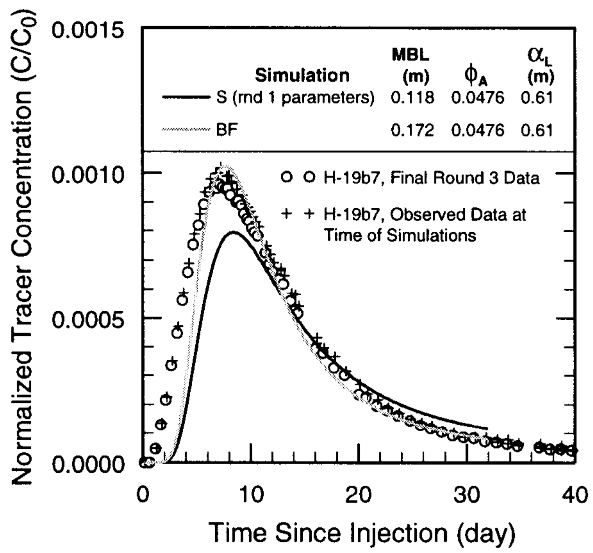

Figure P-7. **Observed and simulated tracer-breakthrough curves for the H-19b7 Round 3 data. Two sets of observed data are shown; one set is the final data (open circles) and the other set is the data at the time of the simulations (plus signs). Simulations show the results predicted for the Round 3 data using the parameter values determined from calibration to the Round 1 data (black curve) and the best fit to the Round 3 data (gray curve). All simulations assumed best-estimate values for the fixed parameters and a homogeneous hydraulic-conductivity field.**

multiple rates of diffusion, rather than a single rate, can do a better job of reproducing similar peak heights for different pumping rates.

The best-fit simulation to the H-19b7 Round 3 data provides a reasonable match to the observed tracer-breakthrough curve. However, the simulated results overpredict the time of tracer breakthrough and the slope of the rising limb. As a result, simulated mass recovery is lower than observed mass recovery at all times.

P.5.2 Results for MWCF Tracer Data from the H-11 Hydropad

The well configuration for the H-11 hydropad is shown in Figure 3-1. Reasonable matches to the observed tracer-breakthrough curves are presented for all data from both the 1988 and 1996 tests with one exception. No attempt was made to match the 1996 H-11b2 Round 1 data. The tracer test conducted in 1988 is described briefly in Appendix F and in detail in Stensrud et al. (1990) and Jones et al. (1992). The tracer test conducted in 1996 is described in Chapter 3.

Results of homogeneous interpretations of the 1988 and 1996 Round 2 data for injections into H-19b2 are shown in Figure P-8. The 1988 data were matched using both best-estimate and stressed values for the fixed parameters. In all cases, the rising limb and peak concentration of the observed data are reasonably matched but the simulations significantly overpredict the amount of mass recovered after the peak. Consequently, total mass recovery for the simulations was over 40% higher than that observed. Although many attempts were made to reduce the width of the

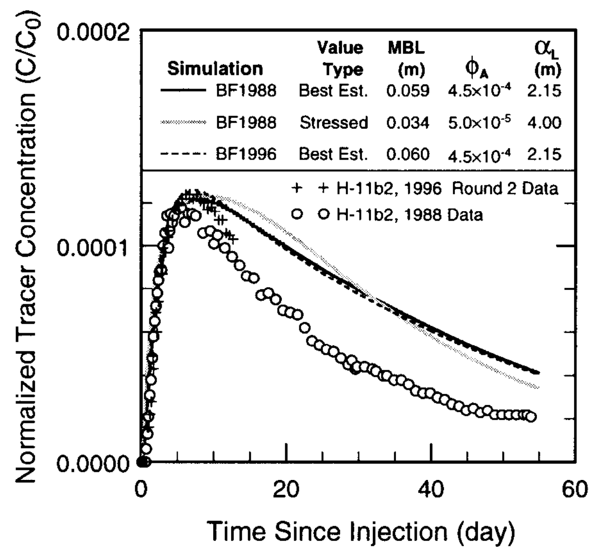

Figure P-8. **Observed and simulated tracer-breakthrough curves for the H-11b2 1988 data (open circles) and Round 2 data (plus signs). The simulations show the best match to the observed 1998 data using both best-estimate (black curve) and stressed (gray curve) values for the fixed parameters and show the best match to the observed Round 2 data using best-estimate values for the fixed parameters (dashed curve). All simulations assumed a homogeneous hydraulic-conductivity field.**

simulated peak, no combination of parameters was found that produced a peak width consistent with that observed.

Figures P-9, P-10, and P-11 show results for interpretations of the tracer data from the 1988, 1996 Round 1, and 1996 Round 2 injections into H-11b3, respectively, assuming a homogeneous hydraulic-conductivity field. The simulations of the 1988 and Round 1 data used best-estimate values for the fixed parameters and the simulations of the Round 2 data used both best-estimate and stressed values for the fixed parameters. In all cases, the simulated results overpredict the time to peak arrival and the width of the peak. Overprediction of the peak width results in an overprediction of the amount of mass recovered after the peak. For all three data sets, total mass recovery predicted by the simulations is over 15% higher than the total mass recovery calculated from the observed data.

Although the pumping rate was lower during Round 1 (0.22 L/s) than during Round 2 (0.38 L/s) of the 1996 test, the observed H-11b3 data for these two rounds have very similar peak heights

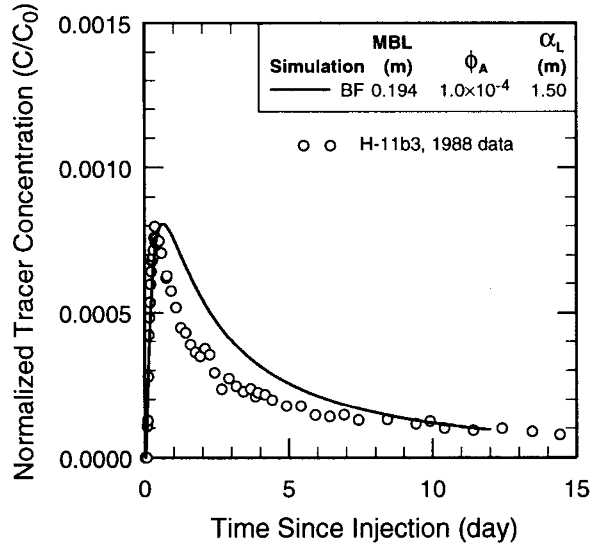

Figure P-9. Observed and simulated tracer-breakthrough curves for the H-11b3 1988 data. The simulation shows the best match to the observed data assuming best-estimate values for the fixed parameters and a homogeneous hydraulic-conductivity field.

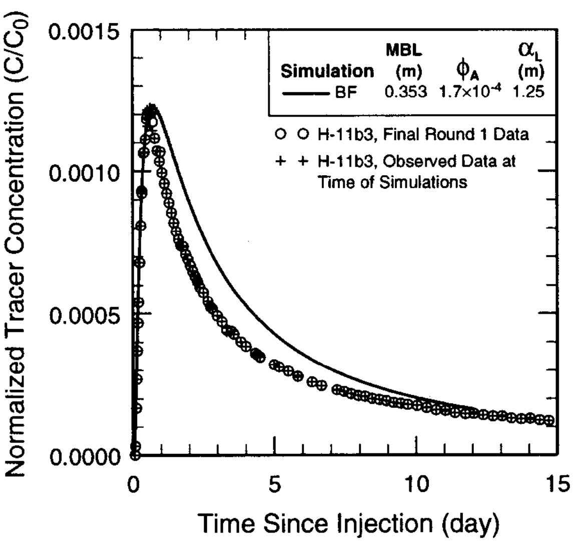

Figure P-10. Observed and simulated tracer-breakthrough curves for the H-11b3 Round 1 data. Two sets of observed data are shown; one set is the final data (open circles) and the other set is the data at the time of the simulation (plus signs). The simulation shows the best match to the observed data assuming best-estimate values for the fixed parameters and a homogeneous hydraulic-conductivity field.

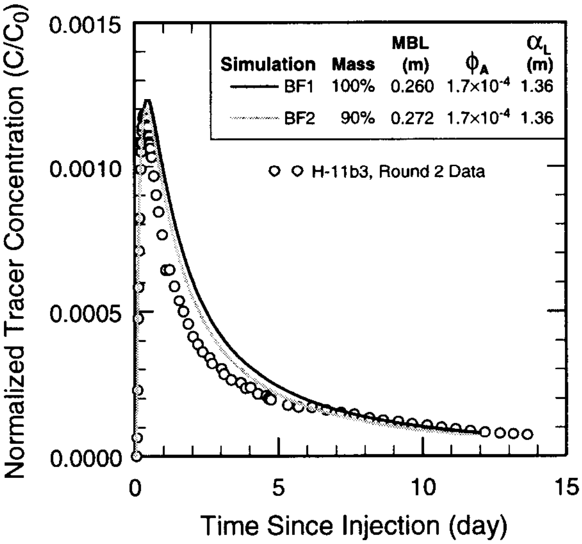

Figure P-11. Observed and simulated tracer-breakthrough curves for the H-11b3 Round 2 data. Simulations show the best match to the observed data assuming best-estimate values for the fixed parameters (black curve) and assuming that the percentage of tracer mass participating in the test is 90% rather than 100% (gray curve). Both simulations assumed a homogeneous hydraulic-conductivity field.

(see Figure 3-5). In order to match both peak concentrations, the interpreted matrix-block length was higher for the Round 1 data than for the Round 2 data (see Table P-3). Because the residence time in the formation was longer during Round 1 due to the lower pumping rate, a higher matrix-block length (i.e., less diffusion) was required to produce the same peak height as was obtained when the pumping rate was higher.

The best match to the data from the 1988 injection into H-11b4 obtained using the homogeneous model is shown in Figure P-12. The simulated results provide a reasonable match to the rising limb and peak of the observed data but overpredict mass recovery after the peak. A comparison of the mass recovery shows good agreement throughout the test and only a 4% difference between the observed and simulated total mass recovered at the end of the test.

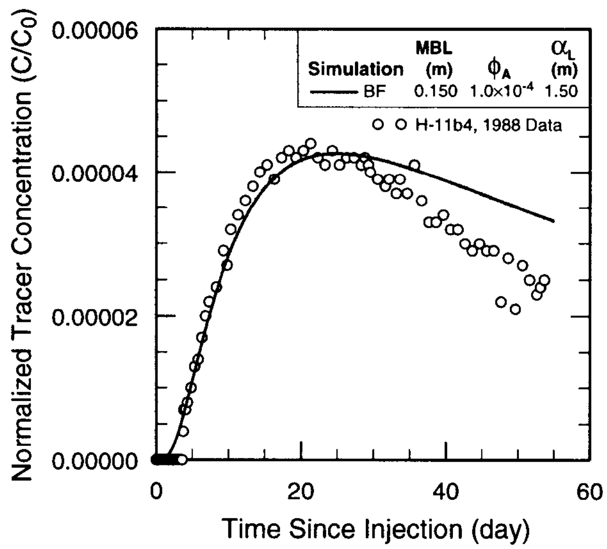

Figure P-12. Observed and simulated tracer-breakthrough curves for the H-11b4 1988 data. The simulation shows the best match to the observed data assuming best-estimate values for the fixed parameters and a homogeneous hydraulic-conductivity field.

P.5.3 Results for MWCF Tracer Data from the H-3 Hydropad

The well configuration for the H-3 hydropad is shown in Figure F-2. A MWCF tracer test was conducted at H-3 in 1984. A brief discussion of that test can be found in Appendix F and detailed discussions can be found in Hydro Geo Chem (1985), INTERA Technologies (1986), and Jones et al. (1992). Reasonable matches to the observed data for the injection of m-TFMBA into H-3b1 assuming homogeneous and heterogeneous hydraulic-conductivity fields are presented here. No attempt was made to match the data for the injection of PFBA into H-3b2 because the observed tracer-breakthrough curve has a poorly defined peak and essentially no data after the peak.

Figure P-13 shows two matches to the observed data assuming a homogeneous hydraulic-

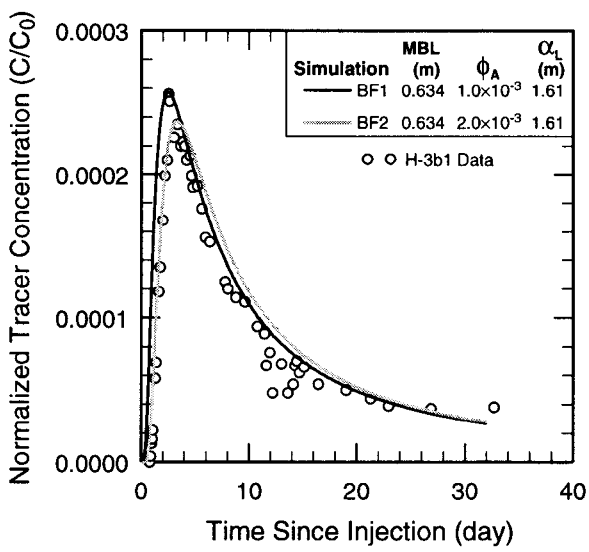

Figure P-13. Observed and simulated tracer-breakthrough curves for the H-3b1 data. Simulations show the best match to the observed data based on matching to the two highest concentration values (black curve) and matching to the third-highest concentration value (gray curve). Both simulations assumed best-estimate values for the fixed parameters and a homogeneous hydraulic-conductivity field.

conductivity field and best-estimate values for the fixed parameters. One of the best-fit simulations matched to the two highest observed data points and the other matched to the third-highest observed data point. A match to the third-highest data point was performed because that point appears to be most consistent with the trend of the rest of the observed curve. The simulations underpredict the time of tracer breakthrough, match the peak concentration well, and predict a slightly shallower slope immediately after the peak than is observed in the data. The total amount of mass recovered at the end of the test predicted by the simulations is a little over 10% higher than the observed total.

The observed data were also matched with the homogeneous model assuming stressed values for the fixed parameters using the two highest concentration values to define the peak (Figure P-14). The stressed values selected were designed to maximize the amount of diffusion and thus require a higher matrix-block length in order to calibrate to the data. Two of the simulations used a thickness equal to that of the lower Culebra (4.2 m) and one simulation used a thickness equal to that of the full Culebra (7.2 m). Values for the fixed parameters were the same for the simulations that used a thickness of 4.2 m, with the exception of the percentage of mass assumed to participate during the test (100% versus 90%). The matrix-block length that best fit the data was higher for the simulation that assumed 90% mass participation than for the simulation that assumed 100%. If the amount of mass in the system is decreased, less mass reduction by matrix diffusion is needed to achieve the same amount of mass recovery at the pumping well and, therefore, the matrix-block length required to match the data increases.

Figure P-15 shows two matches to the observed data using the homogeneous model, stressed values for the fixed parameters, and the third-highest observed data point to define the peak. These

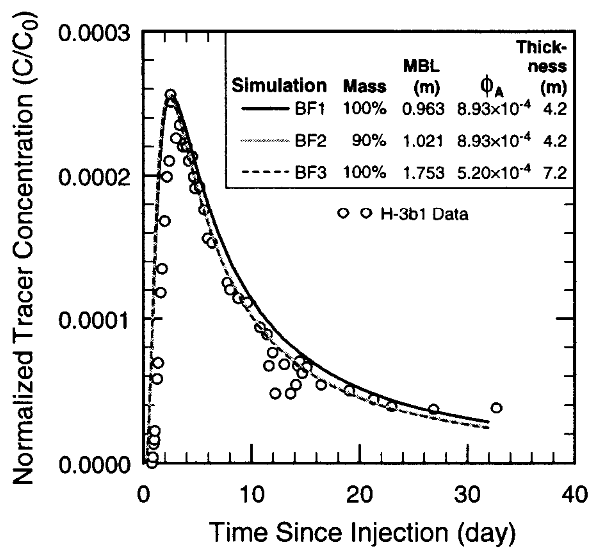

Figure P-14. Observed and simulated tracer-breakthrough curves for the H-3b1 data. Simulations show the best match to the observed data based on matching to the two highest concentration values assuming stressed values for the fixed parameters and a homogeneous hydraulic-conductivity field.

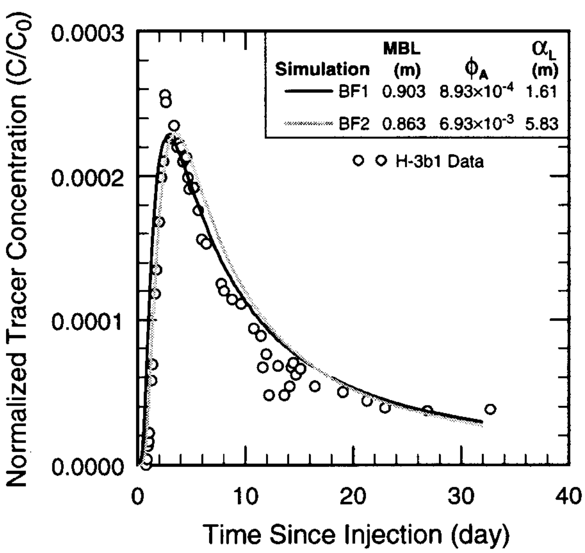

Figure P-15. Observed and simulated tracer-breakthrough curves for the H-3b1 data. Simulations show the best match to the observed data based on matching to the third-highest concentration value assuming stressed values for the fixed parameters and a homogeneous hydraulic-conductivity field.

simulations were designed to evaluate the sensitivity of the calibrated parameters to simultaneous changes in the flow-path length, pumping rate, and free-water diffusion coefficient. The values for these three parameters were selected to reduce the amount of diffusion for simulation BF2 (i.e., smallest flow-path length, fastest pumping rate, and smallest free-water diffusion coefficient) and to increase the amount of diffusion for simulation BF1 (i.e., largest flow-path length, slowest pumping rate, and largest free-water diffusion coefficient). The simulations show that the matrix-block length needed to fit the data decreases as the effects of the other parameters contributing to diffusion decrease. For both simulations, the results show earlier tracer arrival and a shallower falling-limb slope immediately after the peak than were observed.

Heterogeneous simulations using best-estimate values for the fixed parameters considered two realizations for the hydraulic-conductivity field. For each realization, the model results could be matched to the observed data using several combinations of matrix-block length and advective porosity. Figures P-16a and b show two best-fit simulations for realization #1 and realization #2, respectively. Best-fit results for three realizations of the hydraulic-conductivity field for simulations using stressed values for the fixed parameters are shown in Figure P-17. In general, the heterogeneous simulations slightly underpredict the time to tracer breakthrough but match the peak concentration, peak-arrival time, and falling limb of the observed data well. The difference in the total amount of simulated and observed mass recovered at the end of the test is about 9%, with the simulated results predicting greater mass recovery.

The matrix-block lengths determined from the homogeneous and heterogeneous models of the H-3b1 data are similar (Table P-3), indicating minimal effects of heterogeneous flow on the simulated results. In contrast, the interpretations of the H-19b3 data from the H-19 hydropad yielded a higher matrix-block length using the heterogeneous model than using the homogeneous model. This difference in results when comparing matrix-block lengths obtained for homogeneous

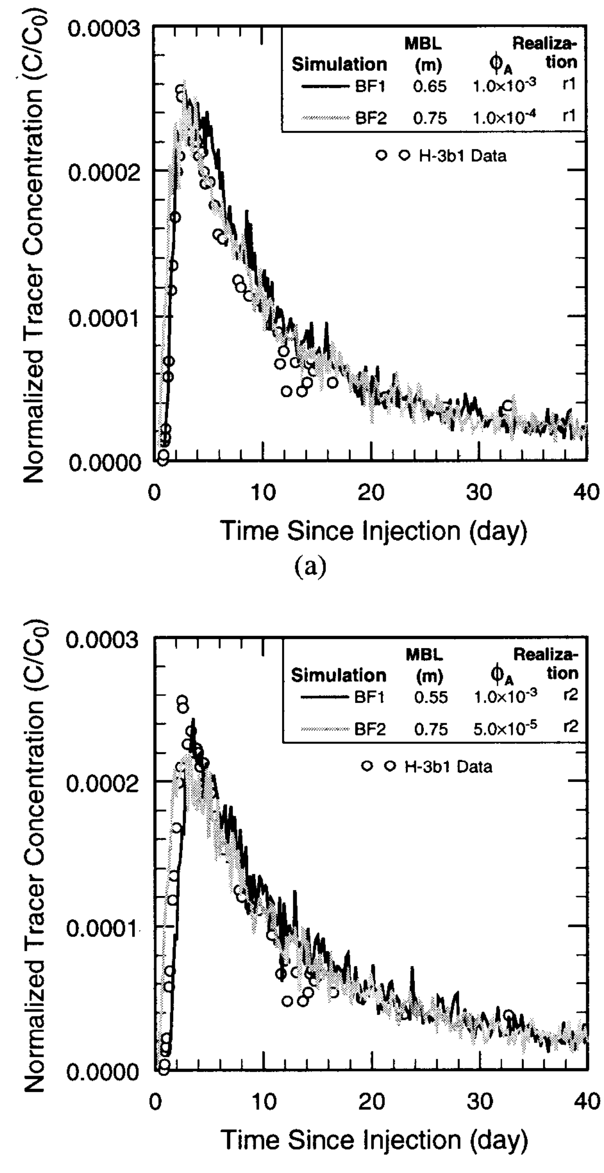

(b)

Figure P-16. **Observed and simulated tracer-breakthrough curves for the H-3b1 data. The simulations show two matchs to the observed data for realization #1 (a) and realization #2 (b) of the hydraulic-conductivity field. All simulations assumed best-estimate values for the fixed parameters.**

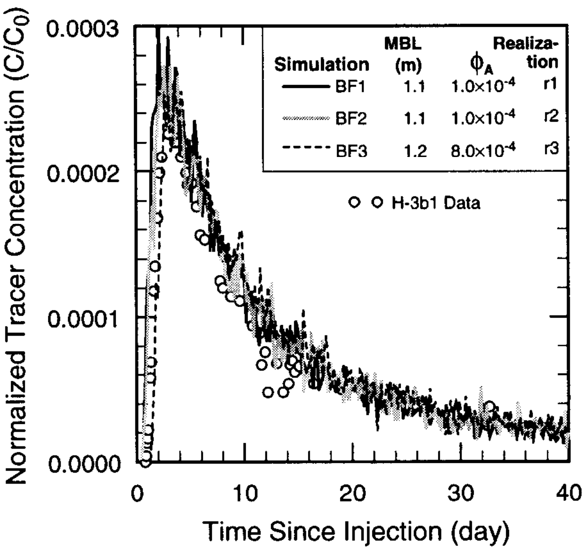

Figure P-17. **Observed and simulated tracer-breakthrough curves for the H-3b1 data. The simulations show one match to the observed data for each of three realizations of the hydraulic-conductivity field. All simulations assumed stressed values for the fixed parameters.**

and heterogeneous hydraulic-conductivity fields may be due to the nature of the heterogeneous hydraulic-conductivity fields used for the H-19 and H-3 simulations. As indicated in Table P-1, the field used for the H-19 simulations was created using a larger variance and a smaller correlation length than were used to create the field for the H-3 simulations. As a result, the field used for the H-19 simulations was more heterogeneous, leading to more tracer spreading, than the field used for the H-3 simulations. The heterogeneity in the hydraulic-conductivity field used for the H-3 simulations was slight, and that field was very similar to a homogeneous field. Therefore, heterogeneity made little contribution to tracer spreading, and retardation was largely ascribed to diffusion. As a result, both the homogeneous and heterogeneous models calculated similar matrix-block lengths.

P.5.4 Results for MWCF Tracer Data from the H-6 Hydropad

The well configuration for the H-6 hydropad is shown in Figure F-4. A series of five convergent-flow tracer tests was conducted at this hydropad between August 1981 and November 1982. A brief discussion of the H-6 tests and the suitability of the observed data for analysis can be found in Appendix F. Details of the tests can be found in Hydro Geo Chem (1985) and Jones et al. (1992). The current analysis considered data for two of the tracers injected during test #1 (PFBA injected into H-6b and m-TFMBA injected into H-6a) and one tracer injected during test #2 (p-FB injected into H-6b). All of the interpretations assumed best-estimate values for the fixed parameters and a homogeneous hydraulic-conductivity field.

Best-fit matches to the observed data from tests #1 and #2 for tracers injected into H-6b are shown in Figures P-18 and P-19, respectively. The simulated results are almost identical to the observed data for test #1 and closely match the test #2 data with the exception of slightly overpredicting tracer tailing. The test conditions for these two tracers were essentially identical, which is reflected by the nearly identical interpretation results (see Table P-3). The simulated total amount of mass recovered is about 2% higher than that observed for test #1 and about 11% higher than that observed for test #2. The best match to the data for the tracer injected into H-6a during test #1 is shown in Figure P-20. As indicated by the figure, calibration of the model to these data was not possible for the Culebra conceptualization and model assumptions used here. Numerous combinations of values for the matrix-block length, advective porosity, and dispersivity were investigated. In each case, the simulated curve significantly overpredicted mass recovery at all times. Jones et al. (1992), however, were able to obtain a reasonable fit to the H-6a data from test #1. Additional investigation is warranted to evaluate why model improvements (see section P.3.2) resulted in an inability to reproduce the observed data.

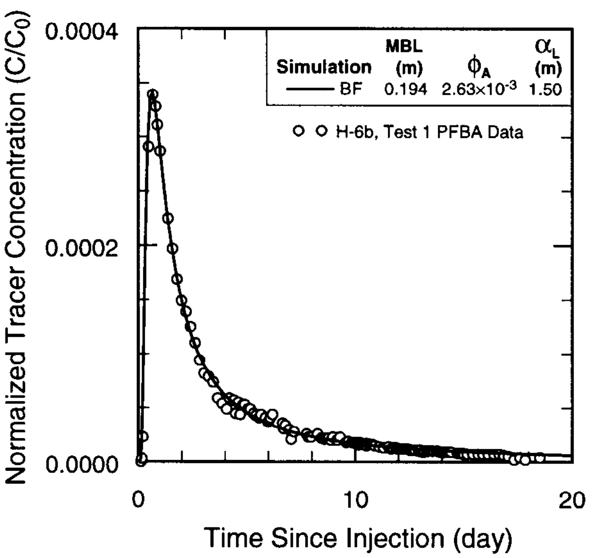

Figure P-18. **Observed and simulated tracer-breakthrough curves for the H-6b Test #1 PFBA data. The simulation shows the best match to the observed data assuming best-estimate values for the fixed parameters and a homogeneous hydraulic-conductivity field.**

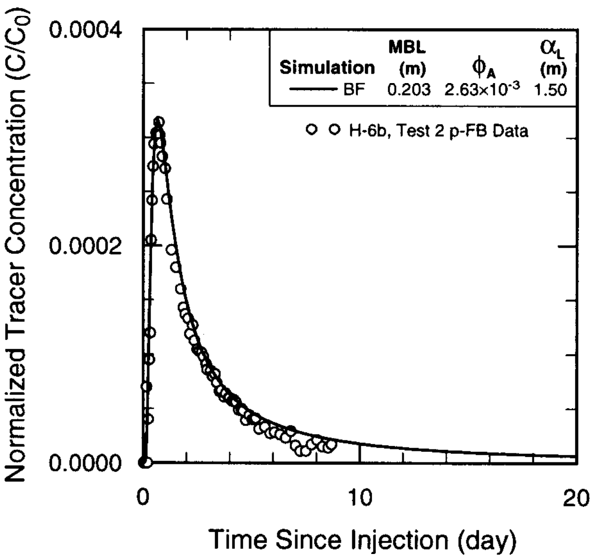

Figure P-19. **Observed and simulated tracer-breakthrough curves for the H-6b Test #2 p-FB data. The simulation shows the best match to the observed data assuming best-estimate values for the fixed parameters and a homogeneous hydraulic-conductivity field.**

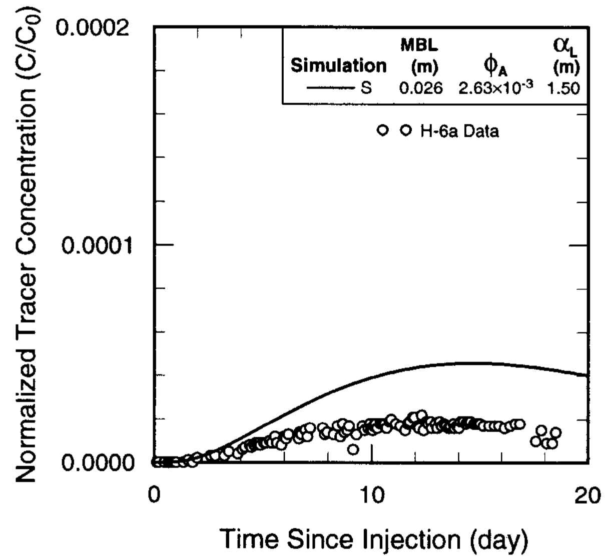

Figure P-20. **Observed and simulated tracer-breakthrough curves for the H-6a Test #1 m-TFMBA data. The simulation shows the best match to the observed data assuming best-estimate values for the fixed parameters and a homogeneous hydraulic-conductivity field.**

P.6 Summary and Conclusions

Observed data from MWCF tracer tests conducted at the H-19, H-11, H-3, and H-6 hydropads at the WIPP site were interpreted using conventional double-porosity models. The interpretations considered both homogeneous and heterogeneous hydraulic-conductivity fields. Results that provided reasonable matches to the observed data are presented along with several instances when the observed data could not be reproduced by the model.

All of the individual data sets from the H-19 tracer test considered by the analysis could be reasonably matched with the model. However, the conventional double-porosity model could not reproduce the similar peak concentrations observed in the data for tracers injected at the same well but transported under different flow regimes (i.e., different pumping rates) using the same parameters. Both the homogeneous and heterogeneous models predicted a lower peak concentration for the same matrix-block length when the pumping rate was lower. This result is inconsistent with the observed data, indicating that all transport processes at work in the formation are not incorporated in the conventional double-porosity model. Simulations discussed in Chapter 7 and Appendix S suggest that a double-porosity model with multiple rates of diffusion rather than a single rate can do a better job of reproducing similar peak concentrations for different pumping rates.

One H-19 data set was interpreted with both the homogeneous and heterogeneous models. The homogeneous model determined a slightly higher advective porosity and lower matrix-block length than did the heterogeneous model. The fact that a higher matrix-block length (i.e., less diffusion) was needed to fit the data with the heterogeneous model may support the theory that some tracer spreading may be due to heterogeneous flow rather than diffusion.

Tracer data for all three flow paths at the H-11 hydropad were interpreted using the homogeneous model. In all cases, the simulated results significantly overpredict the width of the peak and, consequently, overpredict the amount of mass recovered after the peak. This result is inconsistent with the interpretations of the H-19 tracer data that produced simulated results closely matching the observed peak widths. The observed data for tracers injected into H-11b3 under two pumping regimes show similar peak concentrations. The interpretations of those data required a larger matrix-block length (i.e., less diffusion) when the pumping rate was lower in order to reproduce the similar peak concentrations. In summary, the simulations were unable to match similar peak heights for different pumping rates using the same matrix-block length. This result was also found for the H-19 data. The inability of the conventional double-porosity model to match the general trends of the data indicates that this model does not include key processes affecting tracer transport at H-11.

One data set from the H-3 hydropad was interpreted using both the homogeneous and heterogeneous models. In both cases, a good match between the observed and simulated data was obtained, suggesting that a conventional double-porosity conceptualization for the Culebra is appropriate at H-3. However, no attempt was made to match the data for the tracer injected into H-3b2. Therefore, the conventional double-porosity model has not been evaluated with respect to all of the available data at this hydropad. The matrix-block lengths determined by the homogeneous and heterogeneous models using best-estimate values for the fixed parameters were very similar. The simulations of the H-19b3 Round 1 data, on the other hand, yielded a higher matrix-block length with the heterogeneous model than with the homogeneous model. This difference in trend when comparing heterogeneous and homogeneous simulation results is due to the difference in the nature of the heterogeneous hydraulic-conductivity fields used for the two simulations. The field used for the H-19 simulations was more heterogeneous than the field used for the H-3 simulations due to the use of a higher variance and lower correlation length. Consequently, the difference in matrix-block lengths determined for the heterogeneous and homogeneous simulations was greater for interpretations of the H-19 data than for the interpretations of the H-3 data.

For the H-6 hydropad, two tracer data sets for the H-6b to H-6c flow path and one set for the H-6a to H-6c flow path were interpreted using the homogeneous model. Excellent agreement between the simulated and observed tracer-breakthrough curves was obtained for both sets of H-6b data. On the other hand, the model could not be calibrated to the H-6a data. This inconsistency suggests that, at the H-6 hydropad, the Culebra can not be represented by a conventional double-porosity conceptualization.

Although the homogeneous and heterogeneous conventional double-porosity models were able to match the observed data (except from the H-6a to H-6c flow path) reasonably well when considering each data set individually, the conventional double-porosity model is inconsistent with the observed data in the following ways: (1) it can not reproduce the similar peak concentrations observed in the H-19 and H-11 data for tracers transported along the same flow paths at different pumping rates; (2) it significantly overpredicts mass recovery after the peak for all H-11 data; and (3) it provides an excellent match to the observed data for one flow path at the H-6 hydropad but can not be calibrated to the data for the other flow path.

These inconsistencies suggest that crucial transport processes within the Culebra are not incorporated in a conventional double-porosity model. Simulations discussed in Chapter 7 and Appendix S suggest that some of these inconsistencies between model results and observed data can be eliminated by using a double-porosity model that incorporates multiple rates of diffusion (multirate model) rather than limiting diffusion to a single rate.

P.7 References

Bear, J., and C. Braester. 1972. Simultaneous Flow of Immiscible Liquids in a Fractured Medium, from *Fundamentals of Transport Phenomena in Porous Media.* New York, NY: American Elsevier Publishing Company.

Beauheim, R.L. 1987. *Interpretations of Single-Well Hydraulic Tests Conducted At and Near the Waste Isolation Pilot Plant (WIPP) Site, 1983-1987.* SAND87-0039. Albuquerque, NM: Sandia National Laboratories.

Finley, N.C., and M. Reeves. 1981. *SWIFT Self-Teaching Curriculum: Illustrative Problems to Supplement the User's Manual for the Sandia Waste-Isolation Flow and Transport Model (SWIFT).* SAND81-0410, NUREG/CR-1968. Albuquerque, NM: Sandia National Laboratories.

Gelhar, L.W., A. Mantoglou, C. Welty, and K.R. Rehfeldt. 1985. *A Review of Field-Scale Physical Solute Transport Processes in Saturated and Unsaturated Porous Media.* EPRI EA-4190. Palo Alto, CA: Electric Power Research Institute.

Grisak, G.E., and J.F. Pickens. 1980. "Solute Transport Through Fractured Media, 1. The Effect of Matrix Diffusion," *Water Resources Research.* Vol. 16, no. 4, 719-730.

Gutjahr, A.L., S. Hatch, and B. Bullard. 1995. "Random Field Generation, Conditional Simulations, and Flow Modeling Using the Fast Fourier Transform," [Mathematics Department Technical Report. Socorro, NM: New Mexico Institute of Mining and Technology.] (Copy on file in the Sandia WIPP Central Files (SWCF) as ERMS #510145.)

Hale, F.V., and Y.W. Tsang. 1996. *THEMM User Guide Version 1.0 (7-16-96).* Berkeley, CA: Lawrence Berkeley Laboratory. (Copy on file in the SWCF as ERMS #235261.)

Huyakorn, P.S., B.H. Lester, and J.W. Mercer. 1983. "An Efficient Finite Element Technique for Modeling Transport in Fractured Porous Media, 1. Single Species Transport," *Water Resources Research.* Vol. 19, no. 3, 841-854.

Hydro Geo Chem, Inc. 1985. *WIPP Hydrology Program, Waste Isolation Pilot Plant, SENM, Hydrologic Data Report #1.* SAND85-7206. Albuquerque, NM: Sandia National Laboratories.

INTERA Technologies, Inc. 1986. *WIPP Hydrology Program, Waste Isolation Pilot Plant, Southeastern New Mexico, Hydrologic Data Report #3.* SAND86-7109. Albuquerque, NM: Sandia National Laboratories.

Jones, T.L., V.A. Kelley, J.F. Pickens, D.T. Upton, R.L. Beauheim, and P.B. Davies. 1992. *Integration of Interpretation Results of Tracer Tests Performed in the Culebra Dolomite at the Waste Isolation Pilot Plant Site.* SAND92-1579. Albuquerque, NM: Sandia National Laboratories.

Lallemand-Barrès, A., and P. Peaudecerf. 1978. "Recherche des Relations Entre la Valeur de la Dispersivité Macroscopique d'un Milieu Aquifère, Ses Autres Caractéristiques et les Conditions de Mesure," *Bulletin du B.R.G.M. (Deuxième Série).* Section III, no. 4, 277-284.

Pickens, J.F., and G.E. Grisak. 1981. "Scale-Dependent Dispersion in a Stratified Granular Aquifer," *Water Resources Research.* Vol. 17, no. 4, 1191-1211.

Pruess, K., and T.N. Narasimhan. 1982. "A Practical Method for Modeling Fluid and Heat Flow in Fractured Porous Media." SPE 10509. Richardson, TX: Society of Petroleum Engineers.

Rasmuson, A., T.N. Narasimhan, and I. Neretnieks. 1982. "Chemical Transport in a Fissured Rock: Verification of a Numerical Model," *Water Resources Research.* Vol. 18, no. 5, 1479-1492.

Reeves, M., D.S. Ward, N.D. Johns, and R.M. Cranwell. 1986a. *Theory and Implementation for SWIFT II the Sandia Waste-Isolation Flow and Transport Model for Fractured Media Release 4.84.* NUREG/CR-3328, SAND83-1159. Albuquerque, NM: Sandia National Laboratories.

Reeves, M., D.S. Ward, N.D. Johns, and R.M. Cranwell. 1986b. *Data Input Guide for SWIFT II, the Sandia Waste-Isolation Flow and Transport Model for Fractured Media, Release 4.84.* SAND83-0242, NUREG/CR-3925. Albuquerque, NM: Sandia National Laboratories.

Reeves M., D.S. Ward, P.A. Davis, and E.J. Bonano. 1987. *SWIFT II Self-Teaching Curriculum: Illustrative Problems for the Sandia Waste-Isolation Flow and Transport Model for Fractured Media.* SAND84-1586 Revision, NUREG/CR-3925. Albuquerque, NM: Sandia National Laboratories.

Stensrud, W.A., M.A. Bame, K.D. Lantz, J.B. Palmer, and G.J. Saulnier, Jr. 1990. *WIPP Hydrology Program, Waste Isolation Pilot Plant, Southeastern New Mexico, Hydrologic Data Report #8.* SAND89-7056. Albuquerque, NM: Sandia National Laboratories.

Streltsova-Adams, T.D. 1978. "Well Hydraulics in Heterogeneous Aquifer Formations," *Advances in Hydroscience.* Vol. 11, 357-423.

Tang, D.H., E.O. Frind, and E.A. Sudicky. 1981. "Contaminant Transport in Fractured Porous Media, 1. Analytical Solution for a Single Fracture," *Water Resources Research.* Vol. 17, no. 3, 555-564.

US Department of Energy. 1996. *Title 40 CFR Part 191 Compliance Certification Application for the Waste Isolation Pilot Plant.* DOE/CAO-1996-2184. Carlsbad, NM: US DOE Waste Isolation Pilot Plant, Carlsbad Area Office. Vols. I-XXI.

Ward, D.S., M. Reeves, and L.E. Duda. 1984. *Verification and Field Comparison of the Sandia Waste-Isolation Flow and Transport Model (SWIFT).* SAND83-1154, NUREG/CR-3316. Albuquerque, NM: Sandia National Laboratories.

This page intentionally left blank.

Appendix Q
Laplace-Domain Solution for Multirate Model

By Roy Haggerty[1]

A mathematical model describing advective-dispersive solute transport with multirate diffusion was used in Chapter 6 of this report to analyze SWIW data from the Culebra tracer tests. The solutions to the equations are obtained in the Laplace domain and then numerically inverted using the de Hoog algorithm (de Hoog et al., 1982). The solutions are performed sequentially for each of the injection, resting, and pumping periods of the SWIW test. The purpose of this appendix is to derive the Laplace-domain solutions.

Haggerty and Gorelick (1995, 1998) show that the solute-transport and mass-transfer relationships given in Equations 6-1, 6-2a, 6-3a, 6-3b, and 6-3c in Chapter 6 can be re-written as follows:

$$\frac{\partial c_a}{\partial t} + \int_0^\infty b(\alpha_m)\frac{\partial c_m(\alpha_m)}{\partial t}\,d\alpha_m = \frac{1}{r}\frac{\partial}{\partial r}\left(\frac{r\alpha_L|v|}{R_a}\frac{\partial c_a}{\partial r}\right) - \frac{v}{R_a}\frac{\partial c_a}{\partial r} \qquad \text{(Q-1)}$$

$$b(\alpha_m) = \sum_{j=1}^{\infty} \frac{8\beta_{tot}}{\sqrt{2\pi^5}\,(2j-1)^2\,\sigma_d\alpha_m} \times \exp\left\{-\frac{\left[\ln\left(\frac{4\alpha_m}{\pi^2(2j-1)^2}\right)-\mu_d\right]^2}{2\sigma_d^2}\right\} \qquad \text{(Q-2)}$$

$$c_m(\alpha_m) = \alpha_m\left[c_a - c_m(\alpha_m)\right],\, 0 < \alpha_m < \infty \qquad \text{(Q-3)}$$

All variables not defined in this appendix were previously defined in Chapter 6. The same boundary conditions apply as discussed in Sections 6.2.1 through 6.2.3. The boundary condition given in Equation 6-3c has no equivalent in the above equations, but is dealt with implicitly. Using Equations Q-1 through Q-3 is completely equivalent in every way to using Equations 6-1 through 6-3c. However, the immobile concentrations (c_m) are only mathematical constructs, and are used solely for the purpose of "storing" mass. The advantage of using Equations Q-1 through Q-3 is that they are mathematically simpler to use, and eliminate the need to solve many diffusion equations for concentrations within a distribution of immobile zones (each of which would need to be discretized using finite differences, finite elements, etc.). For a more complete description of this approach to solving a multirate-diffusion problem, see Haggerty and Gorelick (1995, 1998).

We solve for concentrations after the injection period, resting period, and during the pumping period by converting Equations Q-1 through Q-3 to the Laplace domain. The solution to the differential equation(s) is found in the Laplace domain, and then concentrations are obtained by inverting numerically to the time domain. Similar and related solutions have been documented extensively by Chen (1985), Chen and Woodside (1988), Harvey et al. (1994), and Haggerty and Gorelick (1995, 1998). Therefore, we will give only the solutions in the Laplace domain, and not the derivation. The STAMMT-R (Solute Transport And Multirate Mass Transfer in Radial coordinates) code (Haggerty et al., 2000) was constructed to solve this problem and to estimate the parameters of the distribution of diffusion-rate coefficients for SWIW tests and for multiwell tracer tests. This code has undergone QA qualification at Sandia National Laboratories.

---

[1] Oregon State University, Department of Geosciences, 104 Wilkinson Hall, Corvallis, OR 97331-5506. Email: haggertr@geo.orst.edu.

The solution in the Laplace domain to Equations Q-1 through Q-3 during the injection period can be expressed nondimensionally as:

$$\overline{c}_a = \overline{c}_{inj} \exp\left(\frac{\rho - \rho_o}{2}\right) \frac{\mathrm{Ai}\left(P^{1/3} y\right)}{\frac{1}{2}\mathrm{Ai}\left(P^{1/3} y_o\right) - P^{1/3}\mathrm{Ai}'\left(P^{1/3} y_o\right)} \qquad \text{(Q-4)}$$

where:

$$y = \rho + \frac{1}{4P} \qquad \text{(Q-5)}$$

$$P = s\left[1 + \int_0^\infty \frac{b(\omega_m)\omega_m}{s + \omega_m} d\omega_m\right] \qquad \text{(Q-6)}$$

$$T = \frac{Q_{inj} t}{2\pi b \phi_a \alpha_L^2 R_a} \qquad \text{(Q-7)}$$

$$\omega_m = \alpha_m \frac{2\pi b \phi_a \alpha_L^2 R_a}{Q_{inj}} \qquad \text{(Q-8)}$$

$$\rho = \frac{r}{\alpha_L} \qquad \text{(Q-9)}$$

The injected concentrations (c_{inj}) also must be transformed into the Laplace domain, as indicated in Equation Q-4. Although using a non-uniform injected concentration is simple, we assume that injected concentrations begin at zero, then go instantaneously to a uniform value for a given pulse length, and then instantaneously return to zero. The Laplace transform of this square wave, which can be directly substituted into Equation Q-4, is:

$$\overline{c_{inj}} = c_{inj} \frac{\exp\left(sT_{inj,i}\right) - \exp\left(sT_{inj,i-1}\right)}{s} \qquad \text{(Q-10)}$$

Times are nondimensionalized in the same way as in Equation Q-7. For our purposes, we do not bother nondimensionalizing concentration as its nondimensional form does not change the solution.

The solution in the Laplace domain to Equations Q-1 through Q-3 during the resting period can be expressed without need to nondimensionalize as:

$$\overline{c_a} = \frac{c_a' + \int_0^\infty \frac{b(\alpha_m)\alpha_m}{s + \alpha_m} c_m'(\alpha_m) d\alpha_m}{s\left[1 + \int_0^\infty \frac{b(\alpha_m)\alpha_m}{s + \alpha_m} d\alpha_m\right]} \qquad \text{(Q-11)}$$

and

$$\overline{c_m(\alpha_m)} = \frac{\alpha_m}{s + \alpha_m}\overline{c}_a + \frac{c_m'(\alpha_m)}{s + \alpha_m} \qquad \text{(Q-12)}$$

Concentrations are inverted at times defined since the beginning of the resting period.

The solution in the Laplace domain to Equations Q-1 through Q-3 during the pumping period can be expressed nondimensionally as:

$$\overline{c}_a = \exp\left(-\frac{\rho_w}{2}\right)\int_{\rho_w}^\infty \xi \exp\left(\frac{\xi}{2}\right) F(\xi)\, g_1(\rho, s, \xi)\, d\xi \qquad \text{(Q-13)}$$

where T is redefined as:

$$T = \frac{Q_{out}\left(t - t_{rest} - \sum_{i=1}^{N} t_{inj,i}\right)}{2\pi b \phi_a {\alpha_L}^2 R_a} \qquad \text{(Q-14)}$$

Variables in Equation Q-13 are defined as follows:

$$F(\rho) = c_a'(\rho) + \int_0^\infty \frac{b(\omega_m)\omega_m}{s + \omega_m} c_m'(\omega_m, \rho) d\omega_m \qquad \text{(Q-15)}$$

$$\begin{aligned} g_1 = {} & \frac{\pi}{P^{1/3}}\mathrm{Ai}\left(P^{1/3}\Lambda\right)\times \\ & \left[\mathrm{Bi}\left(P^{1/3} y_o\right) - X\ \mathrm{Ai}\left(P^{1/3} y_o\right)\right] \end{aligned} \qquad \text{(Q-16)}$$

$$X = \frac{P^{1/3}\ \mathrm{Bi}'\left(P^{1/3} y_o\right) - \frac{1}{2}\ \mathrm{Bi}\left(P^{1/3} y_o\right)}{P^{1/3}\ \mathrm{Ai}'\left(P^{1/3} y_o\right) - \frac{1}{2}\ \mathrm{Ai}\left(P^{1/3} y_o\right)} \qquad \text{(Q-17)}$$

$$\Lambda = \xi + \frac{1}{4P} \qquad \text{(Q-18)}$$

and all other variables are as previously defined.

References

Chen, C-S. 1985. "Analytical and Approximate Solutions to Radial Dispersion from an Injection Well to a Geological Unit with Simultaneous Diffusion into Adjacent Strata," *Water Resources Research.* Vol. 21, no. 8, 1069-1076.

Chen, C-S., and G.D. Woodside. 1988. "Analytical Solution for Aquifer Decontamination by Pumping," *Water Resources Research.* Vol. 24, no. 8, 1329-1338.

de Hoog, F.R., J.H. Knight, and A.N. Stokes. 1982. "An Improved Method for Numerical Inversion of Laplace Transforms," *SIAM Journal on Scientific and Statistical Computing.* Vol. 3, no. 3, 357-366.

Haggerty, R., and S.M. Gorelick. 1995. "Multiple-Rate Mass Transfer for Modeling Diffusion and Surface Reactions in Media with Pore-Scale Heterogeneity," *Water Resources Research.* Vol. 31, no. 10, 2383-2400.

Haggerty, R., and S.M. Gorelick. 1998. "Modeling Mass Transfer Processes in Soil Columns with Pore-Scale Heterogeneity," *Soil Science Society of America Journal.* Vol. 62, no. 1, 62-74.

Haggerty, R., S.W. Fleming, and S.A. McKenna. 2000. *STAMMT-R, Solute Transport and Multirate Mass Transfer in Radial Coordinates: A FORTRAN Code for Modeling and Analyzing Radial Single-Well and Two-Well Tracer Tests in Formations Exhibiting Multiple Rates of Diffusive Mass Transfer.* SAND99-0164. Albuquerque, NM: Sandia National Laboratories.

Harvey, C.F., R. Haggerty, and S.M. Gorelick. 1994. "Aquifer Remediation: A Method for Estimating Mass Transfer Rate Coefficients and an Evaluation of Pulsed Pumping," *Water Resources Research.* Vol. 30, no. 7, 1979-1991.

This page intentionally left blank.

Appendix R
Estimation of Diffusive Mass-Transfer for Continuous Rate Distributions from a Single-Well Injection-Withdrawal Tracer Test

By Winston Yu[1] and Charles Harvey[2]

Abstract

We present a method for estimating a continuous distribution of mass-transfer rates from single-well injection-withdrawal (push-pull) tracer tests. Data from the H-11 single-well injection-withdrawal (SWIW) tracer test performed in a fractured dolomite by Sandia National Laboratories are investigated. Instead of assuming a particular statistical distribution function, such as a lognormal distribution, a piece-wise linear model is used to facilitate calculation of uncertainties along the entire distribution of rate coefficients. Comparison between the linear piece-wise model and a lognormal rate distribution shows that both models estimate similar cumulative mass-transfer capacities for rate coefficients that span the time scale of the actual experiment. However, the piece-wise model estimated a larger total capacity coefficient than the lognormal model for the data set examined. Finally, the linear piece-wise model provided uncertainty estimates for mass-transfer rate coefficients that generally increased with the time scale.

R.1 Introduction

Accurate models of mobile/immobile domain mass-transfer in the subsurface are important for the prediction of contaminant transport. Mass-transfer between mobile and immobile pore spaces is often modeled as a first-order non-equilibrium process, or as diffusion in and out of immobile regions of idealized geometries such as spheres or layers of uniform size. Recent literature and observations in the field suggest that in natural formations, mass transfer is best described by multiple rate coefficients (Haggerty and Gorelick, 1995; Fong and Mulkey, 1990; Cunningham et al., 1997; Chen and Wagenet, 1995, 1997; Pedit and Miller, 1994; Culver et al., 1997). The work presented in Chapter 6 uses classical least-squares methods to estimate the parameters of a lognormal distribution of rate coefficients from single-well injection-withdrawal (SWIW) tracer tests performed in the Culebra dolomite. It also estimates the advective porosity that, with a known matrix porosity, provides the total mass-transfer capacity. It further estimates uncertainties in the mean and variance of the lognormal distribution and the advective porosity.

The goal of this appendix is to demonstrate a method for estimating a continuous distribution of mass-transfer coefficients, and the uncertainty of this distribution, from SWIW tracer tests without constraining the estimated distribution to a particular shape. This appendix builds upon the estimation method presented in Hollenbeck et al. (1999). They estimated a piece-wise linear distribution of mass-transfer coefficients from laboratory batch and purge experiments. Here we apply the estimation method to SWIW experiments.

The piece-wise linear model has several advantages over distributions borrowed from statistics such as the lognormal or gamma distribution. First, it can be used to model distributions that have arbitrary, even multimodal, shapes. Second, multivariate linear statistics can be used to formulate uncertainty in rate-distribution estimates. Third, we can use the piece-wise linear model to

---

[1] Harvard University, Environmental Sciences and Engineering, Pierce Hall 120, 29 Oxford Street, Cambridge, MA 02138. Email: whyu@deas.harvard.edu.

[2] Ralph M. Parsons Laboratory, Massachusetts Institute of Technology, Cambridge, MA 02139. Email: charvey@mit.edu.

determine the time scales over which predictions can be made using parameters estimated from a particular experiment. With the piece-wise linear model, we can estimate the capacity associated with different sections of a distribution of rate coefficients, and we can also estimate the uncertainty associated with each of these sections. We can then use these estimated uncertainties to determine the time scales over which we can accurately predict solute behavior. Typically, uncertainty increases for time scales much shorter and much longer than the experimental time scale. The piece-wise linear model provides a useful tool for answering questions such as:

- how much does our uncertainty increase for time scales longer than the experimental time scale?
- how does this uncertainty differ for various experimental designs? and
- how can we design experiments that minimize the uncertainty of capacities associated with very slow rates?

R.2 Method

The method used here couples the multi-variate Baysian estimation method presented in Hollenbeck et al. (1999) with a quasi-analytic simulation method similar to that presented in Chapter 6. Here we give a general presentation of these coupled methods. The reader is referred to either Hollenbeck et al. (1999) or Chapter 6 for complete mathematical details.

R.2.1 Quasi-Analytic Model of the Sandia SWIW Tracer Tests

A MATLAB code was constructed to simulate the three stages of a SWIW tracer test: (1) injection of solute into the aquifer followed by a clean chaser (a square wave input at the well), (2) a resting period, and (3) withdrawal of the tracer by pumping.

For all three stages, the governing equations consist of the mass-balance equation in radial coordinates:

$$\frac{\partial C}{\partial t}+\int_0^\infty b(\alpha)\frac{\partial S(\alpha)}{\partial t}d\alpha=\frac{1}{r}\frac{\partial}{\partial r}r\alpha_L|v|\frac{\partial C}{\partial r}-v\frac{\partial C}{\partial r} \tag{R-1}$$

coupled with a multirate mass-transfer equation:

$$\frac{\partial S(\alpha)}{\partial t}=\alpha\left(C-S(\alpha)\right) \tag{R-2}$$

where C is the concentration in the mobile domain [M/L^3], α is the mass-transfer rate coefficient [1/T], $S(\alpha)$ is the concentration in the immobile domain associated with a particular rate coefficient [M/L^3], $b(\alpha)$ describes the distribution of rate coefficients [T], α_L is the longitudinal dispersivity [L], v is the velocity [L/T], r is the distance from the well [L], and t is time [T]. During the injection stage, v is positive, during the resting stage, v is zero (so the right-hand side of Equation R-1 drops out), and during the withdrawal stage, v is negative. The mass-transfer equation is a linear first-order model.

The distribution of rate coefficients $b(\alpha)$ is described by a piece-wise linear function:

$$b(\alpha)=\frac{b_{i+1}-b_i}{\alpha_{i+1}-\alpha_i}\left(\alpha-\alpha_i\right)+b_i \qquad \text{for } \alpha_i\le\alpha\le\alpha_{i+1} \tag{R-3}$$

where the pairs (α_i, b_i) describe the endpoints of linear segments and i goes from 0 to the number of linear segments (see Figure R-1). For values of α_i below the first segment or above the last segment, the capacity b_i is zero.

The formulation of R-1, R-2, and R-3 differ from the formulation given in Chapter 6 in two principal ways. First, the piece-wise linear distribution (Equation R-3) rather than the lognormal distribution is used. Second, a linear non-equilibrium mass-transfer expression (Equation R-2) is used rather than a diffusive mass-transfer expression. This second difference is not of practical significance because a distribution can always be found

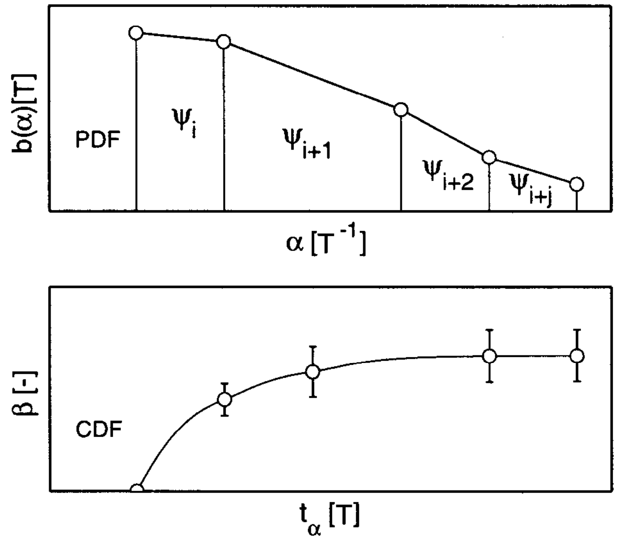

Figure R-1. Example of piece-wise linear *b(α)* function, and the associated cumulative *β(α)* function which describes the integrated piece-wise linear distribution. Note that the X-axis for the cumulative function is the inverse of the mass-transfer coefficient, the time scale of mass-transfer. The cumulative function is curved due to the log transformation.

such that the linear non-equilibrium and diffusive mass-transfer formulations are equivalent. Haggerty and Gorelick (1995) showed that rate coefficient distributions can be translated between the two formulations because any single diffusive mass-transfer rate coefficient can be represented by a series of linear rate coefficients.

Equations R-1 and R-2 are solved by taking the Laplace transform and manipulating the equations into an inhomogeneous Airy equation, determining the Green's function solution for the transformed equations, and then back transforming the Laplace solution numerically into the time domain. Refer to Chapter 6 for the mathematical details. For the numerical inverse transform, we used a version of the de Hoog algorithm (de Hoog et al., 1982).

R.2.2 Multivariate Statistical Method for Estimating a Piece-Wise Linear Distribution of Rate Coefficients

The piece-wise linear function (Equation R-3) is estimated from the observed concentrations in the withdrawn water by anchoring the mass-transfer rate coefficients α_i at the end points of each segment, and estimating the values of the capacity b_i associated with each α_i anchor. In other words, we estimate the piece-wise linear distribution by moving the endpoints of the segments up and down with respect to the capacity axis, but not back and forth with respect to the rate-coefficient axis. In order to guarantee positive values of b_i, the natural logarithm *ln b* is estimated. Assuming that the prior *ln b* and the measurement errors are normally distributed, the classic Bayesian least-squares objective function, *J(ln b)*, is:

$$J(lnb) = \left(C_{obs} - C(lnb)\right)^T Q_v^{-1}\left(C_{obs} - C(lnb)\right) + \left(lnb - ln\bar{b}\right)^T Q_{lnb}^{-1}\left(lnb - ln\bar{b}\right) \tag{R-4}$$

where: Q_v [M/L^3]^2 is the vector of measurement errors, $Q_{ln\ b}$ [M/L^3]^2 is the covariance matrix for the prior $ln\ b_i$ values, *ln b* is the capacity vector, C_{obs} [M/L^3] are the observed concentrations, and the superscript T represents the transpose of the matrix. The first term describes the difference between the model prediction and the observed concentrations weighted by the measurement covariance matrix and the second term describes the difference between the prior and posterior mean *b(α)* function weighted by the prior *b(α)* covariance matrix. If the prior values are completely uncertain, then the second term drops out.

The b_i estimates are found through an iterative optimization of Equation R-4 (a <2% convergence criterion was used):

$$
\begin{aligned}
& ln\, \hat{b}_{k+1} = ln\, \hat{b}_k + \\
& \left\{ \frac{\partial C\,(ln\, b)^T}{\partial\, ln\, b_k}\, Q_v^{-1}\, \frac{\partial C\,(ln\, b)}{\partial\, ln\, b_k} + Q_{ln\, b}^{-1} \right\}^{-1} \times \\
& \left\{ \frac{\partial C\,(ln\, b)^T}{\partial\, ln\, b_k}\, Q_v^{-1} \left(C_{obs} - C\,(ln\, b) \right) + \right. \\
& \left. Q_{ln\, b}^{-1} \left(ln\, \hat{b}_k - ln\, \overline{b} \right) \right\}
\end{aligned}
\tag{R-5}
$$

where the derivatives are evaluated numerically.

Uncertainty in the final parameter estimates is calculated by using a modified Cramer-Rao bound adjusted to incorporate the prior covariance matrix for the initial estimate of $b(\alpha)$. So, the covariance matrix for parameter estimates is a lower bound given by the matrix:

$$
\Sigma_{b(\alpha)} \geq \left(\frac{\partial C\left(\hat{b}\right)^T}{\partial b_k} Q_v^{-1} \frac{\partial C\left(\hat{b}\right)}{\partial b_k} + Q_b^{-1} \right)^{-1}
\tag{R-6}
$$

where the derivatives are numerically calculated about the final estimate. The Cramer-Rao bound may underestimate the uncertainty in some circumstances, such as non-Gaussian measurement errors or strongly non-linear functions.

Once the vector of b_i's has been estimated for each rate coefficient, the cumulative capacity, or integrated distribution, can be calculated as:

$$
\begin{aligned}
\beta_n &= \tfrac{1}{2} \begin{bmatrix} \alpha_{n-1} - \alpha_n \\ \alpha_{n-2} - \alpha_n \\ \vdots \\ \alpha_2 - \alpha_4 \\ \alpha_1 - \alpha_3 \\ \alpha_1 - \alpha_2 \end{bmatrix}^T \begin{bmatrix} b(\alpha_n) \\ b(\alpha_{n-1}) \\ \vdots \\ b(\alpha_3) \\ b(\alpha_2) \\ b(\alpha_1) \end{bmatrix} \\
&\equiv I_n^T b(\alpha_{n \ldots 1})
\end{aligned}
\tag{R-7}
$$

This equation integrates from large to small α, giving a cumulative distribution that goes from small time scale ($1/\alpha$) to large time scale. Note that the end points are handled as special cases.

The variance of the cumulative capacity is:

$$
\sigma_{\beta_n}^2 = I_n^T\, \Sigma_{b(\alpha_{n \ldots 1})}\, I_n \tag{R-8}
$$

This formulation takes account of the information contained in the parameter covariance matrix Σ for describing cross-covariances among estimated $b(\alpha)$'s. In general, the estimated b_i's are negatively correlated – if one goes up, the neighbors to the right and left must go down. This means that when the density function is integrated to the cumulative function, the uncertainties are not simply summed. In fact, the uncertainty may decrease because of the negative correlation. Thus, the uncertainty along the cumulative density function, as shown by error bars along the plot, contains information that is not represented by the uncertainty plotted along the density function.

R.3 Results

To illustrate the estimation procedure outlined, the data for the SWIW injection of 2,4-DCBA (tracer 1) at the H-11 hydropad were truncated from 140 points to 12 points to quicken computation time. We believe that additional data points would not significantly change the final estimated capacity coefficient. All parameters used to model the SWIW test are given in Table R-1.

The 95% confidence intervals (two standard deviations) for each of these data (see Appendix C) are used to construct the diagonal (i.e., the variance) of the error covariance matrix, Q_v. Correlation between measurement errors is assumed to be zero, so the off-diagonal terms of the covariance matrix are assumed zero. We assume no prior knowledge of the $ln(b)$ values, so the second term in Equation R-4 drops out. Five anchor points were established corresponding to mass-transfer time scales ($1/\alpha$) of 1, 10, 100, 1000, and 10000 hr.

The fit to the data is shown in Figure R-2. The root mean square error, defined on concentrations, is 2.25. Note that the estimated fit lies between

Table R-1. Fixed Parameters for H-11 SWIW Test, Tracer 1

Parameter	Value
Solute injection time [hr]	2.2667
Chaser injection time [hr]	4.2833
Pause length [hr]	17.66
Injection rate [m^3/hr]	0.4392
Pumping rate [m^3/hr]	0.8064
Grid radius [m]	8.0
Well radius [m]	0.065
Saturated thickness [m]	4.4
Matrix porosity [-]	0.16
Advective porosity [-]	0.001634*
Dispersivity [m]	0.1

* advective porosity of 0.01 was also used with no change in estimated results

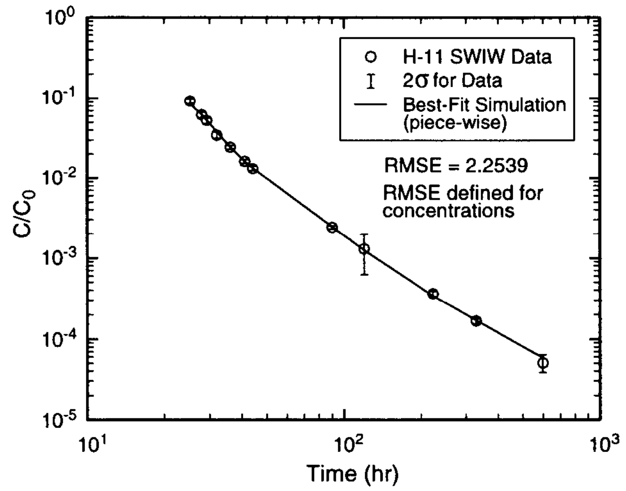

Figure R-2. Best fit to a subset of the H-11 SWIW (2,4-DCBA) data with a piece-wise linear distribution of mass-transfer coefficients.

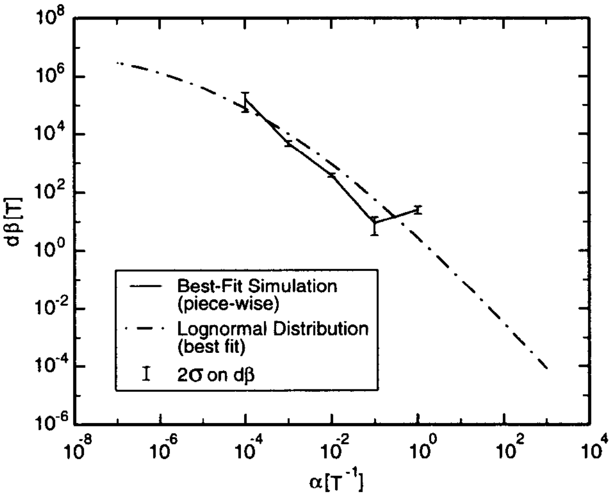

Figure R-3. Final estimated piece-wise linear rate distribution with 2σ confidence intervals estimated with the Cramer-Rao bound, and the estimated lognormal distribution for simulations presented in Chapter 6.

the measurement errors as is expected, even as the observed concentration changes over four orders of magnitude. Figure R-3 shows the estimated multirate distribution with two standard deviation confidence intervals. The estimated piece-wise linear distribution is compared to the lognormal distribution estimated by the simulations presented in Chapter 6 for the same tracer data set. The lognormal distribution for diffusion-rate coefficients given in Chapter 6 has been converted to the equivalent distribution of first-order rate coefficients. (For the mathematical details of this translation, see Haggerty and Gorelick (1995) and Hollenbeck et al. (1999).) Error bars are not calculated for the lognormal distribution. The estimated piece-wise linear distribution has greater capacity than the estimated lognormal model at both the very long and the very short time scales of mass transfer. The larger capacity and small uncertainty at the short time scale ($\alpha = 1$ hr^{-1}) are both presumably due to the fact that $\alpha = 1$ hr^{-1} is the largest rate coefficient considered. Mass transfer that occurs over a shorter time scale (larger rate coefficient) than the time scale of the first anchor will be lumped into this anchor because this mass transfer occurs over a shorter time scale than the time to the first measurement and cannot be accurately distinguished from instantaneous mass transfer.

Figure R-4 shows the cumulative rate coefficient distribution as a function of the time scale of mass transfer, $1/\alpha$. The cumulative $\beta(\alpha)$ function is

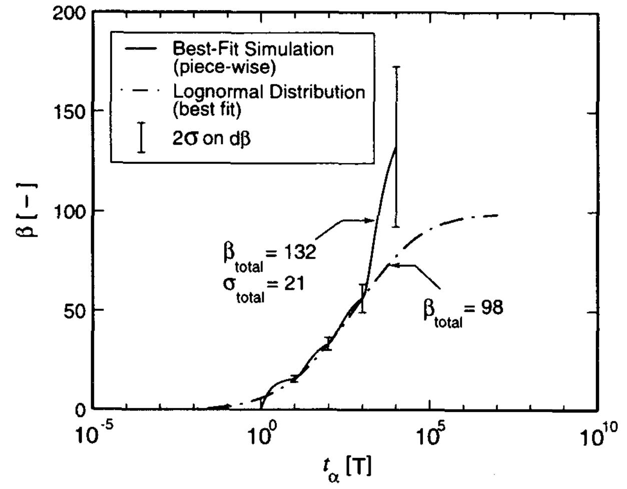

Figure R-4. Estimated cumulative distribution of rate coefficient with error bars for the five anchor points and the estimated cumulative lognormal distribution for the simulations presented in Chapter 6.

obtained by integrating the distribution of rate coefficients shown in Figure R-3 from large rate coefficients to small rate coefficients (i.e., from right to left) using Equation R-7. The uncertainties (i.e., modified Cramer-Rao bound) in the anchor points along the cumulative $\beta(\alpha)$ function are calculated and plotted in Figure R-4. The final estimated β_{total} is 132 with two standard deviations of approximately 40 (calculated from Equation R-8). The error bars grow larger with the time scale of mass-transfer, in part, because most of the data are collected during the first few hours of the SWIW experiment. Uncertainty greatly increases for time scales (~10,000 hr) longer than the time scale of the experiment (~1000 hr). By going one order of magnitude beyond the time scale of the experiment, the uncertainty almost increases by a factor of five. Furthermore, both the lognormal and linear piece-wise models predict similar cumulative capacities during the time scale of the experiment, i.e., 1 to 1000 hr. The linear piece-wise model predicted a larger total capacity in the dolomite (132) than did the lognormal model (98). This may not be of real concern, however, because the error bar on the total capacity predicted using the lognormal model is quite large (see Chapter 6); and in fact will overlap the final error bar computed by the linear piece-wise model.

The shape of the cumulative rate distribution (Figure R-4) predicted by the piece-wise linear distribution is very close to the shape of the lognormal distribution. This suggests that a lognormal distribution is likely to be a good approximation of the actual distribution of rate coefficients for the Culebra dolomite.

R.4 Conclusions

This appendix shows that the $b(\alpha)$ capacity density function can be estimated using a piece-wise linear function for a model of multirate mass transfer. It also shows that uncertainties can be calculated along the entire cumulative $\beta(\alpha)$ function using a modified Cramer-Rao bound. These uncertainties can help determine the range of mass-transfer rate coefficients that can be estimated from a particular SWIW test. Estimation of the 2,4-DCBA data set from the H-11 SWIW test shows that a reasonable fit can be achieved with five anchor points. For five anchor points, the uncertainties associated with each b_i at each α_i anchor point are relatively small, suggesting that mass-transfer rates can accurately be estimated for time scales similar to the experiment. Comparison between the linear piece-wise model and a lognormal rate distribution reveals that both models result in similar capacities for rate coefficients that span the time scale of the actual experiment. However, the piece-wise model estimated a larger total capacity than the lognormal model for the data set examined. The similarity between the piece-wise linear and the lognormal distributions suggest that a lognormal distribution is likely to be a good approximation of the actual distribution of rate coefficients for the Culebra dolomite. However, unlike the lognormal model, use of the linear piece-wise model resulted in uncertainties for all mass-transfer rate coefficients estimated and, in general, uncertainties were increasing with time scale. In future work, the estimated distribution of rate coefficients, and the estimated covariance matrix describing the joint uncertainty of the b_i's, could be used to estimate the uncertainty of solute behavior predicted with the parameters estimated from a SWIW test.

R.5 References

Chen, W., and R. Wagenet. 1995. "Solute Transport in Porous Media with Sorption-Site Heterogeneity," *Environmental Science and Technology.* Vol. 29, no. 11, 2725-2734.

Chen, W., and R. Wagenet. 1997. "Description of Atrazine Transport in Soil with Heterogeneous Nonequilibrium Sorption," *Soil Science Society of America Journal.* Vol. 61, no. 2, 360-371.

Culver, T.B., S.P. Hallisey, D. Sahoo, J.J. Deitsch, and J.A. Smith. 1997. "Modeling the Desorption of Organic Contaminants from Long-Term Contaminated Soil Using Distributed Mass Transfer Rates," *Environmental Science and Technology.* Vol. 31, no. 6, 1581-1588.

Cunningham, J.A., C.J. Werth, M. Reinhard, and P.V. Roberts. 1997. "Effects of Grain-Scale Mass Transfer on the Transport of Volatile Organics Through Sediments 1. Model Development," *Water Resources Research.* Vol. 33, no. 12, 2713-2726.

de Hoog, F.R., J.H. Knight, and A.N. Stokes. 1982. "An Improved Method for Numerical Inversion of Laplace Transforms," *SIAM Journal on Scientific and Statistical Computing.* Vol. 3, no. 3, 357-366.

Fong, F.K., and L.A. Mulkey. 1990. "Solute Transport in Aggregated Media: Aggregate Size Distribution and Mean Radii," *Water Resource Research.* Vol. 26, no. 6, 1291-1303.

Haggerty, R., and S.M. Gorelick. 1995. "Multiple-Rate Mass Transfer for Modeling Diffusion and Surface Reactions in Media with Pore-Scale Heterogeneity," *Water Resources Research.* Vol. 31, no. 10, 2383-2400.

Hollenbeck, K.J., C.F. Harvey, R. Haggerty, and C.J. Werth. 1999. "A Method for Estimating Distributions of Mass Transfer Rate Coefficients with Application to Purging and Batch Experiments," *Journal of Contaminant Hydrology.* Vol. 37, no. 3-4, 367-388.

Pedit, J.A., and C.T. Miller. 1994. "Heterogeneous Sorption Processes in Subsurface Systems. 1. Model Formulations and Applications," *Environmental Science and Technology.* Vol. 28, no. 12, 2094-2104.

This page intentionally left blank.

Appendix S
Double-Porosity Single-Rate and Multirate Interpretations of Multiwell Convergent-Flow Tracer-Test Data

By Michael J. Kelley[1], Lucy C. Meigs[1], Richard L. Beauheim[2], Sean A. McKenna[1], and Roy Haggerty[3]

S.1 Introduction

As previously discussed in Chapters 3 and 6, one of the major objectives of the single-well injection-withdrawal (SWIW) tracer tests was to demonstrate the significance of matrix diffusion in the Culebra Dolomite Member of the Rustler Formation. In addition, incorporated into the series of multiwell convergent-flow (MWCF) tracer tests were features designed to evaluate matrix diffusion (see Chapter 3). Two such features were: (1) pumping the withdrawal well at different pumping rates while performing multiple tracer injections along the same pathway; and (2) co-injecting two conservative tracers having different aqueous diffusion coefficients. During the MWCF tracer tests at the H-19 hydropad, tracers were injected across the full Culebra thickness as well as into isolated upper- and lower-Culebra intervals to investigate vertical variations within the Culebra (see Chapter 3 for complete details).

As described in Chapter 3, a MWCF tracer test involves three steps: (1) extended pumping of the withdrawal well to create a convergent flow field with effectively steady-state gradients; (2) injection of tracer(s) followed by a chaser solution into one or more separate wells; and (3) sampling of the pumped water through time to define a tracer-breakthrough curve. The tracer-breakthrough curves are typically plotted in terms of normalized concentration (normalized with respect to the injected concentration) versus pumping time since injection began. This graph can be plotted in linear-linear or log-log space for examination and interpretation. The advantage of plotting the observed data in log-log space is the ability to examine small concentration changes in the tail of the tracer-breakthrough curve.

MWCF tracer tests have been utilized by a number of researchers to estimate groundwater flow and transport parameters over a volume of aquifer between the injection and pumping wells (see Chapter 5). In addition to investigating matrix diffusion, another objective of the WIPP MWCF tracer tests is interpretation of the observed data to estimate solute-transport parameters that cannot be determined directly from laboratory analysis (e.g., core measurements, static diffusion tests) and/or other field tests (e.g., hydraulic tests, SWIW tests). These parameters include the advective porosity (ϕ_a), matrix-block half-length (½ MBL), capacity coefficient (β_{tot}), and dispersivity (α_L). For non-sorbing tracers, the capacity coefficient is defined as the ratio of the diffusive porosity to the advective porosity. Appendix P presents interpretations of some of the MWCF tracer test data using a conventional double-porosity (i.e., single-rate) model and both homogeneous and heterogeneous transmissivity fields. That analysis is extended here for the condition of multiple, simultaneous diffusion rates in a homogenous transmissivity field. As explained in Chapter 6, the effects of multiple rates of mass transfer have been theoretically predicted in the past and observed at the

---

[1] Sandia National Laboratories, Geohydrology Department, P.O. Box 5800, MS-0735, Albuquerque, NM 87185-0735. Email: mkelle@sandia.gov.

[2] Sandia National Laboratories, Repository Performance and Certification Department, P.O. Box 5800, MS-1395, Albuquerque, NM 87185-1395.

[3] Oregon State University, Department of Geosciences, 104 Wilkinson Hall, Corvallis, OR 97331-5506.

laboratory scale, but until now have not been documented at the field scale. The reader is referred to Chapter 6 for a thorough discussion of the multirate mass-transfer model.

Chapter 7 provides interpretations of the multiwell tracer-test data from single pathways at both the H-19 and H-11 hydropads. It presents the initial interpretations that were conducted to evaluate the tracer-test data and examine the differences in the transport properties of the Culebra between the H-11 and H-19 hydropads. The purpose of this appendix is to present interpretations of most of the tracer data for tests conducted at four WIPP hydropads using the multirate mass-transfer model. The analysis considered fourteen data sets from the 7-well test performed at the H-19 hydropad in 1995 and 1996, seven data sets from the tests performed at the H-11 hydropad in 1988 and 1996, one data set from the test conducted at the H-3 hydropad, and three data sets from tests #1 and #2 conducted at the H-6 hydropad. A discussion of the H-19 tests and the 1996 H-11 tests can be found in Chapter 3. The 1988 test at H-11 and the H-3 and H-6 tests are discussed in Appendix F.

All of the analyses presented here were performed using STAMMT-R (Solute Transport and Multirate Mass Transfer in Radial Coordinates; Haggerty et al., 2000), which is described in Section S.3. In order to compare results for the assumptions of single and multiple rates of mass transfer directly, the data were interpreted using both the single-rate and multirate options in STAMMT-R. The interpretations discussed here are not final and, therefore, the presented results are considered to be preliminary. Additional simulation work is expected to improve upon the results presented below. In general, the interpretation emphasis has been placed on evaluating the ability of the multirate double-porosity model to match data from individual pathways.

S.2 Model Conceptualization

The Culebra was conceptualized as a dual-porosity system consisting of an advective porosity and a diffusive porosity. Advection and dispersion are the dominant processes in the advective porosity and diffusion is the dominant process in the diffusive porosity (see Chapter 2 for additional discussion on advective and diffusive porosity). We modeled the Culebra as a single layer with a thickness equal to that of the lower Culebra (see Chapter 2). The Culebra is underlain by a mudstone with an expected transmissivity orders of magnitude lower than that of the lower Culebra (Chapter 3; Beauheim, 1987). This mudstone is considered to act as an impermeable boundary. The upper Culebra is not expected to participate in the transport of solutes over the scale of the tracer test due to its significantly reduced transmissivity relative to that of the lower Culebra (Chapter 3). In cases where tracer was injected into an isolated upper-Culebra interval, the observed tracer-breakthrough curves were poorly defined and mass recoveries were generally less than 10% of the injected mass. The model conceptualization assumes that the transport parameters (e.g., advective porosity, dispersivity, and tortuosity) along each well-to-well pathway are constant.

Conventional double-porosity models use a single value to describe the movement of solute between the advective porosity and the diffusive porosity. On the other hand, the multirate model uses a statistical distribution rather than a single value to describe the diffusion-rate coefficient ($\alpha_d = D_a / l^2$) (see Chapter 6). For the multirate conceptualization, diffusion is heterogeneous at the pore scale and the interaction of solute between the advective and diffusive porosities is described by a range of diffusion-rate coefficients. A distribution of diffusion-rate coefficients may be caused by variability in any of the following: matrix-block shape or size, cross-sectional area of the pore space normal to the direction of diffusion, pore restrictivity, and tortuosity. Further justification for this variability and a complete literature review of multirate mass-transfer models are provided in Sections 6.1 and 6.2.

S.3 Code Description

STAMMT-R (Haggerty et al., 2000) is a FORTRAN 77 code that solves the advective-dispersive and rate-limited mass-transfer equations for solute transport in groundwater. The solution to the flow and transport equations is analytic in the Laplace domain and inverted to the time domain using a numerical algorithm. Chapters 6 and 7 and Appendix Q provide an in-depth review of the mathematical model and the Laplace-domain solution for this code.

The MWCF tracer simulations were performed by obtaining a steady-state convergent-flow field from the pumping of a withdrawal well. A pulse of tracer is injected at some radial distance, r_o, from the pumping well into the convergent-flow field. A clean chaser is injected immediately thereafter to clear the injection borehole of any remaining tracer. Assumptions incorporated into STAMMT-R include the following: (1) the aquifer is fully confined with a constant thickness; (2) the aquifer is spatially homogeneous and isotropic with respect to hydraulic conductivity; (3) no regional gradient is present in the aquifer; (4) mass transfer between the advective and diffusive porosities is dominated by diffusion; and (5) the diffusion-rate coefficient, D_a/l^2 (where D_a [L^2/T] is the apparent diffusion coefficient in the matrix, l [L] is the length of the diffusion pathway within the matrix, see Chapter 6) is assumed to have either a lognormal distribution or is a single value (i.e., conventional spherical matrix diffusion) (Haggerty et al., 2000). A dispersivity term is used to approximate mechanical mixing due to small-scale variations in the flow field. See Section 7.2 for the equations that describe solute transport and mass transfer with a lognormal distribution of diffusion-rate coefficients.

The assumed lognormal distribution may not be the appropriate distribution to use in all of the tracer-test analyses. The lognormal distribution was chosen *a priori* for reasons discussed in Chapter 6 and for direct comparison to the SWIW tracer-test results. Recent work on the behavior of late-time slopes of tracer-breakthrough curves indicates other statistical distributions may be more appropriate to describe the tracer-test data (Haggerty et al., in review b).

As noted in Chapter 7, the boundary conditions and fluid velocities must be specified at the injection well. During the injection of the tracer and chaser fluid, the pore-water velocity at a radius, r, from the injection well is given by Equation 7-4 and the boundary conditions for the injection phase are presented in Equations 7-5a and b.

The shape of the injected tracer and chaser within the aquifer is assumed to be unaffected by the convergent-flow field during the injection period; it should form a perfect cylindrical shell around the injection well. In general, this assumption is valid provided the following conditions are met: (1) the ratio of the volume of tracer and chaser to the volume of formation porosity in the vicinity of the two wells (injection and pumping) is small; and (2) the ratio of fluid velocity caused by injection to the fluid velocity due to pumping is large at the location of the injection well. If these assumptions are violated, the plume of the injected fluid will not form a perfect ring, but will be oblong. These two constraints are expressed in the following equations, respectively (after Guvanasen and Guvanasen, 1987):

$$\frac{Q_{inj1}T_{inj1} + Q_{inj2}T_{inj2}}{b\pi\phi_a r_o^2} << 1 \qquad \text{(S-1)}$$

$$\frac{Q_{inj}r_o}{Q_{out}r_{iw}} >> 1 \qquad \text{(S-2)}$$

where Q_{inj1}, T_{inj1} and Q_{inj2}, T_{inj2} refer to the injection rates [L^3/T] and times of injection [T] of the tracer and chaser respectively, b is the thickness of the aquifer [L], ϕ_a is the advective porosity [-], and r_o is the distance between the pumping well and the injection well [L]. The injection rate, Q_{inj}, is the larger of the tracer and chaser injection rates [L^3/T], Q_{out} is the discharge rate of the pumping well [L^3/T], and r_{iw} is the radius of the injection well [L]. These equations are used to verify that the assumptions of the conceptual model regarding tracer and chaser injection into the aquifer in the presence of a convergent-flow field are valid. In the remainder of this appendix, Equations S-1 and S-2 are referred to as the G&G1 and G&G2 assumptions, respectively.

When the G&G1 assumption is violated, the simulated spatial distribution of tracer for the analytical solution at the end of the injection period is examined to determine if the injection plume intersected the pumping well. STAMMT-R allows the user to set a maximum radius for the analytical solution to which a specified concentration of tracer can reach during injection. For the tests discussed in this appendix, the threshold relative concentration (C/C_0) was set to approximately 10^{-7}. This value is set empirically (by the user) through trial and error for each of the tests examined below. Altering the value for maximum radius (i.e., increasing the maximum radius by 0.50 m) does not alter the simulated results significantly.

The modeling of tracer movement along the transport pathway from the injection well to the pumping well is a three-step process. This process is used to calculate the tracer-breakthrough curve at the pumping well. First, the post-injection concentration distribution, which is in polar coordinates centered about the injection well (r_{in}, θ_{in}), is transformed to polar coordinates centered about the pumping well (r_{out}, θ_{out}). Second, the dimensionality of the problem is reduced through azimuthal averaging. Finally, the breakthrough curve is simulated by modeling the transport of the tracer through the aquifer to the pumping well under radially convergent flow with multirate diffusion. This process is described in Equations 7-1 through 7-5 and is shown in Figure 7-1. The completion of these steps provides a semi-analytical solution for the breakthrough curve at the pumping well.

As noted in Chapter 7, the ability of the multirate model to estimate the diffusion-rate coefficient distribution is limited by the ratio of the diffusive to advective mass-transfer rates within the tracer-test system. This ratio can be parameterized with the Damkohler number, *DaI*. The reader is directed to Section 7.2 for a discussion of the significance and presentation of equations for the Damkohler number. The Damkohler number is used to determine which portions of the lognormal distribution for the diffusion-rate coefficients can be resolved during the duration of individual tests. In addition, for the single-rate interpretations, the Damkohler number is used to determine if alternate conceptual models may be valid for describing the tracer tests.

S.4 Interpretation Methodology

Most of the physical-transport-related parameters required as input to the model are assigned fixed values based on field and laboratory measurements. These "fixed" parameters and their values can be found in the Transport Input Parameter Spreadsheets (TIPS - Appendix B) and include the distance between the injection and pumping well, the pumping rate, the tracer and chaser injection rates and times, the diffusive porosity and tortuosity, and the aqueous diffusion coefficient of the tracer. A summary of the fixed parameter values used for the simulations can be found in Table S-1.

Generally, the interpretation methodology consisted of calibrating the simulated results to the observed tracer data through a numerical inversion routine. This calibration was conducted with an International Mathematics Statistical Library (IMSL) subroutine linked to the STAMMT-R code. Parameter estimation through numerical inversion was applied to the multirate-diffusion model to obtain the optimal fit of the simulated and observed data. The measure used for goodness of fit was the root mean square error (RMSE) between the log of the observed data and the log of the predicted concentrations. In all cases, four parameters were estimated: (1) the geometric mean *ln* diffusion-rate coefficient, μ_d; (2) the standard deviation of the *ln* diffusion-rate coefficient distribution, σ_d; (3) the advective porosity, ϕ_a; and (4) the longitudinal dispersivity, α_L. The parametric expression of diffusion-rate coefficients used here is a lognormal distribution that is fully characterized by the mean and standard deviation. For comparison purposes, the model was also calibrated to the observed data assuming a single diffusion rate. This calibration was identical to that described above, except the standard deviation of the diffusion-rate coefficient distribution, σ_d, was set to zero and held constant.

In STAMMT-R, when setting the sigma value to zero, the model collapses from a multirate model with layered (slab) matrix blocks to a single-rate model with spherical matrix blocks. These models are not directly comparable because the mean residence time in a sphere is $^1/_{15}\ D_a / l^2$, while the mean residence time in a layer is $^1/_3\ D_a / l^2$. To estimate the same mean residence time in both a sphere and a layer (assuming identical D_a values), one rate coefficient has to be five times the other and the ½ MBL in the layered model must be $\sqrt{5}$ times the ½ MBL for the spherical model. In

Table S-1 Summary of Fixed Parameters Used in MWCF Multirate and Single-Rate Simulations

Hydropad, Round, Path	Pumping Rate (m^3/s)	Well Spacing (m)	Free-Water Diffusion Coefficient (m^2/s)	Tortuosity (-)	Diffusive Porosity Multirate Model (-)	Diffusive Porosity Single-Rate Model (-)	Tracer-Injection Rate (m^3/s)	Tracer-Injection Time (s)	Chaser-Injection Rate (m^3/s)	Chaser-Injection Time (s)
H-19 Hydropad; Round 1										
H-19b2	2.71E-4	25.1	8.0E-10	0.091	0.147	0.100	1.32E-4	1536	1.46E-4	1056
H-19b3	2.71E-4	11.0	7.4E-10	0.091	0.147	0.100	1.83E-4	1080	2.31E-4	750
H-19b3; iodide	2.71E-4	11.0	1.8E-09	0.091	0.147	0.100	1.83E-4	1080	2.31E-4	750
H-19b4	2.71E-4	22.3	8.2E-10	0.091	0.147	0.100	1.17E-4	1698	1.22E-4	1170
H-19b5	2.71E-4	13.9	7.3E-10	0.091	0.147	0.147	1.08E-5	13800	9.26E-6	7020
H-19b6	2.71E-4	19.8	8.2E-10	0.091	0.147	0.100	1.24E-4	1596	1.21E-4	1278
H-19b7	2.71E-4	12.2	8.2E-10	0.091	0.147	0.094	2.06E-4	960	2.16E-4	780
H-19 Hydropad; Round 2										
H-19b3	2.52E-4	11.0	7.4E-10	0.091	0.147	0.100	2.75E-5	7200	3.30E-5	4320
H-19b5	2.52E-4	13.9	7.3E-10	0.091	0.147	0.147	1.92E-4	1035	1.66E-4	1020
H-19b7	2.52E-4	12.2	7.3E-10	0.091	0.147	0.100	1.55E-5	12720	1.47E-5	9480
H-19 Hydropad; Round 3										
H-19b3	1.55E-4	11.0	7.9E-10	0.091	0.147	0.100	1.00E-4	1974	1.15E-4	1500
H-19b6	1.55E-4	19.8	6.8E-10	0.091	0.147	0.100	6.98E-5	2826	6.84E-5	2238
H-19b7	1.55E-4	12.2	8.0E-10	0.091	0.147	0.094	1.17E-4	1698	1.19E-4	1410
H-19b7; iodide	1.55E-4	12.2	1.8E-09	0.091	0.147	0.100	1.17E-4	1698	1.19E-4	1410
H-11 Hydropad; Round 1										
H-11b2	2.23E-4	21.5	8.2E-10	0.11	0.16	0.16	6.82E-5	2772	6.00E-5	3552
H-11b3	2.23E-4	20.9	7.9E-10	0.11	0.16	0.16	9.57E-5	1974	9.76E-5	3810
H-11 Hydropad; Round 2										
H-11b2	3.76E-4	21.5	7.4E-10	0.11	0.16	0.16	7.23E-5	2610	6.24E-5	3408
H-11b3	3.76E-4	20.9	8.2E-10	0.11	0.16	0.16	9.52E-5	1998	9.71E-5	3840
H-11b3; iodide	3.76E-4	20.9	1.8E-09	0.11	0.16	0.16	9.52E-5	1998	9.71E-5	3840
H-11 Hydropad; 1988 Test										
H-11b2	3.80E-4	21.5	7.7E-10	0.11	0.16	0.16	7.31E-5	2580	6.13E-5	3060
H-11b3	3.80E-4	20.9	7.4E-10	0.11	0.16	0.16	9.85E-5	1920	1.00E-4	3720
H-3 Hydropad										
H-3b1	1.90E-4	30.66	7.4E-10	0.11	0.2	0.2	6.31E-5	1200	6.73E-5	4500
H-6 Hydropad										
H-6a; test 1	1.04E-3	29.90	7.4E-10	0.11	0.15	0.15	1.67E-4	600	8.77E-5	1140
H-6b; test 1	1.04E-3	29.87	7.7E-10	0.11	0.15	0.15	1.67E-4	600	8.77E-5	1140
H-6b; test 2	1.04E-3	29.87	9.3E-10	0.11	0.15	0.15	1.28E-4	780	1.28E-4	780

several instances, the multirate model estimated a very low sigma value, indicating a narrow distribution of diffusion rate coefficients (i.e., nearly a single-rate model). When directly comparing the ½ MBLs obtained from the parameter estimation, the single-rate ½ MBLs appear larger. In order to compare the estimated ½ MBL from a multirate model to the ½ MBL from a single-rate model, the ½ MBL obtained from the multirate model must be multiplied by $\sqrt{5}$. When the ½ MBLs for the layered model are corrected in this fashion, the estimated ½ MBLs from the single-rate model generally agree within 40%. Other differences in dispersivity and porosity make direct comparisons difficult.

The observed tracer-breakthrough curves and the 95% confidence intervals based on the analytical errors for the 1995-96 tests conducted at the H-11 and H-19 hydropads can be found in Appendix C. When possible, the entire data set was used during the inversion process. For a select few of the data sets, no more than four data points were removed from the rising limb of the breakthrough curve. This was done exclusively when the estimated 95% confidence interval for that data point was large. In general, we define large as approximately one order of magnitude uncertainty in the data point. After removing the large-confidence-interval data points from the rising limb of the breakthrough curve, agreement between the model and the observed data improved dramatically. For data sets that spanned different pumping rates, the data were truncated when the pumping rate was changed significantly. The observed tracer-breakthrough curves for tests conducted in the 1980's at the H-3, H-6, and H-11 hydropads can also be found in Appendix C.

In summary, for model calibration to the observed data, the values for the fixed parameters remained constant and the values for the four fitting parameters were varied until the lowest RMSE was achieved. For the single-rate diffusion model simulations, the number of fitting parameters was reduced from four to three. For the 25 tracer data sets investigated, the best-fit (based on lowest RMSE) parameter values are presented below.

S.5 Results

This section contains the results of interpretations of data from 25 separate tracer-test pathways at the H-19, H-11, H-6, and H-3 hydropads using single-rate and multirate double-porosity conceptualizations. The purpose of this section is to present the best-fit estimated parameter values from the attempted calibration of each tracer data set. Instances where the multirate double-porosity conceptualization poorly matches the observed breakthrough curve are identified. Additionally, tests where a single-rate double-porosity conceptualization is able to describe the observed data accurately are acknowledged and the differences between the single- and multi-rate results are discussed.

In all cases, the best-fit estimated parameter values are presented below. In the event that tracer data for transport along a given pathway were available for more than one pumping rate (e.g., H-19b3 to H-19b0 pathway, Rounds 1, 2, and 3), the results from the best-fit parameter estimation were varied to bring the estimated parameter values for all data sets into harmony. We attempted to find a unique set of parameter values that could be used to simulate multiple breakthrough curves for different pumping rates but identical transport pathways. For the subset of tracer injections that contained two tracers with different aqueous diffusion coefficients, we attempted to find a unique parameter set to satisfy all breakthrough curves for both different pumping rates and different diffusion characteristics of tracers. To find the unique parameter set matching all data sets, each tracer data set was numerically inverted to find the best-fit parameter values. Once this was done for the data from each pumping rate and for each tracer, the best-fit values were averaged and breakthrough curves were predicted according to the unique (averaged) parameter set. The criterion used to determine whether the unique parameter set approximated field conditions was visual inspection of how well the simulated results matched the observed data. If one of the tracer data sets could not be accurately described by the unique parameter set (e.g., the simulation fell completely outside the 95% confidence intervals of the data), the parameter set was discarded and a new parameter set was tried.

The consistency of the estimated lognormal distributions of mass-transfer rates at each hydropad can be checked by determining the estimated matrix-block sizes. As noted in Chapter 7, all of the variability in the mass-transfer rates is assigned to variations in the ½ MBL by assuming a constant tortuosity. The large-scale spatial variation of the lognormal value of tortuosity is likely to be small. For one-dimensional diffusion paths into the matrix, the distance from the fracture interface to the center of the matrix block, l, (called the ½ MBL) can be found with:

$$l = \sqrt{\frac{D_o \tau}{\alpha_f}} \qquad \text{(S-3)}$$

where D_o is the aqueous diffusion coefficient [L^2/T], τ is the tortuosity [-], and α_f is the first-order mass-transfer coefficient [1/T]. Calculated values for tortuosity and the aqueous diffusion coefficient for individual tracers can be found in Appendix B. By applying the Damkohler limits to the distribution of ½ MBL, the range of ½ MBLs sampled by each test can be determined. These values can be compared to the values obtained from the SWIW interpretations (Chapter 6) and the single-rate double-porosity interpretations (Appendix P).

Although single-valued diffusion rates have previously been applied to the analysis of the MWCF tracer data (Appendix P), these results are not directly comparable to the multirate interpretations presented here. The criterion for accepting or rejecting the calibrated model in Appendix P was based on visual fit between the data and the simulation. In order to compare the results for the assumptions of multirate diffusion and single-rate diffusion, the single-rate simulations presented in this appendix were conducted using the same estimation technique as the multirate simulations. As mentioned previously, the parameter estimation for both assumptions is identical, except the spread about the diffusion coefficient, σ_d, is fixed at zero for the single-rate simulations. For each hydropad, a total porosity ($\phi_a + \phi_d$), based on core analyses, was established. For consistency, both the single-rate and multirate mass-transfer models were constrained to have this total porosity. For the single-rate model, maintaining this total porosity value generally entailed reducing the matrix porosity used in the multirate model in a trial and error fashion and allowing larger values of estimated advective porosity.

As discussed in Section S.3, the combined shape of the injected tracer and chaser within the aquifer was assumed to be unaffected by the convergent flow field during tracer injection. The assumption remains valid if the two criteria outlined by Equations S-1 and S-2 are met. These equations were calculated for every tracer data set interpreted. In some cases, the validity of one or both assumptions is questionable. For those cases, the impact of the violation of the assumption(s) was investigated as discussed below.

The results for the four estimated parameter values for the multirate conceptualization and the three estimated parameter values for the single-rate conceptualization, as well as the calculated mean ½ MBLs, are presented in Tables S-2 and S-3, respectively. The parameter-estimation routine produces an estimate of the 95% confidence interval of the estimated parameter values. Those results are presented in Table S-4 and S-5 and are for information purposes only.

S.5.1 H-19 Hydropad

The two MWCF tracer tests conducted at the H-19 hydropad are described in Chapter 3. The well layout for this hydropad is shown in Figure 3-2. The experimental description and design methodology for these tests are given in Section 3.1 and the details of each test are given in Tables 3-2 and 3-3. For both H-19 tests, the pumping well was H-19b0. Although two tests were conducted at H-19 (the 4-well test and the 7-well test), only the data from the 7-well test have been interpreted using STAMMT-R to date. Three different pumping rates with three rounds of tracer injections were used during the 7-well test. For Round 1, the withdrawal well was pumping at its highest rate, and tracers were injected into each of the six surrounding wells (H-19b2 through H-19b7). The tracer solution injected into H-19b3 consisted of two tracers (a benzoic acid and iodide) with different aqueous diffusion coefficients. For Round 2, the pumping rate was only slightly lower than for the first round and tracers were injected into

Table S-2 Summary of Parameter Estimates for Multirate Model Calibrations

Hydropad & Injection Well	Figure Number and Simulation Name	Mu μ	Sigma σ	Advective Porosity ϕ_a	Dispersivity (m)	RMSE	Matrix-Block Half-Length (m) ½ MBL	Visual Fit to Data*	Comments
H-19 Hydropad; Round 1									
H-19b2	S-1; MR1	-16.58	5.53	3.37E-3	1.23	0.0616	0.03391	G	
H-19b3	S-2; MR1	-12.69	3.88	1.31E-3	0.73	0.2127	0.00467	P	Inj. Conc. = 100%
H-19b3	S-2; MR2	-13.01	3.12	3.40E-3	0.59	0.0911	0.00550	G	Inj. Conc. = 85%
H-19b3	S-2; MR3	-13.09	3.24	2.10E-3	0.68	0.1621	0.00570	G	Inj. Conc. = 85%; Predictive
H-19b3; iodide	S-3; MR1	-13.07	2.64	3.19E-5	0.43	0.377	0.00880	P	Inj. Conc. = 100%
H-19b3; iodide	S-3; MR2	-12.99	2.80	1.32E-4	0.39	0.186	0.00846	F	Inj. Conc. = 85%
H-19b3; iodide	S-3; MR3	-12.20	3.24	2.10E-3	0.68	0.379	0.00570	F	Inj. Conc. = 85%; Predictive
H-19b4	S-6; MR1	-13.13	3.28	1.39E-3	1.73	0.096	0.00612	G	
H-19b5	S-7; MR1	-11.57	0.55	2.78E-2	1.80	0.087	0.00265	F	
H-19b6	S-9; MR1	-17.21	4.87	7.56E-4	0.89	0.066	0.04708	G	
H-19b6	S-9; MR2	-17.19	4.61	5.85E-4	0.84	0.164	0.04671	G	Predictive
H-19b7	S-11; MR1	-14.95	4.27	2.59E-4	0.65	0.097	0.01521	F	
H-19b7	S-11; MR2	-15.59	4.70	1.00E-3	0.65	0.204	0.02100	F	Predictive
H-19 Hydropad; Round 2									
H-19b3	S-4; MR1	-13.09	4.69	1.09E-3	0.96	0.184	0.00570	F	
H-19b3	S-4; MR2	-13.09	3.24	2.10E-3	0.68	0.239	0.00570	F	Predictive
H-19b5	S-8; MR1	-12.89	0.28	6.69E-2	2.21	0.132	0.00512	G	
H-19b7	S-12; MR1	-16.15	6.47	1.79E-4	1.32	0.144	0.02624	G	
H-19b7	S-12; MR2	-15.71	4.70	1.00E-3	0.65	0.227	0.02100	F	Predictive
H-19 Hydropad; Round 3									
H-19b3	S-5; MR1	-12.90	4.04	3.67E-3	0.81	0.194	0.00536	F	
H-19b3	S-5; MR2	-13.02	3.24	2.10E-3	0.68	0.188	0.00570	G	Predictive
H-19b6	S-10; MR1	-17.36	4.34	4.16E-4	0.78	0.0711	0.04631	G	
H-19b6	S-10; MR2	-17.38	4.61	5.85E-4	0.84	0.1074	0.04670	F	Predictive
H-19b7	S-13; MR1	-15.95	5.17	3.06E-3	0.73	0.071	0.02474	G	
H-19b7	S-13; MR2	-15.62	4.70	1.00E-3	0.65	0.075	0.02100	G	Predictive
H-19b7; iodide	S-14; MR1	-15.65	4.96	9.30E-4	0.80	0.167	0.03199	F	
H-11 Hydropad; Round 1									
H-11b2	S-16; MR 1	-15.03	1.68	1.67E-2	4.30	0.0773	0.01747	F	Fixed Dispersivity
H-11b2	S-16; MR2	-14.30	4.50	2.32E-2	10.83	0.0548	0.01211	G	4 Parameter Estimation
H-11b3	S-19; MR1	-17.69	1.35	1.32E-3	4.03	0.0959	0.06482	G	
H-11 Hydropad; Round 2									
H-11b2	S-17; MR1	-14.98	2.04	1.48E-2	4.30	0.106	0.01612	F/P	Fixed Dispersivity
H-11b2	S-17; MR2	-13.82	2.99	3.79E-4	6.82	0.112	0.00904	G	4 Parameter Estimation
H-11b3	S-20; MR1	-17.19	1.12	6.12E-4	3.47	0.121	0.05120	G	
H-11b3; iodide	S-21; MR1	-16.79	1.08	4.44E-4	3.43	0.180	0.06211	G	

Table S-2 Summary of Parameter Estimates for Multirate Model Calibrations (continued)

Hydropad & Injection Well	Figure Number and Simulation Name	Mu μ	Sigma σ	Advective Porosity ϕ_a	Dispersivity (m)	RMSE	Matrix-Block Half-Length (m) ½ MBL	Visual Fit to Data*	Comments
H-11 Hydropad; 1988 Test									
H-11b2	S-15; MR1	-15.36	0.57	3.02E-2	4.30	0.464	0.01992	F/P	Fixed Dispersivity
H-11b2	S-15; MR2	-15.98	1.54	5.60E-2	11.97	0.140	0.02712	G	4 Parameter Estimation
H-11b3	S-18; MR1	-16.36	0.83	5.35E-4	4.09	0.172	0.03215	G	
H-3 Hydropad									
H-3b1	S-22; MR1	-19.67	1.40	4.58E-3	3.50	0.296	0.16875	G/F	
H-6 Hydropad									
H-6a; test 1	S-23; MR1	-11.85	0.62	7.52E-2	11.94	0.184	0.00337	G	4 Parameter Estimation
H-6a; test 1	S-23; MR2	-12.66	0.30	5.29E-2	4.63	0.391	0.00506	P	Low Dispersivity
H-6b; test 1	S-24; MR1	-17.29	0.33	7.85E-3	5.04	0.221	0.05229	G	
H-6b; test 1	S-24; MR2	-17.33	0.24	6.00E-3	4.00	0.233	0.05343	G	Predictive
H-6b; test 2	S-25; MR1	-17.19	0.15	5.01E-3	3.03	0.173	0.05458	G	
H-6b; test 2	S-25; MR2	-17.14	0.24	6.00E-3	4.00	0.212	0.05343	G/F	Predictive

three of the surrounding wells (H-19b3, H-19b5, and H-19b7). The Round 2 injections occurred approximately 26 days after the Round 1 injections. For Round 3, the withdrawal well was pumping at its lowest rate (maximizing exposure time between the tracer and the Culebra) and tracers were injected into H-19b3, H-19b6, and H-19b7. The injections for Round 3 occurred approximately 32 days after the injections for Round 2. Like the Round 1 injection into H-19b3, the Round 3 injection into H-19b7 also consisted of two tracers with different aqueous diffusion coefficients.

Because the difference in pumping rate between Round 1 and 2 was slight (0.27 L/s versus 0.25 L/s), the data for Round 1 were not truncated at the pumping-rate change in order to obtain a more robust data set with an extended tail. In general, all of the Round 1 data were truncated at the time corresponding to the change in pumping rate in preparation for the Round 3 injection because STAMMT-R uses a single pumping rate for the simulation. Multiple or changing pumping rates during the tracer test cannot be simulated with this code. In all cases, the larger pumping rate was used for the simulation pumping rate.

S.5.1.1 H-19b2 to H-19b0 Pathway

The pathway from H-19b2 to H-19b0 is the longest tested at the H-19 hydropad at 25.1 m (Figure 3-2). Only one injection, during Round 1, was performed in this well during the 7-well tracer test. For analysis, the tracer data for this injection were truncated at the end of pumping for Round 2.

The multirate-diffusion model is able to describe all portions of the observed tracer-breakthrough curve accurately with the simulated results falling within the 95% confidence interval along the entire data set (Figure S-1; MR1 sim,). The simulation slightly underestimates the peak concentration but the peak-arrival time is in close agreement with the observed data. The falling limb and tail of the observed breakthrough curve are also very accurately represented by the simulation. The mass recovery for the observed data is accurately represented with only a 1% difference at the end of the tracer test.

Table S-3 Summary of Parameter Estimates for Single-Rate Model Calibrations

Hydropad & Injection Well	Figure Number and Simulation Name	Mu μ	Sigma σ	Advective Porosity ϕ_a	Dispersivity (m)	RMSE	Matrix-Block Half-Length (m) ½ MBL	Visual Fit to Data*	Comments
H-19 Hydropad; Round 1									
H-19b2	S-1; SR1	-23.14	0.00	6.49E-2	3.27	0.116	0.90289	G	
H-19b3	S-2; SR1	-11.30	0.00	7.90E-4	1.73	0.117	0.00233	G	Inj. Conc. = 85%
H-19b3; iodide	S-3; SR1	-12.96	0.00	4.48E-7	0.64	0.248	0.00834	F	Inj. Conc. = 85%
H-19b4	S-6; SR1	-13.47	0.00	1.22E-2	2.68	0.114	0.00726	F	
H-19b5	S-7; SR1	-13.38	0.00	3.23E-2	1.81	0.113	0.00657	F	
H-19b6	S-9; SR1	-20.16	0.00	4.13E-2	3.03	0.101	0.20602	G	
H-19b7	S-11; SR1	-21.34	0.00	5.78E-2	2.90	0.201	0.37183	F	
H-19 Hydropad; Round 2									
H-19b3	S-4; SR1	-11.65	0.00	2.51E-6	1.77	0.258	0.00278	F	
H-19b5	S-8; SR1	-14.05	0.00	6.24E-2	2.49	0.166	0.00915	F/P	
H-19b7	S-12; SR1	-21.20	0.00	5.54E-2	2.14	0.353	0.32712	F	
H-19 Hydropad; Round 3									
H-19b3	S-5; SR1	-11.35	0.00	2.52E-3	1.62	0.212	0.00247	F	
H-19b6	S-10; SR1	-19.44	0.00	3.78E-2	2.68	0.0943	0.13076	G	
H-19b7	S-13; SR1	-21.81	0.00	5.75E-2	2.49	0.140	0.46503	F	
H-19b7; iodide	S-14; SR1	-18.74	0.00	4.80E-2	1.78	0.273	0.14991	F	
H-11 Hydropad; Round 1									
H-11b2	S-16; SR 1	-16.62	0.00	8.77E-3	2.62	0.0749	0.03858	F/P	
H-11b3	S-19; SR1	-19.38	0.00	2.03E-3	5.75	0.110	0.15022	G	
H-11 Hydropad; Round 2									
H-11b2	S-17; SR1	-16.39	0.00	8.39E-3	2.56	0.0992	0.03265	G	
H-11b3	S-20; SR1	-18.98	0.00	1.49E-3	6.72	0.109	0.12549	G	
H-11b3; iodide	S-21; SR1	-18.57	0.00	1.08E-3	5.11	0.132	0.15192	G	
H-11 Hydropad; 1988 Test									
H-11b2	S-15; SR1	-16.77	0.00	2.29E-2	4.89	0.2764	0.04030	F	
H-11b3	S-18; SR1	-18.26	0.00	1.46E-3	6.54	0.178	0.08309	G	
H-3 Hydropad									
H-3b1	S-22; SR1	-21.51	0.00	4.95E-3	3.06	0.345	0.42303	F	
H-6 Hydropad									
H-6a; test 1	S-23; SR1	-14.61	0.00	7.61E-2	8.47	0.197	0.01345	G	
H-6b; test 1	S-24; SR1	-19.65	0.00	7.24E-3	4.23	0.203	0.17043	G	
H-6b; test 2	S-25; SR1	-19.49	0.00	5.03E-3	2.79	0.225	0.17290	F	

* G = Good, F = Fair, P = Poor

Table S-4 Calculated 95% Confidence Intervals for Values Presented in Table S-2

MULTIRATE: H-19

Parameter-Estimation Results for MWCF Tracer Tests

Test	Mu 2 St. Dev. Range	Sigma ln(Sigma ± 2 St.Dev.) Range	Porosity ln(Porosity ± 2 St.Dev.) Range	Dispersivity ln(Disp. ± 2 St.Dev.) Range	RMSE
H-19 Hydropad; Round 1					
H-19b2	-16.58 ± 0.19 -16.76, -16.39	5.53 1.71 ± 0.07 5.13, 5.96	3.37E-3 -5.69 ± 0.35 2.39E-3, 4.77E-3	1.23 0.20 ± 0.12 1.08, 1.39	0.097
H-19b3 Inj. Conc. = 85%	-13.01 ± 0.68 -13.69, -12.34	3.12 1.14 ± 0.78 1.43, 6.83	3.40E-3 -5.68 ± 0.0202 3.34E-3, 3.47E-3	0.59 -0.53 ± 0.350 0.42, 0.84	0.09
H-19b3 Inj. Conc. = 100%	-12.69 ± 0.75 -13.44, -11.94	3.88 1.36 ± 0.35 2.72, 5.55	1.31E-3 -6.64 ± 5.23 6.97E-6, 2.45E-1	0.73 -0.32 ± 0.477 0.45, 1.17	0.21
H-19b3; iodide Inj. Conc. = 85%	-12.99 ± 1.95 -14.93, -11.04	2.80 1.03 ± 1.97 0.39, 20.01	1.32E-4 -8.94 ± 0.0023 1.31E-4, 1.32E-4	0.39 -0.95 ± 0.079 0.36, 0.42	0.19
H-19b3; iodide Inj. Conc. = 100%	-13.07 ± 5.15 -18.22, -7.91	2.64 0.97 ± 4.51 0.029, 240.1	3.19E-5 -10.35 ± 0.0014 3.19E-5, 3.20E-5	0.43 -0.85 ± 0.069 0.40, 0.46	0.38
H-19b4	-13.13 ± 0.44 -13.57, -12.69	3.28 1.19 ± 0.14 2.85, 3.78	1.39E-3 -6.58 ± 3.33 4.97E-5, 3.90E-2	1.73 0.55 ± 0.15 1.49, 2.02	0.096
H-19b5	-11.57 ± 0.85 -12.42, -10.72	0.55 -0.60 ± 0.12 0.48, 0.62	2.78E-2 -3.58 ± 0.37 1.93E-2, 4.01E-2	1.80 0.59 ± 0.46 1.14, 2.85	0.09
H-19b6	-17.21 ± 1.95 -19.16, -15.25	4.87 1.58 ± 3.79 0.11, 214.84	7.56E-4 -7.19 ± 0.12 6.69E-4, 8.54E-4	0.89 -0.12 ± 0.77 0.41, 1.93	0.07
H-19b7	-14.95 ± 0.84 -15.78, -14.11	4.27 1.45 ± 0.81 1.89, 9.63	2.59E-4 -8.26 ± 0.0041 2.58E-4, 2.60E-4	0.65 -0.44 ± 0.41 0.43, 0.97	0.10
H-19 Hydropad; Round 2					
H-19b3	-13.09 ± 0.95 -14.04, -12.14	4.69 1.54 ± 1.48 1.06, 20.67	1.09E-3 -6.82 ± 0.024 1.06E-3, 1.12E-3	0.96 -0.039 ± 0.11 0.86, 1.08	0.18
H-19b5	-12.89 ± 0.99 -13.88, -11.89	0.28 -1.29 ± 1.10 0.091, 0.83	6.69E-2 -2.70 ± 0.099 6.07E-2, 7.39E-2	2.21 0.79 ± 0.18 1.84, 2.65	0.13
H-19b7	-16.15 ± 0.69 -16.85, -15.46	6.47 1.87 ± 1.21 1.93, 21.68	1.79E-4 -8.63 ± 0.0026 1.79E-4, 1.79E-4	1.32 0.28 ± 2.97 0.068, 25.84	0.14
H-19 Hydropad; Round 3					
H-19b3	-12.90 ± 1.26 -13.52, -11.01	4.04 1.66 ± 2.27 0.54, 50.99	3.67E-3 -6.86 ± 2.35 1.00E-4, 1.09E-2	0.81 0.002 ± 0.24 0.79, 1.27	0.19
H-19b6	-17.36 ± 0.67 -18.04, -16.67	4.34 1.47 ± 0.41 2.87, 6.57	4.16E-4 -7.79 ± 0.011 4.20E-4, 4.11E-4	0.78 -0.24 ± 0.15 0.674, 0.905	0.07
H-19b7	-15.95 ± 0.31 -16.25, -15.64	5.17 1.64 ± 0.51 3.10, 8.64	3.06E-3 -5.79 ± 0.0076 3.03E-3, 3.08E-3	0.73 -0.31 ± 0.095 0.66, 0.80	0.07
H-19b7; iodide	-15.65 ± 0.29 -15.94, -15.36	4.96 1.60 ± 0.091 4.53, 5.43	9.30E-4 -6.98 ± 3.21 3.74E-5, 2.31E-2	0.80 -0.23 ± 0.11 0.71, 0.89	0.17

Table S-4 Calculated 95% Confidence Intervals for Values Presented in Table S-2 (continued)

MULTIRATE: H-11, H-3, and H-6					
Parameter-Estimation Results for MWCF Tracer Tests					
Test	Mu 2 St. Dev. Range	Sigma ln(Sigma ± 2 St.Dev.) Range	Porosity ln(Porosity ± 2 St.Dev.) Range	Dispersivity ln(Disp. ± 2 St.Dev.) Range	RMSE
H-11 Hydropad; Round 1					
H-11b2 Fixed Dispersivity	-15.03 ± 0.065 -15.10, -14.97	1.68 -0.52 ± 0.066 1.57, 1.79	1.67E-2 -4.09 ± 0.086 1.53E-2, 1.82E-2	4.30 1.46 ± fixed 4.30, 4.30	0.077
H-11b2 4 Parameter Est.	-14.30 ± 0.31 -14.61, -13.99	4.50 1.15 ± 0.26 3.46, 5.87	2.32E-2 -3.77 ± 0.046 2.21E-2, 2.43E-2	10.83 2.38 ± 0.87 9.92, 11.81	0.055
H-11b3	-17.69 ± 0.063 -17.76, -17.63	1.35 0.30 ± 0.045 1.29, 1.41	1.32E-3 -6.63 ± 0.11 1.18E-3, 1.46E-3	4.03 1.39 ± 0.071 3.75, 4.33	0.096
H-11 Hydropad; Round 2					
H-11b2 Fixed Dispersivity	-14.98 ± 0.13 -15.11, -14.85	2.04 0.71 ± 0.093 1.85, 2.23	1.48E-2 -4.22 ± 0.14 1.28E-2, 1.70E-2	4.30 1.46 ± fixed 4.30, 4.30	0.11
H-11b2 4 Parameter Est.					
H-11b3	-17.19 ± 0.050 -17.24, -17.14	1.12 0.11 ± 0.017 1.10, 1.14	6.12E-4 -7.40 ± 0.12 5.43E-4, 6.90E-4	3.47 1.24 ± 0.030 3.37, 3.58	0.12
H-11b3; iodide	-16.79 ± 1.56 -18.35, -15.22	1.08 0.080 ± 0.19 0.90, 1.31	4.44E-4 -7.72 ± 0.70 2.20E-4, 8.98E-4	3.43 1.23 ± 1.69 0.063, 18.65	0.18
H-11 Hydropad; 1988 Test					
H-11b2 Fixed Dispersivity	-15.36 ± 0.28 -16.64, -15.08	0.57 -0.56 ± 1.15 0.18, 1.80	3.02E-2 -3.50 ± 0.10 2.74E-2, 3.33E-2	4.30 1.46 ± fixed 4.30, 4.30	0.46
H-11b2 4 Parameter Est.	-15.98 ± 0.33 -16.31, -15.64	1.54 0.43 ± 0.13 1.35, 1.75	5.60E-2 -2.88 ± 0.12 4.98E-2, 6.28E-2	11.97 2.48 ± 0.12 10.63, 13.47	0.14
H-11b3	-16.36 ± 0.066 -16.42, -16.29	0.83 -0.19 ± 0.024 0.81, 0.85	5.35E-4 -7.53 ± 0.52 3.18E-4, 9.01E-4	4.09 1.41 ± 0.12 3.63, 4.61	0.17
H3 Hydropad; 1984 Test					
H-3b1	-19.67 ± 4.14 -23.82, -15.53	1.40 0.34 ± 4.16 0.022, 89.74	4.58E-3 -5.38 ± 0.34 3.24E-3, 6.47E-3	3.50 1.25 ± 0.45 2.22, 5.50	0.30
H-6 Hydropad; 1981 Tests					
H-6a; Test 1 4 Parameter Est.	-11.85 ± 0.61 -12.46, -11.23	0.62 -0.48 ± 0.11 0.56, 0.69	7.52E-2 -2.59 ± 1.47 1.73E-2, 3.27E-1	11.94 2.48 ± 0.41 7.90, 18.04	0.18
H-6a; Test 1 Low Dispersivity					
H-6b; Test 1	-17.29 ± 4.19 -21.48, -13.10	0.33 -1.09 ± 1.08 0.11, 0.99	7.85E-3 -4.85 ± 3.99 1.46E-4, 4.22E-1	5.04 1.62 ± 1.05 1.76, 14.44	0.22
H-6b; Test 2	-17.19 ± 1.13 -18.32, -16.06	0.15 -1.91 ± 0.44 0.10, 0.23	5.01E-3 -5.30 ± 1.42 1.21E-3, 2.08E-2	3.03 1.11 ± 0.62 1.63, 5.63	0.17

Table S-5 Calculated 95% Confidence Intervals for Values Presented in Table S-3

SINGLE-RATE: H-19					
Parameter-Estimation Results for MWCF Tracer Tests					
Test	Mu 2 St. Dev. Range	Sigma	Porosity ln(Porosity ± 2 St.Dev.) Range	Dispersivity ln(Disp. ± 2 St.Dev.) Range	RMSE
H-19 Hydropad; Round 1					
H-19b2	-23.14 ± 1.48 -24.62, -21.66	0.00	6.49E-2 -2.73 ± 0.030 6.30E-2, 6.69E-2	3.27 1.18 ± 0.050 3.11, 3.43	0.13
H-19b3 Inj. Conc.= 85%	-11.30 ± 0.15 -11.45, -11.15	0.00	7.90E-4 -7.14 ± 0.20 6.47E-4, 9.65E-4	1.73 0.55 ± 0.038 1.66, 1.79	0.12
H-19b3; iodide	-12.96 ± 1.12 -14.08, -11.83	0.00	4.48E-7 -14.62 ± 14543.8 0, infinity	0.64 -0.44 ± 0.81 0.29, 1.45	0.45
H-19b4	-13.47 ± 0.32 -13.79, -13.14	0.00	1.22E-2 -4.40 ± 0.21 9.92E-3, 1.51E-2	2.68 0.99 ± 0.12 2.37, 3.04	0.11
H-19b5	-13.38 ± 0.11 -13.50, -13.27	0.00	3.23E-2 -3.43 ± 0.043 3.10E-2, 3.38E-2	1.81 0.59 ± 0.014 1.79, 1.84	0.13
H-19b6	-20.16 ± 0.10 -20.26, -20.05	0.00	4.13E-2 -3.19 ± 0.012 4.09E-2, 4.18E-2	3.03 1.11 ± 0.011 2.99, 3.06	0.10
H-19b7	-21.34 ± 0.74 -22.08, -20.60	0.00	5.78E-2 -2.85 ± 0.36 5.57E-2, 5.99E-2	2.90 1.06 ± 0.053 2.75, 3.05	0.20
H-19 Hydropad; Round 3					
H-19b3	-11.65 ± 0.018 -11.67, -11.63	0.00	2.51E-6 -12.90 ± 0.011 2.48E-6, 2.54E-6	1.77 0.57 ± 2.16 0.20, 15.26	0.26
H-19b5	-14.05 ± 0.88 -14.93, -13.16	0.00	6.24E-2 -2.77 ± 0.16 5.35E-2, 7.29E-2	2.49 0.91 ± 0.30 1.84, 3.36	0.17
H-19b7	-21.20 ± 1.86 -23.06, -19.34	0.00	5.54E-2 -2.89 ± 0.058 5.23E-2, 5.87E-2	2.14 0.76 ± 0.10 1.93, 2.37	0.35
H-19 Hydropad; Round 3					
H-19b3	-11.35 ± 0.54 -11.89, -10.81	0.00	2.52E-3 -5.98 ± 1.12 8.20E-4, 7.75E-3	1.62 -0.48 ± 0.079 1.50, 1.76	0.21
H-19b6	-19.44 ± 0.22 -19.66, -19.22	0.00	3.78E-2 -3.28 ± 0.030 3.67E-2, 3.89E-2	2.68 0.99 ± 0.029 2.61, 2.76	0.09
H-19b7	-21.81 ± 1.59 -23.40, -20.22	0.00	5.75E-2 -2.86 ± 0.38 5.54E-2, 5.97E-2	2.49 0.91 ± 0.051 2.37, 2.62	0.14
H-19b7; iodide	-18.74 ± 268.15 -304.88, 267.41	0.00	4.80E-2 -3.04 ± 8.35 1.13E-5, 1	1.78 0.58 ± 13.42 0.00, 1.20E+6	0.27

Table S-5. Calculated 95% Confidence Intervals for Values Presented in Table S-3 (continued)

SINGLE-RATE: H-11, H-3, and H-6					
Parameter-Estimation Results for MWCF Tracer Tests					
Test	Mu 2 St. Dev. Range	Sigma	Porosity ln(Porosity ± 2 St.Dev.) Range	Dispersivity ln(Disp. ± 2 St.Dev.) Range	RMSE
H-11 Hydropad; Round 1					
H-11b2	-16.62 ± 0.034 -16.65, -16.59	0.00	8.77E-3 -4.74 ± 0.099 7.95E-3, 9.68E-3	2.62 0.96 ± 0.026 2.56, 2.69	0.089
H-11b3	-19.38 ± 0.058 -19.43, -19.32	0.00	2.03E-3 -6.20 ± 0.052 1.93E-3, 2.14E-3	5.75 1.75 ± 0.044 5.51, 6.01	0.11
H-11 Hydropad; Round 2					
H-11b2	-16.39 ± 0.076 -16.46, -16.31	0.00	8.39E-3 -4.78 ± 0.45 5.34E-3, 1.32E-2	2.56 0.94 ± 0.24 2.01, 3.27	0.096
H-11b3	-18.98 ± 0.067 -19.05, -18.91	0.00	1.49E-3 -6.51 ± 0.18 1.24e-3, 1.79E-3	6.72 1.90 ± 0.15 5.81, 7.77	0.11
H-11b3; iodide	-18.57 ± 0.079 -18.65, -18.50	0.00	1.08E-3 -6.83 ± 0.25 8.39e-4, 1.39E-3	5.11 1.63 ± 0.17 4.33, 6.04	0.13
H-11 Hydropad; 1988 Test					
H-11b2	-16.39 ± 0.076 -16.46, -16.31	0.00	8.39E-3 -4.78 ± 0.45 5.34E-3, 1.32E-2	2.56 0.94 ± 0.24 2.01, 3.27	0.14
H-11b3	-18.98 ± 0.067 -19.05, -18.91	0.00	1.49E-3 -6.51 ± 0.18 1.24e-3, 1.79E-3	6.72 1.90 ± 0.15 5.81, 7.77	0.11
H-3 Hydropad; 1984 Test					
H-3b1	-21.51 ± 0.54 -22.05, -20.97	0.00	4.95E-3 -5.31 ± 0.51 2.98e-3, 8.22E-3	3.06 1.12 ± 0.72 1.49, 6.31	0.34
H-6 Hydropad; 1981 Tests					
H-6a; Test 1	-14.61 ± 0.48 -15.10, -14.13	0.00	7.61E-2 -2.58 ± 0.10 6.87E-2, 8.43E-2	8.47 2.14 ± 0.20 6.95, 10.31	0.19
H-6b; Test 1	-19.65 ± 0.14 -19.80, -19.51	0.00	7.24E-3 -4.93 ± 0.078 6.70e-3, 7.82E-3	4.23 1.44 ± 0.088 3.87, 4.62	0.20
H-6b; Test 2	-19.49 ± 0.23 -19.73, -19.26	0.00	5.03E-3 -5.29 ± 0.11 4.50e-3, 5.64E-3	2.79 1.03 ± 0.11 2.51, 3.10	0.22

The single-rate double-porosity model is also able to reproduce the observed tracer-breakthrough curve reasonably well (Figure S-1; SR1 sim). This simulation slightly overestimates the rising limb, resulting in more mass being removed from the aquifer at early time. The peak concentration is similar to that predicted with the multirate model, but the peak-arrival time is earlier than that observed. The falling limb of the breakthrough curve is underestimated and the simulated results fall outside of the confidence interval of the data for this portion of the tracer-breakthrough curve. The tail of the breakthrough curve is slightly overestimated by the simulation with a higher concentration of solute leaving the aquifer at late time. The estimated ½ MBL, advective porosity, and dispersivity are larger for the single-rate model than those estimated with the multirate model (see Tables S-2 and S-3). In fact, the ½ MBL is the largest calculated for any simulation. The Damkohler number calculated for the single-rate simulation is 0.0005. A calculated Damkohler number of less than 0.01 for the single-rate model indicates that the rate of diffusion is negligible with respect to the rate of advection. This single-rate interpretation could also be conceptualized as a single-porosity system. To check this conclusion, a single-porosity simulation was performed for this pathway. The results of this simulation (Figure S-1; SP1 sim) show that this pathway can be accurately conceptualized as a single-porosity system with a porosity of 6.5%. For the porosity to be this high, most of it must be in the matrix, not in fractures. That degree of matrix participation, however, suggests that local equilibrium was reached between the fractures and matrix, in which case we would expect the Damkohler number to be >100, as discussed in Section 7.2. We do not currently understand how a high degree of matrix involvement is consistent with a low Damkohler number.

S.5.1.2 H-19b3 to H-19b0 Pathway

The pathway from H-19b3 to H-19b0 is 11.0 m long and trends east to west from the injection well to the pumping well (see Figure 3-2). Injections were made into this well during all three rounds of the 7-well test (Chapter 3). Round 1 was a dual injection of a benzoic acid and iodide, which have different aqueous diffusion coefficients. Due to irregularities in the tracer-breakthrough curve, the Round 1 data were truncated at the end of Round 1 pumping for simulation. The tracer-breakthrough curve displays a secondary concentration peak during the Round 2 injection period (see Figure S-2). The presence of this secondary peak inhibits the parameter-estimation routine and, therefore, the parameter-estimation routine was performed for the breakthrough data corresponding to Round 1 pumping only. The discussion below first summarizes the results of the best-fit parameter estimations based on the lowest RMSE value for each of the four data sets. Subsequently, for this pathway, the attempt to determine a unique parameter set able to simulate all four data sets accurately is discussed.

The multirate-diffusion model does a poor job of describing the Round 1 data set (Figure S-2; MR1 sim). The simulation mimics but overestimates every portion of the observed breakthrough curve. The mass recovery is overestimated by 16% at the end of Round 1 pumping. Following numerous calibration attempts, closer agreement between the simulation and the observed data could not be achieved.

The shape of the simulated breakthrough curve identically mimics that of the observed data. By adjusting the mass under the breakthrough curve, better agreement between the simulation and the data was achievable (Figure S-2; MR2 sim). Examination of Figure C-3 may reveal the cause of the simulated overestimation of total mass recovered. A secondary peak in the tracer-breakthrough curve is apparent early in the second pumping period shortly after the Round 2 tracer injections. The Round 2 injection of tracer into H-19b3 may have caused tracer trapped in the borehole during the Round 1 injection to be released into the aquifer. Additional examination of Figure C-3 shows that the slope of the mass-recovery curve is zero near the end of Round 3 pumping, indicating that mass is no longer being removed from the aquifer at late time. Approximately 13% (±5%) of the injected mass will apparently never be recovered.

Based on these two observations, the mass participating in the model simulation was reduced by setting the injected concentration to 85% of its original value. The value of 85% was obtained by examining the final mass recovered in the mass-recovery curve (Figure C-3). Several values within the confidence intervals of the mass-recovery curve were investigated. The value of 85% produced the best results based on the calculated RMSE value. After adjusting the injected mass, the simulation obtained estimated parameter values for ½ MBL, advective porosity, and dispersivity that are very similar to those obtained by the first calibration attempt (see Table S-2). Following adjustment, the simulated breakthrough curve agrees with all portions of the observed data very well. The simulation slightly overpredicts the slope of the rising limb and predicts a slightly earlier peak time. The peak concentration is very well represented, as are the falling limb and tail of the observed data. The mass-recovery curves for

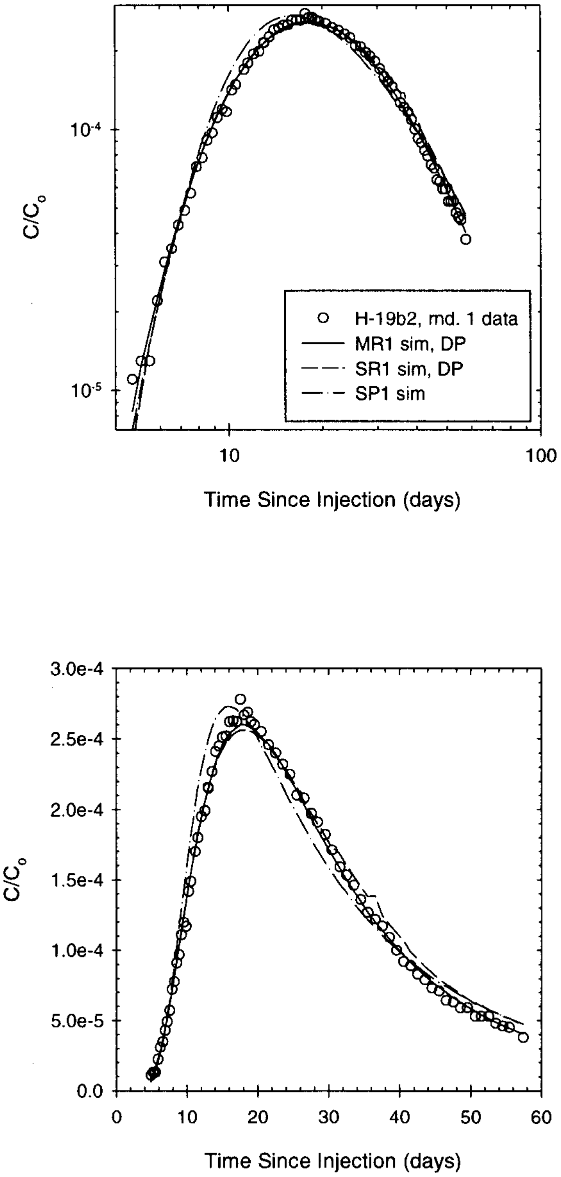

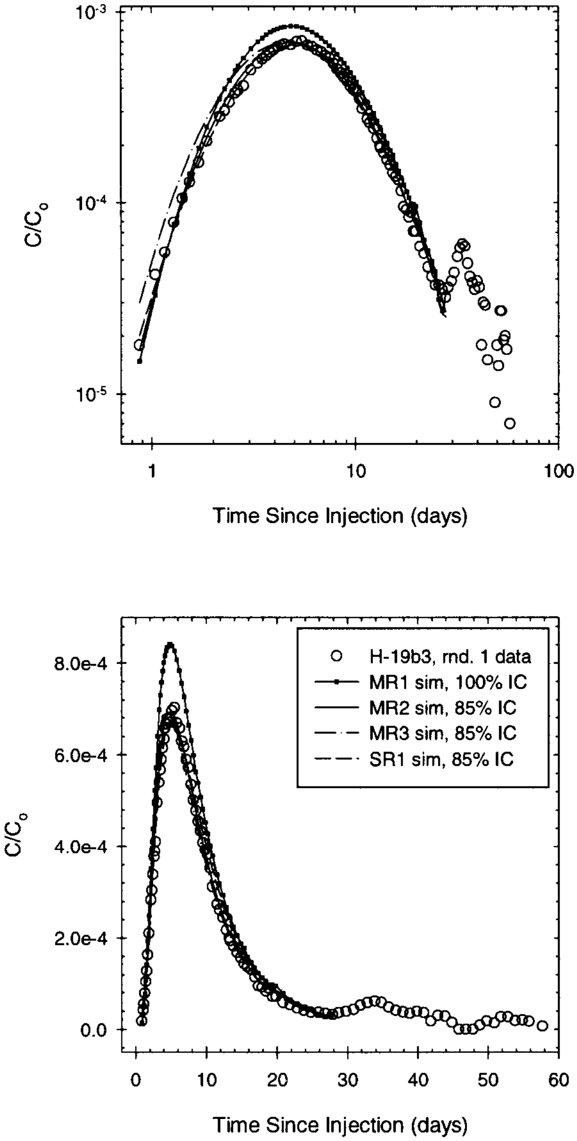

Figure S-1 Single-rate (SR) and multirate (MR) diffusion transport model calibrations to the tracer-breakthrough curve for the H-19 hydropad, pathway H-19b2 to H-19b0, for Round 1 pumping rate, benzoic-acid tracer. Note that for this figure and most other figures two graphs are shown that provide the same data and simulation results. The upper one is plotted in log-log space and the lower one is plotted in linear-linear space.

Figure S-2 Single-rate and multirate diffusion transport model calibrations to the tracer-breakthrough curve for the H-19 hydropad, pathway H-19b3 to H-19b0, for Round 1 pumping rate, benzoic-acid tracer.

the simulation and the data agree within 1% of each other.

The single-rate simulation for this pathway suffered from the same overestimation of total mass recovered as the multirate simulation above. The same technique of lowering the mass under the breakthrough curve was applied, with similar results. A value of 85% of the injection concentration was chosen for consistency with the multirate adjustment. For this pathway, the single-rate model is able to describe the observed breakthrough curve as well as the multirate model (Figure S-2; SR1 sim). The peak concentration is slightly underestimated, but the peak-arrival time is accurate. The simulation overpredicts the concentration of the falling limb and falls outside of the calculated confidence interval. The dispersivity value obtained for this simulation is approximately 16% of the travel distance between the wells and is larger than that estimated with the multirate model. The estimated ½ MBL and advective porosity are lower than predicted with the multirate model (see Tables S-2 and S-3). The mass recovery is overpredicted by 3%.

An iodide tracer was co-injected with the benzoic acid during the Round 1 injection. The iodide data obtained from the ion chromatograph (IC) analyses were used for the simulations. The first two data points in the rising limb were truncated from the data set due to extremely large confidence intervals for those points (see Figure C-9). Similar to the benzoic-acid simulations above, the best-fit calibration overestimates and mimics every portion of the observed data (Figure S-3; MR1 sim). The mass recovery is overestimated by 23% at the end of Round 1 pumping. No set of parameters could be found to match the observed data accurately. Additionally, the same secondary peak on the tracer-breakthrough curve after the pumping for Round 1 is apparent (see Figure C-9). The same technique was used to lower the mass under the breakthrough curve for the iodide data set. The injected concentration was adjusted to 85% for consistency with the benzoic-acid simulation above. After adjusting the injection concentration, the simulation matches the observed data fairly well (Figure S-3; MR2 sim). With the exception of advective porosity, which increased by nearly one order of magnitude, the estimated parameter values are very similar between the two simulations. The estimated advective-porosity value for this simulation is in better agreement with the estimated advective porosities from different pumping rates. The simulation with the adjusted injection concentration overestimates the slope of the rising limb, the peak concentration, and predicts an earlier peak-arrival time of the observed tracer-breakthrough curve. The tail of the data is matched very well by the simulation. The mass recovered at the end of the pumping period is well represented, but slightly overestimated, with the adjusted-injection-concentration simulation.

The single-rate simulation generally overestimates the observed iodide data similar to the multirate simulation above. Several calibration attempts could not match the observed data. The simulations consistently overestimated the mass recovered by 25% at the end of Round 1 pumping. The injected concentration was adjusted to 85% according to the observed mass recovery (Figure C-9) as well as the value used in the benzoic-acid data set. The simulation obtained from the reduced injected mass matches, but overestimates, every portion of the breakthrough-curve data (Figure S-3; SR1 sim). The peak concentration is slightly overestimated, but the peak arrival is accurately represented. The estimated advective porosity is extremely small (4.48×10^{-7}), too small to be realistic. The mass recovered at the end of Round 1 pumping is overestimated by approximately 12%. Additional simulation effort might improve the results of the single-rate simulation by obtaining a more realistic advective-porosity value.

Because the single-rate simulation yields a very low advective porosity when compared to the multirate simulation, the first G&G parameter assumption (Equation S-1) may be violated; the ratio of the injected volume to the fluid volume in the area between the two wells may not be small. This may lead to the plume of the injection fluid intersecting the pumping well during the injection phase. The analytic solution for the injection phase in STAMMT-R allows the user to observe and set the maximum radius the injection solution travels into the aquifer. The apparent violation of the G&G1 assumption was checked for the analytic solution for solute penetration distance and

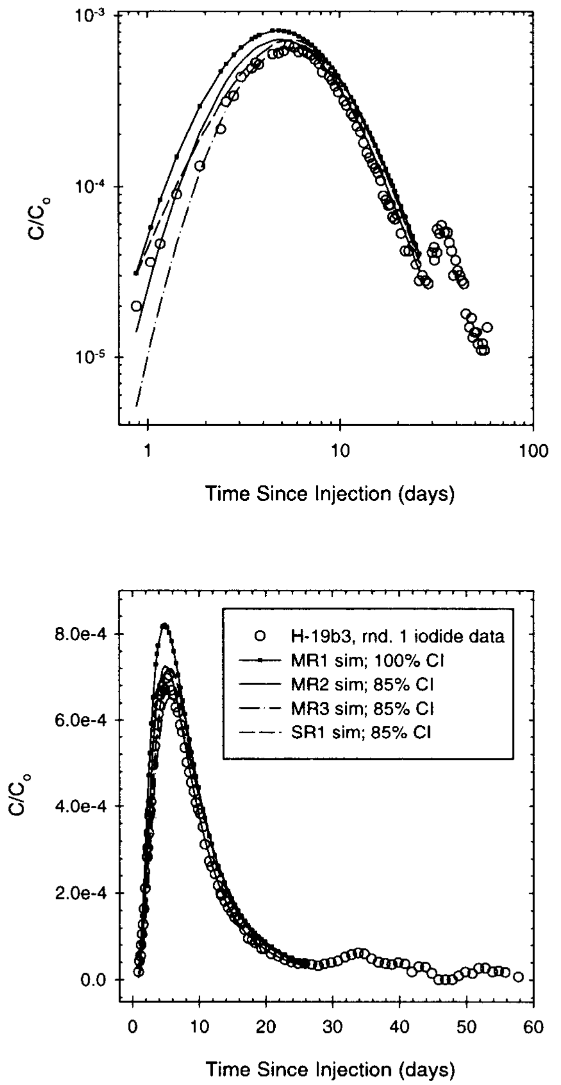

Figure S-3 Single-rate and multirate diffusion transport model calibrations to the tracer-breakthrough curve for the H-19 hydropad, pathway H-19b3 to H-19b0, for Round 1 pumping rate, iodide tracer co-injected with benzoic-acid tracer.

does not affect the simulation results. We believe that sufficient diffusion occurs to prevent the maximum radius of the solute plume from reaching the pumping well.

The multirate-diffusion model is not able to provide a precise match to the observed breakthrough curve for the Round 2 data (Figure S-4; MR1 sim). The data set used for this simulation was obtained from the lower Culebra interval. The simulation overestimates the slope of the rising limb, the peak concentration, and the peak-arrival time. After the peak concentration, the simulation matches the breakthrough curve very well. The mass recovery is overestimated for this simulation by 7%. Simulation of transport along this pathway could benefit from additional effort. This might include attempting to match the rising limb and peak concentration of the observed tracer-breakthrough curve more closely.

Similar to above, the single-rate simulation is not able to match all portions of the data set (Figure S-4; SR1 sim). It is opposite of the multirate simulation in the portions of the observed data that it is able to match. The single-rate simulation matches the rising limb, peak concentration, and peak-arrival time very well. After the peak concentration, it overestimates the concentrations in the falling limb and tail of the observed tracer-breakthrough curve. This simulation obtained an extremely small advective porosity value, similar to the Round 1 single-rate simulation. It also overestimates the mass recovery by 12%. This pathway would benefit from additional simulation effort to obtain a more realistic advective-porosity value which might include constraining the porosity limits. As with Round 1 simulations above, the single-rate simulation obtained an estimated dispersivity that is larger than that from the multirate simulation. The ½ MBL and the advective porosity are lower for the single-rate simulation when compared to the estimated values obtained for the multirate simulation (see Tables S-2 and S-3). Because the single-rate simulation yields a very low advective porosity when compared to the multirate simulation, the G&G1 assumption (Equation S-1) may be violated, similar to the single-rate simulation of the Round 1 iodide data set. The analytical solution for solute penetration indicates this apparent violation should not pose a problem as the maximum radius of the injected solute for the simulation is set to 4.0 m, less than half the distance between the wells.

Similar to the Round 1 benzoic acid and iodide co-injection above, the multirate simulation overestimates and mimics every portion of the observed breakthrough curve for the Round 3 data set (Figure S-5; MR1 sim). The simulation overestimates the slope of the rising limb and the peak concentration. The peak-arrival time is well represented. The falling limb concentration is also overestimated. No parameter set was found to match the simulated concentration breakthrough curve to the observed data precisely. The parameter sets obtained from the estimation routine consistently overestimated the mass recovery by 11% or more.

Similar to the above multirate model and Round 1 injection, the single-rate model also overestimates and mimics every portion of the observed tracer-breakthrough curve (Figure S-5; SR1 sim). The results of the simulation are very similar to that described for the multirate simulation. No parameter set could be found to match the observed breakthrough curve accurately. The estimated ½ MBL and advective porosity are lower for the single-rate simulation while the dispersivity is higher (see Tables S-2 and S-3). The mass recovered at the conclusion of the pumping is consistently overestimated by 12% or more for numerous calibration attempts.

An effort was made to find a unique parameter set that could accurately predict the four tracer-breakthrough curves (three benzoic acids and one iodide data set) from the H-19b3 to H-19b0 pathway. Starting with the best-fit parameters obtained from the parameter-estimation routine, the individual values were averaged (e.g., arithmetic mean, geometric mean) to find a unique set of parameters that could adequately predict the different breakthrough curves obtained from different injection/pumping rates and aqueous diffusion coefficients of the tracers. The averaging approach to find a unique parameter set was not entirely successful and the parameter set was ultimately found by trial and error. If a parameter set could not predict the observed breakthrough curve (i.e., falls outside of the confidence intervals for a significant portion of the data) for any one of the pumping rates or diffusion coefficients, the set was discarded. Figure S-2; MR3 sim, Figure S-3; MR3 sim, Figure S-4; MR2 sim, and Figure S-5; MR2 sim show the results of predicting the four observed data sets with one unique parameter set. For Round 1 (both the benzoic acid and iodide data set) only, the injected concentration was set at the reduced values indicated above. These two tracer-breakthrough curves had the secondary peak after the first round of pumping. Because the technique of lowering the injection concentration found the best-fit parameter set above and the recovered mass would theoretically never reach unity, the same should be done with the forward predictive models. If no adjustments to the injection concentration were made, a unique parameter

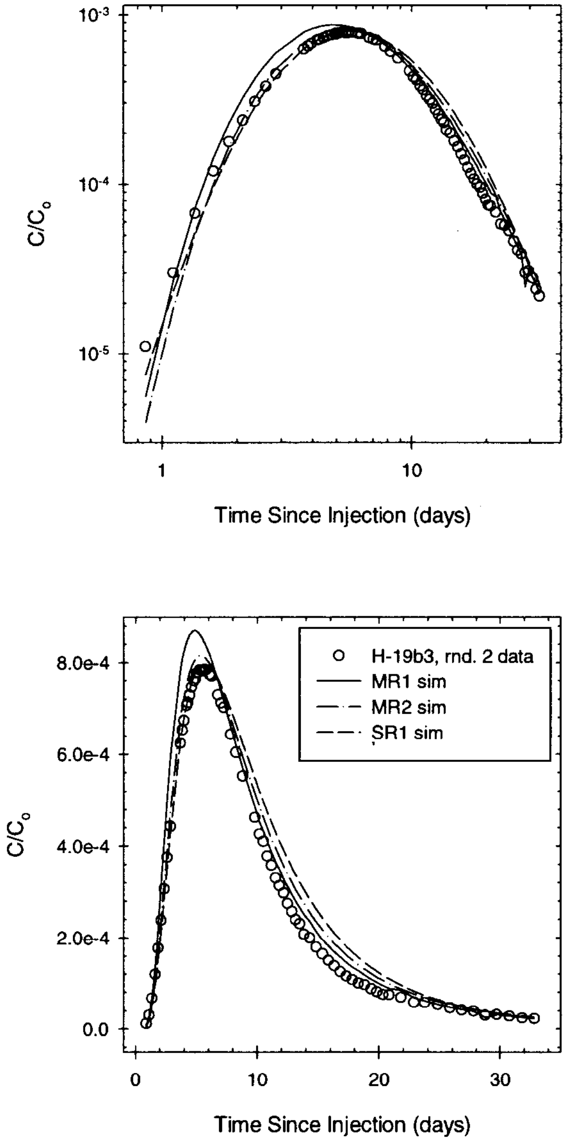

Figure S-4 **Single-rate and multirate diffusion transport model calibrations to the tracer-breakthrough curve for the H-19 hydropad, pathway H-19b3 to H-19b0, for Round 2 pumping rate, benzoic-acid tracer.**

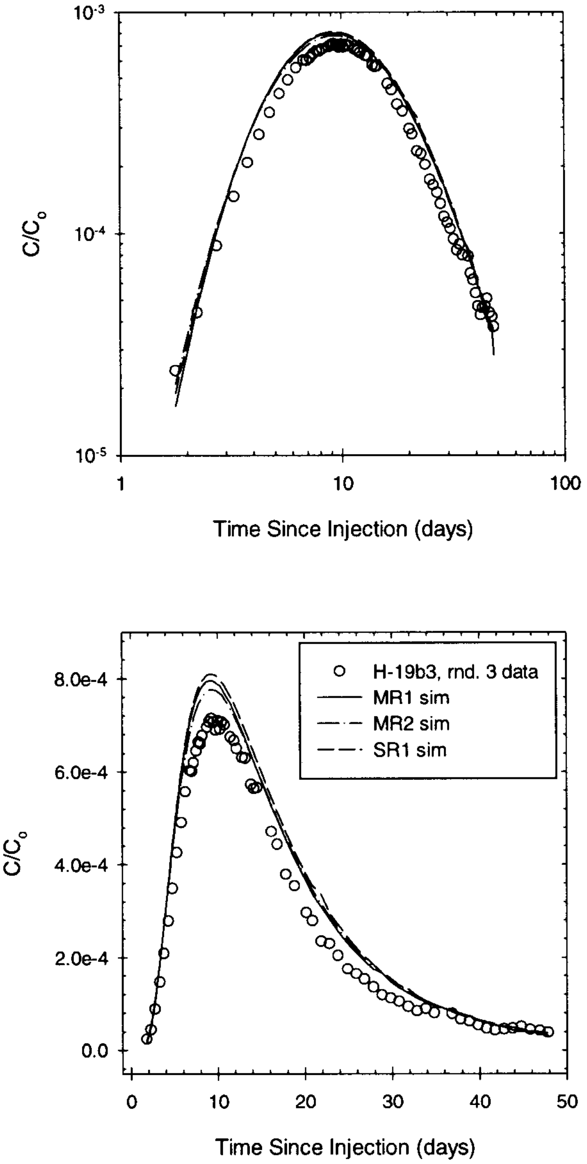

Figure S-5 Single-rate and multirate diffusion transport model calibrations to the tracer-breakthrough curve for the H-19 hydropad, pathway H-19b3 to H-19b0, for Round 3 pumping rate, benzoic-acid tracer.

set would probably not be found to satisfy all of the data sets. Several unsuccessful attempts to predict the observed data with the full injection concentration were made prior to lowering the injection concentration. All other forward predictive models use the full injection concentration for the simulations.

The forward predictive simulations using a unique parameter set for the four tracer-breakthrough curves are fairly successful. In most cases, the predictive model looks very similar, but is never statistically better (according to the calculated RMSE value) than the best-fit simulations presented above. The predictive simulations used a value for the median ½ MBL of 0.0057 m, an advective porosity of 2.10 x 10^{-3}, and a dispersivity of 0.675 m (see Table S-2). In the case of the Round 1 data set, the adjusted injection concentration was utilized because some of the mass of tracer is lost during the tracer test.

A similar attempt to find a unique data set to describe all four data sets with the single-rate model was made. Currently, no unique parameter set has been identified that can adequately predict all of the available data.

S.5.1.3 H-19b4 to H-19b0 Pathway

The pathway from H-19b4 to H-19b0 is the second longest pathway tested at the H-19 hydropad at 22.3 m (see Figure 3-2). This injection well was used for the Round 1 injection only. The data for this simulation were truncated at the conclusion of Round 2 pumping to provide a robust data set for parameter estimation. The peak concentration and tail for this data set are not well defined regardless of the truncation point. The confidence interval for the data is also quite large in comparison to the other data sets (see Figure C-4).

The multirate simulation accurately matches every portion of the observed data (Figure S-6; MR1 sim). The peak concentration is slightly underestimated, but the peak arrival is very accurate. How much the multirate model underestimates the peak concentration is unclear due to two apparent peak concentrations appearing on the tracer-breakthrough curve. The tail of the data set is accurately represented by the multirate simulation. The mass recovered at the conclusion of Round 2 pumping is overestimated by less than 2%.

The single-rate simulation is also able to match the observed data reasonably accurately (Figure S-6; SR1 sim). The peak concentration and arrival time are accurately represented. The tail of the breakthrough curve is overestimated slightly by the simulation. The single-rate model obtained a larger ½ MBL, advective porosity, and dispersivity when compared to the calibration above (see Tables S-2 and S-3). The mass recovered is overestimated by less than 6% at the conclusion of the tracer test. Based on the RMSE value and the mass recovered at the end of the test, the multirate simulation more accurately represents the observed data.

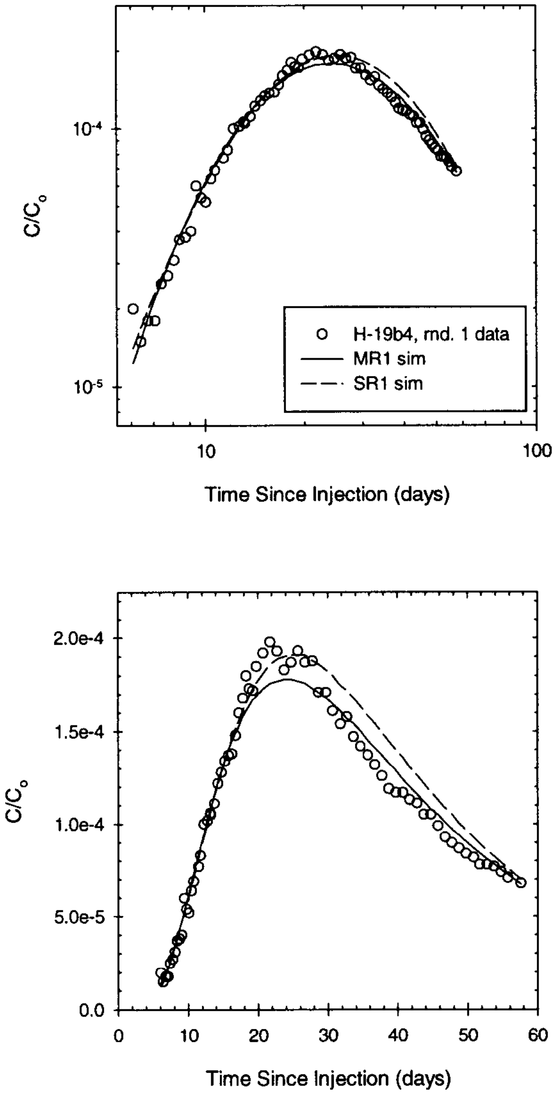

Figure S-6 **Single-rate and multirate diffusion transport model calibrations to the tracer-breakthrough curve for the H-19 hydropad, pathway H-19b4 to H-19b0, for Round 1 pumping rate, benzoic-acid tracer.**

S.5.1.4 H-19b5 to H-19b0 Pathway

Injection well H-19b5 is located 13.9 m from the pumping well (see Figure 3-2) and was utilized for both Round 1 and Round 2 injection periods. During the Round 1 injection, the borehole was separated into upper- and lower-Culebra injection intervals with inflatable packers, and separate, distinct tracers were injected into each interval. The lower injection interval borehole volume was approximately 80 L (Appendix B). The volume of chaser is selected to exceed the borehole volume to flush tracer remaining in the borehole into the formation (see Chapter 3 for details). Due to an injection error, the volume of chaser injected was 65 L (Appendix B) and the entire borehole may not have been flushed of the tracer at the conclusion of the injection phase. The upper injection interval did not yield a suitable data set for model calibration and only the lower injection interval is discussed below. For Round 2 injection, the tracer was injected over the entire Culebra interval.

The multirate and single-rate simulations look very similar to each other for the lower injection interval during Round 1 (Figure S-7; MR1 sim and SR1 sim). Both of the simulations are able to match the rising limb of the observed data. The peak concentration and peak-arrival time are overestimated by both models (e.g., higher peak concentrations that arrive later than observed). The concentrations in the falling limb and most of the tail are overestimated by both models as well. Approximately 9% overestimation of the mass recovered at the end of the observed data is apparent in the simulations. Of all the multirate-diffusion interpretations, this pathway yielded the smallest sigma, σ_d, the spread about the mean diffusion-rate coefficient. This indicates a single-rate model should be adequate to match the observed data. Due to the low injection rate and long

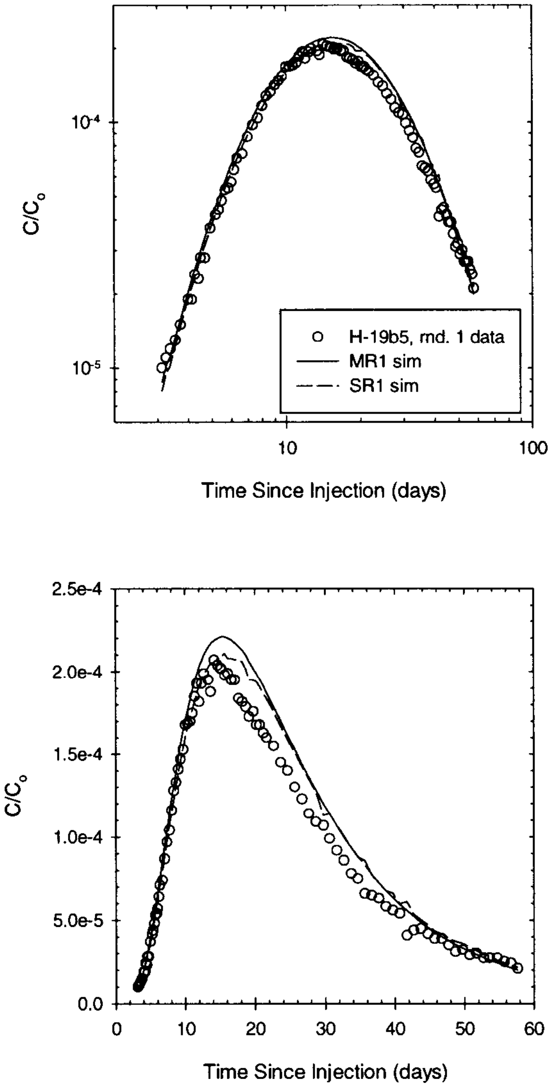

Figure S-7 **Single-rate and multirate diffusion transport model calibrations to the tracer-breakthrough curve for the H-19 hydropad, pathway H-19b5 to H-19b0, for Round 1 pumping rate, benzoic-acid tracer.**

injection time, the G&G2 assumption (Equation S-2) may have been violated during the injection period for both the single-rate and multirate simulations. The velocity of the fluid due to injection may not have been sufficiently greater than the velocity of the groundwater due to pumping the withdrawal well. This will cause the shape of the injection-solution plume to be oblong instead of a perfect ring. This may explain the poor simulation results obtained from this calibration. In addition, because of the flushing error, the injected mass of tracer was reduced similar to the above treatment along pathway H-19b3 to H-19b0. This did not improve the simulation results, however. The advective porosity and dispersivity estimated with both the single-rate and multirate simulations are very similar to each other. The ½ MBL obtained from the single-rate simulation is slightly larger than that obtained from the multirate simulation (see Tables S-2 and S-3).

The Round 2 data set has a poorly defined peak concentration and does not have a developed tail for the tracer-breakthrough curve (Figure S-8). The multirate model matches most of the observed data very well (Figure S-8; MR1 sim). The mass recovery is very accurate with less than 1% error between the simulation and the observed data. Again, the multirate model obtained a sigma value that is close to zero, indicating a single-rate solution to describe the data set should be adequate. However, the best-fit single-rate simulation did not match the data as well as the multirate simulation (Figure S-8; SR1 sim). The peak and falling-limb concentrations are significantly underestimated. The simulated peak-arrival time is also earlier than observed in the data. The estimated advective porosity, dispersivity, and ½ MBL are larger for the single-rate simulation (see Tables S-2 and S-3).

A forward, predictive model using a unique parameter set to simulate the two data sets was not attempted due to the chaser injection error in Round 1 and the poor quality of the data in Round 2.

S.5.1.5 H-19b6 to H-19b0 Pathway

Pathway H-19b6 to H-19b0 was used for Round 1 and Round 3 injections and is the third longest pathway tested on the H-19 hydropad at 19.8 m (see Figure 3-2). The Round 1 data set shows a well-developed tail following a nicely defined peak. This data set was truncated at the end of the Round 2 pumping period. The first three data points in Round 1 data and the first data point in the Round 3 data were removed due to the very large confidence intervals associated with these points (see Figures C-7 and C-16, respectively).

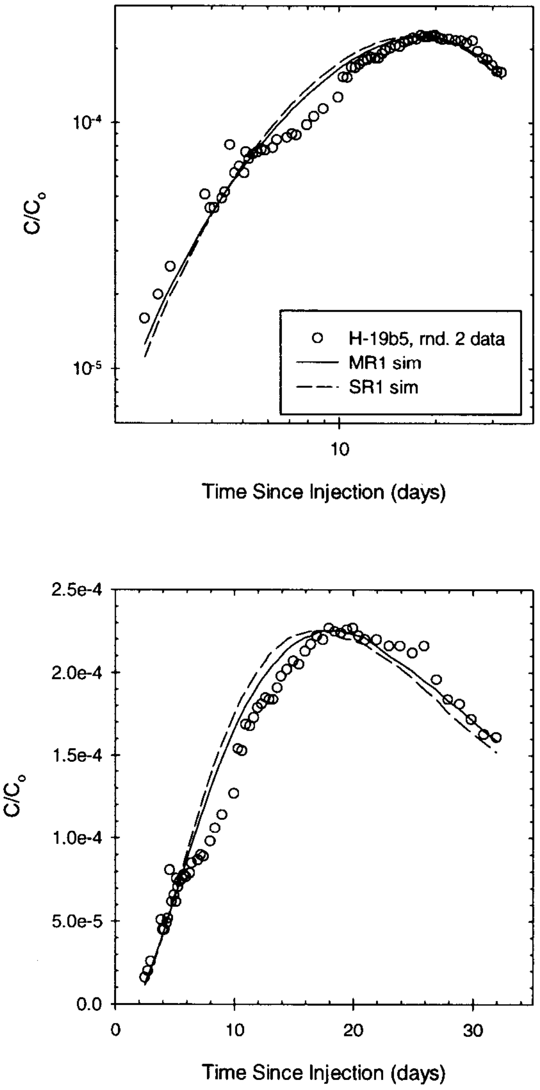

Figure S-8 Single-rate and multirate diffusion transport model calibrations to the tracer-breakthrough curve for the H-19 hydropad, pathway H-19b5 to H-19b0, for Round 2 pumping rate, benzoic-acid tracer.

As with the case of pathway H-19b3 to H-19b0, an attempt to find a unique parameter set to predict the observed data for two different pumping rates was made. This will be presented following the best-fit results below.

The multirate and single-rate simulations are both able to describe the observed tracer-breakthrough curve accurately for the Round 1 data set (Figure S-9; MR1 sim and SR1 sim, respectively). Both simulations predict a slightly higher peak concentration that arrives slightly later than the data set. The single-rate simulation estimates a larger ½ MBL, advective porosity, and dispersivity when compared to the multirate simulation (see Tables S-2 and S-3). The dispersivity value is approximately 15% of the travel distance for the single-rate simulation. The mass recovery is overestimated by 4% and 6% for the single-rate and multirate simulations, respectively. The RMSE value obtained for the single-rate simulation is slightly lower than for the multirate simulation, indicating the single-rate model is statistically better in fitting the data. No attempt to adjust the injection concentration was made for this data set.

The calculated Damkohler number for the single-rate simulation (Figure S-9, SR1 sim) was lower than the 0.01 Damkohler cutoff and had a calculated value of 0.005, indicating this pathway could be conceptualized as a single-porosity system. A calculated Damkohler number of less than 0.01 for the single-rate model indicates that the rate of diffusion is negligible with respect to the rate of advection. A single-porosity simulation was performed for this pathway with adequate results (results not plotted). Increasing the advective porosity to approximately 5 to 6% provides an adequate visual fit, but a less acceptable statistical fit, to the observed breakthrough curve data. Additional simulation effort is required to refine the parameters used in the single-porosity simulation.

Similar to the Round 1 data set, the single-rate and multirate simulations are both able to fit the observed data adequately in Round 3 (Figure S-10; MR1 sim and SR1 sim). The tail of the observed breakthrough curve is not as well developed as that in Round 1. Similar to above, the single-rate simulation obtained a larger ½ MBL, advective porosity, and dispersivity (see Table S-3). The mass recovery is underestimated by the single-rate simulation by approximately 4%, while the multirate simulation overestimates the mass recovered by less than 4%.

The attempt to find a unique parameter set for the multirate-diffusion model to predict the observed breakthrough curves for two different pumping rates was very successful. Both of the simulations

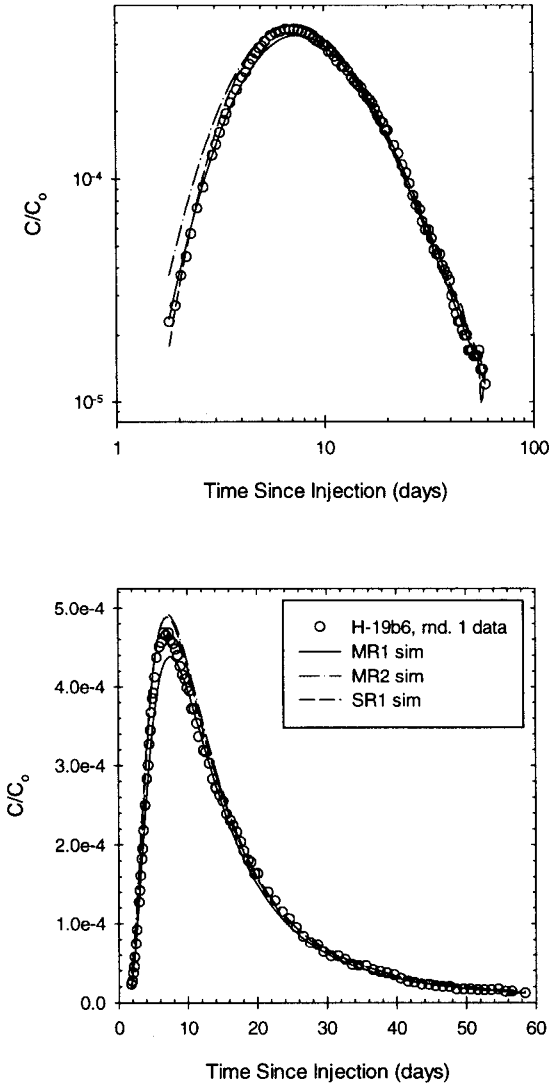

Figure S-9 Single-rate and multirate diffusion transport model calibrations to the tracer-breakthrough curve for the H-19 hydropad, pathway H-19b6 to H-19b0, for Round 1 pumping rate, benzoic-acid tracer.

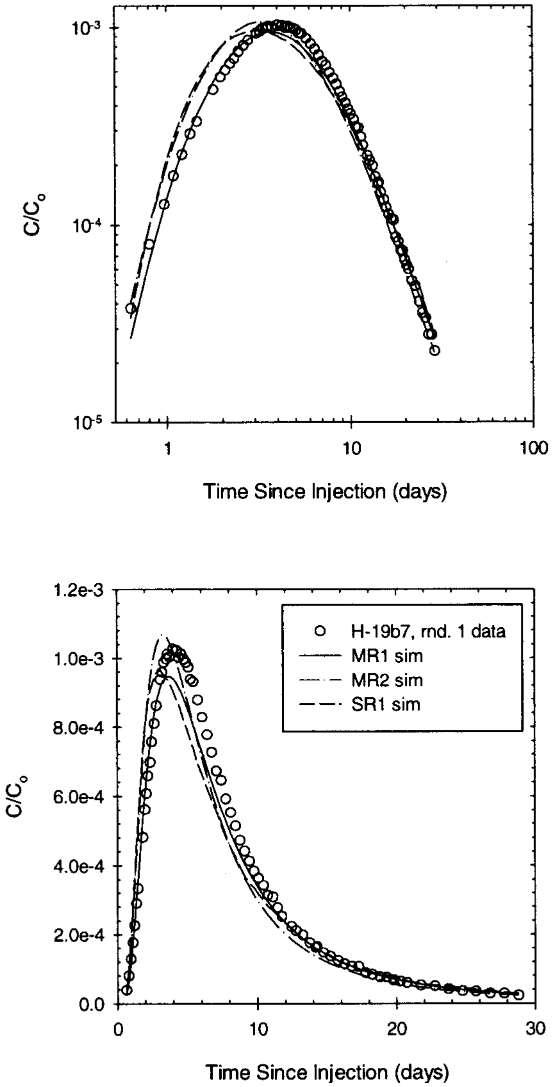

Figure S-10 Single-rate and multirate diffusion transport model calibrations to the tracer-breakthrough curve for the H-19 hydropad, pathway H-19b6 to H-19b0, for Round 3 pumping rate, benzoic-acid tracer.

overestimate the peak concentration, but fall within the confidence intervals of the data. The simulated breakthrough curve from the forward, predictive simulation for Round 1 looks very similar to the tracer-breakthrough curve from the parameter-estimation routine. The forward simulation for the Round 3 data set overestimates the concentration being removed from the aquifer at times after the peak concentration, but matches the tail of the observed data fairly well. A similar attempt to find a unique parameter set for the single-rate model has been made. No unique parameter set for a single-rate simulation has been identified that can accurately predict the observed data.

S.5.1.6 H-19b7 to H-19b0 Pathway

Several data sets are available for pathway H-19b7 to H-19b0. This injection well was used for all three rounds of injection. The Round 3 injection solution contained two tracers, benzoic acid and iodide, which were co-injected into the well. All of the rounds have had the first data point removed for the simulations due to the large confidence intervals associated with the data points (see Appendix C). In general, calibrating the model to the data from this pathway proved to be difficult even though the path is one of the shortest on all of the hydropads. The fast transport of solutes between the injection well and pumping well may be part of the reason this data set was difficult to simulate.Round 1 had the highest mass recovery of all of the (7-well) tracer tests conducted at the H-19 hydropad with 100% of the mass recovered at the end of the pumping period. The confidence interval about this value for mass recovery is quite large at ± 6% (see Figure C-8). Several calibration attempts for both the multirate and single-rate models consistently underestimated the breakthrough curve and the mass recovered at the end of the first pumping period (Figure S-11; MR1 sim and SR1 sim). This is opposite the case of pathway H-19b3 to H-19b0 where the calibration attempts consistently overestimated the breakthrough curve and the mass-recovery curve. The multirate simulation matches the rising limb of the observed data and underestimates the peak concentration, but accurately predicts the peak-arrival time. The simulation falls outside of the confidence interval for the falling limb, but accurately represents the tail of the observed breakthrough curve. The mass recovery is underestimated by approximately 6%. The multirate simulation estimated a very low advective porosity. Because of this, the G&G1 assumption (Equation S-1) is questionable; the front of the injection plume may have intersected the withdrawal well during the injection phase. This should not be a problem for the analytic solution, as the position of the front of the injection plume was manually set to less than half the distance between the injection and pumping wells.

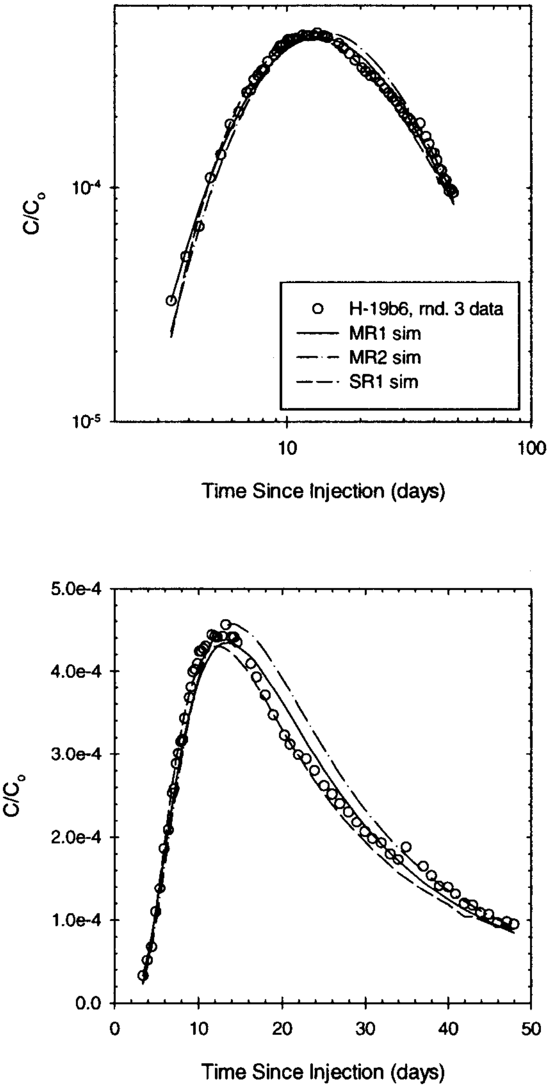

Figure S-11 **Single-rate and multirate diffusion transport model calibrations to the tracer-breakthrough curve for the H-19 hydropad, pathway H-19b7 to H-19b0, for Round 1 pumping rate, benzoic-acid tracer.**

Similar to the multirate simulation above, the single-rate simulation consistently underestimated the observed breakthrough and mass-recovery curves (Figure S-11; SR1 sim). The slope of the rising limb of the observed data is overestimated by the simulation. The peak-arrival time is earlier and the peak concentration is lower than are observed in the data. The concentration of solute being removed from the aquifer after the peak is underestimated by the simulation. The tail of the observed data is matched accurately. The mass recovered at the end of the pumping period is underestimated by approximately 6%. The single-rate simulation obtains estimates for ½ MBL, advective porosity, and dispersivity that are larger than those estimated with the multirate simulation (see Tables S-2 and S-3). The Damkohler number calculated for the single-rate simulation is 0.0006. A calculated Damkohler number of less than 0.01 for the single-rate model indicates that the rate of diffusion is negligible with respect to the rate of advection. This single-rate interpretation could also be conceptualized as a single-porosity system. To check this conclusion, a single-porosity simulation was performed for this pathway (results not plotted). Preliminary visual evaluation of the single-porosity simulation indicates that this conceptualization is adequate to describe the observed breakthrough curve. Additional simulation work is warranted to determine if the single-porosity conceptualization is statistically better at describing the data.

For the Round 2 data set, both the single-rate and multirate simulations overestimate the slope of the rising limb and the peak concentration, and predict an earlier peak-arrival time than is observed in the data set (Figure S-12; MR1 sim and SR1 sim). The single-rate simulation estimates a similar peak-arrival time but a larger peak concentration than the multirate simulation. The portion after the peak is well represented by both simulations. The values estimated for the ½ MBL, advective porosity, and dispersivity are larger for the single-rate simulation when compared to the multirate simulation. The mass recovered at the end of the pumping period is overestimated by 5% and 8% for the multirate and single-rate simulations, respectively. The calculated Damkohler number for the single-rate simulation (0.0008) indicates the single-rate simulation could be conceptualized as a single-porosity system. Increasing the advective porosity to approximately 6% produces results for the single-porosity simulation (not plotted) that are visually identical to the single-rate simulation and the forward predictive simulation discussed below.

Due to the low injection rate for the Round 2 injection period, the G&G2 assumption (Equation S-2) may be questioned. The shape of the injection plume may not be a perfect circle about the injection well, but may have been affected by the fluid velocity created from the pumping of the withdrawal well causing it to have an oblong shape. Additional investigation into this is warranted. In addition, the low advective-porosity estimate obtained from the multirate simulation brings the G&G1 assumption (Equation S-1) into question. Similar to Round 1 above, for the analytic solution, the maximum distance of the injection fluid front is manually set to less than half the distance between the injection well and the pumping well.

The multirate simulation matches the Round 3 observed tracer-breakthrough curve fairly well (Figure S-13; MR1 sim). It overestimates the peak concentration and predicts a slightly earlier peak-arrival time. The portion after the peak concentration is very well matched by the multirate simulation. The single-rate simulation predicts more concentration being removed from the aquifer at early time, and a larger and earlier peak concentration than were observed in the data (Figure S-13; SR1 sim). The single-rate simulation underestimates the concentration of solute being removed from the aquifer at times after the peak concentration. It matches the tail of the observed breakthrough curve fairly well. The mass recovered at the end of Round 3 pumping is accurately represented with approximately 2% error for both simulations. The values obtained for the single-rate simulation for ½ MBL, advective porosity, and dispersivity are larger than those estimated for the multirate simulation (see Tables S-2 and S-3). The single-rate simulation has a calculated Damkohler number of 0.0007, which indicates that the rate of diffusion is negligible when compared to the rate of advection and, therefore, this simulation could be conceptualized as a single-porosity system. A single-porosity simulation was performed for this pathway with results that are visually and statistically the same as the single-rate simulation (results not plotted). The single-porosity simulation increased the advective porosity slightly to 6.25%. Additional simulation work on this pathway is warranted considering all three rounds of pumping for this pathway indicate that it could be conceptualized as a single-porosity system at these particular time and space scales. The iodide co-injection for Round 3 could not be accurately described by either the multirate or single-rate model (Figure S-14; MR1 sim and SR1 sim). Both of the simulations overestimate the slope of the rising

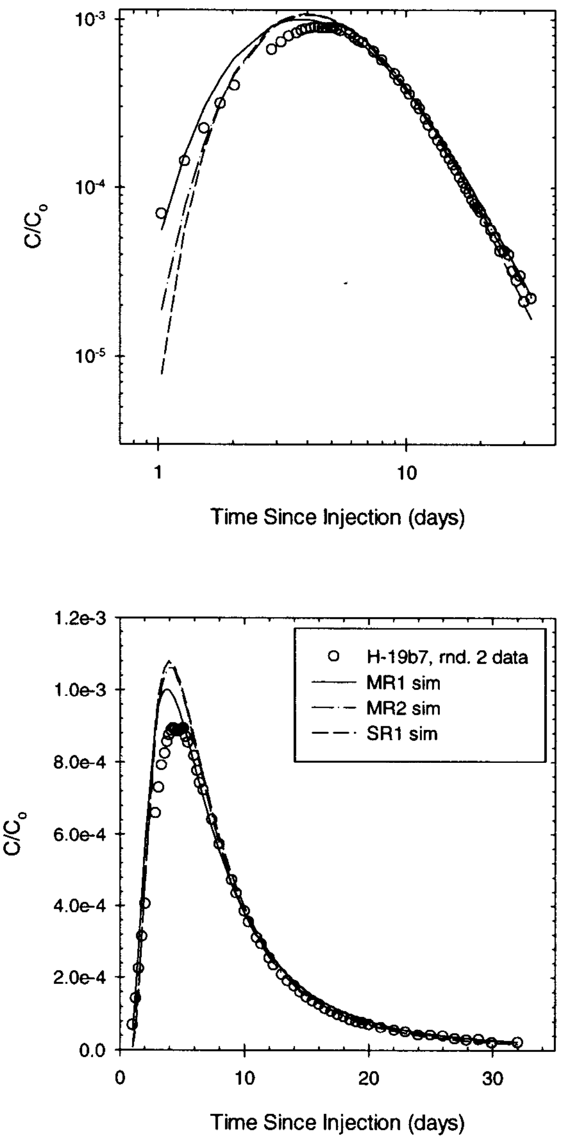

Figure S-12 **Single-rate and multirate diffusion transport model calibrations to the tracer-breakthrough curve for the H-19 hydropad, pathway H-19b7 to H-19b0, for Round 2 pumping rate, benzoic-acid tracer.**

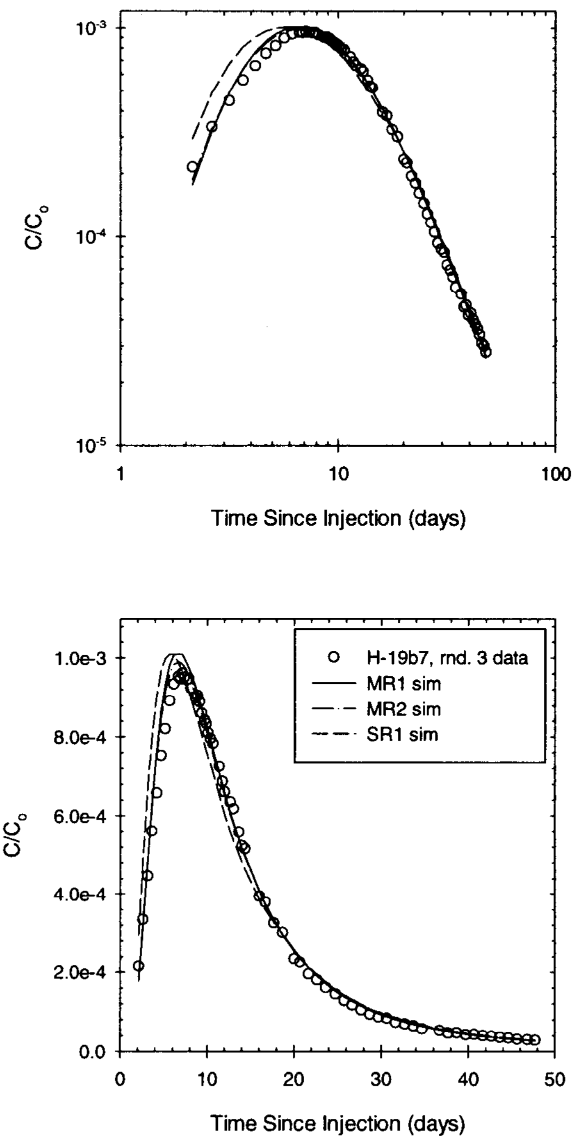

Figure S-13 **Single-rate and multirate diffusion transport model calibrations to the tracer-breakthrough curve for the H-19 hydropad, pathway H-19b7 to H-19b0, for Round 3 pumping rate, benzoic-acid tracer.**

limb, the peak concentration, and estimate an earlier peak-arrival time. This is similar to the benzoic-acid results above. These simulations also underestimate the concentration in the falling limb of the breakthrough curve. Similar to above, the estimated values for ½ MBL, advective porosity, and dispersivity are larger for the single-rate simulation (see Tables S-2 and S-3). The results presented above are directly comparable to the results obtained in Chapter 7. The RMSE value is lower for the simulations presented in this appendix than the results shown in Table 7-2 because the first data point was not used in the inversion (see Section 7.3).

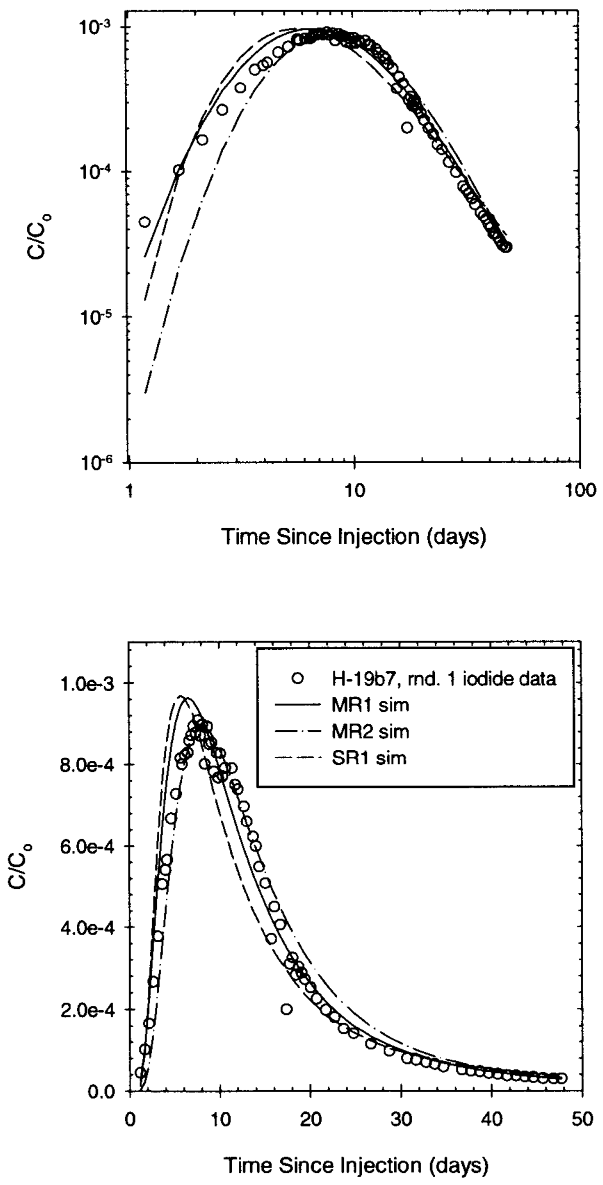

Figure S-14 Single-rate and multirate diffusion transport model calibrations to the tracer-breakthrough curve for the H-19 hydropad, pathway H-19b7 to H-19b0, for Round 3 pumping rate, iodide tracer.

An attempt to find a unique parameter set to describe all of the available data sets was made. Figure S-11; MR2 sim, Figure S-12; MR2 sim, Figure S-13; MR2 sim, and S-14; MR2 sim show the results of finding a unique parameter set to satisfy all of the observed breakthrough curves. The forward, predictive models adequately represent the observed data. For all three rounds of the benzoic-acid data sets, the simulated peak concentrations are larger than those observed. The peak-arrival time is generally fairly well matched to the data. In all but the Round 1 data set, the portion after the peak concentration is very well matched. For the Round 1 data, the general trend of the data is matched, but the simulation underestimates the concentration of solute being removed from the aquifer. For the iodide data set, the rising limb of the data is not well matched. The peak concentration and peak-arrival time are better matched than the best-fit results presented above. Through additional trial and error on the predictive modeling, a more acceptable parameter set able to satisfy all of the available data sets might be found. More than one unique parameter set could likely be found that would be able to describe the data.

Simulation of transport along the H-19b7 to H-19b0 pathway would probably benefit from additional effort. The model calibration for these different pumping rates might be improved upon, and a more suitable parameter set for the predictive simulations might be determined. This may not be the case, however, because the G&G assumptions are called into question in Rounds 1 and 2.

S.5.2 H-11 Hydropad

The MWCF tracer tests at the H-11 hydropad in 1996 had two injection phases: Round 1 injection at a low pumping rate (0.22 L/s); and Round 2 at a high pumping rate (0.38 L/s). Tables 3-2 and 3-3 present the details of the injection phases. For the 1988 tests, three wells were used for injection, with H-11b1 as the pumping well. The 1996 tracer tests utilized paths H-11b2 to H-11b1 and H-11b3 to H-11b1. Because pathway H-11b4 to H-11b1 had a poor tracer resolution and late peak arrival during the 1988 test (see Appendix C), it was not utilized in the 1996 test series. At the H-11 hydropad, tracers were injected over the full Culebra interval only. An injection solution containing both a benzoic acid and iodide was injected in pathway H-11b3 to H-11b1 for the Round 2 injection phase. The 1996 MWCF tracer tests were terminated earlier than planned due to equipment problems.

S.5.2.1 H-11b2 to H-11b1 Pathway

Three tracer test data sets are available for the 21.5-m pathway between the injection well, H-11b2, and the pumping well, H-11b1. All three data sets show a relatively rapid rise to the peak concentration and a broad peak. The 1988 data set shows a long, slowly declining tail in the tracer-breakthrough curve. The more recent data sets do not exhibit a significant tail portion after the peak concentration due to the experiments being terminated earlier than planned. The early termination of these experiments also resulted in a low mass recovery for both Rounds 1 and 2. The pumping rates in 1988 and for 1996 Round 2 were nearly identical, and the pumping duration in 1988 was approximately twice as long as for the later tracer tests.

For the 1988 tracer test, the multirate and single-rate simulations are similar in their ability to match the rising limb of the observed tracer-breakthrough curve (Figure S-15; MR2 sim and SR1 sim). The peak concentration is slightly overestimated by the single-rate simulation and is overestimated, but by a smaller degree, by the multirate simulation. The peak-arrival time is slightly earlier for both simulations compared to the observed data. The concentration in the tail of the breakthrough curve is overestimated by the single-rate simulation with more solute being removed from the aquifer than was observed. The multirate simulation adequately matches the falling limb and tail of the observed data. For the multirate model, the first series of calibration attempts obtained a dispersivity value that we think is unrealistically large at greater than 50% of the travel distance between wells (see Table S-2). Several calibration attempts were unable to obtain a "reasonable" dispersivity value.

We attempted another multirate calibration by fixing the dispersivity at 20% of the distance between the wells and varying only three parameters. The best-fit simulation that could be obtained had a peak concentration that is much greater than observed in the data (Figure S-15; MR1 sim). It is similar in its ability to match the portion after the peak concentration to the single-rate simulation. The single-rate simulation did not have the problem of an extremely high estimated dispersivity.

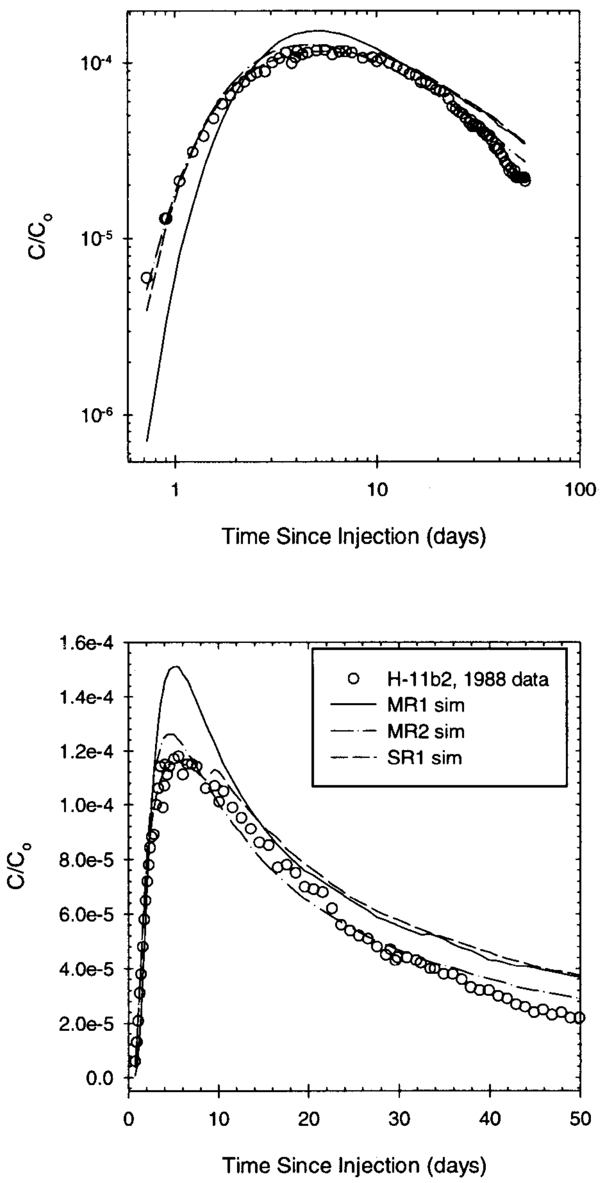

Figure S-15 Single-rate and multirate diffusion transport model calibrations to the tracer-breakthrough curve for the H-11 hydropad, pathway H-11b2 to H-11b1, for 1988 tracer test, benzoic-acid tracer.

The calibration for the single-rate simulation obtained a dispersivity that is approximately 23% of the travel distance. Both simulations obtained a similar advective porosity, while the ½ MBL is larger for the single-rate simulation (see Tables S-2 and S-3). The mass recovery is overestimated by 10% for the single-rate simulation and is slightly higher for the multirate simulation.

For the Round 1 pumping rate during the 1996 test series at the H-11 hydropad, the multirate simulation is able to match all portions and falls entirely within the 95% confidence interval of the observed data (Figure S-16; MR2 sim). The estimated dispersivity value for this simulation is again approximately half the travel distance between the injection well and the pumping well, similar to the case of the 1988 simulation attempt above. No parameter set with a "reasonable" dispersivity value could be found that could match the observed data. As was done with the calibration above, the dispersivity value was fixed at 20% of the distance between the injection well and the pumping well. After fixing the dispersivity value, the single-rate and multirate simulations are visually very similar to each other, and clearly not as good as the multirate simulation with the high dispersivity (Figure S-16; MR1 sim and SR1 sim). The single-rate model conservatively estimated the dispersivity at approximately 10% of the travel distance between wells. The mass recovery for the observed data set is very poor, with less than 25% of the injected mass recovered by the end of the tracer test.

For the Round 2 pumping rate during the 1996 test series at the H-11 hydropad, the multirate simulation matches the rising limb of the observed data (Figure S-17; MR2 sim). The peak concentration is slightly overestimated as are all portions of the data set after the peak concentration. As was observed in the 1988 and 1996 Round 1 tracer-test calibrations, the multirate simulation estimates an unreasonably high dispersivity value (see Table S-2). Consequently, the dispersivity was fixed at 20% of the travel distance between the injection and pumping wells. Following the adjustment of the dispersivity value, the single-rate simulation and the multirate simulation obtain very similar results visually that appear slightly better than the multirate simulation with the high dispersivity (Figure S-17; MR1 sim and SR1 sim). However, very little falling-limb data were collected, and none of the simulations are considered definitive. The single-rate simulation predicts a larger advective porosity and ½ MBL when compared to the multirate simulation.

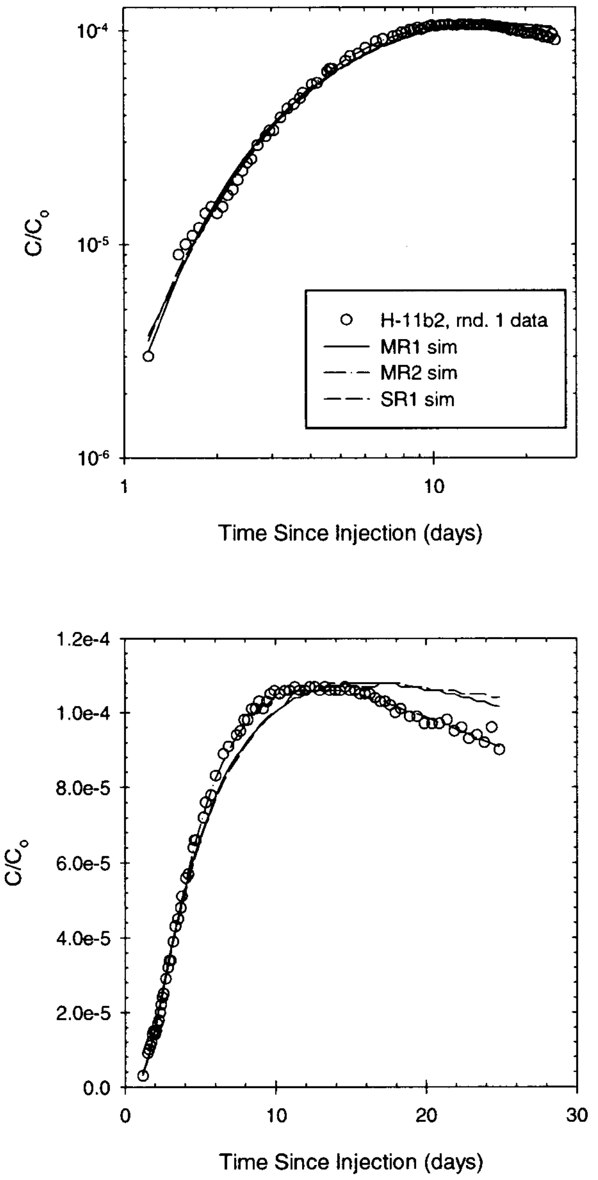

Figure S-16 Single-rate and multirate diffusion transport model calibrations to the tracer-breakthrough curve for the H-11 hydropad, pathway H-11b2 to H-11b1, for Round 1 pumping rate, benzoic-acid tracer.

Additional calibration attention is warranted for the H-11b2 to H-11b1 pathway. Good multirate simulations of the 1988 and 1996 Round 1 data could only be obtained using high values of dispersivity. These high values may reflect significant heterogeneity in permeability that is not represented in the model. The high inferred values

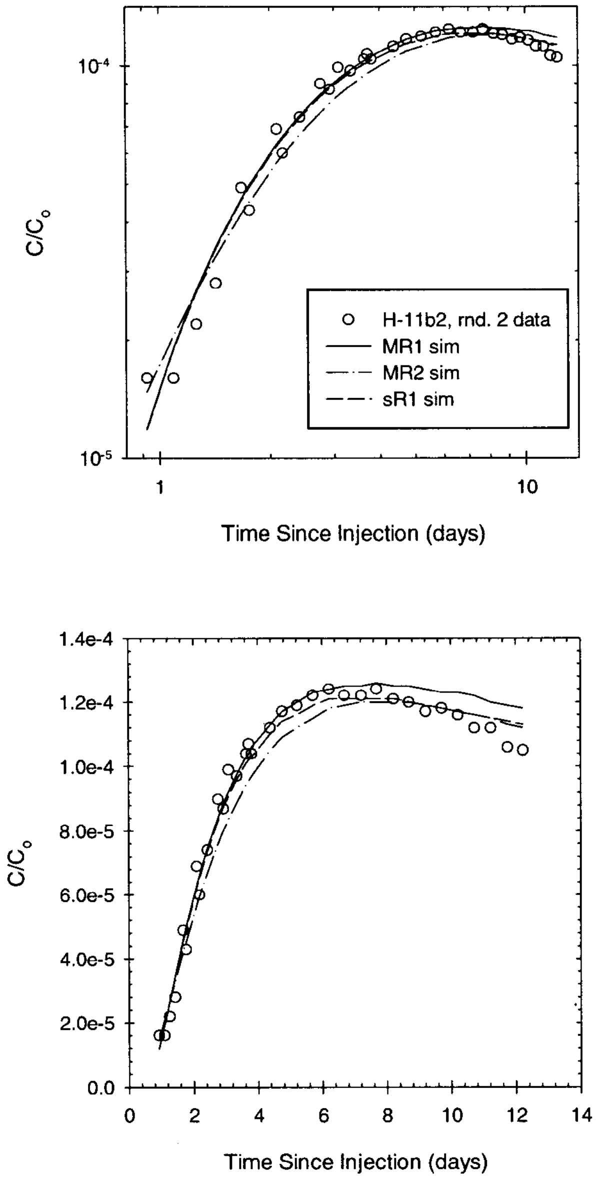

Figure S-17 Single-rate and multirate diffusion transport model calibrations to the tracer-breakthrough curve for the H-11 hydropad, pathway H-11b2 to H-11b1, for Round 2 pumping rate, benzoic-acid tracer.

for dispersivity may also be related in some way to the poor connection between H-11b2 and the Culebra noted in Appendix E. Given the uncertainty in the causes of the apparent high dispersivity, we do not know how much confidence to place in the other parameter values estimated by the model. Overall, the quality of the data from this pathway is poor to marginal, which may contribute to our difficulty in calibrating the model to the observed data.

S.5.2.2 H-11b3 to H-11b1 Pathway

Four tracer tests were analyzed for the 20.9-m H-11b3 to H-11b1 pathway. The available data sets include the 1988 and 1996 tracer tests. The 1996 Round 2 test of this pathway included a co-injection of benzoic acid and iodide. All of the breakthrough curves examined exhibit a similar sharp rise to the peak concentration, a narrow peak width in comparison to those from the H-19 hydropad, and an extended tail after the peak. Additionally, for all the model calibrations conducted for this pathway, the single-rate simulation is able to match the observed breakthrough curve almost as well as the multirate simulation (Figures S-18 through S-21), based on the RMSE value and visual inspection. In most cases, the simulations are nearly identical. All of the simulations, whether single-rate or multirate, underestimate the peak concentration, but are very accurate at predicting the peak-arrival time. The mass recoveries for all of the simulations are accurately represented with less than 5% as the maximum difference between the simulations and the observed data sets.

Without exception, the single-rate simulations predicted a larger ½ MBL, advective porosity, and dispersivity when compared to the multirate simulations. All of the multirate simulations obtained a large dispersivity value of between 15% and 20% of the total travel distance while the single-rate simulations obtained much higher dispersivities of between 25% and 30% of the travel distance between the injection well and the pumping well. We are uncertain why all of the single-rate simulations predicted such high dispersivity values. The multirate simulations presented in Chapter 7 for the lower pumping rate data have a larger RMSE than presented in this appendix, but the estimated dispersivity is smaller. These results highlight the fact that the model fits to the observed data are non-unique.

Additional simulation effort is warranted to try to determine if a different parameter set with a lower dispersivity value exists for the single-rate interpretation. Efforts to calibrate both models using a

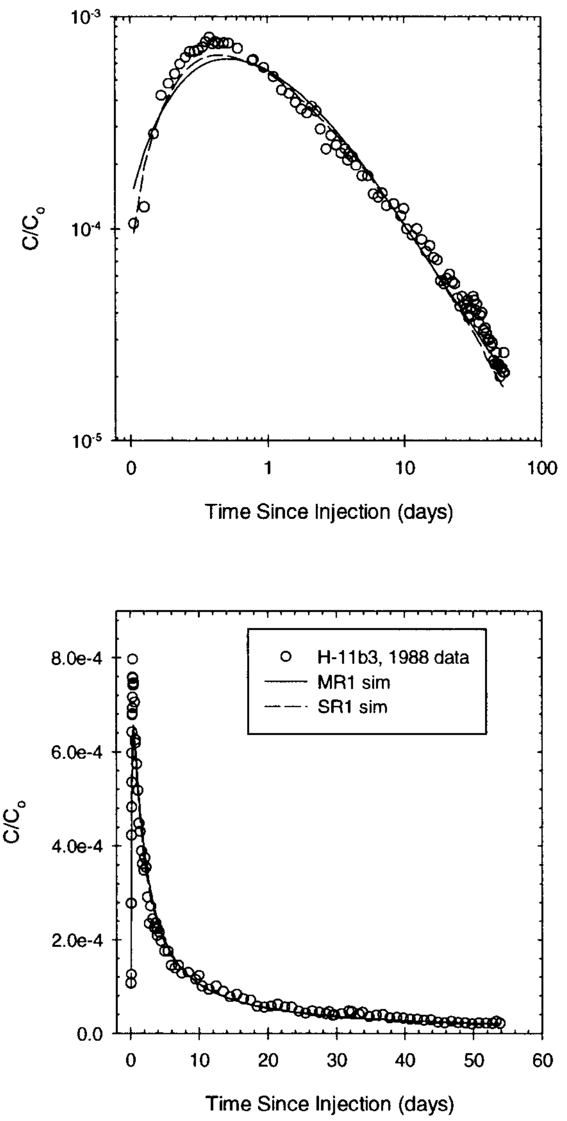

Figure S-18 Single-rate and multirate diffusion transport model calibrations to the tracer-breakthrough curve for the H-11 hydropad, pathway H-11b3 to H-11b1, for 1988 tracer test, benzoic-acid tracer

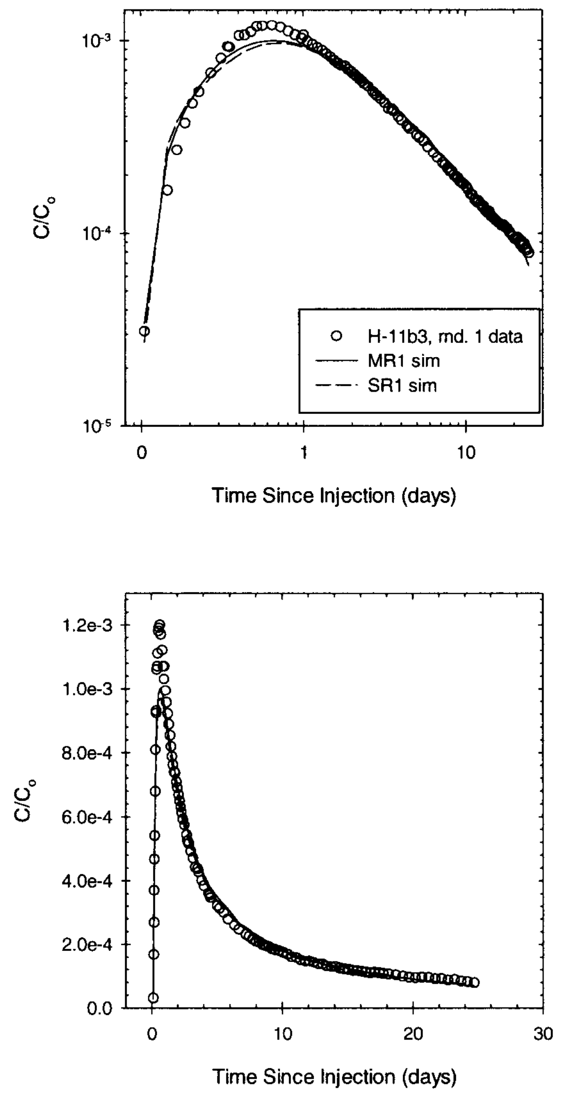

Figure S-19 Single-rate and multirate diffusion transport model calibrations to the tracer-breakthrough curve for the H-11 hydropad, pathway H-11b3 to H-11b1, for Round 1 pumping rate, benzoic-acid tracer.

fixed dispersivity value (10% of the travel distance) while allowing the other parameters to vary were unsuccessful. In all cases where the dispersivity was fixed at 10%, the concentration in the falling limb was overestimated to a large degree. Additionally, the models that used a fixed dispersivity overestimated the mass recovery by several percent. Fixing the dispersivity at different values (between 1% and 20%) and calibrating the models might be investigated in the future. Trying to match the peak concentrations more accurately, while still matching the peak-arrival time, is also warranted.

S.5.3 H-3 Hydropad

One MWCF tracer test with injections into H-3b1 and H-3b2 while pumping H-3b3 was conducted at the H-3 hydropad (Appendix F). Figure 2-2 shows the layout of the injection and pumping wells for this hydropad. The path from injection

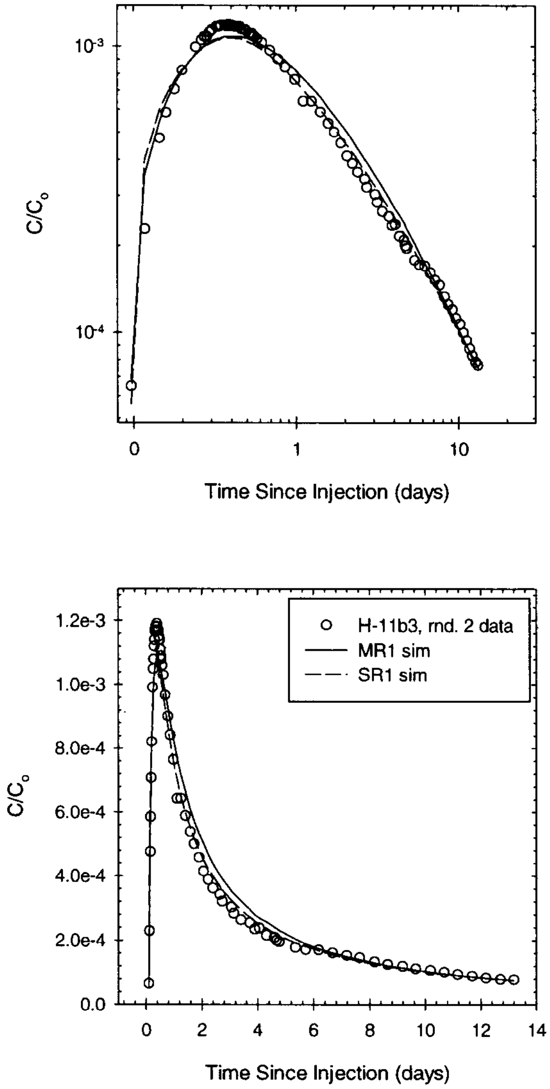

Figure S-20 Single-rate and multirate diffusion transport model calibrations to the tracer-breakthrough curve for the H-11 hydropad, pathway H-11b2 to H-11b1, for Round 2 pumping rate, benzoic-acid tracer.

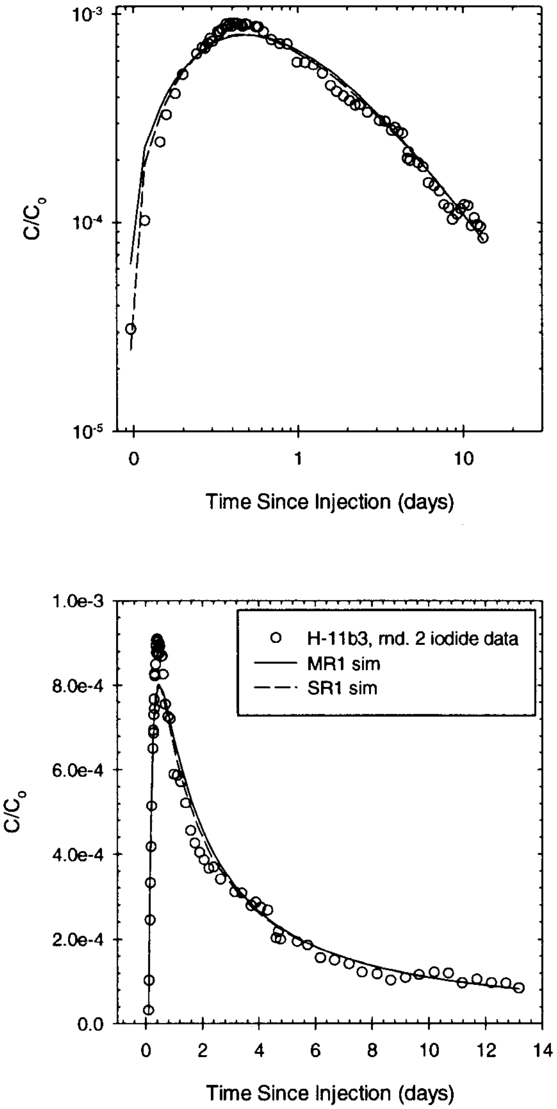

Figure S-21 Single-rate and multirate diffusion transport model calibrations to the tracer-breakthrough curve for the H-11 hydropad, pathway H-11b2 to H-11b1, for Round 2 pumping rate, iodide tracer.

well H-3b2 to pumping well H-3b3 shows a very poor data set with no defined peak concentration or tail. This tracer test achieved a mass recovery of less than 20% at the end of pumping and is omitted from the following discussion. An attempt to find a unique parameter set to predict the observed data might be tried in future investigations.

The 30.66-m pathway from H-3b1 to H-3b3 is the longest path we investigated using STAMMT-R. The multirate simulation is slightly better at matching the observed breakthrough curve than the single-rate simulation (Figure S-22; MR1 sim SR1 sim). Both simulations underestimate the slope of the rising limb of the observed breakthrough curve. The peak concentration is fairly well matched by both simulations, but peak-arrival

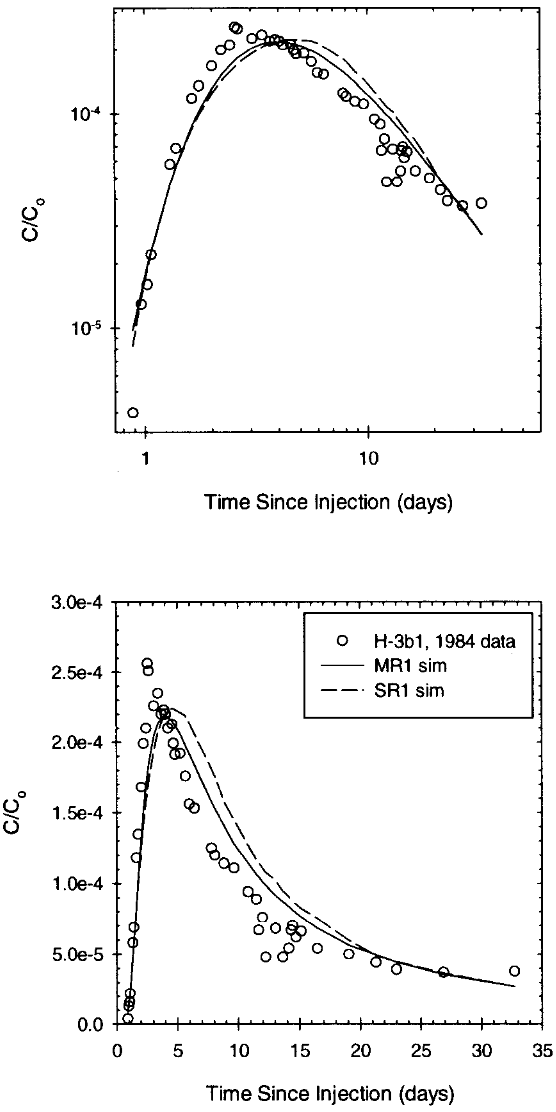

Figure S-22 Single-rate and multirate diffusion transport model calibrations to the tracer-breakthrough curve for the H-3 hydropad, pathway H-3b1 to H-3b3, for 1984 tracer test, benzoic-acid tracer.

time occurs later than is observed in the data set. The concentrations following the peak are overestimated by both simulations, but to a larger degree with the single-rate simulation. The estimated ½ MBL is larger for the single-rate simulation, but the advective porosity and dispersivity values obtained for the different models are very similar (see Tables S-2 and S-3). The mass recovered at the end of the tracer test is more accurately represented by the multirate simulation. The calculated Damkohler number for the single-rate simulation above is 0.0064, indicating this simulation could be conceptualized as a single-porosity system (rate of diffusion is negligible compared to the rate of advection). A single-porosity simulation was investigated for this pathway with poor results. Increasing the advective porosity of the single-porosity simulation did not greatly improve the visual fit to the observed data (results not plotted). Additional simulation work is warranted to determine if a different unique parameter set (i.e., different dispersivity, advective porosity) can be found that can accurately describe the observed breakthrough and mass-recovery curves.

S.5.4 H-6 Hydropad

Several MWCF tracer tests were performed at the H-6 hydropad (see Appendix F). For the reasons outlined in Appendix F, we analyze only a portion of the data from these tracer tests with the multirate-diffusion model. The pumping well for this hydropad is labeled H-6c. Data that are analyzed include pathways H-6a to H-6c for test #1 and H-6b to H-6c for tests #1 and #2. The paths from injection wells H-6a and H-6b to H-6c are also among the longest of all of the paths analyzed in this report, at just less than 30 m each.

S.5.4.1 H-6a to H-6c Pathway (test #1)

The tracer data for H-6a to H-6c show a large amount of data scatter, a poorly defined peak concentration and arrival time, and no developed tail following the peak. Because of these conditions, we are not surprised that both the multirate and single-rate diffusion simulations are able to describe the observed data equally well (Figure S-23; MR1 sim and SR1 sim). Very large dispersivity values of 28% and 40% of the distance between the injection well and pumping well are estimated for the single-rate and multirate simulations, respectively. Efforts to find an acceptable parameter set that fit the data with a dispersivity value of less than 20% were unsuccessful. Figure S-23; MR2 sim shows the results of a multirate simulation that obtained an acceptable dispersivity value, but the visual fit of the simulation to the observed data is

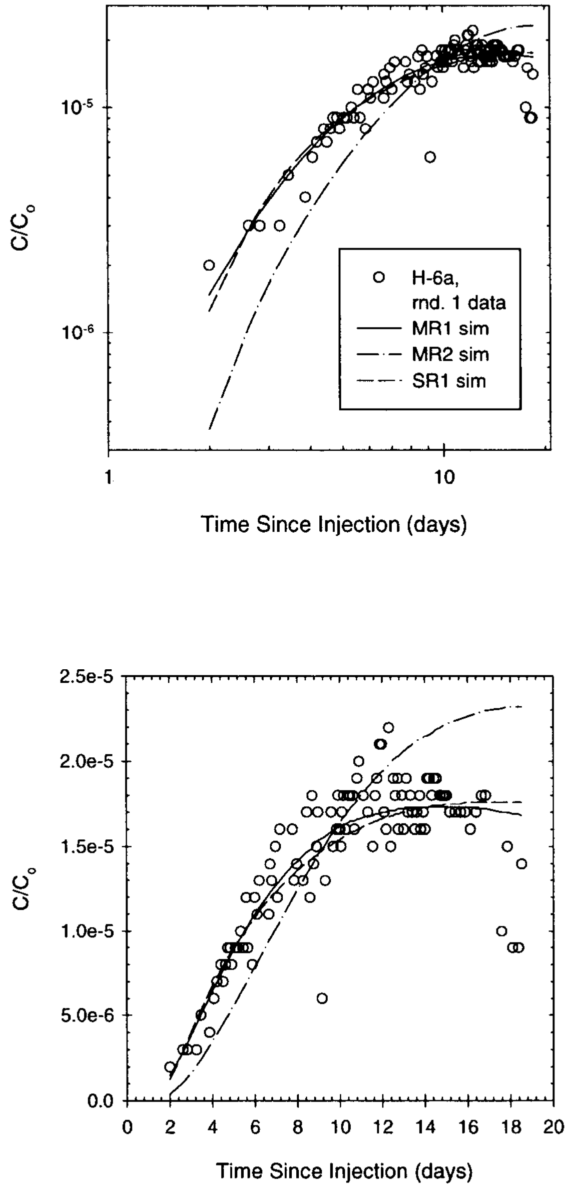

Figure S-23 Single-rate and multirate diffusion transport model calibrations to the tracer-breakthrough curve for the H-6 hydropad, pathway H-6a to H-6c, for 1981 tracer test, Round 1 pumping rate, benzoic-acid tracer.

very poor. Similar advective porosities are estimated with both simulations (see Tables S-2 and S-3) and the mass recovery of approximately 20% at the conclusion of the test is well represented by both simulations.

S.5.4.2 H-6b to H-6c Pathway (tests #1 and #2)

The H-6b to H-6c pathway was used for two tests. These tests had the same pumping rate at the withdrawal well, while the tracer-injection rate for test #1 was greater than the injection rate for test #2. Both of the data sets have only a few data points on the rising limb, a nicely defined peak concentration and arrival time, and an extended tail.

The test #1 tracer data for this pathway are adequately estimated by both the single-rate and multirate-diffusion simulations (Figure S-24; MR1 and SR1 sim). Both simulations match the rising limb and the time of peak arrival fairly well. The single-rate simulation matches the peak concentration more accurately than the multirate simulation. The falling limb is more closely matched by the multirate simulation. Both simulations match the tail very accurately. The parameters obtained for both simulations are very similar, with the exception of the ½ MBL, which is larger for the single-rate simulation. The multirate simulation estimates a very small sigma value, indicating a very narrow diffusion-rate distribution, which essentially reduces the multirate model to a single-rate model (see Table S-2). The dispersivities for both simulations are estimated between 14% and 17% of the travel distance, with the single-rate simulation having the lower value. Both of the simulations accurately represent the mass recovered at the end of the pumping period with only a few percent error.

The multirate simulation is able to match the observed breakthrough curves for test #2 better than the single-rate simulation (Figure S-25; MR1 and SR1 sim). Both simulations match the rising limb of the observed data reasonably well, but the multirate simulation is more accurate in its prediction of the peak concentration and arrival time than the single-rate simulation. Both simulations overestimate the concentration in the early portion of the falling limb, particularly the single-rate simulation. The tail of the observed data is accurately represented by both models. In the same fashion as test #1, the estimated values for advective porosity and dispersivity are very similar for both

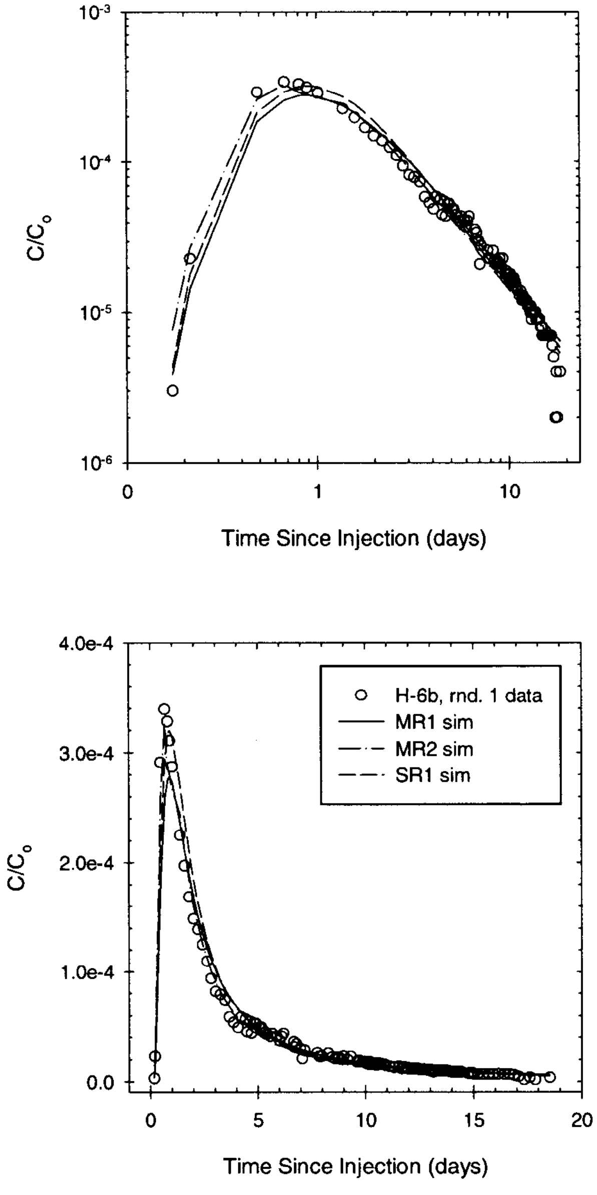

Figure S-24 Single-rate and multirate diffusion transport model calibrations to the tracer-breakthrough curve for the H-6 hydropad, pathway H-6b to H-6c, for 1981 tracer test, Round 1 pumping rate, benzoic-acid tracer.

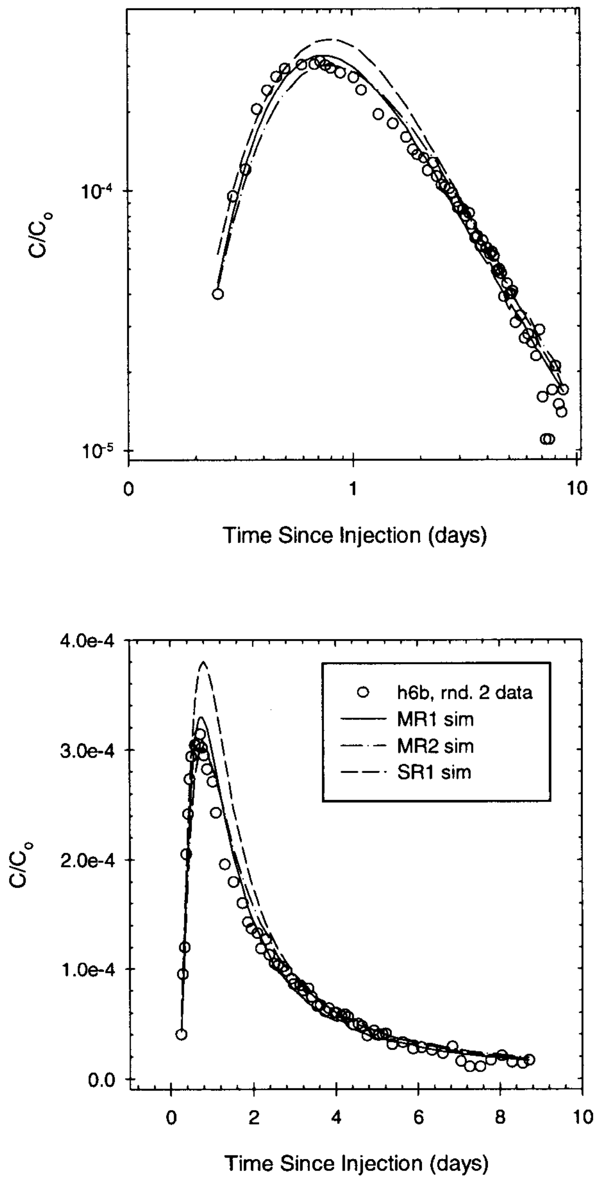

Figure S-25 Single-rate and multirate diffusion transport model calibrations to the tracer-breakthrough curve for the H-6 hydropad, pathway H-6b to H-6c, for 1981 tracer test, Round 2 pumping rate, benzoic-acid tracer.

simulations. The single-rate simulation obtained a ½ MBL larger than that from the multirate simulation. These parameter estimates are very similar to the values obtained for the test #1 data (see Tables S-2 and S-3). Additionally, the multirate simulation obtained a very low value for sigma, the spread about the diffusion coefficient. The mass recovery is overestimated by approximately 10% for the single-rate simulation, but is very accurately represented by the multirate simulation.

The calculated Damkohler numbers for both of the single-rate simulations above are below the 0.01 cutoff. This indicates the rate of diffusion is negligible compared to the rate of advection. Single-porosity simulations have been attempted for this pathway with limited success. The single-porosity simulations do not adequately describe the observed breakthrough curves regardless of increasing the advective porosity (results not plotted). Additional simulation work is required to determine if a different parameter for a single-porosity conceptualization set is able to match the observed breakthrough curves obtained for this pathway.

Attempts at finding a unique parameter set to satisfy both data sets for the multirate model for H-6b have been made (Figure S-24; MR2 sim and Figure S-25; MR2 sim). Both of the forward simulations match the peak concentration and the peak-arrival time. The falling limb and the tail of the observed breakthrough curves are well represented by the forward simulations. The parameters used for these forward simulation are presented in Table S-2.

S.6 Discussion

The observed tracer-breakthrough curves from numerous tracer injections conducted at the H-3, H-6, H-11, and H-19 hydropads are interpreted using both conventional (single-rate) and multirate double-porosity mass-transfer models. Shown in Figures S-1 through S-25 are the results of the single-rate and multirate interpretations. Tables S-2 and S-3 contain the values of the best-fit parameters from the multirate and single-rate model calibrations, respectively, as well as the unique parameter sets used in the predictive simulations. In the case of pathway H-19b3 to H-19b0, the results for the adjusted injection concentration are also reported in the table. Table S-4 and S-5 contains the estimated 95% confidence intervals for the values shown in Tables S-2 and S-3.

For a majority of the tracer data examined, the multirate model is superior to the single-rate model in matching the observed tracer-breakthrough curves. This is the case over a wide range of pathway lengths, ranging from 11.0 to 30.7 m. In the few cases in which the single-rate simulations have lower RMSE's than the multirate simulations (Tables S-2 and S-3), the differences between the simulations appear visually insignificant. In general, the differences between the multirate simulations and the single-rate simulations are slight when the σ_d values inferred from the multirate simulations are less than approximately 1.4. This type of similarity is expected, as the multirate model becomes a single-rate model as σ_d goes to zero. The inferred mean diffusion-rate coefficients are always significantly higher for the multirate simulations than for the single-rate simulations, except for the H-19b3 to H-19b0 pathway, but this is due, in part, to the different matrix-geometry assumptions of the single-rate and multirate models. The multirate model assumes a layered geometry when solving the diffusion equation while the single-rate model assumes a spherical geometry. When comparing the ½ MBL value obtained from a multirate model with a ½ MBL obtained from a single-rate model, the multirate ½ MBL must be multiplied by $\sqrt{5}$. When the ½ MBL for the multirate model is converted in this fashion, the results obtained for the ½ MBL for both the single-rate and multirate models generally agree within 40% of each other and the mean diffusion-rate coefficients are similar.

In most cases, the single-rate model obtained estimated advective porosities and dispersivities that are larger than those estimated by the multirate model. For the H-19b3 to H-19b0 pathway, the single-rate model estimated lower ½ MBLs and advective porosities than the multirate model. The single-rate model also estimated lower advective porosities for the H-11b2 to H-11b1 pathway than the multirate model. The multirate and single-rate models estimated essentially identical advective porosities for the pathways from H-19b5 to H-19b0, H-6a to H-6c, and H-6b to H-6c.

For the pathways evaluated at the H-11 hydropad, the estimated dispersivity values are typically greater than 15% of the travel distances between the injection and withdrawal wells. For pathway H-11b2 to H-11b1, the estimated dispersivities are greater than 20% of the travel distance and the observed tracer-breakthrough curves could not be adequately fit with a lower dispersivity value. At the H-19 hydropad, the estimated dispersivities are generally less than 10% of the travel distances between the wells. This may indicate a larger degree of heterogeneity in transmissivity at the H-11 hydropad.

We attempted to determine unique parameter sets for both the multirate and single-rate models to predict multiple tracer tests along several pathways. Our attempts with the multirate model were fairly successful for four different transport pathways. Four different tracer-test data sets were used for two of the pathways, H-19b3 to H-19b0 and H-19b7 to H-19b0, for this effort. The four data sets consisted of three different pumping rates and one tracer with a different aqueous diffusion coefficient. The third pathway, H-19b6 to H-19b0, used two tracer data sets with different pumping rates. The fourth pathway, H-6b to H-6c, used two tracer data sets with different injection rates but the same pumping rate. The unique parameter sets able to match multiple tests along individual pathways simultaneously are similar to the parameter sets determined from the best-fit matches to the individual tests. No unique parameter sets could be found using the single-rate model that could predict different tracer-breakthrough curves along the same pathways with different pumping rates.

As discussed in Chapter 6, the distribution of diffusion-rate coefficients is particularly sensitive to late-time data. Many of the data sets examined have poorly developed breakthrough-curve tails. This may contribute to the ability of the single-rate model to describe a large portion of the observed breakthrough curves accurately. Accurate estimation of the range of diffusion coefficients for the multirate model relies on accurate concentration data in the tail of the test where the effects of matrix diffusion are dominant over the dispersion of the system.

The cumulative diffusive porosities as functions of the diffusion-rate coefficients as determined from parameter estimation using the multirate interpretations are shown in Figures S-26 and S-27 for the H-19 and H-11 hydropads, respectively. Examination of the figures shows that the estimated distributions of diffusion-rate coefficients are similar for almost all of the flow paths at each individual hydropad, regardless of the pumping rate. At hydropad H-19, pathway H-19b5 to H-19b0 does not follow the observed trend of the rest of the paths at the hydropad, regardless of the pumping rate during the data collection. The estimated distribution of diffusion-rate coefficients is very small for this pathway, indicating the single-rate model could effectively substitute for the multirate model. Additional investigation into why this pathway yields a significantly different diffusion-rate distribution is warranted.

Comparison of Figures S-26 and S-27 reveals the estimated distributions for the H-11 and H-19 hydropads differ significantly. The range of diffusion-rate coefficients is much smaller for the H-11 hydropad than for the H-19 hydropad. Similar results were obtained from the SWIW tests (Chapter 6). The estimated diffusion-rate distribution at the H-3 hydropad (Figure S-28) is similar to those inferred for the H-11 hydropad. The estimated diffusion-rate distributions at the H-6 hydropad (Figure S-28) are extremely narrow, similar to those inferred along the pathway from H-19b5 to H-19b0 (Figure S-26), suggesting a single-rate model should be able to simulate the data accurately.

As discussed in Section 6.4.2, the smaller range in diffusion-rate coefficients at H-11 compared to H-19 is attributed to advective transport being channeled along well-connected fractures that form comparatively direct flow paths between the H-11 wells, whereas advective transport at H-19 occurs in interparticle porosity and vugs in addition to fractures. The diffusion-rate distribution inferred from the H-3 data suggests direct fracture connections between wells similar to those at H-11. The extremely narrow diffusion-rate distributions inferred from the H-6 data might be attributed to flow being concentrated in fewer fracture pathways, allowing less matrix heterogeneity to be encountered, than at H-3 or H-11. They may also be related to the higher pumping rate, and consequent faster tracer recovery, at H-6 allowing less time for diffusion to occur. The capacity coefficients inferred from the H-6 data are smaller than for any other hydropad, which may also reflect limited time for diffusion into the matrix porosity.

The Damkohler limits of 0.01 and 100 can be applied to the lognormal distributions to determine what portions of the distributions can actually be resolved during the tracer tests. As discussed in Section 7.2, a Damkohler number less than or equal to 0.01 reflects negligible diffusion relative to advection (i.e., a single-porosity model) and a

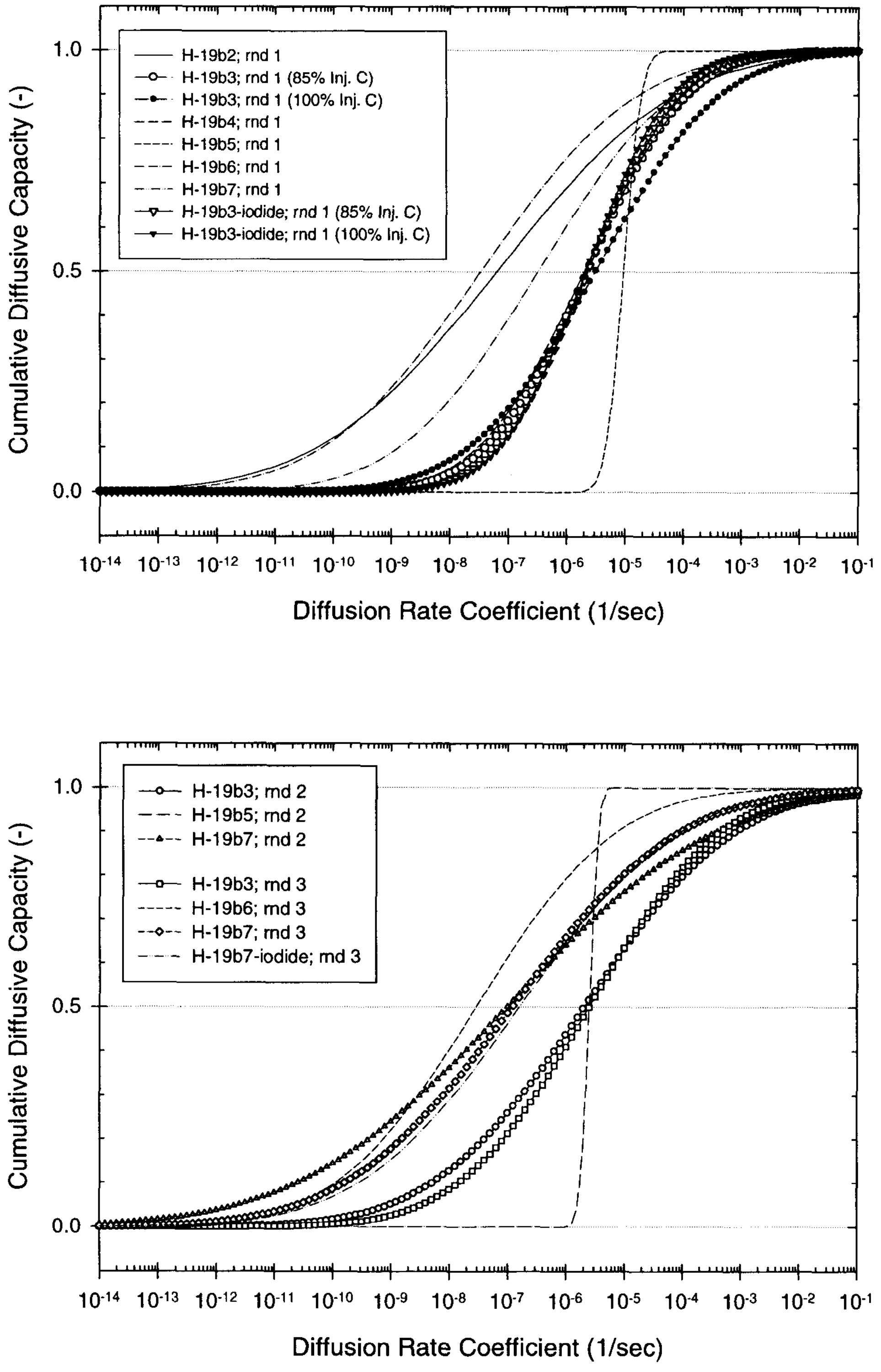

Figure S-26 Cumulative distribution of diffusion rate coefficients for tracer tests analyzed from the H-19 hydropad.

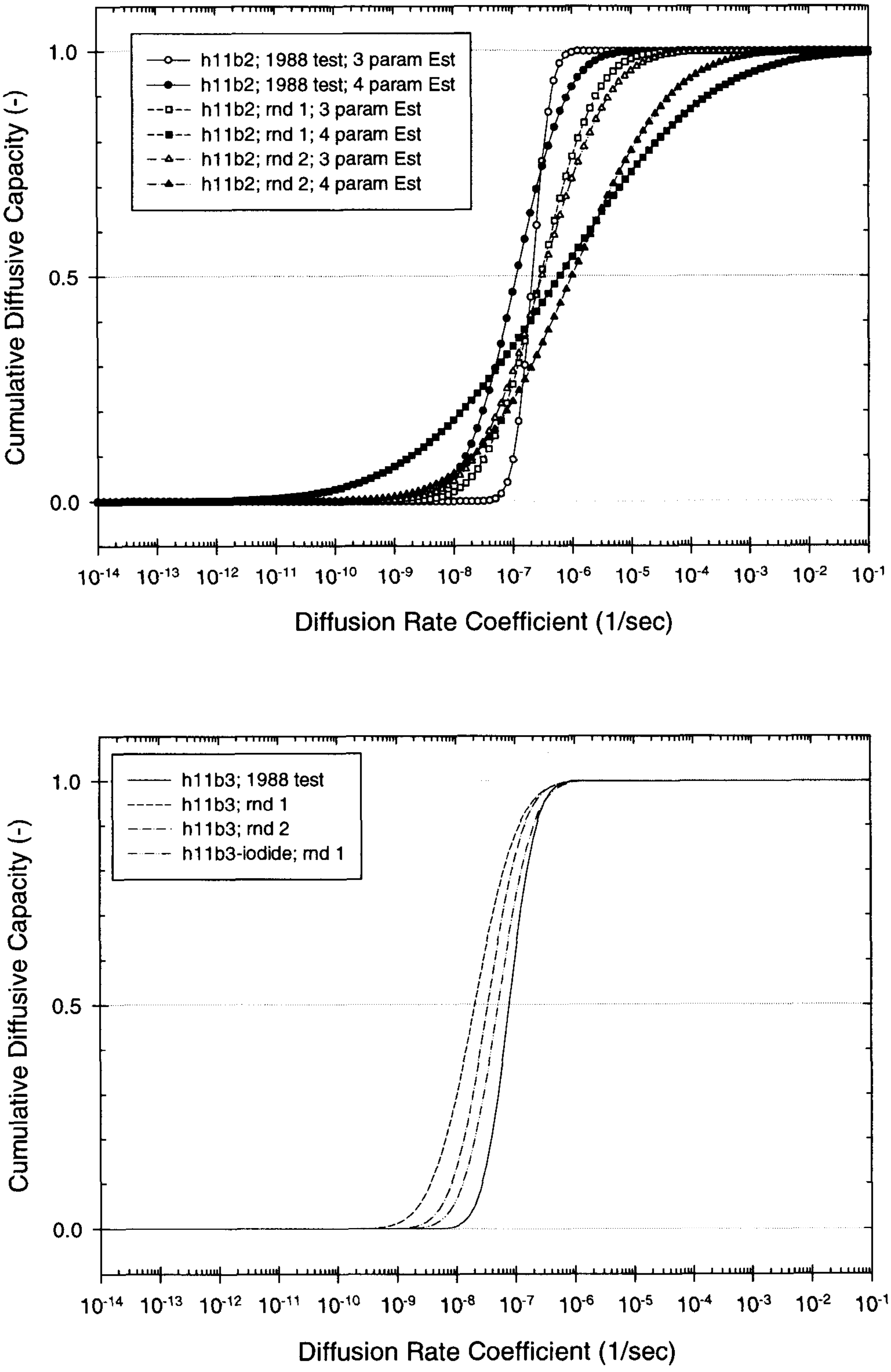

Figure S-27 **Cumulative distribution of diffusion rate coefficients for tracer tests analyzed from the H-11 hydropad.**

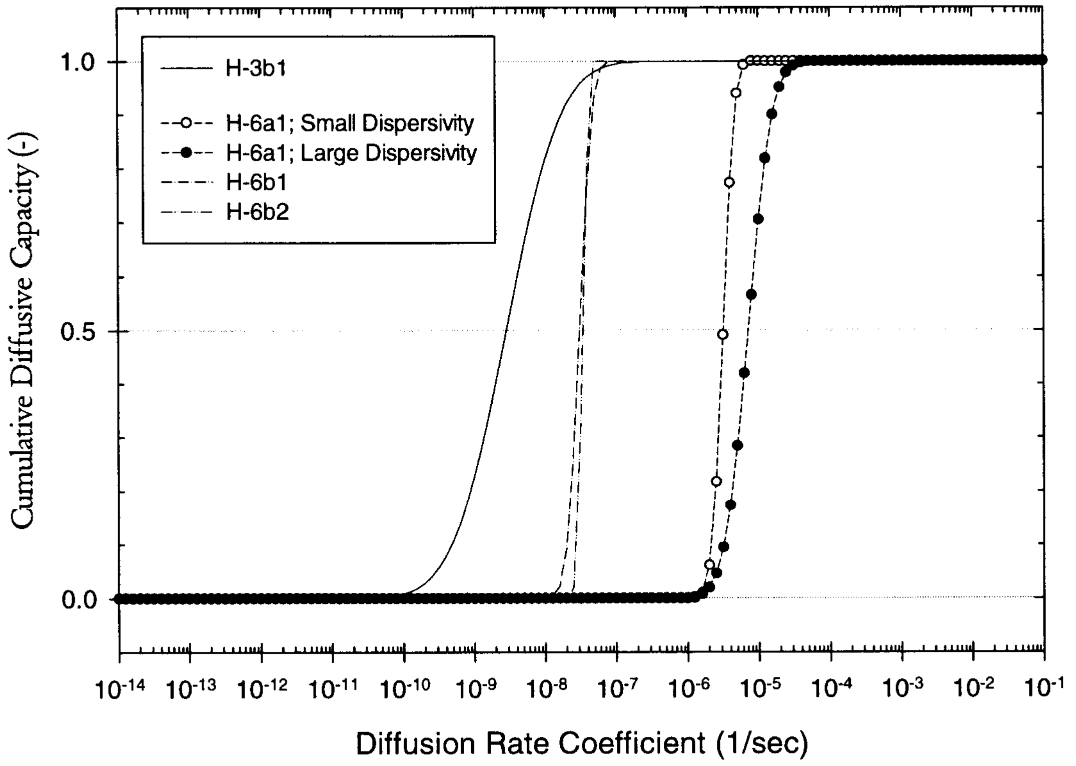

Figure S-28 Cumulative distribution of diffusion rate coefficients for tracer tests analyzed from the H-3 and H-6 hydropads.

value greater than or equal to 100 reflects instantaneous diffusion relative to advection (i.e., local equilibrium assumption). In general, the portion of the distribution of diffusion-rate coefficients able to be observed, over the time period of the tracer tests, is smaller for the H-19 hydropad than for the other hydropads. Approximately 50% to 85% of the diffusion-rate distributions obtained from the H-19 interpretations fall between the Damkohler limits of 0.01 and 100. In contrast, the portions of the diffusion-rate coefficients falling between the Damkohler limits for the remaining hydropads are between 75% and 99%.

Using the calculated Damkohler limits information, the ½ MBLs that the tracer tests were able to observe can be determined. As discussed above, the consistency of the estimated, lognormal distributions of mass-transfer rates can be checked by determining the estimated range of ½ MBLs (Equation S-3). Using the values of tortuosity and aqueous diffusion coefficient in Table S-1, these tests were able to image, within the Damkohler limits of 0.01 and 100, a range of ½ MBLs. Table S-6 and S-7 presents the values of ½ MBL that the multirate model was able to observe. Three values are presented on the table, the first is the ½ MBL at a Damkohler number of 0.01, the second value is the ½ MBL calculated using the estimated μ_d value (called Median ½ MBL on table), and the third value is the ½ MBL at a Damkohler number of 100. The single-rate version of this table presents only the ½ MBL calculated from the estimated mu value. In only one case discussed above, path H-19b2 to H-19b0, was the calculated Damkohler number for the single-rate ½ MBL not within the limits of 0.01 and 100. In this specific case, a value below 0.01 indicates that the tracer test can be imagined as a single-porosity system. This was confirmed through additional simulation efforts (Figure S-1, SP1 sim).

Appendix P investigated the conventional single-rate diffusion model using both homogeneous and heterogeneous transmissivity fields. The results presented differ slightly in their estimated values for dispersivity and ½ MBL. The criterion for accepting or rejecting a model calibration in Appendix P is based on the visual fit in linear space between the model and the observed data. The criterion for accepting or rejecting a model calibration in this appendix is based on the lowest RMSE between the log of the observed data and the log of the predicted concentrations. The difference in fitting criteria is most likely the cause of the difference between the estimated values in the single-rate diffusion simulations.

In general, when comparing the results presented in Appendix P to the multirate STAMMT-R results, the H-19 multirate STAMMT-R simulations obtained lower advective porosities and ½ MBLs than SWIFT II and THEMM. The dispersivity values for STAMMT-R multirate simulations are lower to approximately equal to those reported in Appendix P. For the H-11 hydropad, the multirate STAMMT-R simulations obtained larger advective porosities and dispersivities and lower ½ MBLs.

When comparing the single-rate STAMMT-R results with those in Appendix P, the differences are more varied. For the H-19 hydropad, the single-rate STAMMT-R simulations obtained advective porosities and ½ MBLs that are both higher and lower than those found with SWIFT II and THEMM. The dispersivity values are typically larger for STAMMT-R. For the H-11 hydropad, the single-rate STAMMT-R simulations yielded advective porosities and dispersivities that are larger than those reported in Appendix P, while the ½ MBLs are lower.

S.7 Summary and Conclusions

The observed tracer-breakthrough curves from multiwell tracer tests conducted at the H-3, H-6, H-11, and H-19 hydropads at the WIPP site were interpreted using both single-rate and multirate-diffusion models. Calibration to the observed data adjusted three or four parameters for the single-rate or multirate models, respectively. The multirate model estimated the following values during calibration: (1) the geometric mean *ln* diffusion-rate coefficient, μ_d; (2) the standard deviation of the *ln* diffusion-rate coefficient distribution, σ_d; (3) the advective porosity, ϕ_a; and (4) the longitudinal dispersivity, α_L. The calibration of the single-rate model is identical to that of the multirate model, except σ_d is fixed at zero. The measure of how well a simulation matches the observed data is through the RMSE between the log of the observed data and the log of the predicted concentrations.

For most of the tracer tests investigated above, the multirate-diffusion simulations are better at matching the tracer-breakthrough curves than the single-rate simulations. Even when σ_d values are small, the multirate model estimates higher mean diffusion-rate coefficients than the single-rate model, except for the pathway from H-19b3 to H-19b0. In most cases, the multirate model obtained values for ½ MBL, advective porosity, and dispersivity that are smaller than those obtained from the single-rate model.

The estimated diffusion-rate distributions are widest for the pathways at the H-19 hydropad (except for H-19b5 to H-19b0). The distributions are narrower for pathways at the H-3 and H-11 hydropads, and still narrower for the pathways at the H-6 hydropad. We suspect that as the distributions widen, advective transport shifts from being concentrated in a few fractures to occurring through more fractures and interparticle porosity and vugs.

Unique parameter sets were defined using the multirate model for three pathways that could predict the results of multiple tests along those pathways. The tests involved different pumping rates and/or tracers with different aqueous diffusion coefficients. No unique parameter sets could be found using the single-rate model that could predict different tracer-breakthrough curves along the same pathways.

Table S-6 Calculated Range and Mean Matrix-Block Half-Length (½ MBL) for the Multirate Model

Hydropad & Injection Well	Multirate Figure Number and Simulation Name	½ MBL (m) @ DaI = 0.01	½ MBL (m)	DaI calculated for ½ MBL	½ MBL (m) @ DaI = 100	Comments
H-19 Hydropad; Round 1						
H-19b2	S-1; MR1	0.0555	0.0339	0.0279	0.0004	
H-19b3	S-2; MR1	0.0180	0.0047	0.2143	0.0002	Inj. Conc. = 100%
H-19b3	S-2; MR2	0.0196	0.0055	0.1909	0.0002	Inj. Conc. = 85%
H-19b3; iodide	S-3; MR1	0.0246	0.0088	0.1410	0.0001	Inj. Conc. = 100%
H-19b3; iodide	S-3; MR2	0.0250	0.0085	0.1530	0.0001	Inj. Conc. = 85%
H-19b4	S-6; MR1	0.0323	0.0061	0.5449	0.0003	
H-19b5	S-7; MR1	N/A	0.0027	2.8476	0.0005	
H-19b6	S-9; MR1	0.0418	0.0471	0.0078	0.0002	
H-19b7	S-11; MR1	0.0239	0.0152	0.0267	0.0001	
H-19 Hydropad; Round 2						
H-19b3	S-4; MR1	0.0191	0.0057	0.1410	0.0003	
H19b5	S-8; MR1	N/A	0.0051	4.1864	0.0007	
H-19b7	S-12; MR1	0.0230	0.0262	0.0076	0.0004	
H-19 Hydropad; Round 3						
H-19b3	S-5; MR1	0.0270	0.0054	0.3616	0.0003	
H-19b6	S-10; MR1	0.0495	0.0463	0.0115	0.0002	
H-19b7	S-13; MR1	0.0356	0.0247	0.0215	0.0003	
H-19b7; iodide	S-14; MR1	0.0485	0.0320	0.0241	0.0003	
H-11 Hydropad; Round 1						
H-11b2	S-16; MR 1	0.0681	0.0175	0.2297	0.0007	Fixed Dispersivity
H-11b2	S-16; MR2	0.0856	0.0121	0.5715	0.0012	4 Parameter Estimation
H-11b3	S-19; MR1	0.0594	0.0648	0.0078	N/A	
H-11 Hydropad; Round 2						
H-11b2	S-17; MR1	0.0501	0.0161	0.1338	0.0005	Fixed Dispersivity
H-11b2	S-17; MR2	0.0280	0.0090	0.1622	N/A	4 Parameter Estimation
H-11b3	S-20; MR1	0.0460	0.0512	0.0071	N/A	
H-11b3; iodide	S-21; MR1	0.0623	0.0621	0.0101	N/A	
H-11 Hydropad; 1988 Test						
H-11b2	S-15; MR1	N/A	0.0199	0.1317	0.0007	Fixed Dispersivity
H-11b2	S-15; MR2	0.09034	0.02712	0.1278	N/A	4 Parameter Estimation
H-11b3	S-18; MR1	0.0344	0.0322	0.0136	N/A	
H-3 Hydropad						
H-3b1	S-22; MR1	0.1211	0.1688	0.0044	0.0005	
H-6 Hydropad						
H-6a; test 1	S-23; MR1	N/A	0.0034	6.6853	0.0009	4 Parameter Estimation
H-6a; test 1	S-23; MR2	N/A	0.0051	4.490	0.0007	Low Dispersivity
H-6b; test 1	S-24; MR1	N/A	0.0523	0.0217	N/A	
H-6b; test 2	S-25; MR1	N/A	0.0546	0.0517	N/A	

Table S-7 Calculated Matrix-Block Half-Length (½ MBL) for the Single-Rate Model

Hydropad & Injection Well	Single-Rate Figure Number and Simulation Name	½ MBL (m)	Dal Calculated for ½ MBL	Comments
H-19 Hydropad; Round 1				
H-19b2	S-1; SR1	0.9029	0.0005	
H-19b2	S-1; SP1	0.0000	0.0000	Single Porosity
H-19b3	S-2; SR1	0.0023	7.7915	Inj. Conc. = 85%
H-19b3; iodide	S-3; SR1	0.0083	1.4684	Inj. Conc. = 85%
H-19b4	S-6; SR1	0.0073	4.0544	
H-19b5	S-7; SR1	0.0066	2.7458	
H-19b6	S-9; SR1	0.2060	0.0050	
H-19b7	S-11; SR1	0.3718	0.0006	
H-19 Hydropad; Round 2				
H-19b3	S-4; SR1	0.0028	5.8467	
H19b5	S-8; SR1	0.0092	1.7769	
H-19b7	S-12; SR1	0.3271	0.0008	
H-19 Hydropad; Round 3				
H-19b3	S-5; SR1	0.0025	13.1282	
H-19b6	S-10; SR1	0.1308	0.0175	
H-19b7	S-13; SR1	0.4650	0.0007	
H-19b7; iodide	S-14; SR1	0.1499	0.0145	
H-11 Hydropad; Round 1				
H-11b2	S-16; SR1	0.0386	0.2939	
H-11b3	S-19; SR1	0.1502	0.0169	
H-11 Hydropad; Round 2				
H-11b2	S-17; SR1	0.0327	0.2191	
H-11b3	S-20; SR1	0.1255	0.0149	
H-11b3; iodide	S-21; SR1	0.1519	0.0223	
H-11 Hydropad; 1988 Test				
H-11b2	S-15; SR1	0.0403	0.1609	
H-11b3	S-18; SR1	0.0831	0.0303	
H-3 Hydropad				
H-3b1	S-22; SR1	0.4230	0.0064	
H-6 Hydropad				
H-6a; test 1	S-23; SR1	0.0135	1.2116	
H-6b; test 1	S-24; SR1	0.1704	0.0054	
H-6b; test 2	S-25; SR1	0.1729	0.0063	

The lack of extended tail portions of the tracer-breakthrough curves for some of the MWCF tests may contribute to the close equivalence of some of the single-rate and multirate simulations. As discussed in Chapter 6, the estimation of the range (distribution) of the diffusion coefficients is particularly sensitive to the tail of the breakthrough curve where the effects of matrix diffusion are dominant over the dispersion of the system. The results presented above indicate that the presence of multirate diffusion is best determined by the SWIW tracer tests. The signature of multirate diffusion is more easily evaluated with the SWIW test because the effects of flow-field heterogeneity are mitigated in the design of the test. More investigation is warranted to determine whether the close equivalence of the single-rate and multirate models in simulating some of the MWCF tests is a function of a short tail of the tracer-breakthrough curves or of the larger volume of aquifer interrogated by the MWCF tests compared to the SWIW tests.

To evaluate the data fully and to differentiate more definitively between the single-rate and multirate models, additional simulation work is advised. This should most likely include the evaluation of coupled effects of flow-field heterogeneity and multirate mass transfer. (See Haggerty et al. (in review) for a preliminary evaluation of the effects of heterogeneity.) In addition, evaluation of whether different statistical distributions of diffusion-rate coefficients may provide a better explanation of more data sets or improve the fits to some data sets may be warranted. (See Haggerty et al. (in press) for additional insights into statistical distributions of rate coefficients.)

S.8 References

Beauheim, R.L. 1987. *Interpretations of Single-Well Hydraulic Tests Conducted At and Near the Waste Isolation Pilot Plant (WIPP) Site, 1983-1987.* SAND87-0039. Albuquerque, NM: Sandia National Laboratories.

Guvanasen, V., and V.M. Guvanasen. 1987. "An Approximate Semianalytical Solution for Tracer Injection Tests in a Confined Aquifer with a Radially Converging Flow Field and Finite Volume of Tracer and Chase Fluid," *Water Resources Research.* Vol. 23, no. 8, 1607-1619.

Haggerty, R., S.W. Fleming, L.C. Meigs, and S.A. McKenna. In review. "Tracer Tests in a Fractured Dolomite. 2. Analysis of Mass Transfer in Single-Well Injection-Withdrawal Tests," resubmitted to *Water Resources Research,* 3/00. SAND98-2573J. (Copy on file in the Sandia WIPP Central Files (SWCF) as ERMS #502440)

Haggerty, R, S.A. McKenna, and L.C. Meigs. In press. "On the Late-Time Behavior of Tracer Test Breakthrough Curves," Accepted by *Water Resources Research,* 7/00. SAND99-3120J. (Copy on file in the SWCF as ERMS #508873)

Haggerty R., S.W. Fleming, and S.A. McKenna. 2000. *STAMMT-R, Solute Transport and Multirate Mass Transfer in Radial Coordinates.* Version 1.01. SAND99-0164. Albuquerque, NM: Sandia National Laboratories.

Jones, T.L., V.A. Kelley, J.F. Pickens, D.T. Upton, R.L. Beauheim, and P.B. Davies. 1992. *Integration of Interpretation Results of Tracer Tests Performed in the Culebra Dolomite at the Waste Isolation Pilot Plant Site.* SAND92-1579. Albuquerque, NM: Sandia National Laboratories.

This page intentionally left blank.

WASTE ISOLATION PILOT PLANT (WIPP)
UC721 – Distribution List

Federal Agencies

US Department of Energy (4)
Office of Civilian Radioactive Waste Mgmt.
Attn: Deputy Director, RW-2
Acting Director, RW-10
Office of Human Resources & Admin.
Director, RW-30
Office of Program Mgmt. & Integ.
Director, RW-40
Office of Waste Accept., Stor., & Tran.
Forrestal Building
Washington, DC 20585

Yucca Mountain Site Characterization Office
Director, RW-3
Office of Quality Assurance
Attn: Project Director
P. O. Box 30307
Las Vegas, NV 89036-0307

US Department of Energy
Research & Waste Management Division
Attn: Director
P.O. Box E
Oak Ridge, TN 37831

US Department of Energy (6)
Carlsbad Area Office
Attn: I. Triay
G. T. Basabilvazo
D. Galbraith
M. McFadden
R. A. Nelson
D. Mercer
Mailroom
P.O. Box 3090
Carlsbad, NM 88221-3090

US Department of Energy
Office of Environmental Restoration and
Waste Management
Attn: M. Frei, EM-30
Forrestal Building
Washington, DC 20585-0002

US Department of Energy (3)
Office of Environmental Restoration and
Waste Management
Attn: J. Juri, EM-34, Trevion II
Washington, DC 20585-0002

US Department of Energy
Office of Environmental Restoration and
Waste Management
Attn: S. Schneider, EM-342, Trevion II
Washington, DC 20585-0002

US Department of Energy (2)
Office of Environment, Safety & Health
Attn: C. Borgstrom, EH-25
R. Pelletier, EH-231
Washington, DC 20585

US Department of Energy (2)
Idaho Operations Office
Fuel Processing & Waste Mgmt. Division
785 DOE Place
Idaho Falls, ID 83402

US Environmental Protection Agency (2)
Radiation Protection Programs
Attn: M. Oge
ANR-460
Washington, DC 20460

Boards

Defense Nuclear Facilities Safety Board
Attn: D. Winters
625 Indiana Ave. NW, Suite 700
Washington, DC 20004

Nuclear Waste Technical Review Board (2)
Attn: Chairman
J. L. Cohon
2300 Clarendon Blvd. Ste 1300
Arlington, VA 22201-3367

State Agencies

Attorney General of New Mexico
P.O. Drawer 1508
Santa Fe, NM 87504-1508

Environmental Evaluation Group (3)
Attn: Library
7007 Wyoming NE
Suite F-2
Albuquerque, NM 87109

NM Environment Department (3)
Secretary of the Environment
1190 St. Francis Drive
Santa Fe, NM 87503-0968

NM Bureau of Mines & Mineral Resources
Socorro, NM 87801

Laboratories/Corporations

Battelle Pacific Northwest Laboratories
Battelle Blvd.
Richland, WA 99352

Los Alamos National Laboratory (2)
Attn: B. Erdal, INC-12
P. Reimus, (J534)
P.O. Box 1663
Los Alamos, NM 87545

Golder Associates
Attn: T. W. Doe
4104 148th Avenue NE
Redmond, WA 98052

Westinghouse Electric Corporation (5)
Attn: Library
J. Epstein
J. Lee
R. Kehrman
P.O. Box 2078
Carlsbad, NM 88221

S. Cohen & Associates
Attn: Bill Thurber
1355 Beverly Road
McLean, VA 22101

Stormwater Management
Attn: J. Ogintz
2035 NE Columbia Boulevard
Portland, OR 97211

E.O. Lawrence Berkeley National Laboratory
Attn: Y. W. Tsang
Earth Sciences Division
1 Cyclotron Road
Berkeley, CA 94720

Tech Reps, Inc. (3)
Attn: J. Chapman (1)
Loretta Robledo (2)
5000 Marble NE, Suite 222
Albuquerque, NM 87110

Duke Engineering & Services, Inc. (5)
Attn: T. F. Jones (3)
V. A. Kelley
G. J. Saulnier, Jr.
9111 Research Boulevard
Austin, TX 78758

Waterstone Environmental Hydrology and Engineering, Inc.
Attn: S. W. Fleming
1650 38th St., Suite 201E
Boulder, CO 80301

National Academy of Sciences WIPP Panel

Tom Kiess (15)
Staff Study Director
GF456
2101 Constitution Ave.
Washington, DC 20418

Universities

University of Arizona
Department of Hydrology and Water Resources
Attn: S. P. Neuman
Tucson, AZ 85721

University of Nevada-Las Vegas (4)
Harry Reid Center for Environmental Studies
Attn: I. M. Farnham (3)
K.J. Stetzenbach (1)
4505 Maryland Parkway
Las Vegas, NV 89154-4009

University of New Mexico
Geology Department
Attn: Library
141 Northrop Hall
Albuquerque, NM 87131

University of Washington
College of Ocean & Fishery Sciences
Attn: G. R. Heath
583 Henderson Hall, HN-15
Seattle, WA 98195

University of Wisconsin-Madison (3)
Department of Geology and Geophysics
Attn: M. P. Anderson
H. F. Wang
J. M. Bahr
1215 W. Dayton St.
Madison, WI 53706-1692

Harvard University
Environmental Sciences and Engineering
Attn: W. Yu
Pierce Hall 120
29 Oxford Street
Cambridge, MA 02138

Massachusetts Institute of Technology
Ralph M. Parsons Laboratory
Attn: C. Harvey
Cambridge, MA 02139

New Mexico Institute of Mining and Technology (2)
Department of Geoscience
Attn: J. Wilson
R. Bowman
Socorro, NM 87801

Oregon State University
Department of Geosciences
Attn: R. Haggerty
104 Wilkinson Hall
Corvallis, OR 97331-5506

Libraries

Thomas Brannigan Library
Attn: D. Dresp
106 W. Hadley St.
Las Cruces, NM 88001

Government Publications Department
Zimmerman Library
University of New Mexico
Albuquerque, NM 87131

New Mexico Junior College
Pannell Library
Attn: R. Hill
Lovington Highway
Hobbs, NM 88240

New Mexico State Library
Attn: N. McCallan
325 Don Gaspar
Santa Fe, NM 87503

New Mexico Tech
Martin Speere Memorial Library
Campus Street
Socorro, NM 87810

WIPP Information Center
Attn: J. Mireles
4021 National Parks Highway
Carlsbad, NM 88220

Foreign Addresses

SCK/CEN
Attn: G. Volckaert
Boeretang 200
B-2400 Mol
BELGIUM

Atomic Energy of Canada, Ltd. (2)
Whiteshell Laboratories
Attn: B. Goodwin
C. C. Davison
Pinawa, Manitoba, R0E 1L0
CANADA

Environment Canada
National Water Research Institute
Canada Centre for Inland Waters
Attn: K. S. Novakowski
867 Lakeshore Road
P.O. Box 5050
Burlington, Ontario, L7R 4A6
CANADA

Posiva Oy
Attn: A. Hautojarvi
Mikonkatu 15A
00100 Helsinki
FINLAND

ANDRA (2)
Attn: Francois Chenevier
S. Altman
Parc de la Croix Blanche
1-7 rue Jean Monnet
92298 Chatenay-Malabry Cedex
FRANCE

Centre d'Etudes Nucleaires de la Vallee Rhone
CEN/VALRHO
Attn: Claude Sombret
S.D.H.A. B.P. 171
30205 Bagnols-Sur-Ceze
FRANCE

Commissariat a L'Energie Atomique
Attn: D. Alexandre
Centre d'Etudes de Cadarache
13108 Saint Paul Lez Durance Cedex
FRANCE

Universite Pierre et Marie Curie
Laboratoire de Geologie Appliquee
Attn: G. de Marsily
B 123
4, place Jussieu
F-25252 Paris Cedex 05
FRANCE

Bundesanstalt fur Geowissenschaften und Rohstoffe (2)
Attn: M. Langer
K. Schelkes
Postfach 510 153
D-30631 Hannover
GERMANY

Bundesministerium fur Forschung und Technologie
Postfach 200 706
5300 Bonn 2
GERMANY

Gesellschaft fur Anlagen und Reaktorsicherheit (GRS)
Attn: B. Baltes
Schwertnergasse 1
D-50667 Cologne
GERMANY

Dr.-Ing. Klaus Kuhn
TU Clausthal Institut fur Bergbau
Erzstr. 20
D-38678 Clausthal-Zellerfeld
GERMANY

Shingo Tashiro
Japan Atomic Energy Research Institute
Tokai-Mura, Ibaraki-Ken, 319-11
JAPAN

PNC
Geological Isolation Technology Section
Waste Technology Development Division
Attn: Masahiro Uchida
Tokai Words
Muramatsu, Tokai-Mura
Ibaraki, 319-11
JAPAN

Netherlands Energy Research Foundation ECN
Attn: J. Prij
3 Westerduinweg
P.O. Box 1
1755 ZG Petten
THE NETHERLANDS

Universidad Politechnica de Catalunya
ETSI Caminos
Attn: J. Carrera
Jordi Girona, 1-3
E-08034 Barcelona
SPAIN

Svensk Karnbransleforsorjning AB
Attn: F. Karlsson
Project KBS (Karnbranslesakerhet)
Box 5864
S-102 48 Stockholm
SWEDEN

Royal Institute of Technology
Department of Chemical Engineering
Attn: I. Neretnieks
S-100 44 Stockholm
SWEDEN

GeoSigma AB
Attn: P. Andersson
Box 894
S-751 08 Uppsala
SWEDEN

Conterra AB
Attn: A. Winberg
Ogardesvagen 4
S-433 30 Partille
SWEDEN

SKB
Attn: J.-O. Selroos
Box 5864
S-102 40 Stockholm
SWEDEN

Nationale Genossenschaft fur die Lagerung
Radioaktiver Abfalle (2)
Attn: S. Vomvoris
P. Zuidema
Hardstrasse 73
CH-5430 Wettingen
SWITZERLAND

Paul Scherrer Institute (2)
Attn: W. Heer
A. Jakob
PSI
5232 Villigen
SWITZERLAND

AEA Technology
Attn: J. H. Rees
D5W/29 Culham Laboratory
Abington, Oxfordshire OX14 3DB
UNITED KINGDOM

AEA Technology
Attn: W. R. Rodwell
044/A31 Winfrith Technical Centre
Dorchester, Dorset DT2 8DH
UNITED KINGDOM

AEA Technology
Attn: J. E. Tinson
B4244 Harwell Laboratory
Didcot, Oxfordshire OX11 ORA
UNITED KINGDOM

Internal

MS	Org.	
0771	6800	M. S. Y. Chu
1395	6810	P. E. Shoemaker
1395	6821	M. G. Marietta
1395	6822	M. K. Knowles
1395	6822	R. L. Beauheim (7)
1395	6822	R. M. Roberts
1395	6822	C. R. Bryan
1395	6821	P. Vaughn
0779	6849	D. R. Anderson
0701	6100	P. B. Davies
0735	6115	E. K. Webb
0779	6849	A.R. Lappin
0735	6115	L. C. Meigs (30)
0735	6115	S. J. Altman
0735	6115	S. A. McKenna
0735	6115	M. J. Kelley
0735	6115	T.F. Corbet
0735	6115	V.C. Tidwell
0735	6115	R.J. Holt
0731	6805	J. T. Schneider (2)
0731	6805	NWM Library (20)
9018	8940-2	Central Technical Files
0899	9616	Technical Library (2)
0612	9612	Review and Approval Desk, For DOE/OSTI